frontiers | Research Topics

Insights in viral immunology 2021

Edited by
Alexis M. Kalergis and Shen-Ying Zhang

Published in
Frontiers in Immunology

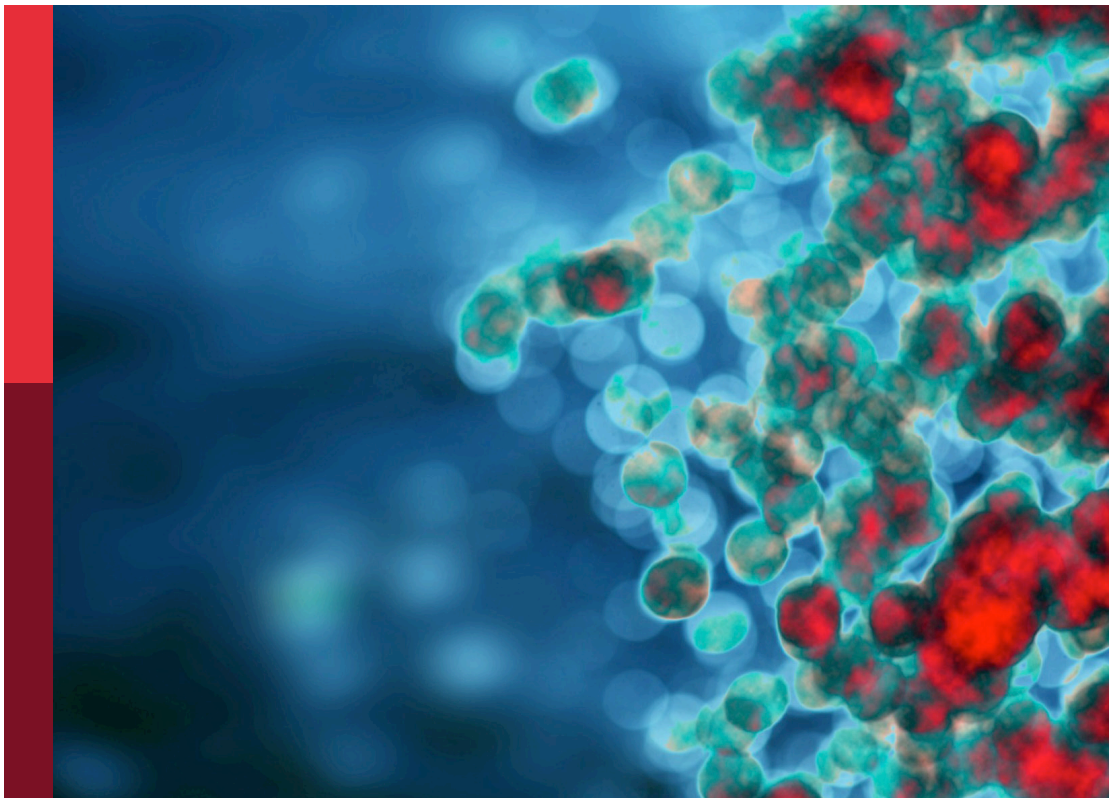

ISSN 1664-8714
ISBN 978-2-8325-2447-3
DOI 10.3389/978-2-8325-2447-3

About Frontiers

Frontiers is more than just an open access publisher of scholarly articles: it is a pioneering approach to the world of academia, radically improving the way scholarly research is managed. The grand vision of Frontiers is a world where all people have an equal opportunity to seek, share and generate knowledge. Frontiers provides immediate and permanent online open access to all its publications, but this alone is not enough to realize our grand goals.

Frontiers journal series

The Frontiers journal series is a multi-tier and interdisciplinary set of open-access, online journals, promising a paradigm shift from the current review, selection and dissemination processes in academic publishing. All Frontiers journals are driven by researchers for researchers; therefore, they constitute a service to the scholarly community. At the same time, the *Frontiers journal series* operates on a revolutionary invention, the tiered publishing system, initially addressing specific communities of scholars, and gradually climbing up to broader public understanding, thus serving the interests of the lay society, too.

Dedication to quality

Each Frontiers article is a landmark of the highest quality, thanks to genuinely collaborative interactions between authors and review editors, who include some of the world's best academicians. Research must be certified by peers before entering a stream of knowledge that may eventually reach the public - and shape society; therefore, Frontiers only applies the most rigorous and unbiased reviews. Frontiers revolutionizes research publishing by freely delivering the most outstanding research, evaluated with no bias from both the academic and social point of view. By applying the most advanced information technologies, Frontiers is catapulting scholarly publishing into a new generation.

What are Frontiers Research Topics?

Frontiers Research Topics are very popular trademarks of the *Frontiers journals series*: they are collections of at least ten articles, all centered on a particular subject. With their unique mix of varied contributions from Original Research to Review Articles, Frontiers Research Topics unify the most influential researchers, the latest key findings and historical advances in a hot research area.

Find out more on how to host your own Frontiers Research Topic or contribute to one as an author by contacting the Frontiers editorial office: frontiersin.org/about/contact

Insights in viral immunology: 2021

Topic editors

Alexis M. Kalergis — Pontificia Universidad Católica de Chile, Chile

Shen-Ying Zhang — The Rockefeller University, United States

Citation

Kalergis, A. M., Zhang, S.-Y., eds. (2023). *Insights in viral immunology: 2021*. Lausanne: Frontiers Media SA. doi: 10.3389/978-2-8325-2447-3

Table of contents

frontiers in Immunology

ORIGINAL RESEARCH
published: 11 March 2022
doi: 10.3389/fimmu.2022.820250

Natural SARS-CoV-2 Infection Affects Neutralizing Activity in Saliva of Vaccinees

*Micaela Garziano[1,2], Olga Utyro[1], Mariacristina Poliseno[3], Teresa Antonia Santantonio[3], Irma Saulle[1,2], Sergio Strizzi[1], Sergio Lo Caputo[3], Mario Clerici[2,4], Andrea Introini[1,5] and Mara Biasin[1]**

[1] Laboratory of Immunobiology, Department of Biomedical and Clinical Sciences L. Sacco, University of Milan, Milan, Italy, [2] Laboratory of Immunology, Department of Pathophysiology and Transplantation, University of Milan, Milan, Italy, [3] Unit of Infectious Diseases, Department of Clinical and Experimental Medicine, University of Foggia, Foggia, Italy, [4] Don C. Gnocchi Foundation, Istituto di Ricovero e Cura a Carattere Scientifico (IRCCS) Foundation, Milan, Italy, [5] Center for Molecular Medicine, Department of Medicine Solna, Division of Infectious Diseases, Karolinska University Hospital, Karolinska Institutet, Solna, Sweden

OPEN ACCESS

Edited by:
Shen-Ying Zhang,
The Rockefeller University,
United States

Reviewed by:
Simone Gonçalves Fonseca,
Universidade Federal de Goiás, Brazil
Anastasia N. Vlasova,
The Ohio State University,
United States

***Correspondence:**
Mara Biasin
mara.biasin@unimi.it

Specialty section:
This article was submitted to Viral Immunology, a section of the journal Frontiers in Immunology

Received: 22 November 2021
Accepted: 14 February 2022
Published: 11 March 2022

Citation:
Garziano M, Utyro O, Poliseno M, Santantonio TA, Saulle I, Strizzi S, Lo Caputo S, Clerici M, Introini A and Biasin M (2022) Natural SARS-CoV-2 Infection Affects Neutralizing Activity in Saliva of Vaccinees. Front. Immunol. 13:820250. doi: 10.3389/fimmu.2022.820250

Background: SARS-CoV-2 transmission mainly occurs through exposure of the upper airway mucosa to infected secretions such as saliva, which are excreted by an infected person. Thus, oral mucosal immunity plays a central role in the prevention of and early defense against SARS-CoV-2 infection. Although virus-specific antibody response has been extensively investigated in blood samples of SARS-CoV-2-infected patients and vaccinees, local humoral immunity in the oral cavity and its relationship to systemic antibody levels needs to be further addressed.

Material and Methods: We fine-tuned a virus neutralization assay (vNTA) to measure the neutralizing activity (NA) of plasma and saliva samples from 20 SARS-CoV-2-infected (SI), 40 SARS-CoV-2-vaccinated (SV), and 28 SARS-CoV-2-vaccinated subjects with a history of infection (SIV) using the "wild type" SARS-CoV-2 lineage B.1 (EU) and the Delta (B.1.617.2) strains. To validate the vNTA results, the presence of neutralizing antibodies (NAbs) to the spike receptor binding domain (RBD) was evaluated with an ELISA assay.

Results: NA to SARS-CoV-2 lineage B.1 (EU) was present in plasma samples from all the tested subjects, with higher titers in SIV compared to both SI and SV. Conversely, NA was detected in saliva samples from 10.3% SV, 45% SI, and 92.6% SIV, with significantly lower titers in SV compared to both SI and SIV. The detection of NAbs in saliva reflected its reduced NA in SV.

Discussion: The difference in NA of plasma vs. saliva was confirmed in a vNTA where the SARS-CoV-2 B.1 and Delta strains were tested head-to-head, which also revealed a reduced NA of both specimens compared to the B.1 variant.

Conclusions: The administration of SARS-CoV-2 vaccines was associated with limited virus NA in the oral cavity, as measured in saliva and in comparison to plasma. This difference was more evident in vaccinees without a history of SARS-CoV-2 infection,

possibly highlighting the importance of local exposure at the site of virus acquisition to effectively prevent the infection and block its spread. Nevertheless, the presence of immune escape mutations as possibly represented by the SARS-CoV-2 Delta variant negatively affects both local and systemic efficacy of NA associated with vaccination.

Keywords: SARS-CoV-2, saliva, neutralizing activity, antibodies, variants

INTRODUCTION

Severe Acute Respiratory Syndrome Coronavirus 2 (SARS-CoV-2), the etiological agent of Coronavirus Disease 2019 (COVID-19) pandemic, has affected more than 250 million people, causing approximately 5 million deaths in the global population as reported by the World Health Organization (WHO, November 2021). At present, the acquisition of immunity by anti-SARS-CoV-2 vaccines represents the most promising chance to contain the COVID-19 pandemic.

The virus uses the receptor binding domain (RBD), within the spike protein, to bind the angiotensin-converting enzyme 2 (ACE2) on the surface of epithelial cells in the upper respiratory tract (1). Viral transmission may occur by asymptomatic, pre-symptomatic, and symptomatic individuals through close exposure to infected secretions such as saliva, respiratory secretions, or respiratory droplets (2, 3). Thus, SARS-CoV-2 infection mainly affects the cells of the superior airways, and the nasopharyngeal swab is the specimen of choice for diagnosis of infection. However, the virus is also able to infect and replicate in the salivary glands, which is why saliva represents a safe and non-invasive sample to detect both viral RNA and SARS-CoV-2-specific antibodies (4–7). Oral tissues, encompassing salivary glands and mucosa, may play a double function: on one side, they are sites of early infection, playing a critical role in viral spreading to the lungs or the gastrointestinal tract *via* saliva (8); at the same time, they represent the first line of defense against a plethora of pathogens as already demonstrated for other microbial-associated diseases, including pneumonia (9) and inflammatory bowel diseases (10).

The mechanisms responsible for the immunological surveillance and tolerance at this site, safeguarding tissue homeostasis, include a complex network orchestrated by dendritic cells (DCs) that process and present specific antigens to resident T cells, which in turn activate B cells producing SARS-CoV-2-specific IgA (30%) and IgG (70%) (11). The induction of a microbe-specific mucosal immunity represents an unequivocal sign of an active infection (12, 13), but whether the intramuscular administration of a vaccine is capable of triggering mucosal immunity is still a matter of debate. For example, in mice, parenteral administration of the influenza vaccine has been shown to fail to induce an effective mucosal immune response (14).

Since the beginning of SARS-CoV-2 vaccination campaign, a large part of the population has already been immunized worldwide, and the presence of neutralizing antibodies (NAbs) in the serum of vaccinated subjects has been assessed. Conversely, the neutralizing response in oral mucosa needs to be further investigated. Given the preponderance of these routes in establishing new infections, we optimized the gold standard virus neutralization assay (vNTA), requiring live pathogen and largely employed to test plasma samples (5–7, 15–17) to detect the presence of neutralizing activity (NA) in saliva samples from infected and/or vaccinated subjects.

Abbreviations: SI, SARS-CoV-2 infected; SV, SARS-CoV-2 vaccinated; SIV, SARS-CoV-2 infected and vaccinated; vNAT, virus neutralization assay.

METHODS

Study Design

An observational study was designed to evaluate the development of humoral immunity in SARS-CoV-2-infected (SI), SARS-CoV-2-vaccinated (SV), and SARS-CoV-2-infected and -vaccinated (SIV) subjects induced by BNT162b2 (Comirnaty) or AZD1222 anti-SARS-CoV-2 vaccines. The primary end point of the study was to optimize a vNTA in order to compare samples representative of the systemic and local response in the oral cavity to SARS-CoV-2, i.e., plasma and saliva, of the same individual, as well as between SV and SIV within each of two compartments. Secondary end points were (i) validation of the vNTA as a surrogate of the presence of SARS-CoV-2-specific NAbs in saliva, and (ii) application of the vNTA to evaluate virus NA of saliva against the currently main variant of concern, Delta. The study design is summarized in **Figure 1**.

Virus and Cell Lines

SARS-CoV-2 variants, including the lineage B.1 (EU) (accession number: EPI_ISL_412973), assumed as comparator virus, and the Delta (lineage B.1.617.2) (accession number: EPI_ISL_1970729) were isolated from positive nasopharyngeal swabs (NPS). All the strains were identified by means of whole genome sequencing and the sequences were submitted to GISAID. The virus was propagated in VeroE6 cells (ATCC® VERO C1008, CRL-1586™) and viral titers were determined by Median Tissue Culture Infectious Dose ($TCID_{50}$) endpoint dilution assay. Briefly, serial 10-fold dilutions of viral suspension, from 10^6 to 10^{-4} $TCDI_{50}$/ml (50 µl), were plated onto 96-well plates, incubated at 37°C in 5% CO_2 and checked daily to monitor the virus-induced cytopathic effect (CPE) by Optical microscope observation (ZOE™ Fluorescent Cell Imager, Bio-Rad, Hercules, CA, USA). Seventy-two hours post infection (hpi) viral titer was determined by crystal violet dyeing method, as previously described (18). All the experiments with SARS-CoV-2 virus were performed in a BSL3 facility.

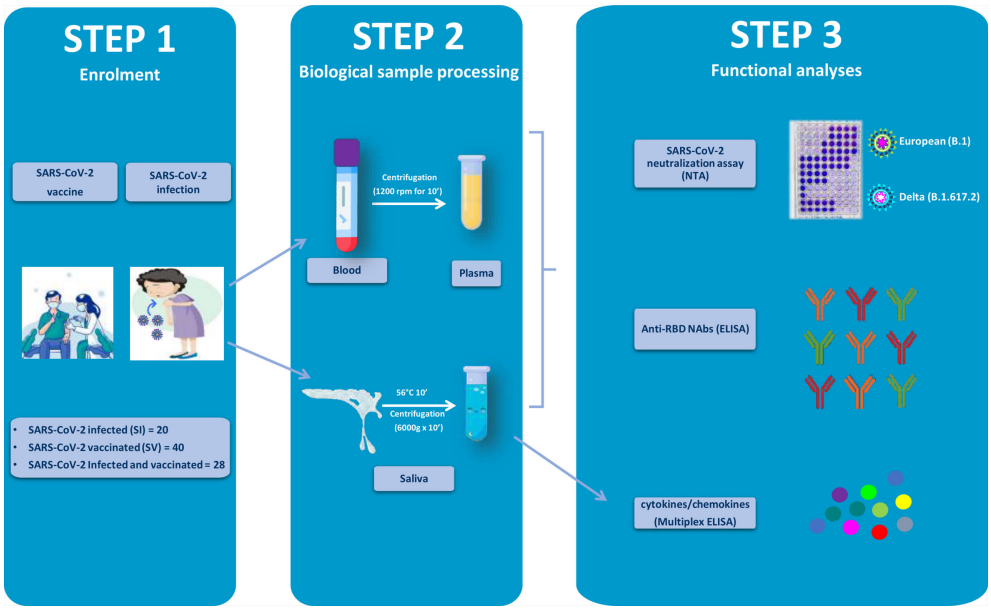

FIGURE 1 | Graphical representation of the study workflow. SARS-CoV-2-infected (SI), vaccinated (SV), and infected–vaccinated (SIV) subjects were enrolled in the study (Step 1). Blood and saliva samples were collected and processed (Step 2) so as to be analyzed for neutralizing activity (NA) by SARS-CoV-2 neutralization assay (NTA), neutralizing antibodies (Nabs) by enzyme-linked immunosorbent assay (ELISA), as well as cytokine production (Multiplex ELISA).

Study Population and Sample Collection

Plasma and saliva samples were obtained from 20 SARS-CoV-2 SI [mean age (years) ± DS: 29.4 ± 20.5; range: 18–83; female: 60%], 40 SARS-CoV-2 SV [mean age (years) ± SD: 34.1 ± 11.5; range: 18–62; female: 67.5%], and 28 SARS-CoV-2 SIV [mean age (years) ± SD: 41.36 ± 19.19; range: 18–61; female: 57.14%], enrolled at Infectious Diseases Unit, Policlinic "Riuniti" of Foggia (Italy). SARS-CoV-2 infection was determined by SARS-CoV-2 molecular test of nasopharyngeal swabs. All the SARS-CoV-2-infected recovered patients were asymptomatic or pauci-symptomatic. The vaccinated subjects were administered either the BNT162b2 or AZD1222 vaccine (SV: 15 AZD1222 and 25 BNT162b2; SIV: 5 AZD1222 and 23 BNT162b2). All the SV and SIV subjects were administered two doses according to the specific vaccination schedules (BNT162b2: dose II administered 21 days after dose I; AZD1222: dose II administered 90 days after dose I). Subjects who were vaccinated within 6 months from SARS-CoV-2 infection recovery received just a single vaccine dose. The administered vaccine, time from infection [mean time (months) ± SE: SI = 5.7 ± 0.5; SIV = 7.9 ± 0.7], and time from vaccination [mean time (months) ± SE: SV = 3.6 ± 0.3; SIV = 3.4 ± 0.5] are reported in **Table 1**. Plasma was obtained by centrifugation of whole blood at 1,200×*g* for 10 min and storage at −20°C until use. Plasma samples were analyzed using iFlash SARS-CoV-2 IgG and IgM (C86095G–C86095M–Shenzhen YHLO Biotech Co, Shenzhen, China) to exclude a possible ongoing asymptomatic infection since the assay targets both nucleocapsid and spike proteins. Only the subjects included in the SI and SIV groups resulted to have SARS-CoV-2 N plus S antigens (**Supplementary Table 1**).

All saliva samples were collected on the same day of testing, by spitting after repeated mouth-washing with water. Saliva was incubated at 56°C for 10 min and centrifuged at 6,000×*g* for 10 min. Supernatants were used for further analyses. Participants were asked not to eat, drink, or smoke at least 30 min prior to collection.

We obtained informed written consent from all the subjects to perform the procedure and analysis, according to CARE guidelines and in compliance with the Declaration of Helsinki principles. The study was approved by the Ethics Committee of Policlinic "Riuniti" of Foggia (protocol number 49/C.E./2021).

SARS-CoV-2 Virus Neutralization Assay

At the time of use, plasma samples were thawed at room temperature and incubated at 56°C for 30 min, to inactivate the complement proteins. Neutralization activity (NA) against SARS-CoV-2 B.1 (EU) and Delta (lineage B.1.617.2) variant by vNTA was performed as follows. Briefly, 50 µl of plasma samples, starting from a 1:10 dilution followed by serial twofold series, was transferred in two wells of 96-well microtiter plates (COSTAR, Corning Incorporated, NY 14831, USA) and mixed with 50 µl of tissue culture infecting dose 50 ($TCID_{50}$) of SARS-CoV-2. All dilutions were made in DMEM with the addition of 1% L-Glutamine, 2% penicillin and streptomycin, and 2% fetal bovine serum. After 2 h of incubation at 37°C and 5% CO_2, 100 µl of the mixture of the supernatant containing the plasma and virus was transferred to microplates seeded with 2×10^4 VeroE6 cells for 72 h at 37°C and 5% CO_2.

As antibody concentration is lower in saliva samples than in plasma (19), and because of saliva's natural composition, it was necessary to set up a vNTA partially modified from the one

TABLE 1 | Cohort study features.

	Subject no.	Gender	Age (years)	PlasmaNAb titer		Saliva NAb titer		%Anti-RBD (ELISA)	Time from infection (months)	Time from vaccination (months)	Vaccine
				WT	Delta	WT	Delta				
SV	1	F	30	80	nd	–	nd	40,5	–	3	AZD1222
	2	F	27	160	nd	–	nd	33	–	3	AZD1222
	3	F	33	640	nd	–	nd	nd	–	3	AZD1222
	4	M	27	40	nd	–	nd	27	–	3	AZD1222
	5	M	24	80	nd	–	nd	nd	–	3	AZD1222
	6	F	36	160	nd	–	nd	33	–	3	AZD1222
	7	F	27	20	nd	–	nd	nd	–	6	BNT-162b2
	8	F	51	40	nd	–	nd	4,5	–	6	BNT-162b2
	9	M	57	80	nd	–	nd	nd	–	6	BNT-162b2
	10	M	39	640	nd	–	nd	18	–	3	AZD1222
	11	F	22	640	nd	–	nd	nd	–	6	BNT-162b2
	12	M	22	320	nd	–	nd	nd	–	6	BNT-162b2
	13	F	30	640	nd	–	nd	nd	–	6	BNT-162b2
	14	F	38	640	nd	–	nd	19	–	3	AZD1222
	15	M	27	640	nd	4	nd	39,5	–	3	BNT-162b2
	16	M	30	160	nd	–	nd	nd	–	3	BNT-162b2
	17	F	30	80	nd	–	nd	nd	–	3	BNT-162b2
	18	F	30	80	nd	–	nd	nd	–	3	BNT-162b2
	19	F	35	320	nd	–	nd	nd	–	6	BNT-162b2
	20	M	23	320	nd	–	nd	nd	–	6	BNT-162b2
	21	F	24	640	nd	–	nd	nd	–	6	BNT-162b2
	22	F	24	1280	nd	–	nd	nd	–	6	BNT-162b2
	23	F	24	320	nd	–	nd	nd	–	4	BNT-162b2
	24	F	18	nd	nd	–	nd	nd	–	1	BNT-162b2
	25	F	18	nd	nd	16	nd	nd	–	1	BNT-162b2
	26	F	60	640	nd	–	nd	nd	–	4	AZD1222
	27	F	40	320	nd	2	nd	40,5	–	4	BNT-162b2
	28	F	62	160	nd	–	nd	nd	–	3	AZD1222
	29	M	36	320	nd	–	nd	58	–	1	BNT-162b2
	30	M	45	2560	nd	2	nd	51	–	0.5	BNT-162b2
	31	M	38	nd	nd	–	nd	61	–	3	AZD1222
	32	F	32	nd	nd	–	nd	21,5	–	4	BNT-162b2
	33	M	37	320	320	8	2	58,5	–	0.5	BNT-162b2
	34	F	50	nd	nd	–	nd	7	–	3	BNT-162b2
	35	F	43	nd	nd	–	nd	16	–	3	AZD1222
	36	M	51	10	–	nd	nd	nd	–	4	AZD1222
	37	F	33	30	20	–	–	nd	–	4	AZD1222
	38	F	45	40	20	–	–	nd	–	4	AZD1222
	39	F	18	nd	nd	–	nd	18,5	–	3	BNT-162b2
	40	F	28	nd	nd	–	nd	27	–	4	BNT-162b2
SI	1	M	52	160	nd	–	nd	nd	6	–	–
	2	M	18	80	nd	–	nd	nd	6	–	–
	3	F	18	160	20	4	nd	nd	6	–	–
	4	F	18	320	40	4	nd	nd	6	–	–
	5	M	19	80	nd	2	nd	21,5	3	–	–
	6	F	80	1280	80	40	nd	nd	3	–	–
	7	M	83	800	400	80	nd	nd	3	–	–
	8	M	18	160	nd	–	nd	nd	6	–	–
	9	M	22	20	nd	–	nd	nd	6	–	–
	10	F	20	80	nd	–	nd	nd	6	–	–
	11	F	20	160	nd	2	nd	nd	6	–	–
	12	F	20	80	nd	–	nd	nd	6	–	–
	13	F	19	20	nd	–	nd	nd	4	–	–
	14	F	30	40	nd	–	nd	nd	7	–	–
	15	F	51	640	nd	2	nd	nd	3	–	–
	16	F	18	nd	nd	–	nd	nd	7	–	–
	17	M	30	160	nd	–	nd	nd	7	–	–
	18	M	18	nd	nd	2	nd	nd	5	–	–
	19	F	18	nd	nd	2	nd	nd	6	–	–
	20	F	18	nd	nd	–	nd	nd	>12	–	–
SIV	1	F	24	1600	nd	8	nd	nd	>12	6	BNT-162b2

(Continued)

TABLE 1 | Continued

Subject no.	Gender	Age (years)	PlasmaNAb titer		Saliva NAb titer		%Anti-RBD (ELISA)	Time from infection (months)	Time from vaccination (months)	Vaccine
			WT	Delta	WT	Delta				
2	M	40	3200	nd	8	nd	54	3	3	BNT-162b2
3	F	55	1600	nd	32	nd	nd	4	1	BNT-162b2
4	F	54	3200	160	16	8	nd	>12	6	AZD1222
5	F	61	12800	nd	32	nd	nd	>12	1	AZD1222
6	M	47	800	nd	2	nd	28,5	>12	6	AZD1222
7	F	25	12800	nd	64	nd	nd	4	2	BNT-162b2
8	F	22	3200	nd	4	nd	nd	>12	6	BNT-162b2
9	F	49	3200	800	32	2	32	>12	6	BNT-162b2
10	M	24	800	nd	–	nd	nd	7	2	BNT-162b2
11	M	18	nd	nd	32	nd	nd	5	0.5	BNT-162b2
12	F	44	6400	nd	8	nd	nd	5	3	BNT-162b2
13	M	18	nd	nd	8	nd	nd	5	1	BNT-162b2
14	F	45	3200	nd	8	nd	nd	>12	3	AZD1222
15	F	38	1600	nd	4	nd	nd	7	5	BNT-162b2
16	F	61	nd	nd	2	nd	47,5	>12	8	BNT-162b2
17	F	18	nd	nd	32	2	68	6	1	BNT-162b2
18	M	18	3200	400	8	4	79	6	3	BNT-162b2
19	M	83	nd	nd	128	32	90	3	1	BNT-162b2
20	M	52	3200	800	16	8	44	6	0.5	BNT-162b2
21	F	18	nd	nd	32	4	61	6	1	BNT-162b2
22	F	56	nd	nd	–	nd	30	10	5	BNT-162b2
23	F	80	nd	nd	128	32	88	3	6	BNT-162b2
24	F	22	nd	nd	16	nd	83	6	3	BNT-162b2
25	M	25	nd	nd	4	nd	45	6	3	BNT-162b2
26	F	55	nd	nd	4	nd	62	6	0.5	BNT-162b2
27	M	59	nd	nd	4	nd	64	6	4	BNT-162b2
28	M	47	120	60	nd	nd	nd	>12	8	AZD1222

-, undetectable.
ND, Not determined.
NAb, neutralizing antibody.
RBD, receptor binding domain.

commonly used to test plasma specimens. One-hundred microliters of saliva was seeded in a 96-well microtiter plate undiluted, and then it was diluted 1:2 in the next 6 wells. Fifty microliters of SARS-CoV-2 $TCID_{50}$ was added to each well and incubated for 2 h at 37°C at 5% CO_2. After incubation, 100 µl of the solution containing saliva and virus was transferred to microplates seeded with 2×10^4 VeroE6 cells and incubated for 72 h at 37°C and 5% CO_2.

At the end of incubation, cells were stained with 0.1% m/v crystal violet solution (Merck KGaA, 64271 Darmstadt, Germany) previously fixed with 4% formaldehyde 37% m/v (Merck KGaA, Darmstadt, Germany) for 20 min. Microtiter plates were then washed with PBS. Wells were scored to evaluate the degree of CPE compared to the virus control. Blue staining of wells indicated the presence of NA. Neutralizing titer corresponds to the maximum dilution with the reduction of 90% of CPE. A positive titer was equal to or greater than 1:10 or 1:2 for plasma and saliva samples, respectively. Every test included plasma control (1:10 dilution) or saliva control (undiluted), cell control (VeroE6 cells alone), and viral control (threefold series dilution).

Anti-RDB NAb Measurement

SARS-CoV-2 anti-RDB NAbs were measured employing a commercial ELISA kit (Viazyme, Delft, Netherlands). Analyses were performed on a subgroup of SV (n = 18) and SIV (n = 15) subjects. Saliva samples were preincubated with HRP-RBD. After 30 min, they were seeded into an ACE2-coated ELISA plate to reveal the presence of anti-RBD antibodies, according to the manufacturer's guidelines. Anti-RBD quantification [1 − (OD of sample/mean OD of negative control)] × 100% was assessed on a standard curve generated by progressive 1:10 dilutions of the positive control. According to the manufacturer instructions, results below 20% threshold were considered as negative. Undetectable samples were assigned the value 10% as the midpoint between 0 and the threshold for the purpose of statistical analysis.

Cytokine Quantification in Saliva Samples by Multiplex ELISA

The concentration of 8 cytokines/chemokines was assessed on the saliva specimens collected from a subgroup of vaccinated subjects (SV: n = 19; and SIV: n = 21) using magnetic bead-based immunoassays (Bio-Rad, CA, USA), according to the manufacturer's protocol *via* Bio-Plex 200 technology (Bio-Rad, CA, USA). Some of the targets resulted in having values above the normal range, and an arbitrary value of 10,000 pg/ml was assigned, while 0 pg/ml was assigned to values below the limit of detection.

Statistical Analyses

For the study variables, medians and ranges were reported for quantitative variables, and absolute and relative frequencies were

reported for categorical variables. The Student's *t*-test and analysis of variance (ANOVA) were applied when appropriate for statistical analysis to compare variables among the analyzed groups. A *p*-value < 0.05 was set as cutoff for significance. The analyses were performed using GraphPad Prism 9.

All the procedures were carried out in accordance with the GLP guidelines adopted in our laboratories.

RESULTS

Neutralizing Activity in Plasma and Saliva Samples From SARS-CoV-2-Infected and/or Vaccinees

NA was not tested for plasma samples from 4 SI, 8 SV, and 12 SIV subjects, and saliva samples from 1 SV and 1 SIV because their samples were not available. Results of systemic humoral response elicited by infection and or vaccine administration showed that NA was present in 16/16 SI (100%), 32/32 SV (100%), and 16/16 SIV (100%) plasma samples. Notably, NA in plasma samples was comparable in SI (mean value ± SE: 265 ± 87.15) and SV (mean value ± SE: 388.12 ± 86.98) but significantly lower compared to SIV (mean value ± SE: 3807.5 ± 719.36) ($p < 0.001$ in both cases) (**Figure 2A**).

A different trend was observed in NA in saliva samples by vNTA. Thus, NA was present only in saliva of 5 out of 39 SV subjects (12.8%), 9/20 SI subjects (45%), and 25/27 SIV subjects (92.6%) (**Figure 2A**). In line with the results observed in plasma samples, saliva NA was significantly higher in SIV (mean value ± SE: 23.4 ± 6.48) compared to both SI (mean value ± SE: 6.9 ± 4.32) ($p < 0.001$) and SV (mean value ± SE: 0.8 ± 0.46) ($p < 0.0001$) (**Figure 3A**).

To address the potential impact of the variability in the period of time between sample collection and infection and/or vaccination, we stratified samples within each group into two subgroups according to the time of sample collection (early vs. late). Although we observed a clear decline in NA over time in both plasma and saliva samples for SI, SV, and SIV (**Supplementary Figure S1**), such change did not affect the comparison between SI and SIV, and SV vs. SIV, whose findings were replicated by analyzing samples belonging to the two identified time points separately (**Supplementary Figure S2**). Nevertheless, we were not able to validate the comparison SI vs. SV due to a substantial difference between the time from infection (approximately 6 months) and time from vaccination (approximately 3 months) for these two groups.

Of note, a superior fraction of saliva sample from SI returned a positive NA test result compared to SV in spite of such longer period of time.

By dividing SV subjects according to the vaccine they were administered, we observed that NA in plasma was higher in BNT162b2 (mean value ± SE: 487 ± 128.35)- compared to AZD1222 (mean value ± SE: 223.33 ± 74)-vaccinated subjects

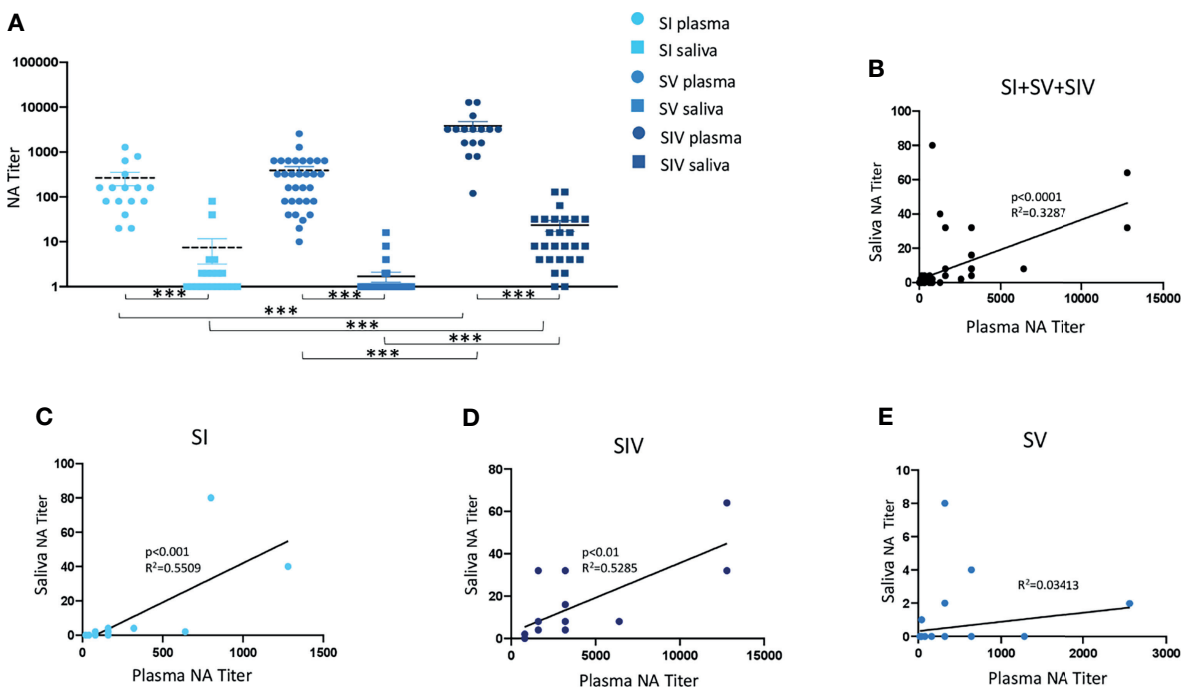

FIGURE 2 | Neutralizing activity (NA) from plasma and saliva of SARS-CoV-2-infected and/or vaccinated subjects, measured by virus neutralization assay (vNTA). NA in plasma and saliva samples are reported in panel **(A)**. Correlation between NA in plasma and saliva samples of all tested subjects are showed in panel **(B)**, while correlation between NA in plasma and saliva specimens of SARS-CoV-2-infected (SI), SARS-CoV-2-infected and vaccinated (SIV), and SARS-CoV-2-vaccinated (SV) subjects are represented in panels **(C–E)**, respectively. ***$p < 0.0001$.

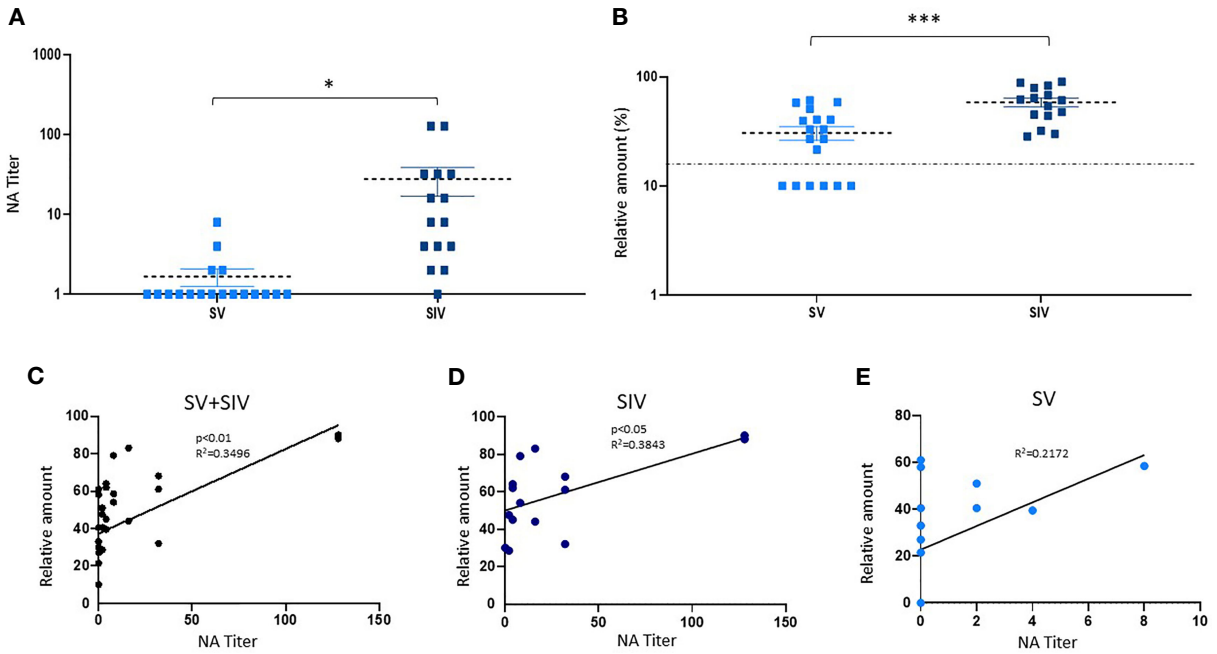

FIGURE 3 | Neutralizing activity (NA) and anti-RBD NAbs titer in saliva samples from SARS-CoV-2-infected and/or vaccinated subjects. **(B)** NA quantified by vNTA in a subgroup of SV (n = 18) and SIV (n = 15) subjects is reported in panel **(A).** In the same subgroup, anti-RBD NAb production was detected by ELISA assay. The dashed line is representative of a cutoff equal to 20%. *$p < 0.05$, ***$p < 0.001$. **(C)** Taking into account all the subjects (SV+SIV), we observed a positive correlation between salivary NA tested by the two techniques (vNTA and ELISA). The production of anti-RBD NAbs quantified by ELISA was positively correlated to the NA tested by NTA in SIV **(D)** but not in the SV group **(E)**.

($p < 0.05$) (**Supplementary Figure S3A**). Likewise, all the SV subjects who displayed a NA in saliva received the BNT162b2 vaccine (5/25 = 20%) (**Supplementary Figure S3B**).

No correlation with sex or age was detected with NA neither in plasma nor in saliva samples from the enrolled groups (data not shown).

Correlation Between SARS-CoV-2 NA Quantified by vNTA in Plasma and Saliva Samples

NA measured by vNTA was soundly correlated in plasma and saliva samples from all of the subjects enrolled in the study (SI + SV + SIV) ($p < 0.0001$) (**Figure 2B**). By analyzing these three groups independently, we observed that such correlation was maintained for SI ($p < 0.001$) (**Figure 2C**) as well as SIV subjects ($p < 0.01$) (**Figure 2D**), but not in SV (**Figure 2E**). Moreover, by dividing SIV subjects according to the vaccine they were administered, the positive correlation between plasma and saliva NA was maintained for BNT162b2-vaccinated individuals ($p < 0.01$) (**Supplementary Figure S3C**), but not for the AZD1222 vaccines (data not shown).

Quantification of Anti-RBD NAbs (ELISA) and Correlation With vNTA

According to the NA data obtained by vNTA on salivary samples from a subgroup of subjects (SV = 18; SIV = 15) (mean value ± SE: SV = 1.66.6 ± 0.42; SIV = 27.8 ± 11.28) ($p < 0.05$) (**Figure 3A**), the concentration of anti-RBD NAbs quantified by ELISA commercial kit was higher in SIV (mean value% ± SE: 58.40 ± 5.33) compared to SV (mean value% ± SE: 30.58 ± 4.48) ($p < 0.0001$) (**Figure 3B**). Indeed, taking into account all the subjects (SV + SIV), we observed a positive correlation between NA quantified by the two techniques (vNTA and ELISA) ($p < 0.01$) (**Figure 3C**). In particular, all of the 18 individuals who had saliva vNTA produced even anti-RBD NAbs (**Table 1**). However, of the 15 subjects who were negative for the vNTA assay, 9 (60%) tested positive to the production of anti-RBD NAbs (**Table 1**), suggesting that the two technical approaches cannot be used interchangeably because they identify different parameters.

Moreover, the production of anti-RBD NAbs quantified by ELISA was positively correlated to the production of salivary NA tested by vNTA in SIV ($p < 0.05$) (**Figure 3D**); conversely, we observed a trend towards a positive correlation, which did not reach statistical significance ($p = 0.0512$) in SV group (**Figure 3E**).

NA in Saliva and Plasma Samples to B.1.617.2 (Delta) Strain

Saliva (n = 11) and plasma (n = 13) collected from a subgroup of subjects enrolled in the study, who displayed NA against the lineage B.1 (EU), assumed as reference virus, were tested against the Delta (lineage B.1.617.2) variant. Mean values ± SE were 1,221.5 ± 427.2 for the EU strain and 240 ± 86.7 for the Delta strain, in plasma samples ($p < 0.05$) (**Figure 4A**); and 36.4 ± 16.6 for the EU strain and 8.5 ± 4.2 for the Delta strain, in saliva

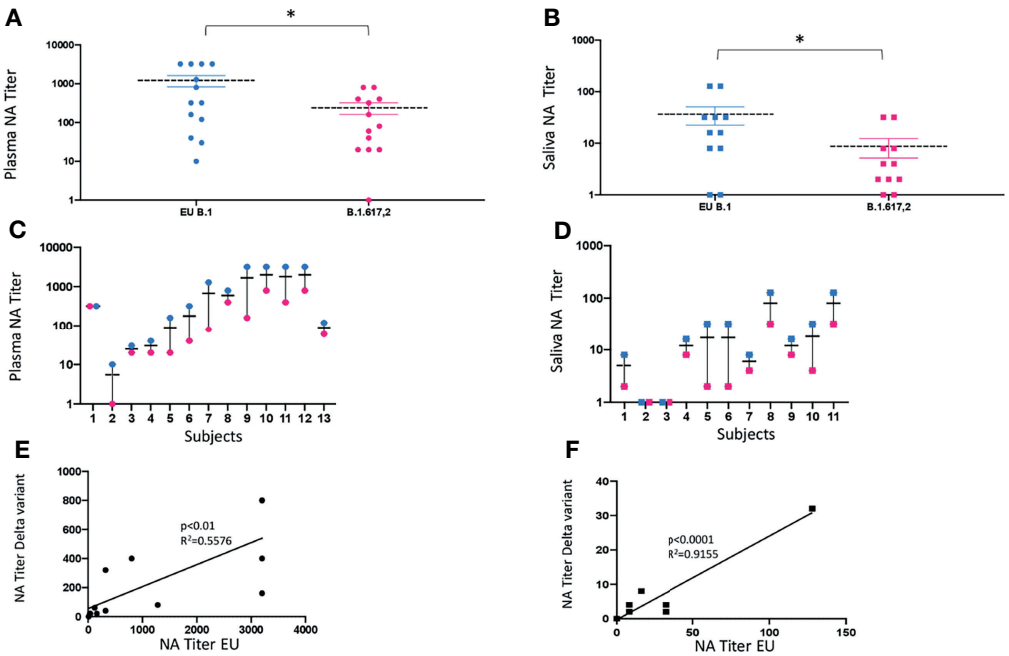

FIGURE 4 | vNTA against SARS-CoV-2 lineage EU (B.1) and Delta variant (B.1.617.2). Virus neutralization assay (vNTA) titer on the Delta variant was significantly lower compared to the «wild type» SARS-CoV-2 (EU) in both plasma **(A)** and saliva **(B)** samples. *$p < 0.05$. Comparison between the EU variant and Delta variant in plasma and saliva samples from each enrolled subject is reported in panels **(C, D)**, respectively. Lines connect the NAbs of each individual subject. In panels **(E)** (plasma) and **(F)** (saliva), vNTA correlation between the EU and the Delta variant is described.

specimens ($p < 0.05$) (**Figure 4B**). Thus, there was a 5-fold and 4-fold reduction in the neutralization titers against the Delta variant in plasma and saliva samples, respectively (**Figures 4C, D**), although at lower titers, NA against the Delta variant was still detectable in both biological samples from subjects who showed NA against the EU lineage. As a whole, the NA of vaccine immune sera against the EU variant was maintained to that against the Delta strain in both plasma ($p < 0.01$) (**Figure 4E**) and saliva ($p < 0.0001$) (**Figure 4F**) strain.

Cytokine/Chemokine Quantification in Saliva Samples

In order to verify if the higher NA detected in samples from BNT162b2-vaccinated subjects was associated with an increased immune activation, we assessed the levels of 8 cytokines, including classic pro- and anti-inflammatory mediators like IL-6, IL-8, IL-10, IFNγ, and TNF, in saliva samples from SV and SIV subjects. No differences in cytokine concentration were observed by comparing saliva samples from SV and SIV, suggesting that infection does not influence the release of cytokines in the oral mucosa in response to vaccination (data not shown). However, overall cytokine production was higher in saliva specimens from BNT162b2 (SIV+SV: $n = 28$)- compared to AZD1222 (SIV+SV: $n = 12$)-vaccinated individuals with a statistically significant difference for IL-6 ($p < 0.05$), IL-10 ($p < 0.01$), and IFNγ ($p < 0.05$) (**Supplementary Figure S4**). The time of sample collection from vaccination was comparable between AZD1222 and BNT162b2 groups (mean month value ± SE: AZD1222 = 3.4 ± 0.3; BNT162b2 = 3.3 ± 0.3).

DISCUSSION

SARS-CoV-2 is an airborne virus that infects epithelial cells of the mucosa of the upper airways to eventually spread further, causing pulmonary and multi-organ infection and damage in some patients (20). Several studies have shown that saliva contains infectious SARS-CoV-2 particles in both symptomatic and asymptomatic individuals, and it can provide useful information on local immunity at the primary site of virus acquisition (8, 19, 21, 22). Such knowledge is of pivotal importance for the development of effective immunomodulatory strategies to prevent and cure the infection, including vaccines. Although they have been widely tested and used in humans, the outcome of SARS-CoV-2 vaccines on local virus-specific immune responses in the airway mucosa is still poorly characterized. To this end, we decided to optimize and validate a virus neutralization test, which has long been used to estimate antibody-mediated protection upon vaccination in plasma samples, to investigate the NA of saliva in a cohort of subjects with different history of SARS-CoV-2 infection and/or vaccination.

As previously documented by other authors (6, 23, 24), our current results showed that NA is present in 100% of serum samples from all the enrolled groups (SI, SV, and SIV), although

the neutralization titer was significantly higher in SIV compared to both SI and SV. Conversely, NA in saliva specimens was detected in almost all SIV individuals (92%), but just in half of SI and 20% of SV and only following BNT162b2 vaccination in the latter. In line with two recent studies on virus-specific antibody detection in saliva of vaccines (25, 26), our results suggest that intramuscular SARS-CoV-2 vaccination alone elicited long-lasting (3 months post-administration) oral mucosal immunity only in a minority of subjects who received two doses, while one dose of vaccine boosted an anti-SARS-CoV-2 response in those individuals who were previously infected.

This possibly underlines the importance of local exposure at the site of virus transmission to efficiently prevent the infection and avoid its spreading, a condition that is not or is partly fulfilled by intramuscular vaccination in the absence of local pre-existing immunity. In fact, the intramuscular vaccine administration route reportedly stimulates systemic immunity, whereas intranasal or oral vaccinations trigger a local immune response also characterized by active secretion of mucosal antibodies passing into the fluids wetting the mucosa (27). Current vaccines intended to elicit local protection against viruses comprise intranasal spray (FluMist) for influenza (28) and oral drops for rotavirus (RotaTeq/Rotarix) (29, 30), polio (31), and typhoid (Vivotif) (32). The biology concerning the new SARS-CoV-2 vaccine preparations, mainly mRNA vaccines, which may stimulate distinctive kinds of antibody responses in different anatomical districts, is still largely unknown and deserves dedicated investigations. In line with previous reports (33, 34), we observed a decline in NA over time in plasma for all three groups. As expected, such decline was also observed in saliva samples. Of note, although the lack of differences in NA titers between SI and SV might be explained by a longer period of time elapsed from infection in SI (6 months) than that from vaccination in SV (3 months), a 3-fold larger fraction of SI (45%) than SV (13%) displayed NA in saliva. We cannot rule out episodes of re-exposure and/or asymptomatic infection after the reported time of diagnosis for SI. However, a possible explanation to a greater longevity or efficacy of the immune response induced by natural infection may be the persistent exposure to virus antigens associated with a sub-clinical infection as detected in the intestine of recovered COVID-19 patients up to 4 months after diagnosis (35). Nevertheless, while the time from infection was comparable between SIV and SI, the vast majority of SIV (92%) displayed a superior NA in saliva as well as plasma samples collected 3 months after vaccination, thus highlighting the efficacy of the vaccine booster regimen also in subjects recovered from COVID-19.

Even if vaccination *per se* does not result in effective and/or durable antibody responses at the site of virus transmission, other determinants of mucosal immunity, that were not evaluated in the present study, may account for local protection against SARS-CoV-2. On the other hand, some recently published papers reported a different overview of salivary antibodies in SARS-CoV-2-vaccinated subjects. Nahass et al. found IgG and IgA anti-RBD antibodies as well as NA in plasma and saliva specimens from both convalescent and mRNA-vaccinated subjects (7). Likewise, Ketas and colleagues reported that anti-S-protein IgG was present in every saliva sample from recipients of 2 mRNA vaccine doses (6). Even more recently, S1-specific IgA and IgG responses with neutralizing activity were detected in the nasal mucosa of mRNA SARS-CoV-2 vaccinees (36). Yet, it should be noted that salivary antibody detection, in these studies, was assessed by techniques other than vNTA, namely ELISA, chemiluminescent immunoassay (CLIA), flow cytometry, and pseudoviruses neutralization assays. Soon after the very early stage of the pandemic, these tests have been extensively used, allowing for faster and greater testing capacity. Although they provide useful indications, these assays do not unbiasedly evaluate the ability of a biological specimen, and/or the antibodies contained therein, to neutralize the infectivity of viral particles. In fact, RBD-binding tests account for an important fraction of NAbs, but do not quantify the NA directed against epitopes other than those commonly recognized by commercial CLIA/ELISA, such as the N-terminal domain of the spike protein (37–40). Likewise, the use of pseudoviruses could lead to incongruent results because they do not entirely recapitulate the life cycle of primary isolates. In line with this observation, in our study, the results on salivary anti-RBD NAbs quantified by ELISA were not fully mirrored by those obtained by vNTA, as some samples that did not display NA in the vNTA tested positive in the ELISA test. In support of our results, Sheikh-Mohamed and colleagues (5) recently published a study providing evidence of robust anti-Spike/RBD IgG and sIgA Ab in the saliva of vaccinated subjects, but only modest levels of neutralizing capacity in saliva specimens at 2 weeks after the second vaccine dose. Additionally, Mileto et al. did not observe a correlation between the quantity of systemic antibodies detected by CLIA assays and their NA tested by vNTA in plasma from SARS-CoV-2-vaccinated healthcare workers (24). These discrepancies suggest that SARS-CoV-2 serological tests may provide incomplete information on the protective feature of systemic or local immunity. Multiple tests addressing different mechanisms underlying humoral as well as cell-mediated virus specific immune responses are, therefore, needed to address the full extent of immunity associated with natural infection and vaccination.

The appearance of new variants of concerns (VOC), with lowered susceptibility to neutralizing antibodies, raises some worries on the possibility of evading vaccination-induced NA, as already documented on plasma samples (16, 17, 41–46). To verify if SARS-CoV-2 vaccines confer immunity in the oral cavity against mutated strains, we tested the NA of saliva and plasma samples from SV and SIV in a head-to-head comparison between B.1.617.2 (Delta) and B.1 (EU) variants in the same vNTA. In SV and SIV, the Delta strain displayed a partial immune escape in both specimens as demonstrated by lower NA titers compared to the EU lineage. However, a strong positive correlation in NA titers between the two strains confirmed the observation that existing vaccines can protect from severe disease even against potential new variants (34).

Another intriguing observation rising from this study concerns the higher protective efficacy apparently triggered by

BNT162b2 compared to AZD1222. Indeed, at the systemic level, the NA was significantly higher in SV vaccinated with BNT162b2 compared to AZD1222; even more oddly, salivary NA was detected only in 5 SV subjects, all of whom received the BNT162b2 vaccine. A plausible explanation stems from a recently published paper suggesting that BNT162b2 administration elicited higher IgG and IgA titers compared to adenoviral vector AZD1222, thus providing mucosal immunity activation to prevent infection at oral and nasopharyngeal mucosa (47). The degree of immune protection offered by different vaccine types is likely associated with multiple factors, possibly reflected by variations in local immunological milieu as evidenced by our cytokine analysis. *Ad hoc* studies on larger cohorts are necessary to validate this hypothesis and pinpoint the role played by each factor in the observed response.

There are some limitations to our study: this was a non-randomized observational study, and it was not planned to investigate neither the production of the different antibody subtypes (i.e., IgA, IgG, and IgM) nor their maintenance over time post infection and/or vaccination. Also, while the main antiviral function of Ab is to neutralize virions, they may also display non-neutralizing effector functions mediated *via* their Fc fragments (i.e., Ab-dependent cellular phagocytosis, Ab-dependent cellular cytotoxicity, and Ab-dependent activation of classical complement cascade), whose activity should be monitored for completeness, as already performed in previous studies (48). Moreover, the study was not prospective, and therefore, it was limited by sample availability and suffers from some variability in specimen collection time points. To be validated, these results need more detailed, prospectively designed, and randomized studies, for instance, following the administration of a third dose. Notwithstanding, in our hands, the salivary vNTA was reliable and reproducible and offered many potential advantages: (1) saliva collection is simple, safe, non-invasive, and can be collected by any individual without the need of a phlebotomist; (2) the test is easy and relatively inexpensive using standard laboratory equipment; (3) vNTA is still considered the gold standard for determining antibody protective efficacy (15) and none of the tests developed to mimic NA, by means of anti-RBD NAbs detection, can currently replace it for the functional evaluation of antibodies (49); (4) the vNTA test may be useful to evaluate the level of cross-reactivity between vaccine antisera and variant strains that may correlate with cross-protection in the host; and (5) saliva offers a glimpse into circulating antibodies, attributed to vascular leakage from the gingival crevicular epithelium. Nonetheless, compared to other commercial techniques, vNTA requires cell culture, high biocontainment laboratories (i.e., BSL-3), more time and labor, and specific technical skills, resulting in being too cumbersome to be employed in routine testing of a large number of samples. To the best of our knowledge, this is one of the first studies to assess the NA of saliva using a vNTA and multiple variants of SARS-CoV-2. We hope that the results of this study will contribute to streamline the use of relevant samples to address local immunity at mucosal sites of interest and will highlight the importance of including such analysis for an improved estimate of the efficacy of prophylactic and therapeutic interventions.

DATA AVAILABILITY STATEMENT

The raw data supporting the conclusions of this article will be made available by the authors, without undue reservation.

ETHICS STATEMENT

The studies involving human participants were reviewed and approved by Policlinic "Riuniti" of Foggia (protocol number 49/C.E./2021). The patients/participants provided their written informed consent to participate in this study.

AUTHOR CONTRIBUTIONS

Each author has approved the submitted version and agrees to be personally accountable for the author's own contributions and for ensuring that questions related to the accuracy or integrity of any part of the work are appropriately investigated and resolved. Conceptualization: MB and MG. Subject enrolment: SC, TS, and MP. Methodology: MG, OU, SS, and IS. Formal Analysis: IS and MG. Data Curation: MG and MB. Writing—Original Draft Preparation: MG, AI, and MB. Writing—Review and Editing: MB, MC, and AI. Supervision: MB. Funding Acquisition: MB. All authors contributed to the article and approved the submitted version.

FUNDING

This research was partially funded by the following grants: Bando Regione Lombardia DG Welfare cod. RL_DG-WEL20MBIAS_01; CARIPLO - EXTRABANDO E PROGETTI TER-RITORIALI cod. CAR_EXT20MBIAS_01.

ACKNOWLEDGMENTS

We would like to thank Loretelli C. and Abdelsalam A. from Fiorina P. laboratory for multiplex analysis assistance (Department of Biomedical and Clinical Sciences "L. Sacco", University of Milan, Milan, Italy).

SUPPLEMENTARY MATERIAL

The Supplementary Material for this article can be found online at: https://www.frontiersin.org/articles/10.3389/fimmu.2022.820250/full#supplementary-material

Supplementary Figure 1 | Neutralizing activity (NA) from plasma and saliva of SARS-CoV-2 infected and/or vaccinated subjects, measured by Neutralisation

assay (NTA) over time. NA in plasma and saliva samples of SI, and SIV analyzing according to the time from infection are reported in panel **(A, B)**, respectively. **(C, D)** panels show NA in plasma and saliva of SV and SIV divided according to the time from vaccine administration. No statistically significant differences were observed in neither plasma nor saliva specimens from the enrolled groups over time.

Supplementary Figure 2 | Comparison of Neutralizing activity (NA) in plasma and saliva of subjects stratified according to the time from infection and/or vaccination. NA in plasma **(A)** and saliva **(B)** specimens from SI and SIV groups sampled before and after 6 months from symptoms onset. Plasma and saliva NA of SV and SIV groups are compared respectively in panel **(C, D)** before and after 3 months from vaccine administration. Significance difference are reported into the graph: *p<0.05, **p<0.01, ***p<0.001.

Supplementary Figure 3 | Neutralizing activity (NA) in plasma and saliva samples of SV and SIV subjects, measured by virus neutralisation assay (vNTA). NA in plasma and saliva samples are reported in panel **(A, B)**, respectively. Vaccinated subjects were divided according to the administrated vaccine: adenovirus-based (AZD1222) or mRNA (BNT162b2). *p<0.05, **p<0.01, ***p<0.001. In panel **(C)** the positive correlation between NA quantified in plasma and saliva samples from BNT-162b2 vaccinated subjects is shown.

Supplementary Figure 4 | Cytokine quantification in saliva samples from SV and SIV subjects. Cytokine concentration in saliva samples from SV (n=19) and SIV (n=21) subjects divided according to the anti-SARS-CoV-2 vaccine they were administered (AZD1222: n°=12; BNT162b2: n°=28). Mean values ± SE are reported. *p<0.05; **p<0.01.

REFERENCES

1. Yang J, Petitjean SJL, Koehler M, Zhang Q, Dumitru AC, Chen W, et al. Molecular Interaction and Inhibition of SARS-CoV-2 Binding to the ACE2 Receptor. *Nat Commun* (2020) 11:4541. doi: 10.1038/s41467-020-18319-6
2. Zhu N, Zhang D, Wang W, Li X, Yang B, Song J, et al. A Novel Coronavirus From Patients With Pneumonia in China, 2019. *N Engl J Med* (2020) 382:727–33. doi: 10.1056/NEJMoa2001017
3. Zhang R, Li Y, Zhang AL, Wang Y, Molina MJ. Identifying Airborne Transmission as the Dominant Route for the Spread of COVID-19. *Proc Natl Acad Sci U S A* (2020) 117:14857–63. doi: 10.1073/pnas.2009637117
4. Pisanic N, Randad PR, Kruczynski K, Manabe YC, Thomas DL, Pekosz A, et al. COVID-19 Serology at Population Scale: SARS-CoV-2-Specific Antibody Responses in Saliva. *J Clin Microbiol* (2020) 59:e02204-20. doi: 10.1128/JCM.02204-20
5. A Mucosal Antibody Response is Induced by Intra-Muscular SARS-CoV-2 mRNA Vaccination, in: *Medrxiv*. Available at: https://www.medrxiv.org/content/10.1101/2021.08.01.21261297v2 (Accessed November 19, 2021).
6. Ketas TJ, Chaturbhuj D, Portillo VMC, Francomano E, Golden E, Chandrasekhar S, et al. Antibody Responses to SARS-CoV-2 mRNA Vaccines Are Detectable in Saliva. *Pathog Immun* (2021) 6:116–34. doi: 10.20411/pai.v6i1.441
7. Intramuscular SARS-CoV-2 Vaccines Elicit Varying Degrees of Plasma and Salivary Antibody Responses as Compared to Natural Infection, in: *Medrxiv*. Available at: https://www.medrxiv.org/content/10.1101/2021.08.22.21262168v1 (Accessed November 19, 2021).
8. Huang N, Pérez P, Kato T, Mikami Y, Okuda K, Gilmore RC, et al. SARS-CoV-2 Infection of the Oral Cavity and Saliva. *Nat Med* (2021) 27:892–903. doi: 10.1038/s41591-021-01296-8
9. Muhlebach MS, Zorn BT, Esther CR, Hatch JE, Murray CP, Turkovic L, et al. Initial Acquisition and Succession of the Cystic Fibrosis Lung Microbiome is Associated With Disease Progression in Infants and Preschool Children. *PloS Pathog* (2018) 14:e1006798. doi: 10.1371/journal.ppat.1006798
10. Kitamoto S, Nagao-Kitamoto H, Jiao Y, Gillilland MG, Hayashi A, Imai J, et al. The Intermucosal Connection Between the Mouth and Gut in Commensal Pathobiont-Driven Colitis. *Cell* (2020) 182:447–62.e14. doi: 10.1016/j.cell.2020.05.048
11. Moutsopoulos NM, Konkel JE. Tissue-Specific Immunity at the Oral Mucosal Barrier. *Trends Immunol* (2018) 39:276–87. doi: 10.1016/j.it.2017.08.005
12. Badia-Boungou F, Sane F, Alidjinou EK, Ternois M, Opoko PA, Haddad J, et al. Marker of Coxsackievirus-B4 Infection in Saliva of Patients With Type 1 Diabetes. *Diabetes Metab Res Rev* (2017) 33:1–7. doi: 10.1002/dmrr.2916
13. Saccoccio FM, Gallagher MK, Adler SP, McVoy MA. Neutralizing Activity of Saliva Against Cytomegalovirus. *Clin Vaccine Immunol* (2011) 18:1536–42. doi: 10.1128/CVI.05128-11
14. Tomar J, Patil HP, Bracho G, Tonnis WF, Frijlink HW, Petrovsky N, et al. Advax Augments B and T Cell Responses Upon Influenza Vaccination *via* the Respiratory Tract and Enables Complete Protection of Mice Against Lethal Influenza Virus Challenge. *J Control Release* (2018) 288:199–211. doi: 10.1016/j.jconrel.2018.09.006
15. Matusali G, Colavita F, Lapa D, Meschi S, Bordi L, Piselli P, et al. SARS-CoV-2 Serum Neutralization Assay: A Traditional Tool for a Brand-New Virus. *Viruses* (2021) 13:655. doi: 10.3390/v13040655
16. Liu Y, Liu J, Xia H, Zhang X, Fontes-Garfias CR, Swanson KA, et al. Neutralizing Activity of BNT162b2-Elicited Serum. *N Engl J Med* (2021) 384:1466–8. doi: 10.1056/NEJMc2102017
17. Edara VV, Hudson WH, Xie X, Ahmed R, Suthar MS. Neutralizing Antibodies Against SARS-CoV-2 Variants After Infection and Vaccination. *JAMA* (2021) 325:1896–8. doi: 10.1001/jama.2021.4388
18. Barrow KA, Rich LM, Vanderwall ER, Reeves SR, Rathe JA, White MP, et al. Inactivation of Material From SARS-CoV-2-Infected Primary Airway Epithelial Cell Cultures. *Methods Protoc* (2021) 4:7. doi: 10.3390/mps4010007
19. Heinzel C, Pinilla YT, Elsner K, Friessinger E, Mordmüller B, Kremsner PG, et al. Non-Invasive Antibody Assessment in Saliva to Determine SARS-CoV-2 Exposure in Young Children. *Front Immunol* (2021) 12:753435. doi: 10.3389/fimmu.2021.753435
20. Harrison AG, Lin T, Wang P. Mechanisms of SARS-CoV-2 Transmission and Pathogenesis. *Trends Immunol* (2020) 41:1100–15. doi: 10.1016/j.it.2020.10.004
21. Chiang SH, Tu M, Cheng J, Wei F, Li F, Chia D, et al. Development and Validation of a Quantitative, non-Invasive, Highly Sensitive and Specific, Electrochemical Assay for Anti-SARS-CoV-2 IgG Antibodies in Saliva. *PloS One* (2021) 16:e0251342. doi: 10.1371/journal.pone.0251342
22. Alkharaan H, Bayati S, Hellström C, Aleman S, Olsson A, Lindahl K, et al. Persisting Salivary IgG Against SARS-CoV-2 at 9 Months After Mild COVID-19: A Complementary Approach to Population Surveys. *J Infect Dis* (2021) 224:407–14. doi: 10.1093/infdis/jiab256
23. Krammer F, Srivastava K, Alshammary H, Amoako AA, Awawda MH, Beach KF, et al. Antibody Responses in Seropositive Persons After a Single Dose of SARS-CoV-2 mRNA Vaccine. *N Engl J Med* (2021) 384:1372–4. doi: 10.1056/NEJMc2101667
24. Mileto D, Fenizia C, Cutrera M, Gagliardi G, Gigantiello A, De Silvestri A, et al. SARS-CoV-2 mRNA Vaccine BNT162b2 Triggers a Consistent Cross-Variant Humoral and Cellular Response. *Emerg Microbes Infect* (2021) 10 (1):2235–43. doi: 10.1080/22221751.2021.2004866
25. Pinilla YT, Heinzel C, Caminada L-F, Consolaro D, Esen M, Kremsner PG, et al. SARS-CoV-2 Antibodies Are Persisting in Saliva for More Than 15 Months After Infection and Become Strongly Boosted After Vaccination. *Front Immunol* (2021) 12:798859. doi: 10.3389/fimmu.2021.798859
26. Azzi L, Dalla Gasperina D, Veronesi G, Shallak M, Ietto G, Iovino D, et al. Mucosal Immune Response in BNT162b2 COVID-19 Vaccine Recipients. *eBioMedicine* (2022) 75:103788. doi: 10.1016/j.ebiom.2021.103788
27. Weniger BG, Papania MJ. Alternative Vaccine Delivery Methods. *Vaccines* (2008), 1357–92. doi: 10.1016/B978-1-4160-3611-1.50065-9
28. Calzas C, Chevalier C. Innovative Mucosal Vaccine Formulations Against Influenza A Virus Infections. *Front Immunol* (2019) 10:1605. doi: 10.3389/fimmu.2019.01605
29. Folorunso OS, Sebolai OM. Overview of the Development, Impacts, and Challenges of Live-Attenuated Oral Rotavirus Vaccines. *Vaccines (Basel)* (2020) 8:341. doi: 10.3390/vaccines8030341

30. Soares-Weiser K, Bergman H, Henschke N, Pitan F, Cunliffe N. Vaccines for Preventing Rotavirus Diarrhoea: Vaccines in Use. *Cochrane Database Syst Rev* (2019) 2019:CD008521. doi: 10.1002/14651858.CD008521.pub5
31. Kirkpatrick BD, Colgate ER, Mychaleckyj JC, Haque R, Dickson DM, Carmolli MP, et al. The "Performance of Rotavirus and Oral Polio Vaccines in Developing Countries" (PROVIDE) Study: Description of Methods of an Interventional Study Designed to Explore Complex Biologic Problems. *Am J Trop Med Hyg* (2015) 92:744–51. doi: 10.4269/ajtmh.14-0518
32. Milligan R, Paul M, Richardson M, Neuberger A. Vaccines for Preventing Typhoid Fever. *Cochrane Database Syst Rev* (2018) 2018:CD001261. doi: 10.1002/14651858.CD001261.pub4
33. Cohen KW, Linderman SL, Moodie Z, Czartoski J, Lai L, Mantus G, et al. Longitudinal Analysis Shows Durable and Broad Immune Memory After SARS-CoV-2 Infection With Persisting Antibody Responses and Memory B and T Cells. *Cell Rep Med* (2021) 2:100354. doi: 10.1016/j.xcrm.2021.100354
34. Dupont L, Snell LB, Graham C, Seow J, Merrick B, Lechmere T, et al. Neutralizing Antibody Activity in Convalescent Sera From Infection in Humans With SARS-CoV-2 and Variants of Concern. *Nat Microbiol* (2021) 6:1433–42. doi: 10.1038/s41564-021-00974-0
35. Gaebler C, Wang Z, Lorenzi JCC, Muecksch F, Finkin S, Tokuyama M, et al. Evolution of Antibody Immunity to SARS-CoV-2. *Nature* (2021) 591:639–44. doi: 10.1038/s41586-021-03207-w
36. Frontiers. The Mucosal and Serological Immune Responses to the Novel Coronavirus (SARS-CoV-2) Vaccines, in: *Immunology* (Accessed November 19, 2021).
37. Chi X, Yan R, Zhang J, Zhang G, Zhang Y, Hao M, et al. A Neutralizing Human Antibody Binds to the N-Terminal Domain of the Spike Protein of SARS-CoV-2. *Science* (2020) 369:650–5. doi: 10.1126/science.abc6952
38. Yoshida S, Ono C, Hayashi H, Fukumoto S, Shiraishi S, Tomono K, et al. SARS-CoV-2-Induced Humoral Immunity Through B Cell Epitope Analysis in COVID-19 Infected Individuals. *Sci Rep* (2021) 11:5934. doi: 10.1038/s41598-021-85202-9
39. McCallum M, De Marco A, Lempp FA, Tortorici MA, Pinto D, Walls AC, et al. N-Terminal Domain Antigenic Mapping Reveals a Site of Vulnerability for SARS-CoV-2. *Cell* (2021) 184:2332–47.e16. doi: 10.1016/j.cell.2021.03.028
40. Suryadevara N, Shrihari S, Gilchuk P, VanBlargan LA, Binshtein E, Zost SJ, et al. Neutralizing and Protective Human Monoclonal Antibodies Recognizing the N-Terminal Domain of the SARS-CoV-2 Spike Protein. *Cell* (2021) 184:2316–31.e15. doi: 10.1016/j.cell.2021.03.029
41. Chen RE, Zhang X, Case JB, Winkler ES, Liu Y, VanBlargan LA, et al. Resistance of SARS-CoV-2 Variants to Neutralization by Monoclonal and Serum-Derived Polyclonal Antibodies. *Nat Med* (2021) 27:717–26. doi: 10.1038/s41591-021-01294-w
42. Jangra S, Ye C, Rathnasinghe R, Stadlbauer DPersonalized Virology Initiative study group, , Krammer F, et al. SARS-CoV-2 Spike E484K Mutation Reduces Antibody Neutralisation. *Lancet Microbe* (2021) 2:e283–4. doi: 10.1016/S2666-5247(21)00068-9
43. The Effect of Spike Mutations on SARS-CoV-2 Neutralization, in: *Crick*. Available at: https://www.crick.ac.uk/research/publications/the-effect-of-spike-mutations-on-sars-cov-2-neutralization (Accessed November 19, 2021).
44. Weisblum Y, Schmidt F, Zhang F, DaSilva J, Poston D, Lorenzi JC, et al. Escape From Neutralizing Antibodies by SARS-CoV-2 Spike Protein Variants. *eLife* (2020) 9:e61312. doi: 10.7554/eLife.61312
45. Neutralization of SARS-CoV-2 Spike 69/70 Deletion, E484K and N501Y Variants by BNT162b2 Vaccine-Elicited Sera, in: *Nature Medicine*. Available at: https://www.nature.com/articles/s41591-021-01270-4 (Accessed November 19, 2021).
46. Zani A, Caccuri F, Messali S, Bonfanti C, Caruso A. Serosurvey in BNT162b2 Vaccine-Elicited Neutralizing Antibodies Against Authentic B.1, B.1.1.7, B.1.351, B.1.525 and P.1 SARS-CoV-2 Variants. *Emerg Microbes Infect* (2021) 10:1241–3. doi: 10.1080/22221751.2021.1940305
47. Tauzin A, Nayrac M, Benlarbi M, Gong SY, Gasser R, Beaudoin-Bussières G, et al. A Single Dose of the SARS-CoV-2 Vaccine BNT162b2 Elicits Fc-Mediated Antibody Effector Functions and T Cell Responses. *Cell Host Microbe* (2021) 29:1137–50.e6. doi: 10.1016/j.chom.2021.06.001
48. Klingler J, Lambert GS, Itri V, Liu S, Bandres JC, Enyindah-Asonye G, et al. Detection of Antibody Responses Against SARS-CoV-2 in Plasma and Saliva From Vaccinated and Infected Individuals. *Front Immunol* (2021) 12:759688. doi: 10.3389/fimmu.2021.759688
49. Johnson S, Bergthaler A, Graw F, Flatz L, Bonilla WV, Siegrist C-A, et al. Protective Efficacy of Individual CD8+ T Cell Specificities in Chronic Viral Infection. *J Immunol* (2015) 194 (4):1755–62. doi: 10.4049/jimmunol.1401771

Conflict of Interest: The authors declare that the research was conducted in the absence of any commercial or financial relationships that could be construed as a potential conflict of interest.

frontiers in Immunology

ORIGINAL RESEARCH
published: 22 March 2022
doi: 10.3389/fimmu.2022.824746

Microbial Protein Binding to gC1qR Drives PLA2G1B-Induced CD4 T-Cell Anergy

Julien Pothlichet[1], Annalisa Meola[1†], Florence Bugault[1†], Louise Jeammet[1], Anne G. Savitt[2], Berhane Ghebrehiwet[2], Lhousseine Touqui[3,4], Philippe Pouletty[5], Frédéric Fiore[6], Alain Sauvanet[7] and Jacques Thèze[1]**

[1] DIACCURATE, Paris, France, [2] Division of Rheumatology, Allergy, and Clinical Immunology, Department of Medicine, SUNY Stony Brook, Stony Brook, NY, United States, [3] Cystic Fibrosis and Bronchial Diseases team - INSERM U938, Institut Pasteur, Paris, France, [4] Centre de Recherche Saint-Antoine (CRSA) - INSERM UMRS938, Sorbonne Université, Paris, France, [5] Truffle Capital, Paris, France, [6] Centre d'Immunophénomique, Aix Marseille Université, INSERM, CNRS, Marseille, France, [7] Service de Chirurgie Hépatobiliaire et Pancréatique - Department of HBP Surgery, Hôpital Beaujon - University of Paris, Clichy, France

The origin of the impaired CD4 T-cell response and immunodeficiency of HIV-infected patients is still only partially understood. We recently demonstrated that PLA2G1B phospholipase synergizes with the HIV gp41 envelope protein in HIV viremic plasma to induce large abnormal membrane microdomains (aMMDs) that trap and inactivate physiological receptors, such as those for IL-7. However, the mechanism of regulation of PLA2G1B activity by the cofactor gp41 is not known. Here, we developed an assay to directly follow PLA2G1B enzymatic activity on CD4 T-cell membranes. We demonstrated that gp41 directly binds to PLA2G1B and increases PLA2G1B enzymatic activity on CD4 membrane. Furthermore, we show that the conserved 3S sequence of gp41, known to bind to the innate sensor gC1qR, increases PLA2G1B activity in a gC1qR-dependent manner using gC1qR KO cells. The critical role of the 3S motif and gC1qR in the inhibition of CD4 T-cell function by the PLA2G1B/cofactor system in HIV-infected patients led us to screen additional microbial proteins for 3S-like motifs and to study other proteins known to bind to the gC1qR to further investigate the role of the PLA2G1B/cofactor system in other infectious diseases and carcinogenesis. We have thus extended the PLA2G1B/cofactor system to HCV and *Staphylococcus aureus* infections and additional pathologies where microbial proteins with 3S-like motifs also increase PLA2G1B enzymatic activity. Notably, the bacteria *Porphyromonas gingivalis*, which is associated with pancreatic ductal adenocarcinoma (PDAC), encodes such a cofactor protein and increased PLA2G1B activity in PDAC patient plasma inhibits the CD4 response to IL-7. Our findings identify PLA2G1B/cofactor system as a CD4 T-cell inhibitor. It involves the gC1qR and disease-specific cofactors which are gC1qR-binding proteins that can contain 3S-like motifs. This mechanism involved in HIV-1 immunodeficiency could play

OPEN ACCESS

Edited by:
Alexis M Kalergis,
Pontificia Universidad Católica de Chile, Chile

Reviewed by:
Alexander G. Gabibov,
Institute of Bioorganic Chemistry (RAS), Russia
Stanley Nithianantham,
St. Jude Children's Research Hospital, United States

***Correspondence:**
Julien Pothlichet
julien.pothlichet@diaccurate.com
Jacques Thèze
jacques.theze@diaccurate.com

†Present address:
Annalisa Meola,
Structural Virology Unit, CNRS UMR 3569, Institut Pasteur, Paris, France
Florence Bugault,
Immunobiology of Infection Unit, INSERM U1221, Institut Pasteur, Paris, France

Specialty section:
This article was submitted to Viral Immunology, a section of the journal Frontiers in Immunology

Received: 29 November 2021
Accepted: 28 February 2022
Published: 22 March 2022

Citation:
Pothlichet J, Meola A, Bugault F, Jeammet L, Savitt AG, Ghebrehiwet B, Touqui L, Pouletty P, Fiore F, Sauvanet A and Thèze J (2022) Microbial Protein Binding to gC1qR Drives PLA2G1B-Induced CD4 T-Cell Anergy. Front. Immunol. 13:824746. doi: 10.3389/fimmu.2022.824746

a role in pancreatic cancer and several other diseases. These observations suggest that the PLA2G1B/cofactor system is a general CD4 T-cell inhibitor and pave the way for further studies to better understand the role of CD4 T-cell anergy in infectious diseases and tumor escape.

Keywords: HIV, PLA2G1B, CD4 T cell, gC1qR, HCV, staphylococcus aureus, porphyromonas gingivalis, infectious disease

INTRODUCTION

CD4 T cells orchestrate efficient antimicrobial and antitumoral immunity. Impairment of CD4 T cells function plays a critical role in several diseases. One of the most highly studied is the severe immunodeficiency of HIV-infected patients. We recently showed that more than 80% of CD4 T cells from HIV-infected patients exhibited morphological anomalies characterized by numerous large abnormal membrane microdomains (aMMDs) that trap and inactivate physiological receptors, resulting in CD4 T-cell unresponsiveness (anergy) (1). Such aMMD-bearing cells were named "Bumpy T cells", due to their appearance upon microscopic observation. We identified phospholipase A2 group 1B (PLA2G1B) as the key molecule responsible for the formation of aMMDs in HIV viremic patients (VP) plasma. Treatments of CD4 T cells isolated from healthy donors (HD) with purified recombinant PLA2G1B induced Bumpy T cells, similarly to HIV VP plasma. HD plasma had no effect. Immunodepletion experiments, as well as experiments with an antibody that inhibits the enzymatic activity of PLA2G1B, confirmed that the PLA2G1B molecule is the active component in the plasma of HIV-infected VP that inhibits the CD4 T-cell response to IL-7, IL-2, and IL-4. These large aMMDs were shown to trap the IL-7R alpha chain and the gamma-c chain which is common to IL-7, IL-2, and IL-4 receptors. These cytokine receptors lose their function when embedded in such aMMDs. Consequently, the Jak/STAT pathway was not functional and IL-7-induced phospho-STAT5 nuclear translocation (pSTAT5-NT) was inhibited and used as a standard assay to follow PLA2G1B activity (1).

PLA2G1B was initially named pancreatic PLA2 due to its primary production in pancreatic tissue. Two forms of PLA2G1B are present in the pancreas, the intestinal tract, and in human plasma (1). It is expressed as an inactive precursor called proPLA2G1B, which contains a propeptide in the N-terminal part that masks the active site of PLA2G1B and blocks the access of the lipid substrate to the catalytic site of the protein (2). Upon digestion by a trypsin protease, the propeptide is removed to generate the active form of PLA2G1B (active PLA2G1B). Immunohistochemistry analysis of normal human pancreatic tissue has shown that active PLA2G1B is present in the exocrine component of the pancreas but not in the endocrine component, whereas proPLA2G1B is also present in the endocrine component (1). Active PLA2G1B was initially described for its role in the intestinal absorption of lipids before our recent demonstration of its role in CD4 T-cell anergy and CD4 T-cell lymphopenia in HIV-infected patients (1).

The inhibitory activity of PLA2G1B that induces the Bumpy phenotype was observed in the plasma of HIV VP but not that of HD, ART-treated patients (ART), or HIV controllers (HIC). The quantification of active PLA2G1B by ELISA showed the protein concentration to be similar in the plasma of VP, ART and HIC, with the median only 1.4-fold higher in VP than in HD plasma. However, PLA2G1B activity was only observed in VP plasma. Thus, we postulated that other factors present in VP plasma may boost the activity of PLA2G1B on CD4 T cells. We showed that recombinant HIV gp41 envelope protein increases PLA2G1B activity on CD4 T cells in a dose-dependent manner using the pSTAT5-NT response to IL-7 as a read-out. The activity of the gp41 cofactor depends on a sequence with three serine amino acids called 3S (3) conserved among HIV strains, as a similar increase in PLA2G1B inhibitory activity was observed with the 3S peptide alone (1).

These findings led us to propose a role for the PLA2G1B/cofactor system as a negative regulator of CD4 T-cell function. We have further shown that both components of the system are essential for its activity in the plasma of VP. PLA2G1B is the active component as anti-PLA2G1B Ab abrogates the inhibitory activity of VP plasma. Moreover, immunodepletion of gp41 from HIV VP plasma, using a polyclonal anti-gp41 antibody or an anti-gp41 antibody directed against the 3S sequence, almost completely abrogates the inhibitory activity of VP plasma on CD4 T cells. In this system, PLA2G1B activity is regulated by gp41 (or 3S) as a cofactor that appears to target PLA2G1B to the CD4 T-cell surface. The PLA2G1B/gp41 pair constitutes a mechanism of immune dysfunction and a compelling target for boosting immune responses in HIV-infected patients. However, the precise mode of action of the effect of the gp41/3S cofactor on the membrane is not known (1).

Here, we first confirmed our previous observations that the inhibitory activity of VP plasma on the pSTAT5-NT response to IL-7 is due to the enzymatic activity of PLA2G1B using several PLA2 inhibitors and the anti-PLA2G1B mAb that we developed to inhibit PLA2G1B. We developed an assay to directly investigate the effect of gp41 protein on the enzymatic activity of PLA2G1B on the cell surface membrane of CD4 T cells based on the labelling of primary human CD4 T cells with tritiated arachidonic acid ([3H]AA). Thus, the enzymatic activity of PLA2G1B can be measured by quantifying the radioactivity in the cell supernatant released from the membrane of the radiolabeled CD4 T cells. We show that [3H]AA is released in a PLA2G1B dose-dependent manner and that this activity correlates with the inhibition of pSTAT5-NT. Moreover, the enzymatic activity of PLA2G1B on CD4 T cells increases in a

gp41 dose-dependent manner, confirming the cofactor effect of gp41, which directly enhances PLA2G1B activity on the membranes of CD4 T cells.

The gp41/3S sequence binds to the receptor for the globular head of complement component C1q, the gC1q receptor (gC1qR) (4, 5). Notably, we showed that the gp41/3S peptide increases PLA2G1B activity on WT but not gC1qR KO cells, showing that the stimulation of PLA2G1B enzymatic activity by 3S is gC1qR-dependent. The gC1qR has been shown to bind to several microbial proteins (6). Thus, we postulated that the regulation of PLA2G1B may not be restricted to the case of HIV infection but shared by other infections. In support of this hypothesis, the HCV core and *Staphylococcus aureus* protein A, two proteins that bind to the gC1qR, also increase the enzymatic activity of PLA2G1B on the CD4 T-cell membrane. Moreover, we performed in-silico screening for 3S-like motifs in protein databases to identify additional gC1qR binding proteins that could also act as PLA2G1B cofactors. We identified 42 candidate proteins, including several proteins encoded by human pathogens. Among them, one was derived from *Porphyromonas gingivalis* (*P. gingivalis*), which is responsible for periodontal infections and has been shown to be associated with a higher risk of pancreatic cancer (7–9). Strikingly, the *P. gingivalis* 3S-like peptide also increases the enzymatic activity of PLA2G1B. We thus tested the plasma of patients with pancreatic ductal adenocarcinoma (PDAC) for the presence of inhibitory PLA2G1B activity that impairs the CD4 T-cell response to IL-7. As shown for HIV, PDAC plasma contains an activity that inhibits pSTAT5-NT in CD4 T cells. PLA2G1B is involved in inhibitory effect of PDAC plasma, as it was partially blocked by a specific anti-PLA2G1B mAb.

Finally, our findings identify a mechanism of inhibition of CD4 T-cell function through the PLA2G1B/cofactor system. PLA2G1B activity is enhanced by cofactors binding to gC1qR. These cofactors are proteins with 3S-like motifs and proteins that bind to the innate sensor gC1qR. This mechanism involved in HIV-1 immunodeficiency is likely to play a role in several diseases.

MATERIALS AND METHODS

Recombinant Proteins and Peptides

Human PLA2G1B was produced in *E. coli* (gift of Gerard Lambeau, purity > 98%) or CHO-S (purity > 98%, Merck or GTP). Human proPLA2G1B, PLA2GIIA, PLA2GIID, PLA2GX, and WT and H48Q porcine PLA2G1B were produced in *E. coli* (gift of Gerard Lambeau, purity > 98%). Recombinant HIV-1 gp41 MN protein was obtained from Antibodies online (gp41 MN (565-771Delta642-725), containing a deletion to remove the transmembrane domain of the protein, ABIN2129703, lot 93-482, purity > 95%) and the 3S peptide NH2-PWNASWSNKSL DDIW-COOH, 3S-like peptide OmpA Pg NH2-SGEGGWSNG SLVDIM-COOH, and scrambled 3S NH2-WNWDSKILSD PAWNS-COOH peptide were ordered from Covalab (purity > 98%). The HCV core protein was obtained from Prospec (HCV-011, purity > 95%) in PBS buffer with 0.002% SDS and the specificity of the effect due to HCV core protein evaluated by comparison with a similar dilution of PBS-0.002% SDS. *Staphylococcus aureus* protein A was obtained from Sigma (P6031). sPLA2 inhibitors were obtained from several providers: Pentapeptide ($sPLA_2$-IIA Inhibitor I, 525145, Calbiochem, ordered from VWR), Varespladib (LY315920, S1110, Selleck ordered from Euromedex), and sPLA2R1 (murine soluble receptor, 5367-PL-050, R&D Systems).

Study Design And Human Sample Collection

The group of viremic patients included in the study of T lymphocytes and plasma consisted of patients with untreated chronic HIV-infection. These patients had never received antiretroviral drugs at the time of blood collection, their CD4 counts were > 300/mm^3, and their viral loads > 10,000 copies/mL (ANRS EP 33). All blood samples from VP were drawn at the Hôpital Bicêtre, Paris. Blood from HD was obtained from healthy volunteers through the Etablissement Français du Sang (Centre Necker-Cabanel and St-Louis, Paris). Blood samples from PDAC patients were drawn at the Hôpital Beaujon (Clichy) or PDAC plasma samples were acquired from BIOIVT. These patients had never received treatments at the time of blood collection.

Study Approval

The study of the effect of VP plasma on the pSTAT5-NT response of CD4 T cells was supported by the ANRS and approved by the "Comité Consultatif de Protection des Personnes dans la Recherche Médicale" under the number 05-15. All participants were adults and provided written informed consent prior to inclusion in the study.

All participants who provided PDAC plasma were adults and provided written informed consent prior to inclusion in the study. The study was registered under the number DC-2021-4516 by the Ministère de l'Enseignement Supérieur, de la Recherche et de l'Innovation.

Purification of Human CD4 T-Lymphocytes

Venous blood was obtained from healthy volunteers through the EFS (Etablissement Français du Sang, Centre Necker-Cabanel, Paris). CD4 T-cells were purified from whole blood using the RosetteSep Human CD4+ T-cell Enrichment Cocktail (Stem Cell, 15062). This cocktail contains mouse and rat monoclonal antibodies purified from mouse ascites fluid or hybridoma culture supernatant, by affinity chromatography using protein A or Protein G Sepharose. These antibodies are bound in bispecific tetrameric antibody complexes directed against cell-surface antigens on human hematopoietic cells (CD8, CD16, CD19, CD36, CD56, CD66b, TCRγ/δ) and glycophorin A on red blood cells. The RosetteSep antibody cocktail crosslinks unwanted cells in human whole blood to multiple red blood cells, forming immunorosettes. This increases the density of unwanted cells, such that they pellet along with the free red blood cells when centrifuged through a buoyant density medium such as lymphocyte separation medium (Eurobio, CMSMSL01-01).

Whole blood was incubated with RosetteSep Human CD4+ T-cell Enrichment Cocktail at 50 µL/mL for 20 min at room temperature under gentle shaking (100 rpm), diluted with an equal volume of PBS + 2% fetal bovine serum (FBS), and mixed gently. The diluted samples were centrifuged for 20 min at 1,200 X g through lymphocytes separation medium. The enriched cells were then collected from the density medium at the plasma interface and washed twice with PBS + 2% FBS. Cells were subsequently resuspended in RPMI 1640 medium (Lonza) supplemented with 5% FBS, 50 mM HEPES pH 7.4, glutamine, penicillin, streptomycin and fungizone (complete medium), and counted using a Moxi Z mini automated cell counter (ORFLO, MXZ000). The cell suspension was adjusted to 7 x 10^6 cells/mL and equilibrated for at least 2 h at 37°C in a 5% CO2 humidified atmosphere.

The enriched CD4-T cell population was analyzed by flow cytometry on a Cytoflex instrument (Beckman coulter). The quiescence of recovered CD4 T cells was verified by the low level of IL-2Rα (CD25). CD4 T cells were labeled with anti-Human CD3 eFluor780 (eBioscience, clone UCHT1, 47-0038-42), anti-Human CD25-PE (Biolegend, clone BC96, 302605), and anti-human CD4-PerCP (BD, clone SK3, 345770). The enriched CD4 T-cell population contains > 95% CD3+CD4+ and < 8% of CD25+.

Phosphorylation and Nuclear Translocation of STAT5 (pSTAT5-NT)

STAT5 phosphorylation and nuclear translocation in HD CD4 T cells were analyzed by microscopy after IL-7 stimulation (2 nM), or in HD CD4 T cells incubated with plasma samples from HD (not shown here), HIV VP or PDAC patients (30 min), human PLA2G1B recombinant proteins, with or without a pretreatment (25 min at room temperature and 5 min at 37°C) with anti-PLA2G1B (14G9, previously described (1)) neutralizing mAb or control isotype (Mouse IgG1, 16-4714-85, Thermofisher) or sPLA2 inhibitors (pentapeptide, varespladib, sPLA2R1) before a 15 min of stimulation with 2 nM IL-7 (recombinant glycosylated human IL-7, Accrobio System). All cell treatments were performed at 37°C. Cell supernatants were removed and stimulation was stopped by the addition of 500 µl of a 4% paraformaldehyde solution in PBS (Fisher, PFA 32% Electron Microscopy Science, 15714) and incubation for 15 min at 37°C. Cells were then permeabilized overnight at -20°C in 500 µL of an ice-cold 90% methanol/water solution.

CD4 T cells were stained using anti-human CD4 (mouse anti-CD4 clone RPA-T4, 555344, BD Biosciences; or goat anti-CD4, AF-379-NA, R&D/Novus), followed by donkey anti-mouse-AlexaFluor488 (A21202, Thermofisher). Phosphorylation of STAT5 in response to IL-7 stimulation was then revealed by staining with rabbit anti-pSTAT5 (9359, Cell Signaling Technology) followed by goat anti-rabbit-Atto 647N (15068; Active Motif) or donkey anti-rabbit AlexaFluor555 (A31572, Life Technologies). Briefly, slides were washed twice after methanol treatment in PBS and cells were rehydrated for 15 min in PBS supplemented with 5% FBS at room temperature. Slides were labeled with primary antibodies (1/120) in 60 µl of PBS-5% FBS for 1 h, washed in PBS buffer 15 times, and washed in PBS/FBS buffer five times. Slides were then stained with secondary antibodies (1/300) for 1 h, washed five times in PBS-5% FBS buffer, rinsed 15 times in PBS, and then mounted in fresh Prolong Gold Antifade (ThermoFisher Scientific, P36930) mounting medium for confocal microscopy.

Images were acquired above the diffraction limit using an inverted laser scanning confocal microscope (LSM700, Zeiss) as previously described (1). The appearance of pSTAT5 was measured using ImageJ software. The number of cells positive for nuclear pSTAT5 among > 200 in response to cytokines was analyzed by confocal microscopy.

PLA2G1B Enzymatic Assay on [3H] Arachidonic Acid-Labeled CD4 T Cells

Purified CD4 T-cells were incubated for 16 h at 2 x 10^6 cells/mL with 1 µCi/mL of arachidonic acid [5,6,8,9,11,14,15-^{3}H(N)] (Perkin Elmer, NET298Z250UC) in RPMI 1640 medium (Lonza) supplemented with 10% FBS, 50 mM HEPES pH 7.4, glutamine, penicillin, streptomycin and fungizone at 2 mL/well in six-well plates at 37°C in a humidified 5% CO2 atmosphere. Cells were washed twice with RPMI containing 10% FBS by centrifugation at 580 x g for 10 min at room temperature and then frozen in 90% FBS 10% DMSO at 10^7 cells/mL/vial at -80°C. The percentage of [3H] arachidonic acid in CD4 T cells (1 minus the ratio of [3H] arachidonic acid in the CD4 T-cell supernatant (cpm/mL) relative to the total [3H] arachidonic acid in the supernatant and cells (cpm/mL)) was measured to control the cell preparation.

To test PLA2G1B activity on [3H] arachidonic acid ([3H]-AA)-labeled CD4 T lymphocytes, cells were first thawed in 10% FBS RPMI preheated to 37°C, centrifuged at 580 x g for 10 min at room temperature, washed twice in 2.5% FBS RPMI, and equilibrated in 2.5% FBS RPMI at 2 x 10^5 CD4 T cells/400µL/well in 24-well polystyrene plates for 90 min at 37°C in a humidified 5% CO2 atmosphere.

To test the effect of H48Q and sPLA2 inhibitors on PLA2G1B activity on [3H]-AA-labeled CD4 T lymphocytes, 100 µL of recombinant WT human (hPLA2G1B) and WT and the catalytic-site mutant H48Q porcine PLA2G1B (pPLA2G1B), or medium or hPLA2G1B pretreated (25 min at room temperature and 5 min at 37°C) with sPLA2 inhibitors (pentapeptide, varespladib) or vehicle, in 2.5% FBS RPMI was added to each well and the plates incubated for 2 h.

To test the effect of viral or bacterial protein cofactors on PLA2G1B activity on [3H]-AA-labeled CD4 T lymphocytes, 100 µL of recombinant protein (gp41 MN (565-771Delta642-725), HCV core protein, *Staphylococcus aureus* protein A), or diluted vehicle, with or without PLA2G1B, in 2.5% FBS RPMI was added to each well and the plates incubated for 2 h. Cells and supernatants were collected in Eppendorf tubes and centrifuged at 580 x g for 10 min at room temperature.

To study PLA2G1B activity on [3H]-AA-labeled CD4 T lymphocytes relative to that of human proPLA2G1B, cells were prepared as above but equilibrated in 2.5% FBS RPMI at 10^6 CD4 T cells/400 µL/well in 24-well polystyrene plates for 90 min at 37°

C in a humidified 5% CO2 atmosphere. Then, 100 µL medium or recombinant sPLA2 proteins in 2.5% FBS RPMI was added to each well and the plates incubated for 2 h.

The [3H]-AA released into the cell supernatant was quantified in 300 µL using 16 mL of Ultima gold (Perkin Elmer, 6013329) in low diffusion vials (Perkin Elmer, 6000477) on a scintillation counter (tri-Carb 2800 TR liquid scintillation analyzer, Perkin Elmer).

To evaluate the effect of the H48Q mutation, the results are expressed as PLA2G1B activity (release of [3H]-AA into the supernatant of cells treated with WT or H48Q PLA2G1B minus the spontaneous release of [3H]-AA by cells treated without PLA2G1B, in cpm/mL).

To evaluate the effect of the sPLA2 inhibitors, the results are expressed as the percentage of inhibition of PLA2G1B activity on cells treated with PLA2G1B and several doses of the inhibitors.

To evaluate the relative effect of PLA2G1B versus that of proPLA2G1B, the results are shown as the percentage of activity with proPLA2G1B relative to that of PLA2G1B activity.

To test the effect of viral or bacterial protein cofactors, the results are expressed as PLA2G1B activity (release of [3H] arachidonic acid into the supernatant of cells treated with recombinant proteins (gp41, HCV core or SA protein A) or buffer together with PLA2G1B minus the spontaneous release of [3H] arachidonic acid by cells treated with recombinant proteins alone or buffer only, without PLA2G1B, in cpm/mL).

PLA2G1B Enzymatic Assay on [3H] Arachidonic Acid-Labeled Jurkat E6.1 T Cells

Jurkat E6.1 T cells (ECACC 88042803) or gC1qR KO Jurkat E6.1 T cells were incubated for 17 h at 5 x 10^5 cells/mL with 1 µCi/mL arachidonic acid [5,6,8,9,11,14,15-^{3}H(N)] (Perkin Elmer, NET298Z250UC) in RPMI 1640 medium (Lonza) supplemented with 10% FBS, 50 mM HEPES pH 7.4, glutamine, penicillin, streptomycin, and fungizone at 2 mL/well in 6-well plates at 37°C in a humidified 5% CO2 atmosphere. Cells were washed twice with RPMI with 10% FBS by centrifugation at 300 x g for 10 min at room temperature and then frozen in 90% FBS 10% DMSO at 10^7 cells/mL/vial at -80°C. The percentage of [3H] arachidonic acid in Jurkat T cells (1 minus ratio of [3H] arachidonic acid in the Jurkat T-cell supernatant (cpm/mL) relative to the total [3H] arachidonic acid in the supernatant and cells (cpm/mL)) was measured to control the cell preparation.

To test PLA2G1B activity on [3H]-AA-labeled Jurkat E6.1 T lymphocytes, cells were thawed in 10% FBS RPMI preheated to 37°C, centrifuged at 300 x g for 10 min at room temperature, washed twice in 2.5% FBS RPMI, and equilibrated in 2.5% FBS RPMI at 5 x 10^4 Jurkat E6.1 T cells/400µL/well in 24-well polystyrene plates for 90 min at 37°C in a humidified 5% CO2 atmosphere. Cells were pretreated with 50 µL of the peptides per well at 110 µM in 2.5% FBS RPMI for 2, 4, or 21 h, as indicated in the figures. Then, 50 µL of 2 µM PLA2G1B in 2.5% FBS RPMI or medium alone were added per well and the plates incubated for 2 h. Cells and supernatants were collected in Eppendorf tubes and centrifuged at 580 x g for 10 min at room temperature. The [3H] arachidonic acid released into the cell supernatant was quantified in 300 µL using 16 mL Ultima gold (Perkin Elmer, 6013329) in low diffusion vials (Perkin Elmer, 6000477) on a scintillation counter (tri-Carb 2800 TR liquid scintillation analyzer, Perkin Elmer).

Results are expressed as ΔPLA2G1B activity with the peptides minus PLA2G1B activity with the Scrambled 3S (the release of [3H] arachidonic acid into the supernatant of cells treated with PLA2G1B and peptide minus the release of [3H] arachidonic acid by cells treated with PLA2G1B and Scrambled 3S peptide, in cpm/mL).

ELISA Study of PLA2G1B and gp41 Interaction

Study of gp41 binding to coated PLA2G1B in ELISA. Microplates were coated with 100 µL of PLA2G1B recombinant proteins at 10 µg/mL in protein-free blocking buffer (37572, Pierce). Then, the binding of serial dilutions (0-1 µg/well) of strep-tagged gp41 (D117 strain in A and MN strain in B) or unrelated proteins (CTL1: EFF-1 or CTL2: IF38 in A and CTL1: EFF1 in B) to PLA2G1B was revealed by the sequential addition of mouse anti-strep-tag mAb (MA5-17283, Invitrogen) and goat anti-mouse HRP-conjugated Ab (31430, Pierce), followed by the HRP reaction with TMB. All dilutions were tested in triplicate.

Study of PLA2G1B binding to coated gp41 in ELISA. Microplates were coated with 100 µL of gp41 (D117III strain in C and MN strain in D) recombinant proteins at 10 µg/mL in protein-free blocking buffer (37572, Pierce). Then, the binding of serial dilutions (0-1 µg/well) of PLA2G1B, to gp41 was revealed by the sequential addition of anti-PLA2G1B mAb (1C11, produced at BIOTEM, described in (1) and HRP-anti-mouse Ab, followed by the HRP reaction with TMB. All dilutions were tested in triplicate.

Pull-Down Assay of PLA2G1B With gp41

Recombinant PLA2G1B (50 µg/mL) in PBS was incubated, or not, with recombinant gp41 (D117 III strains) with a strep-tag at 10 µg/mL in 1.5-mL Eppendorf tubes overnight (Test tube-rotor, 34528, Snijders, Netherlands) at 4°C. Then, gp41 was pulled-down by adding 50 µL of prewashed Strep-Tactin XT-beads (Mag strep "type 3" XT beads, IBA, 2-4090-002) per tube, followed by incubation for 30 min on ice with vortexing from time to time (4X). Beads were washed three times in washing buffer and the pulled-down protein complex was eluted in 50 µL 1X BTX buffer (IBA, 2-1042-025). Then, the proteins in 5 µL of flow through and 30 µL of the eluted sample were separated through 4%–20% Tris-Bis SDS-PAGE (BIO-RAD) gels under reducing conditions. Antigens were transferred to PVDF membranes (BIO-RAD) using a Trans-Blot Turbo (BIO-RAD). After blocking nonspecific binding sites with 5% milk/0.05% tween 20 in PBS, PLA2G1B was revealed using 10 µg/mL 1C11 mouse anti-PLA2G1B mAb and gp41 using 5 µg/mL polyclonal anti-gp41 (PA1-7219, Thermofisher). Goat anti-mouse (31430, Pierce) and donkey anti-goat (705-035-003, Jackson Immunoresearch) HRP-conjugated antibodies were used at a 1:10,000 dilution. Detection occurred directly on the membrane using SuperSignal West Pico Plus Substrate (34580, Thermofisher Scientific).

Generation of gC1qR KO Jurkat E6.1 T Cells

The global strategy for the development of Jurkat cells deprived of C1QBP (the gene for gC1qR) was based on the design of a targeting vector permitting bi-allelic inactivation of the C1QBP gene *via* homologous recombination using CRISPR/Cas9 method as previously described in (10). Homologous human C1QBP regions isogenic with the Jurkat E6.1 T cell line (ECACC 88042803) were used. The targeting vector was synthesized by Genewiz and cloned into the pUC57-Amp vector. The third exon of the human C1QBP gene was targeted by introducing a neomycin resistance gene (NeoR) selection cassette, resulting in the interruption of the open reading frame of C1QBP. The NeoR cassette was cloned using BamHI/NotI restriction sites. The targeting vector was verified by DNA restriction digestion cut with selected restriction enzymes (APaL1, Drd1, Pvu1, Pvu2, BamH1/NotI, Not1/NcoI, NEB) and target region sequencing. The DNA primers corresponding to C1QBP sgRNA (1828-Crispr_1A: CACC-GAAGTGACCGTGATTCTAAAA and 1828-Crispr_1B: AAAC-TTTTAGAATCACGGTCACTTC) were hybridized and cloned (Quick Ligase - New England Biolabs, NEB) into the pX330 plasmid (Addgene, 42230; Feng Zhang, MIT) using the BbsI restriction site (NEB).

The Jurkat cells (5 x 10^6) were resuspended in 100 µL of Opti-MEM and 7 µg of CRISPR/Cas9 plasmid and 2.5 µg of targeting vector were added. The cells were electroporated using a Nepa21 electroporator. After cell selection in G418 selective medium, the Jurkat cell clones were prescreened by PCR genotyping. Independent cell clones knocked-out for the C1QBP gene were amplified and verified by PCR genotyping and target region sequencing. Our validation pipeline for the independent Jurkat cell clones deficient for the C1QBP gene consisted of PCR genotyping. The genomic DNA of gene edited Jurkat cells was isolated by proteinase K treatment and phenol purification. Each cell clone with bi-allelic inactivation of the C1QBP gene was confirmed by PCR genotyping and by target region sequencing. PCR amplification was performed with Platinum HiFi Taq (Life technologies) for 2 min at 50°C with primers 1828_RH5_F: TACTACAGCCCTTGTTCTT and 1828_RH3_R: AGCACTTCC TGAAATGTT. The primers were designed to be in the C1QBP human locus and not in the homologous arms. The wild type (WT) and mutant alleles were distinguished in the same PCR reaction. The WT and mutant alleles resulted in 1,146-bp and 2,362-bp amplification products, respectively. This PCR genotyping protocol allowed the identification of the homozygous Jurkat cell clones knocked-out for both alleles of the C1QBP gene.

Immunoblot Detection of gC1qR in Jurkat E6.1 T Cells

Western-blot analysis of gC1qR protein expression in WT and gC1qR KO Jurkat E6.1 T cell lysates was performed as follows. Cells were lysed in mammalian protein extraction reagent (M-PER, 11884111, Thermo Scientific) buffer and the amount of protein quantified using the BCA Protein assay kit on cleared supernatants (23227, Pierce, Thermo Scientific). An equal amount of total protein was loaded for WT and gC1qR KO Jurkat E6.1 T cells (40 µg) and fractionated by SDS-PAGE on 8-16% Mini-PROTEAN TGX Stain Free Gels (4568104, BIORAD), electro-transferred, and probed by immunoblotting using a specific antibody against gC1qR (60.11 Santa Cruz at 1:50, 74.5.2 Abcam at 1:1,000) or ß-actin (AC-74, Sigma at 1:2,000) in PBS-0.05% Tween-5% BSA at room temperature for 2 h and goat anti-mouse-IgG-HRP (1:20,000, 31430, Invitrogen) in PBS-0.05% Tween-5% BSA for 1 h. Bound antibodies were detected using the ECL immunoblotting detection system (NEL103001EA, PerkinElmer).

Statistics

Statistical parameters, including the exact value of n, precise measures (mean ± SD in all Figures, with the exception of the mean ± SEM in **Figure 4**), statistical significance, and tests used for each analysis are reported in the figures and figure legends. Analyses were performed using GraphPad Prism (GraphPad Software Inc.).

For the pSTAT5-NT experiments, one donor represents one experiment. For the [3H]AA assays, the number of experiments is indicated and certain experiments were repeated on cells from the same donor. The number of donors is indicated in certain figure legends.

Correlations between two variables were evaluated by Pearson's correlation and linear regression.

Data were analyzed using the two-tailed unpaired *t*-test for two groups or ANOVA with Tukey's correction for multiple comparisons for data with a Gaussian distribution according to the D'Agostino & Pearson omnibus test. For data that were not Gaussian, the Mann-Whitney non-parametric test was used to compare two groups and the Kruskal-Wallis test when more than two groups were compared. If the Kruskal-Wallis test was significant, two-by-two comparisons were conducted to identify groups that differed, but applying a Bonferroni correction. The level of significance is indicated as $^*p < 0.05$, $^{**}p < 0.01$, and $^{***}p < 0.001$ in all figures.

RESULTS

The Enzymatic Activity of PLA2G1B on CD4 T-Cell Membranes Is Increased by gp41

To formally demonstrate that the effect of HIV VP plasma on CD4 T cells is due to the enzymatic activity of PLA2G1B we performed additional experiments to complete our previous article (1). We first determined the IC50 of three different PLA2 inhibitors, varespladib, pentapeptide, and soluble mouse PLA2R1 receptor (sPLA2R1), on PLA2G1B protein in our standard IL-7-induced pSTAT5-NT inhibition assay (**Supplementary Figure 1A**). Based on the determined IC50s, we treated VP plasma with the inhibitors. All three almost completely blocked the effect of VP plasma on CD4 T cells (**Figure 1A**). We obtained similar results when VP plasma was treated with the anti-PLA2G1B mAb 14G9, selected to inhibit the enzymatic activity of PLA2G1B (**Figure 1B**). These results

confirm that the inhibitory activity of VP on the CD4 T-cell response is dependent on the enzymatic activity of PLA2G1B.

We previously showed that gp41 is involved in the inhibitory activity of PLA2G1B in VP plasma and that it can increase such activity on the pSTAT5-NT response in CD4 T cells (1). This effect is likely due to an increased enzymatic activity of PLA2G1B on the CD4 T-cell membrane. Thus, we developed an assay to directly study the effect of gp41 on the enzymatic activity of PLA2G1B on the cell surface membranes of CD4 T cells. PLA2 family proteins are known to release fatty acids by digesting lipid membranes. One of the hallmarks of PLA2G1B activity on cell membranes is the release of arachidonic acid (AA). Thus, we labeled primary CD4 T cells purified from HD with tritiated arachidonic acid [3H]AA. The IC50 of the inhibitory activity of PLA2G1B on the pSTAT5-NT response in CD4 T cells (IC50 = 77 nM, **Figure 1C**) was very similar to the EC50 of PLA2G1B activity measured by monitoring the release of [3H]AA in cell supernatants (EC50 = 78 nM, **Figure 1D**), with a release of AA proportional to the PLA2G1B concentration. More remarkably, there was a positive correlation between the release of AA and the inhibition of pSTAT5-NT (**Figure 1E**). To demonstrate that the [3H]AA release upon PLA2G1B treatment of CD4 T cells is an appropriate assay to study the enzymatic activity of PLA2G1B, we studied the effect of the catalytic-site mutant H48Q (**Figure 1F**) and that of several PLA2 enzymatic inhibitors (**Figure 1G** and **Supplementary Figure 1B**) in this assay. H48Q was previously shown to inhibit the PLA2G1B-dependent induction of aMMDs, inhibition of pSTAT5-NT and digestion of phosphatidylserine on the membrane of primary human CD4 T cells (1). As expected, the catalytic-site mutant H48Q showed no activity in this assay (**Figure 1F**) and all PLA2 enzymatic inhibitors, varespladib, pentapeptide (**Figure 1G**), sPLA2R1, and the anti-PLA2G1B mAb 14G9 (**Supplementary Figure 1B**), inhibited the [3H]AA release in a dose-dependent manner. Furthermore, inactive proPLA2G1B, in which the propeptide blocks the active catalytic site and enzymatic activity, did not induce [3H]AA release (**Figure 1H**). In further support of the correlation between pSTAT5-NT inhibition and PLA2G1B enzymatic activity (**Figure 1E**), the IC50s of varespladib, pentapeptide and sPLA2R1 in the [3H]AA release assay (**Figure 1G** and **Supplementary Figure 1B**) were similar to those in the pSTAT5-NT assay (**Supplementary Figure 1A**). In addition, the enzymatic activity showed complete specificity relative to PLA2GIIA and PLA2GIID but PLA2GX was more active than PLA2G1B (**Supplementary Figure 1C**). Notably, the inhibitory effect in HIV VP plasma was blocked by anti-PLA2G1B but not anti-PLA2GX Abs (1) and PLA2GX protein was not detected in HIV plasma. Overall, these results suggest that the enzymatic activity of PLA2G1B in HIV VP plasma on CD4 T-cell membranes controls intracellular events, such as pSTAT5-NT.

We observed that recombinant gp41 protein increases PLA2G1B enzymatic activity on the membrane of CD4 T cells in a gp41 dose-dependent manner using the [3H]AA release assay (**Figure 1I**), with a significant increase from 34 to 340 nM of gp41 (**Figure 1J**, $p < 0.01$). The observation that the activity of PLA2G1B was significantly higher with 136 nM than 34 nM of gp41 for each PLA2G1B concentration tested (middle panel, **Figure 1J**, $p < 0.01$) confirms that PLA2G1B activity is regulated by gp41 in a dose-dependent manner. PLA2G1B activity was more than 20-fold higher with 340 nM of gp41 than with PLA2G1B alone (63 nM, $p < 0.0022$). Overall, these results confirmed our previous observations using the pSTAT5-NT assay. Gp41 can increase the effect of PLA2G1B on CD4 T cells and showed that gp41 directly increases the enzymatic activity of PLA2G1B on the membranes of CD4 T cells.

PLA2G1B Directly Interacts With gp41 Protein

Gp41 has been shown to bind to CD4 T-cell membranes (4). It led us to postulate that gp41 increases the enzymatic activity of PLA2G1B on CD4 T cells by interacting with CD4 T-cell membranes and PLA2G1B, which would increase the PLA2G1B concentration at the cell membrane and, thus, its enzymatic activity. We first tested the interaction of gp41 and PLA2G1B by solid-phase microplate binding assays. Gp41 from two different HIV strains, D117III and MN, bound to PLA2G1B when it was used to coat microwells, whereas other control proteins with the same tag, to reveal protein binding, did not (CTL1: EFF1 (11), CTL2: IF38 (12), **Figures 2A, B**). The reverse experiments with coated gp41, from the same two HIV strains (**Figures 2C, D**) confirmed the interaction between PLA2G1B and gp41. We then tested the interaction of recombinant gp41 and PLA2G1B in solution *in vitro* by pull-down assays of gp41. When gp41 was pulled-down (**Figure 2E**) we observed that PLA2G1B was present in the pulled-down proteins (**Figure 2E**), whereas no PLA2G1B was observed upon pull-down with beads in the absence of gp41 (**Figure 2E**). This experiment was repeated five times with gp41 D117III and three times with gp41 MN (**Supplementary Figure 2**). Therefore, these results indicate that PLA2G1B can directly bind to gp41. It suggests that this interaction could increase PLA2G1B activity on CD4 T-cell membranes after the binding of gp41 to the membrane.

Several gC1qR-binding Proteins Encoded by Human Pathogens can Increase PLA2G1B Activity on CD4 T-Cell Membranes

Gp41 and its conserved sequence 3S are known to bind to the gC1qR (4, 5). We previously showed that inhibition of the CD4 T-cell response due to PLA2G1B activity in VP plasma is 3S-dependent and that the 3S peptide alone can increase the inhibitory activity of PLA2G1B on CD4 T cells (1). Thus, we postulated that gp41 may bind to the gC1qR to increase PLA2G1B activity on CD4 T-cell membranes. The gC1qR is an innate sensor known to bind to several proteins of microbial origins (6). One possibility is that the gC1qR-dependent regulation of PLA2G1B activity may be a common mechanism used by pathogens to inhibit CD4 T-cell responses and impair the immune response.

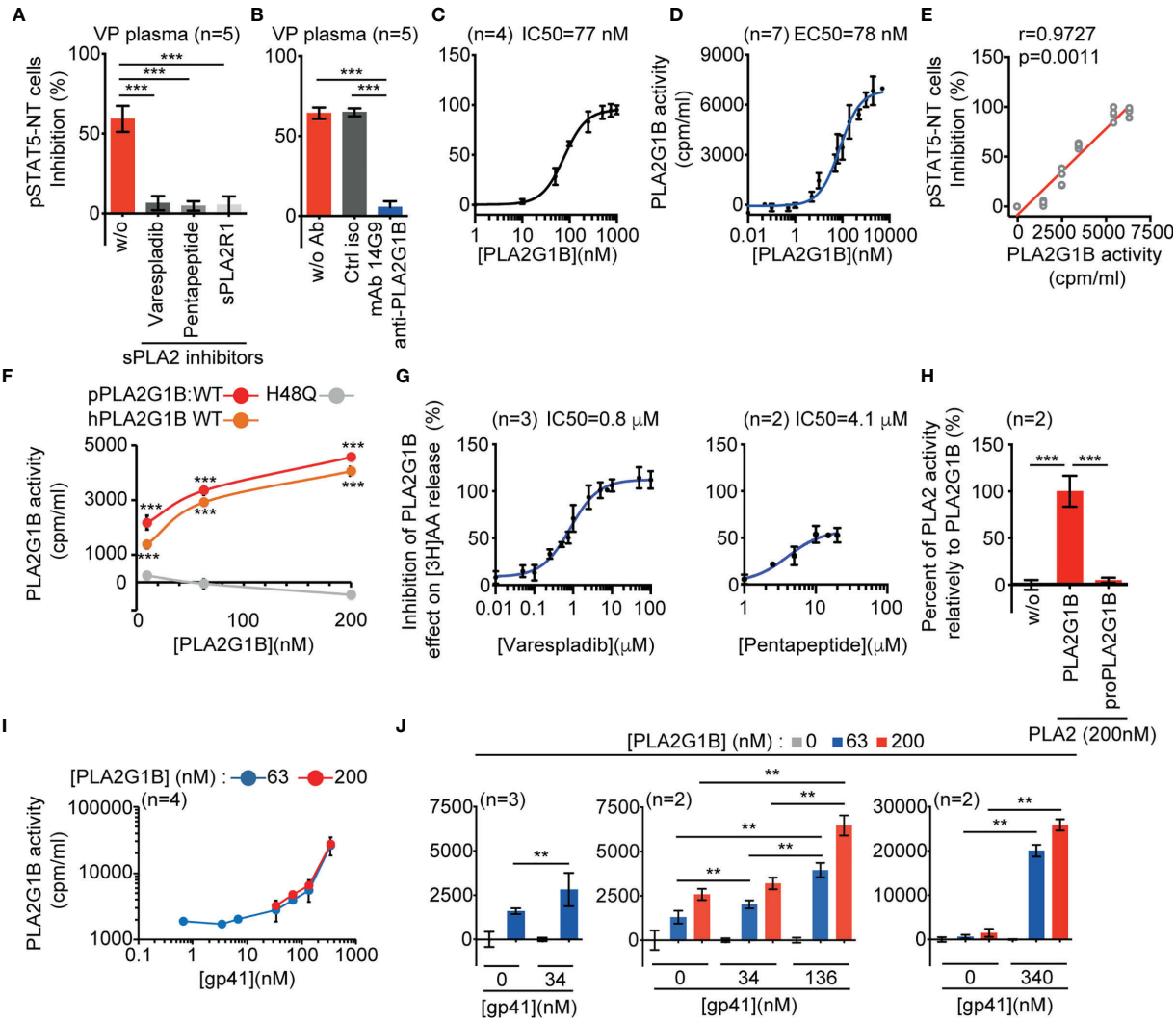

FIGURE 1 | HIV gp41 protein increases PLA2G1B enzymatic activity on CD4 T-cell membranes. **(A, B)** The sPLA2 inhibitors varespladib, pentapeptide, and sPLA2R1 and the anti-PLA2G1B mAb 14G9 strongly inhibit PLA2G1B activity in HIV viremic plasma. Purified HD CD4 T cells from two donors **(A)** and three donors **(B)** were treated with 3% of VP plasma from five viremic HIV patients together with varespladib (50 μM), pentapeptide (15 μM), sPLA2R1 (160 nM), or not **(A)** or control isotype (ctrl iso) or 14G9 mAb (667 nM, B) and the pSTAT5-NT cell response to IL-7 was analyzed by confocal microscopy. **(C)** PLA2G1B inhibits the pSTAT5-NT cell response to IL-7 in a dose-response manner. HD CD4 T cells were purified from four donors. The IC50 value is indicated. Results are shown as the mean ± SD of the percentage of pSTAT5-NT cell inhibition for A-C. **(D)** PLA2G1B activity can be followed in a dose-response manner on human CD4 T cells labeled with tritiated arachidonic acid. CD4 T cells purified from four donors were incubated with several concentrations of PLA2G1B (0.1 nM-5 μM) for 2 h. Then, the release of [3H]-AA in the cell supernatant due to PLA2G1B activity was quantified with a radioactivity counter (tri-Carb 2800 TR liquid scintillation analyzer, Perkin Elmer). Results are shown as the mean ± SD of PLA2G1B activity in cpm/mL from a pool of seven experiments. The EC50 value is indicated. **(E)** pSTAT5-NT cell inhibition positively correlates with PLA2G1B enzymatic activity on [3H]-AA-labeled CD4 T cells. Potential correlations were analyzed using the Pearson r test and a linear regression is presented. **(F)** [3H]-AA release is dependent on PLA2G1B enzymatic activity. [3H]-AA-labeled CD4 T cells were treated with several concentrations (10, 63, 200 nM) of WT human (hPLA2G1B) or WT or the catalytic-site mutant H48Q porcine PLA2G1B (pPLA2G1B). Results are shown as the mean of PLA2G1B activity ± SD of one experiment with the treatment in triplicate. **(G)** Varespladib, and pentapeptide strongly inhibit PLA2G1B enzymatic activity on [3H]-AA-labeled CD4 T cells. Results are shown as the percentage of inhibition of PLA2G1B activity on cells treated with PLA2G1B (65 nM) and several doses of inhibitors. IC50 values are presented. **(H)** ProPLA2G1B is inactive in the [3H]-AA release assay on CD4 T-cell membranes. [3H]-AA-labeled CD4 T cells were treated in triplicate with PLA2G1B or proPLA2G1B at 200 nM. Results are shown as the percentage of activity with proPLA2G1B relative to that of PLA2G1B. **(I, J)** HIV gp41 increases PLA2G1B activity in a dose-dependent manner on human CD4 T cells. [3H]-AA-labeled CD4 T cells were incubated alone or with PLA2G1B (63 nM or 200 nM) in the presence or not of several concentrations of recombinant gp41 protein (0.68 nM-340 nM). Results are shown as the mean ± SD from a pool of four experiments for I and n = 2-3 experiments for **(J)** $^{**}p < 0.01$ and $^{***}p < 0.001$ by two-way ANOVA with Tukey's correction for multiple comparisons **(A, B, F, H)** and the Kruskal-Wallis test, followed by the Mann-Whitney test with p-values adjusted for multiple comparisons between groups **(J)**. For F, only comparisons between H48Q and WT hPLA2G1B or pPLA2G1B at each PLA2G1B concentration are shown.

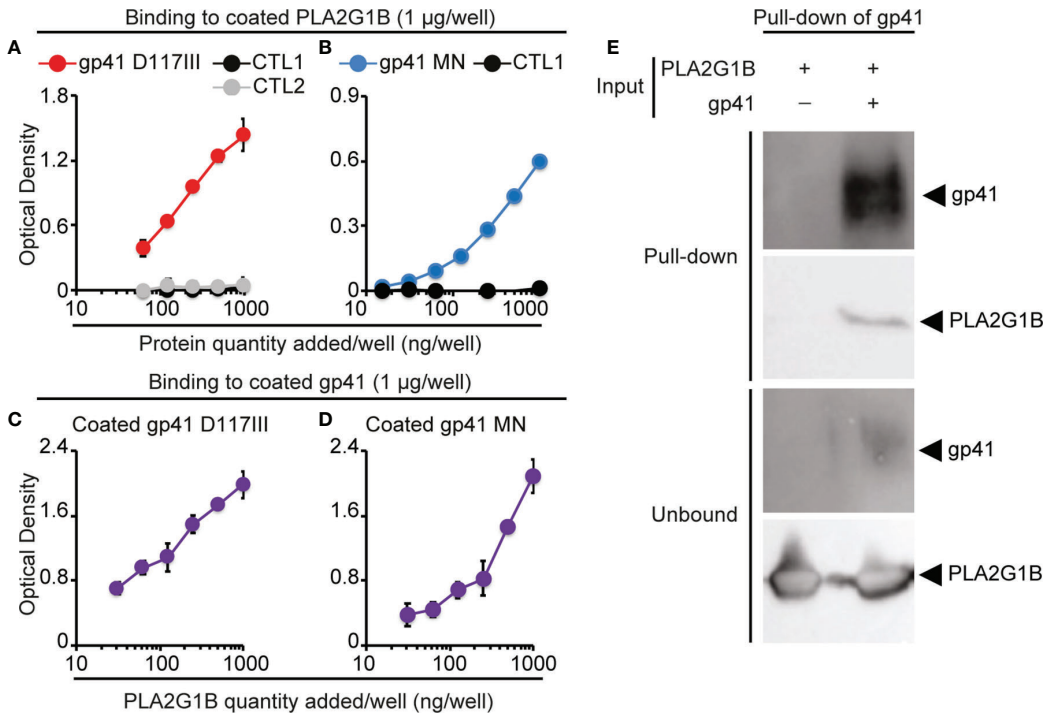

FIGURE 2 | PLA2G1B directly binds to gp41. **(A, B)** gp41 binds to coated PLA2G1B by ELISA. Binding to coated PLA2G1B of serial dilutions (0-1 µg/well) of gp41 (D117III strain on A and MN strain on B), or unrelated proteins (CTL1: EFF-1 on A and B or CTL2: IF38 on A). **(C, D)** PLA2G1B binds to coated gp41 by ELISA. Binding of serial dilutions (0-1 µg/well) of PLA2G1B to coated gp41 (D117III on C, or MN on D) was tested in triplicate by ELISA. Results are shown as the mean ± SD of the OD value of one representative experiment among two **(A)**, five **(B)**, one **(C)** and five **(D)**. **(E)** gp41 binds to PLA2G1B in pull-down assays. Recombinant PLA2G1B protein was incubated with strep-tagged-gp41 (D117III strain, gp41+PLA2G1B) or not (PLA2G1B only). PLA2G1B-gp41 complexes were pulled-down with strep-tactin XT-beads that pull-down gp41. Pulled-down products and unbound proteins were revealed by immunoblotting with goat polyclonal anti-gp41 Ab or mouse anti-PLA2G1B mAb. One representative experiment of five experiments with similar results with D117III gp41 is presented. Similar results were obtained in three experiments with MN gp41 (**Supplementary Figure 2**).

We thus tested the effect of two representative microbial proteins known to bind to the gC1qR (6) on the enzymatic activity of PLA2G1B on CD4 T-cell membranes: the viral HCV core protein (5, 13) and the bacterial protein A of *Staphylococcus aureus* (SA) (14, 15). Both HCV core protein (**Figures 3A, B**) and SA protein A (**Figure 3C**) significantly increased the enzymatic activity of PLA2G1B on the membranes of CD4 T cells in a microbial protein dose-dependent manner. HCV core protein was a very potent inducer of PLA2G1B enzymatic activity. The effect of HCV core was significant with 238 nM of HCV core (**Figure 3B**, $p < 0.001$). PLA2G1B (at 63 nM) activity was 26-fold higher in the presence of 595 nM HCV core than PLA2G1B alone at the same concentration (**Figure 3B**). Although SA protein A was also a significant inducer of PLA2G1B enzymatic activity (**Figure 3C**, $p < 0.001$), the effect was less strong, showing only three-fold more PLA2G1B activity with 1,190 nM SA protein A and PLA2G1B (at 200 nM) than with PLA2G1B alone. Because gp41, HCV core, and SA protein A are all gC1qR-binding proteins, these results support the hypothesis that several microbial proteins could play the role of cofactor in the PLA2G1B/cofactor system and increase the enzymatic activity of PLA2G1B *via* the binding to the gC1qR.

gC1qR Plays a Critical Role in the Regulation of PLA2G1B Enzymatic Activity by gp41

We sought a CD4 T-cell line that could be labeled with [3H]AA to directly demonstrate the role of the gC1qR in the regulation of PLA2G1B activity by microbial proteins. We used the 3S peptide, as it has been shown to bind to the gC1qR (4, 5). We found that gC1qR is expressed by Jurkat T cells and that the gp41-derived 3S peptide (**Figures 4A, B**) can increase the enzymatic activity of PLA2G1B on the membranes of Jurkat T cells. The effect of the 3S peptide required pretreatment of the Jurkat T cells for 4 or 21 h before the addition of PLA2G1B to significantly increase its enzymatic activity relative to scrambled 3S peptide-treated cells, with a major effect occurring after 21 h of pretreatment (**Figure 4A**, $p < 0.0001$). We confirmed this last experimental condition to be the best for studying the effect of 3S on the enzymatic activity of PLA2G1B in several experiments (**Figure 4B**, $p < 0.0001$).

We then generated clones of Jurkat T cells deprived of gC1qR (gC1qR KO) using the CRISPR-Cas9 method. We confirmed the loss of the gC1qR protein in gC1qR KO cells relative to WT Jurkat CD4 T cells by immunoblotting using two anti-gC1qR

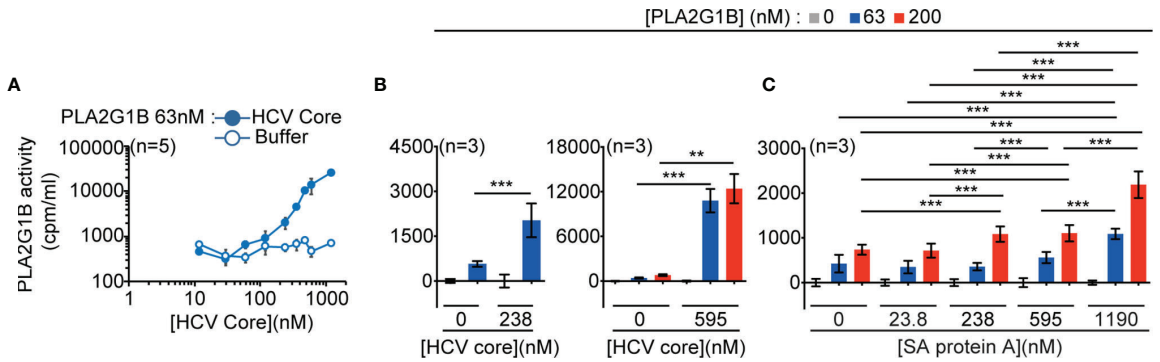

FIGURE 3 | PLA2G1B activity on CD4 T cells is increased by several gC1qR-binding microbial proteins. **(A, B)** HCV core increases PLA2G1B activity on human CD4 T cells in a dose-dependent manner. [3H]-AA-labeled CD4 T cells were incubated alone or with PLA2G1B (63 nM or 200 nM) in the presence or not of several concentrations of recombinant HCV Core protein (11.9 nM-1190 nM) or equivalent concentrations of buffer alone (Buffer for A or 0 nM for B). **(C)** *Staphylococcus aureus* (SA) protein A increases PLA2G1B activity on human CD4 T cells in a dose-dependent manner. [3H]-AA-labeled CD4 T cells were incubated alone or with PLA2G1B (63 nM or 200 nM) in presence or not of several concentrations of SA protein A (23.8 nM-1190 nM). Results are shown as the mean ± SD from a pool of five experiments for A, and three experiments for B and C. $^{**}p < 0.01$ and $^{***}p < 0.001$ by the Kruskal-Wallis test followed by the Mann-Whitney test, with p-values adjusted for multiple comparisons between groups.

mAbs that bind to different epitopes of the gC1qR protein (**Figure 4C**). Notably, 3S peptide significantly increased the enzymatic activity of PLA2G1B on WT cells relative to scrambled 3S peptide ($p < 0.01$), whereas there was no significant difference in PLA2G1B activity between 3S and scrambled 3S peptide-treated cells deficient for the gC1qR (**Figure 4D**). Overall, these results show that gp41 can increase PLA2G1B activity through its conserved 3S region in a gC1qR-dependent manner.

3S-Like Motifs Are Present in Proteins Encoded by Several Human Pathogens

We next screened protein sequence databases for similarity to identify other microbial proteins that could regulate the enzymatic activity of PLA2G1B on CD4 T cells and inhibit the immune response using Blastp with an expect threshold of 100 and a 3S amino-acid substitution matrix (AASM) based on the 3S sequence of the peptide with cofactor activity (**Figure 4** and reference (1) and major amino-acid substitutions found in natural HIV-1 sequence variants (**Supplementary Figure 3**). We identified 42 peptides with 3S-like motifs (**Supplementary Figure 3**). Eleven selected peptides encoded by human pathogens are presented in **Supplementary Table 1**. They are derived from eight bacterial species (*Porphyromonas gingivalis* (7, 8, 16, 17), *Proteus mirabilis* (18), *Leptospira weilii* (19), *Terrisporobacter glycolicus* (20), *Bacteroides fragilis* (21, 22), *Aggregatibacter actinomycetemcomitans* (23, 24), *Porphyromonas somerae* (25), *Aggregatibacter aphrophilus* (23, 26) and one fungus (*Candida glabrata* (27, 28) that are involved in several human infections or have been shown to be associated with autoimmune diseases or with an increased risk of developing cancer (more detailed references on these pathogens are provided in **Supplementary Table 1** and in the **supplementary Material File**). These results show that 3S-like motifs are not restricted to HIV or viruses but are also present in several pathogens, such as bacteria and fungi.

PLA2G1B Plays a Role in the Inhibitory Activity of Pancreatic Ductal Adenocarcinoma Plasma on the pSTAT5-NT Response in CD4 T Cells

Among pathogens encoding proteins with 3S-like motifs, bacterial infection with *P. gingivalis* has been shown to be associated with an increased risk of gastrointestinal cancer, including pancreatic cancer (7–9). This pathogen encodes seven peptides with 3S-like motifs (**Supplementary Figure 3**). Based on previous publications, amino acids W6, S7, N8, and S10 of the 3S HIV peptide PWNAS**WSNK**SLDDIW (**Supplementary Table 1**) are the most critical for induction of the NKp44L by the 3S peptide (29). This effect is due to the binding of 3S to the gC1qR (4), as for the increased of PLA2G1B activity described here. We thus focused on the OmpA pg peptide of *P. gingivalis*, which is the only one from this pathogen that contains W6, S7, N8, and S10 (**Supplementary Table 1** and **Supplementary Figure 3**). We postulated that the OmpA Pg peptide may regulate PLA2G1B activity. If this is true, it is possible that PDAC plasma may contain PLA2G1B activity that inhibits the CD4 T-cell response, based on our previous findings with HIV VP plasma. Thus, 3S-like peptides derived from *P. gingivalis* could play the role of cofactor in increasing PLA2G1B activity.

We first tested the effect of the OmpA Pg peptide on the enzymatic activity of PLA2G1B in parallel with the 3S peptide, used as a positive control (**Figure 5A**). As for 3S from gp41, OmpA Pg increased PLA2G1B activity over that of cells treated with scrambled 3S. We also found there to be no difference between the active PLA2G1B and proPLA2G1B concentrations in PDAC and HD plasma (**Figure 5B**), similar to our observations for HIV VP and HD plasma (1).

Treatment of CD4 T cells with 3% PDAC plasma (PDACp) impaired the pSTAT5-NT response to IL-7 (38% inhibition) to a similar level as recombinant PLA2G1B protein (38% of inhibition, **Figure 5C**). Furthermore, this effect was partially

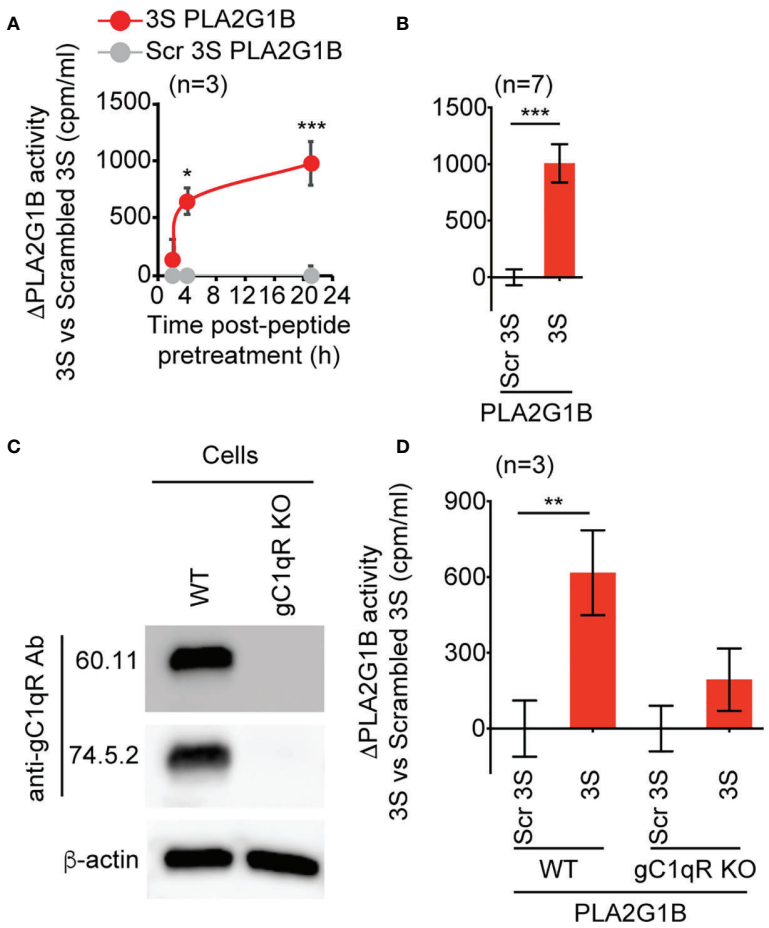

FIGURE 4 | The 3S/gp41 peptide regulates PLA2G1B activity in a gC1qR-dependent manner. **(A, B)** The HIV 3S peptide increases PLA2G1B activity on human Jurkat T cells. [3H]AA-labeled Jurkat T cells were pretreated with 3S gp41 (3S) or scrambled 3S (Scr 3S) peptides (11 μM) for various times (2, 4, or 21 h for A) or 21 h (for B) and incubated alone or with PLA2G1B (200 nM). **(C)** The gC1qR protein is detected in WT but not in gC1qR-deficient (gC1qR KO) Jurkat T cells by immunoblot. Two different anti-gC1qR mAbs were used (60.11 and 74.5.2), as well as anti-ß-actin mAb as an endogenous control of protein load. **(D)** The 3S peptide increases PLA2G1B activity on WT but not on gC1qR KO cells. WT and gC1qR KO [3H]-AA-labeled Jurkat T cells were pretreated with 3S or Scr 3S peptides at 11 μM for 21 h. Then, peptide-pretreated cells were incubated with PLA2G1B (200 nM) for 2 h. Results are expressed as the mean ± SEM of a pool of three **(A, D)** and seven **(B)** experiments performed in triplicate and as ΔPLA2G1B activity (activity with the 3S peptide minus that with the Scr 3S peptide). The level of [3H]AA released in the cell supernatant was quantified in cpm/mL. $^{*}p < 0.05$, $^{**}p < 0.01$ and $^{***}p < 0.001$ by two-way ANOVA with Tukey's correction for multiple comparisons **(A, D)** or an unpaired t-test **(B)**.

dependent on PLA2G1B activity, as anti-PLA2G1B mAb significantly inhibited the activity of PDACp relative to cells treated with plasma alone or plasma treated with a control isotype antibody ($p < 0.01$, **Figure 5C**). Anti-PLA2G1B mAb (14G9) significantly inhibited PDACp activity relative to a control isotype ($p < 0.01$, **Figure 5D**). PLA2G1B appeared to be involved in the plasma of only certain PDAC patients, with 25 to 45% inhibition of PDAC plasma activity by anti-PLA2G1B mAb for 66% (4/6) of the plasma samples tested (**Figure 5D**). Overall, these data suggest that plasma from patients with PDAC can inhibit the CD4 T-cell response to IL-7 by a mechanism likely similar to that we describe for HIV plasma involving the PLA2G1B/cofactor system. It is possible that the PLA2G1B activity in PDAC plasma may be increased by a cofactor derived from *P. gingivalis*, as it encodes a protein containing a 3S-like motif that increases PLA2G1B enzymatic activity at the cell surface membrane.

DISCUSSION

In a recent study, we demonstrated that the PLA2G1B/cofactor system is an inhibitor of CD4 T cells that is involved in the induction of anergy and lymphopenia of CD4 T cells in HIV-infected patients (1). PLA2G1B induces aMMDs on CD4 T cells that trap and inactivate cytokine receptors. PLA2G1B inhibitory activity in HIV VP plasma is dependent on the HIV-1 gp41 envelope protein. We showed that gp41, through a conserved 3S motif, drives PLA2G1B activity on CD4 T cells.

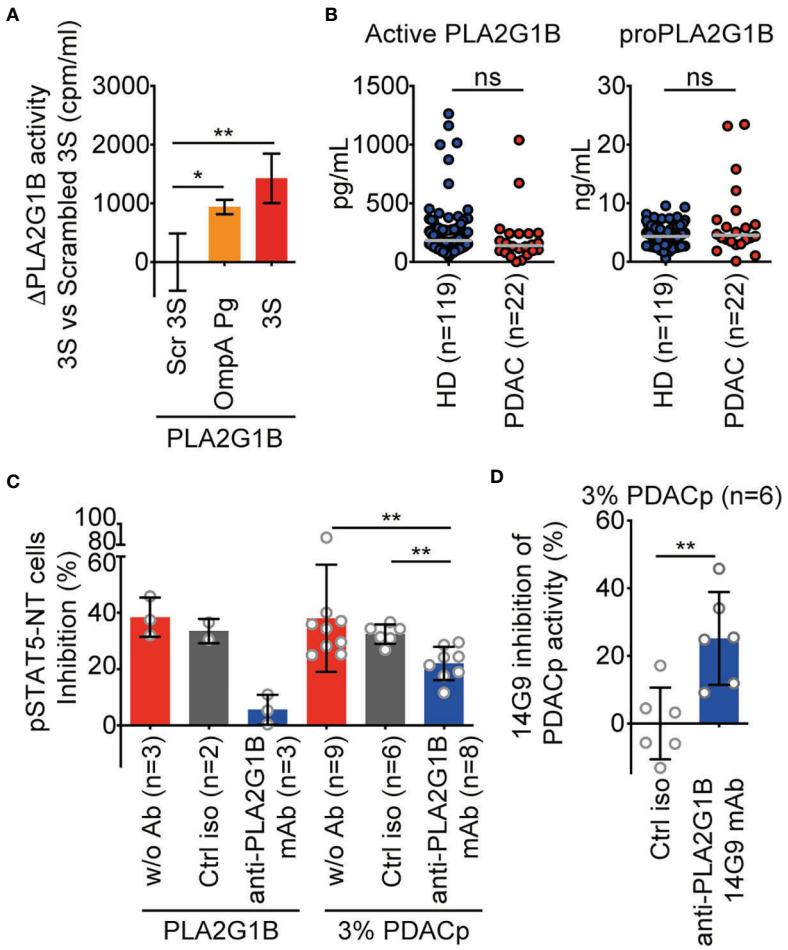

FIGURE 5 | PLA2G1B is involved in PDAC plasma inhibition of the CD4 T-cell pSTAT5-NT response. **(A)** A 3S-like peptide from *P. gingivalis* (OmpA Pg) increases PLA2G1B enzymatic activity. [3H]-AA-labeled Jurkat T cells were pretreated with 3S, OmpA Pg or scrambled 3S (Scr 3S) peptides (11μM) for 21 h and incubated alone or with PLA2G1B (200 nM). Results are shown as the mean ± SD of PLA2G1B activity with the 3S or OmpA Pg minus PLA2G1B activity with Scr 3S from one representative experiment of two with similar results. **(B)** ELISA quantification of active PLA2G1B and proPLA2G1B in plasma from HD and PDAC donors (the median is shown). **(C)** Anti-PLA2G1B mAb inhibits PLA2G1B activity in PDAC plasma. HD CD4 T cells from three donors were treated with PLA2G1B (75 nM), 3% of PDAC plasma (PDACp) alone (w/o Ab, n = 9 plasma samples), with control isotype (ctrl iso, 667 nM, n = 6 plasma samples) or anti-PLA2G1B mAb (14G9, 667 nM, n = 8 plasma samples) and the pSTAT5-NT cell response to IL-7 was analyzed by confocal microscopy. Results are shown as the mean ± SD of percentage of pSTAT5-NT cells inhibition. **(D)** Heterogeneity of anti-PLA2G1B mAb 14G9 inhibition of PLA2G1B activity in PDAC plasma. Results are shown as the mean ± SD of the percentage of inhibition of PDACp activity from six patients on pSTAT5-NT by 14G9 relative to that of control isotype-treated plasma. *$p < 0.05$, and **$p < 0.01$, by two-way ANOVA with Tukey's correction for multiple comparisons for A, by the Mann-Whitney test for B and D, and by the Kruskal-Wallis test followed by the Mann-Whitney test, with p-values adjusted for multiple comparisons between groups, for C. ns, non significant.

However, the mode of action of gp41 to increase PLA2G1B activity on CD4 T cells was yet to be elucidated.

We investigated this mechanism by developing a radioactive assay based on the measurement of [3H]AA release upon treatment of [3H]AA-labeled CD4 T cells with PLA2G1B. We demonstrated that this assay measures the enzymatic activity of PLA2G1B, as the H48Q catalytic site mutant was inactive (**Figure 1F**) and all PLA2G1B enzymatic inhibitors studied (varespladib, pentapeptide, soluble mouse PLA2R1 receptor), a neutralizing anti-PLA2G1B mAb, and the propeptide inhibited the release of [3H]AA by PLA2G1B (**Figures 1G, H** and **Supplementary Figure 1B**). Moreover, PLA2G1B enzymatic activity measured by this assay (**Figure 1D**) is strongly and positively correlated with PLA2G1B inhibitory activity on CD4 T cells as measured by the inhibition of IL-7-induced pSTAT5-NT (**Figures 1C, E**). More importantly, we showed that gp41 increases the enzymatic activity of PLA2G1B on the membranes of CD4 T cells (**Figures 1I, J**), explaining the gp41-driven increase of the inhibitory activity of PLA2G1B on CD4 T-cell response to IL-7 that we previously observed with the plasma of HIV-infected viremic patients. We also further defined the various steps of the mechanism involved.

In vitro, high amounts of PLA2G1B (from 10 nM to 200 nM) directly acted on CD4 T-cell membranes (**Figure 1D**). This indicates that its substrates (phospholipids) are spontaneously expressed at the surface of CD4 T cells. However, the

concentration of PLA2G1B in the plasma of VP is very low (0.025 nM) and thus it cannot act alone. Therefore, cofactor(s) act at the surface of CD4 T cells by either increasing the presence of PLA2G1B or by modifying the quality or quantity of substrate accessible to PLA2G1B. Two types of mechanism are possible.

Here, we showed that gp41 directly interacts with PLA2G1B by solid-phase microplate binding and pull-down assays (**Figure 2**). Gp41 was shown to bind *via* its conserved 3S domain to the gC1qR on CD4 T-cell membranes (4). In addition, the 3S peptide increased PLA2G1B enzymatic activity on WT but not on gC1qR KO Jurkat cells (**Figure 4**). Overall, these results suggest that a gp41-PLA2G1B complex may bind to the gC1qR, resulting in an increase in the PLA2G1B concentration at the CD4 T-cell membrane followed by an increased enzymatic activity on the membrane and the inhibition of CD4 T-cell function.

Alternatively, another mechanism concerning the mode of action of the PLA2G1B/gp41 pair is possible. Based on the pluripotent role of the gC1qR (6), gp41 could also act by changing the membrane composition of CD4 T cells by a gC1qR-dependent mechanism that would increase the concentration of the phospholipid substrates of PLA2G1B, thus increasing its activity. Consistent with this hypothesis, it was shown that 3S binding to gC1qR can induce the fusion of exocytotic vesicles with CD4 T-cell membranes (4). The fusion of exocytotic vesicles with the plasma membrane changes its lipid composition, which could also increase PLA2G1B activity. Both mechanisms, together or independently, could increase the fluidity of the membrane and the formation of aMMDs, which induces anergy of the CD4 T cells by blocking the function of physiological receptors.

The gC1qR is an innate sensor that binds to several pathogens (6). Our discovery of a gC1qR-dependent activation of PLA2G1B by gp41 led us to hypothesize that other gC1qR-binding microbial proteins could also increase PLA2G1B activity. We demonstrate that two other microbial proteins that bind to gC1qR, HCV core and *Staphylococcus aureus* protein A, also increase the enzymatic activity of PLA2G1B on CD4 T cells (**Figure 3**). These observations suggest that PLA2G1B may also be involved in hepatitis C virus infection or several diseases due to *Staphylococcus aureus* infection. HCV core has been shown to bind to the gC1qR and to inhibit T-cell responsiveness and has been suggested to play a role in the persistence of HCV (13). Thus, PLA2G1B activity could also be increased by HCV core binding to the gC1qR in HCV-infected patients and contribute to the inhibition of T-cell responses and HCV persistence. *Staphylococcus aureus* infections, such as superficial skin infections (30), infective endocarditis (31) and sepsis (32) could also be affected by the PLA2G1B/SA protein A cofactor pair.

Importantly, we found that 3S-like motifs are present in several human infectious pathogens (**Supplementary Table 1** and **Supplementary Figure 3**) and that the one we tested increases the enzymatic activity of PLA2G1B (**Figure 5A**). This peptide is encoded by *P. gingivalis*, a Gram-negative anaerobic bacteria involved in periodontitis infection that is also associated with an increased risk of gastrointestinal cancer, including PDAC (90% of the pancreatic cancers) (7–9, 16). Among oral cancers, *P. gingivalis* has been found in oral squamous cell carcinoma (OSCC) and its role in carcinogenesis has been directly established (33). Numerous studies have shown that *P. gingivalis* may have systemic effects through its LPS (34). Very recently, *P. gingivalis* was directly identified inside pancreatic tumors (7). PDAC has also been shown to be associated with immune dysfunctions involving a paucity of dendritic cells (35) and the upregulation of PD-L1 (36). T-cell dysfunction, as well as decreased CD4 and CD8 counts, have also been described in PDAC (37), as in the terminal stages of HIV-infected patients.

The results reported here may partially explain such immunological defects. Plasma from PDAC patients diminished IL-7-induced pSTAT5-NT of HD CD4 T cells (**Figure 5C**). This inhibitory activity was partially due to PLA2G1B, as anti-PLA2G1B mAb, but not a control isotype, partially blocked the effect (**Figure 5C**). A detailed analysis of the effect of an anti-PLA2G1B mAb relative to that of a control isotype antibody on six plasma samples showed heterogeneous involvement of PLA2G1B. Only 25 to 45% specific inhibition of PDAC plasma activity with anti-PLA2G1B mAb was found in the plasma of 4/6 patients (**Figure 5D**). Heterogeneity of this response may reflect the stage of the disease, as well as the intensity of the degradation of the immune system. Further studies should be performed to clarify this point. One of the hallmarks of PLA2G1B/cofactor activity on CD4 T cells is the release of arachidonic acid. Notably, high levels of arachidonic acid in plasma, which could be due to higher PLA2G1B/cofactor system activity, have been positively associated with the risk of pancreatic cancer (38).

At both the cellular and molecular level, our data support the hypothesis that the PLA2G1B/cofactor system may be involved at least in certain patients. The hypothesis that *P. gingivalis* may be a cofactor merits further investigation. The 3S-like motif is exposed at the surface of the bacteria, as it is part of an outer membrane protein called OmpA family protein (WP_097552551.1 in the NCBI protein database, **Supplementary Figure 3** and **Supplementary Table 1**). In addition, it may act directly on CD4 T cells (39) and on their membranes, as OmpA Pg peptide increases PLA2G1B enzymatic activity (**Figure 5A**). The role of the PLA2G1B/cofactor system in PDAC plasma needs to be further investigated. Such studies would help our understanding of the immune disorders found in PDAC patients.

The origin of the two components of the PLA2G1B/cofactor system need to be clarified. We previously found that the major source of PLA2G1B is the pancreas, followed by the duodenum, jejunum, and ileum [see **Supplemental Data** in (1)]. We also observed that *pla2g1b* transcripts are primarily expressed in the pancreas, followed by the duodenum, whereas they were found in low amounts in lymphoid cells, including CD4 T cells, and they were almost undetectable in myeloid cells (see **Supplemental Data** in [1)]. According to these results, active PLA2G1B is mainly produced in the pancreas and intestinal tract from an inactive precursor (proPLA2G1B) that is activated by trypsin digestion and then participates in the digestion of phospholipids. The leaking of PLA2G1B may explain the presence of proPLA2G1B and active PLA2G1B in the blood. The origin of the cofactor appears to be specific for each disease.

Taking the examples studied here, it may be a component of an external protein of the microorganism (HIV, *P. gingivalis* and *Staphylococcus aureus*) or an internal protein recovered in the plasma after degradation of the microorganism. These cofactors are proteins with 3S-like motifs and proteins that bind to gC1qR and drive PLA2G1B activity *via* the gC1qR. As PLA2G1B is the active component of the PLA2G1B/cofactor system, the therapeutic potential of anti-PLA2G1B mAbs should also be tested in certain pathologies that involve the PLA2G1B/cofactor system to determine whether it will be a useful candidate to block PLA2G1B activity and restore CD4 T cells to improve immune responses and patient outcomes.

In conclusion, we provide lines of evidence of a PLA2G1B/cofactor system that inhibits CD4 T-cell function. It helps understanding of the physiopathology of various infections, including some infections involved in oncogenesis. This study further demonstrates the capacity of microbes to disable the immune system by hijacking the activity of a natural endogenous enzyme and making it harmful. Our results establish this study as a pivotal element in the understanding of impaired CD4 T-cell immune response upon infection.

DATA AVAILABILITY STATEMENT

The raw data supporting the conclusions of this article will be made available by the authors, without undue reservation.

ETHICS STATEMENT

The studies involving human participants were reviewed and approved by "Comité Consultatif de Protection des Personnes dans la Recherche Médicale" under the number 05-15 and was supported by the ANRS for the study of the effect of VP plasma on the pSTAT5-NT response of CD4 T cells. The study of PDAC plasma was registered under the number DC-2021-4516 by the Ministère de l'Enseignement Supérieur, de la Recherche et de l'Innovation. The patients/participants provided their written informed consent to participate in this study.

AUTHOR CONTRIBUTIONS

JP and JT conceived and designed the study. JP, AM, FB, and LJ conducted experiments at DIACCURATE. JP analyzed all data and performed enzymatic activity assays and LT provided expertise and feedback in the setting up of the assay. AM performed gp41 and PLA2G1B interaction studies. FB performed pSTAT5-NT assays. LJ performed ELISAs. AGS and BG provided expertise and feedback in the design of experiments to test the role of gC1qR. FF generated gC1qR KO cells. JP, JT and PP were involved in the identification of 3S-like motifs in microbes. AS selected and collected plasma samples from PDAC patients. JP and JT supervised the study. JT and PP secured funding. JP and JT wrote the manuscript with input from all authors. All authors contributed to the article and approved the submitted version.

FUNDING

This work was part of the ANRS program EP33.

ACKNOWLEDGMENTS

We are grateful to J.-F. Delfraissy and O. Lambotte that were principal investigators of the clinical study of HIV patients (the ANRS program EP33) and were involved in patient selection and the characterization of biological parameters. We thank G. Lambeau for helpful discussions and the gift of PLA2G1B proteins. We wish to thank E. Perret, P. Roux, A. Salles, and S. Shorte (UTechS PBI/C2RT, Institut Pasteur) for their microscopy expertise. We also wish to thank P. Casanova and S. Rosario (Service Prévention des Risques, Direction Ressources Techniques et Environnement, Institut Pasteur) for their help in the radioactivity platform. We are grateful to F. Rey, I. Fernandez, and P. Guardado Calvo for helpful discussions concerning the gp41 protein. We also thank B. Georges for the search for 3S-like peptide motifs in sequence databases. We gratefully acknowledge B. Malissen for his critical review of the manuscript.

SUPPLEMENTARY MATERIAL

The Supplementary Material for this article can be found online at: https://www.frontiersin.org/articles/10.3389/fimmu.2022.824746/full#supplementary-material

REFERENCES

1. Pothlichet J, Rose T, Bugault F, Jeammet L, Meola A, Haouz A, et al. PLA2G1B Is Involved in CD4 Anergy and CD4 Lymphopenia in HIV-Infected Patients. *J Clin Invest* (2020) 130:2872–87. doi: 10.1172/JCI131842
2. Lambeau G, Gelb MH. Biochemistry and Physiology of Mammalian Secreted Phospholipases A2. *Annu Rev Biochem* (2008) 77:495–520. doi: 10.1146/annurev.biochem.76.062405.154007
3. Vieillard V, Strominger JL, Debré P. NK Cytotoxicity Against CD4+ T Cells During HIV-1 Infection: A Gp41 Peptide Induces the Expression of an NKp44 Ligand. *Proc Natl Acad Sci USA* (2005) 102:10981–6. doi: 10.1073/pnas.0504315102
4. Fausther-Bovendo PH, Vieillard V, Sagan S, Bismuth G, Debré P. HIV Gp41 Engages Gc1qr on CD4+ T Cells to Induce the Expression of an NK Ligand Through the PIP3/H2O2 Pathway. *PloS Pathog* (2010) 6:1–14. doi: 10.1371/journal.ppat.1000975
5. Pednekar L, Valentino A, Ji Y, Tumma N, Valentino C, Kadoor A, et al. Identification of the Gc1qr Sites for the HIV-1 Viral Envelope Protein Gp41 and the HCV Core Protein: Implications in Viral-Specific Pathogenesis and Therapy. *Mol Immunol* (2016) 74:18–26. doi: 10.1016/J.MOLIMM.2016.03.016

6. Ghebrehiwet B, Geisbrecht BV, Xu X, Savitt AG, Peerschke EIB. The C1q Receptors: Focus on Gc1qr/P33 (C1qBP, P32, HABP-1)1. *Semin Immunol* (2019) 45:101338. doi: 10.1016/j.smim.2019.101338
7. Gnanasekaran J, Gallimidi AB, Saba E, Pandi K, Berchoer LE, Hermano E, et al. Intracellular Porphyromonas Gingivalis Promotes the Tumorigenic Behavior of Pancreatic Carcinoma Cells. *Cancers (Basel)* (2020) 12:1–14. doi: 10.3390/cancers12082331
8. Fan X, Alekseyenko AV, Wu J, Peters BA, Jacobs EJ, Gapstur SM, et al. Human Oral Microbiome and Prospective Risk for Pancreatic Cancer: A Population-Based Nested Case-Control Study. *Gut* (2018) 67:120–7. doi: 10.1136/gutjnl-2016-312580
9. Michaud DS, Izard J, Wilhelm-Benartzi CS, You DH, Grote VA, Tjønneland A, et al. Plasma Antibodies to Oral Bacteria and Risk of Pancreatic Cancer in a Large European Prospective Cohort Study. *Gut* (2013) 62:1764–70. doi: 10.1136/gutjnl-2012-303006
10. Celis-Gutierrez J, Blattmann P, Zhai Y, Jarmuzynski N, Ruminski K, Grégoire C, et al. Quantitative Interactomics in Primary T Cells Provides a Rationale for Concomitant PD-1 and BTLA Coinhibitor Blockade in Cancer Immunotherapy. *Cell Rep* (2019) 27:3315–30.e7. doi: 10.1016/J.CELREP.2019.05.041
11. Pérez-Vargas J, Krey T, Valansi C, Avinoam O, Haouz A, Jamin M, et al. Structural Basis of Eukaryotic Cell-Cell Fusion. *Cell* (2014) 157:407–19. doi: 10.1016/j.cell.2014.02.020
12. Fédry J, Liu Y, Péhau-Arnaudet G, Pei J, Li W, Tortorici MA, et al. The Ancient Gamete Fusogen HAP2 Is a Eukaryotic Class II Fusion Protein. *Cell* (2017) 168:904–915.e10. doi: 10.1016/j.cell.2017.01.024
13. Kittlesen DJ, Chianese-Bullock KA, Yao ZQ, Braciale TJ, Hahn YS. Interaction Between Complement Receptor Gc1qr and Hepatitis C Virus Core Protein Inhibits T-Lymphocyte Proliferation. *J Clin Invest* (2000) 106:1239–49. doi: 10.1172/JCI10323
14. Peerschke EIB, Bayer AS, Ghebrehiwet B, Xiong YQ. Gc1qr/P33 Blockade Reduces Staphylococcus Aureus Colonization of Target Tissues in an Animal Model of Infective Endocarditis. *Infect Immun* (2006) 74:4418–23. doi: 10.1128/IAI.01794-05
15. Nguyen T, Ghebrehiwet B, Peerschke EIB. Staphylococcus Aureus Protein A Recognizes Platelet Gc1qr/P33: A Novel Mechanism for Staphylococcal Interactions With Platelets. *Infect Immun* (2000) 68:2061–8. doi: 10.1128/IAI.68.4.2061-2068.2000
16. Olsen I, Yilmaz Ö. Possible Role of Porphyromonas Gingivalis in Orodigestive Cancers. *J Oral Microbiol* (2019) 11:1563410. doi: 10.1080/20002297.2018.1563410
17. Mei F, Xie M, Huang X, Long Y, Lu X, Wang X, et al. Porphyromonas Gingivalis and Its Systemic Impact: Current Status. *Pathogens* (2020) 9:1–23. doi: 10.3390/pathogens9110944
18. Armbruster CE, Mobley HLT, Pearson MM. Pathogenesis of Proteus Mirabilis Infection. *EcoSal Plus* (2018) 8(1):10. doi: 10.1128/ECOSALPLUS.ESP-0009-2017
19. Jayasundara D, Senavirathna I, Warnasekara J, Gamage C, Siribaddana S, Kularatne SAM, et al. 12 Novel Clonal Groups of Leptospira Infecting Humans in Multiple Contrasting Epidemiological Contexts in Sri Lanka. *PloS Negl Trop Dis* (2021) 15(3):e0009272. doi: 10.1371/journal.pntd.0009272
20. Cheng MP, Domingo MC, Lévesque S, Yansouni CP. A Case Report of a Deep Surgical Site Infection With Terrisporobacter Glycolicus/T. Mayombei and Review of the Literature. *BMC Infect Dis* (2016) 16(1):529. doi: 10.1186/S12879-016-1865-8
21. Chung L, Thiele Orberg E, Geis AL, Chan JL, Fu K, DeStefano Shields CE, et al. Bacteroides Fragilis Toxin Coordinates a Pro-Carcinogenic Inflammatory Cascade *via* Targeting of Colonic Epithelial Cells. *Cell Host Microbe* (2018) 23:203–214.e5. doi: 10.1016/j.chom.2018.01.007
22. Cheng Y, Ling Z, Li L. The Intestinal Microbiota and Colorectal Cancer. *Front Immunol* (2020) 11:615056. doi: 10.3389/fimmu.2020.615056
23. Berge A, Morenius C, Petropoulos A, Nilson B, Rasmussen M. Epidemiology, Bacteriology, and Clinical Characteristics of HACEK Bacteremia and Endocarditis: A Population-Based Retrospective Study. *Eur J Clin Microbiol Infect Dis* (2021) 40:525–34. doi: 10.1007/S10096-020-04035-Y
24. Kuijper EJ, Wiggerts HO, Jonker GJ, Schaal KP. Gans J De. Disseminated Actinomycosis Due to Actinomyces Meyeri and Actinobacillus Actinomycetemcomitans. *Scand J Infect Dis* (1992) 24:667–72. doi: 10.3109/00365549209054655
25. Summanen PH, Durmaz B, Väisänen ML, Liu C, Molitoris D, Eerola E, et al. Porphyromonas Somerae Sp. Nov., a Pathogen Isolated From Humans and Distinct From Porphyromonas Levii. *J Clin Microbiol* (2005) 43:4455–9. doi: 10.1128/JCM.43.9.4455-9.2005
26. Maraki S, Papadakis IS, Chronakis E, Panagopoulos D, Vakis A. Aggregatibacter Aphrophilus Brain Abscess Secondary to Primary Tooth Extraction: Case Report and Literature Review. *J Microbiol Immunol Infect* (2016) 49:119–22. doi: 10.1016/J.JMII.2013.12.007
27. Mushi MF, Bader O, Taverne-Ghadwal L, Bii C, Groß U, Mshana SE. Oral Candidiasis Among African Human Immunodeficiency Virus-Infected Individuals: 10 Years of Systematic Review and Meta-Analysis From Sub-Saharan Africa. *J Oral Microbiol* (2017) 9(1):1317579. doi: 10.1080/20002297.2017.1317579
28. Miceli MH, Díaz JA, Lee SA. Emerging Opportunistic Yeast Infections. *Lancet Infect Dis* (2011) 11:142–51. doi: 10.1016/S1473-3099(10)70218-8
29. Petitdemange C, Achour A, Dispinseri S, Malet I, Sennepin A, Fang RHT, et al. A Single Amino-Acid Change in a Highly Conserved Motif of Gp41 Elicits HIV-1 Neutralization and Protects Against CD4 Depletion. *Clin Infect Dis* (2013) 57:745–55. doi: 10.1093/CID/CIT335
30. Foster TJ. Immune Evasion by Staphylococci. *Nat Rev Microbiol* (2005) 3:948–58. doi: 10.1038/nrmicro1289
31. Archer GL. Staphylococcus Aureus: A Well-Armed Pathogen. *Clin Infect Dis* (1998) 26:1179–81. doi: 10.1086/520289
32. Powers ME, Wardenburg JB. Igniting the Fire: Staphylococcus Aureus Virulence Factors in the Pathogenesis of Sepsis. *PloS Pathog* (2014) 10(2):e1003871. doi: 10.1371/journal.ppat.1003871
33. Qi YJ, Jiao YL, Chen P, Kong JY, Gu BL, Liu K, et al. Porphyromonas Gingivalis Promotes Progression of Esophageal Squamous Cell Cancer *via* Tgfβ-Dependent Smad/YAP/TAZ Signaling. *PloS Biol* (2020) 18:e3000825. doi: 10.1371/JOURNAL.PBIO.3000825
34. Bahar B, Singhrao SK. An Evaluation of the Molecular Mode of Action of Trans-Resveratrol in the Porphyromonas Gingivalis Lipopolysaccharide Challenged Neuronal Cell Model. *Mol Biol Rep* (2021) 48:147–56. doi: 10.1007/S11033-020-06024-Y
35. Hegde S, Krisnawan VE, Herzog BH, Zuo C, Breden MA, Knolhoff BL, et al. Dendritic Cell Paucity Leads to Dysfunctional Immune Surveillance in Pancreatic Cancer. *Cancer Cell* (2020) 37:289–307.e9. doi: 10.1016/J.CCELL.2020.02.008
36. Adel-Khattab D, Groeger S, Domann E, Chakraborty T, Lochnit G, Meyle J. Porphyromonas Gingivalis Induced Up-Regulation of PD-L1 in Colon Carcinoma Cells. *Mol Oral Microbiol* (2021) 36:172–81. doi: 10.1111/OMI.12332
37. Chang JH, Jiang Y, Pillarisetty VG. Role of Immune Cells in Pancreatic Cancer From Bench to Clinical Application An Updated Review. *Med (Baltimore)* (2016) 95:e5541. doi: 10.1097/MD.0000000000005541
38. Ghamarzad Shishavan N, Mohamadkhani A, Ghajarieh Sepanlou S, Masoudi S, Sharafkhah M, Poustchi H, et al. Circulating Plasma Fatty Acids and Risk of Pancreatic Cancer: Results From the Golestan Cohort Study. *Clin Nutr* (2021) 40:1897–904. doi: 10.1016/j.clnu.2020.09.002
39. Gonzales JR, Groeger S, Johansson A, Meyle J. T Helper Cells From Aggressive Periodontitis Patients Produce Higher Levels of Interleukin-1 Beta and Interleukin-6 in Interaction With Porphyromonas Gingivalis. *Clin Oral Investig* (2014) 18:1835–43. doi: 10.1007/s00784-013-1162-5

Conflict of Interest: JT is cofounder and CSO of DIACCURATE, a spin-off of the Institut Pasteur. JP, AM, FB, and LJ are, or were, employees of DIACCURATE. PP was employed by company Truffle Capital. BG receives royalties from the sale of anti-gC1qR antibodies and gC1qR detection assay kit.

The remaining authors declare that the research was conducted in the absence of any commercial or financial relationships that could be construed as a potential conflict of interest.

Publisher's Note: All claims expressed in this article are solely those of the authors and do not necessarily represent those of their affiliated organizations, or those of the publisher, the editors and the reviewers. Any product that may be evaluated in

this article, or claim that may be made by its manufacturer, is not guaranteed or endorsed by the publisher.

frontiers | Frontiers in Immunology

ORIGINAL RESEARCH
published: 27 April 2022
doi: 10.3389/fimmu.2022.840976

Early Post-Vaccination Gene Signatures Correlate With the Magnitude and Function of Vaccine-Induced HIV Envelope-Specific Plasma Antibodies in Infant Rhesus Macaques

*K. K. Vidya Vijayan[1], Kaitlyn A. Cross[2], Alan D. Curtis II[1], Koen K. A. Van Rompay[3], Justin Pollara[4,5,6], Christopher B. Fox[7], Mark Tomai[8], Tomáš Hanke[9,10], Genevieve Fouda[4], Michael G. Hudgens[2], Sallie R. Permar[11] and Kristina De Paris[1]**

[1] Department of Microbiology and Immunology, Center for AIDS Research, and Children's Research Institute, School of Medicine, University of North Carolina at Chapel Hill, Chapel Hill, NC, United States, [2] Department of Biostatistics, Gillings School of Public Health, University of North Carolina at Chapel Hill, Chapel Hill, NC, United States, [3] California National Primate Research Center, University of California, Davis, Davis, CA, United States, [4] Duke Human Vaccine Institute, Duke University Medical Center, Durham, NC, United States, [5] Departent of Surgery, Duke University School of Medicine, Durham, NC, United States, [6] Department of Molecular Genetics and Microbiology, Duke University Medical Center, Durham, NC, United States, [7] Infectious Disease Research Institute, Seattle, WA, United States, [8] 3M Corporate Research Materials Laboratory, Saint Paul, MN, United States, [9] The Jenner Institute, University of Oxford, Oxford, United Kingdom, [10] Joint Research Center for Human Retrovirus Infection, Kumamoto University, Kumamoto, Japan, [11] Department of Pediatrics, Weill Cornell Medical College, New York, NY, United States

A better understanding of the impact of early innate immune responses after vaccine priming on vaccine-elicited adaptive immune responses could inform rational design for effective HIV vaccines. The current study compared the whole blood molecular immune signatures of a 3M-052-SE adjuvanted HIV Env protein vaccine to a regimen combining the adjuvanted Env protein with simultaneous administration of a modified Vaccinia Ankara vector expressing HIV Env in infant rhesus macaques at days 0, 1, and 3 post vaccine prime. Both vaccines induced a rapid innate response, evident by elevated inflammatory plasma cytokines and altered gene expression. We identified 25 differentially-expressed genes (DEG) on day 1 compared to day 0 in the HIV protein vaccine group. In contrast, in the group that received both the Env protein and the MVA-Env vaccine only two DEG were identified, implying that the MVA-Env modified the innate response to the adjuvanted protein vaccine. By day 3, only three DEG maintained altered expression, indicative of the transient nature of the innate response. The DEG represented immune pathways associated with complement activation, type I interferon and interleukin signaling, pathogen sensing, and induction of adaptive immunity. DEG expression on day 1 was correlated to Env-specific antibody responses, in particular antibody-dependent

OPEN ACCESS

Edited by:
Alexis M. Kalergis, Pontificia Universidad Católica de Chile, Chile

Reviewed by:
Mark L. Lang, University of Oklahoma Health Sciences Center, United States
Tara Marlene Strutt, University of Central Florida, United States

***Correspondence:**
Kristina De Paris
abelk@med.unc.edu

Specialty section:
This article was submitted to Viral Immunology, a section of the journal Frontiers in Immunology

Received: *21 December 2021*
Accepted: *28 March 2022*
Published: *27 April 2022*

Citation:
Vijayan KKV, Cross KA, Curtis AD II, Van Rompay KKA, Pollara J, Fox CB, Tomai M, Hanke T, Fouda G, Hudgens MG, Permar SR and De Paris K (2022) Early Post-Vaccination Gene Signatures Correlate With the Magnitude and Function of Vaccine-Induced HIV Envelope-Specific Plasma Antibodies in Infant Rhesus Macaques. Front. Immunol. 13:840976. doi: 10.3389/fimmu.2022.840976

cytotoxicity responses at week 34, and Env-specific follicular T helper cells. Results from network analysis supported the interaction of DEG and their proteins in B cell activation. These results emphasize that vaccine-induced HIV-specific antibody responses can be optimized through the modulation of the innate response to the vaccine prime.

Keywords: systems biology, innate gene signatures, vaccine-induced antibody response, early life HIV vaccine, rhesus macaque model

INTRODUCTION

Novel antiretroviral treatment (ART) options and improved prevention services have resulted in a major decline of new HIV infections in the last decade. Yet, the 90-90-90 goals have not been reached, with 10 million people living with HIV (>25%) still not receiving ART (1). The number of new HIV infections, 1.5 million globally, was three times as high as prioritized in the United Nations Sustainable Development Goals for 2020. In Eastern Europe and central Asia, new HIV infections have increased by >70% since 2010 (1). In sub-Saharan Africa, young women aged 15-24 years accounted for 25% of new HIV infections in 2020 although they only represent 10% of the population (1). Two fifths of all HIV-infected children (0-14 years) remain undiagnosed and only 40% of children with known HIV status and receiving ART are fully suppressed (1). These numbers emphasize the continuous and pressing need for an effective HIV vaccine to curb the pandemic, especially among young people. Our group is pursuing the idea that an HIV vaccine regimen started in early life - with booster immunizations in childhood - would provide the necessary time to mature vaccine-induced HIV-specific antibody responses that could protect against HIV acquisition in the high-risk group of adolescents prior to sexual debut.

Challenges in HIV vaccine development include the immense diversity of the virus, the difficulty in designing Env immunogens that can capture this diversity and present epitopes of vulnerability to the immune system, and the possible need for strategies that can target the various arms of the immune system to induce protective immunity. Systems vaccinology approaches, including transcriptomics, plasma proteomics, structure-based immunogens and rational adjuvant design, have emerged as important tools to inform vaccine design and to predict vaccine immunogenicity and efficacy (2–14). Notably, retrospective analyses of vaccine trials have demonstrated that innate immune responses induced by the vaccine prime impact the subsequent vaccine-induced adaptive immunity (6, 8–14). As the infant immune system is highly dynamic in the first few months of life, it is important to determine if early immune signatures induced by the vaccine prime can also predict immunogenicity and/or efficacy in pediatric vaccines. The goal of our current study was to determine whether early innate immune responses after the vaccine prime were associated with functional antibody responses in the memory phase after immunization of infant rhesus macaques with two different HIV envelope (Env) vaccine regimens.

Our group has previously demonstrated that infant rhesus macaques can mount potent and persistent HIV Env-specific antibody responses to an HIV Env protein vaccine mixed with the TLR7/8-based 3M-052 adjuvant in stable emulsion (SE) and to a vaccine regimen consisting of both the adjuvanted Env protein and a modified Vaccinia Ankara vector expressing HIV Env (MVA-Env) (15, 16). In the current study, we determined plasma cytokine levels and the whole blood transcriptome at days 1 and 3 after the vaccine prime in comparison to day 0 and tested for correlations between early innate immune responses and later adaptive vaccine-induced cellular and humoral responses during the memory phase and in response to a late boost. Our results demonstrate a rapid, systemic innate response to the vaccine prime at day 1. The response was more pronounced in animals receiving the 3M-052-SE adjuvanted Env protein vaccine compared to the animals immunized simultaneously with the adjuvanted protein plus the MVA-Env vaccine. Several of the differentially expressed genes (DEG) on day 1 were positively correlated with Env-specific plasma IgG responses at week 14, and with Env-specific antibody-mediated cellular cytotoxicity (ADCC) and Env-specific follicular T helper cells (T_{FH}) at week 34. In contrast, early molecular signatures were negatively correlated with HIV Env-specific $CD8^+$ T cell responses. These findings imply that vaccine-induced HIV-specific immune responses could be optimized through targeted modulation of innate responses to the vaccine prime.

METHODS

Study Design

The current study utilized whole blood samples from a previously reported vaccine study in infant rhesus macaques (15, 16). Study design, sample collection, and sample processing have been described in detail previously (15, 16). Briefly, infant RMs were immunized during the first week of life with (i) 15 μg 1086.c HIV Env protein administered intramuscularly (IM) with 10 μg 3M-052 adjuvant in 2% v/v stable emulsion (Group 1 or Protein group; n=10), or with (ii) Env Protein in 3M-052-SE and 10^8 pfu MVA expressing 1086.c Env (Group 2 or MVA/Protein group; n=10). In addition, both groups received an IM immunization with the Chimpanzee Adenovirus vector Ox1t that expresses conserved regions of SIV Gag/Pol to promote SIV-specific T cell responses on day zero (D0) (17). ChAdOx1.tSIVconsv239 ($5x10^{10}$ virus particles [vp]) immunizations were divided equally over the left and right gluteus (15, 16) (**Figure 1**). Animals in both groups received booster immunizations at weeks 6 and 12 and a late boost at week 32 (15, 16). The vaccine boosts were identical to the vaccine

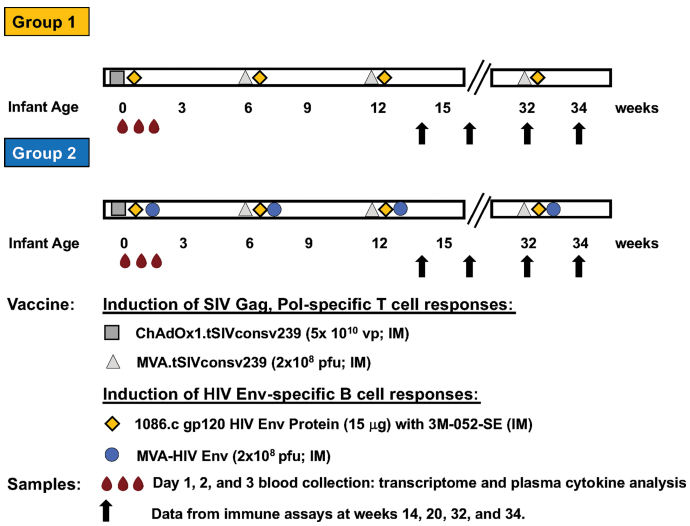

FIGURE 1 | Vaccine study overview. The timeline of immunization with the specific vaccine regimens and timepoints of immunizations for Group 1 and Group 2 are illustrated in horizontal bars. Each vaccine is indicated by a distinct symbol; vaccine dose and route of administration are listed in the legend. Blood samples (red droplets) are the vaccine prime were collected at days 0 (immediately prior to immunization) and at days 1 and 3 post prime. Vaccine-induced adaptive immune responses were measured at weeks 14, 20, 32 and 34, with results having been reported previously (15, 16).

prime, except for the use of MVA.tSIVconsv239 (10^8 pfu) as boost for the initial ChAdOx1.tSIVconsv239 prime (15, 16) (**Figure 1**). As reported previously, animals were euthanized at week 34 to analyze vaccine-induced immune responses in blood, lymph nodes, and in intestinal tissues (15, 16).

To summarize, Group 1 and Group 2 animals received the same vaccine to induce SIV Gag/Pol-specific T cell responses but differed in the vaccine components aimed at inducing HIV Env-specific antibody responses (**Figure 1**).

Whole Blood RNA Isolation and Gene Expression Analysis With NanoString nCounter®

For the purpose of the current study, EDTA-anticoagulated venous blood samples (3 x 200 μl) were collected on day 0 (= vaccine prime) just prior to immunization and at days 1 (24 hrs) and 3 (72 hrs) post prime and immediately resuspended in PAXgene reagent (552 μl). Samples were incubated for 2 hrs at room temperature and then stored at -80^{0}C until analysis.

RNA was extracted using the PAXgene Blood RNA kit (PreAnalytix GmbH, Hombrechtikon, Switzerland) following the manufacturer's protocol, except for incubating the samples for 60 minutes at 55^{0}C - instead of the recommended 10 minutes - after the addition of BR2 and Proteinase K. The extracted RNA was further purified with the RNA Clean and Concentrator Kit (Zymo Research Cooperation, Irvine, CA, USA). RNA was quantified using the Qubit RNA HS assay (ThermoFisher, Waltham, MA, USA). We obtained sufficient RNA for n=17 day 0, n=17 day 1, and n=14 day 3 samples to proceed with transcriptome analysis (**Table 1**). RNA samples (50 ng) were analyzed with the Nanostring Non-Human Primate Immunology Panel comprised of 754 immune-related genes and 16 internal reference genes. Gene expression analysis was conducted according to the manufacturer's protocol utilizing the NanoString nCounter® Prep Station and NanoString nCounter® Digital Analyzer.

Gene Expression Data Analysis

Raw gene expression data across days 0, 1, and 3 were analyzed using the NanoString® software nSolver v3.0.22 with the Advanced Analysis Module v2.0. The raw data files underwent quality evaluation applying nSolver Imaging and Binding Density Quality Control (QC) metrics, checking for Positive Control Linearity, and assessing Limit of Detection parameters. One day 0 (D0) sample (Group 1 RM 8) was flagged for low binding density and low limit of detection and therefore removed from further analysis. To delineate false positives, background correction was performed using a threshold value of 20; samples with counts <20 being adjusted to the value 20. Genes with altered expression levels on D1 or D3 compared to D0 were identified utilizing the Advanced Analysis Module v2.0 in nSolver™ that uses open-source R programs for QC, normalization, Differential Expression (DE) analysis, pathway scoring, and gene-set enrichment analysis. Data normalization employs the geNorm algorithm (18) through the function selectHKs in the Bioconductor package NormqPCR. The overall sample quality was represented by an assigned normalization factor and mean squared error (MSE). One D0 sample (Group 2 RM 12) and two day 1 (D1) samples (RM2 and RM7, both Group 1) had high MSE values far distinct from other samples and were, thus, designated as outliers and excluded from further analysis. Therefore, we had a total of n=15 D0, n=15 D1, and n=14 D3 samples for analysis (**Table 1**).

Genes with altered expression levels on D1 or D3 compared to D0 were identified employing multivariate linear regression

TABLE 1 | List of animals and samples for transcriptome analysis.

Group	Animal No.	Sample Availability		
		Day 0	Day 1	Day 2
1	RM1	x	x	x
	RM2	x		
	RM3	x	x	x
	RM4	x	x	x
	RM5	x	x	
	RM6	x	x	x
	RM7			x
	RM8		x	x
	RM9	x	x	
	Total:	n=7	n=7	n=6
2	RM10	x	x	x
	RM11	x	x	x
	RM12		x	x
	RM13	x	x	x
	RM14	x		x
	RM15	x	x	
	RM16	x	x	x
	RM17	x	x	x
	RM18	x	x	x
	Total:	n=8	n=8	n=8

models; raw p values were adjusted by Benjamini-Yekutieli method to minimize the false discovery rate. DEG were defined as having a $\log_2$ fold-change ≥1.32 (or 2.5-fold linear change) in expression and an adjusted p-value ≤0.1. ClustVis (http://biit.cs.ut.ee/clustvis/) was used for principal component analysis (PCA) using $\log_2$ transcript count values. In addition, we utilized nSolver™ to generate pathway scores to define potential immune pathways altered by the innate response to the vaccine prime. Pathway scores are based on the first principal component of the normalized relative gene expression of genes belonging to a specific immune pathway. The scores are further standardized by Z scaling. Therefore, pathway scores can have positive or negative values.

Gene expression data have been uploaded to Gene Expression Omnibus (GEO) at NCBI (submission number GSE192584).

Network Analysis

Network analyses for interactions of proteins encoded by differentially expressed genes on D1 compared to D0 were performed using the Search Tool for the Retrieval of Interacting Genes/Proteins (STRING) database version 11.5 (http://stringdb.org/), which curates both experimental and predicted protein interactions. Interactions with an interaction score >0.4 were visualized with Cytoscape v3.8.2 (www.Cytoscape.org/), with nodes representing significant genes/proteins and edge width indicating the combined interaction score. Protein-protein interactions were also visualized using NetworkAnalyst 3.0 (networkanalyst.ca) (19), an open source software, that utilizes the Human Interactome of the STRING v11.5 database (20).

Multiplex Cytokine Analysis

Plasma cytokine concentrations were measured using a custom-designed NHP Procartaplex Mix and Match 14-plex (ThermoFischer Scientific Inc) consisting of granulocyte-monocyte-colony stimulating factor (GM-CSF), interferon alpha (IFN-α), IFN gamma (IFN-γ), interleukin 1 beta (IL-1β), IL-1 receptor antagonist (IL-1RA), IL-6, IL-8 (CXCL8), IL-10, IL-12p70, IL-18, IL-23, interferon-inducible protein 10 (IP-10 or CXCL10), monocyte-chemoattractant protein 1 (MCP-1 or CCL2), and tumor necrosis factor alpha (TNF-α). Data were acquired on MAGPIX instrument with Luminex xPONENT software version 4.2. Cytokine concentrations were determined using ProcartaPlex Analyst software version1.0.

Statistical Analysis

Plasma cytokine concentrations of Group 1 or Group 2 animals on D1 or D3 were compared to D0 plasma cytokine concentrations by Mann-Whitney test using GraphPad Prism version 9.0, with $p<0.05$ being considered significant. Similarly, differences in mRNA expression or in pathway scores of Groups 1 or Group 2 animals on D1 compared to D0 were assessed by Mann-Whitney test.

To test for correlations between early gene signatures and/or plasma cytokines and adaptive immune responses at later timepoints, we combined data from Group 1 and Group 2 animals for D1 and D3. This sample size provides 80% power to detect a Spearman correlation of 0.7, and 66% power to detect a Spearman correlation of 0.5 at the $\alpha = 0.05$ level. To adjust for multiple comparisons, the Benjamini–Hochberg (BH) procedure was used to control the false discovery rate (FDR). Adjustments to control the FDR at $\alpha = 0.05$ were performed separately for humoral and cellular immune responses. Humoral responses included Env-specific plasma IgG responses (weeks 14, 20, 32 and 34), ADCC responses (weeks 14, 20, 32, and 34), and neutralizing antibody titers (weeks 14, 32, and 34) for a total of 661 correlation tests. Cellular responses included total peripheral blood and lymph node memory B cells and lymph node germinal center B cells (week 34), Env-specific follicular T helper cell (T_{FH}) responses (week 34), and

HIV Env and SIV Gag specific CD8$^+$ T cell responses (week 34) for a total of 366 correlation tests. Spearman rank correlation coefficients between early mRNA expression and/or plasma cytokines and vaccine-elicited adaptive immune parameters were calculated, tested, and FDR adjustments were performed using SAS version 9.4 (Cary, NC, USA).

RESULTS

Overview of the Study Design

The current study leveraged samples and vaccine-induced immune response data from a previously reported pediatric HIV vaccine study in infant rhesus macaques that was comprised of 2 groups, each with 10 animals (15, 16). On day 0 (D0), animals in both groups received an IM immunization with ChAdOx1.tSIVconsv239 expressing conserved Gag/Pol epitopes (17) to promote SIV Gag/Pol-specific T cell responses (**Figure 1**). Both vaccine groups received booster immunizations with MVA.tSIVconsv239 (10^8 pfu) at weeks 6 and 12, and a late boost at week 32 (15, 16) (**Figure 1**). The two vaccine groups differed in the component designed to induce HIV envelope-specific antibody responses. Animals in Group 1 were vaccinated with 1086.c Env protein administered IM with 3M-052 adjuvant in stable emulsion and Group 2 was immunized with the same adjuvanted HIV Env protein vaccine and with modified Vaccinia Ankara expressing 1086.c Env (MVA-Env) (15, 16). HIV Env protein was given IM into the left and right quadriceps and MVA-Env was administered IM into the left and right biceps (**Figure 1**). Blood was collected just prior to immunization (D0 or baseline), and on days 1 (D1) and 3 (D3) after the initial immunization (vaccine prime) (**Figure 1**). Animals in both vaccine groups received booster immunizations identical to the vaccine prime at weeks 6 and 12, and a late boost at week 32 (15, 16) (**Figure 1**).

Changes in soluble immune mediators in plasma in response to the vaccine prime were measured by multiparameter bead arrays and changes in gene expression were determined using the Nanostring® NHP Immunology Panel. Innate immune responses were correlated to previously reported vaccine-induced HIV 1086.c Env-specific IgG responses at the peak of the antibody responses after the initial 3 immunizations (week 14), during the memory phase of vaccine-induced antibody responses at weeks 20 and 32, and two weeks after the late boost (week 34) (15, 16). We also tested for correlations between innate responses induced by the vaccine prime and cellular immune responses at week 34, including total memory B cells, germinal center (GC) B cells in lymph nodes, Env-specific follicular T helper cells (T_{FH}), and HIV Env- or SIV Gag-specific CD8$^+$ T cell responses (**Figure 1**; see **Supplemental Figures S1-3** for flow cytometry gating strategies).

Impact of Vaccination on Soluble Immune Mediators in Plasma

To assess the systemic effect of the vaccine prime, we measured 14 immune mediators on days 0, 1, and 3 in plasma. On D1, the proinflammatory cytokines IFN-α, IL-6, IL-18, IFN-γ, MCP-1 (aka CCL2) and the anti-inflammatory cytokine IL-1RA were increased in both groups and at a similar magnitude (**Figure 2**). By D3, all 6 cytokines had returned to baseline levels in Group 1, whereas in Group 2 IFN-α and IFN-γ remained slightly elevated compared to D0 (**Figure 2**). These results implied that both vaccine regimens induced a transient inflammatory response.

To further interrogate this point, we determined whether the mRNA levels of the corresponding genes of the elevated plasma cytokines were also increased on D1 compared to D0. The mRNA levels of IL1RN, the gene encoding IL-1RA, were increased on D1 in both groups (**Figure 3**). In Group 1, IL6 mRNA levels were also increased on D1 and there was a trend towards higher median mRNA levels of IFNA2, IL18, and MCP1, but these did not reach statistical significance (**Figure 3**). On D3, consistent with a transient inflammatory response, mRNA levels of all six cytokines were indistinguishable from D0 mRNA levels in animals of both groups (**Figure 3**).

Differential Gene Expression in Response to the Vaccine Prime

We performed whole blood transcriptomics analysis to define the genes and immune pathways associated with immune activation by the two vaccine regimens. We first compared D0 mRNA expression levels of animals in Group 1 and Group 2 to confirm that baseline parameters did not differ between the two groups. Applying principal component analysis (PCA), our results demonstrated that the D0 transcript profile of the

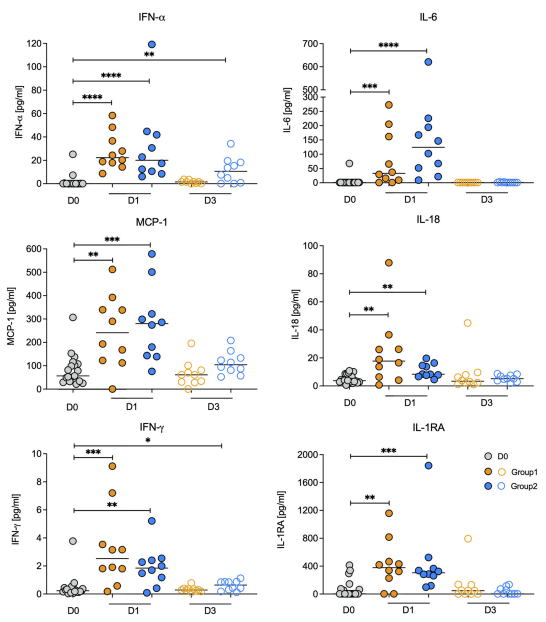

FIGURE 2 | Changes in plasma cytokine concentrations post vaccination. Plasma cytokine concentrations for IFN-a, IL-6, IL-18, IFN-g, MCP-1, and IL-1RA on day 0 (vaccine prime; grey circles) and on days 1 (filled circles) and day 3 (open circles) post vaccination for Group 1 (orange circles) and Group 2 (blue circles) animals. Note that D0 includes animals from both Group 1 and Group 2. Horizontal lines represent median values. Data between two time points were compared by Mann-Whitney test with *, **, ***, **** indicating p<0.05, p<0.01, p<0.001, or p<0.0001 respectively.

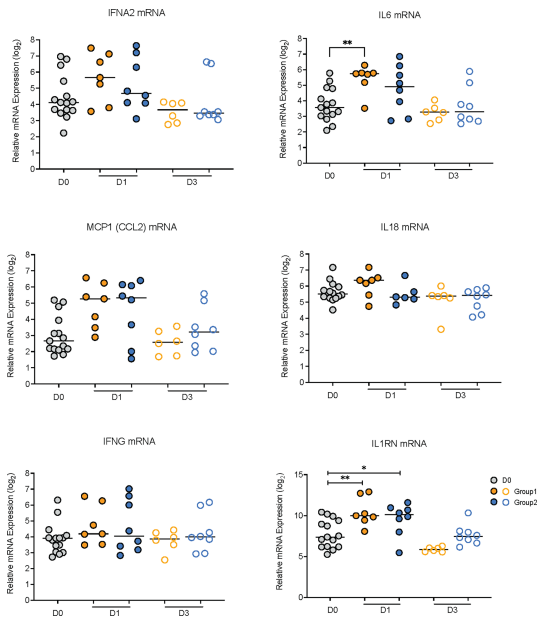

FIGURE 3 | Relative mRNA expression values of genes encoding elevated plasma cytokines. The graphs show relative log_2 mRNA levels of IFNA2, IL6, MCP1, IL18, IFNG, and IL1RN on day 0 (vaccine prime; grey circles) and on days 1 (filled circles) and day 3 (open circles) post vaccination for Group 1 (orange circles) and Group 2 (blue circles) animals. Horizontal lines represent median values. Data between two time points were compared by Mann-Whitney test with * or ** indicating $p < 0.05$ or $p < 0.01$, respectively.

animals from Group 1 (n=8) was indeed similar to the transcript profile of Group 2 animals (n=7) (**Supplemental Figure S4**). Therefore, we combined the D0 mRNA expression data from Group 1 and Group 2 (n=15) in subsequent analyses to assess changes in gene expressions on D1 and D3 in response to the vaccine prime on D0, and to determine whether the early post-prime innate gene signatures of Groups 1 and 2 differed dependent on the vaccine regimen.

In Group 1, more than twice as many genes were upregulated (n=375) than downregulated (n=164) on D1 compared to D0 (**Figure 4A**); the change in mRNA levels of several of these genes (n>20) reached an adjusted p value of p<0.05 (**Figure 4A**). By D3, an opposite trend was noted, with most genes (n=318) being downregulated in Group 1. In Group 2, about an equal number of genes were up- or down-regulated on D1 and D3 compared to D0 (**Figure 4B**). In contrast to Group 1, no genes were induced with adjusted p<0.05 on D1 or D3 in Group 2. This result implied that the MVA-Env vaccine in Group 2 may have altered the innate response induced by the 3M-052-SE adjuvanted Env Protein vaccine that was administered to both groups. Nonetheless, there was large overlap between Group 1 and Group 2 in the number of genes that were up- or down-regulated on D1 and D3 (**Figures 4C, D**).

To identify the genes that had undergone the greatest increase or decrease in mRNA expression in response to the vaccine prime, we applied the combined criteria of a ≥1.32 log_2 (or 2.5-fold change) increase or decrease in mRNA levels on D1 or D3 compared to D0 and the gene expression change having an adjusted $p \leq 0.1$. On D1, we identified 22 DEG in Group 1 that were upregulated and 3 genes that were downregulated (**Figure 5**). In Group 2, only two genes fulfilled these criteria on D1, and both of these genes (KIT and IL1RL1) were downregulated (**Figure 5**). Increased mRNA expression appeared to be transient and only two of the DEG with higher mRNA expression levels on D1 (CLU and GP1BB) still had increased mRNA levels on D3 in Group 1 (**Figure 5**). Among the D1 downregulated DEG, IL1RL1 also had decreased mRNA levels on D3 (**Figure 5**). Two additional downregulated genes in Group 2, IL1R2 and BCL2L1, fulfilled DEG criteria (**Figure 5**).

Consistent with elevated plasma levels of IFN-α on D1 (**Figure 2**), interferon-inducible genes (e.g., OAS3, IRF7, IFITM1, IFI35, SOCS3, TNFIAP3, NFKBIA) represented a large number of D1 DEG. Furthermore, the DEG IL1RN encodes IL-1RA, one of the plasma cytokines that were elevated on D1 (see **Figure 2**). Other proteins encoded by DEG included complement activation factors (e.g., C3AR1), proteins associated with interleukin signaling (e.g., IL1RN, IL1RL1, NFKBIA), genes encoding inflammatory mediators (e.g., TNFSF10), chemotactic molecules (e.g., CCR1), and mediators of monocyte and dendritic cell activation (e.g., CSF3R) (**Supplemental Table S1**). KIT encodes a receptor tyrosine kinase III that is expressed on most hematopoietic cells and has been suggested to interfere with dendritic cell activation by T helper 1 cytokines (21, 22). Of the 25 D1 DEG, 19 could be integrated into a molecular interaction network (**Supplemental Figure S2**). For the remaining 6 genes (LILAR3, ARG2, CD82, DDIT3, GP1BB, and HLA-DMA) no direct interactions with the other DEG could be identified. Major hubs included IL1RN, NFKBIA, and IRF7 with 7 links each, followed by SOCS3 and TNFAIP3 (both 6 links), and by TNFSF10 and C3AR1 with 5 links (**Supplemental Figure S2**). The low number of DEG on D3 did not allow for the assembly of a molecular network and further emphasized that, although the vaccine prime induced an innate response, the response was transient in nature.

Immune Pathway Analysis

To gain more insights into the biological functions of the DEG, we performed pathway analysis utilizing nSolver™. Pathway scores are based on the first principal component of the normalized relative gene expression and the number of genes belonging to a specific immune pathway. Therefore, pathway scores can have positive or negative values. Overall, the Group 1 vaccine regimen resulted in increased scores for 15 of the 17 pathways included in the NanoString NHP Immunology Panel on D1 (**Figure 6**). In contrast, in Group 2, only the score for the interferon signaling pathway was increased on D1 and by D3 pathway scores were indistinguishable from D0 scores (**Figure 6**). However, pathway scores for 8 of the signaling pathways were reduced in Group 1 on D3 compared to D0 (**Figure 6**).

To further interrogate how the two different vaccine regimens impacted these immune pathways, we compared the expression of genes within a specific pathway. Overall, the majority of genes within each of the pathways was detected in the transcriptome analysis (**Supplemental Table S3**). We focused on genes with a

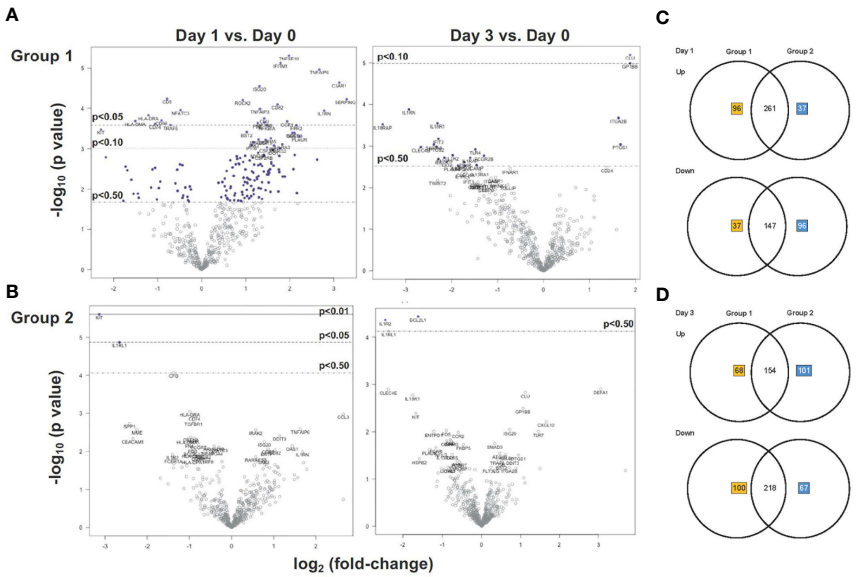

FIGURE 4 | Gene expression analysis of Group 1 and Group 2 prior and post vaccination. **(A, B)** Volcano plots displaying the log_2 change in mRNA expression on D1 (left plots) and D3 (right plots) versus D0 in Group 1 **(A)** and Group 2 **(B)**. The x-axis lists the log_2 fold-change and the y-axis the corresponding $-log_{10}$ p-value for each gene (each gene is represented by a circle). Dashed horizontal lines indicate the adjusted p-value thresholds of $p < 0.05$ and $p < 0.1$ determined by Benjamini-Yekutieli procedure. Genes highlighted by red boxes indicate representative examples of the identical gene in Group 1 and Group 2 with the same direction (up- or down-regulation) in the change of mRNA expression on day1 (left plots) or day 3 (right plots). **(C, D)** Venn diagrams depicting the number of unique and shared up-regulated and downregulated genes at D1 **(A)** and D3 **(B)** after vaccination in Groups 1 and 2. Unique genes in Group 1 or Group 2 are indicated by orange or blue numbers respectively, the number of shared genes is listed in black.

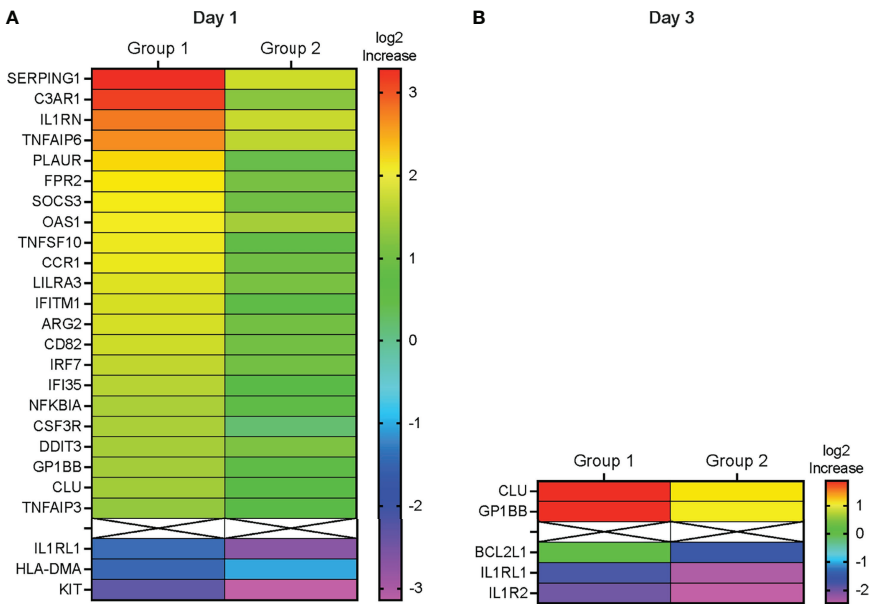

FIGURE 5 | Differentially expressed genes. **(A, B)** Heatmap depicting the log_2 fold-increase (FI) of differentially expressed genes at D1 compared to D0 **(A)** or at D3 compared to D0 **(B)** with an adjusted $p \leq 0.1$. DEG are ordered from top to bottom according the highest (red) to the lowest (purple) fold-increase (FI) in log2 gene expression in Group 1 as indicated by the color legend bar. The corresponding Group 2 log_2 gene expression values are also shown.

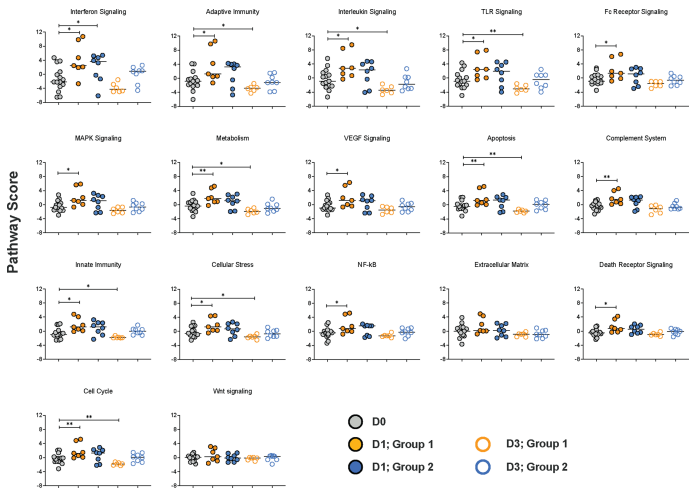

FIGURE 6 | Immune pathways affected by the vaccine prime. Based on the first principal component of the normalized relative gene expression and the number of genes belonging to a specific immune pathway, a pathway score standardized by Z scaling was generated by the nSolver™ software. Each pathway is represented by a specific graph displaying the pathway scores on D0 (grey circles), and on days 1 (filled circles) and day 3 (open circles) post vaccination for Group 1 (orange circles) and Group 2 (blue circles) animals. Differences in pathway scores were determined by Mann-Whitney test with * and ** representing $p < 0.05$ or $p < 0.01$, respectively.

$\log_2$ increase or decrease ≥1.32 on D1 *vs* D0 (**Figure 7A**) or D3 *vs*. D0 (**Figure 7B**) in Group 1 to the mRNA expression of the same genes in Group 2 without considering whether the raw or adjusted p value was <0.05 (**Supplementary Table S4**). We selected the five pathways with the highest increase or decrease in pathway score on D1 or D3 compared to D0. Consistent with the finding that several of the DEG were part of the interferon signaling pathway, the highest D1 pathway score was observed for the Interferon Signaling Pathway (mean: 4.15). The adaptive immunity pathway was the next highest ranked pathway in (mean score: 3.65), followed by the interleukin (mean score: 3.60), Toll-like receptor (TLR) (mean score: 2.94), and the Fc receptor (FcR) (mean score: 2.25) signaling pathways. Upregulated genes on D1, with the exception of the TLR3

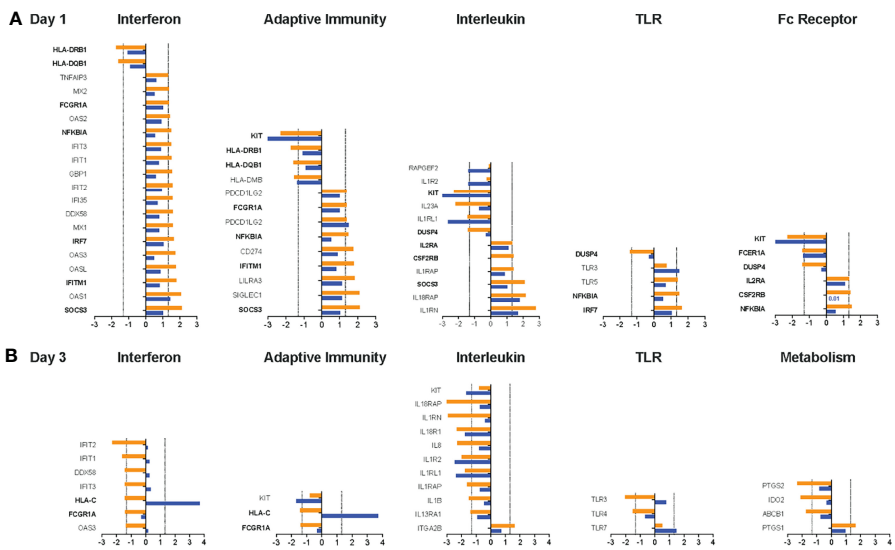

FIGURE 7 | Changes in gene expression between Group 1 and Group 2 animals for the top pathways impacted by the vaccine prime. For each of the top 5 pathways, the mean $\log_2$ increase in mRNA levels on D1 compared to D0 **(A)** or D3 compared to D0 **(B)** is shown for genes within the pathway that had a $\log_2$ increase ≥1.3.2 or decrease (dashed lines) in Group 1 (orange bars). The mean change in mRNA levels of the same genes in animals of Group 2 is indicated by blue bars. Genes for each pathway are listed on the y-axis. Bolded genes indicate genes that are present in more than one pathway. 0.

gene, were expressed at higher levels in Group1 compared to Group 2. The downregulated genes KIT and IL1RL1 were more strongly reduced in Group 2 compared to Group 1. Several genes with $\log_2 \geq 1.32$ increased or decreased mRNA expression were represented in multiple pathways, indicative of some redundancy and crosstalk between the pathways. Some of the shared genes on D1 were part of the DEG (SOCS3, IFITM1, IRF7, NFKBIA, KIT), whereas other common genes (IL2RA, FCGRIA, HLA-DRB1, HLA-DQB1, CSF2RB, DUSP4) were not identified in the DEG analysis because the adjusted p value for the change in mRNA expression for D1 versus D0 was greater than 0.1.

An opposite picture emerged on D3 when most genes were downregulated (**Figure 7B**). The top 5 pathways with the most altered gene expression on D3 were the Interferon (mean: -3.81), Interleukin (mean:-3.33), TLR (mean: -2.93), Adaptive Immunity (mean: -2.89), and the Metabolism (mean: -1.88) pathways. However, most of the genes in the interferon pathway that were downregulated $\log_2 \geq 1.32$ in Group 1 still had increased mRNA levels in Group 2 (**Figure 7B**). As was observed on D1, the downregulation of IL1RL1 was more pronounced in Group 2 and this was also true for the related gene IL1R2 (**Figure 7B**). Few genes (e.g., HLA-C, FCGRIA) were shared between pathways on D3 and those did not represent DEG.

Association of Early Innate Responses With Vaccine-Induced Antibody Responses

To address the question whether innate gene expression signatures on D1 or D3 post vaccine prime could predict the magnitude and function of vaccine-elicited Env-specific antibody responses to vaccination, we tested for correlations between D1 or D3 DEG, additional genes with increased or decreased mRNA expression that were common to at least two top scoring pathways (see **Figure 7**) and elevated plasma cytokines with the magnitude of vaccine-induced 1086.c Env-specific plasma IgG responses, neutralizing antibodies, and antibody-dependent cytotoxicity function (15, 16). Time points were selected to represent peak vaccine-elicited adaptive immune responses after the initial three immunizations (week 14 or 2 weeks post the 3rd immunization), vaccine-induced memory responses (week 20: 8 weeks post 3rd immunization; week 32: 20 weeks post the 3rd immunization and time of 4th immunization), and week 34, the peak response to the late boost (2 weeks post the 4th and final immunization) (15, 16). Although our two vaccine regimens were primarily designed to enhance Env-specific antibodies with Fc-mediated effector function (15, 16), we also assessed the impact of D1 or D3 gene expression and plasma cytokines on vaccine-induced neutralizing antibodies. As the direction of changes in mRNA levels and plasma cytokines on D1 was similar in both groups (**Supplemental Table S2** and see **Figure 4**) and our group sizes were limited in number, we combined the data of Group 1 and Group 2 to test for biologically meaningful correlation between innate vaccine prime-induced signatures and vaccine-induced adaptive immune responses.

The mRNA expression of six DEG on D1 were positively correlated with plasma Env-specific IgG at week 14 and for four of these genes (C3AR1, TNFSF10, LILRA3, and IFITM1) a positive correlation was also seen at week 32 (**Table 2**). In contrast, higher HLA-DQB1 mRNA levels on D1 were associated with lower Env-specific plasma IgG concentrations at week 32. The magnitude of Tier 1 neutralizing antibodies at week 14, week 32, or week 34 could be associated with one, three, or four DEG respectively (**Table 3**). It should be noted that the mRNA expression levels of the D1 DEG LILRA3, IFITM1, IRF7, and DDIT3 were positively associated with Env-specific plasma IgG and neutralizing antibody responses and the shared pathway gene HLA-DQB1 negatively correlated with both responses (**Tables 2**, **3**). On D3, the higher mRNA levels of IL1RL1, the lower were Env-specific IgG and neutralizing antibody responses (**Tables 2**, **3**). Associations of innate immune parameters unique to Env-specific plasma IgG were the inverse correlation with IL6 mRNA on D1 and with MCP1 mRNA on D3. The D1 gene expression of C3AR1, TNFSF10, and CSF3R was positively associated with both Env-specific IgG and ADCC responses (**Tables 2**, **4**). Overall, the induction of 9 DEG on D1 was positively correlated with Env-specific IgG-mediated ADCC responses at week 34, two weeks after the late boost (**Table 4**). Similarly, D1 mRNA expression of the shared pathway genes IL2RA, CSF2RB, and FCGR1A were correlated with ADCC responses at week 34 (**Table 4**). Among the elevated plasma cytokines at D1, IL-6 was negatively associated plasma IgG at weeks 32 and 34. Although increased plasma cytokine levels on D1 did not appear to impact ADCC responses at week 34, IFNG mRNA levels were inversely correlated with ADCC responses at week 14 (**Table 4**), whereas the mRNA expression of CCL2, the gene encoding MCP-1, were positively correlated with ADCC at week 34 (**Table 4**). On D3, few associations between mRNA expression and antibody responses were noted. Furthermore, with the exception of BCL2L1, these associations represented inverse correlations (**Tables 2**–**4**). In particular, the lower IL18 mRNA expression was, the lower were Env-specific plasma IgG, ADCC, and neutralizing antibody responses (**Tables 2**–**4**).

Based on these findings, we assessed whether vaccine prime-induced responses also correlated with B cell populations as antibody producing cells. The mRNA levels of SOCS3 were positively and the mRNA levels of HLA-DMA were negatively correlated with total CD27$^+$ memory B cells in peripheral blood at week 34, but not with lymph node memory B cells (**Table 5**). However, there was a positive correlation of six DEG with lymph node CXCR5$^+$ germinal center (GC) B cell frequencies at week 34 (**Table 5**; see **Supplemental Figure S1**). The latter were also associated with IL6 mRNA levels, but not with IL-6 plasma concentrations on D1 (**Table 5**). There was no overlap between the genes that correlated with peripheral blood memory B cells or with lymph node GC B cells. Follicular T helper cells (T_{FH}) provide critical signals for B cell activation and antibody maturation in lymph nodes (23–26), and, in turn, the T_{FH} responses are directly dependent on the priming by antigen presenting cells and the local immune milieu in lymph nodes (27–30). Env-specific lymph node T_{FH} frequencies (see **Supplemental Figure S2**) were correlated with mRNA levels of 19 of the 25 DEG with increased mRNA on D1, one shared pathway gene (CSF2RB), and with IL6 and CCL2 (MCP1) mRNA levels (**Table 5**). The frequencies of Env-specific lymph

TABLE 2 | Correlation of early gene expression with vaccine-induced Env-specific IgG.

Parameter	Spearman Correlation											
	week 14			week 20			week 32			week 34		
	r	p	q	r	p	q	r	p	q	r	p	q
D1 DEG												
SERPING1	0.3464	0.2061	0.6314	0.0250	0.9336	0.9682	0.4536	0.0915	0.5484	0.3393	0.2161	0.6415
C3AR1	**0.5321**	**0.0438**	**0.5158**	0.3607	0.1870	0.6212	**0.5964**	**0.0213**	**0.5158**	0.3821	0.1607	0.6147
IL1RN	0.4036	0.1370	0.5932	0.1500	0.5934	0.8379	0.4286	0.1127	0.5771	0.3714	0.1735	0.6182
TNFAIP6	0.4679	0.0808	0.5470	0.1893	0.4983	0.7907	0.3607	0.1870	0.6212	0.4643	0.0834	0.5470
PLAUR	-0.0750	0.7925	0.9346	-0.1857	0.5067	0.7907	-0.1357	0.6297	0.8695	-0.0107	0.9744	0.9907
FPR2	0.5071	0.0562	0.5158	0.2107	0.4498	0.7820	0.4071	0.1334	0.5900	0.4464	0.0972	0.5625
SOCS3	0.4893	0.0666	0.5318	0.2571	0.3538	0.7378	0.5000	0.0602	0.5158	0.3107	0.2592	0.6848
OAS1	0.3571	0.1917	0.6278	0.0821	0.7728	0.9263	0.3071	0.2649	0.6973	0.3607	0.1870	0.6213
TNFSF10	0.4929	0.0644	0.5207	0.3000	0.2767	0.6999	***0.6786***	***0.0068***	***0.4927***	0.4071	0.1334	0.5900
CCR1	0.4000	0.1408	0.5999	0.0143	0.9642	0.9833	0.2107	0.4498	0.7820	0.4357	0.1063	0.5737
LILRA3	**0.6036**	**0.0195**	**0.5158**	0.3500	0.2012	0.6314	**0.5214**	**0.0488**	**0.5158**	**0.5393**	**0.0406**	**0.5158**
IFITM1	**0.5321**	**0.0438**	**0.5158**	0.2536	0.3607	0.7379	**0.6036**	**0.0195**	**0.5158**	0.4607	0.0861	0.5470
ARG2	0.4821	0.0711	0.5358	0.1821	0.5150	0.7960	0.3929	0.1485	0.6004	0.3964	0.1446	0.6003
CD82	0.4179	0.1227	0.5900	0.2107	0.4498	0.7820	0.3464	0.2061	0.6313	0.2321	0.4039	0.7633
IRF7	**0.5607**	**0.0322**	**0.5158**	0.2500	0.3677	0.7433	0.4429	0.1002	0.5650	0.5107	0.0543	0.5158
IFI35	0.2607	0.3469	0.7378	-0.2250	0.4189	0.7633	0.0357	0.9031	0.9557	0.2964	0.2827	0.6999
NFKBIA	0.4429	0.1002	0.5650	0.1571	0.5756	0.8341	0.3750	0.1692	0.6169	0.3571	0.1917	0.6277
CSF3R	**0.5500**	**0.0362**	**0.5158**	0.2250	0.4189	0.7633	0.4357	0.1063	0.5737	0.5071	0.0562	0.5158
DDIT3	**0.5214**	**0.0488**	**0.5158**	0.2036	0.4657	0.7881	0.3000	0.2767	0.6999	**0.5607**	**0.0322**	**0.5158**
GP1BB	0.2036	0.4657	0.7881	0.1143	0.6858	0.8988	0.1500	0.5934	0.8379	0.2607	0.3469	0.7378
CLU	0.0786	0.7827	0.9263	0.0357	0.9031	0.9557	0.1857	0.5067	0.7907	0.0464	0.8726	0.9547
TNFAIP3	0.5107	0.0543	0.5158	0.2036	0.4657	0.7810	0.3964	0.1446	0.6003	0.4107	0.1297	0.5900
IL1RL1	0.3643	0.1824	0.6212	-0.0750	0.7925	0.9346	0.3107	0.2592	0.6848	0.4786	0.0735	0.5358
HLA-DMA	-0.2607	0.3469	0.7378	0.1000	0.7208	0.9098	-0.2214	0.4266	0.7633	-0.2143	0.4407	0.7785
KIT	-0.1000	0.7241	0.9098	-0.3214	0.2424	0.6804	-0.1464	0.6024	0.8473	0.1000	0.7241	0.9098
D1 Shared Pathway Genes[c]												
IL2RA	0.3429	0.2111	0.6408	0.1179	0.6763	0.8933	0.2357	0.3966	0.7633	0.2179	0.4342	0.7750
CSF2RB	0.4821	0.0711	0.5358	0.2214	0.4266	0.7633	0.5036	0.0582	0.5158	0.4071	0.1333	0.5900
FCGR1A	0.2071	0.4578	0.7876	0.2821	0.3074	0.7138	0.2893	0.2949	0.7046	0.1857	0.5067	0.7907
DUSP4	-0.0464	0.8764	0.9547	0.1429	0.6115	0.8548	0.1821	0.5151	0.7960	-0.0786	0.7827	0.9262
HLA-DQB1	**-0.5714**	**0.0286**	**0.5158**	-0.3464	0.2061	0.6314	**-0.6036**	**0.0195**	**0.5158**	-0.4107	0.1297	0.5900
HLA-DRB1	0.1000	0.7241	0.9098	0.1071	0.7041	0.9060	0.2393	0.3892	0.7592	0.0393	0.8929	0.9547
D1 Cytokine Genes[d]												
IFNA2	-0.1857	0.5067	0.7906	-0.2714	0.3269	0.7335	-0.2429	0.3820	0.7548	-0.0036	0.9948	0.9999
IL6	-0.0321	0.9132	0.9558	-0.0857	0.7630	0.9220	-0.0250	0.9336	0.9682	0.0321	0.9132	0.9557
IL18	0.1964	0.4819	0.7881	-0.1036	0.7144	0.9098	0.2321	0.4039	0.7633	0.1786	0.5235	0.7960
IFNG	-0.3536	0.1964	0.6314	-0.3250	0.2370	0.6739	-0.1857	0.5067	0.7907	-0.2750	0.3203	0.7310
MCP1	0.0786	0.7827	0.9262	-0.0786	0.7827	0.9262	-0.1179	0.6763	0.8933	0.1179	0.6763	0.8933
D1 Cytokine Proteins												
IFN-α	-0.3750	0.1692	0.6169	-0.1214	0.6669	0.8932	-0.3464	0.2061	0.6314	-0.2571	0.3538	0.7378
IL-6	-0.4540	0.0905	0.5470	-0.3843	0.1573	0.6147	**-0.5290**	**0.0447**	**0.5158**	**-0.5827**	**0.0248**	**0.5158**
IL-18	-0.2643	0.3402	0.7378	-0.2643	0.3402	0.7378	-0.3107	0.2592	0.6848	-0.2393	0.3892	0.7592
IFN-γ	-0.2073	0.4553	0.7873	-0.2288	0.4090	0.7633	-0.0447	0.8753	0.9547	-0.0840	0.7654	0.9220
MCP-1	-0.2321	0.4039	0.7633	-0.3214	0.2425	0.6804	0.0036	0.9948	0.1000	-0.4786	0.0734	0.5358
IL-1RA	0.1786	0.5235	0.7960	-0.1607	0.5667	0.8284	-0.0429	0.8828	0.9547	0.1214	0.6669	0.8932
D3 DEG												
CLU	-0.2396	0.4086	0.7633	0.0418	0.8915	0.9547	-0.4198	0.1368	0.5932	-0.2263	0.4356	0.7753
GP1BB	-0.2835	0.3253	0.7335	0.1165	0.6930	0.9029	-0.4286	0.1281	0.5900	-0.2440	0.3998	0.7633
BCL2L1	-0.0637	0.8319	0.9451	**0.5472**	**0.0458**	**0.5158**	0.2659	0.3573	0.7378	-0.1472	0.6158	0.8590
IL1RL1	-0.5297	0.0544	0.5158	-0.1956	0.5022	0.7907	-0.1165	0.6930	0.9029	**-0.6483**	**0.0144**	**0.5158**
ILR2	-0.2967	0.3026	0.7047	-0.2483	0.3911	0.7606	-0.0549	0.8557	0.9506	-0.4374	0.1198	0.5900
D3 Shared Pathway Genes												
HLA-C	-0.1253	0.6706	0.8933	-0.2615	0.3656	0.7433	-0.2747	0.3411	0.7378	0.2396	0.4086	0.7633
FCGR1A	-0.2527	0.3825	0.7548	-0.0637	0.8319	0.9451	0.1033	0.7270	0.9101	-0.2703	0.3492	0.7378
D3 Cytokine Genes												
IFNA2	-0.4330	0.1239	0.5900	-0.4154	0.1412	0.5999	0.0242	0.9396	0.9729	-0.3670	0.1973	0.6314
IL6	-0.2044	0.4827	0.7881	-0.0769	0.7965	0.9360	0.0593	0.8438	0.9484	-0.2044	0.4827	0.7881
IL18	**-0.7231**	**0.0047**	**0.4927**	-0.4725	0.0905	0.5470	-0.2703	0.3492	0.7378	**-0.6879**	**0.0082**	**0.4927**
IFNG	-0.3978	0.1602	0.6147	-0.1516	0.6051	0.8494	-0.0461	0.8795	0.9547	-0.4725	0.0905	0.5470

(Continued)

TABLE 2 | Continued

Parameter	Spearman Correlation											
	week 14			week 20			week 32			week 34		
	r	p	q	r	p	q	r	p	q	r	p	q
MCP1	-0.5516	0.0438	0.5158	-0.2747	0.3411	0.7378	-0.2176	0.4541	0.7873	**-0.6000**	**0.0261**	**0.5158**
IL1RN	-0.3714	0.1918	0.6277	0.1121	0.7043	0.9060	-0.0989	0.7385	0.9136.	-0.2352	0.4175	0.7633
D3 Cytokine Proteins												
IFN-α	-0.0632	0.8382	0.9484	0.1348	0.6589	0.8896	0.3026	0.3121	0.7212	0.2944	0.3264	0.7335
IL-6	0.3232	0.2949	0.7046	-0.0961	0.7564	0.9211	0.0874	0.7820	0.9263	0.3319	0.2820	0.6999
IL-18	-0.0660	0.8231	0.9451	0.2552	0.3757	0.7526	0.1694	0.5597	0.8284	-0.1012	0.7298	0.9117
IFN-γ	-0.3160	0.2689	0.6988	-0.0022	0.9968	0.1000	0.3005	0.2870	0.7021	-0.0354	0.9062	0.9557
MCP-1	**-0.7890**	**0.0013**	**0.4228**	-0.2835	0.3253	0.7335	0.2527	0.3825	0.7548	-0.5165	0.0615	0.5158
IL-1RA	0.0399	0.8967	0.9556	-0.0446	0.8839	0.9547	0.1948	0.5030	0.7907	0.1338	0.6483	0.8824

[a]*bold font corresponds to p<0.05.*

[b]*bold and italic font corresponds to p<0.01*

[c]*Genes shared between the top five scoring pathways on D1 also included IL1RN, SOCS3, IFITM1, IRF7, NFKBIA, and KIT, genes that are included in the DEG.*

[d]*The gene encoding IL-1RA is ILRN that is included in the DEG.*

node T_{FH} were only weakly associated with GC B cells (r=0.4941, p=0.0540); the caveat being that these B cells were not HIV Env-specific but represented total GC B cells. Note that Env-specific lymph node T_{FH} frequencies were positively correlated with $OX40^+CD137^+$ T_{FH} frequencies (r=0.5956, p=0.0274) after *in vitro* SEB stimulation. SEB-activated $OX40^+CD137^+$ T_{FH} frequencies were also weakly correlated with GC B cells (r=0.5235, p=0.0567) and showed a positive correlation with lymph node $CD27^+$ memory B cells (r=0.7363, p=0.0037). Combined, these data support the idea that the measurement of total GC B cells was likely representative of Env-specific GC B cells in our study. B cell frequencies or Env-specific lymph node T_{FH} frequencies were not associated with D3 cytokines or gene signatures.

We further evaluated the potential impact of the innate response to the vaccine prime on HIV Env-and SIV Gag-specific $CD8^+$ T cell responses in peripheral blood at week 34. SIV Gag-specific $CD8^+$ T cell responses were included because both vaccine regimens involved an adenoviral vector prime with ChAdOx1.tSIVconsv239 that was followed by two booster immunizations with MVA.tSIVconsv239 (15, 16). Peripheral blood SIV-Gag-specific $CD8^+$ T cell responses (see **Supplemental Figure S3**) at week 34 were negatively correlated to plasma IFN-α concentrations on D1, but positively correlated with mRNA levels of IFNA2 and IL18 on D3 (**Table 6**). Correlations were not observed with peripheral blood HIV Env-specific $CD8^+$ T cells (**Table 6**). Representative examples of correlations between vaccine prime-induced innate immune responses and adaptive immune responses are provided in **Figure 8**.

Although none of the correlations remained statistically significant after adjusting for multiple comparison testing at the 0.05 significance level, the fact that correlations of early DEG mRNA with Env-specific ADCC responses were almost exclusively observed at week 34, suggested that these associations were non-random. Additionally, the distribution of unadjusted p-values in each hypothesis group (**Supplemental Figure S6**) is favored more heavily in lower p-values. As the tests for moderate correlations were underpowered given the current sample size, this shape suggested qualitatively that there may be potential true correlation estimates that were not detectable as statistically significant in this study due to lack of power after FDR correction.

In summary, we discovered several correlations between early vaccine prime-induced immune responses and vaccine-induced adaptive immune parameters (**Figure 9**). The induction of several D1 DEG appeared to promote Env-specific antibody responses, whereas elevated plasma cytokines on D1 inversely affected antibody responses. The most pronounced effect of the D1 innate responses was on Env-specific T_{FH} (**Figure 9**). In agreement with the transient upregulation of genes, by D3 positive correlations between gene expression and vaccine-induced antibody responses were no longer detectable. The mRNA levels of most cytokine-encoding genes were inversely correlated with Env-specific plasma IgG, neutralizing antibodies, and ADCC responses (**Figure 9**). Furthermore, among the genes with altered expression on D1, a subset of eight genes (IL1RN, CCR1, TNFAIP3, HLA-DMA, IL2RA, CSF2RB, FCGR1A, and MCP1; **Table 4**) only correlated with ADCC function, but not with Env-specific IgG or neutralizing antibodies.

Discussion

The results of the current study demonstrate that the vaccine prime with an HIV Env protein mixed with 3M-052-SE induced a rapid, but transient, innate immune response characterized by an increase in inflammatory cytokines and elevated mRNA levels of genes associated with chemotaxis, type I interferon responses, and the sensing and priming of adaptive immune responses. Our results also suggest that the inclusion of the MVA-HIV vaccine in addition to the HIV Env protein vaccine modified this inflammatory response. Nonetheless, the mRNA levels of differentially expressed genes on day 1 in animals of both groups correlated with the magnitude and function of vaccine-induced adaptive immune responses assessed between weeks 14 to 34 post prime. The latter finding is consistent with other

TABLE 3 | Correlation of early gene expression with vaccine-induced Env-specific neutralizing antibodies.

Parameter	Spearman Correlation								
	week 14			week 32			week 34		
	r	p	q	r	p	q	r	p	q
D1 DEG									
SERPING1	0.1500	0.5934	0.8379	0.2000	0.4738	0.7881	0.2679	0.3334	0.7378
C3AR1	0.3107	0.2592	0.6848	0.3786	0.1649	0.6147	0.3464	0.2061	0.6313
IL1RN	0.2393	0.3892	0.7592	0.3250	0.2370	0.6739	0.4393	0.1032	0.5737
TNFAIP6	0.3214	0.2425	0.6804	0.3607	0.1870	0.6212	**0.5214**	**0.0488**	**0.5158**
PLAUR	-0.4750	0.0759	0.5415	-0.5143	0.0524	0.5158	-0.1929	0.4901	0.7907
FPR2	0.1429	0.6115	0.8548	0.1857	0.5067	0.7907	0.3714	0.1735	0.6182
SOCS3	0.4821	0.0711	0.5358	**0.5357**	**0.0422**	**0.5158**	0.4571	0.0888	0.5470
OAS1	0.4179	0.1227	0.7907	0.1929	0.4901	0.7378	-0.3714	0.1735	0.5900
TNFSF10	0.2893	0.2949	0.7046	0.4107	0.1297	0.5900	0.3893	0.1525	0.6055
CCR1	0.0179	0.9540	0.9803	0.0714	0.8025	0.9365	0.4679	0.0808	0.5470
LILRA3	0.4071	0.1334	0.5900	0.4500	0.0944	0.5506	**0.5357**	**0.0422**	**0.5158**
IFITM1	**0.5964**	**0.0213**	**0.5158**	**0.6429**	**0.0116**	**0.4927**	0.5000	0.0602	0.5158
ARG2	0.3393	0.2161	0.6415	0.3750	0.1692	0.6169	0.4179	0.1227	0.5900
CD82	0.2607	0.3469	0.7378	0.3107	0.2592	0.6848	0.2929	0.2888	0.7021
IRF7	0.3929	0.1485	0.6004	0.4429	0.1002	0.5650	**0.5679**	**0.0297**	**0.5158**
IFI35	-0.1964	0.4819	0.7881	-0.2500	0.3678	0.7433	0.1607	0.5667	0.8284
NFKBIA	0.1893	0.4983	0.7907	0.2571	0.3538	0.7378	0.3607	0.1870	0.6212
CSF3R	0.3393	0.2160	0.6415	0.3821	0.1607	0.6147	0.5179	0.0506	0.5158
DDIT3	0.2857	0.3012	0.7047	0.2964	0.2827	0.6999	**0.6464**	**0.0110**	**0.4927**
GP1BB	0.0321	0.9132	0.9557	0.0536	0.8525	0.9506	0.2071	0.4578	0.7876
CLU	-0.2214	0.4266	0.7633	-0.1964	0.4819	0.7880	-0.1929	0.4901	0.7907
TNFAIP3	0.1893	0.4983	0.8824	0.1286	0.6482	0.7907	0.4714	0.0783	0.5470
IL1RL1	-0.0964	0.7337	0.9117	-0.1536	0.5844	0.8379	0.1893	0.4983	0.7907
HLA-DMA	-0.4286	0.1127	0.5771	-0.3786	0.1649	0.6147	-0.2536	0.3607	0.7379
KIT	-0.4786	0.0735	0.5358	**-0.5464**	**0.0376**	**0.5158**	-0.2214	0.4266	0.7633
D1 Shared Pathway Genes[c]									
IL2RA	0.0893	0.7532	0.9189	0.1250	0.6575	0.8895	0.1214	0.6669	0.8932
CSF2RB	0.2214	0.4266	0.7633	0.3286	0.2317	0.6722	0.4071	0.1334	0.5900
FCGR1A	0.2393	0.3892	0.7592	0.3179	0.2479	0.6804	0.3643	0.1824	0.6212
DUSP4	-0.3429	0.2111	0.6408	-0.2214	0.4266	0.7633	-0.1607	0.5667	0.8284
HLA-DQB1	***-0.6857***	***0.0061***	***0.4927***	***-0.6964***	***0.0051***	***0.4927***	-0.4571	0.0888	0.5470
HLA-DRB1	0.0714	0.8025	0.9365	0.1500	0.5934	0.8379	-0.0070	0.9847	0.9980
D1 Cytokine Genes[d]									
IFNA2	-0.3786	0.1649	0.6147	-0.4321	0.1094	0.5737	-0.1500	0.5934	0.8379
IL6	-0.4321	0.1094	0.5737	-0.3964	0.1446	0.6003	-0.1000	0.7241	0.9098
IL18	-0.3893	0.1525	0.6055	-0.4607	0.0861	0.5470	-0.2286	0.4114	0.7633
IFNG	-0.4607	0.0861	0.5470	-0.5071	0.0562	0.5158	-0.5000	0.0602	0.5158
MCP1	-0.2321	0.4039	0.7633	-0.2107	0.4498	0.7820	0.2250	0.4190	0.7633
D1 Cytokine Proteins									
IFN-α	-0.1321	0.6389	0.8785	-0.0464	0.8726	0.9547	-0.2036	0.4657	0.7880
IL-6	0.0643	0.8196	0.9557	0.0304	0.9158	0.9450	-0.2574	0.3514	0.7378
IL-18	-0.1250	0.6575	0.8898	-0.0429	0.8828	0.9547	-0.2679	0.3334	0.7378
IFN-γ	0.3378	0.2170	0.6415	0.4004	0.1394	0.5996	0.0840	0.7654	0.9220
MCP-1	-0.0321	0.9132	0.9557	0.1786	0.5235	0.7960	-0.3500	0.2012	0.6314
IL-1RA	-0.2000	0.4738	0.7880	-0.2036	0.4657	0.7880	-0.0786	0.7827	0.9263
D3 DEG									
CLU	-0.3978	0.1602	0.6147	-0.1780	0.5423	0.8141	-0.0901	0.7616	0.9220
GP1BB	-0.1736	0.5526	0.8239	0.0945	0.7500	0.9189	0.0154	0.9637	0.9833
BCL2L1	0.0769	0.7965	0.9360	0.4330	0.1239	0.5900	-0.0153	0.9637	0.9833
IL1RL1	-0.0374	0.9035	0.9557	0.0637	0.8319	0.9451	***-0.6835***	***0.0088***	***0.4927***
ILR2	-0.3275	0.2530	0.6848	-0.2088	0.4731	0.7881	**-0.6132**	**0.0224**	**0.5158**
D3 Shared Pathway Genes									
HLA-C	0.0154	0.9638	0.9833	-0.0901	0.7616	0.9220	0.4681	0.0938	0.5506
FCGR1A	-0.4110	0.1458	0.6003	-0.3802	0.1808	0.6212	-0.3407	0.2335	0.6724
D3 Cytokine Genes									
IFNA2	-0.1165	0.6930	0.9029	-0.3099	0.2806.	0.6999	-0.5297	0.0543	0.5158
IL6	-0.1121	0.7042	0.9060	-0.2615	0.3656	0.7433	-0.1692	0.5629	0.8284
IL18	-0.3011	0.2951	0.7046	-0.3319	0.2464	0.6804	***-0.8242***	***0.0005***	***0.3471***
IFNG	0.0418	0.8915	0.9547	-0.0505	0.8676	0.9547	-0.4286	0.1281	0.5900

(Continued)

TABLE 3 | Continued

Parameter	Spearman Correlation								
	week 14			week 32			week 34		
	r	p	q	r	p	q	r	p	q
MCP1	-0.0549	0.8557	0.9506	-0.0022	1.0000	1.0000	-0.4945	0.0750	0.5411
IL1RN	-0.2307	0.4265	0.7633	-0.0725	0.8083	0.9400	-0.0417	0.8915	0.9547
D3 Cytokine Proteins									
IFN-α	0.3439	0.2484	0.6804	0.4044	0.1706	0.6181	0.4237	0.1494	0.6005
IL-6	0.2096	0.5000	0.7907	-0.0262	0.9487	0.9764	0.0262	0.9487	0.9764
IL-18	-0.1848	0.5243	0.7960	0.0726	0.8049	0.9377	-0.1210	0.6784	0.8944
IFN-g	-0.2077	0.4732	0.7881	-0.0530	0.8581	0.9517	-0.0972	0.7402	0.9136
MCP-1	-0.1077	0.7156	0.9098	-0.0066	0.9879	0.9983	-0.3319	0.2464	0.6804
IL-1RA	-0.5328	0.0532	0.5158	-0.4811	0.0843	0.5470	0.0023	1.0000	1.0000

[a]*bold font corresponds to p < 0.05.*

[b]*bold and italic font corresponds to p < 0.01.*

[c]*Genes shared between the top five scoring pathways on D1 also included IL1RN, SOCS3, IFITM1, IRF7, and NFKBIA, genes that are included in the DEG.*

[d]*The gene encoding IL-1RA is ILRN that is included in the DEG.*

studies documenting a link between early innate immune responses and vaccine-induced immunogenicity at later timepoints (8, 10, 13, 14, 31).

Relevant to the current study, a recent analysis of samples from the RV144 HIV vaccine trial in human adults found that several genes were upregulated on day 1 after the vaccine prime, and then, analogous to our results, rapidly returned to baseline (pre-vaccine) levels (14). In addition, the authors noted an increase in several plasma cytokines on day 1. Among those cytokines were IL-6, MCP-2, and IFN-γ, cytokines that were also found at elevated plasma levels in our study. In RV144 participants, increases in cytokines at day 1 were positively correlated with the vaccine-induced Env-specific plasma antibodies at 6.5 months, whereas the early gene signature was not correlated with plasma Env-specific IgG responses (14). The early gene signature was, however, positively correlated with ADCC and antibody-dependent phagocytosis function at 6.5 months (14). In our study, with the exception of IFN-α that was inversely correlated with SIV Gag-specific $CD8^+$ T cell responses, we did not find a correlation between day 1 elevated plasma cytokines and vaccine-induced adaptive immune responses between weeks 14 to 34. However, on D3 IFN-α and IL-18 plasma concentrations were positively correlated with SIV Gag-specific $CD8^+$ T cell responses, while MCP-1 was inversely correlated to plasma IgG and ADCC function.

Similar to the findings in the RV144 analysis, several of the DEG identified in the current study were positively correlated with Env-specific antibody responses. It was notable that the correlation of early genes with the magnitude of Env-specific ADCC responses was primarily found at week 34, a result consistent with maturation of functional antibody responses over time. This question should be addressed in future studies to determine at what timepoint correlations between early vaccine-prime-induced responses and specific functional adaptive immune parameters should be assessed to predict vaccine immunogenicity and potential efficacy. We identified several genes that were only correlated with ADCC, but not with plasma IgG and neutralizing antibody responses. A study analyzing the transcriptome of adult rhesus macaques vaccinated with a mosaic adenovirus 26-based SIV vaccine that provided partial efficacy against infection with SIV and/or SHIV challenge identified a specific B cell signature that was associated with immune correlates of protection (32). Importantly, this molecular signature could be validated in human adult participants of the RV144 trial that were protected against HIV acquisition (32). One of the genes, TNFSF13, correlated specifically with ADCC and ADCP responses in vaccinees. The D1 mRNA levels of the related genes TNFSF10, TNFIAP3, and TNFIAP6 were also correlated with ADCC responses in the current study. Conversely, we need to determine whether functionally distinct adaptive immune responses can be foretold by specific innate immune or molecular signatures. This question is important for HIV vaccine design to modulate innate immune responses in a targeted fashion to optimize the induction of broadly neutralizing antibodies, antibodies with Fc-mediated effector function, and/or antiviral T cell responses.

Earlier studies have demonstrated that distinct vaccine strategies (live attenuated versus inactivated viral vaccines versus polysaccharide vaccines) differ in the early immune response (9). A comparative study examining the early peripheral blood transcriptome in response to five different vaccines found that despite vaccine-specific gene signatures, similar innate immune response pathways, such as complement activation, inflammation, and antigen-sensing and presentation, were targeted (10). The DEG identified in the current study support these earlier findings. Adjuvants are important means in modulating the early innate response and enhancing specific adaptive immune responses (7, 33). In fact, we and others have previously reported how different adjuvants can alter the magnitude and quality of HIV Env-specific antibody responses (34–36). In the current study, several of the DEG (e.g., the type I interferon inducible genes OAS1, IRF7, IFITM1, SOCS3, IFI35) likely reflected the host response to the TLR7/8-agonist-based adjuvant 3M-052-SE (37–39). This conclusion was supported when a network and enrichment analysis that included all D1 genes that were positively correlated with antibody responses analysis identified the TLR7/8 cascade as one of the important pathways (FDR p=2.01E-08)

TABLE 4 | Correlation of early gene expression with vaccine-induced Env-specific ADCC.

Parameter	Spearman Correlation											
	week 14			week 20			week 32			week 34		
	r	p	q	r	p	q	r	p	q	r	p	q
D1 DEG												
SERPING1	-0.0464	0.8726	0.9547	0.0964	0.7337	0.9117	0.2679	0.3334	0.7378	0.4684	0.0799	0.5470
C3AR1[a]	-0.0893	0.7532	0.9189	0.3929	0.1485	0.6004	0.2964	0.2827	0.6999	**0.6363**	**0.0129**	**0.5121**
IL1RN[b]	-0.0071	0.9847	0.9981	0.3179	0.2479	0.6804	0.4321	0.1094	0.5737	***0.6768***	***0.0073***	***0.4927***
TNFAIP6	0.1571	0.5756	0.8342	0.1214	0.6669	0.8932	0.1393	0.6205	0.8621	0.5016	0.0590	0.5158
PLAUR	-0.3714	0.1735	0.6182	0.0607	0.8324	0.9450	0.0214	0.9438	0.9758	0.3689	0.1751	0.6184
FPR2	0.1071	0.7049	0.9060	0.1143	0.6858	0.8988	0.1786	0.5253	0.7960	0.3947	0.1453	0.6003
SOCS3	0.3000	0.2767	0.6999	**0.5429**	**0.0391**	**0.5158**	***0.7393***	***0.0023***	***0.4664***	**0.5275**	**0.0458**	**0.5158**
OAS1	0.1286	0.6482	0.8824	0.0357	0.9031	0.9557	0.1571	0.5756	0.8342	0.4316	0.1091	0.5737
TNFSF10	-0.0393	0.8929	0.9547	0.3679	0.1779	0.6212	0.4571	0.0888	0.5470	**0.5699**	**0.0292**	**0.5158**
CCR1	0.2857	0.3012	0.7047	0.2143	0.4421	0.7785	0.3500	0.2012.	0.6314	**0.6436**	**0.0117**	**0.4927**
LILRA3	0.2000	0.4738	0.7881	0.2929	0.2888	0.7021	0.2786	0.3139	0.7212	0.4980	0.0611	0.5158
IFITM1	0.2750	0.3203	0.7310	0.2286.	0.4114	0.7633	0.3393	0.2161	0.6415	0.4832	0.0700	0.5358
ARG2	0.2679	0.3335	0.7378	0.1500	0.5934	0.8379	0.2571	0.3538	0.7378	0.3523	0.1964	0.6314
CD82	0.1750	0.5320	0.8022	0.1607	0.5667	0.8284	0.2857	0.3012	0.7047	0.3043	0.2673	0.6979
IRF7	0.2929	0.2888	0.7021	0.2214	0.4266	0.7633	0.3286	0.2317	0.6722	**0.5662**	**0.0304**	**0.5158**
IFI35	0.2250	0.4189	0.7633	0.0607	0.8324	0.9451	0.2250	0.4189	0.7633	0.4057	0.1336	0.5900
NFKBIA	0.1393	0.6205	0.8621	0.0571	0.8425	0.9484	0.1929	0.4901	0.7907	0.4131	0.1263	0.5900
CSF3R	0.2786	0.3139	0.7212	0.1643	0.5580	0.8283	0.2643	0.3401	0.7378	**0.5348**	**0.0425**	**0.5158**
DDIT3	0.0893	0.7532	0.9189	0.1786	0.5253	0.7960	0.1286	0.6482	0.8824	**0.5275**	**0.0458**	**0.5158**
GP1BB	0.0036	0.9949	0.9999	-0.2464	0.3748	0.7526	-0.2929	0.2888	0.7021	0.0664	0.0814	0.9444
CLU	-0.0786	0.7827	0.9263	-0.3286	0.2317	0.6723	-0.1750	0.5320	0.8022	-0.0646	0.8187	0.9451
TNFAIP3	-0.0250	0.9336	0.9682	0.3500	0.2012	0.6314	0.4286	0.1127	0.5771	***0.6584***	***0.0096***	***0.4927***
IL1RL1	-0.0536	0.8505	0.9506	-0.1357	0.6297	0.8695	-0.1179	0.6763	0.8933	0.4186	0.1209	0.5900
HLA-DMA	-0.5071	0.0562	0.5158	-0.3143	0.2536	0.6848	**-0.5607**	**0.0322**	**0.5158**	-0.3025	0.2703	0.6988
KIT	-0.3250	0.2370	0.6739	-0.2143	0.4421	0.7785	-0.3036	0.2708	0.6988	0.1778	0.5239	0.7960
D1 Shared Pathway Genes[c]												
IL2RA	0.3357	0.2212	0.6510	0.4571	0.0888	0.5470	**0.5607**	**0.0322**	**0.5158**	**0.5496**	**0.0364**	**0.5158**
CSF2RB	0.1286	0.6482	0.8824	0.2964	0.2827	0.6999	0.4321	0.1094	0.5737	**0.5939**	**0.0221**	**0.5158**
FCGR1A	-0.1964	0.4819	0.7880	**0.5571**	**0.0335**	**0.5158**	0.3393	0.2161	0.6414	**0.5625**	**0.0317**	**0.5158**
DUSP4	-0.4714	0.0783	0.5470	0.2036	0.4657	0.7881	0.3107	0.2592	0.6848	0.3799	0.1618	0.6147
HLA-DQB1	-0.4964	0.0623	0.5158	-0.3179	0.2479	0.6804	-0.4357	0.1063	0.5737	-0.3596	0.1867	0.6212
HLA-DRB1	-0.2429	0.3820	0.7548	-0.1500	0.5934	0.8379	-0.3000	0.2767	0.6999	-0.0922	0.7421	0.9136
D1 Cytokine Genes[d]												
IFNA2	-0.1678	0.5492	0.8226	0.0536	0.8525	0.9506	0.0856	0.7630	0.9220	0.2545	0.3561	0.7378
IL6	-0.4036	0.1370	0.5931	-0.0250	0.9336	0.9682	-0.0321	0.9132	0.9557	0.3043	0.2673	0.6979
IL18	-0.4214	0.1193	0.5900	-0.2250	0.4189	0.7633	-0.1036	0.7144	0.9098	0.2102	0.4478	0.7820
IFNG	**-0.5500**	**0.0362**	**0.5158**	-0.2643	0.3402	0.7378	-0.1643	0.5579	0.8283	-0.0387	0.8917	0.9550
MCP1	-0.1500	0.5934	0.8379	0.5179	0.0506	0.5158	0.3786	0.1649	0.6147	***0.6621***	***0.0091***	***0.4927***
D1 Cytokine Proteins												
IFN-α	-0.0714	0.8025	0.9365	-0.0714	0.8025	0.9365	-0.3536	0.1964	0.6313	0.0590	0.8342	0.9455
IL-6	0.1144	0.6829	0.8984	-0.1001	0.7212	0.9098	-0.0536	0.8497	0.9506	-0.3840	0.1567	0.6147
IL-18	0.2214	0.4266	0.7633	-0.0893	0.7532	0.9188	-0.2214	0.4266	0.7633	0.0387	0.8917	0.9547
IFN-γ	0.1001	0.7213	0.9098	-0.0572	0.8396	0.9484	-0.0947	0.7361	0.9130	0.0406	0.8849	0.9547
MCP-1	0.1036	0.7144	0.9098	-0.0786	0.7827	0.9262	0.2536	0.3607	0.7379	-0.1070	0.7021	0.9060
IL-1RA	0.1964	0.4819	0.7881	-0.1500	0.5934	0.8379	-0.1321	0.6389	0.8785	0.1180	0.6726	0.8933
D3 DEG												
CLU	0.1121	0.7043	0.9036	-0.3275	0.2530	0.6906	**-0.5736**	**0.0349**	**0.5243**	-0.2978	0.2981	0.7089
GP1BB	0.0549	0.8557	0.9504	-0.1692	0.5629	0.8312	-0.5033	0.0694	0.5446	-0.2556	0.3742	0.7604
BCL2L1	-0.2528	0.3825	0.7650	-0.0330	0.9155	0.9565	-0.1429	0.6266	0.8651	-0.0133	0.9663	0.9836
IL1RL1	-0.3143	0.2735	0.7036	-0.1560	0.5944	0.8376	0.1253	0.6706	0.8904	-0.3911	0.1663	0.9196
ILR2	-0.1604	0.5838	0.8376	-0.2967	0.3025	0.7089	0.0637	0.8319	0.9446	-0.3400	0.2324	0.6774
D3 Shared Pathway Genes												
HLA-C	0.1033	0.7270	0.9115	0.1868	0.5221	0.7999	-0.0637	0.8319	0.9446	0.1978	0.4942	0.7962
FCGR1A	-0.2351	0.4174	0.7633	-0.1076	0.7156	0.9098	0.2307	0.4265	0.7633	0.0422	0.8870	0.9547
D3 Cytokine Genes												
IFNA2	-0.3802	0.1808	0.6282	-0.5209	0.0591	0.5243	0.0066	0.9879	0.9982	-0.4422	0.1144	0.5820
IL6	-0.2835	0.3253	0.7382	-0.2088	0.4731	0.7933	-0.0637	0.8319	0.9446	-0.3022	0.2907	0.7081
IL18	-0.6352	0.0171	0.5243	-0.2659	0.3573	0.7453	***-0.7534***	***0.0028***	***0.4741***	***-0.7231***	***0.0047***	***0.5001***
IFNG	-0.3758	0.1862	0.6282	-0.1604	0.5838	0.8376	0.2044	0.4827	0.7933	-0.5111	0.0641	0.5292

(Continued)

TABLE 4 | Continued

Parameter	Spearman Correlation											
	week 14			week 20			week 32			week 34		
	r	p	q	r	p	q	r	p	q	r	p	q
MCP1	-0.2044	0.4827	0.7933	0.2967	0.3025	0.7089	**0.6176**	**0.0212**	**0.5243**	0.0333	0.9114	0.9565
IL1RN	-0.1780	0.5423	0.8183	0.0593	0.8438	0.9480	0.1912	0.5121	0.7999	-0.0022	0.9970	0.9999
D3 Cytokine Proteins												
IFN-α	-0.2063	0.4958	0.7962	0.1183	0.6991	0.9036	0.1898	0.5316	0.8063	0.1936	0.5224	0.7999
IL-6	0.1922	0.5513	0.8281	-0.0437	0.8974	0.9563	-0.0874	0.7821	0.9235	-0.0133	0.9615	0.9830
IL-18	-0.0968	0.7413	0.9152	-0.1298	0.6562	0.8862	0.0484	0.8707	0.9552	-0.0645	0.8521	0.9446
IFN-γ	-0.3624	0.2021	0.6388	-0.1658	0.5684	0.8318	0.0685	0.8159	0.9432	0.0391	0.8935	0.9552
MCP-1	**-0.5692**	**0.0366**	**0.5243**	-0.2659	0.3573	0.7453	-0.0462	0.8796	0.9552	-0.3845	0.1741	0.6217
IL-1RA	0.1009	0.7327	0.9131	-0.2229	0.4417	0.7872	-0.0211	0.9482	0.9759	0.0427	0.8856	0.9552

[a]*bold font corresponds to p < 0.05.*

[b]*bold and italic font corresponds to p < 0.01.*

[c]*Genes shared between the top five scoring pathways on D1 also included IL1RN, SOCS3, IFITM1, IRF7, NFKBIA, and KIT, genes that are included in the DEG.*

[d]*The gene encoding IL-1RA is ILRN that is included in the DEG.*

TABLE 5 | Correlation of early gene expression with follicular T helper cells (T_{FH}) or with memory or germinal center (GC) B cells (week 34).

Parameter	Spearman Correlation											
	PBMC			Lymph Nodes								
	Memory B cells			Memory B cells			GC B cells			Env-specific T_{FH}		
	r	p	q	r	p	q	r	p	q	r	p	q
D1 DEG												
SERPING1[a,b]	0.3914	0.1492	0.7379	0.1464	0.6024	0.8743	**0.6214**	**0.0155**	**0.3200**	***0.6536***	***0.0099***	***0.3200***
C3AR1	0.1487	0.5209	0.8529	0.1036	0.7144	0.9287	0.3393	0.2161	0.7714	**0.5429**	**0.0391**	**0.4579**
IL1RN	0.3968	0.1432	0.7379	0.2679	0.3334	0.7868	**0.5286**	**0.0454**	**0.4825**	**0.7286**	**0.0029**	**0.3153**
TNFAIP6	0.1877	0.5002	0.8523	0.2821	0.3074	0.7861	0.4107	0.1297	0.7202	***0.7143***	***0.0037***	***0.3153***
PLAUR	0.2735	0.3216	0.7861	0.1571	0.5756	0.8658	**0.6286**	**0.0141**	**0.3200**	**0.5393**	**0.0406**	**0.4578**
FPR2	0.2413	0.3835	0.8163	0.3107	0.2592	0.7714	0.3643	0.1824	0.7458	**0.6500**	**0.0105**	**0.3200**
SOCS3	**0.5594**	**0.0324**	**0.4578**	0.3429	0.2111	0.7714	0.3107	0.2592	0.7714	0.3857	0.1566	0.7379
OAS1	0.3021	0.2719	0.7729	0.2929	0.2888	0.7729	0.4357	0.1063	0.6703	***0.7643***	***0.0014***	***0.3153***
TNFSF10	0.4004	0.1394	0.7378	0.2964	0.2827	0.7729	0.4000	0.1408	0.7378	**0.5679**	**0.0297**	**0.4426**
CCR1	0.2520	0.3622	0.8163	0.3750	0.1692	0.7379	0.4214	0.1193	0.6857	**0.6250**	**0.0148**	**0.3200**
LILRA3	0.1859	0.5041	0.8523	0.3571	0.1917	0.7667	0.3107	0.2592	0.7714	**0.5429**	**0.0391**	**0.4578**
IFITM1	0.1680	0.5466	0.8543	0.0143	0.9642	0.9907	0.1714	0.5406	0.8529	0.3500	0.2012	0.7714
ARG2	0.2806	0.3087	0.7861	0.2464	0.3748	0.8163	0.3107	0.2592	0.7714	**0.5393**	**0.0462**	**0.4578**
CD82	0.3682	0.1763	0.7379	0.2714	0.3269	0.7861	0.3250	0.2370	0.7714	**0.6214**	**0.0155**	**0.3200**
IRF7	0.1930	0.4875	0.8512	0.2321	0.4039	0.8167	0.2750	0.3203	0.7861	**0.5714**	**0.0286**	**0.4426**
IFI35	0.3682	0.1763	0.7379	0.2143	0.4421	0.8367	**0.5393**	**0.0406**	**0.4578**	**0.5250**	**0.0471**	**0.4864**
NFKBIA	0.2520	0.3621	0.8163	0.1964	0.4819	0.8512	0.3679	0.1779	0.7379	***0.6893***	***0.0057***	***0.3166***
CSF3R	0.1180	0.6735	0.9054	0.2393	0.3892	0.8163	0.3393	0.2161	0.7714	**0.5500**	**0.0362**	**0.4578**
DDIT3	0.1662	0.5512	0.8544	0.2714	0.3268	0.7861	0.3321	0.2264	0.7714	***0.7071***	***0.0042***	***0.3153***
GP1BB	0.1019	0.7167	0.9287	0.3071	0.2649	0.7729	0.3536	0.1964	0.7714	***0.6571***	***0.0094***	***0.3200***
CLU	0.1948	0.4837	0.8512	0.1750	0.5320	0.8529	0.4214	0.1193	0.6857	0.4500	0.0944	0.6415
TNFAIP3	0.3342	0.2221	0.7714	0.2857	0.3012	0.7861	0.4536	0.0915	0.6415	***0.7214***	***0.0033***	***0.3135***
IL1RL1	-0.0858	0.7602	0.9302	0.0500	0.8626	0.9550	***0.6786***	***0.0068***	***0.3166***	0.4607	0.0861	0.6415
HLA-DMA	**-0.5719**	**0.0281**	**0.4426**	-0.0179	0.9540	0.9907	-0.3036	0.2708	0.7729	-0.0929	0.7435	0.9202
KIT	0.0393	0.8901	0.9709	0.0607	0.8324	0.9483	**0.5714**	**0.0286**	**0.4426**	0.4571	0.0888	0.6415
D1 Shared Pathway Genes[c]												
IL2RA	0.4021	0.1377	0.7378	0.2393	0.3892	0.8163	0.2107	0.4498	0.8367	0.3000	0.2767	0.7729
CSF2RB	0.3181	0.2461	0.7714	0.2929	0.2888	0.7729	0.3893	0.1525	0.7379	**0.5929**	**0.0222**	**0.3933**
FCGR1A	0.4629	0.0838	0.6414	0.3179	0.2479	0.7714	0.3821	0.1607	0.7379	0.4893	0.0666	0.5629
DUSP4	0.0626	0.8249	0.9483	0.2143	0.4421	0.8367	0.4250	0.1159	0.6857	0.1821	0.5150	0.8529
HLA-DQB1	-0.2270	0.4130	0.8189	-0.1929	0.4901	0.8512	-0.1464	0.6023	0.8743	-0.1786	0.5235	0.8529
HLA-DRB1	-0.4147	0.1249	0.7038	-0.2821	0.3074	0.7861	-0.3250	0.2370	0.7714	-0.0036	0.9948	0.9969

(Continued)

TABLE 5 | Continued

Parameter	Spearman Correlation											
	PBMC			Lymph Nodes								
	Memory B cells			Memory B cells			GC B cells			Env-specific T_{FH}		
	r	p	q	r	p	q	r	p	q	r	p	q
D1 Cytokine Genes[d]												
IFNA2	0.3682	0.1763	0.7379	0.1929	0.4901	0.8512	0.5179	0.0506	0.4951	0.3250	0.2370	0.7714
IL6	0.2967	0.2807	0.7729	0.2500	0.3678	0.8163	**0.5536**	**0.0349**	**0.4578**	***0.6857***	***0.0061***	***0.3166***
IL18	-0.1948	0.4837	0.8512	-0.2857	0.3011	0.7861	0.5107	0.0543	0.5031	0.1964	0.4819	0.8512
IFNG	0.1537	0.5817	0.8658	-0.2429	0.3820	0.8163	0.4679	0.0808	0.6399	0.2107	0.4498	0.8367
MCP1	**0.5326**	**0.0431**	**0.4716**	0.3750	0.1692	0.7379	0.5179	0.0506	0.4951	**0.6393**	**0.0122**	**0.3201**
D1 Cytokine Proteins												
IFN-α	-0.1716	0.5380	0.8529	-0.0929	0.7435	0.9302	-0.2750	0.3203	0.7861	0.1464	0.6023	0.8743
IL-6	0.3399	0.2132	0.7714	-0.5076	0.0554	0.5031	-0.4486	0.0948	0.6415	-0.0286	0.9206	0.9871
IL-18	0.1287	0.6455	0.8959	0.0571	0.8425	0.9483	-0.1000	0.7241	0.9287	0.4071	0.1334	0.7295
IFN-γ	0.2952	0.2820	0.7729	-0.2324	0.4016	0.8166	-0.0840	0.7539	0.9302	0.2717	0.3246	0.7861
MCP-1	0.5094	0.0545	0.5031	-0.2286	0.4114	0.8189	0.0571	0.8425	0.9483	0.3357	0.2212	0.7714
IL-1RA	-0.0197	0.9465	0.9907	0.0786	0.7827	0.9414	0.2250	0.4189	0.8212	0.4429	0.1002	0.6657
D3 DEG												
CLU	0.1342	0.6452	0.8881	0.4374	0.1198	0.6852	0.0044	0.9911	0.9966	0.1516	0.6051	0.8703
GP1BB	0.0528	0.8587	0.9582	0.4549	0.1044	0.6588	-0.0902	0.7582	0.9305	0.1385	0.6375	0.8872
BCL2L1	0.3410	0.2313	0.7550	0.5209	0.0591	0.8463	0.1782	0.5391	0.8463	0.4769	0.0872	0.6249
IL1RL1	0.2464	0.3929	0.7988	-0.1956	0.5022	0.8424	0.2926	0.3074	0.7734	-0.2440	0.3998	0.7988
ILR2	-0.1276	0.6622	0.8979	-0.1604	0.5838	0.8616	0.0946	0.7467	0.9305	-0.2440	0.3998	0.7988
D3 Shared Pathway Genes												
HLA-C	-0.0990	0.7352	0.9305	0.0637	0.8319	0.9532	-0.2332	0.4194	0.8037	0.0593	0.8438	0.9532
FCGR1A	0.3850	0.1736	0.7180	0.0374	0.9035	0.9842	0.4158	0.1396	0.7180	-0.0330	0.9155	0.9911
D3 Cytokine Genes												
IFNA2	0.1210	0.6784	0.9030	-0.2747	0.3411	0.7803	0.4422	0.1143	0.6852	0.0242	0.9396	0.9911
IL6	0.3256	0.2543	0.7550	-0.1077	0.7126	0.9288	0.2794	0.3305	0.7741	0.1780	0.5423	0.8463
IL18	0.1716	0.5549	0.8498	-0.3890	0.1703	0.7180	0.1496	0.6076	0.8703	-0.1956	0.5022	0.8424
IFNG	0.0616	0.8349	0.9532	-0.3363	0.2399	0.7550	-0.0572	0.8468	0.9536	-0.1780	0.5423	0.8463
MCP1	**0.6161**	**0.0213**	**0.3870**	-0.0154	0.9638	0.9911	0.2444	0.3969	0.7988	0.0418	0.8915	0.9769
IL1RN	0.3476	0.2222	0.7550	0.2528	0.3825	0.7988	-0.0946	0.7466	0.9305	-0.0198	0.9517	0.9911
D3 Cytokine Proteins												
IFN-α	-0.2672	0.3737	0.7988	0.0908	0.7678	0.9332	-0.3444	0.2477	0.7550	0.1513	0.6196	0.8824
IL-6	-0.1706	0.5833	0.8616	-0.5154	0.0769	0.6185	0.0088	0.9872	0.9953	-0.4193	0.1666	0.7180
IL-18	0.1828	0.5262	0.8463	0.4004	0.1561	0.7180	-0.0903	0.7579	0.9305	0.3476	0.2221	0.7550
IFN-γ	0.2500	0.3846	0.7988	0.1503	0.6059	0.8703	0.1018	0.7291	0.9288	0.1635	0.5740	0.8616
MCP-1	0.0792	0.7878	0.9412	-0.0637	0.8319	0.9532	-0.1254	0.6673	0.8979	0.0286	0.9276	0.9911
IL-1RA	0.3195	0.2622	0.7550	0.4577	0.1022	0.6565	0.2350	0.4139	0.8014	0.4858	0.0811	0.6185

[a]*bold font corresponds to p < 0.05.*

[b]*bold and italic font corresponds to p < 0.01.*

[c]*Genes shared between the top five scoring pathways on D1 also included IL1RN, SOCS3, IFITM1, IRF7, NFKBIA, and KIT, genes that are included in the DEG.*

[d]*The gene encoding IL-1RA is ILRN that is included in the DEG.*

(**Supplemental Figure S7**). When we limited the analysis to genes that were only correlated with ADCC function, the Toll-like receptor signaling pathway (FDR p=6.36E-06), the BCR signaling pathway (FDR p=0.0002), and the NK cell-mediated cytotoxicity pathway (FDR p=0.0028) were also identified in the enrichment analysis (**Supplemental Table S5**). It should be noted though that enrichment analysis of the data in our study here is biased as we performed a targeted transcriptome analysis and therefore only a limited number of genes could be identified.

The type I interferon response could have also been induced by the administration of the viral ChAd vector (40–43). The coadministration of MVA in Group 2 appeared to modify the innate response observed in Group 1. The current study did not include an adjuvant only group or groups being only immunized with the ChAd vector or MVA. Therefore, we were not able to study the innate response to the individual vaccine components (adjuvant, ChAdV, or MVA). As the individual components of the vaccine regimen were administered at different sites, the potential interference in innate immune responses must have been due to a rapid systemic effect. Interestingly, it was reported previously that the simultaneous administration of HAdV5 and MVA vectors resulted in vaccine interference, evident in suppressed $CD8^+$ T cell responses (44). It is also well established that MVA encodes several immune evasion genes that could have suppressed the innate response, especially the type I interferon response, induced by the 3M-052-SE adjuvanted HIV Env protein (45, 46). In fact, novel MVA vaccine vectors are being developed to improve the immunogenicity of MVA (47, 48). However, it is also well documented that MVA can induce potent innate responses

TABLE 6 | Correlation of early gene expression with antigen-specific $CD8^+$ T cell responses.

Parameter	SIV Gag-specific $CD8^+$ T			HIV Env-specific $CD8^+$ T		
	Spearman Correlation[a]					
	r	p	q	r	p	q
D1 DEG						
SERPING1	0.2272	0.4123	0.8014	-0.1841	0.5085	0.8460
C3AR1	-0.0966	0.7308	0.9288	-0.3378	0.2170	0.7550
IL1RN	0.0322	0.9106	0.9889	-0.2985	0.2779	0.7550
TNFAIP6	-0.0125	0.9667	0.9911	-0.1341	0.6319	0.8861
PLAUR	0.0575	0.8397	0.9532	0.0518	0.8551	0.9571
FPR2	0.1306	0.6406	0.8881	0.0572	0.8396	0.9532
SOCS3	0.2666	0.3342	0.7741	-0.3146	0.2516	0.7550
OAS1	0.0286	0.9208	0.9911	-0.1528	0.5729	0.8616
TNFSF10	0.1073	0.7019	0.9241	-0.2931	0.2867	0.7550
CCR1	-0.2111	0.4471	0.8274	-0.3682	0.1764	0.7181
LILRA3	0.0859	0.7601	0.9305	-0.0089	0.9771	0.9953
IFITM1	-0.0054	0.9872	0.9953	-0.3450	0.2070	0.7550
ARG2	0.1699	0.5419	0.8463	0.0107	0.9717	0.9934
CD82	0.2039	0.4629	0.8346	-0.0232	0.9363	0.9911
IRF7	-0.0608	0.8296	0.9532	-0.2055	0.4595	0.8341
IFI35	0.1127	0.6875	0.9117	-0.1323	0.6362	0.8872
NFKBIA	0.0376	0.8952	0.9781	-0.0822	0.7700	0.9332
CSF3R	-0.0590	0.8346	0.9532	-0.1787	0.5209	0.8463
DDIT3	0.0072	0.9821	0.9953	-0.1430	0.6088	0.8703
GP1BB	0.0877	0.7551	0.9305	0.2752	0.3181	0.7734
CLU	0.2326	0.4012	06852	0.3592	0.1878	0.7393
TNFAIP3	0.0250	0.9309	0.9911	-0.3825	0.1592	0.7180
IL1RL1	0.0125	0.9667	0.9911	-0.1984	0.4756	0.8413
HLA-DMA	-0.3757	0.1673	0.1780	0.0214	0.9410	0.9911
KIT	0.0734	0.7946	0.9412	0.2752	0.3181	0.7734
D1 Shared Pathway Genes[c]						
IL2RA	-0.0447	0.8749	0.9675	0.1233	0.6598	0.8979
CSF2RB	-0.0143	0.9616	0.9911	-0.1930	0.4875	0.8413
FCGR1A	-0.0054	0.9872	0.9953	-0.1984	0.4756	0.8413
DUSP4	-0.1002	0.7212	0.9288	-0.1519	0.5865	0.8621
HLA-DQB1	-0.1342	0.6313	0.8861	0.2359	0.3942	0.7988
HLA-DRB1	-0.2701	0.3275	0.7734	-0.2359	0.3942	0.7988
D1 Cytokine Genes[d]						
IFNA2	0.1664	0.5506	0.8477	0.3146	0.2516	0.7550
IL6	0.0572	0.8397	0.9532	0.1215	0.6641	0.8979
IL18	0.1252	0.6546	0.8973	-0.1734	0.5340	0.8463
IFNG	0.2630	0.3409	0.7803	0.2073	0.4552	0.8332
MCP1	-0.0805	0.7748	0.9359	-0.1912	0.4919	0.8413
D1 Cytokine Proteins						
IFN-α	**-0.6440**	**0.0113**	**0.3149**	0.2431	0.3797	0.7988
IL-6	0.0161	0.9553	0.9911	0.1682	0.5434	0.8463
IL-18	-0.3846	0.1567	0.7180	0.5004	0.0593	0.5055
IFN-γ	-0.0877	0.7539	0.9305	0.0734	0.7943	0.9412
MCP-1	0.1360	0.6268	0.8861	-0.0590	0.8350	0.9532
IL-1RA	-0.0608	0.8296	0.9532	0.3199	0.2435	0.7550
D3 DEG						
CLU	-0.0022	0.9969	0.9969	0.1696	0.5596	0.8533
GP1BB	-0.1411	0.6281	0.8861	0.1960	0.4989	0.8424
BCL2L1	0.1676	0.5641	0.8567	0.1234	0.6727	0.8997
IL1RL1	0.3462	0.2240	0.7550	0.1256	0.6672	0.8979
ILR2	-0.1147	0.6948	0.9180	-0.0154	0.9607	0.9911
D3 Shared Pathway Genes						
HLA-C	-0.2272	0.4316	0.8185	0.0771	0.7933	0.9412
FCGR1A	0.3664	0.2170	0.7550	-0.3106	0.2778	0.7550
D3 Cytokine Genes						
IFNA2	**0.6615**	**0.0119**	**0.3149**	0.2643	0.3583	0.7988
IL6	0.4851	0.0806	0.6185	0.0793	0.7873	0.9412
IL18	**0.6262**	**0.0189**	**0.3641**	0.3811	0.1785	0.7180
IFNG	0.1610	0.5798	0.8616	0.2137	0.4603	0.8341

(Continued)

TABLE 6 | Continued

Parameter	SIV Gag-specific CD8+ T			HIV Env-specific CD8+ T		
	Spearman Correlation[a]					
	r	p	q	r	p	q
MCP1	0.2315	0.4226	0.8055	0.0551	0.8525	0.9571
IL1RN	0.0220	0.9424	0.9911	0.0440	0.8822	0.9726
D3 Cytokine Proteins						
IFN-α	-0.2666	0.3742	0.7988	0.3200	0.2833	07550
IL-6	0.2851	0.3718	0.7988	0.1051	0.7308	0.9288
IL-18	-0.1004	0.7302	0.9288	0.2183	0.4494	0.8274
IFN-γ	0.2661	0.3538	0.7988	0.1008	0.7279	0.9288
MCP-1	0.1874	0.5180	0.8463	0.3040	0.2885	0.7550
IL-1RA	0.0494	0.8672	0.9618	-0.0141	0.9643	0.9911

[a]*bold font corresponds to p < 0.05.*

[b]*bold and italic font corresponds to p < 0.01.*

[c]*Genes shared between the top five scoring pathways on D1 also included IL1RN, SOCS3, IFITM1, IRF7, NFKBIA, and KIT, genes that are included in the DEG.*

[d]*The gene encoding IL-1RA is ILRN that is included in the DEG.*

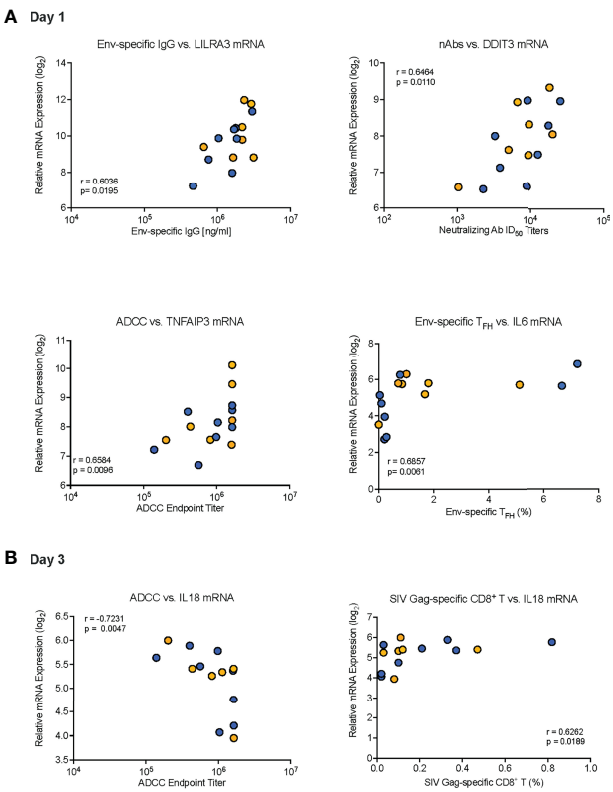

FIGURE 8 | Examples of correlations between day 1 or day 3 innate immune responses and adaptive immune responses. Representative examples of correlations between innate immune responses on Day 1 **(A)** or Day 3 **(B)** with distinct adaptive immune responses are presented. **(A)** Correlation between (i) Env-specific IgG at week 14 and D1 LILRA3 mRNA expression, (ii) neutralizing ID50 titers at week 34 and D1 DDIT3 mRNA expression, (iii) endpoint ADCC titers at week 34 and D1 TNFAIP3 mRNA, and (iv) week 34 Env-specific T_{FH} frequencies and D1 IL6 mRNA expression. **(B)** Correlation between (i) week 34 ADCC endpoint titers and D3 IL18 mRNA levels and (ii) week 34 SIV Gag-specific $CD8^+$ T cell frequencies and D3 IL18 mRNA levels. Each symbol represents an individual animal of Group 1 (orange circles) or Group 2 (blue circles). The "r" and "p" values were determined by Spearman rank analysis and represent the correlation coefficient and the unadjusted p values, respectively.

(49–51). In fact, animals in Group 2 had increased plasma concentrations of several inflammatory cytokines on day 1. It is plausible that the induction of genes in response to the vaccine prime peaked prior to our first sampling timepoint at 24 hours in Group 2. Alternatively, the kinetics of mRNA induction in Group 2 could have been delayed and occurred between day 1 and day 3. In fact, in Group 2 animals some cytokines were still elevated on day 3 compared to day 0. Furthermore, specific genes

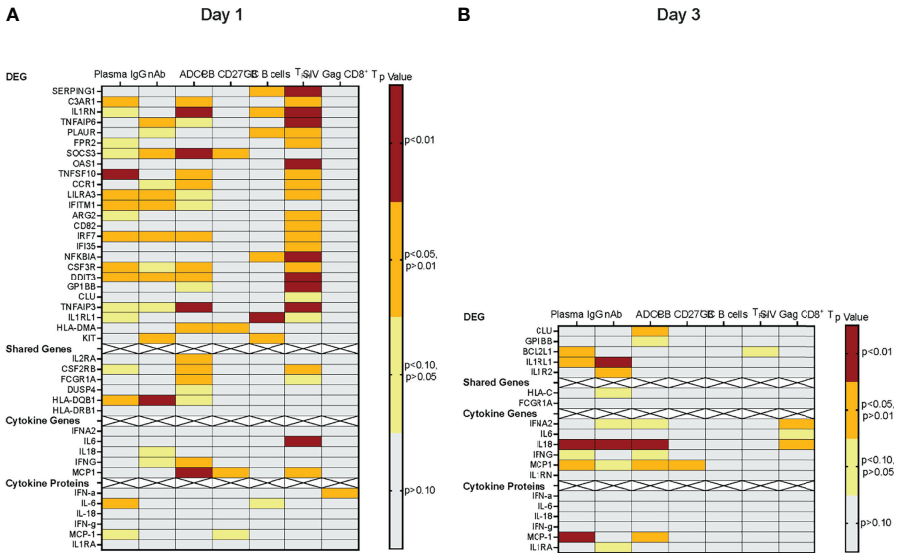

FIGURE 9 | Correlations of early vaccine prime-induced and vaccine-induced adaptive immune responses. Correlations for D1 or D3 are illustrated in Panels **(A)** or **(B)**, respectively. The left y-axis lists the various genes or proteins included in the correlation analyses: (i) DEG, (ii) shared pathway genes, (iii) genes of elevated plasma cytokines, or (iv) plasma cytokines. The strength of the correlation between gene expression and a specific immune parameter is indicated by a heatmap using the relevant Spearman rank correlation unadjusted p values (see color legend). Each column represents a specific immune response, including - from left to right– Env-specific plasma IgG, tier 1 MW965-specific neutralizing antibody ID_{50} titers, ADCC endpoint titers, peripheral blood memory B cells at week 34, germinal center B cells in axillary lymph nodes at week 34, Env-specific follicular T helper cells in axillary lymph nodes at week 34, and SIV Gag-specific peripheral blood $CD8^+$ T cell responses at week 34.

and proteins are induced by distinct cell types and, thus, changes in relative frequencies of peripheral blood cell populations on days 1 and 3 compared to day 0 could have altered results obtained in the whole blood gene expression analysis. Our findings emphasize the need to assess the impact of individual vaccine components on vaccine immunogenicity at a more granular level, including in individual cell populations and over a more frequent sampling interval.

Both the induction of type I interferons and the activation of Myd88 by TLR-based adjuvants have been demonstrated to enhance the inflammatory response through NF-kB activation (7, 52–54). TLR signaling has also been linked to germinal center formation, isotype switching, and antibody maturation (55, 56). While TLR agonists can directly activate B cells, they also indirectly enhance antibody responses through the activation of T_{FH} [reviewed in (23)]. In fact, the D1 expression of several DEG in the current study were correlated with Env-specific lymph node T_{FH} frequencies at week 34 (**Table 6**). Although we found few correlations between DEG and memory or GC B cells at week 34 (**Table 6**), it should be noted that we measured total memory and GC B cells and not Env-specific B cells.

Due to the limited sample size, we could not validate our findings in a different study setting or with a different data set. Furthermore, because we did not challenge the animals, we do not know whether and how the correlations between early gene induction and vaccine-induced adaptive immune responses inform predictions about vaccine efficacy. However, the conclusion that the observed correlations between early innate immune signatures and later vaccine-induced adaptive immune responses are biologically relevant is supported by data demonstrating the role of complement (57), type I interferons (58, 59), IL-6 (60–62), and TLR signaling (55, 56) in B cell activation and maturation. The result of the network and enrichment analyses with genes that were associated with one or more adaptive immune parameters that identified predicted partners involved in the BCR signaling pathway further substantiated this conclusion (**Supplementary Figure X**). Overall, the results support the idea that through modulation of innate immune responses by targeted modifications in the vaccine prime, we can direct specific HIV-specific antibody and T cell responses to optimize vaccine-induced immunity. The latter might be especially important for pediatric vaccines due to the dynamic nature of the immune systems during neonatal and infant development.

DATA AVAILABILITY STATEMENT

The original contributions presented in the study are included in the article/supplementary files, further inquiries can be directed to the corresponding author.

ETHICS STATEMENT

The animal study was reviewed and approved by UC Davis Institutional Animal Care and Use Committee.

AUTHOR CONTRIBUTIONS

KDP and SRP conceived and planned the study. KKVV and KDP wrote the manuscript. KKVV, ADC, and JP performed the experiments and analyzed the data. KKAVR oversaw the animal studies. KAC and MGH conducted the statistical analysis. MT and CF provided the 3M-052-SE adjuvant, and TH the ChAdOx1t.SIVcons239 and MVA.tSIVconsv239 vaccines. All authors critically reviewed and edited the manuscript. All authors contributed to the article and approved the submitted version.

FUNDING

The work was supported by National Institutes of Health grants 1R01 DE028146 (KDP), P01 AI117915 (SRP, KDP), T32 5108303 (ADC), the Office of Research Infrastructure Programs/OD P510D011107 (CNPRC), and the Center for AIDS Research award P30AI050410 (UNC). The UNC Flow Cytometry Core Facility is supported in part by P30 CA016086 Cancer Center Core Support Grant to the UNC Lineberger Comprehensive Cancer Center. Research reported in this publication was supported by the Center for AIDS Research award number 5P30AI050410.

ACKNOWLEDGMENTS

We thank Dr. David Pickup for supplying the MVA-Env vaccine. The authors would like to thank the staff of the UNC Delta Translational Services Recharge Center.

SUPPLEMENTARY MATERIAL

The Supplementary Material for this article can be found online at: https://www.frontiersin.org/articles/10.3389/fimmu.2022.840976/full#supplementary-material

Supplementary Figure 1 | Assessment of Memory and GC B Cell Frequencies by Flow Cytometry. Tissue samples were processed into single cell suspensions and stained with surface markers prior to fixation and analysis *via* flow cytometry. Only events in the R1 lymphocyte gate were recorded (Top left). Single live lymphocytes that were negative for lineage markers CD3, CD14 and CD16 (top right) were assessed for CD20 and CD27 expression. CD20+CD27- B (bottom right) and CD20+CD27+ memory B (bottom left) cells were analyzed for expression of CXCR5 (CD185).

Supplementary Figure 2 | Gating strategy for Env-specific follicular T helper cells. Samples were cultured for 18-24 hours in the presence of vehicle DMSO (negative control), Staphylococcal enterotoxin B (SEB) (positive control), or HIV-1 Clade C Consensus Peptide Pool and analyzed by flow cytometry for surface expression of activation induced T_{FH} markers. Top row: Viable $CD3^+$ lymphocyte events were assessed for the presence of CD4 (thick black gate). Middle row: $CD4^+$ events were further classified as follicular T cells based on the presence of CD185 (CXCR5) and CD279 (PD-1) signal (blue gate). Activation Induced Marker (AIM) T follicular helper cells were defined as $CD134^+CD137^+$ events (magenta gate). Env-specific AIM T_{FH} were calculated by normalizing the frequency against the DMSO control samples.

Supplementary Figure 3 | Flow cytometric identification of SIV Gag-specific $CD8^+$ T cells. Samples were stimulated with media only (negative control), PMA/Ionomycin (positive control) or overlapping peptides of SIV p27 Gag for 6 hours in the presence of Brefeldin-A for the final 5 hours. Samples were stained with surface markers and subsequently fixed, permeabilized, and subjected to intracellular staining. Top row: viable events from the lymphocyte gate were assessed for CD3 and CD8. Gating for TNF-α, IFN-γ, IL-2 or IL-17 is shown for each experimental treatment. SIV Gag-specific responses were reported as the frequency of single-stained (Boolean logic) cytokine-positive events normalized to the frequency of the corresponding 'media only' control sample.

Supplementary Figure 4 | Gene expression analysis of Group 1 and Group 2 prior and post vaccination. *Panel A:* Principal component plot of PC1 and PC2 mRNA data of D0 samples from Group 1 (red circles) and Group 2 (blue circles). Image was generated using Clustviz.

Supplementary Figure 5 | Interaction network of differentially expressed genes. The network was created in Cytoscape as degree-directed layout using the Human String Protein Database. Interactions between the individual proteins are indicated by connecting lines. Note that for the D1 DEG LILAR3, ARG2, CD82, DDIT3, GP1BB, and HLA-DMA no interactions were identified.

Supplementary Figure 6 | Distribution of unadjusted p-values from two-sided tests for Spearman correlations. **(A, B)** show the distribution of unadjusted p-values from two-sided tests for Spearman correlations (H_a: rho ≠ 0) between differentially regulated transcripts and **(A)** humoral (Env-specific plasma IgG, ADCC, and neutralizing antibody responses; total tests: n=661) or **(B)** cellular (memory B and germinal center B cells, T_{FH} cells, and HIV Env- and SIV Gag-specific $CD8^+$ T-cells; total tests: n=366) immune responses. Unadjusted p values in 0.05 increments are listed on the x-axis. The y-axis lists the percentage of unadjusted p values falling into the range of each increment. The number on top of each bar represents the absolute number of tests within each p value range. The dashed line indicates the expected percentage if correlations were randomly distributed.

Supplementary Figure 7 | Potential interactions between day 1 induced genes and specific signaling pathways. Genes that were increased on D1 and correlated to vaccine-induced antibody responses were entered into NetworkAnalyst to assemble a network based on the String v11 Human Interactome. Major hubs (nodes) are indicated by red and orange circles. Predicted interactions between the genes are indicated by edges (black lines), with dark blue circles symbolizing predicted interaction partners. In Panels A and B genes that are part of the KEGG B cell receptor or the TLR7/8 signaling pathway, respectively, are represented by light blue circles.

REFERENCES

1. UNIADS.org. *2021- Global Aids Update* (2021) (Accessed November 24).
2. Pulendran B. Systems Vaccinology: Probing Humanity's Diverse Immune Systems With Vaccines. *Proc Natl Acad Sci USA* (2014) 111:12300–6. doi: 10.1073/pnas.1400476111
3. Hagan T, Nakaya HI, Subramaniam S, Pulendran B. Systems Vaccinology: Enabling Rational Vaccine Design With Systems Biological Approaches. *Vaccine* (2015) 33:5294–301. doi: 10.1016/j.vaccine.2015.03.072
4. Cable J, Srikantiah P, Crowe JE Jr., Pulendran B, Hill A, Ginsberg A, et al. Vaccine Innovations for Emerging Infectious Diseases-a Symposium Report. *Ann NY Acad Sci* (2020) 1462:14–26. doi: 10.1111/nyas.14235
5. Derking R, Sanders RW. Structure-Guided Envelope Trimer Design in HIV-1 Vaccine Development: A Narrative Review. *J Int AIDS Soc* (2021) 24 Suppl 7: e25797. doi: 10.1002/jia2.25797
6. Obermoser G, Presnell S, Domico K, Xu H, Wang Y, Anguiano E, et al. Systems Scale Interactive Exploration Reveals Quantitative and Qualitative Differences in Response to Influenza and Pneumococcal Vaccines. *Immunity* (2013) 38:831–44. doi: 10.1016/j.immuni.2012.12.008
7. Pulendran B, SA P, O'Hagan DT. Emerging Concepts in the Science of Vaccine Adjuvants. *Nat Rev Drug Discov* (2021) 20:454–75. doi: 10.1038/s41573-021-00163-y
8. Kazmin D, Nakaya HI, Lee EK, Johnson MJ, van der Most R, van den Berg RA, et al. Systems Analysis of Protective Immune Responses to RTS,s Malaria

Vaccination in Humans. *Proc Natl Acad Sci USA* (2017) 114:2425–30. doi: 10.1073/pnas.1621489114
9. Li S, Nakaya HI, Kazmin DA, Oh JZ, Pulendran B. Systems Biological Approaches to Measure and Understand Vaccine Immunity in Humans. *Semin Immunol* (2013) 25:209–18. doi: 10.1016/j.smim.2013.05.003
10. Li S, Rouphael N, Duraisingham S, Romero-Steiner S, Presnell S, Davis C, et al. Molecular Signatures of Antibody Responses Derived From a Systems Biology Study of Five Human Vaccines. *Nat Immunol* (2014) 15:195–204. doi: 10.1038/ni.2789
11. Nakaya HI, Pulendran B. Systems Vaccinology: Its Promise and Challenge for HIV Vaccine Development. *Curr Opin HIV AIDS* (2012) 7:24–31. doi: 10.1097/COH.0b013e32834dc37b
12. Nakaya HI, Wrammert J, Lee EK, Racioppi L, Marie-Kunze S, Haining WN, et al. Systems Biology of Vaccination for Seasonal Influenza in Humans. *Nat Immunol* (2011) 12:786–95. doi: 10.1038/ni.2067
13. Querec TD, Akondy RS, Lee EK, Cao W, Nakaya HI, Teuwen D, et al. Systems Biology Approach Predicts Immunogenicity of the Yellow Fever Vaccine in Humans. *Nat Immunol* (2009) 10:116–25. doi: 10.1038/ni.1688
14. Andersen-Nissen E, Fiore-Gartland A, Ballweber Fleming L, Carpp LN, Naidoo AF, Harper MS, et al. Innate Immune Signatures to a Partially-Efficacious HIV Vaccine Predict Correlates of HIV-1 Infection Risk. *PloS Pathog* (2021) 17:e1009363. doi: 10.1371/journal.ppat.1009363
15. Curtis AD2nd, Dennis M, Eudailey J, Walter KL, Cronin K, Alam SM, et al. HIV Env-Specific Igg Antibodies Induced by Vaccination of Neonatal Rhesus Macaques Persist and can be Augmented by a Late Booster Immunization in Infancy. *mSphere* (2020) 5:e00162-20. doi: 10.1128/mSphere.00162-20
16. Dennis M, Eudailey J, Pollara J, McMillan AS, Cronin KD, Saha PT, et al. Co-Administration of CH31 Broadly Neutralizing Antibody Does Not Affect Development of Vaccine-Induced Anti-HIV-1 Envelope Antibody Responses in Infant Rhesus Macaques. *J Virol* (2019) 93:e01783-18. doi: 10.1128/JVI.01783-18
17. Ondondo B, Murakoshi H, Clutton G, Abdul-Jawad S, Wee EG, Gatanaga H, et al. Novel Conserved-Region T-Cell Mosaic Vaccine With High Global HIV-1 Coverage is Recognized by Protective Responses in Untreated Infection. *Mol Ther* (2016) 24:832–42. doi: 10.1038/mt.2016.3
18. Vandesompele J, De Preter K, Pattyn F, Poppe B, Van Roy N, De Paepe A, et al. Accurate Normalization of Real-Time Quantitative RT-PCR Data by Geometric Averaging of Multiple Internal Control Genes. *Genome Biol* (2002) 3:RESEARCH0034. doi: 10.1186/gb-2002-3-7-research0034
19. Raudvere U, Kolberg L, Kuzmin I, Arak T, Adler P, Peterson H, et al. G: Profiler: A Web Server for Functional Enrichment Analysis and Conversions of Gene Lists (2019 Update). *Nucleic Acids Res* (2019) 47:W191–8. doi: 10.1093/nar/gkz369
20. Szklarczyk D, Gable AL, Lyon D, Junge A, Wyder S, Huerta-Cepas J, et al. STRING V11: Protein-Protein Association Networks With Increased Coverage, Supporting Functional Discovery in Genome-Wide Experimental Datasets. *Nucleic Acids Res* (2019) 47:D607–13. doi: 10.1093/nar/gky1131
21. Gaestel M, Kotlyarov A, Kracht M. Targeting Innate Immunity Protein Kinase Signalling in Inflammation. *Nat Rev Drug Discov* (2009) 8:480–99. doi: 10.1038/nrd2829
22. Ray P, Krishnamoorthy N, Oriss TB, Ray A. Signaling of C-Kit in Dendritic Cells Influences Adaptive Immunity. *Ann NY Acad Sci* (2010) 1183:104–22. doi: 10.1111/j.1749-6632.2009.05122.x
23. Belanger S, Crotty S. Dances With Cytokines, Featuring TFH Cells, IL-21, IL-4 and B Cells. *Nat Immunol* (2016) 17:1135–6. doi: 10.1038/ni.3561
24. Crotty S. A Brief History of T Cell Help to B Cells. *Nat Rev Immunol* (2015) 15:185–9. doi: 10.1038/nri3803
25. Dan JM, Lindestam Arlehamn CS, Weiskopf D, da Silva Antunes R, Havenar-Daughton C, Reiss SM, et al. A Cytokine-Independent Approach to Identify Antigen-Specific Human Germinal Center T Follicular Helper Cells and Rare Antigen-Specific CD4+ T Cells in Blood. *J Immunol* (2016) 197:983–93. doi: 10.4049/jimmunol.1600318
26. Havenar-Daughton C, Reiss SM, Carnathan DG, Wu JE, Kendric K, Torrents de la Pena A, et al. Cytokine-Independent Detection of Antigen-Specific Germinal Center T Follicular Helper Cells in Immunized Nonhuman Primates Using a Live Cell Activation-Induced Marker Technique. *J Immunol* (2016) 197:994–1002. doi: 10.4049/jimmunol.1600320
27. Ma CS, Suryani S, Avery DT, Chan A, Nanan R, Santner-Nanan B, et al. Early Commitment of Naive Human CD4(+) T Cells to the T Follicular Helper (T (FH)) Cell Lineage is Induced by IL-12. *Immunol Cell Biol* (2009) 87:590–600. doi: 10.1038/icb.2009.64
28. Moser B, Schaerli P, Loetscher P. CXCR5(+) T Cells: Follicular Homing Takes Center Stage in T-Helper-Cell Responses. *Trends Immunol* (2002) 23:250–4. doi: 10.1016/S1471-4906(02)02218-4
29. Vinuesa CG, Tangye SG, Moser B, Mackay CR. Follicular B Helper T Cells in Antibody Responses and Autoimmunity. *Nat Rev Immunol* (2005) 5:853–65. doi: 10.1038/nri1714
30. Linterman MA, Hill DL. Can Follicular Helper T Cells be Targeted to Improve Vaccine Efficacy? *F1000Res* (2016) 5. doi: 10.12688/f1000research.7388.1
31. Zak DE, Andersen-Nissen E, Peterson ER, Sato A, Hamilton MK, Borgerding J, et al. Merck Ad5/HIV Induces Broad Innate Immune Activation That Predicts CD8(+) T-Cell Responses But is Attenuated by Preexisting Ad5 Immunity. *Proc Natl Acad Sci USA* (2012) 109:E3503-12. doi: 10.1073/pnas.1208972109
32. Ehrenberg PK, Shangguan S, Issac B, Alter G, Geretz A, Izumi T, et al. A Vaccine-Induced Gene Expression Signature Correlates With Protection Against SIV and HIV in Multiple Trials. *Sci Transl Med* (2019) 11(507): eaaw4236. doi: 10.1126/scitranslmed.aaw4236
33. Di Pasquale A, Preiss S, Tavares Da Silva F, Garcon N. Vaccine Adjuvants: From 1920 to 2015 and Beyond. *Vaccines (Basel)* (2015) 3:320–43. doi: 10.3390/vaccines3020320
34. Francica JR, Zak DE, Linde C, Siena E, Johnson C, Juraska M, et al. Innate Transcriptional Effects by Adjuvants on the Magnitude, Quality, and Durability of HIV Envelope Responses in Nhps. *Blood Adv* (2017) 1:2329–42. doi: 10.1182/bloodadvances.2017011411
35. Phillips B, Van Rompay KKA, Rodriguez-Nieves J, Lorin C, Koutsoukos M, Tomai M, et al. Adjuvant-Dependent Enhancement of HIV Env-Specific Antibody Responses in Infant Rhesus Macaques. *J Virol* (2018) 92:e01051-18. doi: 10.1128/JVI.01051-18
36. Kwissa M, Nakaya HI, Oluoch H, Pulendran B. Distinct TLR Adjuvants Differentially Stimulate Systemic and Local Innate Immune Responses in Nonhuman Primates. *Blood* (2012) 119:2044–55. doi: 10.1182/blood-2011-10-388579
37. Dowling DJ. Recent Advances in the Discovery and Delivery of TLR7/8 Agonists as Vaccine Adjuvants. *Immunohorizons* (2018) 2:185–97. doi: 10.4049/immunohorizons.1700063
38. Gibson SJ, Imbertson LM, Wagner TL, Testerman TL, Reiter MJ, Miller RL, et al. Cellular Requirements for Cytokine Production in Response to the Immunomodulators Imiquimod and s-27609. *J Interferon Cytokine Res* (1995) 15:537–45. doi: 10.1089/jir.1995.15.537
39. Tomai MA, Gibson SJ, Imbertson LM, Miller RL, Myhre PE, Reiter MJ, et al. Immunomodulating and Antiviral Activities of the Imidazoquinoline s-28463. *Antiviral Res* (1995) 28:253–64. doi: 10.1016/0166-3542(95)00054-P
40. Hartman ZC, Kiang A, Everett RS, Serra D, Yang XY, Clay TM, et al. Adenovirus Infection Triggers a Rapid, Myd88-Regulated Transcriptome Response Critical to Acute-Phase and Adaptive Immune Responses *in Vivo*. *J Virol* (2007) 81:1796–812. doi: 10.1128/JVI.01936-06
41. Yamaguchi T, Kawabata K, Koizumi N, Sakurai F, Nakashima K, Sakurai H, et al. Role of Myd88 and TLR9 in the Innate Immune Response Elicited by Serotype 5 Adenoviral Vectors. *Hum Gene Ther* (2007) 18:753–62. doi: 10.1089/hum.2007.016
42. Nociari M, Ocheretina O, Schoggins JW, Falck-Pedersen E. Sensing Infection by Adenovirus: Toll-Like Receptor-Independent Viral DNA Recognition Signals Activation of the Interferon Regulatory Factor 3 Master Regulator. *J Virol* (2007) 81:4145–57. doi: 10.1128/JVI.02685-06
43. Zhu J, Huang X, Yang Y. Innate Immune Response to Adenoviral Vectors is Mediated by Both Toll-Like Receptor-Dependent and -Independent Pathways. *J Virol* (2007) 81:3170–80. doi: 10.1128/JVI.02192-06
44. Yashima S, Yoshizaki S, Shinoda K, Yoshida A, Kondo A, Mizuguchi H, et al. Co-Administration of Viral Vector-Based Vaccines Suppresses Antigen-Specific Effector CD8 T Cells. *Vaccine* (2010) 28:3257–64. doi: 10.1016/j.vaccine.2010.01.065
45. Waibler Z, Anzaghe M, Frenz T, Schwantes A, Pohlmann C, Ludwig H, et al. Vaccinia Virus-Mediated Inhibition of Type I Interferon Responses is a Multifactorial Process Involving the Soluble Type I Interferon Receptor B18 and Intracellular Components. *J Virol* (2009) 83:1563–71. doi: 10.1128/JVI.01617-08

46. Volz A, Sutter G. Modified Vaccinia Virus Ankara: History, Value in Basic Research, and Current Perspectives for Vaccine Development. *Adv Virus Res* (2017) 97:187–243. doi: 10.1016/bs.aivir.2016.07.001
47. Falivene J, Del Medico Zajac MP, Pascutti MF, Rodriguez AM, Maeto C, Perdiguero B, et al. Improving the MVA Vaccine Potential by Deleting the Viral Gene Coding for the IL-18 Binding Protein. *PloS One* (2012) 7:e32220. doi: 10.1371/journal.pone.0032220
48. Chea LS, Wyatt LS, Gangadhara S, Moss B, Amara RR. Novel Modified Vaccinia Virus Ankara Vector Expressing Anti-Apoptotic Gene B13R Delays Apoptosis and Enhances Humoral Responses. *J Virol* (2019) 93(5):e01648-18. doi: 10.1128/JVI.01648-18
49. Delaloye J, Roger T, Steiner-Tardivel QG, Le Roy D, Knaup Reymond M, Akira S, et al. Innate Immune Sensing of Modified Vaccinia Virus Ankara (MVA) is Mediated by TLR2-TLR6, MDA-5 and the NALP3 Inflammasome. *PloS Pathog* (2009) 5:e1000480. doi: 10.1371/journal.ppat.1000480
50. Waibler Z, Anzaghe M, Ludwig H, Akira S, Weiss S, Sutter G, et al. Modified Vaccinia Virus Ankara Induces Toll-Like Receptor-Independent Type I Interferon Responses. *J Virol* (2007) 81:12102–10. doi: 10.1128/JVI.01190-07
51. Palgen JL, Tchitchek N, Elhmouzi-Younes J, Delandre S, Namet I, Rosenbaum P, et al. Prime and Boost Vaccination Elicit a Distinct Innate Myeloid Cell Immune Response. *Sci Rep* (2018) 8:3087. doi: 10.1038/s41598-018-21222-2
52. Mosaheb MM, Reiser ML, Wetzler LM. Toll-Like Receptor Ligand-Based Vaccine Adjuvants Require Intact Myd88 Signaling in Antigen-Presenting Cells for Germinal Center Formation and Antibody Production. *Front Immunol* (2017) 8:225. doi: 10.3389/fimmu.2017.00225
53. Smith AJ, Li Y, Bazin HG, St-Jean JR, Larocque D, Evans JT, et al. Evaluation of Novel Synthetic TLR7/8 Agonists as Vaccine Adjuvants. *Vaccine* (2016) 34:4304–12. doi: 10.1016/j.vaccine.2016.06.080
54. Vasilakos JP, Tomai MA. The Use of Toll-Like Receptor 7/8 Agonists as Vaccine Adjuvants. *Expert Rev Vaccines* (2013) 12:809–19. doi: 10.1586/14760584.2013.811208
55. Heer AK, Shamshiev A, Donda A, Uematsu S, Akira S, Kopf M, et al. TLR Signaling Fine-Tunes Anti-Influenza B Cell Responses Without Regulating Effector T Cell Responses. *J Immunol* (2007) 178:2182–91. doi: 10.4049/jimmunol.178.4.2182
56. Rawlings DJ, Schwartz MA, Jackson SW, Meyer-Bahlburg A. Integration of B Cell Responses Through Toll-Like Receptors and Antigen Receptors. *Nat Rev Immunol* (2012) 12:282–94. doi: 10.1038/nri3190
57. Harwood NE, Batista FD. Early Events in B Cell Activation. *Annu Rev Immunol* (2010) 28:185–210. doi: 10.1146/annurev-immunol-030409-101216
58. Fink K, Lang KS, Manjarrez-Orduno N, Junt T, Senn BM, Holdener M, et al. Early Type I Interferon-Mediated Signals on B Cells Specifically Enhance Antiviral Humoral Responses. *Eur J Immunol* (2006) 36:2094–105. doi: 10.1002/eji.200635993
59. Braun D, Caramalho I, Demengeot J. IFN-Alpha/Beta Enhances BCR-Dependent B Cell Responses. *Int Immunol* (2002) 14:411–9. doi: 10.1093/intimm/14.4.411
60. Dienz O, Eaton SM, Bond JP, Neveu W, Moquin D, Noubade R, et al. The Induction of Antibody Production by IL-6 is Indirectly Mediated by IL-21 Produced by CD4+ T Cells. *J Exp Med* (2009) 206:69–78. doi: 10.1084/jem.20081571
61. Diehl SA, Schmidlin H, Nagasawa M, Blom B, Spits H. IL-6 Triggers IL-21 Production by Human CD4+ T Cells to Drive STAT3-Dependent Plasma Cell Differentiation in B Cells. *Immunol Cell Biol* (2012) 90:802–11. doi: 10.1038/icb.2012.17
62. Matthews K, Chung NP, Klasse PJ, Moore JP, Sanders RW. Potent Induction of Antibody-Secreting B Cells by Human Dermal-Derived CD14+ Dendritic Cells Triggered by Dual TLR Ligation. *J Immunol* (2012) 189:5729–44. doi: 10.4049/jimmunol.1200601

Author Disclaimer: The content is solely the responsibility of the authors and does not necessarily represent the official views of the National Institutes of Health.

Conflict of Interest: Author MT was employed by the company 3M Corporate Research Materials Laboratory.

The remaining authors declare that the research was conducted in the absence of any commercial or financial relationships that could be construed as a potential conflict of interest.

Publisher's Note: All claims expressed in this article are solely those of the authors and do not necessarily represent those of their affiliated organizations, or those of the publisher, the editors and the reviewers. Any product that may be evaluated in this article, or claim that may be made by its manufacturer, is not guaranteed or endorsed by the publisher.

frontiers | Frontiers in Immunology

ORIGINAL RESEARCH
published: 04 May 2022
doi: 10.3389/fimmu.2022.855230

A Case Study to Dissect Immunity to SARS-CoV-2 in a Neonate Nonhuman Primate Model

*Claire-Maëlle Fovet[1], Camille Pimienta[1], Mathilde Galhaut[1], Francis Relouzat[1], Natalia Nunez[2], Mariangela Cavarelli[1], Quentin Sconosciuti[1], Nina Dhooge[1], Ilaria Marzinotto[3], Vito Lampasona[3], Monica Tolazzi[4], Gabriella Scarlatti[4], Raphaël Ho Tsong Fang[1], Thibaut Naninck[1], Nathalie Dereuddre-Bosquet[1], Jérôme Van Wassenhove[1], Anne-Sophie Gallouët[1], Pauline Maisonnasse[1], Roger Le Grand[1], Elisabeth Menu[1,5] and Nabila Seddiki[1]**

[1] Université Paris-Saclay, INSERM, CEA, Center for Immunology of Viral, Auto-immune, Hematological and Bacterial Diseases (IMVA-HB/IDMIT), Fontenay-aux-Roses, France, [2] Life and Soft, Fontenay-aux-Roses, France, [3] Diabetes Research Institute, IRCCS Ospedale San Raffaele, Milan, Italy, [4] Viral Evolution and Transmission Unit, Division of Immunology, Transplantation and Infectious Diseases, IRCCS Ospedale San Raffaele, Milan, Italy, [5] MISTIC Group, Department of Virology, Institut Pasteur, Paris, France

OPEN ACCESS

Edited by:
Alexis M. Kalergis,
Pontificia Universidad Católica de Chile, Chile

Reviewed by:
Stephanie N. Langel,
Duke University, United States
Rita Carsetti,
Bambino Gesù Children's Hospital (IRCCS), Italy

***Correspondence:**
Nabila Seddiki
nabila.seddiki@cea.fr

Specialty section:
This article was submitted to Viral Immunology, a section of the journal Frontiers in Immunology

Received: 14 January 2022
Accepted: 05 April 2022
Published: 04 May 2022

Citation:
Fovet C-M, Pimienta C, Galhaut M, Relouzat F, Nunez N, Cavarelli M, Sconosciuti Q, Dhooge N, Marzinotto I, Lampasona V, Tolazzi M, Scarlatti G, Ho Tsong Fang R, Naninck T, Dereuddre-Bosquet N, Van Wassenhove J, Gallouët A-S, Maisonnasse P, Le Grand R, Menu E and Seddiki N (2022) A Case Study to Dissect Immunity to SARS-CoV-2 in a Neonate Nonhuman Primate Model. Front. Immunol. 13:855230. doi: 10.3389/fimmu.2022.855230

Most children are less severely affected by coronavirus-induced disease 2019 (COVID-19) than adults, and thus more difficult to study progressively. Here, we provide a neonatal nonhuman primate (NHP) deep analysis of early immune responses to severe acute respiratory syndrome coronavirus 2 (SARS-CoV-2) infection in blood and mucosal tissues. In addition, we provide a comparison with SARS-CoV-2-infected adult NHP. Infection of the neonate resulted in a mild disease compared with adult NHPs that develop, in most cases, moderate lung lesions. In concomitance with the viral RNA load increase, we observed the development of an early innate response in the blood, as demonstrated by RNA sequencing, flow cytometry, and cytokine longitudinal data analyses. This response included the presence of an antiviral type-I IFN gene signature, a persistent and lasting NKT cell population, a balanced peripheral and mucosal IFN-γ/IL-10 cytokine response, and an increase in B cells that was accompanied with anti-SARS-CoV-2 antibody response. Viral kinetics and immune responses coincided with changes in the microbiota profile composition in the pharyngeal and rectal mucosae. In the mother, viral RNA loads were close to the quantification limit, despite the very close contact with SARS-CoV-2-exposed neonate. This pilot study demonstrates that neonatal NHPs are a relevant model for pediatric SARS-CoV-2 infection, permitting insights into the early steps of anti-SARS-CoV-2 immune responses in infants.

Keywords: SARS-CoV-2, innate immunity, type-I IFN, pediatric, neonate, children, COVID-19, nonhuman primate, microbiota

INTRODUCTION

Severe acute respiratory syndrome coronavirus 2 (SARS-CoV-2)-infected children are often asymptomatic or develop mild symptoms, and thus, compared with adults, are less frequently in need of hospitalization and show a lower mortality rate (1–5). Dysregulated innate immune responses, such as anti-interferon (IFN) antibodies or delayed responsiveness, have been reported in some severe COVID-19 cases but cannot account for the majority of severe infections (6–8). A rare and serious postinfectious condition that can occur 2–6 weeks after SARS-CoV-2 infection, termed pediatric inflammatory multisystem syndrome (PIMS-TS) or multisystem inflammatory syndrome (MIS-C), has been reported (9). Several hypotheses have been proposed to explain why children are protected from more severe outcomes with COVID-19 compared with adults, although not always conclusive. These include differences in the expression of the angiotensin-converting enzyme 2 (ACE2) receptor resulting in lower viral RNA loads (10–12), the presence of antibodies to common cold coronaviruses that might provide partial protection (6, 7), and a robust innate response early in the course of infection (8, 13–16). This latter explanation seems more robust and would clarify why children are less affected by COVID-19 (12), but further investigations are needed to fully support this.

Longitudinal data from early viral and immunological events following SARS-CoV-2 infection of children are difficult to obtain, and the reason is often linked to symptoms onset that go unnoticed in this population (1–4). Moreover, concomitant sample collection from the blood, lungs, and gastrointestinal compartments where the virus can be found, is difficult to perform in humans. Thus, the use of a preclinical pediatric model is valuable in this context. Several animal species were evaluated as models of initial SARS-CoV and MERS-CoV human diseases and while most laboratory animals, including mice, hamsters, ferrets, and nonhuman primates (NHP), could be productively infected, only a few species displayed overt clinical disease without requirement of adaptation of viral strains to the animals (17). Macaques have been shown to be reproducibly susceptible to infection to coronaviruses affecting humans and develop acute respiratory syndrome recapitulating the disease (18–26). Because of their phylogenetic proximity, macaques share a similar organization of the immune system with humans. Regarding SARS-CoV-2, ACE2 is expressed in both humans and macaques, with similar distribution and functionalities (13, 19). In recent studies, we have shown that adult cynomolgus macaques reliably develop infection upon intranasal and intratracheal exposure, and mild to moderate lesions were observed in the lungs during the first-week postchallenge, similar to human cases (27, 28).

Here, we describe an experimental SARS-CoV-2 infection in neonate NHP in which we longitudinally studied for 2 months viral kinetics, innate and adaptive immune responses, and microbiota profiles in different compartments, including blood, nasal, oropharyngeal, gastrointestinal, ocular, and vaginal sites. The neonate developed an asymptomatic infection, while its unexposed breastfeeding mother exhibited a low viral RNA load close to the quantification limit, despite their very close contact. Peak viral load in the neonate correlates with the development of an early innate immune response with an IFN gene signature, as demonstrated by RNA sequencing, flow cytometry, and cytokine longitudinal data analyses. Viral kinetics and immune responses correlate with changes in the microbiota profile composition in the oropharyngeal and rectal mucosae. Altogether, these findings support the use of neonate NHP as a suitable model to get insights into early pathogenic mechanisms of the human pediatric SARS-CoV-2 infection.

MATERIALS AND METHODS

Animals

A healthy pregnant female rhesus macaque (*Macaca mulatta*), 6 years old with a body weight of 6 kg, was imported from the *Station de Primatologie* (CNRS, Rousset-sur-Arc, France). Pregnancy was monitored until vaginal delivery of a full-term healthy female neonate. No complications were noted during delivery or subsequent breastfeeding. Seven adult female rhesus macaques (Hartelust, Tilburg, Netherlands), from three different studies conducted in our laboratory, aged 4–5 years old with a body weight of 5–7 kg, were also used in this study.

All animals were housed in the BSL3 facilities of the Infectious Disease Models and Innovative Therapies (IDMIT) infrastructure (CEA, Fontenay-aux-Roses, France). CEA complies with French national regulation (facilities authorization number #D92-032-02), the European Directive 2010/63/EU, and the Standards for Human Care and Use of Laboratory Animals (OLAW animal welfare assurance number #A5826-01, United States). The study was approved by the local ethical committee (CEtEA#44) and the French Research, Innovation and Education Ministry under registration number APAFIS #24434-20200030216532863 V3.

For all procedures, the mother was sedated with ketamine (Imalgene 1000, 10 mg/kg, Rhône-Mérieux, France)/medetomidine (Domitor, 0.5 mg/kg, Vetoquinol, France) to access the neonate. The neonate was either sedated for imaging or blood collection or restrained for fluid collection, the neonate was anesthetized with ketamine (5 mg/kg) and medetomidine (0.5 mg/kg). Anesthesia was reversed with atipamezole 2.5 mg/kg (Antisedan®, Vetoquinol, France) first in the neonate until fully awaken, then in the mother. Both were monitored until complete recovery and total reattachment. Adult females were anesthetized following the same procedure. The volume of blood sampling per week for both the neonate and mother was performed according to ethics and protocols.

Study Design and Clinical Follow-Up

The longitudinal follow-ups are summarized in **Figure 1** and **Supplementary Table S1** for the neonate/mother pair and adult females, respectively. Animals were observed 7 days a week, and any abnormal behavior was reported in a specific individual file. Clinical examination, body weight, rectal temperature, oxygen saturation, and respiratory and heart rates were recorded at each bleeding. Blood and biological fluids (nasal, vaginal, rectal, oropharyngeal, and tears) were collected for the neonate/mother pair at day postinfection (DPI) −7, 0, 2, 4, 6, 8, 10, 12, 16, 21, 35, 42, 49, and

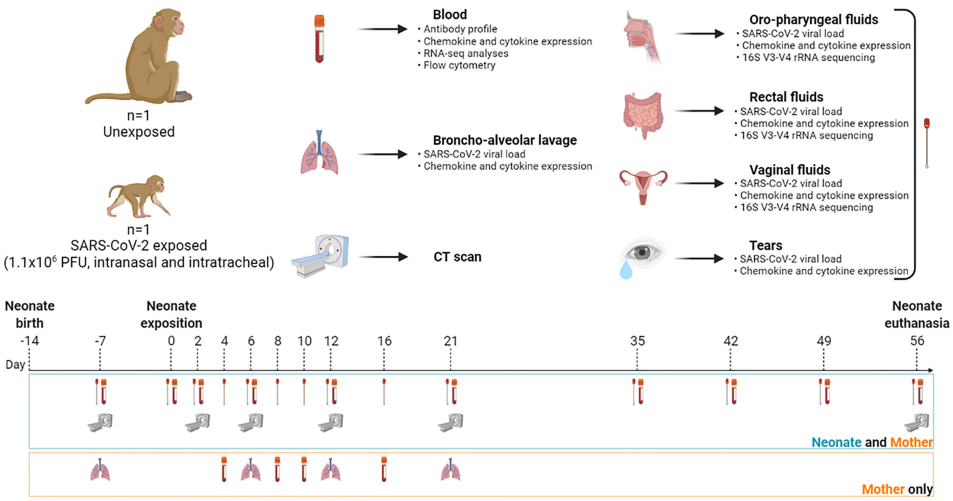

FIGURE 1 | Study design and workflow. A female rhesus macaque neonate was exposed at 14 days of life to a total dose of 1.1×10^6 PFU of SARS-CoV-2 by the intranasal and intratracheal routes. Symbols: blood tube for bleeding; lungs for bronchoalveolar lavage; scan machine for CT session; swab for biological fluid collection (nasal, oropharyngeal, vaginal, rectal, and tears). Samples were collected at day postinfection (DPI) −7, 0, 2, 4, 6, 8, 10, 12, 16, 21, 35, 42, 49, and 56. Analysis of peripheral blood and fluids included viral RNA load kinetics and chemokine/cytokine quantification. Microbiota identification was done in every fluid compartment. Antibody profiling, RNA-seq analyses, and flow cytometry were also performed in blood. Created with BioRender.com.

56. To limit collected blood volume and frequency of sedation, the neonate was not anesthetized nor bled at DPI 4, 8, 10, and 16. Only fluids were sampled under restraint at these time points. Bronchoalveolar lavages were performed on the mother at DPI −7, 6, 12, and 21. Blood and biological fluids (nasal, rectal, bronchoalveolar lavages) were collected from adult females according to the schedule of their respective studies and described in **Supplementary Table S1**. Complete blood count was determined using an HMX A/L analyzer (Beckman Coulter, USA) and biochemical parameters (C-reactive protein, haptoglobin, creatinine, urea, alanine–aspartate–aminotransferase (ASAT/ALAT), lactate dehydrogenase (LDH), troponin I, and total proteins) were assessed using an ADVIA1800 analyzer (Siemens). After 2 months, the neonate was euthanized with an intravenous administration of 180 mg/kg of sodium pentobarbital (Dolethal, Vetoquinol, France) under anesthesia.

SARS-CoV-2 Virus and Infection

SARS-CoV-2 virus (hCoV-19/France/lDF0372/2020 strain, passaged twice in Vero E6 cells) was provided by the National Reference Centre for Respiratory Viruses (Institut Pasteur) as previously described (23). Neonate macaque was inoculated 14 days after birth with 1.1×10^6 plaque-forming units (PFU) of SARS-CoV-2 and adult females with 1×10^5, 1×10^6, or 1×10^7 (see **Supplementary Table S1**) through a combination of intranasal and intratracheal routes after a premedication of atropine sulfate 0.04 mg kg^{-1} (Aguettant, France) and under anesthesia. The challenge took place under a class II biological safety cabinet with the animal placed in a supine position.

Virus preparation was applied slowly into each nostril (50 or 250 µl each for neonates and adults, respectively) using a 100-µl micropipette. The nostrils were slowly massaged for 1 min. After nasal exposure using a laryngoscope to visualize the epiglottis and larynx, a 1-mm diameter bladder catheter (neonate, ref#706537, Coveto, France) or a 3.5-mm diameter endotracheal probe (adults, ref#647587, Coveto, France) was introduced and stopped before the carina, then connected to a 1-ml syringe to apply the virus into the trachea (450 µl or 4.5 ml for neonate and adults, respectively). A 1-ml syringe of air was injected inside the probe to make sure that all virus preparation was injected. The animal's face was wiped to clean off any residual virus. Oxygen saturation and heart rate were monitored for 10 min after inoculation. Anesthesia was reversed first in the neonate, then in the mother, as described above.

Chest CT *In Vivo* Imaging

Chest computed tomography (CT) scans were performed on neonate and mother at DPI −7, 2, 6, 12, 21, and 56, as described in **Figure 1**. All imaging acquisitions were performed on a CT system (Vereos-Ingenuity, Philips) as previously described (27–30). CT scans were performed using the following parameters: CT detector collimation of 64 × 0.6 mm, tube voltage of 80 kV (neonate) or 120 kV (mother and adult animals), and intensity of about 350 mAs (neonate) or 150 mAs (mother and adult animals), 1.25-mm slice sickness, and 0.25-pixel spacing. Animals were placed in a supine position with thermal support (Bear Hugger, 3M) on the machine bed with heart rate, oxygen saturation, and temperature monitoring. Pulmonary lesions were defined as ground-glass opacity, crazy-paving pattern, or consolidation as previously described (29, 30). Lesion features detected by CT imaging were blindly assessed by two persons independently, and final CT score results were reached by consensus.

Viral Quantification

Viral RNA loads were assessed for both mother and neonate in nasal, oropharyngeal, vaginal, and rectal fluids, tears, and maternal bronchoalveolar lavages by RT-qPCR with a plasmid standard concentration range containing an RdRp gene fragment, including the RdRp-IP4 RT-PCR target sequence. Viral RNA loads in adult females were determined in nasal, rectal, and bronchoalveolar lavage fluids when available (see **Supplementary Table S1**), following the same procedure. The protocol describing the procedure for the detection of SARS-CoV-2 is available on the WHO website (https://www.who.int/docs/default-source/coronaviruse/real-time-rt-pcr-assays-for-the-detection-of-sars-cov-2-institut-pasteur-paris.pdf?sfvrsn=3662fcb6_2). The limit of detection was estimated at 2.37 log10 copies/ml, and the limit of quantification was estimated at 3.37 log10 copies/ml.

Lentiviral Vector-Based SARS-CoV-2 Neutralization Assay

Plasmid pSpike-C3 expressing the codon-optimized SARS-CoV-2 Spike protein open reading frame (ORF) (GenBank: NC_045512.2) containing a 21-amino acid deletion at the cytoplasmic tail (delta21) of Spike protein was previously described (31). The Lenti-X 293T human embryonic kidney cell line (Clontech, Mountain View, CA, USA) was used for the production of LV-Luc pseudotyped with Wuhan-Hu-1 Spike by transient transfection. LV-Luc preparations were titered on VeroE6 cells (African green monkeys, epithelial kidney), and dilutions providing 150,000–200,000 relative luciferase units (RLU) were used in the neutralization assay. Briefly, heat-inactivated serum serial 3-fold dilutions starting from the 1/40 dilution for the adult macaque and 1/20 for the neonate were incubated in duplicate with the LV-Luc for 30 min at 37°C in 96-well plates and thereafter added to VeroE6 cells at a density of 20,000 cells/well. After 48 h, luciferase expression was determined with a luciferase assay system (Bright-Glo, Promega) and measured in a Mithras luminometer (Berthold, Germany). The 50% inhibitory serum dilution (ID50) was calculated with a linear interpolation method using the mean of the duplicates (32). Neutralization was expressed as the reciprocal of the serum dilution giving 50% inhibition of RLU compared with the mean of the virus control wells. An ID50 below the lowest serum dilution used was considered negative.

IgG-Binding Antibody Luciferase Immunoprecipitation System Assay

Using luciferase immunoprecipitation system (LIPS) (33), we measured IgG binding to recombinant nanoluciferase-tagged antigens corresponding to SARS-CoV-2 Wuhan-Hu-1 spike RBD domains, as previously described (34). Viral sequences used in this study corresponded to the deposited sequence Genebank NC_045512.2 for SARS-CoV-2 Wuhan. Briefly, we cloned recombinant nanoluciferase-tagged antigens and expressed them by transient transfection into Expi293F™ cells (Expi293™ Expression System, ThermoFisher Scientific Life Technologies, Carlsbad, CA, USA). For LIPS, we incubated in liquid phase each antigen with test serum (1 µl) for 2 h and then captured immune complexes with rProtein A-sepharose. After washing (5 times) the sepharose pellets, we quantified bound IgG by measuring the recovered luciferase activity in a Berthold Centro XS3 luminometer (Berthold Technologies GmbH & Co. KG, Bad Wildbad, Germany) using the MikroWin version 5.22 software. We then converted raw data into arbitrary units (AU), using a local positive index serum for SARS-CoV-2-specific antibodies.

Flow Cytometry

Immune profiling analysis was performed on fresh heparin–lithium whole blood by flow cytometry. Two antibody panels (myeloid/lymphoid) were established, using for each one 20 or 50 µl of blood from the neonates and the adults, respectively. Staining was performed with Blue-Vid for cell viability (Invitrogen) and anti-human antibodies that cross-react with NHP antigens, including CD45, CD3, CD4, CD95, CD69, HLA-DR (Becton Dickinson), CD8 (Miltenyi, Germany), and CD20 (Fisher Scientific). After two washes, erythrocytes were lysed and PBMCs were fixed (paraformaldehyde (PFA)) before acquisition with an LSRII flow cytometer (BD Bioscience, USA). Analyses were performed using FlowJo software (version 10.7.1; Treestar Inc., CA, USA).

Cytokines Analyses

Cytokine quantification (25 µl/sample) was performed for neonate and its mother in serum and fluids (nasal, oropharyngeal, rectal, and vaginal) and in the serum of adult females with the Milliplex MAP kit for nonhuman primates, which is based on Luminex® xMAP multiplex technology for the detection of 23 cytokines: G-CSF, GM-CSF, IFNγ, IL-1β, IL-1Ra, IL-2, IL-4, IL-5, IL-6, IL-8, IL-10, IL-12/23, IL-13, IL-15, IL-17A, MCP-1, MIP-1α, MIP-1β, sCD40L, TGF-α, VEGF, and IL-18, according to manufacturer's instructions.

RNA Sequencing

Frozen whole blood Tempus samples were processed for RNA extraction using Tempus Spin RNA Isolation Kit (Applied Biosystems, USA). RNA was then concentrated using RNA Clean XP beads (Beckman Coulter, USA). RNA was quantified using QuBit (ThermoFisher), and a quality check was performed on the Agilent TapeStation system. A total of 100 ng of RNA per sample was denatured at 65°C and retrotranscribed by a strand-switching technique using Maxima H Minus Reverse Transcriptase (ThermoFisher, USA) to synthesize a double-stranded cDNA. PCR, barcode, and adapter attachment were performed according to SQL-PCB109 cDNA-PCR Sequencing Kit (Oxford Nanopore Technologies, Oxford, UK). Samples were quantified using QuBit dsDNA HS (ThermoFisher, USA) kit before loading on R9.4.1 Flow cells using the GridION instrument.

Transcriptome Analysis

Sequence reads were converted into FASTQ files. Reads under 100 bp or with a quality score under seven were discarded. The remaining reads were aligned on the *Macaca mulatta*

transcriptome of reference (GeneBank assembly accession number GCA_003339765.3) using minimap2 (35) version 2.17. To quantify transcripts, the resulting alignments were given to Salmon version 1.4.0 (36). To explore single replicates, samples were duplicated to use DESeq2 version 1.32.0 (37).

We performed a gene set enrichment analysis with both upregulated and downregulated genes Log2FC>2 or Log2FC<2, respectively, using Enrichr, a web server enrichment analysis tool (38–40), and BioPlanet 2019 database for cellular and signaling pathway analysis (41). To determine the type-I IFN protein-protein association network and identify a type-I IFN signature for innate response at DPI 2, we used the STRING database, a web resource of known and predicted gene-gene or protein-protein interactions (https://string-db.org/). The network predicts associations for a particular gene dataset (42). More lines between the nodes, more types of evidence found in the interaction.

Of note, since differential expression with DESeq2 version 1.32.0 (37) requires at least two biological replicates for each condition, which was not possible for this part of the study, the samples were artificially duplicated for further analysis. The differentially expressed genes were thus, considered exploratory. Nevertheless, the several longitudinal time points available enabled us to analyze and interpret the data by comparison with the literature.

Microbiota Sequencing

DNA from the oropharyngeal, rectal, and vaginal swabs were extracted using the PowerFecal DNA Pro Kit (Qiagen®, Germany) following the manufacturers' instructions. Purified DNA was quantified using a QuBit fluorometer. Samples were concentrated with the magnetic AMPure XP beads (Beckman Coulter) and stored at −20°C until use.

Sequencing of the V3–V4 region of the 16S rRNA gene was performed using the 16S Metagenomic Sequencing Library Preparation protocol for MiSeq System (Illumina). Briefly, 16S rRNA V3–V4 regions were amplified using 5′ CCTACGGGNGGCWGCAG and 5′ GACTACHVGGG TATCTAATCC primers with overhanging adapters. Amplicons were purified to remove free or dimerized primers with the AMPure XP beads (Beckman Coulter). Dual Indexes and Illumina sequencing adapters were attached using TrueSeq Index Plate (Illumina). Samples were quantified using QuBit, and a 4nM library was denatured. PhiX library was integrated as an internal control. The library was sequenced using the MiSeq device (Illumina).

Metagenomics Sequencing Data Processing and Taxonomic Assignation

FASTQ sequences were processed using the Find Rapidly OTU with Galaxy Solution (FROGS) pipeline (43) implemented on a galaxy instance (http://migale.jouy.inra.fr/galaxy/). Bacterial 16S rRNA-matched readings were merged with a maximum rate of 0.1 mismatches in the overlapping region using Vsearch (44). Each of the samples was a unique time point; thus, after dereplication, the clusterization step ran with an aggregation distance equal to 1 (maximum number of differences between all of our sequences), and thus denoising was not needed. Chimeras were removed using Vsearch, and 99% of the total sequence abundance was kept. OTUs with less than 0.00001% abundance were filtered out. Finally, taxonomic affiliation was performed using SILVA 138 pintail 100 databases. Data normalization was performed to the lowest sequencing depth using both mother and neonate reads.

Statistical Analysis

We used GraphPad Prism 8.0.2 software to analyze viral and immunological data as well as microbiota OTUs and bacterial abundance and cytokine quantification. The mean value of normalized read counts was calculated for each taxon. Taxa having less than 1% of relative mean abundance were assigned to the category "Others". All relative mean abundances are represented in cumulative histograms. For correlations between cytokines, viral RNA load, and microbiota, a nonparametric test of Spearman was performed, heatmaps were generated based on the obtained R correlation factors, and one or more (*) are shown according to the p-value indicated in the figure legends. Percentages of cell populations from flow cytometry analyses and cytokines were expressed as a fold change from the baseline at DPI −7 for each time point. The log of fold change was indicated in the figures when applied.

RESULTS

Clinical Parameters

After infection, the neonate exhibited asymptomatic clinical signs and had no major changes in temperature, oxygen saturation, respiratory rate, and heart rate (**Supplementary Figure S1A**). The newborn weighed around 450 g at birth and gained weight throughout the study, consistent with expected standards (45) (**Supplementary Figure S1B**).

As previously reported (46), we observed elevated levels of creatinine, ASAT, and LDH at baseline, followed by a physiological decrease as early as the second week of life. Interestingly, we detected an increase in the ASAT and LDH levels at DPI 2 in the neonate (**Supplementary Figure S1C**).

No variations in the different leukocyte subpopulations, red blood cells, and hemoglobin were observed (**Supplementary Figure S2A**). The mother showed lymphocytosis and neutropenia at DPI 2, probably due to the stress of the manipulations.

Overall, this follow-up of clinical monitoring showed normal myeloid and lymphoid cell population counts at different time points in the neonate and the mother. As expected, we observed an inverse lymphocyte to neutrophil count ratio between neonate and adult blood that started to normalize at 10 weeks of life (47) (**Supplementary Figure S2B**).

As for the infected adult females, we did not see any symptoms nor variation in the clinical parameters (**Supplementary Figure S3A**). However, we did observe signs of inflammation through increased levels of hepatic transaminases and C-reactive protein (CRP) throughout their follow-up, and a transient lymphopenia at DPI 2 (**Supplementary Figures S3B, S4**, respectively).

SARS-CoV-2 Neonate Infection and Follow-Up

The neonate had a high viral RNA load, i.e., 7 × log10 copies/ml as early as DPI 2 in the oropharyngeal samples, as evaluated by RT-qPCR genomic viral RNA. The viral RNA load progressively decreased to undetectable levels from DPI 10 and remained undetectable until the end of the follow-up. The virus was also detected in the neonate's rectal fluids with higher levels than those of adults (**Figure 2A**). In nasal fluids, the viral RNA load peaked at almost 5 × log10 copies/ml. Adult animals, displaying no differences between virus doses tested (**Supplementary Figure S5**), showed similar viral RNA load kinetics in nasal fluids, although at a higher level (**Figure 2A**). The anatomical differences between adults and newborns might explain the variation in viral RNA load detection, given that we barely entered the nostril in the newborn while we reached the nasal turbinates in adults. Finally, in vaginal fluids and the tears, the viral RNA load was lower than in oropharyngeal and rectal fluids, peaking at almost 5 and 4 × log10 copies/ml, respectively (**Figure 2A**).

To exclude a potential transmission of infection from the neonate to the mother, we tested her virus load. Only tears and vaginal fluids showed a minimal positive signal above the detection limit, while no virus was detected above the detection limit in the oropharyngeal, nasal, rectal, or bronchoalveolar space compartments (**Figure 2A**).

Overall, these data indicate that the newborn was infected in the respiratory tract. As for the potential infection of the digestive tract, we observed a high rectal viral RNA load that persisted over time with a slower clearance compared with adults. Whether it is the result of the swallowing of viral particles that replicated in the throat or an active infection of SARS-CoV-2 in the gastrointestinal tract needs to be confirmed. As for the mother, despite the close contact with the baby, especially during breastfeeding, we did not detect the presence of SARS-CoV-2 by RT-qPCR above the detection limit in the respiratory or intestinal tracts (**Figure 2A**).

We next assessed the kinetics of antibodies to SARS-CoV-2. We used the lentiviral vector-based SARS-CoV-2 neutralization assay and the LIPS assays to profile the antibody response to spike antigen of SARS-CoV-2 Wuhan-Hu-1. IgG to RBD and neutralizing antibody to SARS-CoV-2 were negative at baseline DPI −7 and DPI 2 in the neonate, while the sera from DPI 35 onwards showed a gradual increase (**Figure 2B**). In agreement with the low to undetectable viral RNA load assessed by RT-qPCR, no antibody response was detected in the maternal serum samples.

To characterize lung lesions, we used *in vivo* imaging at crucial time points postinfection. No pulmonary changes were observed in the neonate's lungs, as evidenced by the CT scan (**Figure 2C**, left image), compared with what can be found in the adult's lungs (right images) at DPI 2 and DPI 6. SARS-CoV-2-infected adult animals that developed a mild infection after virus inoculation showed ground-glass opacities by CT scan (**Figure 2C**, right panel and blue arrows), especially in the dorsal area of the middle and lower lobes. No lesions were observed in the mother.

In addition to RT-qPCR and CT scans that showed the presence of virus and signs of infection, respectively, we sought to use RNA-sequencing data analysis to reveal the presence of host responding genes to COVID-19 in longitudinal whole blood samples in the neonate compared with the mother. First, our analysis indicated no association and a sharp distinction between neonate and mothers' gene sets, as demonstrated by the principal component analysis (PCA) (**Figure 3A**). Further data analyses showed an increase in host responding genes to SARS-CoV-2 infection at DPI 2 and DPI 6 compared with the baseline in the neonate (**Figure 3B**, upper panel) but not in the mother (**Figure 3B**, lower panel), adding a further level of evidence for infection.

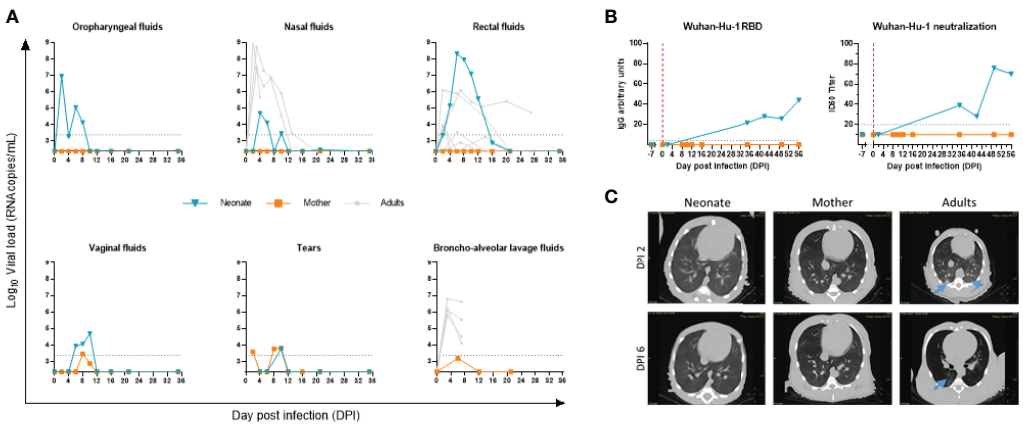

FIGURE 2 | Follow-up of SARS-CoV-2 infection. **(A)** Viral RNA load measured by RT-qPCR in the oropharyngeal, nasal, rectal, vaginal, tears, and bronchoalveolar fluidic compartments. The blue line is for the neonate, orange line for the mother, and gray lines for adult NHPs. The limit of detection was estimated at 2.37 log10 copies/ml, and the limit of quantification was estimated at 3.37 log10 copies/ml (dotted horizontal line). **(B)** Line plots of RBD IgG arbitrary units (AU) and 50% inhibitory serum dilution (ID50) against SARS-CoV-2 Wuhan-Hu-1 in sequential serum samples of the neonate. **(C)** Thoracic CT scan at DPI 2 (upper panel) and DPI 6 (lower panel) for neonate (left), mother (middle), and infected adult (right). Blue arrows point to ground-glass opacities.

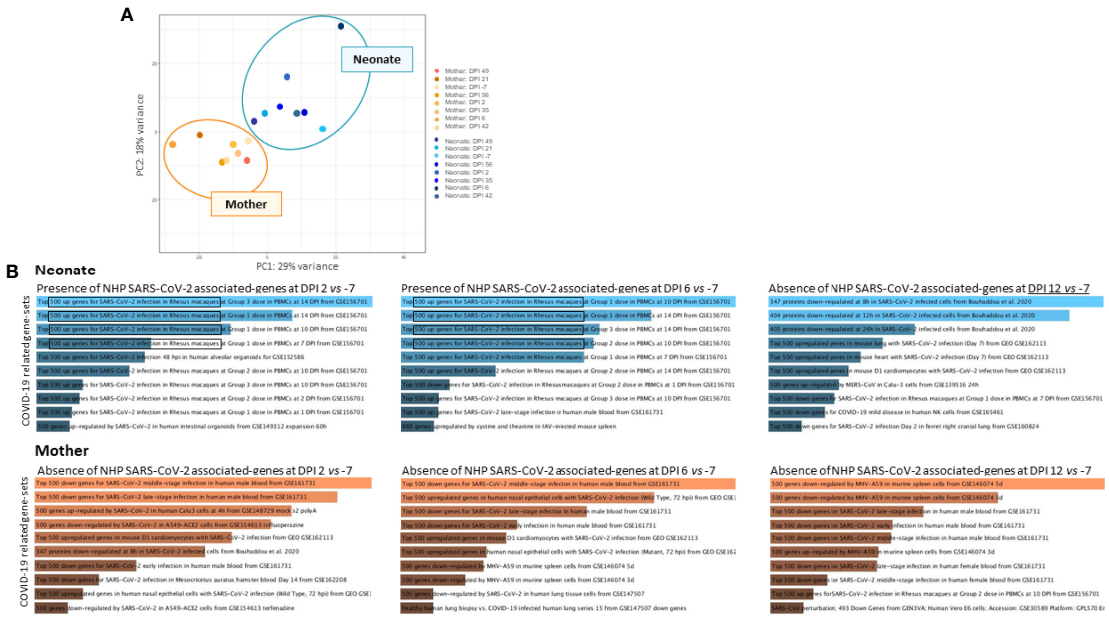

FIGURE 3 | RNA-sequencing analyses of whole blood. RNA-sequencing experiments on longitudinal whole blood samples (DPI –7, 2, 6, 12, 21, 35, 42, 49, and 56) to detect the presence of COVID-19-associated gene sets. **(A)** Principal component analysis (PCA) of neonate samples (blue) and mother samples (orange) show no association between individuals where mother and neonate samples are presented. **(B)** Increased host-responding genes to SARS-CoV-2 infection at DPI 2 and DPI 6 compared with the baseline at DPI –7 were observed, in the neonate (upper panel in blue) but not in the mother (lower panel in orange). SARS-CoV-2-associated genes decrease at DPI 12 in the neonate.

SARS-CoV-2-Exposed Neonate Shows an Early Type-I IFN Response in the Blood

Using an RNA-sequencing-based approach, we aimed to reveal the very early antiviral gene signature that emerges following SARS-CoV-2 exposure using longitudinal neonate's whole blood.

Using the Enrichr server and BioPlanet database, we explored only upregulated genes in the infected neonate compared with the baseline at DPI –7. The radar chart shows a high activation of IFN signaling pathways (–log10(*p*-value)>5) at DPI 2 (peak viral RNA load in oropharyngeal fluids) that remains significantly high at DPI 6. As time progresses, we observe a shift in the key biological process and molecular functions that show activation of transcription, RNA processing, regulation, and degradation (**Figure 4A**). We then focused on DPI 2, which shows a higher IFN pathway activation. Comparing DPI 2 with DPI –7, we found 2,110 differentially expressed genes (DEGs; fold change >2), including 907 that were upregulated and 1,203 downregulated (**Figure 4B**). To follow expression level dynamics of type-I IFN genes throughout the collected blood samples, we then generated a heatmap plotting Log2FC expression values at every time point (**Figure 4C**). Type-I IFN gene expression levels peak at DPI 2 and were maintained at DPI 6 for most of the genes except for IFI35, IFI3, IFI2, SAMHD1, TYK2, and IRF3 (**Figure 4C**). MX1 and IFIT1 were maintained at DPI 12 and 35, unlike the other genes, which decreased at DPI 12, except for IFI35 and IRF3. Finally, we identified confident interactions (at least 4 differently colored lines) between STAT2, TYK2, IRF3, MX1, ISG15, IFIT1, IFIT2, IFIT3, and IFI35 (**Figure 4D**), where STAT2 seems to be the key signal transducer and the transcription activator of some IFN-associated genes (48).

To assess the presence of gene sets related to cell markers that identify cell populations and determine the quality of the immune response induced after infection and throughout all time points, we used the Enrichr/CellMarkerAugmented2021 and Appyter applications. We generated volcano plots showing the presence and significance of each gene set (dark blue dots, **Figure 5**). As shown in the figure, the presence of natural killer T-cell (NKT) gene sets persisted at each time point (DPI 2, 6, 12, 35, 42, 49, and 56). We also revealed the presence of gene sets related to populations of dendritic cells (DC), regulatory T cells (Treg), and subsets of plasmablast and memory B cells.

Overall, these findings show the development of an early innate response in neonate NHP coinciding with increased viral RNA load at DPI 2.

SARS-CoV-2-Exposed Neonate Shows a High Humoral B-Cell Response in Whole Blood

We performed flow cytometry analyses of longitudinal whole blood samples to study the dynamics of cell populations before and after SARS-CoV-2 exposure of the neonate. Data from two infected adults were used for comparison. To avoid intrinsic differences between neonate and adult cell count

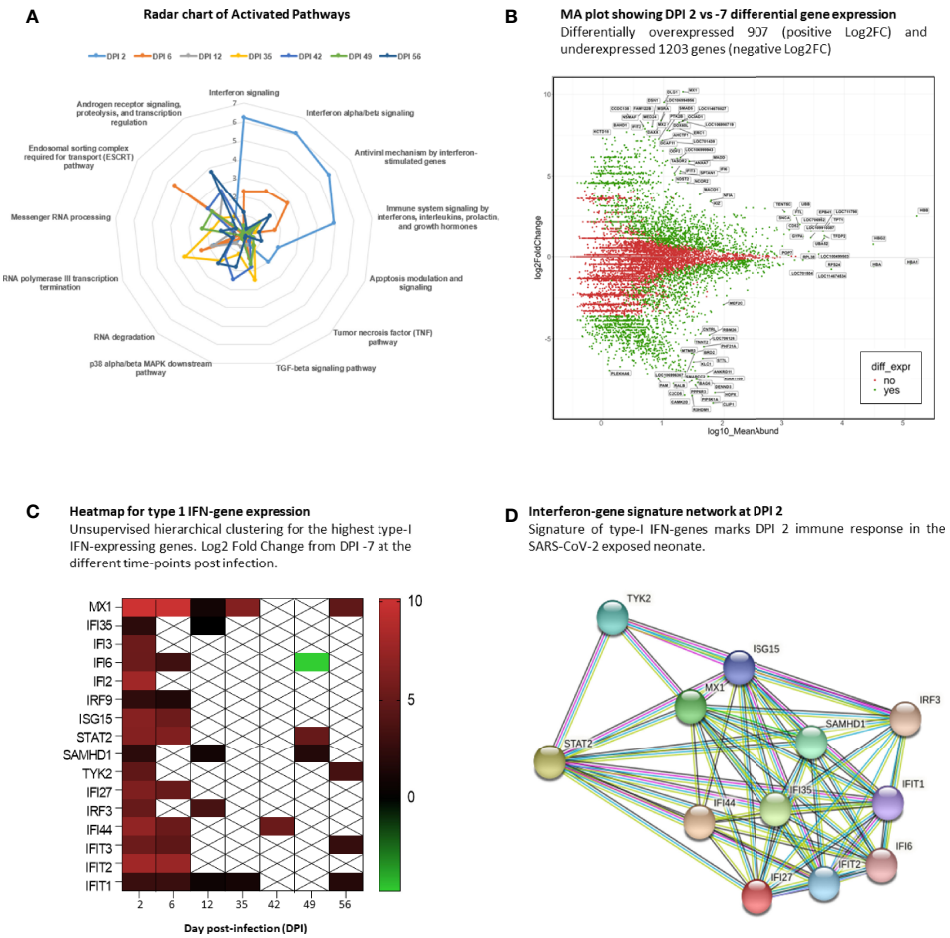

FIGURE 4 | Interferon signature at DPI 2. RNA-sequencing analysis of neonate whole blood. **(A)** Radar chart of upregulated genes at the infected time points and their associated activation pathways. **(B)** MA plot of DPI 2 showing 2,110 differentially expressed genes in green, with 907 upregulated and 1,203 downregulated genes. **(C)** Heatmap showing the gene-expression level of type-I IFN signature genes at different time points. White crossed rectangles are for no gene-expression changes between corresponding time points. **(D)** The STRING network inference for type-I IFN-associated genes at DPI2.

(**Supplementary Figure S2B**), we chose to present the results as a fold increase from the baseline at DPI −7.

White blood cell (WBC) counts results showed no major changes throughout the follow-up in the neonate (**Supplementary Figure S2A**). By flow cytometry, however, we observed a high fold increase of $CD45^{+}CD20^{+}$ B cells from the baseline in the neonate compared with adults, which started from DPI 6 and peaked at DPI 35 to then plateau at DPI 42 and 49 before decreasing (**Figure 6**). This increase coincided with B-cell activation ($CD69^{+}CD20^{+}$ cells peak at DPI 6 and 10; **Figure 6**) and an increase of SARS-CoV-2 RBD binding IgG and neutralizing antibodies (starting at DPI 35, **Figure 2C**). This increase also coincided with enrichment in B-cell populations starting from DPI 12 and onwards, as shown by RNA-sequencing data (**Figure 5**). Our data are in line with previous studies showing the presence of specific plasmablast B cells as well as neutralizing antibodies in children with low viral RNA load 1 week after disease onset (49). Our results show an increase in humoral B-cell responses in the blood of SARS-CoV-2-exposed neonates.

SARS-CoV-2-Exposed Neonate Shows Longitudinal Cytokine Changes in Whole Blood, Oropharyngeal, and Rectal Mucosae

Local and systemic innate and adaptive responses were monitored by measuring cytokine concentration in oropharyngeal and rectal fluids, as well as in peripheral blood from the infected neonate at all time points (**Supplementary Table S2**).

In the oropharyngeal compartment, IL-1Ra, IL-8, VEGF, MCP-1, and TNF-α were increased at DPI 2. As for flow cytometry, the results are presented as a fold increase from the baseline at DPI −7. VEGF and TNF-α levels were relatively weak and transient, whereas

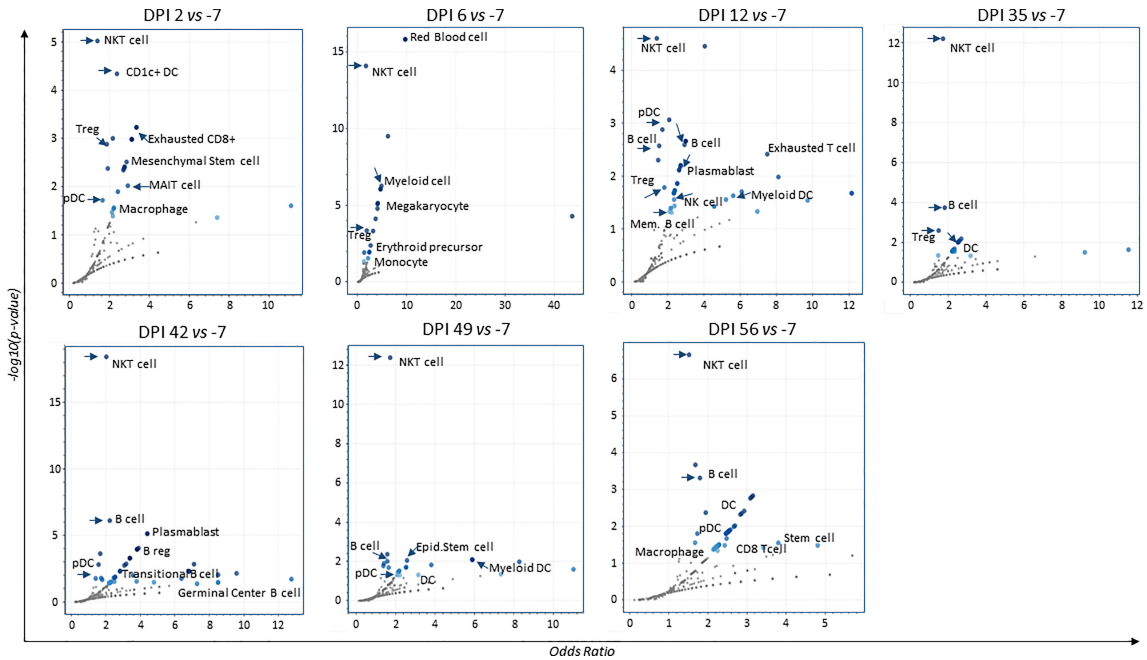

FIGURE 5 | Volcano plots for augmented cell-populations following infection. RNA-sequencing of whole blood cell-populations at each time-point compared to baseline (DPI – 7) (analyses using Enrichr/CellMarkerAugmented2021 and Appyter applications). Each volcano plot shows the significance of each gene-set (dark blue dots). x-Axis measures the odds ratio (0, inf) calculated for the gene-set, while the y-axis gives the –log10(*p*-value) of the gene set. Larger blue points represent significant terms (*p*-value < 0.05); smaller gray points represent non-significant terms. The darker the blue color of a point, the more significant it is.

IL-1Ra, IL-8, and MCP-1 levels were high and were maintained at different time points following infection (**Figure 7A**; **Supplementary Table S2**). IL-1Ra, IL-8, and VEGF were positively and significantly correlated with the oropharyngeal viral RNA load (**Figure 7B**), as shown by the overlay of synchronized curve kinetics before and after infection (**Figure 7C**).

In the blood, we observed increased levels of IFN-γ, IL-2, IL-5, IL-10, IL-13, IL-15, TNF-α, IL-1Ra, IL-8, IL-12/23, IL-18, MIP-1α, VEGF, and G-CSF with a peak at DPI 2, whereas IL-5 peaked at DPI 6, VEGF and G-CSF remained elevated during the whole follow-up (**Figure 8A**; **Supplementary Table S2**). Compared with the adult control group, the main differences we observed in the neonate were high levels of MCP-1 and IL-8 at baseline and high levels of IL-10 at DPI 2 in the neonate but not in the adults, with only a slight increase at DPI 13 in one animal (**Supplementary Figure S6**).

Unlike the mucosae sites, no blood samples were available at DPI 10, 12, 16, and 21 for cytokine analyses. IL-10, IL-13, IL-15, TNF-α, IFN-γ, IL-1Ra, VEGF, and G-CSF were positively and significantly correlated with the oropharyngeal viral RNA load (**Figure 8B**). As shown in **Figure 8C**, the peak of cytokine levels in blood matched with the peak of oropharyngeal viral RNA load.

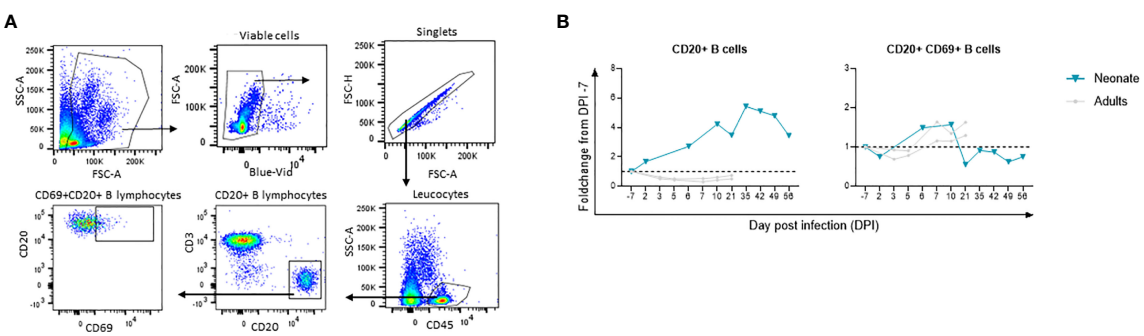

FIGURE 6 | Flow cytometry analyses for longitudinal B cell immune response following infection. Fold-changes from the baseline are shown for each cell population. The neonate is shown in blue line whereas adults (n=2) are shown in grey lines. **(A)** Gating strategy for B cell subsets. **(B)** CD45+CD20+B cells and activated $CD69^{+}CD20^{+}$B cell fold change from the baseline. The dashed line represents the baseline (Fold change 1).

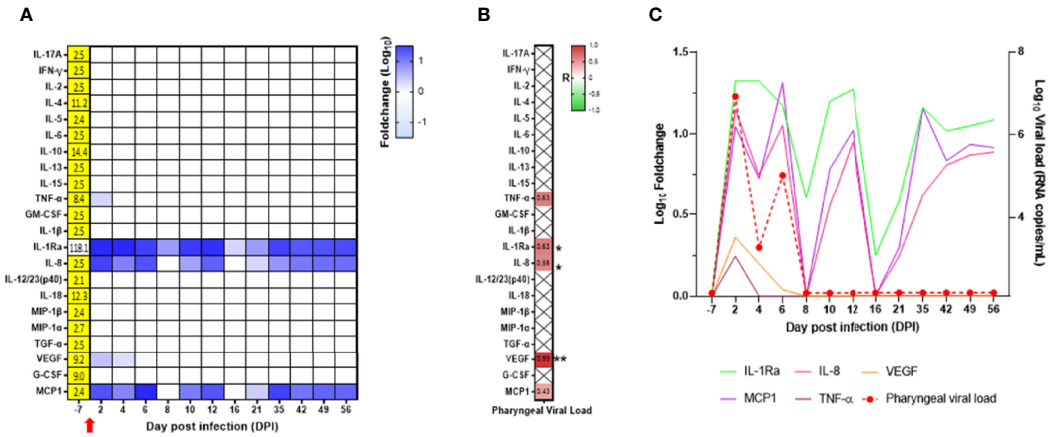

FIGURE 7 | Cytokine analyses in the neonate oropharyngeal compartment. **(A)** Heatmap for the evolution of cytokines over time (in the log of fold change from the baseline). Variations are shown on a blue scale. Basal concentrations (pg/ml) are shown on the left side of the heatmap. Highlighted yellow values correspond to the detection threshold. **(B)** Spearman correlation analysis between SARS-CoV-2 viral RNA load in the oropharyngeal compartment and the kinetics of cytokines in the same compartment was performed. The obtained correlation factors, which have been determined on the whole kinetics, are shown on the heatmap with a red to green scale. *$p < 0.04$ and **$p < 0.003$. **(C)** Graph overlapping the kinetics of the cytokines in the log of fold change (left scale) with the oropharyngeal viral RNA load on the logarithmic scale (right scale).

In the rectal mucosa, levels of IFN-γ, IL-10, and IL-12/IL-23 increased at DPI 2 and were maintained at DPI 4 and DPI 6, whereas IL-4, IL-13, IL-15, TNF-α, IL-18, VEGF, and G-CSF had intermediate levels and returned to baseline level after DPI 6 (**Figure 9A**; **Supplementary Table S2**). In contrast to blood and oropharyngeal cytokines, there was no correlation between rectal cytokines and rectal viral RNA load (**Figure 9B**). However, we observed a positive and significant correlation in rectal cytokines with oropharyngeal viral RNA load (**Figure 9B**). The peak of cytokine levels in rectal mucosa matched with the peak of oropharyngeal viral RNA load (**Figure 9C**). Overall, our results show the presence of an early cytokine increase in the blood, oropharyngeal, and rectal mucosae compartments following SARS-CoV-2 infection.

Microbiota Composition Changes in Oropharyngeal and Rectal Mucosae Following SARS-CoV-2 Infection

We assessed microbiota composition in the oropharyngeal and rectal compartments of the neonate using the V3–V4 16S sequencing. In the oropharyngeal microbiota, the three dominant phyla found were *Firmicutes*, *Proteobacteria*, and *Bacteroides*. Seventeen genera were present at more than 1% of relative abundance throughout the follow-up (**Figure 10A**). The

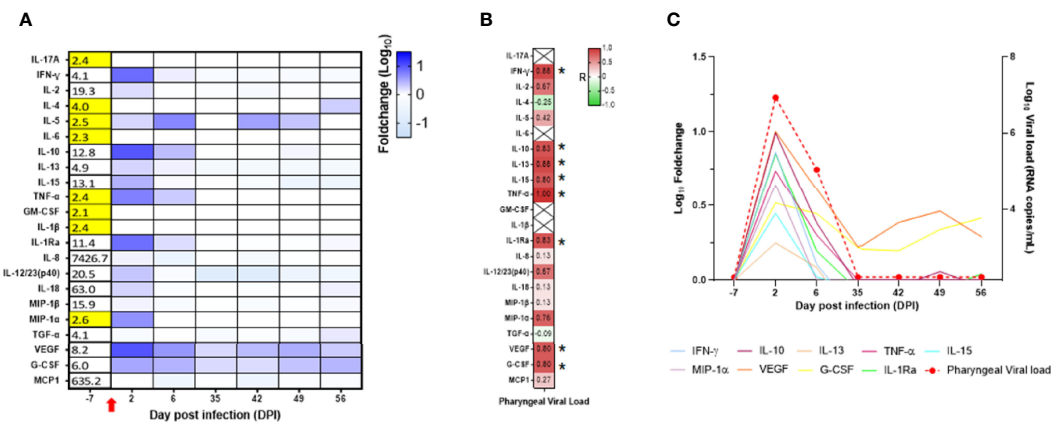

FIGURE 8 | Cytokine analyses in the neonate blood. **(A)** Heatmap representing the evolution of cytokines over time (in the log of fold change from the baseline). Variations are shown on a blue scale. Basal concentrations (pg/ml) are shown on the left side of the heatmap. Highlighted yellow values correspond to the detection threshold. **(B)** Spearman correlation analysis between SARS-CoV-2 viral RNA load in the oropharyngeal compartment neonate and the kinetics of cytokines in the blood. Correlation factors determined on the whole kinetics are shown on the heatmap with a red to green scale. *$p < 0.03$. **(C)** Graphs overlapping the kinetics of the blood cytokines in the log of fold change (left scale) with the oropharyngeal viral RNA load on the logarithmic scale (right scale).

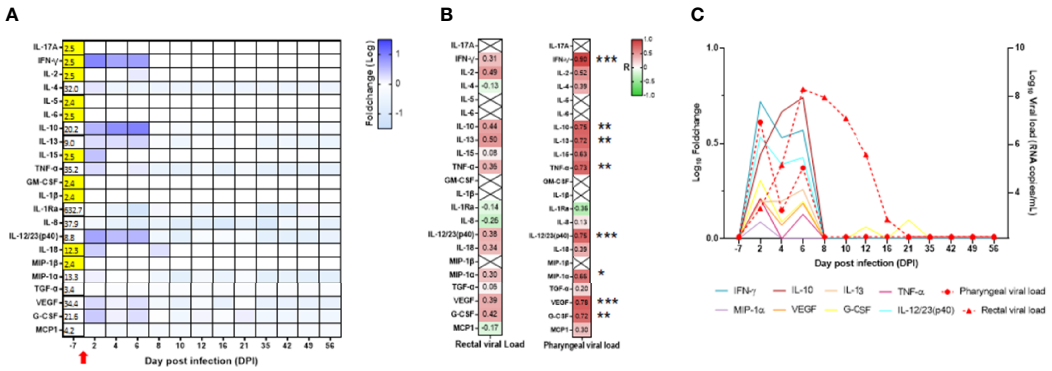

FIGURE 9 | Cytokine analyses in the neonate rectal compartment. **(A)** Heatmap representing the evolution of cytokines over time (in the log of fold-change from the baseline). Variations are shown on a blue scale. Basal concentrations are shown on the left side of the heatmap. Highlighted yellow values correspond to the detection threshold. **(B)** Spearman correlation analysis between SARS-CoV-2 viral RNA load in the rectal (left) or oropharyngeal (right) compartment and the kinetics of cytokines in the rectal compartment. Correlation factors determined on the whole kinetics are shown on the heatmap with a red to green scale. $*p < 0.03$*; $**p < 0.008$; $***p = 0.0006$. **(C)** Graphs overlapping the kinetics of the rectal cytokines in the log of fold change (left scale) with the oropharyngeal and rectal viral RNA load on the logarithmic scale (right scale).

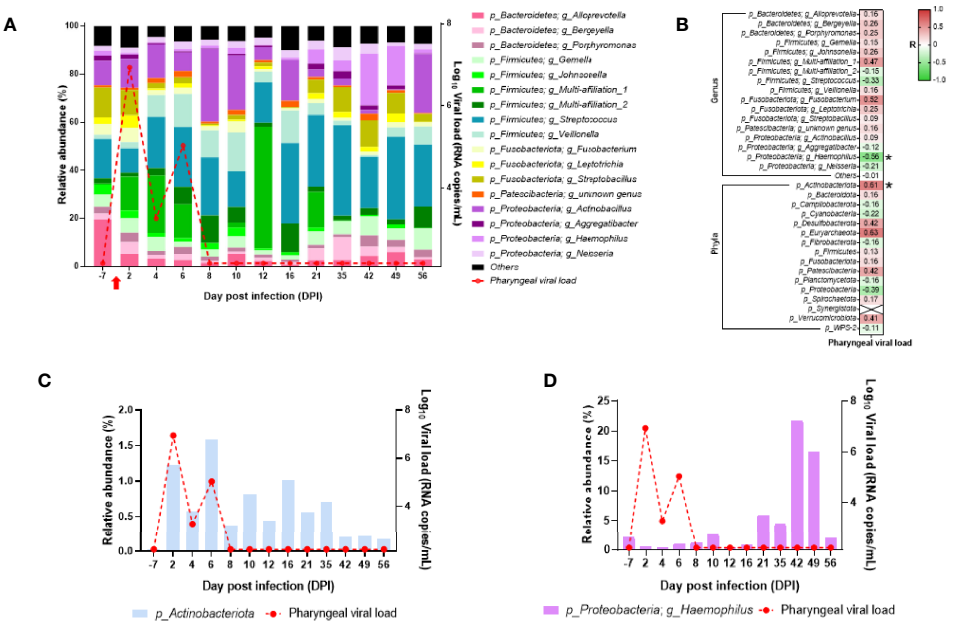

FIGURE 10 | Analyses of the neonate oropharyngeal microbiota composition. **(A)** Bar plots represent the oropharyngeal microbiota composition. Relative abundance is represented for each time point (left scale). The red curve represents the oropharyngeal viral RNA load (logarithmic scale) of SARS-CoV-2 detected in the neonate over time (right scale). p-Firmicutes and g_Multi-affiliation_1 correspond to c_Bacilli and p-Firmicutes; g_Multi-affiliation_2 corresponds to o_Lactobacillales. **(B)** Spearman correlation analysis between the SARS-CoV-2 oropharyngeal viral RNA load and the oropharyngeal microbiota composition. On the heatmap, the correlation factors of each phylum or genus are represented according to the oropharyngeal viral RNA load. Correlation factors are indicated on a red to green scale. $*p < 0.036$. **(C)** *Actinobacteria* (phylum) relative abundance (left scale) overlapped with oropharyngeal viral RNA load on the logarithmic scale (right scale). **(D)** *Haemophilus* (genus) relative abundance (left scale) overlapped with oropharyngeal viral RNA load on the logarithmic scale (right scale).

oropharyngeal microbiota composition was similar throughout the follow-up, except at DPI 12 where *Streptococcus* and *Veillonella* genus decreased and *Bacilli* class increased. However, those changes seemed to be independent of the SARS-CoV-2 infection (**Figure 10A**). During the follow-up, some fluctuations were observed in the phylum *Actinobacteriota* and the genus *Haemophilus* that correlated positively and negatively, respectively, with the oropharyngeal viral RNA load (**Figures 10B–D**).

In the rectal microbiota, the three dominant phyla varied over time (**Figure 11A**). In fact, at baseline (DPI −7), the rectal microbiota was dominated by *Firmicutes*, *Bacteroidetes*, and *Proteobacteria*, but during infection (detectable viral RNA

load), *Firmicutes*, *Actinobacteriota*, and *Bacteroidetes* become the dominant phyla (**Figure 11A**). After infection (back to undetectable viral RNA load), the dominant phyla were *Campilobacterota*, *Firmicutes*, and *Bacteroidetes* (**Figure 11A**). At the genus level, *Collinsella* and *Bacteroides* increased during infection, and *Helicobacter* and *Prevotella* increased after infection (**Figure 11A**). Many genus or phylum variations were significantly correlated with the rectal viral RNA load (**Figure 11B**). Among the significant correlation, the abundance of the *Actinobacteriota* phylum, mainly driven by the *Collinsella* genus, perfectly followed the viral kinetics (**Figures 11B, C**). In the *Bacteroidetes* phylum, three genera were significantly correlated with rectal viral RNA load: *Alloprevotella* and *Bacteroides* with a positive correlation and *Prevotella* with a negative correlation (**Figures 11B, D**). *Spirochaetota* variation was negatively correlated with rectal viral RNA load variation (**Figures 11B, E**). These results show that the microbiota composition of the oropharyngeal and rectal mucosae changed in the SARS-CoV-2-exposed neonate.

DISCUSSION

Our pilot study shows that SARS-CoV-2 infection of neonates may represent a suitable model to study early viral and immune response dynamics, with the advantage of having a well-defined onset of an asymptomatic infection, which is difficult to obtain in humans.

We show an effective and asymptomatic infection of the neonate NHP. We observed a correlation of the viral RNA load with the development of an early (DPI 2) innate immune response, accompanied with a balanced IL-10/IFN-γ response in peripheral and mucosal sites. Moreover, these parameters correlated with changes in the oropharyngeal and rectal microbiota profile composition. In the mother, viral RNA loads were low and close to the detection limit, despite the very close contact with SARS-CoV-2-exposed neonate, as demonstrated by RT-qPCR and RNA-sequencing data. In infected adults, we observed a mild asymptomatic infection with transient signs of inflammation, more pronounced than the rapidly resolving form observed in the neonate.

There is a debate on the fact that children are more exposed to common cold coronaviruses and have therefore developed cross-reactive antibodies with some ability to protect them against SARS-CoV-2 (13, 50, 51). However, adults are also exposed and thus should have such immunity (50). Recently, a study reported that in adults and upon exposure to SARS-CoV-2, the influence of pre-existing memory responses in combination with potentially slower activation of the memory B-cell response may contribute to a less rapid and effective antibody response. In contrast, children, who have less-experienced humoral immunity to seasonal coronaviruses, may mount a more specific immune response towards antigens from SARS-CoV-2, by inducing more targeted and Fc functional immunity against SARS-CoV-2 antigens in comparison with adults (14). Whether this mechanism applies here in the SARS-Cov-2-exposed

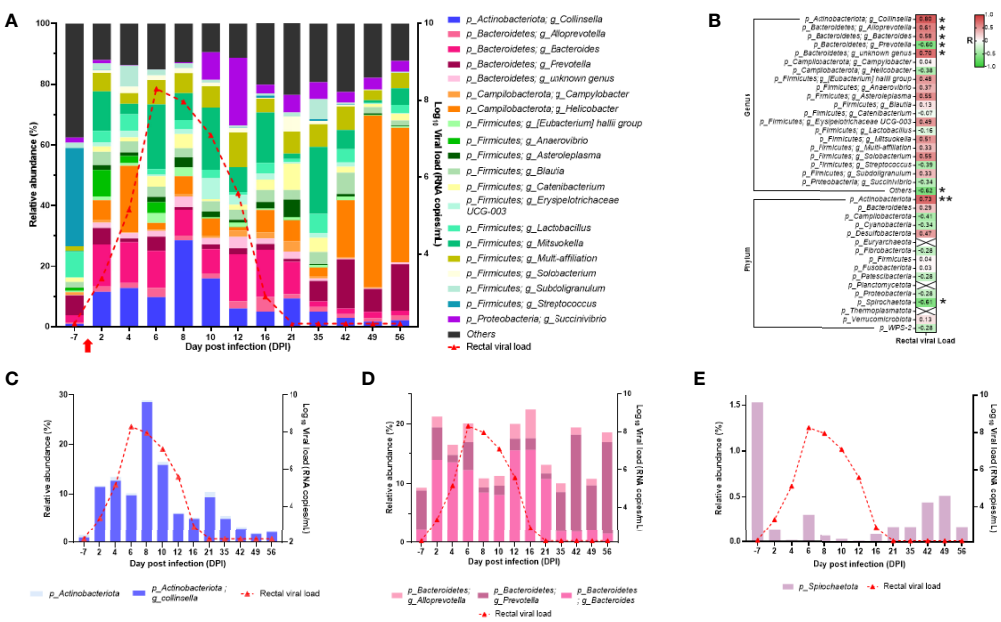

FIGURE 11 | Analyses of the neonate rectal microbiota composition. **(A)** Bar plots represent the rectal microbiota composition. Relative abundance is represented for each time point (left scale). The red curve represents the rectal viral RNA load (logarithmic scale) of SARS-CoV-2 detected in neonate over time (right scale). **(B)** Spearman correlation analysis between the SARS-CoV-2 rectal viral RNA load and the rectal microbiota composition. On the heatmap, the correlation factors of each phylum or genus are represented according to the rectal viral RNA load. Correlation factors are indicated on a red to green scale. $^{*}p < 0.03$; $^{**}p < 0.001$. **(C)** *Actinobacteria* (phylum) and *Collinsella* (genus) relative abundance (left scale) overlapped with rectal viral RNA load on the logarithmic scale (right scale). **(D)** *Alloprevotella*, *Bacteroides*, and *Prevotella* (genus) relative abundance (left scale) overlapped with rectal viral RNA load on the logarithmic scale (right scale). **(E)** *Spirochaetota* (phylum) relative abundance (left scale) overlapped with rectal viral RNA load on the logarithmic scale (right scale).

neonate NHP or not is an additional question that can be addressed in future studies. Of note, the neonate in our study was born to a healthy mother in our clean and protected facility.

In our study, we observed an early and high fold increase of B cells in the neonate compared with adults, which started from DPI 6, persisted, and peaked at DPI 35 and DPI 42. The physiological increase of B cells from 1 month described in human neonate (16) might partly explain the observed B-cell expansion. Nonetheless, this increase also coincided with infection-related B-cell enrichment and activation, together with the kinetics of the IgG to RBD and neutralizing antibodies, though the latter were not tested throughout. Antibody titers in the neonate NHP were lower compared with those we previously detected in nonhospitalized COVID-19 adult patients at similar time points postinfection (31).

Furthermore, we observed the presence of gene sets related to some cell populations, namely dendritic, B, and T cells, as assessed by RNA sequencing of whole blood. The presence of NKT gene sets was persistent at every time point, as shown by the volcano plots. These cells are important as they are involved in both innate and adaptive immunity during respiratory infections (52) and have the capacity to not only rapidly produce some key cytokines but also interact with B cells for prolonged antibody responses with isotype switch and affinity maturation, and development of long-lasting B-cell memory (53–55). We also observed an increase in some innate and adaptive cytokines, chemokines, and growth factors. More specifically, IFN-γ but not IL-17 was highly expressed as early as DPI 2 in the neonate's blood, which confirms previous data obtained in SARS-CoV-2-infected children (13). We also found an increase in IL-10, TNF-α, IL-1Ra, MIP-1α, and to a lesser extent, IL-5, IL-13, IL-15, IL-12/23, IL-18, and G-CSF at DPI 2. Interestingly, this increase correlated with the peak of oropharyngeal viral RNA load. Some of these cytokines, i.e., IFN-γ, IL-10, IL-15, IL-12/23, TNF-α, IL-1Rα, or IL-8, concomitantly increased in rectal and oropharyngeal mucosae, respectively. Increased blood, oropharyngeal, and rectal cytokines correlated with oropharyngeal viral RNA load at DPI 2. The detection of both regulatory (i.e., IL-10) and effector (i.e., IFN-γ) cytokine expression as early as DPI 2 indicates the existence of a balanced immune response very early following pathogen exposure. This increase of IL-10 was not observed in the blood of adult animals, which is consistent with the tolerogenic profile of the neonate immune system that might participate in the control of potential excessive responses.

Importantly, by using an RNA-sequencing-based approach, we were able to show the presence of an early innate immune response in the infected neonate, but not the mother. In particular, we found a strong IFN gene signature as early as DPI 2 compared with the baseline. Type-I interferon signatures included MX1, IFI2, IFI3, IFI27, IFI44, and ISG15 key genes. Genes' expression was elevated and persistent over DPI 6 and even DPI 12 for some of them. These data are in line with previous studies from SARS-CoV-2-infected children (13, 14) and https://doi.org/10.1101/2022.02.12.480218, and interestingly enough, also in line with other pediatric infections such as respiratory syncytial and influenza viruses (56).

Although the exact mechanism leading to better and faster disease resolution in children remains unclear, it is tempting to suggest that the robust innate response that develops very early following SARS-CoV-2 infection, as shown in this study and previous reports (10, 13, 14, 57), plays a major role in rapid disease resolution. Moreover, the presence of persistent NKT cells very early following infection, with their maintenance at every time point, suggests their crucial role in the early production of cytokines such as IFN-γ. This early innate response probably led to disease resolution with no need for mounting a high cellular response, as demonstrated by our results on T-cell populations' dynamics. These results should be reproduced in a larger cohort of neonate NHP. Future studies are underway to assess the potential role of NKT cells in early events of SARS-CoV-2 infection in humans/children.

Given that microbiota plays an important role in shaping the immune responses (58) and that many factors may be responsible for variation in microbiota composition, such as food or exposure to pathogens (59), we sought to assess microbiota composition before and after SARS-CoV-2-neonate NHP exposure, and determine whether we could identify virus-specific bacteria profiles. In adult macaques and humans, SARS-CoV-2 infection causes a transient variation in gut microbiota composition and inflammatory profile (60, 61).

Our results showed some variations of the oropharyngeal microbiota composition, with an increase of the *Actinobacteriota* that correlated with the viral RNA load and of *Haemophylus* spp. from DPI 21 to DPI 49. This increase of *Haemophylus* spp. was reported in children 3 months after antibiotics treatment (62), suggesting that it could be an indicator of dysbiosis in the oropharyngeal microbiota of the neonate. The SARS-CoV-2 effects on the rectal microbiota composition were more pronounced, and the number of the bacterial genus was directly impacted by SARS-CoV-2 infection. While most genera return to normal after infection, *Helicobacter* spp. stayed high. Usually, this genus is not detected in the rectal microbiota of macaques (63), while in humans, it was correlated with several intestinal and hepatobiliary diseases (64). We can therefore reason that SARS-CoV-2 infection in the neonate macaque caused dysbiosis in oropharyngeal and rectal mucosae. The consequences of such dysbiosis on the implementation of immunity and long-term immunity effects should be investigated.

Our study has a few limitations. Only one neonate NHP was studied, which was mainly due to the urgent need for rapidly developing a pediatric SARS-CoV-2 neonate model when the COVID-19 pandemic started (65–67). In a context of strong pressure for SARS-CoV-2 studies on macaque supply, only one animal was available. Consequently, a noninfected SARS-CoV-2 neonate NHP was also unavailable to compare the immune responses and the evolution of the microbiota. Another limitation is the lack of bronchoalveolar lavage and larger blood samples from the neonate for further virological and extended immunological explorations due to ethical reasons. Indeed, larger cohorts are needed to confirm the results from this pilot study.

In summary, we have identified an early innate response in a SARS-CoV-2-infected neonate NHP with mild disease. This

response included the presence of an antiviral type-I IFN genes signature, a persistent and lasting NKT cell population, a balanced peripheral and mucosal IFN-γ/IL-10 cytokine response, and a high increase in B cells that was accompanied with anti-SARS-CoV-2 IgG response. These results suggest an age-dependent differential immune response to SARS-CoV-2 infection will have to be confirmed in a larger number of animals to explore the pathogenesis in children.

DATA AVAILABILITY STATEMENT

The datasets presented in this study can be found in online repositories. The names of the repository/repositories and accession number(s) can be found below: NCIO BioProject, PRJNA800739.

ETHICS STATEMENT

The animal study was reviewed and approved by CEA and complies with the French national regulation (facility authorization number #D92-032-02), the European Directive 2010/63/EU, and the Standards for Human Care and Use of Laboratory Animals (OLAW animal welfare assurance number #A5826-01, United States). The study was approved by the local ethics committee (CEtEA#44) and the French Research, Innovation, and Education Ministry under registration number APAFIS #24434-20200030216532863 V3.

AUTHOR CONTRIBUTIONS

C-MF, MG, CP, NN, RG, EM, and NS conceived, designed, performed experiments, analyzed data, supervised and managed the project, provided funding, and wrote the manuscript (original draft). FR, MC, RF, TN, PM, IM, MT, QS, ND, and JW performed experiments and analyzed the results. VL and GS provided funding and assisted in data interpretation. ND-B supervised the RT-PCR and cytokine experiments. A-SG supervised the flow cytometry experiments. All authors contributed to the reviewing and editing of the final manuscript.

FUNDING

This work was supported by the "Programme Investissements d'Avenir" (PIA) managed by the ANR under reference ANR-11-INBS-0008, funding the Infectious Disease Models and Innovative Therapies (IDMIT, Fontenay-aux-Roses, France) infrastructure, and ANR-10-EQPX-02-01, funding the FlowCyTech facility (IDMIT, Fontenay-aux-Roses, France). The Fondation Bettencourt Schueller and the Region Ile-de-France contributed to the implementation of IDMIT's facilities and imaging technologies. The NHP model of SARS-CoV-2 infection have been developed thanks to the support from REACTing, the Fondation pour la Recherche Medicale (FRM; AM-CoV-Path), and the European Infrastructure TRANSVAC2 (730964). The virus stock used in NHPs was obtained even through the EVAg platform (https://www.european-virus-archive.com/), funded by H2020 (653316). The work performed at IRCCS Ospedale San Raffaele (OSR) was funded by Program Project COVID-19 OSR-UniSR and Ministero della Salute (COVID-2020-12371617). The funders had no role in the design of the study, data collection or interpretation, or the decision to submit the work for publication. We thank Foundation Dormeur, Vaduz for the donation of laboratory instruments relevant to this project to the Viral Evolution and Transmission Unit at OSR.

ACKNOWLEDGMENTS

We thank Sylvie van Der Werf at the National Reference Centre for Respiratory Viruses (Institut Pasteur) for providing SARS-CoV-2 virus; Benoît Delache, Julien Lemaitre, and all ASW staff for their help with animal experiments; Maxence Galpin-Lebreau, Marco Leonec, and Laurine Moenne-Loccoz for RT-PCR experiments; Laetitia Bossevot and Julie Morin for the Luminex experiments; Léo D'Agata, Ségolène Diry, and Cassandra Gaspar for RNA/DNA extraction, sequencing, and data analyses; Catherine Chapon and Nidhal Kahlaoui for their help with the CT scans; Mario Gomez-Pacheco and Wesley Gros for flow cytometry experiments; Mylinda Barendji, Julien Dinh, and Elodie Guyon for the macaque sample processing; Marie-Thérèse Nugeyre, Claude Cannou, and Cindy Adapen for DNA extraction and microbiota data analysis; Vanessa Contreras, Romain Marlin, and Camille Bouillier for adult data analysis; Frédéric Ducancel, Yann Gorin, Brice Targat, and Isabelle Mangeot for their help with the logistics, safety, and resource management; and Andrea Cara and Donatella Negri for providing the Lentiviral-Luc-Spike preparations.

SUPPLEMENTARY MATERIAL

The Supplementary Material for this article can be found online at: https://www.frontiersin.org/articles/10.3389/fimmu.2022.855230/full#supplementary-material

Supplementary Figure 1 | Clinical parameters of the neonate/mother pair. **(A)** Temperature, oxygen saturation, respiratory and heart rate for the neonate (blue line) and its mother (orange line). The horizontal dashed line(s) is for the physiological accepted values. **(B)** Neonate body weight. **(C)** Biochemical parameters values for ASAT/ALAT, creatinine, CRP, haptoglobin, LDH, total protein, troponin I and urea. The vertical red dashed line indicates viral inoculation at DPI 0.

Supplementary Figure 2 | Hematological parameters of the neonate/mother pair. **(A)** Hemoglobin concentration and absolute numbers of white blood cells, neutrophils, lymphocytes, red blood cells, monocytes, eosinophils, basophils in the neonate (blue line) and its mother (orange line). The vertical red dashed line indicates viral inoculation at DPI 0. **(B)** Evolution of the leukocytes subpopulations count in the neonate blood during the first ten weeks of life compared to adult profile.

Supplementary Figure 3 | Clinical parameters of infected adults. **(A)** Temperature, oxygen saturation, respiratory and heart rate of seven adults from three studies (pink, green and blue lines). The horizontal dashed line(s) is for the physiological accepted values. **(B)** Biochemical parameters values for ASAT/ALAT, creatinine, CRP, haptoglobin, LDH, total protein and troponin I. The horizontal

dashed lines stand for median with standard deviations according to reference values (68, 69). The vertical red dashed line indicates viral inoculation at DPI 0.

Supplementary Figure 4 | Hematological parameters of infected adults. Hemoglobin concentration and absolute numbers of white blood cells, neutrophils, lymphocytes, red blood cells, monocytes, eosinophils, basophils in adults from three studies (pink, green and blue lines). The horizontal dashed lines stand for median with standard deviations according to reference values (68, 69). The vertical red dashed line indicates viral inoculation at DPI 0.

Supplementary Figure 5 | SARS-CoV-2 infection in adults. Viral RNA load measured by RT-qPCR in the fluidic compartments. The limit of detection was estimated at 2.37 log10 copies per ml and the limit of quantification was estimated at 3.37 log10 copies per ml (dotted horizontal line). Macaques were included in three studies with specific SARS-CoV-2 inoculated doses: MM1-4 received $1x10^5$ CFU (pink), MM5 received $1x10^6$ CFU (green) and MM6-7 received $1x10^7$ CFU (blue).

Supplementary Figure 6 | Cytokine analyses in blood from infected adults. Heatmap representing the evolution of cytokines over-time in three adults (in log of fold-change from the baseline). Variations are shown on a blue scale. Basal concentrations (pg/ml) are shown on the left side of the heatmap. Highlighted yellow values correspond to the detection threshold.

Supplementary Table 1 | Individual data of infected adult rhesus macaques. SARS-CoV-2 inoculation protocol and sampling planning for mucosal swabs and blood collection of seven adult females. MM1-4 received $1x10^5$ CFU and had a 28 DPI follow-up (pink), MM5 received $1x10^6$ CFU and had a 4 DPI follow-up (green), and MM6-7 received $1x10^7$ CFU with 28 DPI follow-up (blue). Samples included heparin-lithium blood and fluids from nasal, rectal and broncho-alveolar lavages compartments.

Supplementary Table 2 | Cytokine concentrations in the neonate compartments. Cytokine quantification was performed in blood, oropharyngeal and rectal fluids with the Milliplex MAP kit for NHP, based on Luminex® xMAP multiplex technology.

REFERENCES

1. Castagnoli R, Votto M, Licari A, Brambilla I, Bruno R, Perlini S, et al. Severe Acute Respiratory Syndrome Coronavirus 2 (SARS-CoV-2) Infection in Children and Adolescents: A Systematic Review. *JAMA Pediatr* (2020) 174 (9):882–9. doi: 10.1001/jamapediatrics.2020.1467
2. Dong YY, Mo X, Hu YB, Qi X, Jiang F, Jiang ZY, et al. Epidemiology of COVID-19 Among Children in China. *Pediatrics* (2020) 145(6):e20200702. doi: 10.1542/peds.2020-0702
3. Ludvigsson JF. Systematic Review of COVID-19 in Children Shows Milder Cases and a Better Prognosis Than Adults. *Acta Paediatr* (2020) 109(6):1088–95. doi: 10.1111/apa.15270
4. Qiu H, Wu J, Hong L, Luo Y, Song Q, et al. Clinical and Epidemiological Features of 36 Children With Coronavirus Disease 2019 (COVID-19) in Zhejiang, China: An Observational Cohort Study. *Lancet Infect Dis* (2020) 20 (6):689–96. doi: 10.1016/S1473-3099(20)30198-5
5. Parri N, Lenge M, Buonsenso D. Children With Covid-19 in Pediatric Emergency Departments in Italy. *N Engl J Med* (2020) 383(2):187–90. doi: 10.1056/NEJMc2007617
6. Anderson EM, Goodwin EC, Verma A, Arevalo CP, Bolton MJ, Weirick ME, et al. Seasonal Human Coronavirus Antibodies are Boosted Upon SARS-CoV-2 Infection But Not Associated With Protection. *Cell* (2021) 184 (7):1858. doi: 10.1016/j.cell.2021.02.010
7. Heald-Sargent T, Muller WJ, Zheng XT, Rippe J, Patel AB, Kociolek LK. Age-Related Differences in Nasopharyngeal Severe Acute Respiratory Syndrome Coronavirus 2 (SARS-CoV-2) Levels in Patients With Mild to Moderate Coronavirus Disease 2019 (COVID-19). *JAMA Pediatr* (2020) 174(9):902–3. doi: 10.1001/jamapediatrics.2020.3651
8. Weatherhead JE, Clark E, Vogel TP, Atmar RL, Kulkarni PA. Inflammatory Syndromes Associated With SARS-CoV-2 Infection: Dysregulation of the Immune Response Across the Age Spectrum. *J Clin Invest* (2020) 130 (12):6194–7. doi: 10.1172/JCI145301
9. Verdoni L, Mazza A, Gervasoni A, Martelli L, Ruggeri M, Ciuffreda M, et al. An Outbreak of Severe Kawasaki-Like Disease at the Italian Epicentre of the SARS-CoV-2 Epidemic: An Observational Cohort Study. *Lancet* (2020) 395 (10239):1771–8. doi: 10.1016/S0140-6736(20)31103-X
10. Pierce CA, Sy S, Galen B, Goldstein DY, Orner E, Keller MJ, et al. Y Natural Mucosal Barriers and COVID-19 in Children. *JCI Insight* (2021) 6(9):e148694. doi: 10.1172/jci.insight.148694
11. Zhang Z, Guo L, Huang L, Zhang C, Luo R, Zeng L, et al. Distinct Disease Severity Between Children and Older Adults With COVID-19: Impacts of ACE2 Expression, Distribution, and Lung Progenitor Cells. *Clin Infect Dis* (2021) 73(11):e4154–65. doi: 10.1093/cid/ciaa1911
12. Yonker L. Virologic Features of SARS-CoV-2 Infection in Children. *MedRxiv* (2021) 17:2021.05.30.21258086. doi: 10.1101/2021.05.30.21258086
13. Pierce CA, Preston-Hurlburt P, Dai YL, Aschner CB, Cheshenko N, Galen B, et al. Immune Responses to SARS-CoV-2 Infection in Hospitalized Pediatric and Adult Patients. *Sci Trans Med* (2020) 12(564):eabd5487. doi: 10.1126/scitranslmed.abd5487
14. Vono M, Huttner A, Lemeille S, Martinez-Murillo P, Meyer B, Baggio S, et al. Robust Innate Responses to SARS-CoV-2 in Children Resolve Faster Than in Adults Without Compromising Adaptive Immunity. *Cell Rep* (2021) 37 (1):109773. doi: 10.1016/j.celrep.2021.109773
15. Gilbert C, Lefeuvre C, Preisser L, Pivert A, Soleti R, Blanchard S, et al. Age-Related Expression of IFN-Lambda1 Versus IFN-I and Beta-Defensins in the Nasopharynx of SARS-CoV-2-Infected Individuals. *Front Immunol* (2021) 12:750279. doi: 10.3389/fimmu.2021.750279
16. Loske J, Rohmel J, Lukassen S, Stricker S, Magalhaes VG, Liebig J, et al. Pre-Activated Antiviral Innate Immunity in the Upper Airways Controls Early SARS-CoV-2 Infection in Children. *Nat Biotechnol* (2022) 40(3):319–24. doi: 10.1038/s41587-021-01037-9
17. Roberts A, Lamirande EW, Vogel L, Jackson JP, Paddock CD, Guarner J, et al. Animal Models and Vaccines for SARS-CoV Infection. *Virus Res* (2008) 133 (1):20–32. doi: 10.1016/j.virusres.2007.03.025
18. Brody IB, Calcedo R, Connell MJ, Carnathan DG, Nason M, Lawson BO, et al. Susceptibility to SIV Infection After Adenoviral Vaccination in a Low Dose Rhesus Macaque Challenge Model. *Pathog Immun* (2019) 4(1):1–20. doi: 10.20411/pai.v4i1.241
19. Chen YX, Liu L, Wei Q, Zhu H, Jiang H, Tu XM, et al. Rhesus Angiotensin Converting Enzyme 2 Supports Entry of Severe Acute Respiratory Syndrome Coronavirus in Chinese Macaques. *Virology* (2008) 381(1):89–97. doi: 10.1016/j.virol.2008.08.016
20. de Wit E, Feldmann F, Cronin J, Jordan R, Okumura A, Thomas T, et al. Prophylactic and Therapeutic Remdesivir (GS-5734) Treatment in the Rhesus Macaque Model of MERS-CoV Infection. *Proc Natl Acad Sci USA* (2020) 117 (12):6771–6. doi: 10.1073/pnas.1922083117
21. Fouchier RA, Kuiken T, Schutten M, van Amerongen G, van Doornum GJ, van den Hoogen BG, et al. Aetiology: Koch's Postulates Fulfilled for SARS Virus. *Nature* (2003) 423(6937):240. doi: 10.1038/423240a
22. Haagmans BL, Osterhaus AD. Nonhuman Primate Models for SARS. *PloS Med* (2006) 3(5):e194. doi: 10.1371/journal.pmed.0030194
23. Kuiken T, Fouchier RAM, Schutten M, Rimmelzwaan GF, van Amerongen G, van Riel D, et al. Newly Discovered Coronavirus as the Primary Cause of Severe Acute Respiratory Syndrome. *Lancet* (2003) 362(9380):263–70. doi: 10.1016/S0140-6736(03)13967-0
24. Liu L, Wei Q, Lin Q, Fang J, Wang H, Kwok H, et al. Anti-Spike IgG Causes Severe Acute Lung Injury by Skewing Macrophage Responses During Acute SARS-CoV Infection. *JCI Insight* (2019) 4(4):e123158. doi: 10.1172/jci.insight.123158
25. Luo F, Liao FL, Wang H, Tang HB, Yang ZQ, Hou W. Evaluation of Antibody-Dependent Enhancement of SARS-CoV Infection in Rhesus Macaques Immunized With an Inactivated SARS-CoV Vaccine. *Virol Sin* (2018) 33(2):201–4. doi: 10.1007/s12250-018-0009-2
26. Rockx B, Feldmann F, Brining D, Gardner D, LaCasse R, Kercher L, et al. Comparative Pathogenesis of Three Human and Zoonotic SARS-CoV Strains in Cynomolgus Macaques. *PloS One* (2011) 6(4):e18558. doi: 10.1371/journal.pone.0018558

27. Brouwer PJM, Brinkkemper M, Maisonnasse P, Dereuddre-Bosquet N, Grobben M, Claireaux M, et al. Two-Component Spike Nanoparticle Vaccine Protects Macaques From SARS-CoV-2 Infection. *Cell* (2021) 184 (5):1188. doi: 10.1016/j.cell.2021.01.035
28. Maisonnasse P, Guedj J, Contreras V, Behillil S, Solas C, Marlin R, et al. Hydroxychloroquine Use Against SARS-CoV-2 Infection in non-Human Primates. *Nature* (2020) 585(7826):584. doi: 10.1038/s41586-020-2558-4
29. Pan F, Ye T, Sun P, Gui S, Liang B, Li L, et al. Time Course of Lung Changes at Chest CT During Recovery From Coronavirus Disease 2019 (COVID-19). *Radiology* (2020) 295(3):715–21. doi: 10.1148/radiol.2020200370
30. Shi H, Han X, Jiang N, Cao Y, Alwalid O, Gu J, et al. Radiological Findings From 81 Patients With COVID-19 Pneumonia in Wuhan, China: A Descriptive Study. *Lancet Infect Dis* (2020) 20(4):425–34. doi: 10.1016/S1473-3099(20)30086-4
31. Dispinseri S, Secchi M, Pirillo MF, Tolazzi M, Borghi M, Brigatti C, et al. Neutralizing Antibody Responses to SARS-CoV-2 in Symptomatic COVID-19 is Persistent and Critical for Survival. *Nat Commun* (2021) 12(1):2670. doi: 10.1038/s41467-021-22958-8
32. Fenyo EM, Heath A, Dispinseri S, Holmes H, Lusso P, Zolla-Pazner S, et al. International Network for Comparison of HIV Neutralization Assays: The NeutNet Report. *PloS One* (2009) 4(2):e4505. doi: 10.1371/journal.pone.0004505
33. Burbelo PD, Goldman R, Mattson TL. A Simplified Immunoprecipitation Method for Quantitatively Measuring Antibody Responses in Clinical Sera Samples by Using Mammalian-Produced Renilla Luciferase-Antigen Fusion Proteins. *BMC Biotechnol* (2005) 5:22. doi: 10.1186/1472-6750-5-22
34. Secchi M, Bazzigaluppi E, Brigatti C, Marzinotto I, Tresoldi C, Rovere-Querini P, et al. COVID-19 Survival Associates With the Immunoglobulin Response to the SARS-CoV-2 Spike Receptor Binding Domain. *J Clin Invest* (2020) 130 (12):6366–78. doi: 10.1172/JCI142804
35. Li H. Minimap2: Pairwise Alignment for Nucleotide Sequences. *Bioinformatics* (2018) 34(18):3094–100. doi: 10.1093/bioinformatics/bty191
36. Patro R, Duggal G, Love MI, Irizarry RA, Kingsford C. Salmon Provides Fast and Bias-Aware Quantification of Transcript Expression. *Nat Methods* (2017) 14(4):417–9. doi: 10.1038/nmeth.4197
37. Love HC, Timms DL, Nestler F, Frazier OH, Cohn WE. A Mock Circulatory Loop for Designing and Evaluating Total Artificial Hearts. *Annu Int Conf IEEE Eng Med Biol Soc* (2014) 2014:5667–70. doi: 10.1109/EMBC.2014.6944913
38. Chen EY, Tan CM, Kou Y, Duan Q, Wang Z, Meirelles GV, et al. Enrichr: Interactive and Collaborative HTML5 Gene List Enrichment Analysis Tool. *BMC Bioinform* (2013) 14:128. doi: 10.1186/1471-2105-14-128
39. Kuleshov MV, Jones MR, Rouillard AD, Fernandez NF, Duan Q, Wang Z, et al. Enrichr: A Comprehensive Gene Set Enrichment Analysis Web Server 2016 Update. *Nucleic Acids Res* (2016) 44(W1):W90–7. doi: 10.1093/nar/gkw377
40. Xie Z, Bailey A, Kuleshov MV, Clarke DJB, Evangelista JE, Jenkins SL, et al. Gene Set Knowledge Discovery With Enrichr. *Curr Protoc* (2021) 1(3):e90. doi: 10.1002/cpz1.90
41. Huang R, Grishagin I, Wang Y, Zhao T, Greene J, Obenauer JC, et al. The NCATS BioPlanet - An Integrated Platform for Exploring the Universe of Cellular Signaling Pathways for Toxicology, Systems Biology, and Chemical Genomics. *Front Pharmacol* (2019) 10:445. doi: 10.3389/fphar.2019.00445
42. Szklarczyk D, Gable AL, Lyon D, Junge A, Wyder S, Huerta-Cepas J, et al. STRING V11: Protein-Protein Association Networks With Increased Coverage, Supporting Functional Discovery in Genome-Wide Experimental Datasets. *Nucleic Acids Res* (2019) 47(D1):D607–13. doi: 10.1093/nar/gky1131
43. Escudie F, Auer L, Bernard M, Mariadassou M, Cauquil L, Vidal K, et al. FROGS: Find, Rapidly, OTUs With Galaxy Solution. *Bioinformatics* (2018) 34 (8):1287–94. doi: 10.1093/bioinformatics/btx791
44. Rognes T, Flouri T, Nichols B, Quince C, Mahe F. VSEARCH: A Versatile Open Source Tool for Metagenomics. *PeerJ* (2016) 4:e2584. doi: 10.7717/peerj.2584
45. Merino KM, Richardson N, Reaman G, Ande A, Zvada S, Liu C, et al. Clinical and Immunological Metrics During Pediatric Rhesus Macaque Development. *Front Pediatr* (2020) 8:388. doi: 10.3389/fped.2020.00388
46. Adeli K, Higgins V, Trajcevski K, White-Al Habeeb N. The Canadian Laboratory Initiative on Pediatric Reference Intervals: A CALIPER White Paper. *Crit Rev Clin Lab Sci* (2017) 54(6):358–413. doi: 10.1080/10408363.2017.1379945
47. Bohn MK, Higgins V, Tahmasebi H, Hall A, Liu E, Adeli K, et al. Complex Biological Patterns of Hematology Parameters in Childhood Necessitating Age- and Sex-Specific Reference Intervals for Evidence-Based Clinical Interpretation. *Int J Lab Hematol* (2020) 42(6):750–60. doi: 10.1111/ijlh.13306
48. Duncan CJA, Hambleton S. Human Disease Phenotypes Associated With Loss and Gain of Function Mutations in STAT2: Viral Susceptibility and Type I Interferonopathy. *J Clin Immunol* (2021) 41(7):1446–56. doi: 10.1007/s10875-021-01118-z
49. Cotugno N, Ruggiero A, Bonfante F, Petrara MR, Zicar S, Pascucci GR, et al. Virological and Immunological Features of SARS-CoV-2-Infected Children Who Develop Neutralizing Antibodies. *Cell Rep* (2021) 34(11):108852. doi: 10.1016/j.celrep.2021.108852
50. Ng KW, Faulkner N, Cornish GH, Rosa A, Harvey R, Hussain S, et al. Preexisting and De Novo Humoral Immunity to SARS-CoV-2 in Humans. *Science* (2020) 370(6522):1339–+. doi: 10.1126/science.abe1107
51. Dowell AC, Butler MS, Jinks E, Tut G, Lancaster T, Sylla P, et al. Children Develop Robust and Sustained Cross-Reactive Spike-Specific Immune Responses to SARS-CoV-2 Infection. *Nat Immunol* (2022) 23(1):40–9. doi: 10.1038/s41590-021-01089-8
52. Trottein F, Paget C. Natural Killer T Cells and Mucosal-Associated Invariant T Cells in Lung Infections. *Front Immunol* (2018) 9:1750. doi: 10.3389/fimmu.2018.01750
53. Lang ML. How do Natural Killer T Cells Help B Cells? *Expert Rev Vaccines* (2009) 8(8):1109–21. doi: 10.1586/erv.09.56
54. Bai L, Deng S, Reboulet R, Mathew R, Teyton L, Savage PB, et al. Natural Killer T (NKT)-B-Cell Interactions Promote Prolonged Antibody Responses and Long-Term Memory to Pneumococcal Capsular Polysaccharides. *Proc Natl Acad Sci USA* (2013) 110(40):16097–102. doi: 10.1073/pnas.1303218110
55. Chen Z, Zhu S, Wang L, Xie D, Zhang H, Li X, et al. Memory Follicular Helper Invariant NKT Cells Recognize Lipid Antigens on Memory B Cells and Elicit Antibody Recall Responses. *J Immunol* (2018) 200(9):3117–27. doi: 10.4049/jimmunol.1701026
56. Heinonen S, Velazquez VM, Ye F, Mertz S, Acero-Bedoya S, Smith B, et al. Immune Profiles Provide Insights Into Respiratory Syncytial Virus Disease Severity in Young Children. *Sci Transl Med* (2020) 12(540):eaaw0268. doi: 10.1126/scitranslmed.aaw0268
57. Mallapaty S. Kids and COVID: Why Young Immune Systems are Still on Top. *Nature* (2021) 597(7875):166–8. doi: 10.1038/d41586-021-02423-8
58. Tanaka M, Nakayama J. Development of the Gut Microbiota in Infancy and its Impact on Health in Later Life. *Allergol Int* (2017) 66(4):515–22. doi: 10.1016/j.alit.2017.07.010
59. Nunez N, Reot L, Menu E. Neonatal Immune System Ontogeny: The Role of Maternal Microbiota and Associated Factors. How Might the Non-Human Primate Model Enlighten the Path? *Vaccines (Basel)* (2021) 9(6):584. doi: 10.3390/vaccines9060584
60. Sokol H, Contreras V, Maisonnasse P, Desmons A, Delache B, Sencio V, et al. SARS-CoV-2 Infection in Nonhuman Primates Alters the Composition and Functional Activity of the Gut Microbiota. *Gut Microbes* (2021) 13(1):1–19. doi: 10.1080/19490976.2021.1893113
61. Vodnar DC, Mitrea L, Teleky BE, Szabo K, Calinoiu LF, Nemes SA, et al. Coronavirus Disease (COVID-19) Caused by (SARS-CoV-2) Infections: A Real Challenge for Human Gut Microbiota. *Front Cell Infect Microbiol* (2020) 10:575559. doi: 10.3389/fcimb.2020.575559
62. Thapa S, Runge JK, Venkatachalam A, Denne C, Luna RA, et al. The Nasopharyngeal and Gut Microbiota in Children in a Pediatric Otolaryngology Practice. *Pediatr Infect Dis J* (2020) 39(9):e226–33. doi: 10.1097/INF.0000000000002703
63. Cui YF, Wang FJ, Yu L, Ye HH, Yang GB. Metagenomic Comparison of the Rectal Microbiota Between Rhesus Macaques (Macaca Mulatta) and Cynomolgus Macaques (Macaca Fascicularis). *Zool Res* (2019) 40(2):89–93. doi: 10.24272/j.issn.2095-8137.2018.061
64. Smet A, Flahou B, Mukhopadhya I, Ducatelle R, Pasmans F, Haesebrouck F, et al. The Other Helicobacters. *Helicobacter* (2011) 16(Suppl 1):70–5. doi: 10.1111/j.1523-5378.2011.00884.x
65. Livingston E, Bucher K. Coronavirus Disease 2019 (COVID-19) in Italy. *JAMA* (2020) 323(14):1335. doi: 10.1001/jama.2020.4344

66. Team CC-R. Coronavirus Disease 2019 in Children - United States, February 12-April 2, 2020. *MMWR Morb Mortal Wkly Rep* (2020) 69(14):422–6. doi: 10.15585/mmwr.mm6914e4
67. Wu Z, McGoogan JM. Characteristics of and Important Lessons From the Coronavirus Disease 2019 (COVID-19) Outbreak in China: Summary of a Report of 72314 Cases From the Chinese Center for Disease Control and Prevention. *JAMA* (2020) 323(13):1239–42. doi: 10.1001/jama.2020.2648
68. Koo BS, Lee DH, Kang P, Jeong KJ, Lee S, Kim K, et al. Reference Values of Hematological and Biochemical Parameters in Young-Adult Cynomolgus Monkey (Macaca Fascicularis) and Rhesus Monkey (Macaca Mulatta) Anesthetized With Ketamine Hydrochloride. *Lab Anim Res* (2019) 35:7. doi: 10.1186/s42826-019-0006-0
69. Krogh AK, Lundsgaard JF, Bakker J, Langermans JA, Verreck FA, Kjelgaard-Hansen M, et al. Acute-Phase Responses in Healthy and Diseased Rhesus Macaques (Macaca Mulatta). *J Zoo Wildl Med* (2014) 45(2):306–14. doi: 10.1638/2013-0153R.1

Conflict of Interest: Author Natalia Nunez was employed by Life and Soft, Fontenay-aux-Roses, France.

The remaining authors declare that the research was conducted in the absence of any commercial or financial relationships that could be construed as a potential conflict of interest.

Publisher's Note: All claims expressed in this article are solely those of the authors and do not necessarily represent those of their affiliated organizations, or those of the publisher, the editors and the reviewers. Any product that may be evaluated in this article, or claim that may be made by its manufacturer, is not guaranteed or endorsed by the publisher.

frontiers | Frontiers in Immunology

ORIGINAL RESEARCH
published: 01 June 2022
doi: 10.3389/fimmu.2022.887892

Dynamic Immune Landscape and VZV-Specific T Cell Responses in Patients With Herpes Zoster and Postherpetic Neuralgia

Qiao Peng[1†], Xuejiao Guo[2†], Yang Luo[3†], Guocan Wang[1], Lingyu Zhong[1], Jiamin Zhu[2], Yunze Li[2], Xun Zeng[1‡] and Zhiying Feng[2*‡]*

[1] State Key Laboratory for Diagnosis and Treatment of Infectious Diseases, National Clinical Research Center for Infectious Diseases, National Medical Center for Infectious Diseases, Collaborative Innovation Center for Diagnosis and Treatment of Infectious Diseases, The First Affiliated Hospital, Zhejiang University School of Medicine, Hangzhou, China, [2] Department of Pain Medicine, The First Affiliated Hospital, Zhejiang University School of Medicine, Hangzhou, China, [3] Center for Stem Cell and Regenerative Medicine, Zhejiang University School of Medicine, Hangzhou, China

OPEN ACCESS

Edited by:
Shen-Ying Zhang, The Rockefeller University, United States

Reviewed by:
Werner Ouwendijk, Erasmus Medical Center, Netherlands
Megan Steain, The University of Sydney, Australia

***Correspondence:**
Xun Zeng
xunzeng@zju.edu.cn
Zhiying Feng
Fengfzy1972@zju.edu.cn

†These authors have contributed equally to this work

‡These authors have contributed equally to this work

Specialty section:
This article was submitted to Viral Immunology, a section of the journal Frontiers in Immunology

Received: *02 March 2022*
Accepted: *29 April 2022*
Published: *01 June 2022*

Citation:
Peng Q, Guo X, Luo Y, Wang G, Zhong L, Zhu J, Li Y, Zeng X and Feng Z (2022) Dynamic Immune Landscape and VZV-Specific T Cell Responses in Patients With Herpes Zoster and Postherpetic Neuralgia. Front. Immunol. 13:887892. doi: 10.3389/fimmu.2022.887892

Objectives: Varicella-zoster virus (VZV) can induce herpes zoster (HZ) and postherpetic neuralgia (PHN). Immune cells play an important role in regulating HZ and PHN pathogenesis, but the dynamic immune profiles and molecular mechanisms remain unclear. This study aimed to screen dynamic immune signatures during HZ progression and elucidate the mechanism of VZV-specific T cells in PHN.

Methods: We used cytometry by time-of-flight (CyTOF) to analyze peripheral blood mononuclear cells (PBMC) samples from 45 patients with HZ and eight age-sex-matched healthy controls, eight PHN samples and seven non-PHN samples. Correlations between the immune subsets and clinical pain-related scores were performed. Further, the characteristics of VZV-specific T cells between PHN and non-PHN patients were evaluated by VZV peptide pools stimulation. The expression level of cytokines, including granzyme B, interleukin (IL)-2, interferon (IFN)-γ, and tumor necrosis factor (TNF)-α was performed *via* cytometric bead array. Finally, we analyzed the alteration of Ca^{2+} signals in dorsal root ganglion (DRG)-derived cells after TNF-α stimulation.

Results: We investigated the dynamic characteristics of the immune landscape of peripheral blood samples of patients with HZ and PHN, and depicted two major dynamic signatures in NK, $CD4^+$ and $CD8^+$ T subsets in patients with HZ, which closely correlated with clinical pain-related scores. The frequency of PD-1^+CD4^+ T cells, VZV-specific PD-1^+CD4^+ T cells, and the amount of TNF-α produced by VZV-specific T cells were higher in patients with PHN than without PHN. Furthermore, we showed that TNF-α could induce calcium influx in DRG-derived cells in a dose-dependent manner.

Conclusions: Our results profiled the dynamic signatures of immune cells in patients with HZ and highlighted the important role of VZV-specific T cells in the pathogenesis of PHN.

Keywords: varicella-zoster virus, herpes zoster, postherpetic neuralgia, CyTOF, VZV-specific T cells

INTRODUCTION

Herpes zoster (HZ), often known as shingles, is caused by the reactivation of varicella-zoster virus (VZV), a human host-restricted α-herpes virus with a high incidence worldwide, particularly in immunocompromised or elderly individuals (1, 2). Postherpetic neuralgia (PHN) is defined as persistent pain for at least 3 months after HZ initiation and is the most common and debilitating complication following HZ in approximately 20% of patients (3, 4). PHN may cause physical disability, psychological depression, and financial burden that reduce the quality of life of patients (5). One of the most common syndromes for HZ and PHN is pain (6). However, current clinical pain indicators, such as rating scales and symptom-based questionnaires, have low sensitivity and reliability and fail to point out the underlying pathogenesis of pain (7, 8). Therefore, more accurate, sensitive, and objective pain indicators are required in the clinic. In addition, current therapies for both HZ and PHN, including anti-virus treatment, medication, nerve blocks, and radiofrequency, have many adverse effects or limited efficacy (9, 10). Thus, investigating the disease pathogenesis to explore the new targets for efficient therapies of HZ and PHN is urgent and important, which may improve the efficacy of HZ therapy and prevent the incidence of PHN from acute HZ.

The immune system is crucial in VZV infection. Natural killer (NK) cells and monocytes, vital components of the innate immune system, are significantly elevated in HZ patients (11). NK cell expansion is associated with more pronounced inflammation during HZ (11), and monocytes produce IL-6, IL-8, IL-12, IFN-γ, and TNF-α in response to VZV infection (12, 13). Apart from the innate immune system, adaptive immunity, especially T cell-mediated response, plays a definitive role in host defense against VZV infection. T cell xenografts in severe combined immunodeficiency (SCID) mice *in vivo* or tonsil T cells *in vitro* have validated that T cells can be infected with VZV. Furthermore, VZV-infected T cells are fully permissive to VZV replication and release (10, 14). The VZV-infected T cells predominantly display $CD69^+CD45RA^-$, an activation and memory phenotype (14). Part of them also express cutaneous leukocyte antigen and chemokine receptor 4 (CCR4), which enhances the skin homing ability of VZV-infected T cells and promotes VZV dissemination to the cutaneous site of replication (14). Moreover, VZV infection inhibits the IFN-γ production of VZV-specific $CD8^+$ T cells by upregulating the expression of immunoinhibitory proteins programmed death-1 (PD-1) and PD-L1 (15). Along with these phenotypic alterations, VZV-infected T cells show a loss of CD3ϵ expression, leading to TCR-CD3 complex dysregulation and destruction of immune function (16). Fortunately, VZV must infect each T cell individually and cannot induce the fusion of infected T cells (10). The non-infected T cell-triggered immune response is essential for virus clearance and recovery from HZ. In detail, the proportion of $CD4^+$ T cells from PBMCs negatively correlated, while regulatory T cells (Tregs) positively correlated with the severity of HZ (11, 17). Besides VZV-specific $CD4^+$ T cells are more abundant in PBMCs than $CD8^+$ T cells (18, 19). Moreover, the frequency of VZV-specific $CD4^+$ T cells peaks at about 2 weeks after HZ onset, then decreases at 3–6 weeks and remains stable for many years (20). Recently, dense $CD4^+$ and $CD8^+$ T cell infiltrates in ganglia have been observed during HZ (21, 22). Evidence also confirm the key roles of the immune system in the development of PHN, albeit with limited information. A significant decrease of $CD4^+$ T cells, $CD8^+$ T cells, as well as CD4/CD8 T cell ratio, while an increased percentage of Tregs are validated in patients with PHN compared with those in non-PHN and normal controls, suggesting the more severely impaired T cell-mediated immunity in patients with PHN (11, 23). Thus, a deeper understanding of the immune response of HZ and PHN warrants further investigation to develop potential targets for new immunotherapies.

To illustrate the immune signatures in PBMCs of patients with HZ and the mechanisms of immune cells in patients with PHN, we utilized the CyTOF to visualize the dynamic immune landscape of PBMCs in patients with HZ and PHN (**Figure 1A**). Our findings depicted two major kinetic signatures of NK and T cell clusters, which closely correlated with clinical pain-related scores. We further demonstrated that patients with PHN had more $PD\text{-}1^+CD4^+$, VZV-specific $PD\text{-}1^+CD4^+$ T cells, and more TNF-α production than non-PHN patients. Finally, we showed that TNF-α could induce calcium influx in DRG-derived cell lines, suggesting that VZV-specific T cells secreted TNF-α could induce pain. These data illustrated the dynamic signatures of the immune landscape in the peripheral, which closely correlated with clinical features in patients with HZ and revealed the molecular mechanism of VZV-specific T cells induced pain in patients with PHN.

MATERIALS AND METHODS

Patients and Samples

PBMCs for CyTOF analysis were collected from 60 patients at different time points after the onset of rash and eight age-sex-matched healthy donors as controls (HC) (**Supplementary Table 1**, **Figure S1A**). patients with HZ were diagnosed clinically by a typical vesicular rash in dermatome distribution, and medications prescribed were in standard criterion. Exclusion criteria included known serious immunity disorders or malignant disease, serious cardiocerebrovascular or hepatorenal insufficiency, diabetes, hypersensitivity to antiviral or analgesic drugs, and previous use of corticosteroid therapy, and breastfeeding or pregnancy. Clinical pain-related scores, including Numbering Rating Score (NRS), Touch induced NRS, Numbness degree, DN4, ID-pain, GAD7, PHQ9, impact of pain on mood, and impact of pain on daily life were documented in each patient. The clinical characteristics of all the samples were summarized in **Supplementary Table 1**.

We recruited another cohort of 35 patients with five samples at each time point and five HC (**Supplementary Table 2**) to further explore the function of VZV-specific cell subsets. This study was approved by the ethics committee at the First Affiliated Hospital, School of Medicine, Zhejiang University (NO.2018-

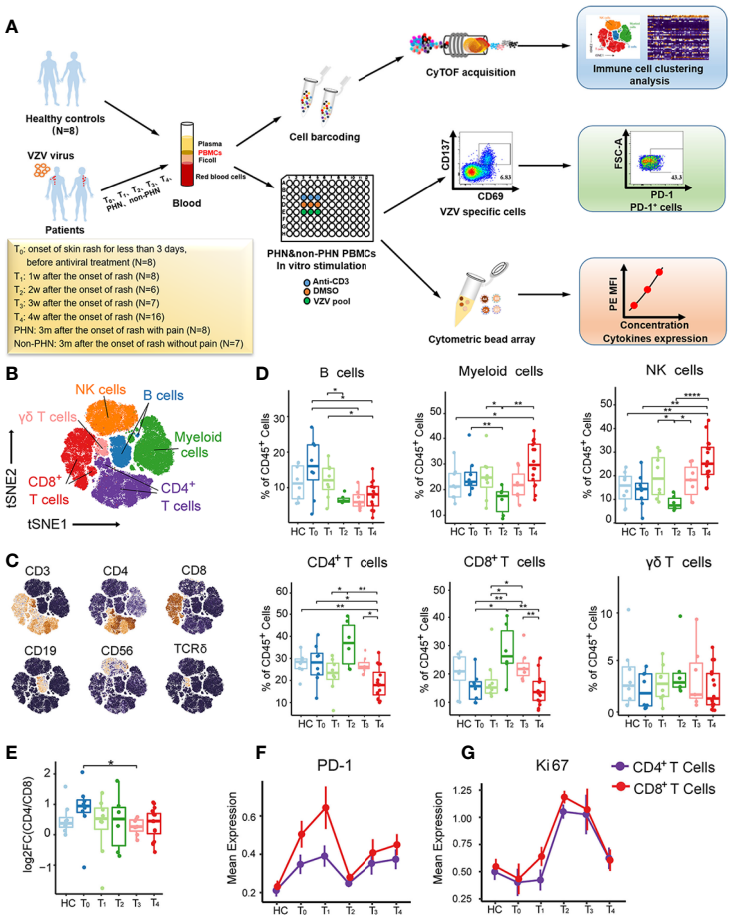

FIGURE 1 | Immune cell profiles of PBMCs from patients with HZ revealed by CyTOF. **(A)** Experimental design of this project. **(B)** t-SNE plot identifying the six major immune cell populations from PBMCs, including $CD4^+$ T cells, $CD8^+$ T cells, γδ T cells, NK cells, B cells, and myeloid cells. **(C)** t-SNE analysis defining the immune cell populations according to the expression of the main surface markers. **(D)** Boxplots demonstrating the frequencies of the six major immune cells in $CD45^+$ cells among healthy controls (HC) and patients with each time point. **(E)** Boxplots showing alteration of CD4/CD8 T cell ratio among HC and patients from T_0 to T_4. **(F, G)** The kinetic features of cell markers with PD-1 **(E)** and Ki67 **(F)** in both $CD4^+$ T cells and $CD8^+$ T cells. *P < 0.05, **P < 0.01, ****P < 0.0001.

530), in accordance with the ethical principles of the Declaration of Helsinki. Written informed consent was obtained from all participants before study entry.

PBMCs Isolation

For PBMCs isolation, whole blood of patients infected with VZV and HC were collected in 10 mL K_2EDTA coated vacutainer tubes (BD Biosciences). PBMCs were isolated by Ficoll-Paque PLUS (GE Healthcare). PBMCs were washed twice using FACS buffer (0.2% BSA in PBS) at 400 g for 10 min, resuspended, and cryopreserved at a density of 5×10^6 cells for storage.

CyTOF Samples Processing, Acquisition and Analysis

All the CyTOF data were collected at PLT Company (Hangzhou, China) following their protocols. Briefly, Mass cytometry antibodies are shown in **Supplementary Table 3**. For each sample, 3×10^6 PBMCs were stained with mass-tagged barcodes for 30 min. After washing, every 10 samples were combined and stained with 1μM Cisplatin (Fluidigm) to distinguish live/dead cells at room temperature for 5 min. After washing, cells were incubated with total mouse and human IgG for blocking for 20 min, followed by cell surface markers staining for 30 min on ice. Subsequently, cells were fixed and permeabilized with paraformaldehyde and labeled with DNA Intercalator-Ir overnight, and then incubated with intracellular antibodies. Finally, cells were washed twice with deionized water and diluted with EQ normalization beads containing ^{140}Ce, ^{151}Eu, ^{153}Eu, ^{165}Ho, and ^{175}Lu (Fluidigm), and the data were acquired by the CyTOF system (Helios, Fluidigm).

A doublet filtering scheme with mass-tagged barcodes was firstly used to debarcode the CyTOF data. Next, the live, singlet, and valid immune cells were obtained *via* manually gating. The data from different batches have been normalized by the bead normalization method. The X-SHIFT (Phenograph) algorithm was used for all samples. CyTOF data was visualized using the t-SNE algorithm, an implemented function in the Rtsne package.

The top 1% was deleted, and the 99th was defined as the maximum intensity to exclude extreme marker intensity. The intensity of all markers was then rescaled between 0 and 1. Heatmap of normalized mean expression of markers was generated by R package pheatmap. Spearman correlation was used to explore the relationships between clusters, and clinical traits and visualized using ggplot2.

Antigen-Specific T Cell Stimulation

Cryopreserved PBMCs were thawed in a complete PRMI 1640 medium containing 10% FBS, 1% penicillin/streptomycin, and 1% L-glutamine at 1×10^7 cells per mL. Three VZV-specific peptide pools (gE, IE62, IE63) (JPT Peptide Technologies, Germany) were mixed together, and PBMCs with 100μL/well were stimulated with 1 μg/mL mixed VZV-specific peptide pools in U-bottom 96-well plate (Jet Bio-Filtration Co., Ltd. China). The same volume of DMSO (Sigma) 1% (vol/vol) was used as a negative Control group and 10 μg/mL purified anti-human CD3ϵ antibody (OKT3, Biolegend) was performed as a positive Control group. After 24 hr stimulation, supernatants were harvested and stored at −80°C for cytokine detection. PBMCs were stained for flow cytometry analysis.

Flow Cytometry

All the antibodies for flow cytometry were purchased from Biolegend unless otherwise stated. After VZV peptide pools stimulation, the cells were stained with live/dead Zombie violet™ Fixable Viability Kit (Biolegend), Pacific Blue™ anti-human CD56 (clone 5.1H11), Pacific Blue™ anti-human CD14 (clone HCD14), Pacific Blue™ anti-human CD19 (clone HIB19), PE/Dazzle™ 594 anti-human CD3ϵ (clone HIT3a), FITC anti-human CD4 (clone A161A1), Percp/Cyanine5.5 anti-human CD8 (clone SK1), APC anti-human CD137 (clone 4B4-1), PE anti-human CD69 (Clone FN50), and APC/Cyanine7 anti-human PD-1 (clone EH12.2H7). After 30 min incubation, samples were washed twice with FACS buffer, resuspended in 300 μL FACS buffer, and then analyzed on a BD FACSFortessa multicolor flow cytometer (BD Biosciences).

Cytometric Bead Array

The cytometric bead array (CBA, BD Biosciences) was performed as per the manual instructions. Briefly, the collected supernatants were incubated with human granzyme B (D7 channel), human IL-2 (A4 channel), human IFN-γ (B8 channel), and human TNF-α (C4 channel) beads for 1hr at room temperature in darkness, followed by 50 μL PE detection reagent for another 1hr. Beads were centrifuged, washed, resuspended with wash buffer, and performed on BD FACSFortessa multicolor flow cytometer (BD Biosciences). The data were analyzed using FCAP array software (BD Biosciences).

ND7/23 Cell Line Culture and Differentiation

DRG neuron-derived ND7/23 cell lines (National Infrastructure of Cell Line Resource, China) were expanded in DMEM medium containing 10% FBS, 1% penicillin/streptomycin, and 1% L-glutamine. The cells were cultured at 1×10^6 cells per mL and passaged every 2 days. When the cells were under logarithmic growth phase, 5000 cells were seeded into a confocal dish (Wuxi NEST Biotechnology Co., Ltd, China) with a medium with 1 mM N6,2'-O-Dibutyryladenosine 3',5'-cyclic monophosphate sodium salt (cAMP, Sigma-Aldrich) and 10 ng/mL recombinant rat β-nerve growth factor (NGF; R&D Systems Inc.) for differentiation. Cells were maintained in differentiation media for 3 days and then performed a further experiment.

Measurement of Cytosolic Ca^{2+}

As previously described by Ma et al. (24), the calcium imaging method was performed. Briefly, the differentiated ND7/23 cells were washed with FACS buffer containing 2 mM $CaCl_2$ for three times and then incubated with 5 μM Fluo-4 AM (Yeasen Biotechnology Co., Ltd, China) for 40 minutes at 37°C. Following this, cells were washed by FACS for another three times and then preserved in 200 μL FACS buffer. Time-lapse images were acquired by Olympus IX83-FV3000-OSR (Olympus Optical Co., Ltd, Tokyo, Japan) with excitation at 488 nm and emission at 500–600 nm. Before the addition of stimulators, seven baseline fluorescence readings were taken, followed by fluorescent readings every second for 300s. The ratio of real-time fluorescence divided by baseline fluorescence (F/F_{base}) was utilized for each well to normalize the Ca^{2+} signals.

Statistical Analysis

All data were expressed as mean ± SEM and analyzed by SPSS 25.0 statistical software (SPSS lnc., Chicago, IL, USA). Data were analyzed by the Kolmogorov-Smirnov test to identify the normal distribution. Non-parametric Wilcoxon test was used for the two groups' comparison. Spearman's correlation analysis was used to identify the clinical correlations. A value of $P < 0.05$ was considered statistically significant (**** $P < 0.0001$, *** $P < 0.001$, ** $P < 0.01$, * $P < 0.05$).

RESULTS

High-Dimensional Immune Cell Profiling of PBMCs From Patients With HZ During Acute Phase

To comprehensively understand the immunological cell profiles of PBMCs in HZ, we performed CyTOF to analyze PBMC samples from 45 patients and eight age-sex-matched HC (**Figure S1A**). The samples were collected from the designated HZ patient cohort at different time points, including the onset of skin rash for less than 3 days (T_0, N = 8), 1 week (T_1, N = 8), 2 weeks (T_2, N = 6), 3 weeks (T_3, N = 7), and 4 weeks (T_4, N = 16) (**Figure 1A**). The detailed sample information and clinical characteristics were listed in **Supplementary Table 1**. To explore the signature of major immune lineages of patients' PBMCs, we clustered $CD45^+$, ProMBP-1^-, and $CD66b^-$ cells to analyze immune cells without granulocytes. We then characterized six major clusters according to the main immune cell markers, including $CD4^+$ T cells, $CD8^+$ T cells, γδ T cells, NK cells, B cells and myeloid cells, as displayed *via* t-distributed

Stochastic Neighbor Embedding (t-SNE) analysis (**Figures 1B, C**, and **S1B**). It is noteworthy that all these clusters presented their specific kinetics at the different time points (**Figure 1D**). Specifically, B cells showed the highest frequency at T_0 while decreasing from T_1 to T_4, whereas myeloid cells and NK cells reached the lowest percentage at T_2, then increased at T_3 and arrived at a peak at T_4. The frequency of γδ T cells stably maintained at low levels during all the acute phases for T cells. $CD4^+$ T cells were firstly upregulated to the peak at T_2, and then gradually downregulated from T_3 to T_4, consistent with the consensus that adaptive immune response usually reaches its maximum two weeks after antigens stimulate T cells. Such a similar kinetic trend was also visualized for $CD8^+$ T cells. In addition, a decreased tendency of CD4/CD8 T cell ratio during the acute phases was observed, indicating a faster proliferation velocity of $CD8^+$ T cells (**Figure 1E**).

Next, we analyzed the dynamic changes of several vital cellular markers of $CD4^+$ and $CD8^+$ T cells (**Figures 1F, G**, and **S1C**). The expression of PD-1 on both subsets presented two peaks at T_1 and T_4 (**Figure 1F**). For Ki67, only one peak at T_2 was detected, indicating the strongest proliferation capacity of $CD4^+$ and $CD8^+$ T cells (**Figure 1G**). This was consistent with their highest frequencies in $CD45^+$ cells at T_2 (**Figure 1D**). Collectivelly, these data emphasize the dynamic fluctuation of six major clusters from PBMCs, especially for $CD4^+$ and $CD8^+$ T cells.

Dynamic Characteristics of Different Immune Subsets

To further characterize the detailed phenotypes of these six major clusters, we analyzed immune cell clusters with 40 cell markers by algorithm X-shift and visualized them in a heatmap (**Figure 2A**). In general, we identified 5 B cell subsets (B01–B05), 10 myeloid cell subsets (M01–M10), 6 NK cell subsets (NK01–NK06), 16 $CD4^+$ T cell subsets (T02–T17), 13 $CD8^+$ T cell subsets (T18–T30), and 4 γδ T cell subsets (T31–T34) (**Figure 2A**, **Supplementary Table 4**). Using principal component analysis (PCA), we revealed that the signature of immune cells at different time points was distinct and manifested a rhythmic change (**Figures 2B, C**). Compared to that in HC, the immune signature of patients gradually increased from T_0 to T_2, but progressively went back from T_3 to T_4, showing a good correlation between the dynamic immune signature and the disease development during acute phases (**Figure 2C**).

Next, we performed the frequencies of all immune cell subsets at each time point from T_0 to T_4 to investigate the specific dynamic features of each phenotype (**Figures 2D, E**, and **S2A**). Among the 6 NK cell subsets, NK02 ($CD56^{low}CD16^+$) frequency only increased at T_4. In contrast, NK05 and NK06 ($CD56^{high}CD16^-$) frequencies reached the peak at T_1 (**Figure 2D**). This phenomenon suggested that the fundamental functions of distinct NK cell subsets varied at different stages. There were also two major dynamic patterns in the case of T cell subsets: quick response pattern and slow response pattern (**Figure 2E**). In a quick response pattern, T cell subsets, such as T13 ($CD25^+FOXP3^+CD45RO^+CD4^+$), T14 ($CD27^{low}CD45RO^+CD4^+$), T15, and T16 ($GranzymeB^+Tbet^+CD45RO^+CD4^+$), T17 ($CD161^+CD45RO^+CD4^+$), T20 ($PD\text{-}1^+CD45RO^+CD8^+$) and T28 ($CD161^+CD45RO^+CD8^+$), responded quickly and reached the highest frequencies at T_2, and then gradually decreased at T_3 and T_4, which was similar to the trend of total $CD4^+$ and $CD8^+$ T cells (**Figure 1D**). In slow response pattern, the frequencies of T cell subsets, such as T02 ($BTLA^+CD27^+CD127^+CD57^{low}CD4^+$), T03 ($CD127^{high}CD45RO^+CD4^+$), T10 ($CD28^+CD45RO^+CD4^+$), T18 ($BTLA^+CD27^+CD127^+CD57^{low}CD8^+$), and T25 ($CD27^{low}CD45RO^{low}CD8^+$), stably maintained at low levels from T_0 to T_3, and only increased at T_4 (**Figure 2E**). Together, these results suggest two major dynamic signatures in NK, $CD4^+$ and $CD8^+$ T subsets in patients with HZ.

Correlations Between Immune Subsets and Clinical Pain-Related Scores

Clinical pain-related scores, including NRS, touch induced NRS, numbness degree, DN4 (Douleur Neuropathique 4 Questions), ID-pain, generalized anxiety disorder (GAD7), patient health questionnaire-9 (PHQ9), the impact of pain on mood, and impact of pain on daily life are important parameters to describe the pain levels of patients with HZ. However, these clinical pain-related scores are highly subjective and lack objective clinical indicators. We wondered whether the immune characteristics in PBMCs could be considered objective biomarkers for pain description and potential targets for future immunotherapy for pain-release. Thus, we analyzed the correlation between clinical pain-related scores and immune subsets by Spearman's correlation (**Figure 3A**). Prior to the correlation analysis, we validated that the clinical parameters significantly increased in patients compared with that in HC, but there was no difference among different time points (**Figure S3A**). This observation hinted the practicability of combining the data at all-time points for clinical parameter-related analysis. B cells and myeloid cells displayed little association with clinical pain-related scores among all the immune clusters. For NK cells, the $CD56^{high}CD16^-$ NK subset (NK05, NK06) positively correlated with clinical pain-related scores, while the $CD56^{low}CD16^+$ NK subset (NK02) presented a negative correlation (**Figure 3A**).

Similar to NK cells, the correlation between clinical pain-related scores and different T cell subsets was also confirmed. Interestingly, we revealed that most T cell subsets with quick response patterns, such as T13, T14, T15, T16, T17, T20, and T28, positively correlated with clinical pain-related scores. However, all T cell subsets with slow response patterns, such as T02, T03, T10, T18, and T25, showed a negative correlation with clinical pain-related scores (**Figures 2E**, **3A**). In addition, at one month after the onset of rash (T_4 time point), some patients still suffered persistent pain, but the others felt relieved (**Supplementary Table 1**). As the frequencies of immune subsets with slow response patterns only increased at T_4, we divided patients at T_4 into pain group and pain-release group and examined the difference between all NK and T cell subsets with slow response patterns in these two groups. We found that T02, T03, T10, T18, and T25 subsets significantly increased in the pain-release group (**Figure 3B**).

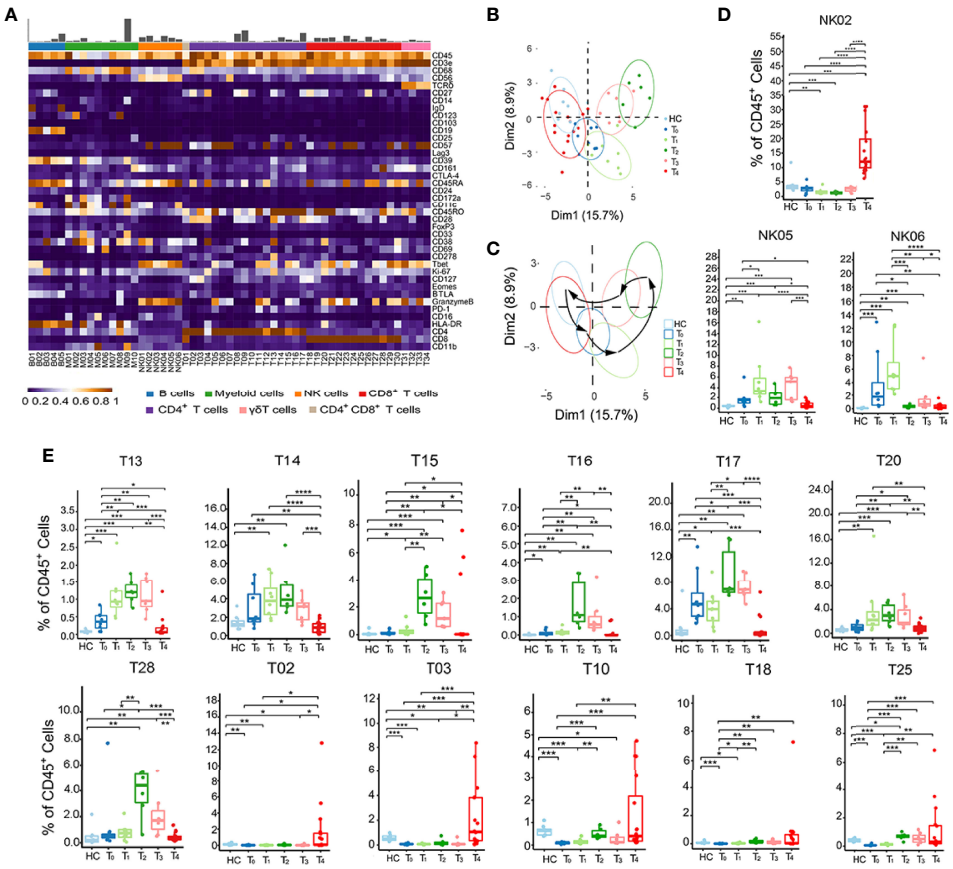

FIGURE 2 | Identification of dynamic signatures of each immune subset. **(A)** Heatmap showing the normalized mean expression of 40 membranous or intracellular markers to identify the phenotypes of the main six immune cell clusters. We characterized five B cell clusters (B01–B05), 10 myeloid cell clusters (M01–M10), six NK cell clusters (NK01–NK06), 16 $CD4^+$ T cell clusters (T02–T17), 13 $CD8^+$ T cell clusters (T18–T30), four γδ T cell clusters (T31–T34). Relative frequency was shown as a bar graph on the top. **(B, C)** Principal component analysis (PCA) showing **(B)** the distinct immune signatures among HC and patients with each time point from T_0 to T_4. **(C)** Black arrows indicate the rhythmic changes with the disease development. **(D, E)** Boxplots revealing the dynamic characteristics and frequencies of different immune cell clusters, NK cells shown in **(D)** and T cells shown in **(E)**. *P < 0.05, **P < 0.01, ***P < 0.001, **** P < 0.0001.

We further analyzed the correlation between each immune subset (**Figure S3B**). T cell subsets with quick response patterns (T13-T17, T28-T32) were positively correlated. Similarly, the slow response pattern of T cell subsets between T02 and T03, T10, T18, subsets between T03 and T10, T18, T25, subsets between T10 and T18, T25 also showed positive correlations (**Figures 3C**, **S3B**). T02 ($BTLA^+CD27^+CD127^+$ $CD57^{low}CD4^+$) and T18 ($BTLA^+CD27^+CD127^+CD57^{low}CD8^+$) were negatively correlated with most of the clinical pain-related scores and positively correlated with each other, indicating the involvement of $BTLA^+CD27^+CD127^+CD57^{low}$ T cells in the pathogenesis patients with HZ (**Figures 2A**, **3A, C**). Further investigations are required to explore the functions of $BTLA^+CD27^+CD127^+CD57^{low}$ T cells in the progression of the acute phase of HZ.

Comparison of the Immune Landscape Between PHN and Non-PHN Patients

A new cohort was set up with 8 PHN samples and 7 non-PHN samples (**Figure 1A**, **Supplementary Table 1**) to investigate the immune signature in PBMCs between non-PHN and PHN groups by CyTOF analysis. The distribution among non-PHN subjects is similar, and so it is in PHN subjects (**Figure S4A**). However, the distribution of different immune cells varied between non-PHN and PHN groups in t-SNE projections (**Figure 4A**). Compared with the non-PHN group, the percentage of $CD4^+$ T cells in the PHN group was significantly decreased, accompanied by a significant increase in myeloid cells (**Figure 4B**). PCA analysis further confirmed the distinct immune signature between the non-PHN and PHN groups (**Figure 4C**). Previous studies showed that patients with PHN had a lower CD4/CD8 T cell ratio than non-PHN patients (11, 23). We observed a similar decrease in CD4/CD8 T cell ratio in PHN but with no significant difference, which the insufficient sample size might cause in each group (**Figure 4D**). Since PD-1 expression was upregulated at the late acute stage of HZ and was indicated as an exhaustion marker (**Figure 1F**). We wondered whether the percentage of PD-1^+ T cells in peripheral blood differed between PHN and non-PHN group. We found that the

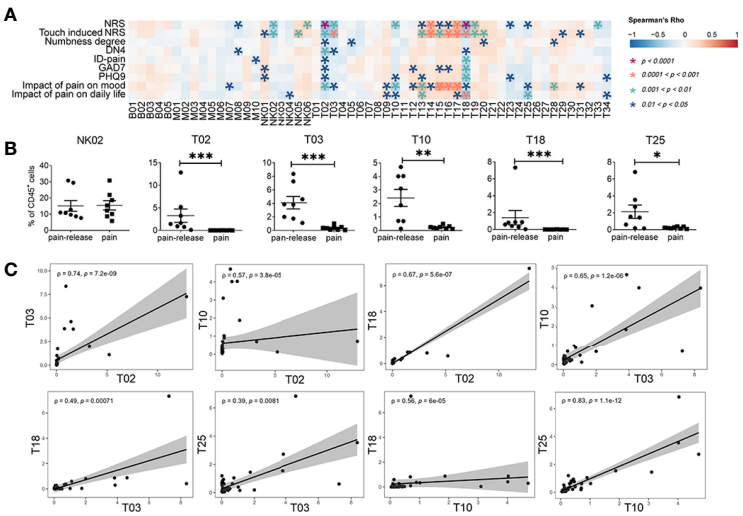

FIGURE 3 | Correlations between immune subsets and clinical pain related scores. **(A)** Spearman's correlation analysis showing the correlations between each immune cluster and clinical pain-related scores. **(B)** The difference in the frequency of different immune subsets with slow response patterns that negatively correlated with clinical pain-related scores (**Figure 2E**) in the pain or the pain-release groups at the T_4 time point. **(C)** The correlation analysis between each immune subset with slow response patterns. *P < 0.05, **P < 0.01, ***P < 0.001.

frequencies of PD-1$^+$CD4$^+$ T cells, but not PD-1$^+$CD8$^+$ T cells, significantly increased in PHN group (**Figure 4E**).

Next, we analyzed the mean expression level of distinct cellular markers on the total CD4$^+$ and CD8$^+$ T cells between the PHN and non-PHN groups. In PHN group, the markers that are related to T cell activation and proliferation (e.g., CD28, Ki67, and IL-7Ra) were significantly declined in both CD4$^+$ and CD8$^+$ T cells compared with that in non-PHN group, suggesting the inefficiency of CD4$^+$ T cells and CD8$^+$ T cells on VZV clearance in patients with PHN (**Figure 4F**). Besides these cellular markers, we also assessed frequencies of different immune cell subsets between the PHN and non-PHN groups (**Figures 4G**, **S4B**). For T cells, compared to the non-PHN group, T13, T17 and T28 subsets were significantly decreased, whereas T05, T06, T11, T22, T24, T25, and T27 subsets were significantly increased in the PHN group (**Figure 4G**). Interestingly, both T17 and T28 were CD161$^+$, indicating the involvement of CD161$^+$ T cells in PHN development (**Figure 2A**). Among other immune cells, M01 and NK05 clusters dramatically decreased in the PHN group (**Figure S4A**). These data might indicate that the signature of αβ T subsets dominated the difference between the PHN and non-PHN groups. Collectively, these data reveal that many T cell subsets of the PHN group are much different from that of the non-PHN group, which might ultimately be one of the reasons for the initiation and progression of PHN.

The Different Characteristics of VZV-Specific T Cells Between PHN and Non-PHN Patients

T cells that are activated by TCR signals can express multiple activation markers, including CD69, CD137, CD154, and OX40, which are used to identify pathogen-specific T cells (25, 26). We used VZV peptide pools to stimulate PBMCs from patients with HZ at different time points after the onset of rash to elucidate the role of VZV-specific T cells play in patients with HZ. VZV-specific T cells were referred as CD69$^+$CD137$^+$, and the gating strategies were displayed in **Figure S5A**. For PBMCs stimulation, three VZV peptide pools (gE, IE62, IE63) were mixed as stimulators, and the anti-human CD3ϵ and DMSO were performed as positive and negative controls, respectively (**Figures 5A**, **S5B**). We identified VZV-specific CD4$^+$ and CD8$^+$ T cells in all patients with HZ using VZV peptide pools compared to DMSO control (**Figures 5B**, **S5C**). Compared with HC, the VZV-specific CD4$^+$ T cells were significantly elevated, which is important for virus clearance (**Figure 5C**). However, no significant increase was found in VZV-specific CD8$^+$ T cells (**Figure S5D**). We revealed the highest frequency of VZV-specific CD4$^+$ T cells at T_3, in accordance with the expression of Ki67 at T_3, suggesting the strongest antiviral response during this time point (**Figures 1F**, **5D**). Although there was no difference for VZV-specific CD8$^+$ T cells, a similar increased tendency was also detected at T_3 (**Figure S5E**). Interestingly, there was no difference between the frequencies of both VZV-specific CD4$^+$ and CD8$^+$ T cells in the PHN and non-PHN groups (**Figures 5D**, **S5E**).

Since a remarkable increase of PD-1$^+$CD4$^+$ T cells in patients with PHN has been identified as previously described (**Figure 4E**), we compared the frequencies of PD-1$^+$ T cells in total CD4$^+$ T cells and VZV-specific CD4$^+$ T cells in non-PHN and PHN groups. Consistent with our CyTOF data, the frequency of both total PD-1$^+$CD4$^+$ T cells and VZV-specific PD-1$^+$CD4$^+$ T cells in the PHN group was higher than that in the non-PHN group (**Figures 5E, F**). In terms of CD8$^+$ T cells, the frequencies of total PD-1$^+$CD8$^+$ T cells and PD-1$^+$ VZV-specific CD8$^+$ T cells were similar in the two groups (**Figures S5F, G**).

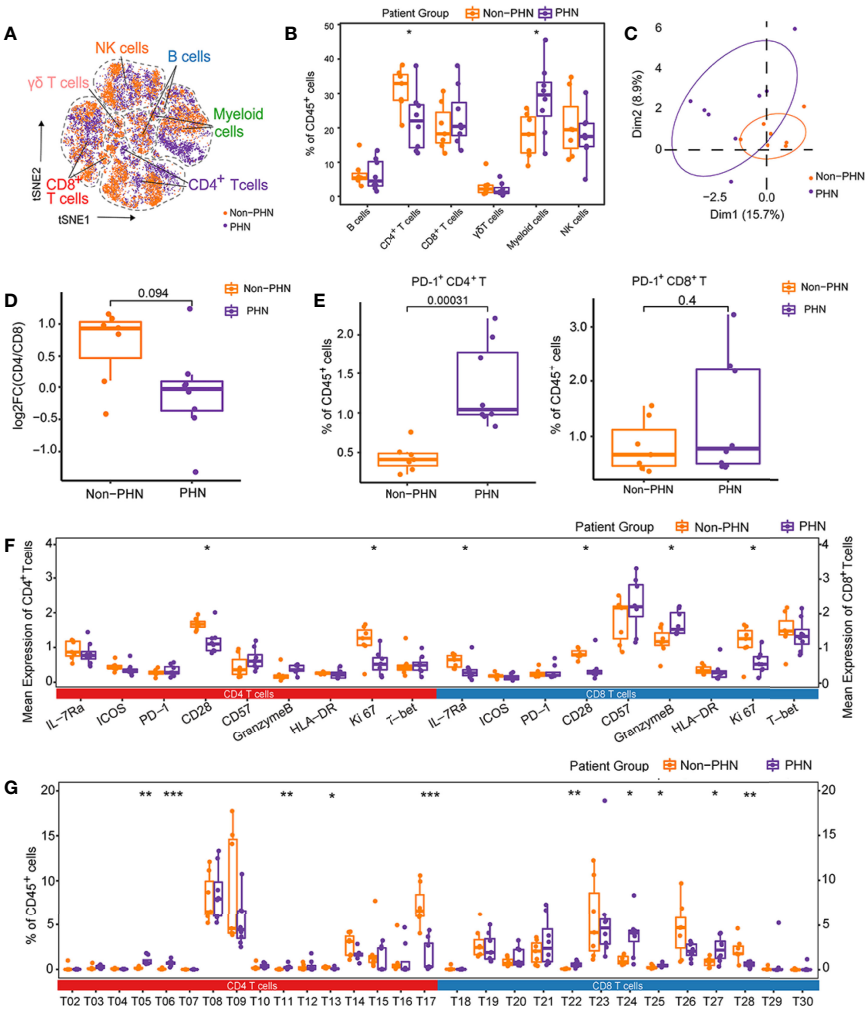

FIGURE 4 | Characteristics of immune landscape of patients with PHN and without PHN. **(A)** t-SNE plots identifying the difference of six main immune cell profiles, as shown in **Figure 1A**, between PHN and non-PHN. **(B)** Boxplots showing the frequencies of indicated clusters in the PHN and non-PHN groups. **(C)** The PCA projections of immune signatures between the PHN and non-PHN groups. **(D)** Boxplots showing the tendency of CD4/CD8 T cells ratio in the PHN group compared with the non-PHN group. **(E)** Boxplots showing the frequencies of PD-1^{+}CD4^{+} T cells and PD-1^{+}CD8^{+} T cells in PHN and non-PHN groups. **(F)** Boxplots displaying the mean expression levels of important cellular markers on CD4^{+} T cells and CD8^{+} T cells in the PHN and non-PHN groups. **(G)** Boxplots exhibiting the frequencies of T cell clusters in the PHN and non-PHN groups. *P < 0.05, **P < 0.01, ***P < 0.001.

To evaluate the function and response of VZV-specific T cells, we further explored the cytokine secretion of PBMCs in the supernatant after stimulation with VZV peptide pools. Among the four cytokines, including TNF-α, IL-2, IFN-γ, and granzyme B, the production of TNF-α was significantly higher in the PHN group than that in the non-PHN group, suggesting the positive effect of TNF-α on PHN progression (**Figures 5G–J**).

TNF-α played an important role in neuropathic pain (27). Calcium influx was one of the indicators for nociceptive responses, such as pain, in dorsal root ganglion (DRG) (28). Since there is no PHN mouse model (29), we visualized the dynamic of Ca^{2+} influx in DRG neuron-derived ND7/23 cells *via* TNF-α stimulation. Compared with the PBS group, the Ca2+ intensity in DRG cells was enhanced after TNF-α stimulation (**Figures 6A–D**), and, more importantly, in a TNF-α dose-dependent manner (**Figure 6E**, **Supplementary video 1–4**). The maximal increased level of Ca^{2+} by 500ng/mL TNF-α stimulation was significantly higher than that by 125ng/mL TNF-α stimulation (**Figure 6F**).

Collectively, our data indicated that VZV-specific CD4^{+} T cells, but not CD8^{+} T cells, dramatically changed in acute stages and were more exhausted in the PHN group. In addition, the observation of higher expression of TNF-α after VZV peptide pool stimulation in PHN than that in non-PHN patients and the subsequent effect on Ca^{2+} influx in DRG-derived cells implies that VZV-specific T cells play a key role in the progression of pain in patients with PHN.

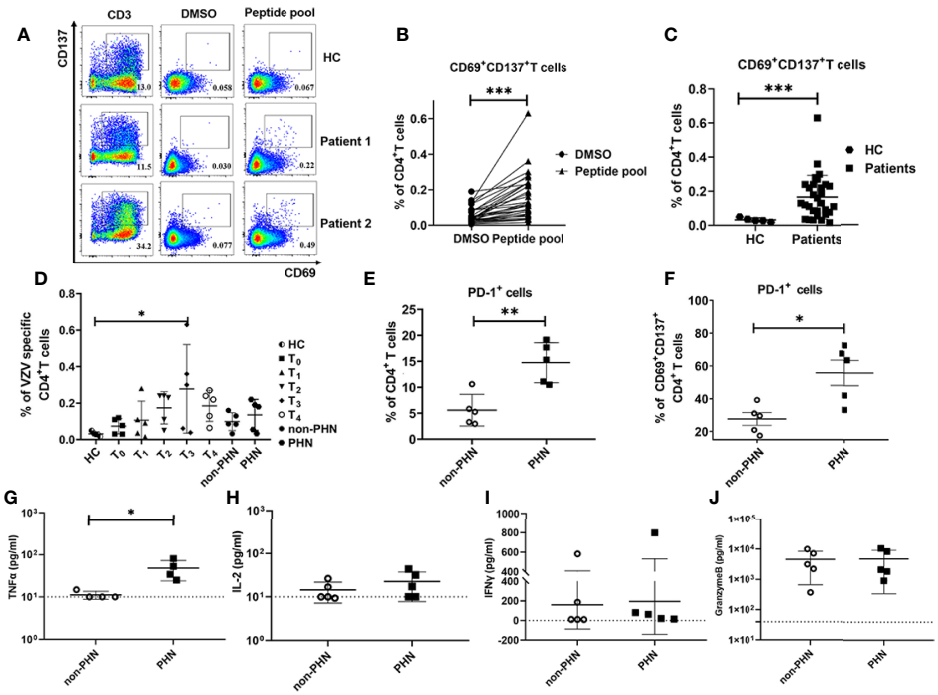

FIGURE 5 | Characteristics of VZV-specific $CD4^+$ T cell response. VZV-specific $CD4^+$ T cells assessed as frequencies of $CD69^+CD137^+CD4^+$ T cells after stimulation of PBMCs by VZV peptide pools (gE, IE62, IE63). **(A)** Examples displaying the Fluorescence-activated cell sorting (FACS) plot, gated on total $CD4^+$ T cells. The anti-human CD3 antibody group and DMSO group were performed as positive control and negative control, respectively. **(B)** Comparison of the frequency of VZV-specific $CD4^+$ T cells in peptide pools or DMSO stimulation. **(C)** Comparison of the frequency of VZV-specific $CD4^+$ T cells in patients and HC. **(D)** The characteristics of dynamics of VZV-specific $CD4^+$ T cells in patients at different time points after the onset of rash. **(E, F)** Frequencies of PD-1^+ cells in total $CD4^+$ T cells **(E)** and VZV-specific $CD4^+$ T cells **(F)** in PHN and non-PHN groups. **(G-J)** Different levels of cytokines in the cultured supernatants of PBMCs with VZV peptide pools stimulation in PHN and non-PHN groups. **(G)**TNF-α, **(H)** IL-2, **(I)** IFN-γ, **(J)** Granzyme B. *P < 0.05, **P < 0.01, ***P < 0.001.

DISCUSSION

In this study, we performed a CyTOF analysis of PBMCs of patients with PHN and HZ in the long-term cohort at six-time points after HZ onset. We further explored the characteristics of VZV-specific T cells by VZV peptide pools stimulation. These data promoted a comprehensive understanding of the immune cell profiles and kinetics and the role of VZV-specific T cells in PHN pathogenesis.

NK cells are important sentinels of the immune system, which function as front-line responders and warn the host of infections. During the early phase of acute inflammation, secondary to an infection, NK cells mainly present regulatory abilities *via* diverse cytokine production upon activation (30). Moreover, the highly proliferative $CD56^{high}CD16^-$ NK cell subset mainly participates in immunomodulatory cytokine production, including IFN-γ, TNF-β, IL-10, IL-13, and GM-CSF (31). We observed that $CD56^{high}CD16^-$ NK cells were the predominant subset of NK cells at T_1 in line with these results. Compared with the $CD16^-$ NK subset, expression of CD16 on NK cells renders strong mediators of antibody-dependent cellular cytotoxicity against IgG coated target cells, because the combination of CD16 and its ligand IgG Fc induces the polarization and degranulation of NK cells (32). The $CD56^{low}CD16^+$ subset, accounting for the majority (~90%), is potently cytotoxic, albeit lowly proliferative (31). In our study, the percentages of the $CD56^{low}CD16^+$ subset increased to the highest level at T_4, indicating the potent cytotoxicity of eliminating VZV-infected cells. We also found that the $CD56^{high}CD16^-$ NK subset positively correlated with pain-related scores, while the $CD56^{low}CD16^+$ NK subset presented a negative correlation. This suggested that the higher frequency of $CD56^{high}CD16^-$ NK cells during the early acute phase indicated the severe VZV infection, and the increasing frequency of $CD56^{low}CD16^+$ NK cells during the late acute phase signified the stronger capacity to obliterate VZV infection.

During HZ, total $CD4^+$ and $CD8^+$ T cells simultaneously reached the highest frequencies with the highest expression of Ki67 at T_2, indicating the strongest antiviral response and proliferation ability of these cells. In addition, a similar trend was observed in T cell subsets with quick response patterns, including T13, T14, T15, T16, T17, T20, and T28. These subsets were memory T cells with $CD45RO^+$ and positively correlated with the pain-related scores. T13, the Tregs ($CD25^+FOXP3^+CD45RO^+CD4^+$), is essential to maintain immune homeostasis *via* governing aggravated and destructive inflammation, exhibiting protective roles in the host during viral infections (33). Investigations have revealed their

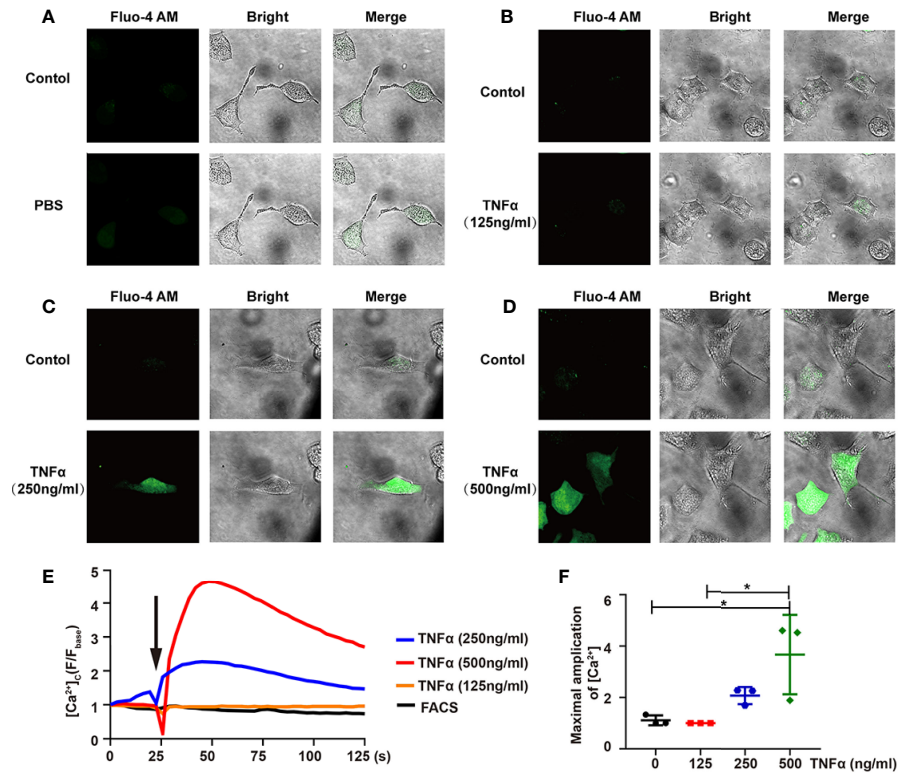

FIGURE 6 | TNF-α induces Ca^{2+} influx in differentiated ND7/23 cells. **(A-D)** The relative intensity of Fluo-4 AM fluorescence - and bright-field images were shown in PBS **(A)**, 125ng/mL TNF-α **(B)**, 250ng/mL TNF-α **(C)**, 500ng/mL TNF-α **(D)**. The Control group indicated the background before adding the stimulator. Images were taken by confocal microscope. **(E)** Confocal microscope analysis of $[Ca^{2+}]$ in ND7/23 cells with PBS and TNF-α stimulation. Arrow indicated cells stimulated by PBS or TNF-α. **(F)** Quantitative analysis of the maximal increased level of cytosolic Ca^{2+} after stimulations. *P < 0.05.

suppressive roles in controlling the antiviral $CD4^+$ and $CD8^+$ T cells in chronic Hepatitis B/C, and HSV-1 infection (34–36). Due to the immune suppression of Tregs, effector T cell-mediated antiviral immune responses are inhibited, thus facilitating viral persistence and disease exacerbation (37).

In contrast to Tregs, T15, and T16 ($Tbet^+CD45RO^+CD4^+$), the typical Th1 effector subsets, mediate immune response against intracellular pathogens and rapidly produce IFN-γ, IL-2, and TNF-α to help control acute infection (38). The higher frequency of these two subsets suggested the severe VZV infection in the early acute HZ phase, leading to the pain-related syndromes. The subsets of T17 and T28 are represented as $CD161^+CD4^+$ and $CD161^+CD8^+$ T cells. It is reported that T cells subsets capable of producing IL-17 are virtually restricted to express CD161 (39, 40). The positive correlation between T17 or T28 and pain-related scores indicated that IL-17 was positively involved in the host immune response related to pain. The T20 ($PD\text{-}1^+CD8^+$) subset presented a transient induction of PD-1 expression on $CD8^+$ T cells in the acute phase. Previous studies have documented that this transient PD-1 upregulation has little influence on early $CD8^+$ T cell activation, expansion, and effector differentiation during acute viral infection (41). Moreover, the transient $PD\text{-}1^+CD8^+$ T cells can exert similar effector molecules, including granzyme B, IFN-γ, TNF-α (41). Coincidentally, the T20 subset was granzyme B positive in our data, which indicated the active antiviral role of T20 in the acute HZ phase.

Compared with the cell subsets with quick response patterns, we noted that several cell subsets with slow response patterns only increased at T_4, such as T02, T03, T10, T18, and T25. In addition, all of these subsets negatively correlated with the pain-related scores and showed increased frequencies in the pain-release group at T_4. Among these subsets, T02 ($BTLA^+CD27^+CD127^+CD57^{low}CD4^+$) and T18 ($BTLA^+CD27^+CD127^+CD57^{low}CD8^+$) subsets showed a significantly positive correlation between each other. BTLA, also known as B and T lymphocyte attenuator, is a co-inhibitory receptor of the CD28 superfamily, which plays an important role in T cell functions *via* binding with its ligand herpesvirus entry mediator (HVEM) (42). Many studies have documented the negative modulation on T cell activation and proliferation in various infectious diseases, such as COVID-19, HBV, and cytomegalovirus (43). In contrast, BTLA can also function as an activating ligand. BTLA expression on αβ T cells is essential for cells to exhibit an active central memory phenotype against *M. tuberculosis* (Mtb) infection with a strong ability to produce IFN-γ and perforin (44). In addition, the BTLA-HVEM

combination in a *cis*-heterodimeric complex can inhibit the activation of the HVEM-dependent NF-κB signaling pathway, and then helps maintain T cells in a naïve state (45). In our study, the negative correlation of $BTLA^+$ αβ T cells with clinical pain-related scores and the significantly elevated frequencies in the pain-release group at T_4 indicated the similarly protective immune response of $BTLA^+$ αβ T cells against VZV infection. Further investigation will be performed to validate this assumption.

T cell exhaustion is reported as a common appearance during persisting infections, such as chronic lymphocytic choriomeningitis virus (LCMV) and HIV (46, 47). The exhausted T cells are characterized by impaired effector functions, sustained expression of multiple inhibitory receptors, especially the typical cellular marker PD-1, and a transcriptional signature that is different from that of functional effector or memory T cells (48). We found a slight increase in PD-1 expression on both $CD4^+$ and $CD8^+$ T cells from T2 to T4 during the acute phase of HZ. In addition, frequencies of PD-1^+CD4^+ T cells in patients with PHN were significantly higher than that in non-PHN patients. The data implied that the severity of the disease, at least partly, correlated with the extent of T cell exhaustion. By stimulating PBMCs with the VZV peptide pools, the expression of PD-1 on $CD69^+CD137^+CD4^+$ T cells was significantly higher in the PHN group than that in the non-PHN group, but the frequency of virus-specific $CD8^+$ T cells was similar in two groups, indicating that virus-specific $CD4^+$ T cells were more exhausted in the PHN group than in the non-PHN group. It has been demonstrated that the blocking axis of PD-1 and PD-1 ligand could reinvigorate virus-specific T cell responses and lead to a lower viral load during chronic LCMV infection (49). Therefore, PD-1 would be a potential target for reversing the dysfunction of exhausted VZV-specific $CD4^+$ T cells to improve the control of VZV infection.

Strikingly, we also identified a significant elevation of TNF-α in the supernatant of PBMCs by VZV peptide pools stimulation in the PHN group. It has been reported that TNF-α is essential for anti-tumoral but not for antiviral response in T cells (50). Therefore, the elevated level of TNF-α in patients with PHN may not benefit VZV clearance but rather pain persistence in patients with PHN. Indeed, TNF-α affected the Ca^{2+} influx of DRG in a dose-dependent manner. These data suggested the active roles of TNF-α in promoting pain symptoms. Wagner et al. has first validated that TNF-α, a well-known immune and pro-inflammatory mediator, exhibits a similar hyperalgesia after the injection into the nerve in 1996 (51). Since then, increasing evidence has put forward the roles of TNF-α in the mechanisms of both peripheral and central neuropathic pain (52, 53). However, we noticed that the concentration of TNF-α in the supernatant after VZV peptide pool stimulation was ~10000 times lower than the concentration of TNF-α for Ca^{2+} influx of DRG-derived cells (**Figures 4G**, **6F**). This difference may be because experiments *in vitro* could not truly reflect situations *in vivo*. We hypothesized that the local concentration of TNF-α surrounding VZV-specific T cells in ganglia was high enough to stimulate DRG neurons. In fact, by analyzing ganglia in cadavers with active shingles before death, the Abendroth group has found that both $CD4^+$ and $CD8^+$ T cells could infiltrate into ganglia and secrete granzyme B (22). Therefore, it is possible that during HZ, the infection of VZV induces T cell-mediated immune response, then these VZV-specific T cells infiltrate into ganglia, stimulated by VZV antigens, and secrete TNF-α to induce pain in patients with PHN. This hypothesis requires to be examined by establishing a new PHN animal model. Regardless, we found TNF-α produced by VZV-specific T cells could be one of the reasons for persistent pain in patients with PHN, and the effective blockade of TNF-α would be a promising treatment in the mediation of pain induced by VZV infection.

In conclusion, we have comprehensively shown the dynamic immune landscape of patients with HZ, and documented two major dynamic features and their close correlation with clinical pain-related scores. We also revealed the enhanced frequencies of total PD-1^+CD4^+, VZV-specific PD-1^+CD4^+ T cells, and TNF-α content in the PHN group. Moreover, TNF-α could induce the Ca^{2+} influx of DRG-derived cells in a dose-dependent manner. Based on these results, we consider that the TNF-α secreted by VZV-specific T cells that function on DRG then induce pain. These findings provide a better understanding of VZV pathogenesis and immunity mechanisms, offering a fundamental basis for exploring new therapies for VZV infection.

DATA AVAILABILITY STATEMENT

The original contributions presented in the study are included in the article/**Supplementary Material**. Further inquiries can be directed to the corresponding authors.

ETHICS STATEMENT

The studies involving human participants were reviewed and approved by the First Affiliated Hospital, School of Medicine, Zhejiang University (NO.2018-530). The patients/participants provided their written informed consent to participate in this study. Written informed consent was obtained from the individual(s) for the publication of any potentially identifiable images or data included in this article.

AUTHOR CONTRIBUTIONS

XZ and ZF designed and supervised the project. QP performed the experiments. XG collected the patient samples and clinical characteristics. YL (3rd author) analyzed the CyTOF data. QP, GW and LZ processed the samples. QP and XZ wrote the manuscript and revised the manuscript. All authors contributed to the article and approved the submitted version.

FUNDING

This work was supported by Zhejiang Provincial Department of Science and Technology (2022C03081 to ZF), the National Natural Science Foundation of China (31870899, 32070899 to XZ, and 82103304 to QP) and the Independent Task of State Key Laboratory for Diagnosis and Treatment of Infectious Diseases (2022zz07 to QP).

SUPPLEMENTARY MATERIAL

The Supplementary Material for this article can be found online at: https://www.frontiersin.org/articles/10.3389/fimmu.2022.887892/full#supplementary-material

Supplementary Figure 1 | Overview of markers expression by CyTOF data analysis (related to **Figure 1**). **(A)** The comparison of age and sex between patients and HC for CyTOF analysis. **(B)** The t-SNE plots of selected markers as shown in **Figure 1B**. **(C)** The dynamic features of mean expression level of cell markers in $CD4^+$ and $CD8^+$ T cells.

Supplementary Figure 2 | Dynamic signatures of immune subsets in HZ patients at different time point after the onset of rash (related to **Figure 2**). **(A)** Boxplots revealing the dynamic characteristics of immune subsets as shown in .

Supplementary Figure 3 | The clinical pain-related scores at different time point and correlation analysis between each immune cluster in HZ patients (related to **Figure 3**). **(A)** Comparisons of clinical pain-related scores, including NRS, Touch induced NRS, Numbness degree, DN4, ID-pain, GAD7, PHQ-9, Impact of pain on mood, and Impact of pain on daily life among HC and patients from T_0 to T_4. **(B)** The correlation analysis among immune subsets identified by CyTOF. The red boxes indicate positive correlation and blue boxes indicate negative correlation.

Supplementary Figure 4 | The immune landscape of PBMCs in PHN and non-PHN patients (related to **Figure 4**). **(A)** the merged tSNE plot of each PHN and non-PHN sample. **(B)** Boxplots exhibiting the frequencies of different phenotypes of B cells, myeloid cells, NK cells, and γδ T cells in PHN and non-PHN groups.

Supplementary Figure 5 | The characteristics of VZV specific $CD8^+$ T cell response (related to **Figure 5**). **(A)** The gating strategy for getting $CD69^+CD137^+CD4^+$ T cells or $CD69^+CD137^+CD8^+$ T cells. Dead cells and pacific blue positive cells are excluded for analysis (details in method). **(B)** Examples displaying the FACS plot, gated on total $CD8^+$ T cells. **(C)** Comparison of frequency of VZV specific $CD8^+$ T cells in peptide pools or DMSO. **(D)** Comparison of frequency of VZV specific $CD8^+$ T cells in patients and HC. **(E)** The characteristics of dynamics of VZV-specific $CD8^+$ T cells in patients at different time point after the onset of rash. **(F, G)** Percentages of PD-1^+ cells in total $CD8^+$ T cells **(F)** and VZV specific $CD8^+$ T cells **(G)** at different time point after the onset of rash.

Supplementary Video 1–4 | (related to **Figure 6**). The changes of Fluo-4 AM signal intensity of ND7/23 cell line with the stimulation by PBS (Video1) and 125ng/mL TNF-α (Video2), 250ng/mL TNF-α (Video3), 500ng/mL TNF-α (Video4). The videos were taken by confocal microscope.

REFERENCES

1. Oliver SL, Zhou M, Arvin AM. Varicella-Zoster Virus: Molecular Controls of Cell Fusion-Dependent Pathogenesis. *Biochem Soc Trans* (2020) 48(6):2415–35. doi: 10.1042/BST20190511
2. Kennedy PGE, Gershon AA. Clinical Features of Varicella-Zoster Virus Infection. *Viruses* (2018) 10(11):609. doi: 10.3390/v10110609
3. Johnson RW, Rice AS. Clinical Practice. Postherpetic Neuralgia. *N Engl J Med* (2014) 371(16):1526–33. doi: 10.1056/NEJMcp1403062
4. Nagel MA, Bubak AN. Varicella Zoster Virus Vasculopathy. *J Infect Dis* (2018) 218(suppl_2):S107–S12. doi: 10.1093/infdis/jiy425
5. Shrestha M, Chen A. Modalities in Managing Postherpetic Neuralgia. *Korean J Pain* (2018) 31(4):235–43. doi: 10.3344/kjp.2018.31.4.235
6. Schmader K. Herpes Zoster. *Ann Intern Med* (2018) 169(3):ITC19–31. doi: 10.7326/AITC201808070
7. Tracey I, Woolf CJ, Andrews NA. Composite Pain Biomarker Signatures for Objective Assessment and Effective Treatment. *Neuron* (2019) 101(5):783–800. doi: 10.1016/j.neuron.2019.02.019
8. Smith SM, Amtmann D, Askew RL, Gewandter JS, Hunsinger M, Jensen MP, et al. Pain Intensity Rating Training: Results From an Exploratory Study of the ACTTION PROTECCT System. *Pain* (2016) 157(5):1056–64. doi: 10.1097/j.pain.0000000000000502
9. Ngo AL, Urits I, Yilmaz M, Fortier L, Anya A, Oh JH, et al. Postherpetic Neuralgia: Current Evidence on the Topical Film-Forming Spray With Bupivacaine Hydrochloride and a Review of Available Treatment Strategies. *Adv Ther* (2020) 37(5):2003–16. doi: 10.1007/s12325-020-01335-9
10. Zerboni L, Sen N, Oliver SL, Arvin AM. Molecular Mechanisms of Varicella Zoster Virus Pathogenesis. *Nat Rev Microbiol* (2014) 12(3):197–210. doi: 10.1038/nrmicro3215
11. Xing Q, Hu D, Shi F, Chen F. Role of Regulatory T Cells in Patients With Acute Herpes Zoster and Relationship to Postherpetic Neuralgia. *Arch Dermatol Res* (2013) 305(8):715–22. doi: 10.1007/s00403-013-1367-0
12. Wang JP, Kurt-Jones EA, Shin OS, Manchak MD, Levin MJ, Finberg RW. Varicella-Zoster Virus Activates Inflammatory Cytokines in Human Monocytes and Macrophages *via* Toll-Like Receptor 2. *J Virol* (2005) 79 (20):12658–66. doi: 10.1128/JVI.79.20.12658-12666.2005
13. Torigo S, Ihara T, Kamiya H. IL-12, IFN-Gamma, and TNF-Alpha Released From Mononuclear Cells Inhibit the Spread of Varicella-Zoster Virus at an Early Stage of Varicella. *Microbiol Immunol* (2000) 44(12):1027–31. doi: 10.1111/j.1348-0421.2000.tb02599.x
14. Arvin AM, Moffat JF, Sommer M, Oliver S, Che X, Vleck S, et al. Varicella-Zoster Virus T Cell Tropism and the Pathogenesis of Skin Infection. *Curr Top Microbiol Immunol* (2010) 342:189–209. doi: 10.1007/82_2010_29
15. Jones D, Como CN, Jing L, Blackmon A, Neff CP, Krueger O, et al. Varicella Zoster Virus Productively Infects Human Peripheral Blood Mononuclear Cells to Modulate Expression of Immunoinhibitory Proteins and Blocking PD-L1 Enhances Virus-Specific CD8+ T Cell Effector Function. *PloS Pathog* (2019) 15(3):e1007650. doi: 10.1371/journal.ppat.1007650
16. Sen N, Mukherjee G, Sen A, Bendall SC, Sung P, Nolan GP, et al. Single-Cell Mass Cytometry Analysis of Human Tonsil T Cell Remodeling by Varicella Zoster Virus. *Cell Rep* (2014) 8(2):633–45. doi: 10.1016/j.celrep.2014.06.024
17. Weinberg A, Zhang JH, Oxman MN, Johnson GR, Hayward AR, Caulfield MJ, et al. Varicella-Zoster Virus-Specific Immune Responses to Herpes Zoster in Elderly Participants in a Trial of a Clinically Effective Zoster Vaccine. *J Infect Dis* (2009) 200(7):1068–77. doi: 10.1086/605611
18. Ouwendijk WJ, Laing KJ, Verjans GM, Koelle DM. T-Cell Immunity to Human Alphaherpesviruses. *Curr Opin Virol* (2013) 3(4):452–60. doi: 10.1016/j.coviro.2013.04.004
19. Kleemann P, Distler E, Wagner EM, Thomas S, Klobuch S, Aue S, et al. Varicella-Zoster Virus Glycoproteins B and E Are Major Targets of CD4+ and CD8+ T Cells Reconstituting During Zoster After Allogeneic Transplantation. *Haematologica* (2012) 97(6):874–82. doi: 10.3324/haematol.2011.052597
20. Laing KJ, Ouwendijk WJD, Koelle DM, Verjans G. Immunobiology of Varicella-Zoster Virus Infection. *J Infect Dis* (2018) 218(suppl_2):S68–74. doi: 10.1093/infdis/jiy403
21. Gowrishankar K, Steain M, Cunningham AL, Rodriguez M, Blumbergs P, Slobedman B, et al. Characterization of the Host Immune Response in Human Ganglia After Herpes Zoster. *J Virol* (2010) 84(17):8861–70. doi: 10.1128/JVI.01020-10
22. Steain M, Sutherland JP, Rodriguez M, Cunningham AL, Slobedman B, Abendroth A. Analysis of T Cell Responses During Active Varicella-Zoster Virus Reactivation in Human Ganglia. *J Virol* (2014) 88(5):2704–16. doi: 10.1128/JVI.03445-13
23. Wei L, Zhao J, Wu W, Zhang Y, Fu X, Chen L, et al. Decreased Absolute Numbers of CD3(+) T Cells and CD8(+) T Cells During Aging in Herpes Zoster Patients. *Sci Rep* (2017) 7(1):15039. doi: 10.1038/s41598-017-15390-w

24. Ma J, Stefanoska D, Grad S, Alini M, Peroglio M. Direct and Intervertebral Disc-Mediated Sensitization of Dorsal Root Ganglion Neurons by Hypoxia and Low Ph. *Neurospine* (2020) 17(1):42–59. doi: 10.14245/ns.2040052.026
25. Watts TH. TNF/TNFR Family Members in Costimulation of T Cell Responses. *Annu Rev Immunol* (2005) 23:23–68. doi: 10.1146/annurev.immunol.23.021704.115839
26. Grifoni A, Weiskopf D, Ramirez SI, Mateus J, Dan JM, Moderbacher CR, et al. Targets of T Cell Responses to SARS-CoV-2 Coronavirus in Humans With COVID-19 Disease and Unexposed Individuals. *Cell* (2020) 181(7):1489–501.e15. doi: 10.1016/j.cell.2020.05.015
27. Leung L, Cahill CM. TNF-Alpha and Neuropathic Pain–A Review. *J Neuroinflamm* (2010) 7:27. doi: 10.1186/1742-2094-7-27
28. Anderson M, Zheng Q, Dong X. Investigation of Pain Mechanisms by Calcium Imaging Approaches. *Neurosci Bull* (2018) 34(1):194–9. doi: 10.1007/s12264-017-0139-9
29. Laemmle L, Goldstein RS, Kinchington PR. Modeling Varicella Zoster Virus Persistence and Reactivation - Closer to Resolving a Perplexing Persistent State. *Front Microbiol* (2019) 10:1634. doi: 10.3389/fmicb.2019.01634
30. Janeway CA Jr, Medzhitov R. Innate Immune Recognition. *Annu Rev Immunol* (2002) 20:197–216. doi: 10.1146/annurev.immunol.20.083001.084359
31. Cooper MA, Fehniger TA, Caligiuri MA. The Biology of Human Natural Killer-Cell Subsets. *Trends Immunol* (2001) 22(11):633–40. doi: 10.1016/s1471-4906(01)02060-9
32. Moretta A, Marcenaro E, Parolini S, Ferlazzo G, Moretta L. NK Cells at the Interface Between Innate and Adaptive Immunity. *Cell Death Differ* (2008) 15 (2):226–33. doi: 10.1038/sj.cdd.4402170
33. Che JW, Kraft AR, Selin LK, Welsh RM. Regulatory T Cells Resist Virus Infection-Induced Apoptosis. *J Virol* (2015) 89(4):2112–20. doi: 10.1128/JVI.02245-14
34. Feng C, Cao LJ, Song HF, Xu P, Chen H, Xu JC, et al. Expression of PD-L1 on CD4+CD25+Foxp3+ Regulatory T Cells of Patients With Chronic HBV Infection and Its Correlation With Clinical Parameters. *Viral Immunol* (2015) 28(8):418–24. doi: 10.1089/vim.2015.0062
35. Cabrera R, Tu Z, Xu Y, Firpi RJ, Rosen HR, Liu C, et al. An Immunomodulatory Role for CD4(+)CD25(+) Regulatory T Lymphocytes in Hepatitis C Virus Infection. *Hepatology* (2004) 40(5):1062–71. doi: 10.1002/hep.20454
36. Yu W, Geng S, Suo Y, Wei X, Cai Q, Wu B, et al. Critical Role of Regulatory T Cells in the Latency and Stress-Induced Reactivation of HSV-1. *Cell Rep* (2018) 25(9):2379–89.e3. doi: 10.1016/j.celrep.2018.10.105
37. Wan Z, Zhou Z, Liu Y, Lai Y, Luo Y, Peng X, et al. Regulatory T Cells and T Helper 17 Cells in Viral Infection. *Scand J Immunol* (2020) 91(5):e12873. doi: 10.1111/sji.12873
38. Ruterbusch M, Pruner KB, Shehata L, Pepper M. *In Vivo* CD4(+) T Cell Differentiation and Function: Revisiting the Th1/Th2 Paradigm. *Annu Rev Immunol* (2020) 38:705–25. doi: 10.1146/annurev-immunol-103019-085803
39. Fergusson JR, Fleming VM, Klenerman P. CD161-Expressing Human T Cells. *Front Immunol* (2011) 2:36. doi: 10.3389/fimmu.2011.00036
40. Maggi L, Santarlasci V, Capone M, Peired A, Frosali F, Crome SQ, et al. CD161 Is a Marker of All Human IL-17-Producing T-Cell Subsets and is Induced by RORC. *Eur J Immunol* (2010) 40(8):2174–81. doi: 10.1002/eji.200940257
41. Kalia V, Yuzefpolskiy Y, Vegaraju A, Xiao H, Baumann F, Jatav S, et al. Metabolic Regulation by PD-1 Signaling Promotes Long-Lived Quiescent CD8 T Cell Memory in Mice. *Sci Transl Med* (2021) 13(615):eaba6006. doi: 10.1126/scitranslmed.aba6006
42. Sedy JR, Gavrieli M, Potter KG, Hurchla MA, Lindsley RC, Hildner K, et al. B and T Lymphocyte Attenuator Regulates T Cell Activation Through Interaction With Herpesvirus Entry Mediator. *Nat Immunol* (2005) 6 (1):90–8. doi: 10.1038/ni1144
43. Ning Z, Liu K, Xiong H. Roles of BTLA in Immunity and Immune Disorders. *Front Immunol* (2021) 12:654960. doi: 10.3389/fimmu.2021.654960
44. Zeng JC, Lin DZ, Yi LL, Liu GB, Zhang H, Wang WD, et al. BTLA Exhibits Immune Memory for αβ T Cells in Patients With Active Pulmonary Tuberculosis. *Am J Transl Res* (2014) 6(5):494–506.
45. Cheung TC, Oborne LM, Steinberg MW, Macauley MG, Fukuyama S, Sanjo H, et al. T Cell Intrinsic Heterodimeric Complexes Between HVEM and BTLA Determine Receptivity to the Surrounding Microenvironment. *J Immunol* (2009) 183(11):7286–96. doi: 10.4049/jimmunol.0902490
46. Crawford A, Angelosanto JM, Kao C, Doering TA, Odorizzi PM, Barnett BE, et al. Molecular and Transcriptional Basis of CD4(+) T Cell Dysfunction During Chronic Infection. *Immunity* (2014) 40(2):289–302. doi: 10.1016/j.immuni.2014.01.005
47. Macatangay BJC, Gandhi RT, Jones RB, McMahon DK, Lalama CM, Bosch RJ, et al. T Cells With High PD-1 Expression are Associated With Lower HIV-Specific Immune Responses Despite Long-Term Antiretroviral Therapy. *AIDS* (2020) 34(1):15–24. doi: 10.1097/QAD.0000000000002406
48. Wherry EJ. T Cell Exhaustion. *Nat Immunol* (2011) 12(6):492–9. doi: 10.1038/ni.2035
49. Utzschneider DT, Gabriel SS, Chisanga D, Gloury R, Gubser PM, Vasanthakumar A, et al. Early Precursor T Cells Establish and Propagate T Cell Exhaustion in Chronic Infection. *Nat Immunol* (2020) 21(10):1256–66. doi: 10.1038/s41590-020-0760-z
50. Calzascia T, Pellegrini M, Hall H, Sabbagh L, Ono N, Elford AR, et al. TNF-Alpha is Critical for Antitumor But Not Antiviral T Cell Immunity in Mice. *J Clin Invest* (2007) 117(12):3833–45. doi: 10.1172/jci32567
51. Wagner R, Myers RR. Endoneurial Injection of TNF-Alpha Produces Neuropathic Pain Behaviors. *Neuroreport* (1996) 7(18):2897–901. doi: 10.1097/00001756-199611250-00018
52. Campbell JN, Meyer RA. Mechanisms of Neuropathic Pain. *Neuron* (2006) 52 (1):77–92. doi: 10.1016/j.neuron.2006.09.021
53. Marchand F, Perretti M, McMahon SB. Role of the Immune System in Chronic Pain. *Nat Rev Neurosci* (2005) 6(7):521–32. doi: 10.1038/nrn1700

Conflict of Interest: A patent application has been submitted based in part on results presented in this manuscript. QP, XG, XZ and ZF are listed as the inventors.

The remaining authors declare that the research was conducted in the absence of any commercial or financial relationships that could be construed as a potential conflict of interest.

Publisher's Note: All claims expressed in this article are solely those of the authors and do not necessarily represent those of their affiliated organizations, or those of the publisher, the editors and the reviewers. Any product that may be evaluated in this article, or claim that may be made by its manufacturer, is not guaranteed or endorsed by the publisher.

frontiers | Frontiers in Immunology

ORIGINAL RESEARCH
published: 08 July 2022
doi: 10.3389/fimmu.2022.874426

A Prospective Study on Risk Factors for Acute Kidney Injury and All-Cause Mortality in Hospitalized COVID-19 Patients From Tehran (Iran)

Zohreh Rostami[1], Giuseppe Mastrangelo[2], Behzad Einollahi[1], Eghlim Nemati[1], Sepehr Shafiee[3], Mehrdad Ebrahimi[1], Mohammad Javanbakht[1], Seyed Hassan Saadat[1], Manouchehr Amini[4], Zahra Einollahi[5], Bentolhoda Beyram[1] and Luca Cegolon[6,7]**

[1] Nephrology and Urology Research Center, Baqiyatallah University of Medical Sciences, Tehran, Iran, [2] Department of Cardiac, Thoracic, Vascular Sciences and Public Health, Padua University, Padua, Italy, [3] School of Medicine, Shahid Beshest University of Medical Sciences, Tehran, Iran, [4] Nephrology Research Center, Shariati Hospital, Tehran University of Medical Sciences, Tehran, Iran, [5] Scholl of Medicine, Tehran University of Medical Sciences, Tehran, Iran, [6] Department of Medical, Surgical and Health Sciences, University of Trieste, Trieste, Italy, [7] Public Health Department, University Health Agency Giuliano-Isontina (ASUGI), Trieste, Italy

Background: Several reports suggested that acute kidney injury (AKI) is a relatively common occurrence in hospitalized COVID-19 patients, but its prevalence is inconsistently reported across different populations. Moreover, it is unknown whether AKI results from a direct infection of the kidney by SARS-CoV-2 or it is a consequence of the physiologic disturbances and therapies used to treat COVID-19. We aimed to estimate the prevalence of AKI since it varies by geographical settings, time periods, and populations studied and to investigate whether clinical information and laboratory findings collected at hospital admission might influence AKI incidence (and mortality) in a particular point in time during hospitalization for COVID-19.

Methods: Herein we conducted a prospective longitudinal study investigating the prevalence of AKI and associated factors in 997 COVID-19 patients admitted to the Baqiyatallah general hospital of Tehran (Iran), collecting both clinical information and several dates (of: birth; hospital admission; AKI onset; ICU admission; hospital discharge; death). In order to examine how the clinical factors influenced AKI incidence and all-cause mortality during hospitalization, survival analysis using the Cox proportional-hazard models was adopted. Two separate multiple Cox regression models were fitted for each outcome (AKI and death).

Results: In this group of hospitalized COVID-19 patients, the prevalence of AKI was 28.5% and the mortality rate was 19.3%. AKI incidence was significantly enhanced by diabetes, hyperkalemia, higher levels of WBC count, and blood urea nitrogen (BUN). COVID-19 patients more likely to die over the course of their hospitalization were those presenting a joint association between ICU admission with either severe COVID-19 or

OPEN ACCESS

Edited by:
Shen-Ying Zhang,
The Rockefeller University,
United States

Reviewed by:
Stefano Candura,
University of Pavia, Italy
Allan Prochazka,
University of Colorado, United States
Caterina Ledda,
University of Catania, Italy
Amirhesam Alirezaei,
Shahid Beheshti University of Medical Sciences, Iran

***Correspondence:**
Luca Cegolon
l.cegolon@gmail.com;
luca.cegolon@units.it
Mohammad Javanbakht
mhmjvbt81@gmail.com

Specialty section:
This article was submitted to Viral Immunology, a section of the journal Frontiers in Immunology

Received: 12 February 2022
Accepted: 08 June 2022
Published: 08 July 2022

Citation:
Rostami Z, Mastrangelo G, Einollahi B, Nemati E, Shafiee S, Ebrahimi M, Javanbakht M, Saadat SH, Amini M, Einollahi Z, Beyram B and Cegolon L (2022) A Prospective Study on Risk Factors for Acute Kidney Injury and All-Cause Mortality in Hospitalized COVID-19 Patients From Tehran (Iran). Front. Immunol. 13:874426. doi: 10.3389/fimmu.2022.874426

even mild/moderate COVID-19, hypokalemia, and higher levels of BUN, WBC, and LDH measured at hospital admission. Diabetes and comorbidities did not increase the mortality risk among these hospitalized COVID-19 patients.

Conclusions: Since the majority of patients developed AKI after ICU referral and 40% of them were admitted to ICU within 2 days since hospital admission, these patients may have been already in critical clinical conditions at admission, despite being affected by a mild/moderate form of COVID-19, suggesting the need of early monitoring of these patients for the onset of eventual systemic complications.

Keywords: acute kidney injury, COVID-19, electrolyte abnormalities, renal failure, SARS-CoV-2

BACKGROUND

SARS-CoV-2 is known for its ability to invade various organs (1). Earlier studies on the impact of COVID-19 focused on the pulmonary system, and dysfunctions of other organs were attributed to hyper-inflammatory response and thrombophilia-inducing multiorgan failure (MOF).

ACE-2 and TMPRSS-2, surface cell proteins expressed by various tissues, are targeted by SARS-CoV-2. In addition to the respiratory system, ACE-2 and TMPRSS-2 are also expressed in the gastrointestinal tract, brain, and vessels (2–5). Furthermore, ACE-2 is highly expressed in renal proximal tubules, where SARS-CoV-2 particles were detected postmortem in podocytes of COVID-19 patients, suggesting that the kidneys could also be one of the targets of SARS-CoV-2 (6, 7). Acute kidney injury (AKI)—a common finding in hospitalized COVID-19 patients—can interfere with the conventional management of COVID-19, resulting in poorer prognosis in terms of higher risk of mortality, intensive care unit (ICU) admission, and prolonged hospitalization (8, 9). It is unknown, however, whether AKI results from a direct infection of the kidney by SARS-CoV-2 or as a consequence of the physiologic disturbances and therapies used to treat the viral disease (10).

Up until November 14, 2021, the cumulative number of COVID-19 infections globally was 3,800,000,000, with a 1%–2% hospitalization rate and a mortality rate of 194.5/100,000 (11). Prevalence of AKI in COVID-19 patients is inconsistently reported, ranging from 0.5% in China (12) to 80% among critically ill COVID-19 patients in France (13, 14). While AKI prevalence among COVID-19 patients was low in initial reports from China, subsequent figures became much higher, suggesting the kidney as one of the main organs targeted by SARS-CoV-2 (15). For instance, in an observational cohort study conducted in a large tertiary care university hospital in Wuhan (China), enrolling all consecutive COVID-19 inpatients older than 65 years during January 2020, the prevalence of AKI was 14% (16). In a meta-analysis on 6,945 COVID-19 patients from China, Italy, the UK, and the USA recruited from 2019 to May 11, 2020, the incidence of AKI was 8.9% [95% CI: 4.6–14.5] (17). Higher AKI figures (46%) were observed among 3,993 COVID-19 patients aged ≥18 years admitted to the Mount Sinai Health System (New York) from February 27 to May 30, 2020 (18), and in another study (rate of 32%) in New York city on a cohort of 5,216 US veterans hospitalized for COVID-19 from February 1, 2020, to July 23, 2020 (16, 19). Likewise, the incidence of AKI on 5.449 COVID-19 patients admitted to 18 university and community hospitals of New York between March 1 and April 5, 2020, was 36.6% (20). Lower AKI figures have been reported in Europe during the first pandemic wave, for instance in a multicenter study on 1,855 admissions for COVID-19 in London hospitals from January 1, 2020, up to May 14, 2020, where 455 patients (a rate of 24.5%) developed AKI (21). Likewise, prevalence of AKI among hospitalized COVID-19 patients was estimated to be 22.4% in an Italian study (22). By contrast, a study from Brazil reported an incidence of AKI of 71% among critically ill COVID-19 patients (23).

In view of the above, we carried out a prospective study on hospitalized COVID-19 patients in Tehran (Iran) with a double aim:

- To estimate the prevalence of AKI, since it varies by geographical settings, time periods, and populations studied; and
- To investigate the risk factors predicting AKI occurrence, assessing their impact on survival of hospitalized COVID-19 patients.

METHODS

This single-center longitudinal prospective study was conducted at Baqiyatallah general hospital in Tehran (Iran), from October 22, 2020, until January 7, 2021, during the third wave of the COVID-19 pandemic (**Figure 1**) (24). The study received approval from the research ethic committee of Baqiyatallah University of Medical Sciences. COVID-19 diagnosis was confirmed by RT-PCR on nasopharyngeal swabs, as per WHO guidelines (25).

Following triage telephone consultations, 5,890 patients with COVID-19 symptoms were referred to Accident & Emergency (A&E) of Baqiyatallah general hospital of Tehran (Iran) from October 22, 2020, until January 7, 2021. Two thousand COVID-19 patients were randomly selected (using a simple random code generator software) among those 3,099 hospitalized for more than 1 day. Patients receiving alternative experimental treatments (N = 110) were excluded since they were part of other clinical trials.

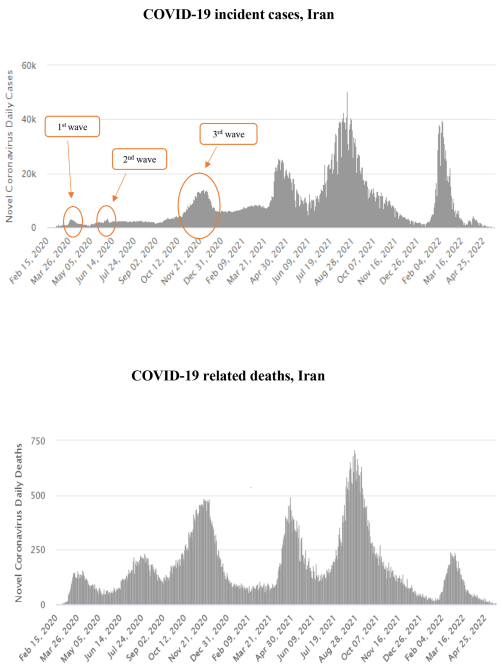

FIGURE 1 | Temporal distribution of COVID-19 incident cases (upper panel) and deaths (lower panel) in Iran, February 2020–April 2022. (24)

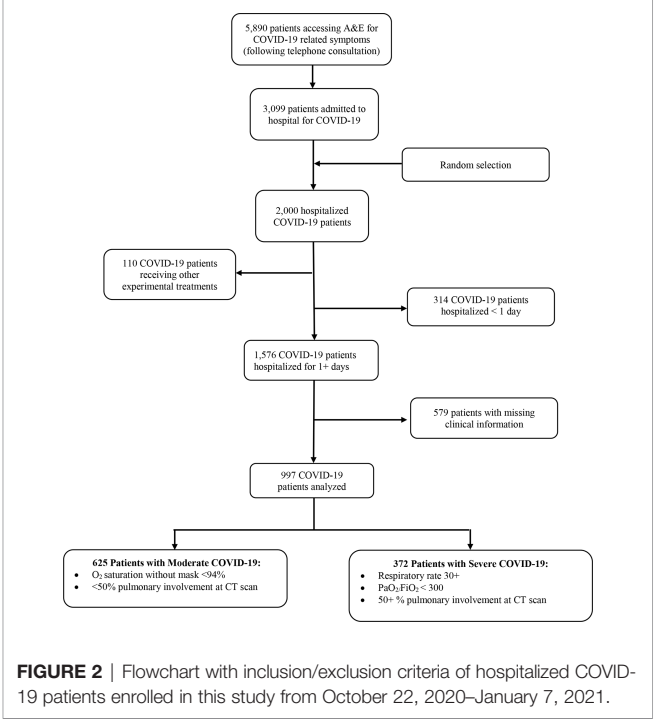

FIGURE 2 | Flowchart with inclusion/exclusion criteria of hospitalized COVID-19 patients enrolled in this study from October 22, 2020–January 7, 2021.

Furthermore, patients with missing data on past medical history and serum creatinine and those with only one documented creatinine measurement were excluded (**Figure 2**). The final number of patients analyzed in this study was 997, broken down into 625 patients affected by mild/moderate COVID-19 and 372 patients with severe disease (**Figure 2**).

Variables

All variables were collected from hospital records (and stratified as follows).

* Oxygen supplement (strata: mask, mask with bag reserve, non-invasive ventilation, intubation);

* Degree of severity of COVID-19.

o Mild COVID-19 (26):

a) Any signs and symptoms of COVID-19 (fever, cough, sore throat, malaise, headache, muscle pain, nausea, vomiting, diarrhea, loss of taste and smell), BUT

b) No shortness of breath, dyspnea, or abnormal chest imaging.

o Moderate COVID-19 (26):

a) ≥94% O_2 saturation without mask, AND

b) <50% lung involvement at imaging.

o Severe COVID-19 (26):

a) SpO_2 <94%; OR

b) Respiratory rate ≥30, OR

c) PaO_2/FiO_2 <300 mmHg; OR

d) Signs of pulmonary involvement at imaging ≥50%.

* Sex (female and male);

* Age (years: mean ± SD; classes: <47; 47–56; 57–65; 66+ years);

* Timeline of AKI onset (days since hospital admission: mean ± SD; classes: <2; 2–3; 4–6; and 7+ days);

* Length of hospital stay (LoS: mean ± SD; classes: <7; 7–9; 10–13; 14+ days);

* ICU admission (no, yes)

* Timeline of ICU (days since hospital admission: mean ± SD; classes: <2; 3–5; 6+ days);

* Mortality (no, yes);

* Comorbidities: diabetes mellitus (no, yes); hypertension (no, yes); ischemic heart disease (IHD: no, yes); chronic heart failure (CHF: no, yes); end-stage liver disease (ESLD: no, yes); chronic obstructive pulmonary disease—interstitial lung disease (COPD-ILD: no, yes); chronic kidney disease (CKD: no, yes if eGFRr <45); [CKD: no, yes if Estimated Glomerular Filtration Rate (eGFR) <45]

* AKI stage (stage 1, stage 2, stage 3).

The International Classification of Diseases (ICD10) was used to evaluate mortality and comorbidities. AKI and stage of renal failure were identified using Kidney Disease: Improving Global Outcomes (KDIGO) guidelines (27) (**Figure 3**).

* eGFR (mL/min/1.73 m^2): mean ± SD. The following formula for modification of diet in renal disease (MDRD) was used to estimate the glomerular filtration rate:

$$\mathbf{eGFR = 186 \times (Cr)^{-1.154} \times (Age)^{-0.203} \times (1.212\ if\ Black) \times (0.742\ if\ Female)}$$

* Electrolyte imbalance: natremia (hypo Na^+ <135 mEq/l; Hyper Na^+ >145 mEq/l); kalemia (Hypo K^+ <3.5 mEq/l; hyper K^+ > 5 mEq/l); magnesemia (hypo Mg^{2+} <1.46 mg/dl; hyper Mg^{2+} >2.68 mg/dl); calcemia (hypo Ca^{2+} <8.8 mg/dl; hyper Ca^{2+} >10.5 mg/dl).

STAGE 1				
Creatinine increase ≥ 0.3 mg/ dl within 48 h	OR	1.5–1.9 Creatinine increase in 7 days, from baseline		
STAGE 2				
2–2.9 fold Creatinine increase over 7 days, from baseline				
STAGE 3				
3+ fold Creatinine increase over 7 days, from baseline	OR	Creatinine ≥ 4 mg/dl in 48 h	OR	Need for renal replacement therapy

FIGURE 3 | Stages of renal failure by kidney disease according to Improving Global Outcomes (KDIGO) guidelines.

* White blood cells, WBC ($\times 10^9$/l): mean ± SD;
* Platelets ($\times 10^9$/l): mean ± SD;
* Hemoglobin (g/dl): mean ± SD;
* Lactate de-hydrogenase, LDH (U/L); mean ± SD;
* Blood creatinine (mg/dL): mean ± SD;
* Blood urea nitrogen (BUN; mg/dL): mean ± SD.

All clinical information but ICU referral was collected at hospital admission. Blood creatinine and BUN were also measured at end of follow-up (hospital discharge or death).

The national guidelines of the Iran Ministry of Health (MoH) and medical education as well as WHO guidelines on management of COVID-19 (26, 28–30) were followed for the hospital management of COVID-19 patients and decision making on ICU admissions.

After the initial admission, all patients were evaluated, monitored, and treated for volume depletion and high blood sugar. All patients were stabilized in A&E department before being transferred to COVID-19 wards and constantly monitored for their hemodynamic status during hospitalization. Treatment of patients was mainly supportive and based on WHO guidelines on COVID-19 patient management at the time of the study. The only non-steroid-anti-inflammatory drug (NSAID) used was naproxen, administered routinely but to patients with low eGFR and with other contradictions. Enoxaparin or heparin was used as anticoagulants. In patients with mild/moderate COVID-19, dexamethasone was administered, whereas in those affected by severe disease methylprednisolone pulse was employed. Antibiotic therapy was administered only in case of secondary bacterial infection.

Treatment drugs were adjusted based upon eGFR and administration of diuretics; ACE inhibitors and angiotensin II receptor blockers were refrained in patients at risk of AKI. Furthermore, remdesivir was not administered in patients with eGFR<30 mg/dl/1.73 m^2, because of its debated nephrotoxicity risk (31).

Statistical Analysis

Distribution of variables by AKI status (yes vs. no) was estimated by chi-squared test in case of categorical terms, whereas ANOVA was employed for comparison of continuous terms by AKI. The distribution of timeline of ICU referral since hospital admission was contrasted by the mean length of hospital stay (LoS, in days), AKI onset (yes vs. no), timeline of AKI onset (days since hospital admission), and vital status at end of follow-up (death or discharge). The mean and median concentration of BUN and blood creatinine were contrasted between hospital admission and end of hospital dischargefollow-up by Wilcoxon test.

This prospective study was conducted over a short period of time collecting both clinical information and several dates (of: birth; hospital admission; AKI onset; ICU admission; hospital discharge; death). In order to examine how the above risk factors influenced mortality risk and AKI incidence during hospitalization in a particular point in time, survival analysis using the Cox proportional-hazard models was adopted. Two separate multiple Cox regression models were fitted for each outcome (AKI and death). The two multivariable models were built up only including variables significant at univariable analysis.

Statistical interaction was modeled by including a product of ICU and severity of COVID-19 in the regression model to evaluate whether COVID-19 severity modified the association between ICU and in-hospital mortality. Similarly, we assessed the interaction between ICU and AKI and between COVID-19 severity and AKI. Results were expressed as hazard ratio (HR) with 95% confidence interval (95% CI). Non-significant terms at multivariable analysis were omitted from the respective tables. The level of significance for each test was set at 0.05. All terms and interactions not being significant were dropped out, and the corresponding results were not shown in the tables.

Statistical analysis was conducted using Stata 14.2 (Stata Corporation, College Station, Texas, USA).

RESULTS

As shown in **Table 1**, 37.3% patients were affected by severe COVID-19, whose average age was 56.6 ± 14.7 years, with 60% (N = 599) of them being males. The mean LoS was 8.8 days, 33% (=330/997) had to be admitted to ICU, and 19% (=192/997) died. AKI was more prevalent in male patients and increased with age and severity of COVID-19 and among those referred to ICU, with a progressively higher prevalence with increasing number of days between hospital admission and ICU referral. The most common comorbidity was diabetes mellitus (49.5% = 493/997) followed by hypertension (31.9% = 318/997), ischemic heart disease and heart

TABLE 1 | Distribution of COVID-19 patients by Acute Kidney Injuries (AKI). Number (N), column percentage (%) and p-value of ANOVA (mean differences) or chi square test (difference in proportions).

FACTORS	STRATA		Total (N=997) N (%)	AKI - N (row %)		p-value
				NO (N=712; 71.5%)	YES (N=285; 28.5%)	
COVID-19	**Mild/Moderate**		625 (62.7)	483 (77.3)	142 (22.7)	<0.001
	Severe		372 (37.3)	229 (61.6)	143 (38.4)	
Oxygen	**Mask**		268 (26.9)	241 (89.9)	27 (10.1)	<0.001
supplement	**Mask with bag reserve**		356 (35.7)	290 (81.6)	66 (18.5)	
	Non-invasive ventilation		141 (14.1)	85 (60.3)	56 (39.7)	
	Intubation		232 (23.4)	96 (41.4)	136 (58.6)	
AKI	**Stage 1**		176 (61.8)	–	176	–
Stage	**Stage 2**		59 (20.7)	–	59	
	Stage 3		50 (17.5)	–	50	
Timeline of	**Mean ± SD**		5.6 ± 3.5	–	–	–
AKI onset	**<2**		46 (16.1)	–	46	–
(days since admission)	**2-3**		55 (19.3)	–	55	
	4-6		96 (33.7)	–	96	
	7+		88 (30.9)	–	88	
LoS	**Mean ± SD**		8.80 ± 4.35	7.84 ± 3.35	11.19 ± 5.52	<0.001
(days)	**<7**		322 (32.3)	270 (83.9)	52 (16.2)	<0.001
	7-9		369 (37.0)	286 (77.5	83 (22.5)	
	10-13		175 (17.6)	109 (62.3)	66 37.7)	
	14+		131 (13.1)	47 (35.9)	84 (64.1)	
Age	**Mean ± SD**		56.6 ± 14.7	55.0 ± 14.7	60.8 ± 13.9	<0.001[a]
(years)	**<47**		246 (24.7)	204 (82.9)	42 (17.1)	<0.001
	47-56		241 (24.2)	181 (75.1)	60 (24.9)	
	57-65		249 (25.0)	166 (66.7)	83 (33.3)	
	66+		261 (26.2)	161 (61.7)	100 (38.3)	
Sex	**Female**		398 (39.9)	308 (77.4)	90 (22.6)	0.001
	Male		599 (60.1)	404 (67.5)	195 (32.6)	
ICU Admission	**No**		667 (66.9)	532 (79.8)	135 (20.2)	<0.001
	Yes		330 (33.1)	180 (54.6)	150 (45.5)	
Timeline of	**Mean ± SD**		3.7 ± 2.5	3.6 ± 2.3	3.9 ± 2.6	0.252
ICU	**<2**		127 (38.5)	73 (57.5)	54 (42.5)	0.277
(days since admission)	**3-5**		120 (36.4)	68 (56.7)	52 (43.3)	
	6+		83 (25.2)	39 (47.0)	44 (53.0)	
Mortality	**No**		805 (80.7)	650 (80.8)	155 (519.3)	<0.001
	yes		192 (19.3)	62 (32.3)	130 (67.7)	
Comorbidities	**Diabetes mellitus**	**No**	504 (50.6)	415 (82.3)	89 (17.7)	<0.001
		Yes	493 (49.5)	297 (60.2)	196 (39.8)	
	Hypertension	**No**	679 (68.1)	529 (77.9)	150 (22.1)	<0.001
		Yes	318 (31.9)	183 (57.6)	135 (42.5)	
	IHD, CHF	**No**	873 (87.6)	642 (73.5)	231 (26.5)	<0.001
		Yes	124 (12.4)	70 (56.5)	54 (43.6)	
	ESLD	**No**	987 (99.0)	706 (71.5)	281 (28.5)	0.422 [b]
		Yes	10 (1.0)	6 (60.0)	4 (40.0)	
	COPD-ILD	**No**	984 (98.7)	703 (71.4)	281 (28.6)	0.861 [b]
		Yes	13 (1.3)	9 69.2)	4 (30.8)	
	CKD (eGFRr<45)	**No**	912 (91.5)	668 (73.3)	244 (26.8)	<0.001
		Yes	85 (8.5)	44 (51.8)	41 (48.2)	
Electrolyte	**Na^+**	**Mean ± SD**	134.91 ± 4.95	135.21 ± 4.69	134.18 ± 5.49	0.004
imbalance	(mEq/L)	<135	435 (44.9)	286 (65.8)	149 (34.3)	<0.001
		135-145	517 (53.4)	396 (76.6)	121 (23.4)	
		>145	16 (1.5)	8 (50.0)	8 (50.0)	
	K^+	**Mean ± SD**	4.17 ± 0.60	4.13 ± 0.53	4.28 ± 0.74	<0.001
	(mEq/L)	<3.5	79 (8.2)	54 (68.4)	25 (31.7)	<0.001
		3.5-5.0	812 (84.0)	598 (73.7)	214 (26.4)	
		> 5	76 (7.9)	36 (47.4)	40 (52.6)	
	Mg^{2+} (md/dL)	**Mean ± SD**	1.89 ± 0.39	1.90 ± 0.36	1.87 ± 0.46	0.370[a]
		<1.7	214 (26.0)	244 (67.4)	118 (32.6)	0.008
		1.7-3	684 (73.4)	444 (73.5)	160 (26.5)	
		>3	5 (0.6)	1 (20.0)	4 (80.0)	
		Mean ± SD	8.81 ± 0.97	8.86 ± 0.92	8.70 ± 1.09	0.080

(Continued)

TABLE 1 | Continued

FACTORS	STRATA		Total (N=997) N (%)	AKI - N (row %)		p-value
				NO (N=712; 71.5%)	YES (N=285; 28.5%)	
	Ca^{2+} (mg/dL)	<8.8	179 (32.2)	117 (63.6)	62 (34.6)	0.047
		8.8-10.5	367 (66.0)	276 (75.2)	91 (24.0)	
		>10.5	10 (1.8)	8 (80.0)	2 (20.0)	
eGFR		**Mean ± SD**	78.35 ± 26.46	79.71 ± 25.49	74.96 ± 28.52	0.010
(ml/min/1.73m^2)		<90	698 (70.0)	248 (24.1)	51 (5.1)	0.934
		90-119	248 (24.9)	175 (70.6)	73 (29.4)	
		120+	51 (5.1)	3 (72.6)	14 (27.5)	
WBC		**Mean ± SD**	8.73 ± 7.19	8.16 ± 6.53	10.15 ± 9.08	<0.001
(× 109/L)		<5.2	238 (23.1)	183 (76.9)	55 (23.1)	<0.001
		5.2-7.1	255 (25.6)	193 (75.7)	62 (24.3)	
		7.2-10.4	253 (25.4)	182 (71.9)	71 (28.1)	
		10.5+	252 (25.2)	154 (61.4)	97 (38.7)	
Platelets		**Mean ± SD**	209.72 ± 93.93	214.25 ± 93.08	198.38 ± 95.26	0.016
(× 109/L)		<147	249 (25.0)	169 (67.9)	80 (32.1)	0.333
		147/190	249 (25.0)	175 (70.3)	74 (29.7)	
		191/260	247 (24.8)	179 (72.5)	68 (275)	
		261+	252 (25.3)	189 (75.0)	63 (25.0)	
LDH		**Mean ± SD**	848.60 ± 619.23	765.63 ± 345.35	1058.57 ± 996.71	<0.001
(U/L)		<564	216 (25.0)	1771 (81.9)	39 (18.1)	<0.001
		564/753	213 (24.6)	166 (77.9)	47 (22.1)	
		754-997	216 (25.0)	150 (69.4)	66 (30.6)	
		978+	220 (25.4)	127 (57.7)	93 (42.3)	
BUN		**Mean ± SD**	19.23 ± 10.51	17.41 ± 9.30	23.80 ± 11.91	<0.001
(mg/dL)		<14	240 (24.1)	211 (87.9)	29 (12.1)	<0.001
		14-15	172 (17.3)	135 (78.5)	37 (21.5)	
		16-20	316 (317)	228 (72.2)	88 (27.9)	
		21+	269 (26.9)	138 (51.3)	131 (48.7)	
Blood Creatinine		**Mean ± SD**	1.14 ± 0.74	1.08 ± 0.74	1.27 ± 0.74	<0.001
(mg/dL)		<0.7	17 (1.7)	15 (88.2)	2 (11.8)	<0.001
		0.7-1.2	749 (75.1)	584 (78.0)	165 (22.0)	
		>1.2	231 (232)	113 (48.9)	118 (51.1)	
Hemoglobin (g/dl)		**Mean ± SD**	13.55 ± 2.10	13.69 ± 1.95	13.21 ± 2.4	0.001

LoS, Length of hospital stay; ICU, Intensive care unit; AKI, Acute kidney injury; IHD, Ischemic heart disease; CHF, Chronic heart failure; CKD, Chronic kidney disease; COPD, chronic obstructive pulmonary disease; ILD, Interstitial lung disease; ESLD, End stage liver disease; WBC, White Blood Cells; LDH, Lactate de-hydrogenase; eGFR, Estimated Glomerular Filtration Rate.

failure (12.4% = 124/997), and chronic kidney disease (8.5% = 85/997). With the exception of COPD and liver disorders, all pre-existing morbidities were significantly higher among patients developing AKI (**Figure 4**). Finally, patients developing AKI were featured by higher levels of BUN, creatinine, WBC, and LDH (**Table 1**).

As is shown in **Table 2**, the majority of patients were referred to ICU within 2 days (N = 127, 38.5%) or 3–5 days (N = 120; 36.4%) since hospital admission, and the increasing timeline between hospitalization and ICU referral translated into longer LoS. Prevalence of AKI was higher among patients affected by a milder form of COVID-19 referred to the ICU within 2 days since hospital admission, whereas among those developing AKI 3+ days since admission to hospital, it progressively increased with days since hospital admission to ICU referral (42.5% for patients admitted <2 days since hospital admission to 53.0% among those referred to the ICU 6+ days since hospital admission). The death rate was 19.3% (=192/997), 67.7% (=130/192) vs. 32.3% (=62/192) among those not developing AKI (**Table 2**). The majority of COVID-19 patients developed AKI after ICU referral, and the death rate also increased with days since hospital admission to ICU referral (**Table 2**).

As is shown in **Table 3**, both BUN and blood creatinine increased considerably more for COVID-19 patients developing AKI, from admission to end of follow-up.

Table 4 displays the results of a multiple Cox regression model on AKI onset among study subjects hospitalized for COVID-19. COVID-19 patients who at hospital admission were affected by diabetes mellitus (HR = 1.72; 95% CI: 1.26; 2.38), hyperkalemia (HR = 1.64; 95% CI: 1.08; 2.48), progressively higher levels of BUN (>14 mg/dl), and WBC count (>5.1 × 10^9/L) were more likely to develop AKI during hospitalization.

Table 5 displays the results of a multivariable Cox regression model for in-hospital mortality. The untoward prognostic risks were found among patients who at admission were affected by hypokalemia (HR = 2.23; 95% CI: 1.32; 3.78), higher levels of BUN (>16 mg/dl), and LDH and increasing WBC count (>7.2 × 10^9/l). At multivariable analysis, ICU admission significantly increased the risk of death from severe COVID-19 (HR = 7.34;

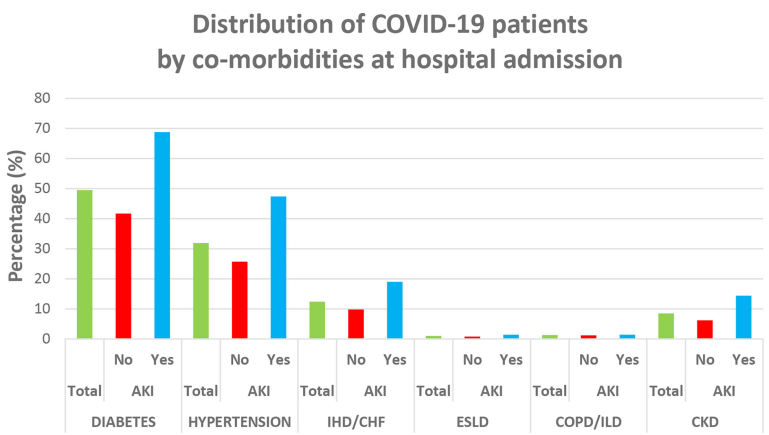

FIGURE 4 | Distribution of comorbidities among COVID-19 patients at hospital admission. IHD, ischemic heart disease; CHF, chronic heart failure; CKD, chronic kidney disease; COPD, chronic obstructive pulmonary disease; ILD, interstitial lung disease; ESLD, end-stage liver disease.

95% CI: 2.41; 22.35) and even more from mild/moderate COVID-19 (HR = 10.14; 95% CI: 3.55; 28.98). No other interactions (between ICU and AKI, and between COVID-19 and AKI) were statistically significant.

DISCUSSION

Key Findings

The prevalence of AKI in the present study was 28.5%, a figure fairly in line with reports from different settings and time periods (32). The risk of AKI increased with diabetes mellitus as well as hyperkalemia, higher WBC count, and increasing level of BUN measured at hospital admission. On the other hand, the overall mortality risk among COVID-19 patients was 19.3%. Factors associated with a higher risk of death were ICU admission for severe COVID-19 as well as for mild/moderate COVID-19, hypokalemia, higher level of BUN, increasing WBC, and increasing LDH measured at hospital admission.

Interpretation of Findings

In a systematic review and meta-analysis on 14,415 COVID-19 patients from different countries, the prevalence of AKI was 11% (95% CI: 0.07–0.15; $p < 0.01$), hence a figure much lower than the present study. Moreover, in the latter meta-analysis AKI was significantly associated with death (OR = 8.45; 95% CI: 5.56–12.56; $p < 0.001$) and severe COVID-19 (OR = 13.52; 95% CI: 5.43–33.67; $p < 0.001$) among hospitalized patients (33). In our prospective study—where a survival analysis by Cox proportional-hazard models was employed to examine risk factors influencing AKI incidence and mortality risk in a particular point in time during hospitalization—although 28.5% COVID-19 patients developed AKI and the crude death rate was higher among patients developing it (67.7%), AKI did not increase the adjusted mortality risk at multivariable analysis, a rather unexpected finding. The majority of COVID-19 patients developed AKI after ICU referral; therefore, the risk of death appeared to rise following ICU admission rather than AKI. Almost 40% patients were referred to the ICU within 2 days since hospital admission, suggesting critical clinical conditions of these patients even with less severe form of COVID-19.

Kidney involvement and AKI onset in COVID-19 patients have multiple risk factors, and several explanatory mechanisms have been proposed (**Figure 5**), including electrolyte imbalance, medication-induced injury, organ failure in late stages of the disease, impairment of gas exchange, hemodynamic alterations including right heart failure, systemic congestion due to fluid overload, and secondary infections/sepsis, among others (32, 34).

AKI is reportedly a frequent pattern in patients dying from COVID-19 (15, 35–38), with acute tubular injury being the most common morpho-pathologic finding in kidney autopsies (37–39). Furthermore, ACE-2 and TMPRSS2 are highly expressed in proximal tubules, where SARS-CoV-2 particles could be detected postmortem in the respective podocytes from COVID-19 patients (40), hinting that the novel coronavirus can directly target the kidneys (7, 10, 34, 41). Experimental and epidemiological studies evidenced that SARS-CoV-2 can infect and damage target renal epithelial cells expressing ACE-2 and TMPRSS2, triggering a cytokine storm (sustained especially by IL-6 and interferon) and directly causing AKI by increasing vascular permeability, shock, and multiorgan failure or aggravating/perpetuating a kidney injury already initiated by non-viral processes (37, 38, 42). Less frequent autoptic findings include micro-angiopathy and collapsing glomerulopathy (40), a frequent cause of proteinuria rapidly progressing to kidney failure (43–45), which predominantly affect patients with homozygous apolipoprotein L1 (APOL-1) high-risk alleles (45–46).

This single-center clinical study was conducted from October 22, 2020, to January 7, 2021, during the third pandemic wave in Iran (**Figure 1**), before large-scale vaccination campaigns against COVID-19 were deployed globally. The massive surge of

TABLE 2 | Distribution of timeline of intensive care unit (ICU) admission, by severity of COVID-19, length of hospital stay (LoS, in days), acute kidney injury (AKI) onset (yes vs. no), and patient outcome (death vs. survival). Number (N), percentages (%), mean (M) ± standard deviation (SD).

ICU admission			LoS (days)	AKI onset Number (row %)					Patient outcome N (row %)			
Timeline (days since hospital admission)	Patients' breakdown	N (%)	M ± SD	No N = 712 (71.5)	Yes N = 285 (28.5)	Before ICU admission (N = 30)	Same day as ICU admission (N = 22)	After ICU admission (N = 98)	Survived		Deceased	
									All patients N = 805 (80.7)	AKI N = 155 (19.3)	All patients N = 192 (19.3)	AKI N = 130 (45.6)
<2	All	127 (38.5)	9.5 ± 5.9	73 (57.5)	54 (42.5)	5 (9.3)	7 (13.0)	42 (77.8)	72 (56.7)	15 (27.8)	55 (43.3)	39 (72.2)
	Mild/moderate COVID-19	47 (37.0)	8.9 ± 4.9	29 (61.7)	18 (30.3)	4 (22.2)	4 (22.2)	10 (55.6)	30 (63.8)	8 (44.4)	17 (36.2)	10 (55.6)
	Severe COVID-19	80 (63.0)	9.8 ± 6.4	44 (55.4)	36 (45.0)	1 (2.8)	3 (8.3)	32 (88.9)	42(52.5)	29 (80.6)	38 (47.5)	7 (19.4)
3–5	All	120 (36.4)	11.0 ± 5.1	68 (56.7)	52 (43.3)	13 (25.0)	7 (13.5)	32 (61.5)	53 (44.2)	6 (11.5)	67 (55.8)	46 (88.5)
	Mild/moderate COVID-19	58 (48.3)	10.6 ± 5.4	37 (65.8)	21 (36.2)	6 (28.6)	3 (14.3)	12 (57.1)	29 (50.0)	4 (19.1)	29 (50.0)	17 (81.0)
	Severe COVID-19	62 (51.7)	11.5 ± 4.9	31 (50.0)	31 (50.0)	7 (22.6)	4 (12.9)	20 (64.5)	24 (38.7)	2 (6.5)	38 (61.3)	29 (93.4)
6+	All	83 (25.2)	13.1 ± 4.7	39 (47.0)	44 (53.0)	12 (27.3)	8 (18.2)	24 (54.6)	27 (32.5)	11 (25.0)	56 (76.5)	13 (75.0)
	Mild/moderate COVID-19	30 (36.1)	13.7 ± 5.2	16 (53.3)	14 (46.7)	1 (7.1)	5 (35.7)	8 (57.1)	12 (40.0)	6 (42.9)	18 (60.0)	8 (57.1)
	Severe COVID-19	53 (63.9)	12.7 ± 4.4	23 (43.4)	30 (56.6)	11 (36.7)	3 (10.0)	16 (53.3)	15 (28.3)	25 (83.3)	38 (71.7)	5 (16.7)

COVID-19 cases did not allow to perform autopsies or biopsies on patients with AKI.

Although SARS-CoV-1 proved capable of infecting kidney cells *in vitro* (47, 48), the evidence supporting persistent infection of the kidney by SARS-CoV-2 is still unconvincing (45). An alternative plausible pathogenetic hypothesis is the "hit and run" model, where the renal injury persists after the clearance of an early direct kidney infection by SARS-CoV-2. However, AKI associated with COVID-19 is probably determined by multiple factors, including an indirect organ damage induced by the physiologic disturbances caused by COVID-19 and the therapies administered to treat the severe acute respiratory syndrome (9, 32, 34, 45). Contrast media, corticosteroids, NSAIDs, ACEs, Angiotensin receptor blockers (ARBs), and various antibiotics are reportedly associated with increased risk of AKI in COVID-19 patients (34, 40), although there is also some evidence that high daily doses (40 mg) of methylprednisolone are associated with increased mortality but lower risk of AKI in COVID-19 patients (49). In a meta-analysis on 23,655 hospitalized, critically ill COVID-19 patients, the incidence of AKI was not significantly different between COVID-19 patients (51%) and critically ill patients infected with ACE2-associated (56%) or non-ACE2-associated viruses (63%). The latter meta-analysis estimated a lower risk of renal replacement therapy in patients affected by COVID-19 or ACE2-associated viruses (featured by a lower risk of shock and use of vasopressors) as compared with patients infected with non-ACE2-binding viruses (50).

As already mentioned, considerable inconsistencies exist regarding the prevalence of AKI in hospitalized COVID-19 patients, with figures widely ranging from 0.5% to 80% (14). Explanatory factors for the inconsistency of the epidemiological evidence on AKI prevalence among COVID-19 patients include ethnicity, genetic polymorphism, type of SARS-CoV-2 variant, the underlying mechanism of kidney injury (either pre-renal, renal, or post-renal), and the methodology employed in various studies (19, 41, 45, 51).

Up until November 14, 2021 (before the spread of the Omicron variant), 56,900,000 cumulative COVID-19 infections were recorded in Iran, where the overall infection/hospitalization rate was 1%–3% and the mortality rate equaled to 277.5/100,000 (11). According to a systematic review and meta-analysis, in Iran the proportion of hospitalized COVID-19 patients developing AKI was 24% (95% CI: 17%–31%), slightly lower than figures from the present study (28.5%) (52). In an earlier study conducted in Iran during February–April 2020, the prevalence of AKI was lower (13.8%) [53]. A lower prevalence of AKI reported from China in the early stages of the COVID-19 pandemic could also be due to underestimation of signs and symptoms not involving the respiratory system (16, 17). Moreover, clinical management of COVID-19 has considerably evolved over time since the early days of the pandemic, and this may account for the inconsistency in AKI figures reported by different studies in diverse periods.

Despite the inconsistencies of prevalence among COVID-19 patients, common risk factors of AKI according to the open literature are advanced age, male gender, and comorbidities such as diabetes mellitus, hypertension, CKD, ischemic heart disease, electrolyte imbalance, and inflammatory markers (22, 23, 32, 36, 41, 54). Likewise, the role of diabetes, electrolyte imbalance, and inflammation in AKI was confirmed in the present study. These factors were already present at hospital admission, reflecting critical clinical conditions of patients entering the hospital independently from the severity of their viral lung disease, thereby supporting the hypothesis that treatment and alterations induced also by mild/moderate forms of COVID-19 may contribute to MOF, including AKI. The enhanced risk of AKI in males may reflect on one side a higher SARS-CoV-2 infection rate in males, on the other side their higher susceptibility to viral infections due to differences in natural immunity linked to sex chromosomes (41). The enhanced expression of ACE2 and TMPRSS2 receptors in males, regulated by androgens, might account for their higher susceptibility to severe COVID-19 (41, 55, 56). In contrast,

TABLE 3 | Variation of blood urea nitrogen (BUN) and blood creatinine from hospital admission to end of follow-up (hospital discharge or death).

CLINICAL PARAMETERS		Patients without AKI				Patients developing AKI			
		Admission	Final	Difference	p-value	Admission	Final	Difference	p-value
BUN	M ± SD	17.41 ± 9.30	19.02 ± 10.62	-1.6 1± 4.49	<0.001	23.8 ± 11.9	40.5 ± 24.2	16.72 ± 21.28	<0.001
(mg/dL)	Median (IQR)	16 (13; 19)	17 (13; 21)	0 (-3; 0)		20 (16; 28)	31 (23; 50)	-10 (24; -4)	
Blood Creatinine	M ± SD	1.08 ± 0.74	1.11 ± 0.76	-0.03 ± 0.16	<0.001	1.27 ± 0.74	2.09 ± 1.53	0.82 ± 1.23	<0.001
(mg/dL)	Median (IQR)	1 (0.9; 1.1)	1 (0.9; 1.1	0 (-0.1; 0)		1 (0.9; 1.4)	1.5 (1.3; 2.2)	-0.4 (-0.9;-0.3)	

MEAN (M) ± standard deviation (SD). Difference, difference between baseline (hospital admission) to end of follow-up (final); Wilcoxon test p-value; IQR, interquartile range (IQR). AKI, acute kidney injury; BUN, blood urea nitrogen.

TABLE 4 | Multiple Cox regression model on the risk of acute kidney injuries (AKI).

Factors	Strata	Univariable analysis HR (95% CI)	Multivariable analysis aHR (95% CI)
Diabetes mellitus	**No**	Reference	Reference
	Yes	1.70 (1.32; 2.19)	1.69 (1.24; 2.33)
Any other comorbidity*	**No**	reference	
	Yes	1.43 (1.13; 1.83)	
Na^+	**<135**	1.36 (1.07; 1.73)	
(mEq/L)	**135–145**	Reference	
	>135	1.56 (0.76; 3.20)	
K^+	**<3.5**	1.25 (0.82; 1.89)	1.16 (0.73; 1.85)
(mEq/L)	**3.5–5**	Reference	Reference
	>5	1.95 (1.39; 2.74)	1.63 (1.08; 2.47)
Mg^{2+}	**<1.7**	0.85 (0.63; 1.15)	
(mg/dL)	**1.7–3.0**	Reference	
	>3.0	3.86 (1.43; 10.47)	
WBC	**<5.2**	Reference	Reference
(× 10^9/L)	**5.2–7.1**	1.45 (1.01; 2.10)	1.53 (1.02; 2.31)
	7.2–10.4	1.42 (1.00; 2.02)	1.43 (0.95; 2.15)
	10.5+	1.80 (1.29; 2.51)	1.52 (1.03; 2.25)
BUN	**<14**	Reference	Reference
(mg/dL)	**14–15**	1.73 (1.06; 2.83)	1.98 (1.12; 3.48)
	16–20	2.33 (1.52; 3.57)	2.44 (1.49; 4.01)
	21+	2.26 (1.49; 3.41)	2.29 (1.43; 3.67)
eGFR	**<90**	0.77 (0.59; 1.00)	
(ml/min/1.73 m^2)	**90–120**	Reference	
	120+	1.41 (0.79; 2.51)	

**Hypertension; ischemic heart disease: chronic heart failure; chronic kidney disease; chronic obstructive pulmonary disease; interstitial lung disease; end-stage liver disease. Hazard ratio unadjusted (HR) and adjusted (aHR) with 95% confidence interval (95%CI). Multiple regression model fitted on 814 complete (case analysis) observations and adjusted for diabetes mellitus, any comorbidity, natremia, kalemia, magnesemia, WBC,white blood cells (WBCs) and blodd urea nitrogen (BUN) at admission.*

estrogen may inhibit the cell invasion of SARS-CoV-2 by reducing the expression of TMPRSS2 (57).

STRENGTHS AND LIMITATIONS

This study has several strengths, including a high number of hospitalized COVID-19 patients and a detailed and thorough collection of clinical variables with a good level of completeness of data, allowing to adjust risk estimates. Furthermore, rather than a cross-sectional design, this study employs a longitudinal approach and it is the first to test the interaction between ICU and severity of COVID-19, thereby disentangling the impact of ICU referral by COVID-19 severity on the mortality risk. Nevertheless, this study was conducted in the midst of the third pandemic wave in Iran, with no capacity to perform postmortem autopsies in AKI patients. Since autopsy and biopsy are essential steps to elucidate the exact mechanism of AKI in COVID-19 patients, future studies should include postmortem examination in COVID-19 patients affected by AKI.

CONCLUSIONS

The prevalence of AKI—a relatively common finding among hospitalized COVID-19 patients—was 28.5% in the present study, and the overall mortality rate was 19.3%. The risk of AKI was associated with diabetes mellitus hyperkalemia, electrolyte imbalance, and inflammation, but not with the severity of COVID-19. However, AKI did not influence the mortality risk, which increased with joint association between

TABLE 5 | Multiple Cox regression model on the risk of death.

Factors	Strata	Univariable analysis HR (95%CI)	Multivariable analysis aHR (95%CI)
Age	**<47**	Reference	
	47–56	1.66 (0.93; 2.97)	
	57–65	2.03 (1.16; 3.56)	
	66+	2.27 (1.32; 3.90)	
AKI	**No**	Reference	
	Yes	1.91 (1.39; 2.63)	
COVID-19	**Mild/Moderate**	Reference	
	Severe	1.72 (1.29; 2.31)	
ICU	**No**	Reference	
admission	**Yes**	10.27 (5.90; 17.87)	
Interaction	**Mild/moderate COVID-19 and no ICU admission**	Reference	Reference
ICU admission	**Severe COVID-19 and no ICU admission**	1.28 (0.43; 3.81)	1.07 (0.25; 4.56)
X	**Mild/moderate COVID-19 and ICU admission**	10.22 (5.05; 20.71)	10.14 (3.55; 28.98)
COVID-19 severity	**Severe COVID-19 and ICU admission**	11.72 (5.89; 23.31)	7.34 (2.41; 22.35)
Diabetes mellitus	**No**	Reference	
	Yes	2.26 (1.62; 3.16)	
Any	**No**	Reference	
comorbidity*	**Yes**	1.81 (1.33; 2.46)	
Na^+	**<145**	1.19 (0.89; 1.61)	
(mEq/L)	**135–145**	Reference	
	>145	2.69 (1.39; 5.19)	
K^+	**<3.5**	2.17 (1.43; 3.30)	2.23 (1.32; 3.78)
(mEq/L)	**3.5–5.0**	Reference	Reference
	>5.0	1.88 (1.22; 2.88)	1.46 (0.80; 2.66)
Mg^{2+}	**<1.7**	0.90 (0.63; 1.29)	
(mg/dL)	**1.7–3**	Reference	
	>3	7.05 (2.57; 19.34)	
Platelets	**<147**	Reference	Reference
(× 10^9/L)	**147/190**	0.67 (0.46; 0.99)	0.80 (0.47; 1.39)
	191/260	0.68 (0.47; 1.00)	0.56 (0.33; 0.94)
	261+	0.84 (0.56; 1.27)	0.70 (0.41; 1.17)
BUN	**<14**	Reference	Reference
(mg/dL)	**14–15**	1.35 (0.70; 2.60)	1.91 (0.86; 4.25)
	16–20	2.55 (1.51; 4.33)	2.31 (1.19; 4.46)
	21+	2.33 (1.40; 3.87)	1.51 (0.78; 2.91)
LDH	**<564**	Reference	Reference
(U/L)	**564/753**	1.03 (0.55; 1.92)	1.44 (0.69; 3.01)
	754–997	1.64 (0.93; 2.89)	1.63 (0.77; 3.48)
	978+	2.59 (1.53; 4.38)	2.53 (1.13; 4.69)
WBC	**<5.2**	Reference	Reference
(× 10^9/L)	**5.2–7.1**	1,34 (0.83; 2.16)	1.75 (0.93; 3.26)
	7.2–10.4	1.53 (0.98; 2.38)	1.88 (1.04; 3.40)
	10.5+	2.30 (1.53; 3.45)	2.51 (1.41; 4.46)

Hazard ratio (HR) with 95% confidence interval (95% CI). Model fitted on 755 complete (case analysis) observations and adjusted for severity of COVID-19, AKI, diabetes, any comorbidity.
**Natremia, kalemia, magnesemia, WBC, platelets, LDH, and BUN at admission.*
**Hypertension; ischemic heart disease: chronic heart failure; chronic kidney disease; chronic obstructive pulmonary disease; interstitial lung disease; end-stage liver disease*
Hazard Ratio unadjusted (HR) and adjusted (aHR) with 95 confidence interval (95%CI). AKI, acute kidney injury; ICU, Intensive care unit; BUN, blood urea nitrogen; LDH, lactate dehydrogenase; WBC, white blood cells.

ICU admission and severe COVID-19 as well as mild/moderate COVID-19, hypokalemia, and higher levels of BUN, WBC, and LDH measured at hospital admission. Diabetes mellitus and comorbidities did not increase the mortality risk among these hospitalized COVID-19 patients. AKI can occur anytime in the course of COVID-19 as a possible complication arising from disturbances and therapies administered to treat even milder forms of the disease. Therefore, considering the crucial importance played by the kidneys in regulating blood pressure and filtering blood from toxic substances, COVID-19 patients should be early monitored for the onset of eventual complications, as they may be already in critical clinical condition at hospital admission.

Future research should focus on biomarkers of tubule damage predicting AKI and whether modulation of ACE2 expression by renin-angiotensin system inhibitors may be beneficial for COVID-19 patients, diminishing the risk of AKI. Finally, since the underlying cause of AKI is invasion of kidney cells by SARS-CoV-2, research should focus on drugs capable of interfering with the binding of SARS-CoV-2 with cell receptors

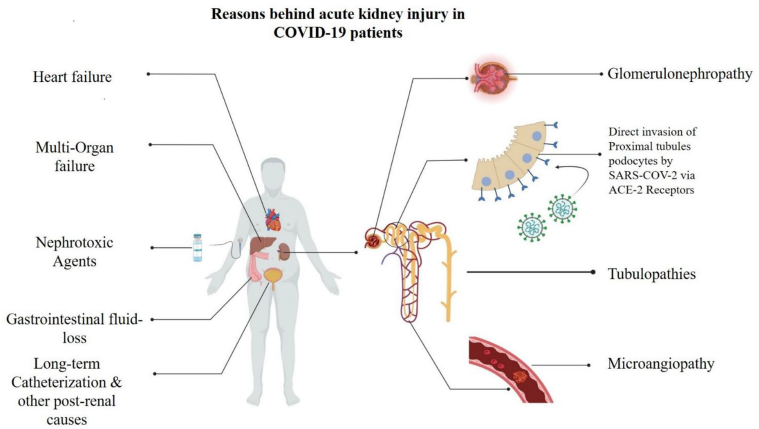

FIGURE 5 | Underlying mechanims contributing to onset of acute kidney injuries (AKI) in COVID-19 patients.

(ACE2 and TMPRSS2), with cell endocytosis of the virus and altering the pH of lysosomes where the virus crosses once inside the cell.

DATA AVAILABILITY STATEMENT

The raw data supporting the conclusions of this article will be made available by the authors, without undue reservation.

ETHICS STATEMENT

The study was approved by the Medical Ethical Committee of Baqiyatallah University of Medical Sciences. Written informed consent for participation was not required for this study in accordance with the national legislation and the institutional requirements.

AUTHOR CONTRIBUTIONS

ZR, BE, EN, SSH, ME, MJ, SHS, MA, ZE, and BHB designed the study etc. designed the study, collected the clinical data and samples, drafted the primary version of the manuscript, and validated the final draft. GM and LC analyzed/interpreted the data and wrote the manuscript. The authors approved the final manuscript.

REFERENCES

1. Kirtipal N, Kumar S, Dubey SK, Dwivedi VD, Babu G, Malý P. Understanding on the possible routes for SARS CoV-2 invasion via ACE2 in the host linked with multiple organs damage.*Genet Evol* (2022) 99:105254
2. Bittmann S, Moschüring-Alieva E, Anne W, Elisabeth L, Gloria V. COVID-19: ACE-2 Receptor, MPRSS2,Cathepsin-L/B and CD-47 Receptor. *J Regen. Biol Med* (2020) 2(3):1–3. doi: 10.37191/Mapsci-2582-385X-2(3)-031
3. Motaghinejad M, Gholami M. Possible Neurological and Mental Outcomes of COVID 19 Infection: A Hypothetical Role of ACE 2\Mas\BDNF Signaling Pathway. *Int J Prev Med* (2020) 11(7):11–84.
4. Shafiee S, Cegolon L, Khafaei M, Gholami N, Zhao S, Khalesi N, et al. Gastrointestinal Cancers, ACE-2/TMPRSS2 Expression and Susceptibility to COVID-19. (2021) 21(1):1–10. doi: 10.1186/s12935-021-02129-x
5. Kihira S, Schefflein J, Mahmoudi K, Rigney B, N. Delman B, Mocco J, et al. Association of Coronavirus Disease (COVID-19) With Large Vessel Occlusion Strokes: A Case-Control Study. *Am J Roentgenol* (2021) 216 (1):150–6. doi: 10.2214/AJR.20.23847
6. Su H, Yang M, Wan C, Yi L-X, Tang F, Zhu H-Y, et al. Renal Histopathological Analysis of 26 Postmortem Findings of Patients With COVID-19 in China. (2020) 98(1):219–27. doi: 10.1016/j.kint.2020.04.003
7. Battle D, Soler MJ, Sparks MA, Hiremath S, South AM, Welling PA, et al. Acute Kidney Injury in COVID-19: Emerging Evidence of a Distinct Pathophysiology. *J Am Soc Nephrol* (2020) 31(7):1380–3. doi: 10.1681/ASN.2020040419
8. Fisher M, Neugarten J, Bellin E, Yunes M, Stahl L, Johns TS, et al. AKI in Hospitalized Patients With and Without COVID-19: A Comparison Study. *J Am Soc Nephrol* (2020) 31(9):2145–57. doi: 10.1681/ASN.2020040509
9. Ronco C, Reis T, Husain-Syed FJTLRM. Management of Acute Kidney Injury in Patients With COVID-19. *Lancet Respir Med* (2020) 8(7):738–42. doi: 10.1016/S2213-2600(20)30229-0
10. Palevsky PM. COVID-19 and AKI: Where Do We Stand? *J Am Soc Nephrol* (2021) 32(5):1029–32. doi: 10.1681/ASN.2020121768
11. COVID-19 Cumulative Infection Collaborators. Estimating Global, Regional, and National Daily and Cumulative Infections With SARS-CoV-2 Through Nov 14, 2021: A Statistical Analysis. *Lancet* (2022) 8;S0140-6736(22)00484-6. doi: 10.1016/S0140-6736(22)00484-6
12. Guan W-j NiZ-y, Hu Y, Liang W-H, Ou C-Q, He J-X, et al. Clinical Characteristics of Coronavirus Disease 2019 in China. *New Engl J Med* (2020) 382:1708–20. doi: 10.1056/NEJMoa2002032
13. Rubin S, Orieux A, Prevel R, Garric A, Bats M-L, Dabernat S, et al. Characterisation of Acute Kidney Injury in Critically Ill Patients With Severe Coronavirus Disease-2019 (COVID-19). *medRxiv* (2020) 13(3):354–61. doi: 10.1101/2020.05.06.20069872
14. Sabaghian T, Kharazmi AB, Ansari A, et al. COVID-19 and Acute Kidney Injury: A Systematic Review. *Front Med (Lausanne)* (2022) 9:705908. doi: 10.3389/fmed.2022.705908
15. Cheng Y, Luo R, Wang K, et al. Kidney Disease is Associated With in-Hospital Death of Patients With COVID-19. *Kidney Int* (2020) 97:829–38. doi: 10.1016/j.kint.2020.03.005

16. Yan Q, Zuo P, Cheng L, Li Y, Song K, Chen Y, et al. Acute Kidney Injury Is Associated With In-Hospital Mortality in Older Patients With COVID-19. *J Gerontol. A Biol Sci Med Sci* (2021) 76(3):456–62. doi: 10.1093/gerona/glaa181
17. Chen YT, Shao SC, Hsu CK, Wu IW, Hung MJ, Chen YC. Incidence of Acute Kidney Injury in COVID-19 Infection: A Systematic Review and Meta-Analysis. *Crit Care* (2020) 24(1):1–4. doi: 10.1186/s13054-020-03009-y
18. Chan L, Chaudhary K, Saha A, Chauhan K, Vaid A, Zhao S, et al. AKI in Hospitalized Patients With COVID-19. *J Am Soc Nephrol* (2021) 32(1):151–60. doi: 10.1681/ASN.2020050615
19. Bowe B, Cai M, Xie Y, Gibson AK, Maddukuri G, Al-Aly Z. Acute Kidney Injury in a National Cohort of Hospitalized US Veterans With COVID-19. *Clin J Am Soc Nephrol* (2020) 16(1):14–25. doi: 10.2215/CJN.09610620
20. Hirsch J, Ng JH, Ross DW, Sharma P, Shah HH, Barnett RL, et al. Acute Kidney Injury in Patients Hospitalized With COVID-19. *Kidney Int* (2020) 98 (1):209–18. doi: 10.1016/j.kint.2020.05.006
21. Wan YI, Bien Z, Apea VJ, Orkin CM, Dhairyawan R, Kirwan CJ, et al. Acute Kidney Injury in COVID-19: Multicentre Prospective Analysis of Registry Data. *Clin Kidney J* (2021) 14(11):2356–64. doi: 10.1093/ckj/sfab071
22. Alfano G, Ferrari A, Fontana F, Mori G, Magistroni R, Meschiari M, et al. Incidence, Risk Factors and Outcome of Acute Kidney Injury (AKI) in Patients With COVID-19. *Clin Exp Nephrol* (2021) 25(11):1203–14. doi: 10.1007/s10157-021-02092-x
23. De Almeida DC, MdCP F, Dos Santos DRP, Santos MC, Maltoni IS, Mascotte F, et al. Acute Kidney Injury: Incidence, Risk Factors, and Outcomes in Severe COVID-19 Patients. *PloS One* (2021) 16(5):e0251048. doi: 10.1371/journal.pone.0251048
24. Worldometer. *Coronavirus Update*. Available at: https://www.worldometers.info/coronavirus/country/iran%20/ (Accessed 10th May 2022).
25. World Health Organization a. *Diagnostic Testing for SARS-CoV-2*. Available at: https://www.who.int/publications/i/item/diagnostic-testing-for-sars-cov-2 (Accessed 14th May 2022).
26. NIH. *Coronavirus Disease 2019 (COVID-19) Treatment Guidelines*. Available at: https://www.covid19treatmentguidelines.nih.gov (Accessed 14th May 2022).
27. Acute Kidney Injury (AKI). *Kidney Disease: Improving Global Outcomes* (2022) Available from: https://kdigo.org/guidelines/acute-kidney-injury/
28. Rahmanzade R, Rahmanzadeh R, Hashemian SM, Tabarsi P. Iran's Approach to COVID-19: Evolving Treatment Protocols and Ongoing Clinical Trials. *Front Public Health* (2020) 8:551889. doi: 10.3389/fpubh.2020.551889
29. World Health Organization b. *Therapeutics and COVID-19: Living Guideliens.* .Available at: https://www.who.int/publications/i/item/WHO-2019-nCoV-therapeutics-2022.3 (Accessed 14th May 2022).
30. Center for Disease Control & Prevention (CDC). *COVID-19 Treatment and Medications*. Available at: https://www.cdc.gov/coronavirus/2019-ncov/your-health/treatments-for-severe-illness.html (Accessed 14th May 2022).
31. Gérard AO, Laurain A, Fresse A, Parassol N, Muzzone M, Rocher F, et al. Remdesivir and Acute Renal Failure: A Potential Safety Signal From Disproportionality Analysis of the WHO Safety Database. *Clin Pharmacol Ther* (2021) 109(4):1021–4. doi: 10.1002/cpt.2145
32. Nadim MK, Forni LG, Mehta RL, Connor JM, Liu KD, Ostermann M, et al. COVID-19-Associated Acute Kidney Injury: Consensus Report of the 25th Acute Disease Quality Initiative (ADQI) Workgroup. *Nat Rev Nephrol* (2020) 16:747–64. doi: 10.1038/s41581-020-00356-5
33. Menon T, Sharma R, Kataria S, Sardar S, Adhikari R, Tousif S, et al. The Association of Acute Kidney Injury With Disease Severity and Mortality in COVID-19: A Systematic Review and Meta-Analysis. *Cureus* (2021) 13(3): e13894. doi: 10.7759/cureus.13894
34. Fanelli V, Fiorentino M, Cantaluppi V, Gesualdo L, Stallone G, Ronco C, et al. Acute Kidney Injury in SARS-CoV-2 Infected Patients. *Crit Care* (2020) 24 (1):1–3. doi: 10.1186/s13054-020-02872-z
35. Pei G, Zhang Z, Peng J, Liu L, Zhang C, Yu C, et al. Renal Involvement and Early Prognosis in Patients With COVID-19 Pneumonia. *J Am Soc Nephrol* (2020) 31:1157–65. doi: 10.1681/ASN.2020030276
36. Arikan H, Ozturk S, Tokgoz B, Dursun B, Seyahi N, Trabulus S, et al. Characteristics and Outcomes of Acute Kidney Injury in Hospitalized COVID-19 Patients: A Multicenter Study by the Turkish Society of Nephrology. *PloS One* (2021) 16(8):e0256023.
37. Faour WH, Choaib A, Issa E. Mechanisms of COVID-19-Induced Kidney Injury and Current Pharmacotherapies. *Inflammation Res* (2022) 71(1):39–56. doi: 10.1007/s00011-021-01520-8
38. Teixeira JP, BArone S, Zahedi K, Soleimani M. Kidney Injury in COVID-19: Epidemiology, Molecular Mechanisms and Potential Therapeutic Targets. *Int J Mol Sci* (2022) 23(4):2242. doi: 10.3390/ijms23042242
39. Smith KD, Akilesh S. Pathogenesis of Coronavirus Disease 2019- Associated Kidney Injury. *Curr Opin Nephrol Hypertens* (2021) 30(3):324–31. doi: 10.1097/MNH.0000000000000708
40. Santoriello D, Khairallah P, Bomback AS, Xu K, Kudose S, Batal I, et al. Postmortem Kidney Pathology Findings in Patients With COVID-19. *J Am Soc Nephrol* (2020) 31:2158–67. doi: 10.1681/ASN.2020050744
41. See YP, Young BE, Ang LW, Ooi XY, Chan CP, Looi WL, et al Risk Factors for Development of Acute Kidney Injury in COVID-19 Patients: A Retrospective Observational Cohort Study. *Nephron*. (2021) 145(3):256–64.
42. He W, Liu X, Hu B, Li D, Chen L, Li Y, et al. Gender and Ethnic Disparities of Acute Kidney Injury in COVID-19 Infected Patients: A Literature Review. *Front Cell Infect Microbiol* (2022) 11:778636. doi: 10.3389/fcimb.2021.778636
43. Minami T, Iwata Y, Wada T. Renal Complications in Coronavirus Disease 2019: A Systematic Review. *Inflamm Regen* (2020) 40(13). doi: 10.1186/s41232-020-00140-9
44. Wu H, Larsen CP, Hernandez-Arroyo CF, Mohamed MMB, Caza T, Sharshir M, et al. AKI and Collapsing Glomerulopathy Associated With COVID-19 and APOL1 High-Risk Genotype. *J Am Soc Nephrol* (2020) 31(8):1688–95. doi: 10.1681/ASN.2020050558
45. Akilesh S, Nast CC, Yamashita M, Henriksen K, Charu V, Troxell ML, et al. Multicenter Clinicopathologic Correlation of Kidney Biopsies Performed in COVID-19 Patients Presenting With Acute Kidney Injury or Proteinuria. *Am J Kidney Dis* (2021) 77:82–93.e1. doi: 10.1053/j.ajkd.2020.10.001
46. Ortega-Paz L, Capodanno D, Montalescot G, Angiolillo DJ. COVID-19 Associated Thrombosis and Coagulopathy: Review of the Pathophysiology and Implications for Antithrombotic Management. *J Am Heart Assoc* (2020) 10:e019650. doi: 10.1161/JAHA.120.019650
47. Niemeyer D, Zillinger T, Muth D, Zielecki F, Horvath G, Suliman T, et al. Middle East Respiratory Syndrome Coronavirus Accessory Protein 4a is a Type I Interferon Antagonist. *J Virol* (2013) 87(22):12489–95. doi: 10.1128/JVI.01845-13
48. Kaye M. SARS-Associated Coronavirus Replication in Cell Lines. *Emerg Infect Dis* (2006) 12(1):128–33. doi: 10.3201/eid1201.050496
49. Kumar G, Patel D, Hererra M, Jefferies D, Sakhuja A, Meersman M, et al. Do High-Dose Corticosteroids Improve Outcomes in Hospitalized COVID-19 Patients? *J Med Virology* (2022) 94(1):372–9. doi: 10.1002/jmv.27357
50. Cau A, Cheng MP, Lee T, Levin A, Lee TC, Vinh DC, et al. Acute Kidney Injury and Renal Replacement Therapy in COVID-19 Versus Other Respiratory Viruses: A Systematic Review and Meta-Analysis. *Can J Kidney Health Dis* (2021) 8:20543581211052185. doi: 10.1177/20543581211052185
51. Darbani B. The Expression and Polymorphism of Entry Machinery for COVID-19 in Human: Juxtaposing Population Groups, Gender, and Different Tissues. *Int J Environ Res Public Health* (2020) 17(10):3433. doi: 10.3390/ijerph17103433
52. Saghafi A, Aghaali M, Saghafi H. Acute Kidney Injury in Hospitalized COVID-19 Patients in Iran; a Systematic Review and Meta-Analysis. *J Renal Inj Prev* (2021) 10(2):e09. doi: 10.34172/jrip.2021.09
53. Mousavi Movahed SM, Akhavizadegan H, Dolatkhani F, Nejadghaderi SA, Aghajani F, Faghir Gangi M, et al. Different Incidences of Acute Kidney Injury (AKI) and Outcomes in COVID-19 Patients With and Without non-Azithromycin Antibiotics: A Retrospective Study. *J Med Virol* (2021) 93 (7):4411–9. doi: 10.1002/jmv.26992
54. Lee JR, Silberzweig J, Akchurin O, Choi ME, Srivatana V, Lin J, et al. Characteristics of Acute Kidney Injury in Hospitalized COVID-19 Patients in an Urban Academic Medical Center. *Clin J Am Soc Nephrol* (2021) 16 (2):284–6. doi: 10.2215/CJN.07440520
55. Mikkonen L, Pihlajamaa P, Sahu B, Zhang FP, Jänne OA. Androgen Receptor and Androgen-Dependent Gene Expression in Lung. *Mol. Cell. Endocrinol* (2010) 317:14–24. doi: 10.1016/j.mce.2009.12.022
56. Sama IE, Ravera A, Santema BT, Van Goor H, Ter Maaten JM, Cleland JGF, et al. Circulating Plasma Concentrations of Angiotensin-Converting Enzyme

2 Inmen and Women With Heart Failure and Effects of Renin-Angiotensin-Aldosterone Inhibitors. *Eur Heart J* (2020) 41:1810–17. doi: 10.1093/eurheartj/ehaa37

57. O'Brien J, Du KY, Peng C. -Incidence, Clinical Features, and Outcomes of COVID-19 in Canada: Impact of Sex and Age. *J of Ovarian Res* (2020) 13:137

Conflict of Interest: The authors declare that the research was conducted in the absence of any commercial or financial relationships that could be construed as a potential conflict of interest.

The reviewer AA declared a shared affiliation with the author SS to the handling editor at the time of review.

Publisher's Note: All claims expressed in this article are solely those of the authors and do not necessarily represent those of their affiliated organizations, or those of the publisher, the editors and the reviewers. Any product that may be evaluated in this article, or claim that may be made by its manufacturer, is not guaranteed or endorsed by the publisher.

frontiers | Frontiers in Immunology

MINI REVIEW
published: 26 July 2022
doi: 10.3389/fimmu.2022.834098

SARS-CoV-2's Variants of Concern: A Brief Characterization

Aline Miranda Scovino[1,2†], Elizabeth Chen Dahab[1,2†], Gustavo Fioravanti Vieira[3], Leonardo Freire-de-Lima[4], Celio Geraldo Freire-de-Lima[4] and Alexandre Morrot[2,5]*

[1] Instituto de Microbiologia Paulo de Goes, Universidade federal do Rio de Janeiro, Rio de Janeiro, Brazil, [2] Instituto Oswaldo Cruz, FIOCRUZ, Rio de Janeiro, Brazil, [3] Universidade La Salle Canoas, Rio Grande de Sul, Brazil, [4] Instituto de Biofísica Carlos Chagas Filho, Universidade Federal do Rio de Janeiro, Rio de Janeiro, Brazil, [5] Faculdade de Medicina, Universidade Federal do Rio de Janeiro, Rio de Janeiro, Brazil

The severe acute respiratory syndrome coronavirus 2 (SARS-CoV-2) disclose the variants of concern (VOC) including Alpha (B.1.1.7), Beta (B.1.351), Gamma (P1), Delta (B.1.617.2), and Omicron (B.1.1.529). Its spike protein (S) present on the surface of the virus is recognized by the host cell receptor, the angiotensin-2 converting enzyme (ACE2) which promotes their entry into the cell. The mutations presented by VOCs are found in RBD and the N-terminal region of S protein. Therefore, mutations occurring in RBD can modify the biological and immunogenic characteristics of the virus, such as modifying the spike affinity for ACE2, increasing the virus transmissibility, or conferring the ability to escape the immune responses. The raise of a potential new SARS-CoV-2 variant capable of evading the host defenses at the same time maintaining its fitness justifies the importance of continued genetic monitoring of the pandemic coronavirus.

Keywords: COVID-19, SARS-CoV-2, COVID-19 vaccination, viral immune escape, SARS-COV-2 variants

OPEN ACCESS

Edited by:
Shen-Ying Zhang, The Rockefeller University, United States

Reviewed by:
Houcemeddine Othman, University of the Witwatersrand, South Africa

***Correspondence:**
Alexandre Morrot
alexandre.morrot@ioc.fiocruz.br

†These authors have contributed equally to this work

Specialty section:
This article was submitted to Viral Immunology, a section of the journal Frontiers in Immunology

Received: *13 December 2021*
Accepted: *13 June 2022*
Published: *26 July 2022*

Citation:
Scovino AM, Dahab EC, Vieira GF, Freire-de-Lima L, Freire-de-Lima CG and Morrot A (2022) SARS-CoV-2's Variants of Concern: A Brief Characterization. Front. Immunol. 13:834098. doi: 10.3389/fimmu.2022.834098

INTRODUCTION

According to the World Health Organization (WHO), in December 31, 2019, the first notification of patients in Wuhan Province, China, presenting an "unknown viral pneumonia" was carried out. In January 9, 2020, the virus was isolated and its genetic sequence was shown to be a "new coronavirus"; two days later, the first death was reported by China. On February 11, 2020, the disease caused by the new coronavirus is officially named COVID-19 (Coronavirus disease 2019) (1).

The clinical symptoms of COVID-19 are fever, fatigue, cough, cardiac injury, breathlessness, sore throat, multi-organ failure, and others manifestations. The worsening of disease is associated with individual risk factors such as age, gender, cardiovascular disease, obesity and other comorbidities (2). Reports from China at the onset of outbreak and from other countries thereafter clearly demonstrated that the majority of patients (81%) have mild symptoms without pneumonia or mild pneumonia. Among patients with more significant symptoms, 14% have severe respiratory distress, and 5% respiratory failure, septic shock and/or multiple organ failure (1, 3).

COVID-19 is caused by the severe acute respiratory syndrome coronavirus 2 (SARS-CoV-2), a betacoronavirus members of the family *Coronaviridae*. SARS-CoV-2 has been characterized as a positive-sense single-stranded RNA. Its spike protein present on the surface of the virus is responsible for its invasion of host cells, being recognized by the angiotensin-2 converting

enzyme (ACE2) in host cells which promotes their cellular entry. The ACE2 receptor is found in several mammalian organs, including lungs, heart, gastrointestinal tract, and kidney. However, the viral entry into the host cell is facilitated *via* proteolytic cleavage of ACE2 mediated by the transmembrane serine protease-2 (TMPRSS2), transforming spike protein into S1 and S2 fragments. The S1 fragment contains the receptor binding domain (RBD), a region of the protein S that binds to ACE2 (4, 5).

The rate at which mutations occur in the SARS-CoV-2 is about 10^{-4} nucleotide substitutions per site per year (6), much less than the rates for influenza virus (7) and HIV (8). However, we have observed a higher mutation rate for SARS-CoV-2 than expected. This is because the transmission rates of this virus are high, infecting a very high number of individuals in the pandemic (9). The more people infected, the greater is the likelihood of mutations appearing. These mutations may then generate viral variants, which may modify the biology of the virus, and impact of disease.

Since the beginning of the pandemic some variants has appeared and continue occurring. The World Health Organization in collaboration with partners, expert networks, national authorities, institutions and researchers have been monitoring and assessing the evolution of SARS-CoV-2 since January 2020. This informal group named Technical Advisory Group on Virus Evolution (TAG-VE), supports a larger WHO-coordinated global risk monitoring and assessment framework for SARS-CoV-2 variants, which include other WHO advisory groups, such as the Expert Advisory Group on COVID-19 Vaccine Composition (TAG-CO-VAC), the Strategic Advisory Group of Experts on Immunization (SAGE), and the Strategic and Technical Advisory Group for Infectious Hazards (STAG-IH) (9).

The TAG-VE shall have up to 30 members, these have experience in virology, bioinformatics, epidemiology, laboratory sciences, pharmacology, clinical management, or in one or several diagnostic, therapeutic and/or vaccine products. In the selection of the TAG-VE Members, consideration shall be given to attaining an adequate distribution of technical expertise, geographical representation and gender balance (9). The group periodically monitors the appearance of new mutations and their impacts on the biology of the virus, evaluating the emergence of variants, their transmissibility, disease severity, diagnosis and treatment, in an attempt to contain the spread of these new potential variants. According to their clinical impact on the pandemic, they are classified as either interest or concern variants (10, 11).

Variants of interest are defined as those with genetic changes that are predicted or known to affect virus characteristics such as transmissibility, disease severity, host immune escape, diagnostic or therapeutic resistance. They are identified to cause significant community transmission or multiple COVID-19 clusters, in multiple countries with an increasing relative prevalence alongside the number of new cases over time, or other apparent epidemiological impacts to suggest an emerging risk for global public health, as it happened for the Lambda variant (10).

The variants of concern, besides having all the characteristics of the variants of interest, can show a sort of different characteristics including increased rates in transmissibility or detrimental change in COVID-19 epidemiology; increased virulence or change in clinical disease symptoms; decrease in the effectiveness of public health and social measures or available diagnostics, vaccines, therapeutics. The major viral mutants identified to date exhibiting one or more of these characteristics (**Table 1**) are named Alpha (B.1.1.7), Beta (B.1.351), Gamma (P1), Delta (B.1.617.2) and Omicron (B.1.1.529) variants (10).

ALPHA VARIANT

The Alpha variant (B.1.1.7) was dominant in the United Kingdom in early 2021 (**Figure 1**), containing several deletions

TABLE 1 | Variants and spike mutations, including specific RBD mutations. The most important RBD positions that interacts with ACE2 are E484, S494, N501, K417, L452 (12–14).

Variants	Deletions	Mutation S1+S2	RBD mutations	Earliest Documented in
Alpha (B.1.1.7)	ΔH69, ΔV70, ΔY144	N501Y, A570D, D614G, E484K, T716I, S982A, P681H, D1118H	E484K, S494P, N501Y	United Kingdon (10, 15)
Beta (B.1.351)	Δ241/4, Δ242, Δ243	N501Y, A701V, D614G, E84K, D215G, K417N, and D80A	K417N, E484K, N501Y	South Africa (10, 16)
Gamma (P1)		N501Y, L18F, D614G, E484K, T1027I, K417T, D138Y, R190S, H655Y, P26S, T20N	K417N, E484K, N501Y	Brazil (10, 17, 18)
Delta (B.1.617.2)	Δ156, Δ157	T478K, L452R, D614G, G142D, D950N, T19R, P681R, R158G, E484Q	L452R, E484Q	India (10, 19)
Omicron (B.1.1.529)	ΔH69-V70, Δ143-145, Δ211-212	A67V, T95I, G142D, G339D, S371L, S373P, S375F, K417N, N440K, G446S, S477N, T478K, E484A, Q493K, G496S, Q498R, N501Y, Y505H, T547K, D614G, H655Y, N679K, P681H, N764K, D796Y, N856K, Q954H, N969K, L981F	K417N, E484A, N501Y	South Africa (10, 20)

Variants and spike mutations, inlcuding specific RBD mutations. The most important RBD positions that interacts with ACE2 are E484, S494, N501, K417, L452 and the countries each of the variants have been initially reported.

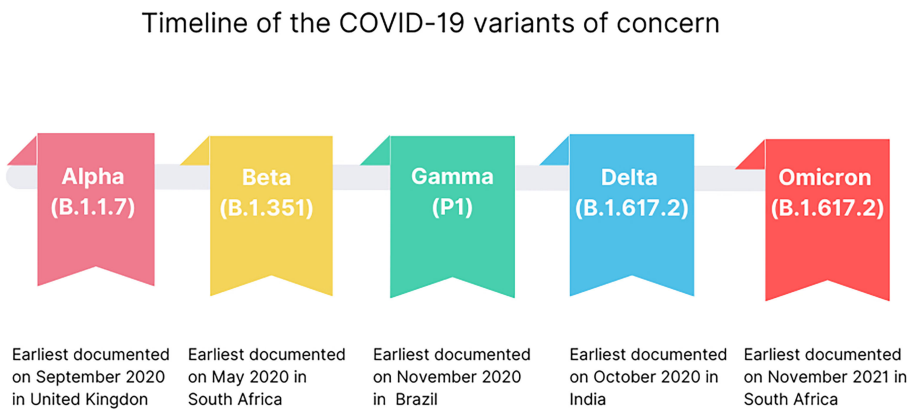

FIGURE 1 | Time line emergence of COVID-19 VOCs.

and mutations in its spike protein (**Figure 2**) such as N501Y, A570D, ΔH69/ΔV70, ΔY144, P681H, T716I, S982A, and D1118H. The N501Y substitution, common to the other variants, seems to be associated with greater transmissibility, as it has a greater affinity for ACE2. After the first identification of B1.1.7 phylogeny, an E484K mutation in the protein S was identified (15). This replacement, as well as the N501Y appears to increase the spike affinity to ACE2, being related to resistance to antibody neutralization targeting the original epitope (21). N501Y mutation slowed the dissociation of the RBD from the ACE2 receptor, resulting in a fourfold greater affinity than wild-type RBD (22).

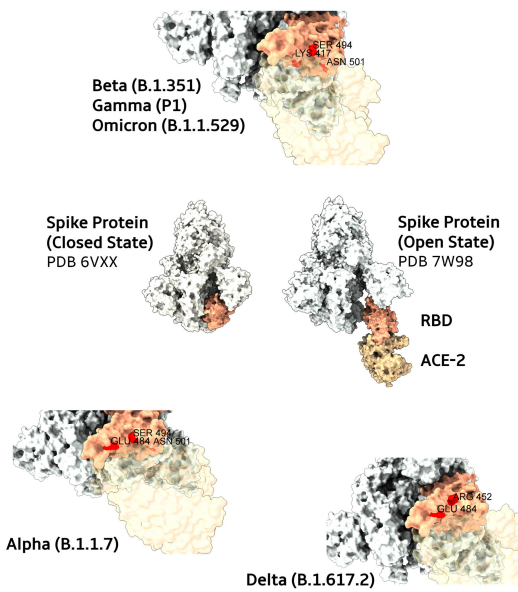

FIGURE 2 | Main mutations present in SARS-CoV-2 Spike protein variants. In the center, structures from Spike proteins (colored in ivory) in their closed and open states (complexed with ACE2, in light brown). The RBD domain is highlighted in salmon. Closes from the ACE2 interaction interfaces of RBD domains are depicted for Beta, Gamma, and Omicron (top), Alpha (bottom left), and Delta (bottom right) variants. Mutated residues are colored in red with their respective name and positions. To improve the visualization of variants mutated regions, transparency was applied to ACE2 protein surfaces.

In vitro studies with serum from patients vaccinated with BNT162b2 or ChAdOx1 has demonstrated that mutation in the spike protein reduce the antibody neutralization of B.1.1.7 variant as compared to the original virus (23, 24). However, other studies show little or no difference in the neutralization antibody capacity of the plasma of vaccinated individuals against the B.1.1.7 variant compared to the original strains (25–27).

In Qatar, the BNT162b2 vaccine effectiveness was estimated with a test-negative case–control study design. This study showed that the effectiveness of this vaccine against the alpha variant was 89.5% to develop the disease and 97.4% against severe and fatal cases of the disease (28).

In Brazil, the effectiveness of ChAdOx1 and CoronaVac/Sinovac was evaluated in two outbreaks of the alpha variant, in a convent and a Long Term Care Facility for the elderly. They observed that vaccination did not prevent people from becoming infected, but there was a reduction in the number of deaths, symptoms and severe cases of the disease, even in this population whose average age was around 77 years, with 1 dose of ChAdOx1 or two from CoronaVac/Sinovac (29).

In UK, a group evaluated a cohort that had already participated in the ChAdOx1 vaccine efficacy trials. These participants received booster doses, according to the vaccination protocol, and periodically provided upper airway swabs on a weekly basis and also if they developed symptoms of COVID-19 disease. In this work, they showed that although the neutralization assays with the plasma of these individuals showed a reduction in neutralization against this variant, the clinical data show an efficacy of the ChAdOx1 vaccine of approximately 70% against the symptomatic cases. This indicates that either a low neutralization rate is already sufficient for protection, there may be complement activation and elimination of infected cells, antibody-

dependent NK cell activation, macrophage opsonization, or other immunological mechanisms such as induction of T cells specific for spike (30).

BETA VARIANT

The Beta variant (B.1.351) was identified in South Africa, appearing after the first wave of the epidemic, becoming prevalent in three provinces (the Eastern Cape, Western Cape and KwaZulu–Natal), during the second wave (**Figure 1**). The Beta variant has eight mutations in the spike (**Figure 2**), three of which are known and common to other variants, such as K417N, E484K and N501Y substitutions, affecting key sites of RBD associated with escape of neutralizing antibodies (31). It is not known whether this combination confers a greater affinity to the host invasion ACE2 receptors. In addition to RBD, the N-terminal domain (NTD) of spike is a target site for antibody neutralization, as mutations in this region show substantial or complete escape from neutralizing antibodies (16).

Recently, a group using a live-virus neutralization assay has compared the neutralization of a non-variant of concern to Beta variant, using plasma collected from adults who were hospitalized with COVID-19 during the two waves of infection in South Africa. The results showed that the Beta variant was efficiently neutralized by plasma from infected individuals in the second wave, but there was a decrease, around 15 times, in the neutralization efficiency when plasma collected from infected individuals who was diagnosed in the first COVID-19 wave (32).

Studies on the effectiveness of available vaccines against the strains of concern found the Oxford-AstraZeneca vaccine with only 10% protection against mild-to-moderate disease associated to Beta variant in young populations with an average median age about 30 in South Africa (33). In contrast, Johnson & Johnson's vaccine showed 64% protection against moderate-to-severe clinical forms of disease (34). The Pfizer/BioNTech was reported to be less effective against Beta variant than other variants based on a small analysis of breakthrough infections in Israel (35). However, a test-negative case–control study design carried out in Qatar showed that the effectiveness of this vaccine against the beta variant was 75%, and against severe and fatal cases, the effectiveness was 97.4% (28).

DELTA VARIANT

The Delta variant, Lineage B.1.617, was first identified in India in the Maharasha city (**Figure 1**), and was shown to have the highest transmissibility, when compared to the Alpha (B.1.1.7), Beta (B.1.351), and Gamma (P.1) variants. People infected with this variant have a viral load about 1,000 times greater than people infected with the wild strain virus (SARS-CoV-2 WT), in addition to its higher replicating rate. This explains why this variant is so transmissible, and why it became the dominant variant worldwide, until the emergence of the Omicron variant (19).

The Delta variant belongs to the B.1 strain, which contains a mutation in the spike protein (D614G) that already exists in the alpha and beta variants, indicating that it can increase the affinity of the Spike protein for the host ACE2 receptors (36, 37). The B.1.617 contains 3 sub lineages identified as B.1.617, B.1.617.2, and B.1.617.3, with B.1.617.2 being the most transmissible in humans. The B.1.617 has also many other mutations inside the lineage. In the spike protein (**Figure 2**), mutations are found in RBD (L452R and T478K), NTD (R158G, T19R, G142D, Δ156-157), S2 region (D950N), and a mutation at the site close to furin cleavage. These mutations may increase the efficiency of replication as well as the regulation of S protein, thus reducing the chances of being recognized by neutralizing antibodies (36).

Recent studies has tested the efficacy of Pfizer/BioNTech and Oxford-AstraZeneca vaccines to Delta variants, showing reduced sensitivity of SARS-CoV-2 variant Delta to antibody neutralization (36, 38). However, a test-negative case–control study design carried out in Israel showed that the effectiveness of these vaccines after the complete vaccine program was similar to the efficacy of clinical trials (39).

In China, due to a public policy of zero tolerance, in 2020 practically all cases of COVID-19 were imported, with almost no internal transmission of the virus. In this way, the immunity of the Chinese population is practically all induced by the vaccine formulations used in the country, which allows a good assessment of the effectiveness of vaccines, in the isolated outbreaks that occurred in 2021 as a result of cases of the Delta variant. This work evaluated the efficacy of two attenuated virus vaccines, CoronaVac/Sinovac and BBIBP-CorV vaccine, as well as an adenovirus vector vaccine, Cansino's Ad5 vaccine, against this variant in this 2021 outbreak, which occurred near Yunnan province. They used a retrospective cohort design among close contacts of infected individuals to determine vaccine effectiveness. They observed that the two inactivated virus vaccines were 74.6% effective against symptomatic COVID-19, and 100% against severe cases of the disease. The same was observed for the adenovirus vector vaccine (40).

A meta-analysis study corroborates these results. This article brought together five papers on vaccine effectiveness from Pfizer/BioNTech, three from Oxford-AstraZeneca and one from CoronaVac/Sinovac. Overall, the three vaccines were effective after the two doses, the Pfizer/BioNTech had approximately 83% of effectiveness after the second dose, and 97% after the third dose. For Oxford-AstraZeneca the effectiveness was approximately 80%, and for CoronaVac/Sinovac approximately 65% after the second dose, and 63% after the third dose. For severe forms of the disease, vaccine effectiveness was approximately 98% for Pfizer/BioNTech, 91% for Oxford-AstraZeneca and 75% for CoronaVac/Sinovac (41).

GAMMA VARIANT

The Gamma variant was detected in Japan in travelers arriving from Brazil in January 2021 (17) (**Figure 1**). By April it had

already been worldwide spread in 36 countries, with local transmission occurring in five, including Brazil. This variant differs from the original Wuhan strain presenting twelve mutations in the spike (**Figure 2**), including N501Y, K417T and E484K (18). Despite having an accumulation of three different mutations, it seems that this variant has replication potential similar to the original strain, and is likewise neutralized with serum from individuals vaccinated with the Pfizer/BioNTec vaccine (18).

The Gamma strain has also been linked to reinfection cases in Manaus, Brazil, suggesting its efficiency to circumvent the acquired immune response from other previous strain infections. This may explain the rapid spread of the Gamma variant in Brazil. In Manaus, at the end of 2020, we have observed a drastic increase in the number of cases for this variant, and consequently in the number of deaths during pandemic. Analyzes integrating viral genomic tracking and mortality data estimate that Gamma variant it is about 1.7 to 2.4 times more transmissible as compared to previous SARS-CoV-2 non-Gamma infection.

One study evaluated the potential of neutralizing antibodies after two doses of CoronaVac/Sinovac vaccine against the original B.1 strain and the Gamma variant. Antibody titers in individuals who had received two doses of CoronaVac/Sinovac 21 days before sample collection were near 1:80 for B.1 and 1:20 for P.1 isolates. Collectively, the data suggest that P.1 lineage virus might escape from neutralizing antibodies induced by an inactivated SARS-CoV-2 vaccine, especially at 5 months after vaccination as immunity wanes (42).

Previous non-P1 lineage infections can induce about 54-79% protection against P1 variant (43). The efficacy of the CoronaVac/Sinovac inactivated virus vaccine in Brazil, where 75% of infections has occurred in the presence of Gamma variant, was estimated about 50% protection against symptomatic infection (44).

A test-negative case–control study design evaluated the efficacy of CoronaVac/Sinovac in elderly people over 70 years of age during the Gamma variant outbreak in São Paulo, Brazil. The data show that this vaccine is 47% effective against symptomatic COVID-19, 57% against severe COVID-19 and 67% against deaths (44).

A multicentric study carried out in Brazil to assess the effectiveness of the Oxford-AstraZeneca vaccine in preventing symptomatic COVID-19 showed that against the Gamma variant this vaccine was 64% effective, but the number of confirmed cases of this variant was small, therefore this estimate is weak (45).

OMICRON VARIANT

The new Omicron variant (B.1.1.529) was first detected in Botswana, on November 11, 2021(**Figure 1**). Soon after, it was detected in Hong Kong in a patient who had arrived from a trip to South Africa (10). In these countries, cases had highly increased from one week to another after its detection, which was partially attributed to the increase in surveillance (20). The Omicron has some deletions, such as 69–70del, which prevents Spike from being detected by the RT-PCR test. It also shows more than 30 mutations in the S protein (**Figure 2**), with about 15 ones present in the RDB, some of them in regions that overlap the mutations of the other variants of concern, such as those that occur in residues K417, E484, and N501 (10). These deletions and mutations are associated with increased transmissibility by increasing the affinity of the spike protein with ACE2, and also associated to host immune escape and reduced neutralization of vaccine-induced antibodies (46–49).

Studies have indicated that the third dose of Pfizer/BioNTech and Moderna mRNA vaccines are efficient to neutralize the Omicron variant. The first and second doses of these vaccines resulted in low to none neutralization for this variant. However, patients who received a third dose exhibited efficient neutralization against the variant (50). The same was observed when the booster was heterologous, with the vaccination schedule being CoronaVac/Sinovac and the booster (third dose) of Pfizer/BioNTech (51), or the vaccination schedule of Oxford-AstraZeneca and the booster of Pfizer/BioNTech (52).

Furthermore, *in vitro* infection experiments demonstrated that the Omicron pseudovirus also depends on the human ACE2 receptor for target cell entry and infects host cells four times more efficiently than the wild-type pseudovirus, and 2 times more when compared to the Delta pseudovirus (50). Corroborating these findings, other studies showed that Omicron had a growth advantage over Delta in Gauteng, South Africa, where it presented 5.4-fold weekly increase in clinical cases as compared to Delta variants (49).

In general, infection with the Omicron variant appears to cause milder symptoms in relation to other variants. In countries where the vaccination programs are advanced it can be demonstrated high index of vaccine protection in all analyzed populations. However, in countries where vaccination is still incipient, the spreading of Omicron variant is associated with an increased number of infection cases, but this epidemiology is not accompanied by an increase in mortality rates, still indicating a low virulence of this variant. In fact, the replication capacity of Omicron is significantly attenuated *in vitro* and *in vivo* as compared to others such as SARS-CoV-2 WT, Alpha, Beta and Delta variants. This is explained by its lower efficiency in using TMPRSS2, as mutations in the spike gene of Omicron variant cause its inefficient cleavage by the host protease, leading to reduced recognition by host protease (53).

IMPLICATIONS ON BOTH HOST IMMUNE RESPONSE AND VACCINE EFFICACY

Some mutations capable of altering the fitness of SARS-CoV-2 were detected in the Spike protein early in the pandemic, due to an international effort in viral monitoring worldwide (10). Some of them are located in the RBD (**Figure 2**). Spike protein is the main neutralizing target for antibodies generated after SARS-CoV-2 infection (more than 90% of neutralizing antibodies) (54),

especially the RBD and is the SARS-CoV-2 component of mRNA and adenovirus-based vaccines licensed for use (55–57). The immunodominant epitopes are present in the region of the RBD that overlaps the ACE2 binding site (54).

The interaction of the Spike protein with the host cell occurs dynamically in a three-dimensional structure. Neutralizing antibodies can act in different ways, first by blocking the binding site (RBD) with ACE2 (58, 59). A few of these, bind to a motif surrounding the N-linked glycan at residue 343. These antibodies, exemplified by S309 (60), do not block ACE2 interaction, and destabilizing the S-trimer may be their mechanism of action. Neutralizing anti-NTD mAbs do not block ACE2 interaction and bind to a so-called supersite on the NTD (61, 62), however, they generally fail to provide a broad protection as the supersite is disrupted by a variety of NTD mutations present in the variants of concern (VOC).

The main vaccines applied today aim to induce an immune response, either humoral or cellular, against the spike protein. This is the case of Oxford-AstraZeneca (55), Pfizer/BioNTech (56) and Moderna (57). The variants of concern have mutations in RBD and the N-terminal region of S protein. Therefore, mutations occurring in RBD could potentially modify the biological and immunogenic characteristics of the virus, may affecting the spike affinity for ACE2, thus affecting the virus transmissibility, or conferring the ability to escape the immune response (63). This may affect the effectiveness of these vaccines. These mutations in the VOCs, without changing the viral fitness, can be selected during the course of the infection, by the host's immune system, by therapy with convalescent plasma, by vaccines and also by treatment with antibodies (64).

Vaccination induces a humoral and cellular response, so it is plausible to assume that the production of antibodies against Spike, preventing its binding to ACE2 and consequently infection, is an important mechanism in the control of the disease (65). Several studies show that vaccines developed against COVID-19 are capable of inducing neutralizing antibodies against Spike. It is not known, however, the amount of neutralizing antibodies needed to control the infection (66), there seems to be a relationship of the higher the neutralizing antibody titers, the greater the protection (67).

Since neutralization is an important mechanism for infection control, concern about variants is legitimate. Some works show that there is a reduction in neutralization by antibodies in *in vitro* assays for existing variants. However, in clinical practice, vaccines are being effective in reducing severe cases of the disease. This only reinforces the doubt about the necessary amount of neutralization to control the disease, as well as its relevance, since vaccines also induce a specific T response to the spike protein (68).

CONCLUDING REMARKS

Mutations would have evolutionary relevance if they could promote phenotypic changes in the viral behavior that promote its susceptibility to natural selection. In most RNA viruses, the variations that confer greater ability to evade the immune system are usually associated with increased fitness, that is, their ability to infect the host and being transmitted. This could be the case of antigenic changes causing viral evasion responses to host defense thus subverting the neutralizing action of antibodies, induced by a natural immune or vaccine responses (69). The HIV virus, for example, is one of the viruses with the greatest capacity to produce high fitness-variants capable of evading the host immune system.

However, when the selective pressure occurs under reverse transcriptase or protease, due to treatment with antiretroviral drugs, the variants that appear resistant to these drugs have a reduced replicative capacity and transmission (70). Influenza`s virus hemagglutinin, for instance, is extremely immunogenic and any variation on it allows evasion of the immune system, without loss of fitness (71). Therefore, much attention is currently given to the continued genetic monitoring of new SARS-CoV-2 variants of concern that could be able to evade the host immune defense mechanisms and promote an deadly wave of epidemiological outbreak (69).

AUTHOR CONTRIBUTIONS

AM, ECD, GFV, LFL, CGFL and ED wrote the manuscript. All authors contributed to the article and approved the submitted version.

REFERENCES

1. Huang C, Wang Y, Li X, Ren L, Zhao J, Hu Y. Clinical Features of Patients Infected With 2019 Novel Coronavirus in Wuhan, China. *Lancet* (2020) 395 (10223):497–506. doi: 10.1016/S0140-6736(20)30183-5
2. Wu Z, Mcgoogan JM. Characteristics of and Important Lessons From the Coronavirus Disease 2019 (COVID-19) Outbreak in China: Summary of a Report of 72 314 Cases From the Chinese Center for Disease Control and Prevention. *JAMA* (2020) 323(13):1239–42. doi: 10.1001/jama.2020.2648
3. Zhang H, Penninger JM, Li Y, Zhong N, Slutsky AS. Angiotensin-Converting Enzyme 2 (ACE2) as a SARS-CoV-2 Receptor: Molecular Mechanisms and Potential Therapeutic Target. *Intensive Care Med* (2020) 46(4):586–90. doi: 10.1007/s00134-020-05985-9
4. Bakhshandeh B, Jahanafrooz Z, Abbasi A, Goli MB, Sadeghi M, Mottaqi MS, et al. Mutations in SARS-CoV-2; Consequences in Structure, Function, and Pathogenicity of the Virus. *Microb Pathog* (2021) 154:104831. doi: 10.1016/j.micpath.2021.104831
5. Sokolowska M, Lukasik ZM, Agache I, Akdis CA, Akdis D, Akdis M, et al. Immunology of COVID-19: Mechanisms, Clinical Outcome, Diagnostics, and Perspectives-A Report of the European Academy of Allergy and Clinical Immunology (EAACI). *Allergy* (2020) 75(10):2445–76. doi: 10.1111/all.14462
6. Lu R, Zhao X, Li J, Niu P, Yang B, Wu H, et al. Genomic Characterisation and Epidemiology of 2019 Novel Coronavirus: Implications for Virus Origins and Receptor Binding. *Lancet* (2020) 395(10224):565–74. doi: 10.1016/S0140-6736(20)30251-8

7. Manzanares-Meza LD, Medina-Contreras O. SARS-CoV-2 and Influenza: A Comparative Overview and Treatment Implications. *Bol Med Hosp Infant Mex* (2020) 77(5):262–73. doi: 10.24875/BMHIM.20000183
8. Fischer W, Giorgi EE, Chakraborty S, Nguyen K, Bhattacharya T, Theiler J, et al. HIV-1 and SARS-CoV-2: Patterns in the Evolution of Two Pandemic Pathogens. *Cell Host Microbe* (2021) 29(7):1093–110. doi: 10.1016/j.chom.2021.05.012
9. WHO. *Terms of Reference for the Technical Advisory Group on SARS-CoV-2 Virus Evolution (TAG-Ve)* (2021). Available at: https://www.who.int/publications/m/item/terms-of-reference-for-the-technical-advisory-group-on-sars-cov-2-virus-evolution-(tag-ve).
10. *Tracking SARS-CoV-2 Variants* (2021). Available at: https://www.who.int/en/activities/tracking-SARS-CoV-2-variants/.
11. *Mutation Profiles of VOC/VOIs* (2021). Available at: https://www.who.int/docs/default-source/coronaviruse/voc_voi_290921.pdf?sfvrsn=61b3acff_5.
12. Negi SS, Schein CH, Braun W. Regional and Temporal Coordinated Mutation Patterns in SARS-CoV-2 Spike Protein Revealed by a Clustering and Network Analysis. *Sci Rep* (2022) 12(1):1128. doi: 10.1038/s41598-022-04950-4
13. Roy U. Comparative Structural Analyses of Selected Spike Protein-RBD Mutations in SARS-CoV-2 Lineages. *Immunol Res* (2021) 70(2):143–51. doi: 10.1101/2021.06.23.449639
14. Lupala CS, Ye Y, Chen H, Su X-D, Liu H. Mutations on RBD of SARS-CoV-2 Omicron Variant Result in Stronger Binding to Human ACE2 Receptor. *Biochem Biophys Res Commun* (2022) 590:34–41. doi: 10.1016/j.bbrc.2021.12.079
15. Volz E, Mishra S, Chand M, Barrett JC, Johnson R, Geidelberg L, et al. Assessing Transmissibility of SARS-CoV-2 Lineage B.1.1.7 in England. *Nature* (2021) 593(7858):266–9. doi: 10.1038/s41586-021-03470-x
16. Tegally H, Wilkinson E, Giovanetti M, Iranzadeh A, Fonseca V, Giandhari J, et al. Detection of a SARS-CoV-2 Variant of Concern in South Africa. *Nature* (2021) 592(7854):438–43. doi: 10.1038/s41586-021-03402-9
17. National Institute Of Infectious Diseases, J. *Brief Report: New Variant Strain of SARS-CoV-2 Identified in Travelers From Brazil*. (National Institute of Infectious Diseases, Japan) (2021).
18. Imai M, Halfmann PJ, Yamayoshi S, Iwatsuki-Horimoto K, Chiba S, Watanabe T, et al. Characterization of a New SARS-CoV-2 Variant That Emerged in Brazil. *Proc Natl Acad Sci U.S.A.* (2021) 118(27):1–9. doi: 10.1073/pnas.2106535118
19. Li B, Deng A, Li K, Hu Y, Li Z, Shi Y, et al. Viral Infection and Transmission in a Large, Well-Traced Outbreak Caused by the SARS-CoV-2 Delta Variant. *Nat Commun* (2022) 13(1):460. doi: 10.1038/s41467-022-28089-y
20. Karim SSA, Karim QA. Omicron SARS-CoV-2 Variant: A New Chapter in the COVID-19 Pandemic. *Lancet* (2021) 398(10317):2126–8. doi: 10.1016/S0140-6736(21)02758-6
21. Starr TN, Greaney AJ, Hilton SK, Ellis D, Crawford KHD, Dingens AS, et al. Deep Mutational Scanning of SARS-CoV-2 Receptor Binding Domain Reveals Constraints on Folding and ACE2 Binding. *Cell* (2020) 182(5):1295–1310.e20. doi: 10.1016/j.cell.2020.08.012
22. Tian F, Tong B, Sun L, Shi S, Zheng B, Wang Z, et al. N501Y Mutation of Spike Protein in SARS-CoV-2 Strengthens its Binding to Receptor ACE2. *Elife* (2021) 10:1–17. doi: 10.7554/eLife.69091
23. Collier DA, De Marco A, Ferreira IATM, Meng B, Datir RP, Walls AC, et al. Sensitivity of SARS-CoV-2 B.1.1.7 to mRNA Vaccine-Elicited Antibodies. *Nature* (2021) 593(7857):136–41. doi: 10.1038/s41586-021-03412-7
24. Supasa P, Zhou D, Dejnirattisai W, Liu C, Mentzer AJ, Ginn HM, et al. Reduced Neutralization of SARS-CoV-2 B.1.1.7 Variant by Convalescent and Vaccine Sera. *Cell* (2021) 184(8):2201–2211.e7.
25. Xie X, Liu Y, Liu J, Zhang X, Zou J, Fontes-Garfias CR, et al. Neutralization of SARS-CoV-2 Spike 69/70 Deletion, E484K and N501Y Variants by BNT162b2 Vaccine-Elicited Sera. *Nat Med* (2021) 27(4):620–1. doi: 10.1038/s41591-021-01270-4
26. Liu Y, Liu J, Xia H, Zhang X, Fontes-Garfias CR, Swanson K, et al. Neutralizing Activity of BNT162b2-Elicited Serum. *N Engl J Med* (2021) 384(15):1466–8. doi: 10.1056/NEJMc2102017
27. Chen Y, et al. Serum Neutralising Activity Against SARS-CoV-2 Variants Elicited by CoronaVac. *Lancet Infect Dis* (2021) 21(8):1071–2. doi: 10.1016/S1473-3099(21)00287-5
28. Abu-Raddad LJ, et al. Effectiveness of the BNT162b2 Covid-19 Vaccine Against the B.1.1.7 and B.1.351 Variants. *N Engl J Med* (2021) 385(2):187–9.
29. de Souza WM, Muraro SP, Souza GF, Amorim MR, Sesti-Costa R, Mofatto LS, et al. Clusters of SARS-CoV-2 Lineage B.1.1.7 Infection After Vaccination With Adenovirus-Vectored and Inactivated Vaccines. *Viruses* (2021) 13 (11):2127–40. doi: 10.3390/v13112127
30. Emary KRW, Golubchik T, Aley PK, Ariani CV, Angus B, Bibi S, et al. Efficacy of ChAdOx1 Ncov-19 (AZD1222) Vaccine Against SARS-CoV-2 Variant of Concern 202012/01 (B.1.1.7): An Exploratory Analysis of a Randomised Controlled Trial. *Lancet* (2021) 397(10282):1351–62.
31. Alenquer M, Ferreira F, Lousa D, Valério M, Medina-Lopes M, Bergman ML, et al. Signatures in SARS-CoV-2 Spike Protein Conferring Escape to Neutralizing Antibodies. *PloS Pathog* (2021) 17(8):e1009772. doi: 10.1371/journal.ppat.1009772
32. Cele S, Gazy I, Jackson L, Hwa SH, Tegally H, Lustig G, et al. Escape of SARS-CoV-2 501y.V2 From Neutralization by Convalescent Plasma. *Nature* (2021) 593(7857):142–6.
33. Madhi SA, Baillie V, Cutland CL, Voysey M, Koen AL, Fairlie L, et al. Efficacy of the ChAdOx1 Ncov-19 Covid-19 Vaccine Against the B.1.351 Variant. *N Engl J Med* (2021) 384(20):1885–98. doi: 10.1056/NEJMoa2102214
34. Sadoff J, Gray G, Vandebosch A, Cárdenas V, Shukarev G, Grinsztejn B, et al. Safety and Efficacy of Single-Dose Ad26.Cov2.S Vaccine Against Covid-19. *N Engl J Med* (2021) 384(23):2187–201.
35. Kustin T, Harel N, Finkel U, Perchik S, Harari S, Tahor M, et al. Evidence for Increased Breakthrough Rates of SARS-CoV-2 Variants of Concern in BNT162b2-mRNA-Vaccinated Individuals. *Nat Med* (2021) 27(8):1379–84. doi: 10.1038/s41591-021-01413-7
36. Planas D, Veyer D, Baidaliuk A, Staropoli I, Guivel-Benhassine F, Rajah MM, et al. Reduced Sensitivity of SARS-CoV-2 Variant Delta to Antibody Neutralization. *Nature* (2021) 596(7871):276–80. doi: 10.1038/s41586-021-03777-9
37. Li M, Lou F, Fan H. SARS-CoV-2 Variants of Concern Delta: A Great Challenge to Prevention and Control of COVID-19. *Signal Transduct Target Ther* (2021) 6(1):349. doi: 10.1038/s41392-021-00767-1
38. Mlcochova P, Kemp SA, Dhar MS, Papa G, Meng B, Ferreira IATM, et al. SARS-CoV-2 B.1.617.2 Delta Variant Replication and Immune Evasion. *Nature* (2021) 599(7883):114–9. doi: 10.1038/s41586-021-03944-y
39. Bernal JL, Andrews N, Gower C, Gallagher E, Simmons R. Effectiveness of Covid-19 Vaccines Against the B.1.617.2 (Delta) Variant. *N Engl J Med* (2021) 385(7):585–94. doi: 10.1056/NEJMoa2108891
40. Ma C, Sun W, Tang T, Jia M, Liu Y, Wan Y, et al. Effectiveness of Adenovirus Type 5 Vectored and Inactivated COVID-19 Vaccines Against Symptomatic COVID-19, COVID-19 Pneumonia, and Severe COVID-19 Caused by the B.1.617.2 (Delta) Variant: Evidence From an Outbreak in Yunnan, China, 2021. *Vaccine* (2022) 40(20):2869–74. doi: 10.1016/j.vaccine.2022.03.067
41. Pormohammad A, Zarei M, Ghorbani S, Mohammadi M, Aghayari Sheikh Neshin S, Khatami A, et al. Effectiveness of COVID-19 Vaccines Against Delta (B.1.617.2) Variant: A Systematic Review and Meta-Analysis of Clinical Studies. *Vaccines (Basel)* (2021) 10(1):23–38. doi: 10.3390/vaccines10010023
42. Souza WM, Amorim MR, Sesti-Costa R, Coimbra LD, Brunetti NS, Toledo-Teixeira DA, et al. Neutralisation of SARS-CoV-2 Lineage P.1 by Antibodies Elicited Through Natural SARS-CoV-2 Infection or Vaccination With an Inactivated SARS-CoV-2 Vaccine: An Immunological Study. *Lancet Microbe* (2021) 2(10):e527–35. doi: 10.1016/S2666-5247(21)00129-4
43. Faria NR, Mellan TA, Whittaker C, Claro IM, Candido DDS, Mishra S, et al. Genomics and Epidemiology of the P.1 SARS-CoV-2 Lineage in Manaus, Brazil. *Science* (2021) 372(6544):815–21. doi: 10.1126/science.abh2644
44. Hitchings MDT, Ranzani OT, Torres MSS, de Oliveira SB, Almiron M, Said R, et al. Effectiveness of CoronaVac Among Healthcare Workers in the Setting of High SARS-CoV-2 Gamma Variant Transmission in Manaus, Brazil: A Test-Negative Case-Control Study. *Lancet Reg Health Am* (2021) 1:100025. doi: 10.1016/j.lana.2021.100025
45. Clemens SAC, Folegatti PM, Emary KRW, Weckx LY, Ratcliff J, Bibi S, et al. Efficacy of ChAdOx1 Ncov-19 (AZD1222) Vaccine Against SARS-CoV-2 Lineages Circulating in Brazil. *Nat Commun* (2021) 12(1):5861. doi: 10.1038/s41467-021-25982-w
46. Greaney AJ, Starr TN, Gilchuk P, Zost SJ, Binshtein E, Loes AN, et al. Complete Mapping of Mutations to the SARS-CoV-2 Spike Receptor-Binding

Domain That Escape Antibody Recognition. *Cell Host Microbe* (2021) 29 (1):44–57.e9. doi: 10.1016/j.chom.2020.11.007
47. Harvey WT, Carabelli AM, Jackson B, Gupta RK, Thomson EC, Harrison EM, et al. SARS-CoV-2 Variants, Spike Mutations and Immune Escape. *Nat Rev Microbiol* (2021) 19(7):409–24. doi: 10.1038/s41579-021-00573-0
48. Garcia-Beltran WF, Lam EC, St Denis K, Nitido AD, Garcia ZH, Hauser BM, et al. Multiple SARS-CoV-2 Variants Escape Neutralization by Vaccine-Induced Humoral Immunity. *Cell* (2021) 184(9):2523. doi: 10.1016/j.cell.2021.04.006
49. Viana R, Moyo S, Amoako DG, Tegally H, Scheepers C, Althaus CL, et al. Rapid Epidemic Expansion of the SARS-CoV-2 Omicron Variant in Southern Africa. *Nature* (2022) 603:679–86. doi: 10.1038/s41586-022-04411-y
50. Garcia-Beltran WF, St Denis KJ, Hoelzemer A, Lam EC, Nitido AD, Sheehan ML, Berrios C, et al, et al. mRNA-Based COVID-19 Vaccine Boosters Induce Neutralizing Immunity Against SARS-CoV-2 Omicron Variant. *Cell* (2022) 185(3):457–66. doi: 10.1101/2021.12.14.21267755
51. Campos GRF, Almeida NBF, Filgueiras PS, Corsini CA, Gomes SVC, Miranda DAPd, et al. Booster Dose of BNT162b2 in a CoronaVac Primary Vaccination Protocol Improves Neutralization of SARS-CoV-2 Omicron Variant. *MedRxiv* (2022). doi: 10.1101/2022.03.24.22272904
52. Andrews N, Stowe J, Kirsebom F, Toffa S, Rickeard T, Gallagher E, et al. Covid-19 Vaccine Effectiveness Against the Omicron (B.1.1.529) Variant. *N Engl J Med* (2022) 386(16):1532–46. doi: 10.1056/NEJMoa2119451
53. Shuai H, Chan JF, Hu B, Chai Y, Yuen TT, Yin F, et al. Attenuated Replication and Pathogenicity of SARS-CoV-2 B.1.1.529 Omicron. *Nature* (2022) 603:693–99. doi: 10.1038/s41586-022-04442-5
54. Piccoli L, Park YJ, Tortorici MA, Czudnochowski N, Walls AC, Beltramello M, et al. Mapping Neutralizing and Immunodominant Sites on the SARS-CoV-2 Spike Receptor-Binding Domain by Structure-Guided High-Resolution Serology. *Cell* (2020) 183(4):1024–1042.e21. doi: 10.1016/j.cell.2020.09.037
55. Voysey M, Clemens SAC, Madhi SA, Weckx LY, Folegatti PM, Aley PK, et al. Safety and Efficacy of the ChAdOx1 Ncov-19 Vaccine (AZD1222) Against SARS-CoV-2: An Interim Analysis of Four Randomised Controlled Trials in Brazil, South Africa, and the UK. *Lancet* (2021) 397(10269):99–111. doi: 10.1016/S0140-6736(20)32661-1
56. Walsh EE, Frenck RW, Falsey AR, Kitchin N, Absalon J, Gurtman A, et al. Safety and Immunogenicity of Two RNA-Based Covid-19 Vaccine Candidates. *N Engl J Med* (2020) 383(25):2439–50. doi: 10.1056/NEJMoa2027906
57. Jackson LA, Anderson EJ, Rouphael NG, Roberts PC, Makhene M, Coler RN, et al. An mRNA Vaccine Against SARS-CoV-2 - Preliminary Report. *N Engl J Med* (2020) 383(20):1920–31. doi: 10.1056/NEJMoa2022483
58. Dejnirattisai W, Zhou D, Ginn HM, Duyvesteyn HME, Supasa P, Case JB, et al. The Antigenic Anatomy of SARS-CoV-2 Receptor Binding Domain. *Cell* (2021) 184(8):2183–2200.e22. doi: 10.1016/j.cell.2021.02.032
59. Lan J, Ge J, Yu J, Shan S, Zhou H, Fan S, et al. Structure of the SARS-CoV-2 Spike Receptor-Binding Domain Bound to the ACE2 Receptor. *Nature* (2020) 581(7807):215–20. doi: 10.1038/s41586-020-2180-5
60. Pinto D, Park YJ, Beltramello M, Walls AC, Tortorici MA, Bianchi S, et al. Cross-Neutralization of SARS-CoV-2 by a Human Monoclonal SARS-CoV Antibody. *Nature* (2020) 583(7815):290–5. doi: 10.1038/s41586-020-2349-y
61. Cerutti G, Guo Y, Wang P, Nair MS, Wang M, Huang Y, et al. Neutralizing Antibody 5-7 Defines a Distinct Site of Vulnerability in SARS-CoV-2 Spike N-Terminal Domain. *Cell Rep* (2021) 37(5):109928. doi: 10.1016/j.celrep.2021.109928
62. Chi X, Yan R, Zhang J, Zhang G, Zhang Y, Hao M, et al. A Neutralizing Human Antibody Binds to the N-Terminal Domain of the Spike Protein of SARS-CoV-2. *Science* (2020) 369(6504):650–5. doi: 10.1126/science.abc6952
63. Han P, Su C, Zhang Y, Bai C, Zheng A, Qiao C, et al. Molecular Insights Into Receptor Binding of Recent Emerging SARS-CoV-2 Variants. *Nat Commun* (2021) 12(1):6103. doi: 10.1038/s41467-021-26401-w
64. Liu Z, VanBlargan LA, Bloyet LM, Rothlauf PW, Chen RE, Stumpf S, et al. Identification of SARS-CoV-2 Spike Mutations That Attenuate Monoclonal and Serum Antibody Neutralization. *Cell Host Microbe* (2021) 29(3):477–488.e4. doi: 10.1016/j.chom.2021.01.014
65. Earle KA, Ambrosino DM, Fiore-Gartland A, Goldblatt D, Gilbert PB, Siber GR, et al. Evidence for Antibody as a Protective Correlate for COVID-19 Vaccines. *Vaccine* (2021) 39(32):4423–8. doi: 10.1016/j.vaccine.2021.05.063
66. Khoury DS, Cromer D, Reynaldi A, Schlub TE, Wheatley AK, Juno JA, et al. Neutralizing Antibody Levels are Highly Predictive of Immune Protection From Symptomatic SARS-CoV-2 Infection. *Nat Med* (2021) 27(7):1205–11. doi: 10.1038/s41591-021-01377-8
67. Feng S, Phillips DJ, White T, Sayal H, Aley PK, Bibi S, et al. Correlates of Protection Against Symptomatic and Asymptomatic SARS-CoV-2 Infection. *Nat Med* (2021) 27(11):2032–40. doi: 10.1038/s41591-021-01540-1
68. Tregoning JS, et al. Progress of the COVID-19 Vaccine Effort: Viruses, Vaccines and Variants Versus Efficacy, Effectiveness and Escape. *Nat Rev Immunol* (2021) 21(10):626–36. doi: 10.1038/s41577-021-00592-1
69. Burioni R, Topol EJ. Assessing the Human Immune Response to SARS-CoV-2 Variants. *Nat Med* (2021) 27(4):571–2. doi: 10.1038/s41591-021-01290-0
70. Eriksen J, Albert J, Axelsson M, Berglund T, Brännström J, Gaines H, et al. Contagiousness in Treated HIV-1 Infection. *Infect Dis (Lond)* (2021) 53(1):1–8. doi: 10.1080/23744235.2020.1831696
71. Karlsson Hedestam GB, Fouchier RA, Phogat S, Burton DR, Sodroski J, Wyatt RT, et al. The Challenges of Eliciting Neutralizing Antibodies to HIV-1 and to Influenza Virus. *Nat Rev Microbiol* (2008) 6(2):143–55. doi: 10.1038/nrmicro1819

Conflict of Interest: The authors declare that the research was conducted in the absence of any commercial or financial relationships that could be construed as a potential conflict of interest.

Publisher's Note: All claims expressed in this article are solely those of the authors and do not necessarily represent those of their affiliated organizations, or those of the publisher, the editors and the reviewers. Any product that may be evaluated in this article, or claim that may be made by its manufacturer, is not guaranteed or endorsed by the publisher.

frontiers | Frontiers in Immunology

TYPE Original Research
PUBLISHED 28 July 2022
DOI 10.3389/fimmu.2022.877682

OPEN ACCESS

EDITED BY
Shen-Ying Zhang,
The Rockefeller University,
United States

REVIEWED BY
Kyung-Ho Roh,
University of Alabama in Huntsville,
United States
Kailin Xu,
Xuzhou Medical University, China

*CORRESPONDENCE
Masakazu Kamata
masa3k@uab.edu

†These authors have contributed equally to this work

SPECIALTY SECTION
This article was submitted to Viral Immunology, a section of the journal Frontiers in Immunology

RECEIVED 17 February 2022
ACCEPTED 07 July 2022
PUBLISHED 28 July 2022

CITATION
Kranz E, Kuhlmann CJ, Chan J, Kim PY, Chen ISY and Kamata M (2022) Efficient derivation of chimeric-antigen receptor-modified T_{SCM} cells. *Front. Immunol.* 13:877682. doi: 10.3389/fimmu.2022.877682

Efficient derivation of chimeric-antigen receptor-modified T_{SCM} cells

Emiko Kranz[1†], Charles J. Kuhlmann[2†], Joshua Chan[3], Patrick Y. Kim[3], Irvin S. Y. Chen[1,3] and Masakazu Kamata[2*]

[1]Division of Hematology-Oncology, David Geffen School of Medicine at University of California, Los Angeles (UCLA), Los Angeles, CA, United States, [2]Department of Microbiology, School of Medicine, University of Alabama at Birmingham, Birmingham, AL, United States, [3]Department of Microbiology, Immunology, and Molecular Genetics, David Geffen School of Medicine at University of California, Los Angeles (UCLA), Los Angeles, CA, United States

Chimeric-antigen receptor (CAR) T-cell immunotherapy employs autologous-T cells modified with an antigen-specific CAR. Current CAR-T manufacturing processes tend to yield products dominated by effector T cells and relatively small proportions of long-lived memory T cells. Those few cells are a so-called stem cell memory T (T_{SCM}) subset, which express naïve T-cell markers and are capable of self-renewal and oligopotent differentiation into effector phenotypes. Increasing the proportion of this subset may lead to more effective therapies by improving CAR-T persistence; however, there is currently no standardized protocol for the effective generation of CAR-T_{SCM} cells. Here we present a simplified protocol enabling efficient derivation of gene-modified T_{SCM} cells: Stimulation of naïve CD8+ T cells with only soluble anti-CD3 antibody and culture with IL-7 and IL-15 was sufficient for derivation of CD8+ T cells harboring T_{SCM} phenotypes and oligopotent capabilities. These *in-vitro* expanded T_{SCM} cells were engineered with CARs targeting the HIV-1 envelope protein as well as the CD19 molecule and demonstrated effector activity both *in vitro* and in a xenograft mouse model. This simple protocol for the derivation of CAR-T_{SCM} cells may facilitate improved adoptive immunotherapy.

KEYWORDS

T_{SCM}, CAR, gene therapy, adoptive immunotherapy, HIV-1

Abbreviations: T_{SCM}, stem cell memory T; CAR, chimeric antigen receptor; HIV-1, human immunodeficiency virus type 1.

Introduction

Gene-engineered T cells with desired antigen-specific receptors such as chimeric-antigen receptors (CARs), aim to confer directed and enhanced cytotoxic T lymphocyte responses (1–4). CARs contain an antigen-binding domain specific for targets and an internal-signaling domain derived from CD3ζ chain as well as 41BB, CD28, or other co-stimulatory molecules (5, 6). When a CAR encounters its target ligand, it signals the cell in a T cell receptor-like, but human-leukocyte antigen (HLA)-independent manner, thus allowing this approach to be used in any patient. In human clinical trials for B-cell malignancies, CAR-modified autologous T cells targeting CD19 have shown robust effector responses (5–10). For HIV-1 infection, CD4ζ CAR has been widely and longitudinally tested in patients. Treatment was safe and well-tolerated for over a decade, but antiviral effects were limited due to low levels of gene-modified cell persistence (11–14).

The novel memory T cell subset known as stem cell-memory T (T_{SCM}) harbors self-renewing and oligopotency capabilities. The T_{SCM} subset has been identified in mice (15), non-human primates (16, 17), and humans (18, 19). In humans, approximately 2-4% of peripheral blood T cells consist of T_{SCM} cells (20). The T_{SCM} cells are phenotypically defined as naïve T (T_N) cells by the expression of T_N cell markers, such as CD45RA, CD62L and CCR7, but are distinguishable from T_N cells by two memory T cell markers: CD95 and CD122. Thus, they exhibit a gene profile between T_N and central-memory T (T_{CM}) cells. Of note, the T_{SCM} cells —— unlike other memory T cells —— can be expanded *ex vivo* while maintaining their stemness, allowing enrichment of the gene-modified population prior to transplant.

Increasing evidence indicates that the T_{SCM} cells exhibit a lesser extent of proliferation and effector activities compared to other memory T cells. Upon antigen stimulation, the T_{SCM} cells have the ability to differentiate into T_{CM} (which are thought to be a premature memory subset that differentiates into the effector subset upon antigen re-encounter), followed by effector-memory T (T_{EM}) cells (which are considered to be committed progenitor cells that undergo terminal differentiation after a limited number of cell divisions) (18, 21–24). The frequency and activity of T_{SCM} cells from clinical samples also supports their prolonged precursor potential in humans (25, 26). Importantly, individual gene-modified T_{SCM} cell clones did not show the emergence of clonal dominance for over a decade after infusion, indicating that gene engineering of T_{SCM} cells does not bring in them a tumorigenic change. These evidence well support that T_{SCM} cells would be an ideal host cell for CAR engineering.

We here developed a simple condition for the derivation and expansion of gene-modified-T cells harboring T_{SCM}-surface phenotype and validated its applicability for gene engineering of T cells using both anti-HIV-1 and anti-CD19 CARs. Our results further demonstrate that these cells can effectively differentiate to functional-T cells conferring CAR-dependent effector activity against target cells *in vitro* as well as in a xenograft NSG mouse model.

Methods

Cells

Peripheral blood mononuclear cells (PBMCs) from healthy human donors were obtained from the CFAR Virology Core at UCLA without personal identifying information. To minimize a potential induction of T-cell stimulation by events such as crosslinking of cell-surface molecules, T_N-cell population was negatively selected in one step using an EasySep™ Human Naive CD8+ T Cell Enrichment Kit (StemCell Technologies, Inc., Vancouver, Canada), which consistently provides >95% purity of CD8+ T_N cells (Supplementary Figure 1). Cells were maintained in Iscove's Modified Dulbecco's Medium (IMDM) supplemented with 1% GlutaMAX supplement and Antibiotic-Antimycotic (Life Technologies, Grand Island, NY), 20% FCS (SH30070.03E; GE Healthcare Life Sciences, South Logan, UT), and 0.1 mM 2-mercaptoethanol (Sigma-Aldrich St. Louis, MO) (T-cell medium) as reported previously (27). Prior to lentiviral vector transduction, CD8+ T_N cells were incubated with various concentrations of anti-CD3 antibody (Hit3a; BioLegend, San Diego, CA) with or without 2 μg/mL of anti-CD28 antibodies (CD28.2; BioLegend) for 2 days in T-cell medium supplemented with 5 ng/mL IL-7 and IL-15 (R&D systems, Minneapolis, MN) as summarized in Figure 1A. All cells were incubated at 37°C in 5% CO_2.

Cytotoxic assay

Triple-CD4ζ (27) was used an anti-HIV CAR. For anti-HIV CAR cytotoxicity assays, Jurkat cells encoded without (ΔKS, non-target cells) or with HIV-1_{HXBC2} envelope protein (HXBC2, target cells), where the expression can be induced by removal of doxycycline from culture medium (28), were used. As an additional target cell for *in vivo* cytotoxicity assay, TF228.1.16 cells —— which are BJAB cells constitutively expressing HIV-1_{BH10} envelope protein (29) —— were used. ΔKS, HXBC2, and TF228.1.16 cells were genetically labeled with TagBFP (30), mCherry (31), and mStrawberry (31), respectively. In an assay for anti-CD19 CAR (FMC63-IgG4ζ (32)), we used BCBL-1 (33) (CD19-, non-target cells) and Ramos cells (CD19+, target cells). BCBL-1 and Ramos cells were genetically labeled with TagBFP and mStrawberry, respectively. All cells were obtained from the NIH-AIDS Reagent Program and cultured as recommended.

For *in vitro* cytotoxicity assay, 5 x 10^4 CAR- or EGFP-modified CD8+ T cells as a negative control were plated using

10.3389/fimmu.2022.877682

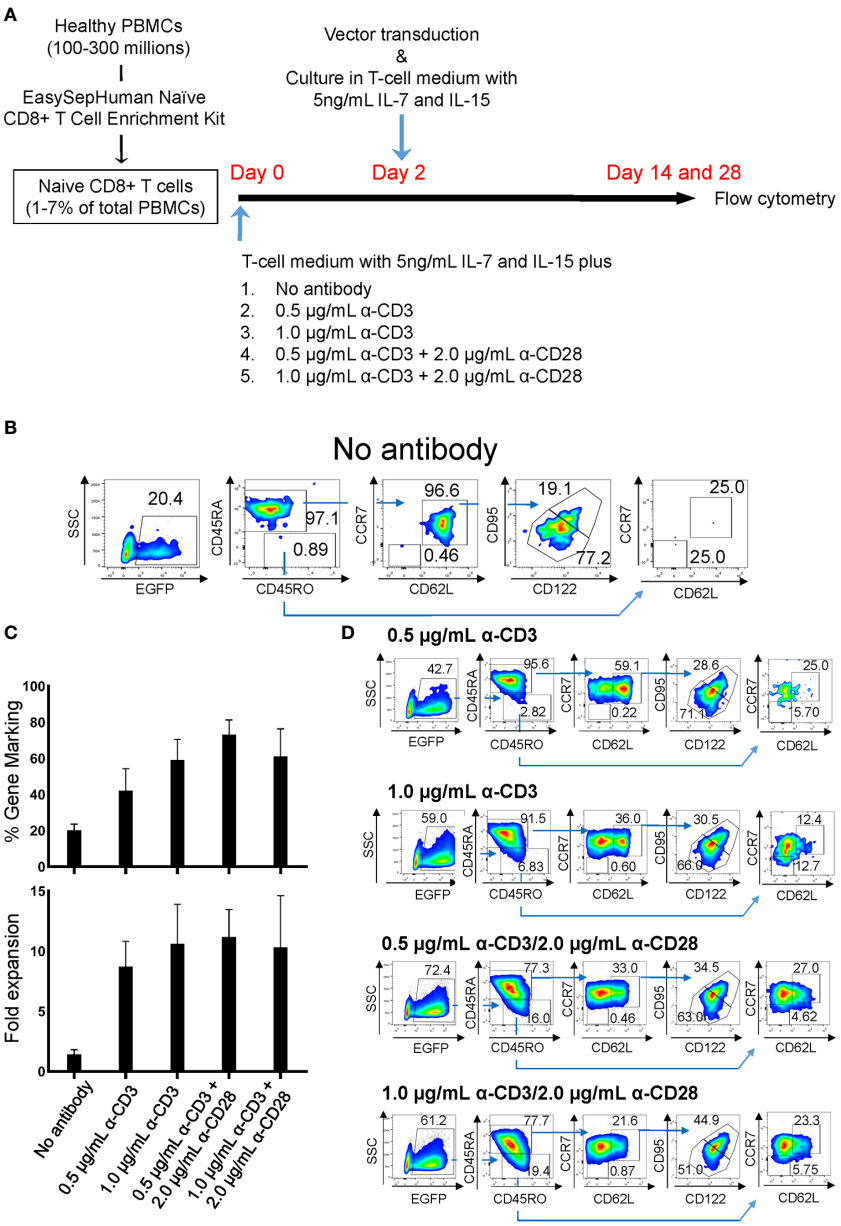

FIGURE 1
Derivation of gene-marked CD8+ T cells harboring T_{SCM}-surface phenotype under different stimulation conditions. Freshly isolated human PBMCs were separated for CD8+ T_N cells using an EasySep™ Human Naïve CD8+ T Cell Enrichment kit. Cells were stimulated for 2 days with the condition as in **(A)**, followed by transduction with lentiviral vector encoding EGFP as a transduction marker. Cells were cultured for an additional 12 days in the presence of 5 ng/mL of IL-7 and IL-15, and cell-surface marker profiles were analyzed by flow cytometry. **(A)** Summary for derivation of T_{SCM} cells procedure. **(B)** Flow cytometry analyses of CD8+ T_N cells genetically marked by EGFP with no antibody stimulation. **(C)** % positivity of EGFP-marked cells (Top bars) and fold changes in cell number following 14 days of culture (Bottom bars). **(D)** Flow cytometry analyses of EGFP-engineered CD8+ T_N cells. All experiments were repeated at least three times. Error bars in **(C)** show the standard deviation of a data set. One representative experiment is shown for **(B, D)**.

100μL of T-cell medium in a 96-well round bottom plate. The same numbers of genetically-labeled ΔKS and HXBC2 cells for CD4ζ or BCBL-1 and Ramos cells for FMC63-IgG4ζ were added to each well and co-incubated for 4 or 16 hours [Effector: Target (E:T) ratio = 1:1]. Antigen specificity of both CARs was also validated with HXBC2 cells culturing with doxycycline to suppress HIV-1_{HXBC2} envelope protein expression for CD4ζ CAR which cells cannot be a target for CD4ζ CAR, as well as human CD19 overexpressing HXBC2 cells culturing with doxycycline for FMC63-IgG4ζ CAR (data not shown). Total

numbers of each cell were determined by MACSQuant (Milteny Biotech, Germany) and relative cytotoxicity of target cells relative to non-target cells was determined by the following formula: Relative cytotoxicity (%) =100 x (1 – target cell number/non-target cell number).

Viruses

Lentiviral vectors were generated and transduced as described elsewhere (27, 34, 35). $p24^{Gag}$ ELISA assays were performed by the CFAR Virology Core at UCLA. Lentiviral vector information used in this research will be provided upon request.

Flow cytometry

The following antibodies were used in flow cytometry: BV711-CD4 (OKT4), BV605-CD8 (RPA-T8), APC/Cy7-CD45RO (UCHL1), AlexaFlour700-CD45RA (H100), PerCP/Cy5.5-CD62L (DREG-56), BV785-CCR7 (G043H7) (all from BioLegend), eFluor650NC-CD3 (OKT3; eBioscience, San Diego, CA), APC-CD95 (LT95; Thermo Fisher, Pittsburgh, PA), and BV421-CD122 (Mik-β3; BD Biosciences, San Jose, CA). Cells were acquired using FACSDiva on BD LSRFortessa. Data for each cell with different cell surface phenotypes were analyzed using FlowJo software (BD Biosciences) as summarized in Supplementary Figure 2. Absolute cell counts were determined using MACSQuant analyzer. Cell sorting was performed by the CFAR Flow Cytometry Core Facility at UCLA.

In vivo tumor-killing assay

Animal research was conducted under UCLA's Chancellor's Animal Research Committee. Two million of TF228.1.16 or HXBC2 cells in 50 µL of PBS were mixed with 50 µL of Matrigel (BD Biosciences) and subcutaneously engrafted to the left or right hind limbs of NOD.CB17-Prkdc^{scid}/J (NOD-SCID) mice (n=4) (Jackson Laboratory, Bar Harbor, Maine), respectively. On day 14, either Triple-CD4ζ- or FMC63-IgG4ζ–modified T cells ($5x10^5$) were infused *via* the retro-orbital vein. Biofluorescence images and the weight of xenograft tumors were obtained 42 days post-engraftment.

Statistical analyses

Results are expressed as mean ± standard deviations (SDs). Errors depict SD. Comparisons between two groups were performed using an unpaired two-tailed t-test with Welch's correction. A p-value less than 0.05 was considered statistically significant.

Results

Stimulation of CD8+ T_N cells with soluble anti-CD3 antibody enables efficient gene-modification by lentiviral vector while minimizing T-cell differentiation

Two independent protocols for the derivation of T_{SCM} have been described by Gattinoni et al. (18) and Cieri et al. (19). The major differences between those two protocols are that the former used an inhibitor of glycogen synthase kinase 3β (GSK-3β), TWS119 (15, 36), and the latter used a low concentration of two cytokines, IL-7 and IL-15 with no chemical inhibitor. Our preliminary experiments for a side-by-side comparison of those two protocols showed that there was minimal benefit of the use of TWS119 for the derivation of T_{SCM} cells due to a poor cell expansion by the former protocol. Whereas, the latter protocol was able to yield a nearly 5-fold higher number of cells harboring surface phenotypes corresponding to T_{SCM} (0.41×10^6 *vs* 1.88×10^6, Supplementary Table 1). However, a considerable number of T_{EM} cells were derivated under both conditions, presumably due to the potent stimulation condition of using anti-CD3/CD28 antibody coated beads. We thus assessed alternative stimulation conditions for their ability to derive large numbers of T_{SCM} while minimizing T-cell differentiation and allowing for gene modification *via* lentiviral vectors. Negatively selected CD8+ T_N cells were incubated with different amounts of soluble anti-CD3 antibody with or without anti-CD28 antibody. The cells were then transduced with a lentiviral vector encoding EGFP as a marker gene and cultured for an additional 12 days with IL-7 and IL-15 followed with Cieri's protocol (Figure 1A). In the no antibody condition, approximately 20% of CD8+ T_N cells were successfully gene-modified, indicating that a small portion of CD8+ T cells are transducable without active stimulation and that culturing in the presence of IL-7 and IL-15 allows maintenance of the CD8+ T_N cell phenotype for at least 14 days (Figure 1B). However, the no antibody condition resulted in extremely poor expansion of the cells (<2-fold, Figure 1C). The inclusion of increasing concentrations of anti-CD3 antibody and/or the presence of anti-CD28 antibody increased the levels of gene marking and T-cell expansion (Figure 1C), but also increased the proportion of differentiated cells as defined by the loss of CD45RA or CD62L expression (37–39) (Figures 1D, 2A). The differences shown above became more obvious after an additional 14 days of culture (total 28 days of culture) (Figure 2B, Day 28), indicating that cells harboring T_{SCM}-surface phenotype slowly but continuously expanded in the presence of IL-7 and IL-15. The average numbers from each population in EGFP-positive cells after a total of 28 days of culture in Figure 2B were summarized in Supplementary Table 2: a higher recovery of the EGFP-marked T_{SCM} cells was observed with 0.5 µg (7.35×10^6) or 1.0 µg/mL anti-

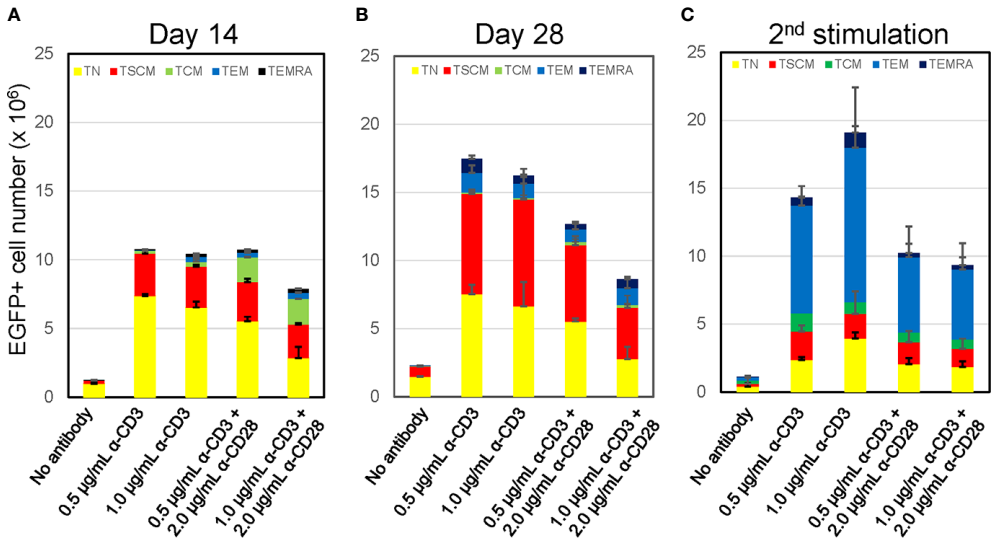

FIGURE 2
Prolonged culture increases % population of CD8+ T cells harboring T_{SCM}-surface phenotype with maintaining oligopotency Freshly isolated CD8+ T_N cells were transduced with lentiviral vector encoding EGFP following stimulation with various antibody conditions shown in Figure 1A. The cells were cultured for an additional 12 days (**A**, Day14) or 26 days (**B**, Day 28) in the presence of 5 ng/mL of IL-7 and IL-15. A half million of cells in A was co-stimulated by 0.5 µg/mL anti-CD3 and 2.0 µg/mL anti-CD28 antibodies and further cultures for 14 days (**C**, 2nd stimulation). Cells were staining for CD45RA, CD45RO, CCR7, CD62L, CD95 and CD122, and surface marker of EGFP-marked cells were analyzed by flow cytometry. Each cell number of EGFP-marked cells with T_N, T_{SCM}, T_{CM}, T_{EM}, and T_{EMRA} phenotypes was plotted. Experiments were repeated three times. Error bars show the standard deviation of a data set.

CD3 (7.84 x 10^6) stimulation rather than the condition with 0.5 µg/mL anti-CD3 + 2.0 µg of anti-CD28 antibody (5.61 x 10^6), which generated the highest gene marking as in Figure 1C. Importantly, EGFP-marked T_{SCM} cells were expanded nearly 2-fold following a total of 28 days of culture, whereas the number of T_{SCM} cells in other populations decreased over the course of the culture (Supplementary Figure 3). These results indicate that stimulation of CD8+ T_N cells with only soluble anti-CD3 antibody (0.5-1.0 µg/mL) and prolonged-expansion (28 days) in the presence of IL-7 and IL-15 allowed for the most efficient derivation of gene-marked CD8+ T cells harboring T_{SCM}-surface phenotype with a minimum level of T-cell differentiation.

A key feature of the T_{SCM} subset is its oligopotency allowing differentiation into more terminal subsets upon antigen stimulation (18, 19). We confirmed the differentiation ability of these *in-vitro* generated T_{SCM} cells *via* anti-CD3/CD28 co-stimulation. The status of T-cell differentiation was evaluated by surface phenotypes at 14-days after the 2nd stimulation (Figure 2C, 2nd stimulation). The number and prevalence of CD8+ T cells harboring the T_{SCM} and T_N phenotype was substantially reduced after the 2nd stimulation. Concomitantly, the proportion of differentiated cells — especially the T_{EM} population — increased under this condition. Thus, these *in-vitro* generated T_{SCM} cells retain their oligopotency.

Derivation of CAR-modified CD8+ T cells with T_{SCM}-surface phenotype

As above, we were able to validate the oligopotency of the *in-vitro* generated gene-engineered cells with T_{SCM}-surface phenotypes. We next applied this method for the generation of anti-HIV-1 CAR-T cells. We utilized the Triple-CD4ζ CAR that targets HIV-1 gp120 on the infected cell surface (27) with co-expression of two anti-HIV-1 shRNAs: sh1005 which suppresses surface expression of the key HIV-1 co-receptor CCR5 (40) and sh516 which prevents HIV-1 infection to both CD4+ T and CD8+ T cells mediated *via* CD4ζ expression (34). Thus, the Triple-CD4ζ CAR can exert potent anti-HIV-1-effector activity while protecting its transduced cells from HIV-1 infection. We previously demonstrated its potent anti-HIV-1 effects *in vivo* using an HIV-1 challenged-humanized mouse model (41, 41). Although the condition established above allowed successful modification of CD8+ T_N cells with the Triple-CD4ζ CAR while maintaining a population with the T_{SCM}-surface phenotype, the proportion of transduced cells was relatively lower compared to that of control EGFP vector (42.9% *vs* 8.8%, Supplementary Figure 4). This is potentially due to a larger size of the transgene (42). Nevertheless, these gene-marked cells were successfully differentiated to cells harboring surface phenotypes of T_{CM} and T_{EM} cells upon anti-CD3/CD28 stimulation (Figure 3A).

We next assessed the effector function of Triple-CD4ζ-modified CD8+ T cells by a flow-cytometry based cytotoxicity assay. The cells modified with Triple-CD4ζ cells were incubated with their target Jurkat cells expressing HIV-1_{HXBC2} envelope protein (HXBC2) upon doxycycline removal from culture medium (28). To validate the level of non-specific target cell killing, control Jurkat cells which do not encode HIV-1-envelope protein (ΔKS, non-target cell) were included (28). The former is labeled by mCherry and the latter by Tag-BFP, thus both cells can be distinguished by flow cytometry. The numbers of remaining mCherry+ and TagBFP+ cells following incubation with Triple-CD4ζ-modified CD8+ T cells correspond to levels of anti-HIV-1 CAR-dependent and independent cytotoxicity, respectively. Following a co-culture with the above three cells for 4 and 16 hours, the total numbers of mCherry+ and TagBFP+ cells were analyzed by MACSQuant, and relative cytotoxicity against target cells compared to that against non-target cells was determined (Figure 3B). The pre-differentiated cells shown in Figure 3A were used as a positive control for the assay. There were minimal levels of change in the cell surface phenotypes of Triple-CD4ζ following

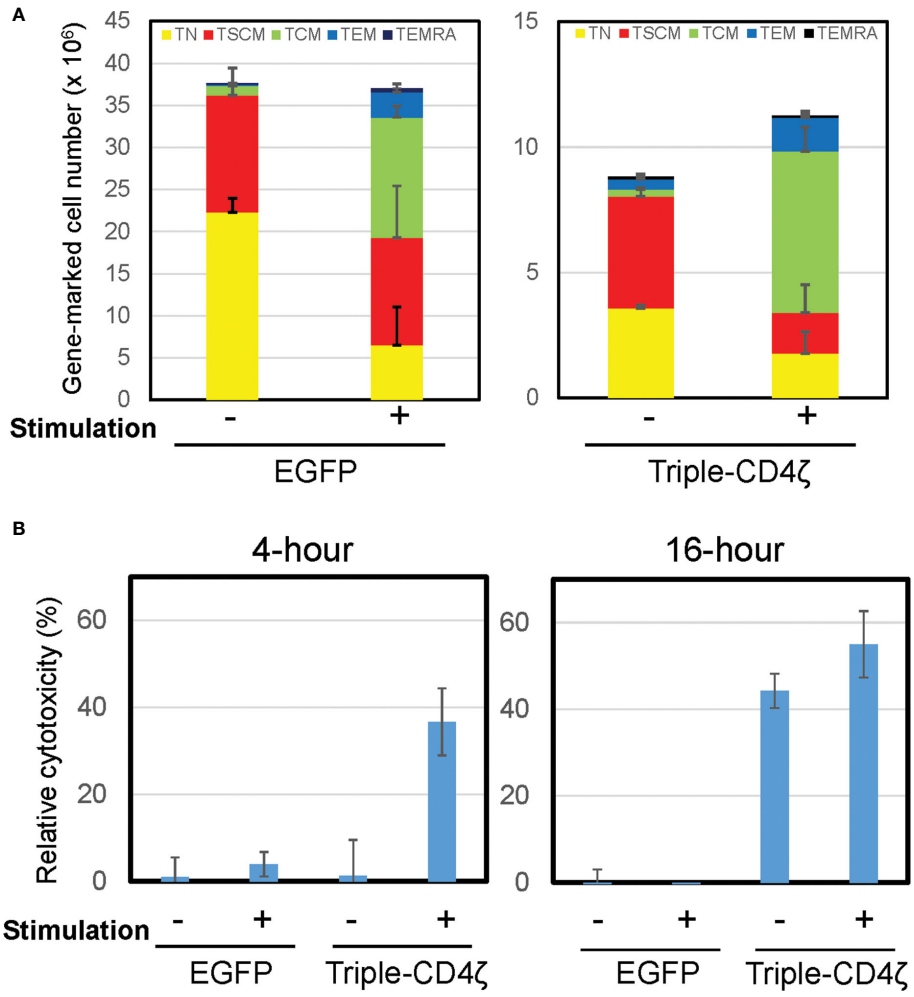

FIGURE 3
Induced differentiation of Triple-CD4ζ modified CD8+ T cells harboring T_{SCM}-surface phenotype with anti-CD3 and CD28 co-stimulation. **(A)** Triple-CD4ζ or EGFP-modified CD8+ T cells were co-stimulated with 0.5 μg/mL of anti-CD3 and 2.0 μg/mL of CD28 antibodies for 2 days (2^{nd} stimulation) at day14 post-1^{st} stimulation. The cells were further cultured for an additional 12 days in the presence of 5 ng/mL of IL-7 and IL-15. Cell-surface profiles of gene-marked CD8+ T cells were analyzed by flow cytometry. Each cell number of EGFP- or Triple-CD4ζ-marked cells with T_N, T_{SCM}, T_{CM}, T_{EM}, and T_{EMRA} phenotypes was plotted with or without 2^{nd} stimulation. Experiments were repeated three times. Error bars show the standard deviation of a data set. **(B)** The cells were plated at 5 x 10^4 cells/100 μL in a 96-well plate. The same number of TagBFP-labeled Jurkat cells (ΔKS, non-target control) and mCherry-labeled Jurkat cells constitutively expressing HIV-1_{HXBC2} envelope protein (HXBC2, target cells) were added to the wells and incubated for 4 or 16 hours. Total numbers of each population were determined by MACSQuant, and relative cytotoxicity of target cells relative to non-target cells was determined. -: unstimulated, +: 2^{nd} stimulated. Experiments were repeated three times. Error bars show the standard deviation of a data set. Cytotoxicity assays were performed in biological triplicate.

4-hour and 16-hour incubations with the target cells (Supplementary Figure 5). A 4-hour incubation was sufficient for the induction of cytotoxic activity by the pre-differentiated cells transduced with Triple-CD4ζ, whereas a 16-hour incubation was required to achieve a similar level of cytotoxicity without pre-differentiation, indicating that longer incubation was required to exert an effector activity for undifferentiated Triple-CD4ζ-modified CD8+ T cells.

Additionally, we generated anti-CD19 (FMC63-IgG4ζ) modified CD8+ T cells using the same conditions as above (Supplementary Figure 6). The level of gene marking by FMC63-IgG4ζ was similarly lower than control vector as seen with Triple-CD4ζ. FMC63-IgG4ζ-modified cells also maintained high levels of expression for T_{SCM} cell markers, and a large portion of the cells harbored T_N- and T_{SCM}-surface phenotypes. Similar to Triple-CD4ζ modified-CD8+ T cells, FMC63-IgG4ζ-modified cells also exerted a potent antigen dependent cytotoxicity following 16, but not 4, hours of incubation.

Triple-CD4ζ CAR-modified CD8+ T cells generated with sole anti-CD3 antibody stimulation exert antigen-specific effector functions in a xenograft NOD-SCID mouse model

As above, CD8+ CAR-T cells carrying the T_{SCM}-surface phenotype were generated *in vitro* with an antigen-specific effector activity. We next tested their effector activity *in vivo* using a xenograft NOD-SCID mouse model. NOD-SCID mice were engrafted with two different lymphoma cell lines: TF228.1.16 —— a derivative of BJAB (29) or HXBC2 —— a derivative of Jurkat (28). These lines express envelope protein from either the HIV-1_{BH10} or HIV-1_{HXBC2} strains, respectively. *In vitro*, the TF228.1.16 cells were killed by Triple-CD4ζ-modified CD8+ T cells like the HXBC2 cells, but relatively weakly by FMC63-IgG4ζ-modified CD8+ T cells. Although TF228.1.16 is CD19+ and can be a target for FMC63-IgG4ζ-modified CD8+ T cells *in vitro* (Supplementary Figure 7), our FMC63-IgG4ζ construct contains an IgG hinge-CH2-CH3 domain, which makes ineffective this CAR *in vivo* due to an Fcγ receptor 1 mediated CAR-T cell elimination (43–46). Thus, the FMC63-IgG4ζ serves as negative control. Those two tumor cells were genetically marked by mStrawberry (TF228.1.16) or mCherry (HXBC2), and subcutaneously engrafted into the left and right hind limbs of NOD-SCID mice, respectively. We confirmed that the expression levels of HIV-1 envelope proteins in tumor tissues developed in xenograft mice were similar to those in cells maintained *in vitro* by western blotting using anti-GP120 (2G12) and anti-GP41 (2F5) antibodies (data not shown).

At 14 days post-engraftment, we infused CD8+ T cells engineered with either Triple-CD4ζ CAR or FMC63-IgG4ζ CAR derived as above. We analyzed these CAR-dependent effector activities by bioimaging using a Maestro 2 multispectral imaging system (Figure 4). As expected, we observed poor *in vivo* effector activity of the cells modified by FMC63-IgG4ζ CAR. On the other hand, the cells modified by Triple-CD4ζ CAR showed stronger anti-tumor effector activity against both tumors, with tumor burdens decreasing approximately 1.9-fold for TF228.1.16 tumors (blue bars, Figure 4B) and 5.5-fold for HXBC2 tumors (orange bars, Figure 4B). Compared to HXBC2 tumor, the effector activity on TF228.1.16 tumor was weaker with no statistical significance; this may be due to the faster growth rate of TF228.1.16 cells. These results provide additional evidence that our simplified protocol allows for the derivation of CAR-modified CD8+ T cells harboring T_{SCM}-surface phenotype while maintaining antigen-specific effector activity *in vivo*.

Discussion

Though there is currently no standardized protocol for CAR-T_{SCM} cell manufacturing, the use of CAR-T_{SCM} products represents a promising approach for improving the outcome of CAR-T based therapies. Here, we refined the protocol for the derivation of CAR-modified CD8+ T cells harboring T_{SCM}-surface phenotype and T_{SCM}-like oligopotency.

The first key to generating CAR-T_{SCM}-like cells is the purification of CD8+ T_N cells as a starting population. Flow-cytometry based cell sorting is commonly used to isolate this population, but has 2 major drawbacks: decreased cell viability (47, 48), and the potential for sorting antibodies to induce unwanted activation *via* binding to T_N cell surface markers. By this reasoning, negative selection may be more effective for isolating T_N populations because these processes leave the cells 'untouched' and also without any antibodies remaining bound to the cells in the final product. By using an EasySep™ Human Naïve CD8+ T Cell Enrichment Kit which enables negative selection of CD8+ T_N cells, we consistently obtained CD8+ T_N cells with >95% purity (Supplementary Figure 1).

Next, we evaluated the utility of different stimulation conditions for generating gene-modified T_{SCM}-like CD8+ T cells and found that stimulation with only soluble anti-CD3 antibody in the presence of IL-7 and IL-15 was the most efficient. Since this condition does not require the use of novel agents, it is readily translatable for clinical applications. Cieri *et al.* also tested a stimulation condition with only anti-CD3 antibody for expansion of cells with a CD8+/CD45RA+/CD62L+/CD95- phenotype, but this attempt was unsuccessful (19). There were several differences compared to our protocol; they used a different anti-CD3 antibody clone —— OKT3 —— at >16-times lower concentration (30 ng/mL) in a plate-bound format. With this condition, they observed a poor expansion of CD8+ T_N cells compared to the cells co-stimulated with anti-CD3/

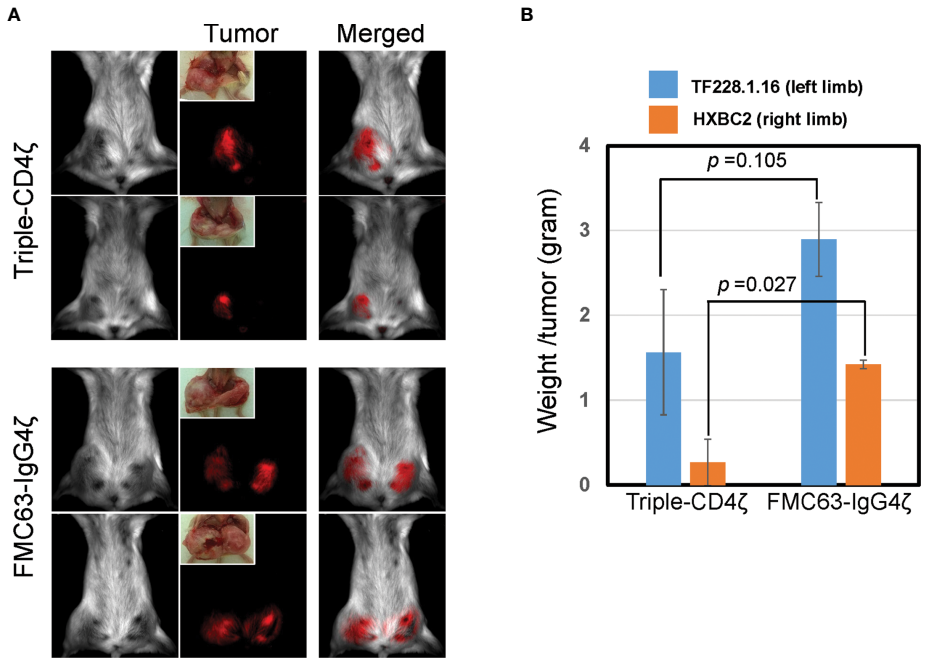

FIGURE 4
Triple-CD4ζ CAR-modified CD8+ T cells harboring T_{SCM}-surface phenotype eliminate tumor cells expressing HIV-1 envelope proteins in a xenograft mouse model. Two million mStrawberry-labeled CD19+ TF228.1.16 cells expressing envelope protein from HIV-1_{BH10} or mCherry-labeled Jurkat cells expressing envelope protein from HIV-1_{HXBC2} (HXBC2), were mixed with Matrigel at a 1:1 ratio and subcutaneously engrafted to the left or right hind limbs of NOD-SCID mice from ventral side, respectively (n = 4). Freshly isolated CD8+ T_N cells were stimulated for 2 days with 0.5 µg/mL of anti-CD3 antibody in T-cell medium, followed by transduction with a lentiviral vector encoding either Triple-CD4ζ or FMC63-IgG4ζ. Following 26 days of culture in the presence of 5 ng/mL of IL-7 and IL-15, cells corresponding to 5 x 10^5 CAR-modified cells were intravenously injected *via* the retro-orbital vein on day 14 post-engraftment of TF228.1.16 and HXBC2. Biofluorescence images **(A)** and the weight of xenograft tumors **(B)** were obtained on day 42 post-engraftment (on day 28 post-transplant of CAR cells). **(B)** Blue or orange bars: average weight of xenograft tumors from TF228.1.16 (left limb, blue bars) or HXBC2 (right limb, orange bars) on day 42 post-engraftment. Experiments were repeated three times with similar results. Two representative animals from each group were shown.

CD28 antibody coated beads. Surprisingly, most of the cells lost expression of CD45RA and CD62L after 16 days of culture with their experimental conditions (19). We did not observe this by the use of soluble form of anti-CD3 antibody, suggesting that the precoated anti-CD3 antibodies probably induced a stronger stimulation *via* TCR crosslinking, resulting in T-cell differentiation.

Whereas both CD4+ and CD8+ T cells are needed for an efficient CAR-T cell therapy (49–51); the former mainly serve as CAR-dependent helper cells and the latter as CAR-dependent effector cells (52). We have already adopted the derivation of CAR-modified CD4+ T_{SCM} cells by the use of EasySep Human Naive CD4+ T cell Isolation kit, which enables negative selection of CD4+ T_N cells (Stemcell technologies, #19555). Unlike CD8+ T_N cells, CD4+ T_N cells required co-stimulation by soluble forms of anti-CD3 (1.0 µg/mL) and anti-CD28 (0.1 µg/mL) antibodies for an efficient expansion of cells with T_{SCM}-surface phenotype (data not shown). The level of gene marking as well as oligopotential activity of CAR-engineered CD4+ T_{SCM} cells were similarly reproduced as those confirmed in CAR-engineered CD8+ T_{SCM} cells. We are currently validating the effector activity of CAR-engineered CD4+ T cells as well as seeking to derivate CAR-engineered T_{SCM} cells from negatively selected naive Pan-T cells using EasySep Human Naive Pan T cell Isolation kit (Stemcell technology, #17961) without pre-separating CD4+ or CD8+ T_N cells. We believe that these approaches will enable more efficient and reproducible procedures for the manufacturing of highly effective CAR-T cells.

CAR-modified CD8+ T cells harboring T_{SCM}-surface phenotype required longer incubation to exert CAR-dependent effector activity compared to the pre-differentiated cells (16 hours *vs* 4 hours, Figures 3B and Supplementary Figure 6B). The pre-differentiated cells consisted of more differentiated cells, which have potent cytotoxicity than cells harboring T_{SCM} cell phenotype. We also confirmed that 16 hours of incubation was not sufficient to fully induce differentiation of the cells with T_{SCM}-surface phenotype to cells with differentiated phenotypes, such as T_{CM} or T_{EM} (Supplementary Figure 5). We thus expected the cells derived with our protocol to have less effector activity

than those with differentiated phenotypes, and to require longer incubation before acquiring cytotoxicity. These possibilities are currently under investigation.

In recent years, immunotherapy utilizing CAR-engineered T cells has become a highly promising approach, especially for the treatment of blood cancers. T_{SCM} cells have the capacity for both self-renewal and oligopotent differentiation into effector cells upon encounter with antigens; thus, T_{SCM} cells re-directed against their targets could be more effective than mature T cells employed in current clinical trials. Due to the low frequency of T_{SCM} cells in peripheral blood, establishing techniques for efficient expansion with high levels of gene modification will be important for translation to clinical purposes. Our protocol described here is applicable for a prompt implementation of T_{SCM} cell-based immunotherapies against not only cancer but also infectious diseases such as AIDS.

Data availability statement

The raw data supporting the conclusions of this article will be made available by the authors, without undue reservation.

Ethics statement

The animal study was reviewed and approved by Guido Eibl, UCLA.

Author contributions

EK, CJK, wrote the paper. EK, JC, and PYK performed the experiments. ISY, interpreted data. MK designed the research, performed the experiments, analyzed data, interpreted data, and wrote the paper. All authors contributed to the article and approved the submitted version.

Funding

This work was supported by the California HIV/AIDS Research Grants Program ID13-LA-563 (M.K.), NIH grants R01AI110200 (MK), and RO1 CA232015 (MK). The following reagents were obtained through the NIH AIDS Reagent Program, Division of AIDS, NIAID, NIH: BCBL-1 (Drs. Michael McGrath and Don Ganem), Jurkat-ΔKS and Jurkat-HXBC2 (4) (Dr. Joseph Sodroski), and TF228.1.16 (Drs. Zdenka Jonak and Steve Trulli). Maestro 2 multispectral imaging system was performed at the CNSI Advanced Light Microscopy/Spectroscopy Shared Resource Facility at UCLA, supported by NIH-NCRR shared resources grant (CJX1-443835-WS-29646) and NSF Major Research Instrumentation grant (CHE-0722519).

Conflict of interest

The authors declare that the research was conducted in the absence of any commercial or financial relationships that could be construed as a potential conflict of interest.

Publisher's note

All claims expressed in this article are solely those of the authors and do not necessarily represent those of their affiliated organizations, or those of the publisher, the editors and the reviewers. Any product that may be evaluated in this article, or claim that may be made by its manufacturer, is not guaranteed or endorsed by the publisher.

Supplementary material

The Supplementary Material for this article can be found online at: https://www.frontiersin.org/articles/10.3389/fimmu.2022.877682/full#supplementary-material

References

1. Wilkie S, van Schalkwyk MC, Hobbs S, Davies DM, van der Stegen SJ, Pereira AC, et al. Dual targeting of ErbB2 and MUC1 in breast cancer using chimeric antigen receptors engineered to provide complementary signaling. *J Clin Immunol* (2012) 32:1059–70. doi: 10.1007/s10875-012-9689-9

2. June CH. Adoptive T cell therapy for cancer in the clinic. *J Clin Invest* (2007) 117:1466–76. doi: 10.1172/JCI32446

3. Gattinoni L, Powell DJJr., Rosenberg SA, Restifo NP. Adoptive immunotherapy for cancer: building on success. *Nat Rev Immunol* (2006) 6:383–93. doi: 10.1038/nri1842

4. Gill S, Maus MV, Porter DL. Chimeric antigen receptor T cell therapy: 25years in the making. *Blood Rev* (2016) 30:157–67. doi: 10.1016/j.blre.2015.10.003

5. Lindner SE, Johnson SM, Brown CE, Wang LD. Chimeric antigen receptor signaling: Functional consequences and design implications. *Sci Adv* (2020) 6: eaaz3223. doi: 10.1126/sciadv.aaz3223

6. Cappell KM, Kochenderfer JN. A comparison of chimeric antigen receptors containing CD28 versus 4-1BB costimulatory domains. *Nat Rev Clin Oncol* (2021) 18:715–27. doi: 10.1038/s41571-021-00530-z

7. Porter DL, Hwang WT, Frey NV, Lacey SF, Shaw PA, Loren AW, et al. Chimeric antigen receptor T cells persist and induce sustained remissions in relapsed refractory chronic lymphocytic leukemia. *Sci Transl Med* (2015) 7:303ra139. doi: 10.1126/scitranslmed.aac5415

8. Maude SL, Frey N, Shaw PA, Aplenc R, Barrett DM, Bunin NJ, et al. Chimeric antigen receptor T cells for sustained remissions in leukemia. *N Engl J Med* (2014) 371:1507–17. doi: 10.1056/NEJMoa1407222

9. Kochenderfer JN, Dudley ME, Feldman SA, Wilson WH, Spaner DE, Maric I, et al. B-cell depletion and remissions of malignancy along with cytokine-associated toxicity in a clinical trial of anti-CD19 chimeric-antigen-receptor-transduced T cells. *Blood* (2012) 119:2709–20. doi: 10.1182/blood-2011-10-384388

10. Kochenderfer JN, Dudley ME, Kassim SH, Somerville RP, Carpenter RO, Stetler-Stevenson M, et al. Chemotherapy-refractory diffuse large b-cell lymphoma and indolent b-cell malignancies can be effectively treated with autologous T cells expressing an anti-CD19 chimeric antigen receptor. *J Clin Oncol* (2015) 33:540–9. doi: 10.1200/JCO.2014.56.2025

11. Mitsuyasu R, Anton P, Deeks S, Scadden D, Connick E, Downs M, et al. Prolonged survival and tissue trafficking following adoptive transfer of CD4zeta gene-modified autologous CD4(+) and CD8(+) T cells in human immunodeficiency virus-infected subjects. *Blood* (2000) 96:785–93. doi: 10.1182/blood.V96.3.785.015k10_785_793

12. Deeks S, Wagner B, Anton P, Mitsuyasu R, Scadden D, Huang C, et al. A phase II randomized study of HIV-specific T-cell gene therapy in subjects with undetectable plasma viremia on combination antiretroviral therapy. *Mol Ther* (2002) 5:788–97. doi: 10.1006/mthe.2002.0611

13. Mitsuyasu R, Zack J, Macpherson J, Symonds G. Phase I/II clinical trials using gene-modified adult hematopoietic stem cells for HIV: Lessons learnt. *Stem Cells Int* (2011). vol. 2011, 393698–705. doi: 10.4061/2011/393698

14. Scholler J, Brady T, Binder-Scholl G, Hwang W, Plesa G, Hege K, et al. Decade-long safety and function of retroviral-modified chimeric antigen receptor T cells. *Sci Trans Med* (2012) 4:132ra53. doi: 10.1126/scitranslmed.3003761

15. Gattinoni L, Zhong XS, Palmer DC, Ji Y, Hinrichs CS, Yu Z, et al. Wnt signaling arrests effector T cell differentiation and generates CD8+ memory stem cells. *Nat Med* (2009) 15:808–13. doi: 10.1038/nm.1982

16. Lugli E, Dominguez M, Gattinoni L, Chattopadhyay P, Bolton D, Song K, et al. Superior T memory stem cell persistence supports long-lived T cell memory. *J Clin Invest* (2013) 123:594–9. doi: 10.1172/JCI66327

17. Lugli E, Gattinoni L, Roberto A, Mavilio D, Price D, Restifo N, et al. Identification, isolation and *in vitro* expansion of human and nonhuman primate T stem cell memory cells. *Nat Protocol* (2013) 8:33–42. doi: 10.1038/nprot.2012.143

18. Gattinoni L, Lugli E, Ji Y, Pos Z, Paulos C, Quigley M, et al. A human memory T cell subset with stem cell-like properties. *Nat Med* (2011) 17:1290–7. doi: 10.1038/nm.2446

19. Cieri N, Camisa B, Cocchiarella F, Forcato M, Oliveira G, Provasi E, et al. IL-7 and IL-15 instruct the generation of human memory stem T cells from naive precursors. *Blood* (2013) 121:573–84. doi: 10.1182/blood-2012-05-431718

20. Li Y, Wu D, Yang X, Zhou S. Immunotherapeutic potential of T memory stem cells. *Front Oncol* (2021) 11:723888. doi: 10.3389/fonc.2021.723888

21. Costa Del Amo P, Lahoz-Beneytez J, Boelen L, Ahmed R, Miners KL, Zhang Y, et al. Human TSCM cell dynamics *in vivo* are compatible with long-lived immunological memory and stemness. *PloS Biol* (2018) 16:e2005523. doi: 10.1371/journal.pbio.2005523

22. Gattinoni L, Restifo N. Moving T memory stem cells to the clinic. *Blood* (2013) 121:567–8. doi: 10.1182/blood-2012-11-468660

23. Gattinoni L, Speiser DE, Lichterfeld M, Bonini C. T Memory stem cells in health and disease. *Nat Med* (2017) 23:18–27. doi: 10.1038/nm.4241

24. Henning AN, Klebanoff CA, Restifo NP. Silencing stemness in T cell differentiation. *Science* (2018) 359:163–4. doi: 10.1126/science.aar5541

25. Biasco L, Scala S, Basso Ricci L, Dionisio F, Baricordi C, Calabria A, et al. *In vivo* tracking of T cells in humans unveils decade-long survival and activity of genetically modified T memory stem cells. *Sci Transl Med* (2015) 7:273ra13. doi: 10.1126/scitranslmed.3010314

26. Biasco L, Izotova N, Rivat C, Ghorashian S, Richardson R, Guvenel A, et al. Clonal expansion of T memory stem cells determines early anti-leukemic responses and long-term CAR T cell persistence in patients. *Nat Cancer* (2021) 2:629–42. doi: 10.1038/s43018-021-00207-7

27. Kamata M, Kim P, Ng H, Ringpis G, Kranz E, Chan J, et al. Ectopic expression of anti-HIV-1 shRNAs protects CD8+ T cells modified with CD4ζ CAR from HIV-1 infection and alleviates impairment of cell proliferation. *Biochem Biophys Res Commun* (2015) 463:216–21. doi: 10.1016/j.bbrc.2015.05.026

28. Cao J, Park IW, Cooper A, Sodroski J. Molecular determinants of acute single-cell lysis by human immunodeficiency virus type 1. *J Virol* (1996) 70:1340–54. doi: 10.1128/jvi.70.3.1340-1354.1996

29. Jonak ZL, Clark RK, Matour D, Trulli S, Craig R, Henri E, et al. A human lymphoid recombinant cell line with functional human immunodeficiency virus type 1 envelope. *AIDS Res Hum Retroviruses* (1993) 9:23–32. doi: 10.1089/aid.1993.9.23

30. Subach OM, Gundorov IS, Yoshimura M, Subach FV, Zhang J, Gruenwald D, et al. Conversion of red fluorescent protein into a bright blue probe. *Chem Biol* (2008) 15:1116–24. doi: 10.1016/j.chembiol.2008.08.006

31. Shaner N, Campbell R, Steinbach P, Giepmans B, Palmer A, Tsien R. Improved monomeric red, orange and yellow fluorescent proteins derived from discosoma sp. red fluorescent protein. *Nat Biotechnol* (2004) 22:1524–5. doi: 10.1038/nbt1037

32. Kochenderfer JN, Feldman SA, Zhao Y, Xu H, Black MA, Morgan RA, et al. Construction and preclinical evaluation of an anti-CD19 chimeric antigen receptor. *J Immunother* (2009) 32:689–702. doi: 10.1097/CJI.0b013e3181ac6138

33. Renne R, Zhong W, Herndier B, McGrath M, Abbey N, Kedes D, et al. Lytic growth of kaposi's sarcoma-associated herpesvirus (human herpesvirus 8) in culture. *Nat Med* (1996) 2:342–6. doi: 10.1038/nm0396-342

34. Ringpis G, Shimizu S, Arokium H, Camba-Colón J, Carroll M, Cortado R, et al. Engineering HIV-1-resistant T-cells from short-hairpin RNA-expressing hematopoietic stem/progenitor cells in humanized BLT mice. *PloS One* (2012) 7:e53492. doi: 10.1371/journal.pone.0053492

35. Kamata M, Nagaoka Y, Chen I. Reassessing the role of APOBEC3G in human immunodeficiency virus type 1 infection of quiescent CD4+ T-cells. *PloS Pathog* (2009) 5:1000342. doi: 10.1371/journal.ppat.1000342

36. Schroeder JH, Bell LS, Janas ML, Turner M. Pharmacological inhibition of glycogen synthase kinase 3 regulates T cell development *in vitro*. *PloS One* (2013) 8:e58501. doi: 10.1371/journal.pone.0058501

37. Brinkman CC, Rouhani SJ, Srinivasan N, Engelhard VH. Peripheral tissue homing receptors enable T cell entry into lymph nodes and affect the anatomical distribution of memory cells. *J Immunol* (2013) 191:2412–25. doi: 10.4049/jimmunol.1300651

38. Butcher EC, Picker LJ. Lymphocyte homing and homeostasis. *Science* (1996) 272:60–6. doi: 10.1126/science.272.5258.60

39. Gunn MD, Kyuwa S, Tam C, Kakiuchi T, Matsuzawa A, Williams LT, et al. Mice lacking expression of secondary lymphoid organ chemokine have defects in lymphocyte homing and dendritic cell localization. *J Exp Med* (1999) 189:451–60. doi: 10.1084/jem.189.3.451

40. An D, Donahue R, Kamata M, Poon B, Metzger M, Mao S, et al. Stable reduction of CCR5 by RNAi through hematopoietic stem cell transplant in non-human primates. *Proc Natl Acad Sci U S A.* (2007) 104:13110–5. doi: 10.1073/pnas.0705474104

41. Zhen A, Kamata M, Rezek V, Rick J, Levin B, Kasparian S, et al. HIV-Specific immunity derived from chimeric antigen receptor-engineered stem cells. *Mol Ther* (2015) 23:1358–67. doi: 10.1038/mt.2015.102

42. N. al Yacoub M, Haritonova N. And j. foerster, optimized production and concentration of lentiviral vectors containing large inserts. *J Gene Med* (2007) 9:579–84. doi: 10.1002/jgm.1052

43. Hudecek M, Sommermeyer D, Kosasih PL, Silva-Benedict A, Liu L, Rader C, et al. The nonsignaling extracellular spacer domain of chimeric antigen receptors is decisive for *in vivo* antitumor activity. *Cancer Immunol Res* (2015) 3:125–35. doi: 10.1158/2326-6066.CIR-14-0127

44. Jonnalagadda M, Mardiros A, Urak R, Wang X, Hoffman LJ, Bernanke A, et al. Chimeric antigen receptors with mutated IgG4 fc spacer avoid fc receptor binding and improve T cell persistence and antitumor efficacy. *Mol Ther* (2015) 23:757–68. doi: 10.1038/mt.2014.208

45. Almasbak H, Walseng E, Kristian A, Myhre MR, Suso EM, Munthe LA, et al. Inclusion of an IgG1-fc spacer abrogates efficacy of CD19 CAR T cells in a xenograft mouse model. *Gene Ther* (2015) 22:391–403. doi: 10.1038/gt.2015.4

46. Hombach A, Hombach AA, Abken H. Adoptive immunotherapy with genetically engineered T cells: modification of the IgG1 fc 'spacer' domain in the extracellular moiety of chimeric antigen receptors avoids 'off-target' activation and unintended initiation of an innate immune response. *Gene Ther* (2010) 17:1206–13. doi: 10.1038/gt.2010.91

47. M. al-Rubeai AN, Chalder S. And M.H. Goldman, a flow cytometric study of hydrodynamic damage to mammalian cells. *J Biotechnol* (1993) 31:161–77. doi: 10.1016/0168-1656(93)90158-J

48. Tomlinson MJ, Tomlinson S, Yang XB, Kirkham J. Cell separation: Terminology and practical considerations. *J Tissue Eng* (2013) 4:2041731412472690. doi: 10.1177/2041731412472690

49. Turtle CJ, Hanafi LA, Berger C, Gooley TA, Cherian S, Hudecek M, et al. CD19 CAR-T cells of defined CD4+:CD8+ composition in adult b cell ALL patients. *J Clin Invest* (2016) 126:2123–38. doi: 10.1172/JCI85309

50. Shah NN, Highfill SL, Shalabi H, Yates B, Jin J, Wolters PL, et al. CD4/CD8 T-cell selection affects chimeric antigen receptor (CAR) T-cell potency and toxicity: Updated results from a phase I anti-CD22 CAR T-cell trial. *J Clin Oncol* (2020) 38:1938–50. doi: 10.1200/JCO.19.03279

51. Zhang H, Zhao P, Huang H. Engineering better chimeric antigen receptor T cells. *Exp Hematol Oncol* (2020) 9:34. doi: 10.1186/s40164-020-00190-2

52. Chmielewski M, Rappl G, Hombach AA, Abken H. T Cells redirected by a CD3zeta chimeric antigen receptor can establish self-antigen-specific tumour protection in the long term. *Gene Ther* (2013) 20:177–86. doi: 10.1038/gt.2012.21

frontiers | Frontiers in Immunology

TYPE Original Research
PUBLISHED 09 August 2022
DOI 10.3389/fimmu.2022.890263

OPEN ACCESS

EDITED BY
Pierre Roques,
CEA Saclay, France

REVIEWED BY
Uladzimir Karniychuk,
University of Saskatchewan, Canada
Pero Lucin,
University of Rijeka, Croatia
Qingtao Liu,
Jiangsu Academy of Agricultural Sciences, China

*CORRESPONDENCE
Dabing Zhang
zdb@cau.edu.cn

SPECIALTY SECTION
This article was submitted to Viral Immunology, a section of the journal Frontiers in Immunology

RECEIVED 05 March 2022
ACCEPTED 20 July 2022
PUBLISHED 09 August 2022

CITATION
Meng R, Yang B, Feng C, Huang J, Wang X and Zhang D (2022) The difference in CD4$^+$ T cell immunity between high- and low-virulence Tembusu viruses is mainly related to residues 151 and 304 in the envelope protein.
Front. Immunol. 13:890263.
doi: 10.3389/fimmu.2022.890263

The difference in CD4$^+$ T cell immunity between high- and low-virulence Tembusu viruses is mainly related to residues 151 and 304 in the envelope protein

Runze Meng, Baolin Yang, Chonglun Feng, Jingjing Huang, Xiaoyan Wang and Dabing Zhang*

Key Laboratory of Animal Epidemiology of the Ministry of Agriculture, College of Veterinary Medicine, China Agricultural University, Beijing, China

Tembusu virus (TMUV) can result in a severe disease affecting domestic ducks. The role of T cells in protection from TMUV infection and the molecular basis of T cell-mediated protection against TMUV remain largely uncharacterized. Here, we used the high-virulence TMUV strain Y and the low-virulence TMUV strain PS to investigate the protective role for TMUV-specific CD4$^+$ and CD8$^+$ T cells. When tested in a 5-day-old Pekin duck model, Y and PS induced comparable levels of neutralizing antibody, whereas Y elicited significantly stronger cellular immune response relative to PS. Using a duck adoptive transfer model, we showed that both CD4$^+$ and CD8$^+$ T cells provided significant protection from TMUV-related disease, with CD8$^+$ T cell conferring more robust protection to recipient ducklings. For TMUV, CD4$^+$ T cells mainly provided help for neutralizing antibody response, whereas CD8$^+$ T cells mainly mediated viral clearance from infected tissues. The difference in T cell immunity between Y and PS was primarily attributed to CD4$^+$ T cells; adoptive transfer of Y-specific CD4$^+$ T cells resulted in significantly enhanced protective ability, neutralizing antibody response, and viral clearance from the brain relative to PS-specific CD4$^+$ T cells. Further investigations with chimeric viruses, mutant viruses, and their parental viruses identified two mutations (T151A and R304M) in the envelope (E) protein that contributed significantly to TMUV-specific CD4$^+$ T cell-mediated protective ability and neutralizing antibody response, with more beneficial effects being conferred by R304M. These data indicate T cell-mediated immunity is important for protection from disease, for viral clearance from tissues, and for the production of neutralizing antibodies, and that the difference in CD4$^+$T cell immunity between high- and low-virulence TMUV strains is primarily related to residues 151 and 304 in the E protein.

KEYWORDS

Tembusu virus, virulence, cellular immune response, CD4$^+$ T cell immunity, CD8$^+$ T cell immunity

Introduction

Tembusu virus (TMUV) is an enveloped mosquito-borne flavivirus with a positive-sense, single-stranded RNA genome of approximately 11 kb. The RNA genome contains one large open reading frame (ORF), which is preceded by a 5' untranslated region (UTR) and followed by a 3' UTR. The ORF encodes ten polypeptides: three structural proteins [(capsid (C), precursor of membrane (prM), and envelope (E)] that form the viral particle and seven nonstructural proteins (NS1, NS2A, NS2B, NS3, NS4A, NS4B, and NS5) that are required for viral replication (1, 2).

TMUV can cause an acute infectious disease affecting ducks, which is of economic importance to all breeder duck farms, layer duck farms, and duck-growing farms (3–6). Affected ducks below 7 weeks of age develop signs of encephalitis consisting of ataxia, reluctance to walk, lameness, and paralysis (1, 4–7). Therefore, TMUV can be regarded as an encephalitic flavivirus. Experimental infections of Pekin ducklings (*Anas platyrhynchos domesticus*) less than 7 weeks of age have shown that the severity of TMUV-caused disease is associated with multiple factors, such as the age of birds, the route of application, the strain of virus, and the infectivity titer. In ducklings less than 9 days of age, TMUV generally causes fatal infection, with mortality ranging from 18% to 100% (1, 6, 8–11).

A better understanding of TMUV-induced adaptive immune response is crucial for the control of the TMUV-related disease. Through the use of plaque reduction neutralization test (PRNT), TMUV has been shown to elicit high, long-lasting neutralizing antibodies after natural infection and vaccination with attenuated vaccine (12). Previous works with E or prM/E-based subunit vaccine (13–16), DNA vaccine (17–19), and live vector vaccine (18–25) have demonstrated that the TMUV E and prM/E proteins induce neutralizing antibodies. The importance of E protein residue 408 in regulation of neutralizing antibodies has been highlighted by a recent investigation into attenuation-induced loss of immunogenicity (26). The C protein expressed by DNA vaccine was also shown to induce neutralizing antibodies (27).

Using duck models of TMUV infection, the TMUV-induced cellular immune response is beginning to be understood. TMUV induces significant up-regulation of IL-2 and IFN-γ at 7 days post infection (pi) (9, 28), and significant increases in numbers of $CD4^+$ and $CD8^+$ T cells at 5 days pi (29). The E, prM/E, and C proteins were shown to induce cellular immune response by measurement of the expression of cytokines (e.g., IL-2, IL-4, IL-6, IFN-γ, and TNF-α) or the change of $CD4^+$ and $CD8^+$ T cell numbers in ducks following immunization with subunit vaccine, DNA vaccine, and live vector vaccine (13, 14, 17, 19, 20, 22, 27).

To date, the role of T cells in protection from TMUV infection and the molecular basis of T cell-mediated protection against TMUV remain largely uncharacterized. Earlier works in our laboratory showed that the natural isolate Y and the plaque-purified strain PS, which exhibited distinct virulence in a 2-day-old Pekin duckling model, elicited comparable levels of neutralizing antibody (11). In this study, we describe the comparative studies on cellular immune responses to Y and PS. Our studies indicate that marked differences in inducing T cell responses exist between Y and PS. On this basis, the molecular determinants responsible for the differences in cellular immune responses observed between Y and PS are described.

Materials and methods

Ducks and cells

Newly hatched Pekin ducklings were derived from Peking duck breeding farm, Institute of Animal Sciences, Chinese Academy of Agricultural Sciences, Beijing, China. Their parents had never received TMUV vaccine. All ducklings were confirmed to be free of TMUV infection by testing serum samples using PRNT for antibodies to TMUV (12) and TMUV-specific real-time quantitative PCR (RT-qPCR) for viral RNA (30). In all cases, ducks in each group were reared separately in different isolators. BHK-21 cells were maintained at 37°C in Dulbecco's modified Eagle's medium (DMEM; Macgene, Beijing, China) supplemented with 10% fetal bovine serum (FBS; Macgene, Beijing, China), 100 U/ml penicillin, and 0.1 mg/ml streptomycin.

Viruses

The BHK-21 cell-derived Y and PS strains of TMUV were isolated and propagated previously, which were shown to display high- and low-virulence for 2-day-old Pekin ducklings respectively (11). Parental backbone viruses rY and rPS were rescued from the full-length cDNAs of Y and PS respectively. Chimeric viruses rPS-YE with the Y entire E gene and rPS-YNS1-3'UTR with the Y NS1-3'UTR region as well as mutant viruses R38K, T151A, and R304M that have K38, A151, and M304 of the E protein of strain Y, respectively, were generated in the backbone of the rPS genome (Supplementary Figure 1). Information relating to the generation of these viruses were described previously (11). Stock viral titers were determined by plaque assay in BHK-21 cells as described previously (12) and are expressed as plaque forming unit (PFU) per ml.

To obtain working stocks, viruses were propagated in BHK-21 cells as described previously (12). For strains Y and PS, working stocks were prepared by four passages in BHK-21 cells. Briefly, BHK-21 cells were infected with viruses at a multiplicity of infection (MOI) of 0.1 PFU/cell at 37°C for 1 h. The cells were washed three times with phosphate-buffered saline (PBS), and

maintenance medium consisting of DMEM supplemented with 2% FBS, 100 U/ml penicillin, and 0.1 mg/ml streptomycin was added. After incubation at 37°C for 60 h, the infected cell cultures were freeze-thawed three times and clarified by centrifugation and filtration.

Duck experiments

The first experiment was conducted to investigate the pathogenicity of strain Y in Pekin ducklings with different ages, employing strain PS as a control virus. A total of 140 newly hatched ducklings were divided into seven groups (n=20). When the ducklings grew to 3, 5, and 7 days of age, they were inoculated with virus by intramuscular (im) route at a dose of 2×10^3 PFU, respectively. The mock-infected control group received 0.2 ml of supernatant prepared from uninfected BHK-21 cells by im inoculation at 3 days of age. The ducklings were monitored for 15 days for mortality.

To systematically compare the virulence of Y and PS in 5-day-old Pekin ducklings, experimental infections were performed as described above. In each group (n=60), 20 ducklings were monitored for 15 days for signs of encephalitis and weight loss as well as mortality, and 40 ducklings were used for examination of gross lesions and sample collection. Signs of encephalitis were divided into 5-grade severities of no change, very mild, mild, moderate, and marked, giving scores 0, 1, 2, 3, and 4, respectively. The ducklings were weighed once every 2 days between 1 and 15 days pi. Three ducks were randomly selected from each group at 1, 3, 5, and 7 days pi, and sera and ethylenediamine tetraacetic acid (EDTA)-anticoagulated bloods were sampled for detection of viremia and counting of $CD4^+$ and $CD8^+$ T cells respectively. Subsequently, the selected ducks were euthanized, tissues (brain, spleen, and thymus) were collected for measurement of TMUV burden and expression of cytokines and T cell markers, and spleens were weighed. Tissues collected at 5 days pi were also used for examination of histopathological changes and viral antigens. At 9, 11, 13, and 15 days pi, serum samples of three ducks were collected from each group. These sera, together with those collected between 1 and 7 days pi, were used for detection of neutralizing antibodies. For isolation of Y- and PS-specific $CD4^+$ and $CD8^+$ T cells and naïve $CD4^+$ and $CD8^+$ T cells, the EDTA-anticoagulated blood samples were collected at 9 day pi from infected and uninfected ducklings.

To identify the protein associated with the difference in cellular immune response between Y and PS, chimeric viruses (rPS-YE and rPS-YNS1-3'UTR) and their parental viruses (rY and rPS) were used to infect 5-day-old ducklings (n=23) as described above. To identify the residues associated with the difference in cellular immune response between Y and PS, mutant viruses (R38K, T151A, and R304M) and their parental viruses (rY and rPS) were used to infect 5-day-old ducklings (n=23). In each case, a mock-infected control (n=23) was included, and tissues (brain and thymus) were sampled from three ducks in each group at 7 days pi for measurement of the expression of cytokines and T cell markers. For isolation of R38K-, T151A-, R304M-, rY-, and rPS-specific $CD4^+$ and $CD8^+$ T cells, the EDTA-anticoagulated blood samples were collected at 9 days pi from ducklings infected with mutant viruses and their parental viruses.

Quantitation of viral loads in tissue and serum samples

Viruses in the tissue and serum samples were quantified using a RT-qPCR assay targeting the E gene. The tissue samples were processed as 20% homogenates in PBS, followed by centrifugation at 10,000 g for 10 min. RNA was extracted from 250 µl of each supernatant or serum using a TRIpure reagent (Aidlab, Beijing, China) and reverse transcribed using a M-MLV Reverse Transcriptase kit (Promega, Madison, USA), according to the manufacturer's instructions. 5 µl of cDNA was mixed with 1 µl of each of forward and reverse primers [Table 1; (30)], 10 µl

TABLE 1 Primers used for measurement of TMUV RNA levels and expression of cellular immune-related genes in tissues of infected Pekin ducklings by RT-qPCR.

Target	Primer sequence (5′→3′)	Primer sequence (3′→5′)
TMUV E[a]	CGCTGAGATGGAGGATTATGG	ACTGATTGTTTGGTGGCGTG
Duck IL-2	TAGAAAACCTGGGAACAAGC	ATTTCTTCCTCCAAGGTGAC
Duck IL-17	TGCCTACGGGAAGGTGATAC	ATTGATGGGGATGGAGTTGA
Duck IFN-α	CCTCCCGCCAACGCCTTCTC	TGTGCGGCTTGCTGCGTGTC
Duck IFN-β	CGCAACCTTCACCTCAGCAT	TCTTCATCCGCCGTATTAGC
Duck IFN-γ	ACCTCGTGGAACTGTCAAAC	ACTGGCTCCTTTTCCTTTTG
Duck CD4	ATTTCAACGCCACAGCAGAT	CCCAGGAGGGTTAGCAGACA
Duck CD8	CCTGCTTGCTGCTTCTCATT	TTGGCACCTTGGGATTCATT
Duck GAPDH[b]	ATGAGAAGTATGACAAGTCC	ACTGTCTTCGTGTG TGGCT

[a]Reported previously (30).
[b]Reported previously (31).

of 2×AceQ qPCR SYBR Green Master Mix (Vazyme, Nanjing, China), and 3 µl of ddH_2O. The RT-qPCR was performed using the conditions reported previously (30).

Histopathological examination

The tissue samples were fixed in 4% formalin at room temperature for 24h. Five-µm-thick paraffin-embedded sections were prepared by a standard protocol (32). After staining with hematoxylin eosin (H & E), the sections were checked for histopathological changes under an Olympus microscope (Olympus, Tokyo, Japan).

Immunohistochemistry

Ten-µm-thick paraffin-embedded sections were prepared by a standard protocol (33). The sections were strained using mouse anti-TMUV E monoclonal antibody F3B4 (1:500 dilution in PBS) (34) and horseradish peroxidase (HRP)-conjugated goat anti-mouse IgG (1:500 dilution in PBS, Thermo Fisher Scientific, Shanghai, China). After counterstaining with hematoxylin, the sections were checked for viral antigen under an Olympus microscope (Olympus, Tokyo, Japan).

Neutralization assay

Neutralizing antibodies in sera were detected using a previously reported PRNT (12). First, serial 10-fold dilutions of each heat-inactivated (56°C for 30 min) sera were mixed with an equal volume of virus, and incubated at 37°C for 1 h. Second, BHK-21 cells were inoculated with the virus-serum mixture and incubated at 37°C in a CO_2 incubator 1 h for adsorption. Finally, the cell cultures were covered with overlay medium consisting of DMEM containing 1% low melting-point agarose (Macgene, Beijing, China) and 2% FBS, and the plaque assay was conducted. Antibody titer is expressed as 50% end point titer (neutralizing dose, ND_{50}).

Measurement of cytokine mRNA levels in tissues

RT-qPCR was applied to detect the expression of several cytokines, including interleukin 2 (IL-2), IL-17, gamma interferon (IFN-γ), and tumor necrosis factor-beta (TNF-β), and T cell markers, including CD4 and CD8. Sample processing, RNA extraction, and cDNA synthesis were the same as described above. 5 µl of cDNA was mixed with 1 µl of each of forward and reverse primers (Table 1) (31), 10 µl of 2×AceQ qPCR SYBR Green Master Mix (Vazyme, Nanjing, China), and 4.2 µl of ddH_2O. Duck glyceraldehyde-3-phosphate-dehydrogenase (GAPDH) was used as an endogenous control. RT-qPCR was performed for GAPDH and each cytokine and T cell marker as follows: 95°C for 5 min, followed by 40 cycles at 95°C for 10 s and 60°C for 30 s, and extension at 72° for 60s. Relative expression was calculated for each cytokine using a $2^{-\triangle\triangle ct}$ method (35).

Flow cytometry

Peripheral blood mononuclear cells (PBMCs) were isolated from the EDTA-anticoagulant blood samples (3ml/duck) using a duck lymphocyte isolation kit (P5720, Solarbio, Beijing, China), according to the manufacturer's instructions. Following sucrose density gradient centrifugation, PBMCs that were located in a layer with relative density of 1.050–1.078 g/ml were harvested. The cells were washed three times and resuspended in 5 ml of PBS. $CD4^+$ (or $CD8^+$) T cells in PBMCs (3 ml/duck) were analyzed on a BD Arial Fusion flow cytometry (BD, Franklin, USA), using mouse anti-duck mAb MCA2478 (or mouse anti-duck CD8 mAb MCA2479) (Bio-Rad, Shanghai, China) and fluorescein isothiocyanate (FITC)-conjugated goat anti-mouse IgG (Thermo, Waltham, USA). Frequencies of $CD4^+$ and $CD8^+$ T lymphocytes in PBMCs were presented with FlowJo 7.6 software (BD, Franklin, USA). To prepare T cells for adoptive transfer, we conducted a fluorescence-activated cell sorting (FACS) on the BD Arial Fusion flow cytometry. $CD4^+$ and $CD8^+$ T cells were sorted from PBMCs.

Adoptive T cell transfer

To compare the T cell-mediated immunity between Y and PS viruses, adoptive T cell transfer protocol was conducted using 3-day-old Pekin ducklings as recipients. Groups of 23 ducklings were inoculated by intravenous (iv) route with Y-specific $CD4^+$, Y-specific $CD8^+$ T cells, PS-specific $CD4^+$, PS-specific $CD8^+$ T cells, naïve $CD4^+$ T cells, naïve $CD8^+$ T cells (1×10^7/duck), or PBS (2 ml/duck). 12 h later, the recipients were challenged by im route with TMUV Y at a dose of 2×10^3 PFU. A mock-transferred, non-challenged group (control) was included, which was inoculated twice with PBS (2 ml/duck). The ducklings were monitored for signs of encephalitis, weight loss, and mortality. Serum samples of three ducklings were collected from each group between 1 and 15 days after challenge for measurement of neutralizing antibodies and viral RNA levels. At 7 days after challenge, three ducklings in each group were euthanized for measurement of spleen weight, and their tissues (brain, spleen, and thymus) were sampled for measurement of viral RNA levels and examination of histopathological changes.

To compare the T cell-mediated immunity between mutant viruses and their parental viruses, rY-, rPS-, T151A-, and

R304M-specific $CD4^+$ and $CD8^+$ T cells were transferred into 3-day-old ducklings as described above. The ducklings in each group (n=23) were monitored for mortality. The serum samples of three ducklings were collected from each of groups receiving $CD4^+$ T cells between 1 and 15 days after challenge for detection of neutralizing antibodies. The brain samples of three ducklings were collected from each of groups receiving $CD4^+$ T cells at 7 days after challenge for measurement of viral RNA levels.

Statistical analysis

All data were analyzed using GraphPad Prism software (version 5.0) (GraphPad Software Inc., San Diego, CA, United States). Survival curves were analyzed by the *Log-rank* test. Viral RNA levels, neutralizing antibody titers, and cytokine and T cell marker mRNA levels were analyzed by two-tailed Student *t* test. Body weight, spleen weight, and frequencies of $CD4^+$ and $CD8^+$ T cells in PBMCs were analyzed by two-way analysis of variance (ANOVA).

Results

TMUV Y exhibits different pathogenicity in pekin ducklings aged 3, 5, and 7 days

Earlier works in our laboratory have shown that following experimental infection of 2-day-old Pekin ducklings with 5×10^4 PFU of Y or its rescued virus rY by intracerebral or subcutaneous routes, mortality as high as 90–100% occurred between 4 and 7 days pi (11), which is unfavorable for evaluation of immune responses against TMUV isolates. Thus, we assessed the pathogenicity of Y in 3- to 7-day-old Pekin ducklings by experimental infections using an im route and a lower infectivity titer (2×10^3 PFU). All of the 20 3-day-old infected ducklings died between 4 and 7 days pi., 10 of the 20 5-day-old infected ducklings died between 7 and 15 days pi., and two of the 20 7-day-old infected ducklings died at 7 days pi (Figure 1A). This suggests that Y exhibits moderate pathogenicity in 5-day-old Pekin duckling model relative to those observed in 3- and 7-day-old Pekin duckling models. PS retained low pathogenicity, similar to previously reported pathogenicity in 2-day-old Pekin duck model (11): 5% (1/20) mortality occurred following infection at 3 and 5 days of age, and no mortality was recorded in the case of 7-day-old infection (Figure 1B). These data indicate that the marked differences in virulence between Y and PS can be retained in the 5-day-old Pekin duck model, with Y-induced pathogenic outcome being reduced as compared to that observed in 2- and 3-day-old Pekin duck models. Thus, use of the 5-day-old Pekin duckling model can ensure enough survivors at each time point after infection for testing of immune responses.

TMUV Y and PS present different virulence in pekin ducklings aged 5 Days

We further investigated the virulence of strains Y and PS in terms of clinical signs, mortality, and tissue injure using the 5-day-old Pekin duck model. Y caused severe signs of encephalitis within 5 to 9 days pi, including listlessness (10/20), tremor (6/20), and paralysis (5/20). In ducklings inoculated with PS, small portion (3/20) displayed signs of listlessness within 7 to 9 days pi (Figure 2A). Ducklings inoculated with Y and PS had 50% (10/20) and 5% (1/20) mortality respectively, like those observed

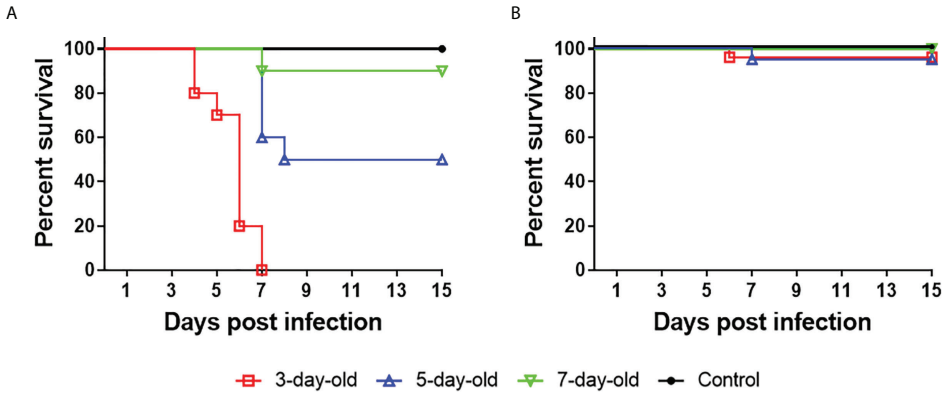

FIGURE 1
TMUV strain Y shows distinct pathogenicity in Pekin ducklings following infection at 3, 5, and 7 days of age. Groups of 20 ducklings were infected by an im route with virus at a dose of 2×10^3 PFU, and monitored for mortality for 15 days. Shown are survival curves of ducklings infected with Y **(A)** and PS **(B)**. For ducklings infected with Y, significant differences in survival existed between 5-day-old and 7-day-old ($P<0.01$), 3-day-old and 5-day-old ($P<0.001$), 3-day-old and 7-day-old ($P<0.0001$) infected groups.

10.3389/fimmu.2022.890263

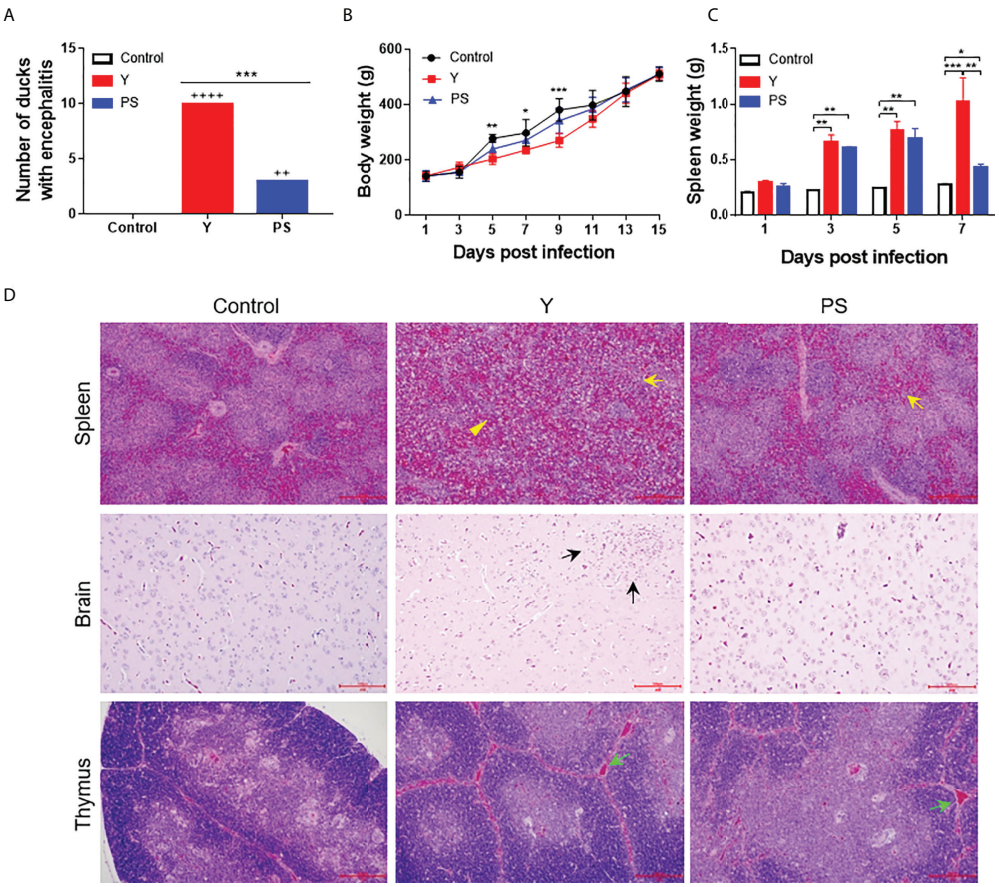

FIGURE 2
TMUV strain Y is more virulent in 5-day-old Pekin ducklings than strain PS. Groups of 60 ducklings were infected by an im route with virus at a dose of 2×10^3 PFU or mock infected, and monitored for 15 days. **(A)** Number of infected ducklings displaying signs of encephalitis. ++, mild; +++, marked. ***, $P<0.001$. **(B)** Body weight of infected ducklings. At each time point, data are presented as mean ± standard deviation (SD) of body weight from all surviving ducklings. Asterisks indicate significant differences between the group infected with Y and the controls (*, $P<0.05$; **, $P<0.01$; ***, $P<0.001$). **(C)** Spleen weight of infected ducklings. At each time point, data are presented as mean ± SD of spleen weight from three ducklings. *, $P<0.05$; **, $P<0.01$; ***, $P<0.001$. **(D)** Histopathological changes of infected ducklings. Shown necrotic vacuole (yellow arrows) and indistinct interface between red-pulp and white-pulp (yellow triangles) in spleen, inflammatory cell aggregation (black arrows) in brain, and increased interstitial hemorrhages of thymic corpuscles (green arrows) in thymus. Bar = 200 μm.

above. Infection with Y affected weight gain between 9 and 13 days pi, with weight loss ranging from 18% to 31%, as compared to uninfected ducklings. Whereas no significant differences in body weight were detected between PS-infected ducklings and controls (Figure 2B). Infection with Y and PS both caused injury to spleen; however, we observed more severe gross lesions (more than 2-fold enlargement at 7 days pi; $P<0.05$; Figure 2C) and microscopic lesions (lymphocyte degeneration, necrosis, vacuolization, and depletion as well as indistinct interface between red and white pulp; Figure 2D, up panel) in spleens of ducklings inoculated with Y when compared to those observed in PS-infected ducklings. Microscopic lesions (perivascular lymphocyte infiltration) were observed in brains of ducklings inoculated with Y, whereas no microscopic lesions were detected in PS-infected ducklings (Figure 2D, middle panel). Similar microscopic lesions were seen in thymuses of ducklings infected with Y and PS (Figure 2D, bottom panel). These data confirm that infection with strain Y causes more severe disease relative to strain PS.

To investigate the contribution of virus replication to virulence in 5-day-old Pekin ducklings, viral RNA levels were measured at different time points pi. During the whole observation period, viral RNA was detectable in all collected samples of infected ducklings. In general, levels of viral RNA in all samples of Y-infected ducklings were significantly higher than in those of PS-infected duckling. Y presented a similar replication kinetics in spleen and thymus, where similar levels of viral RNA were detected at a given time point pi; this was also the case for PS. However, viral RNA levels in Y- and PS-infected ducklings peaked at 1 and 3 days pi respectively. Moreover, Y

produced approximately 4- and 16-fold-higher viral RNA levels in spleen and 7- and 10-fold-higher viral RNA levels in thymus at 1 and 5 days pi, respectively, relative to PS (Figures 3A, B). A similar viremia pattern was observed for Y and PS, both of which produced relatively high levels of viremia as early as 1 day pi and peak levels of viremia at 3 days pi; however, 3- to 24-fold-higher viral RNA levels were detected in Y-infected ducklings than in PS-infected ducklings between 1 and 7 days pi (Figure 3C). Viral RNA levels in brains of both Y- and PS-infected ducklings peaked at 3 days pi; however, Y produced 9- and 4-fold-higher viral RNA levels at 3 and 5 days pi, respectively, as compared to PS (Figure 3D). Immunohistochemical analysis of brain, spleen, and thymus revealed the presence of viral antigens in ducklings infected with both Y and PS. Whereas the immunolabeling was notably more intense in brain and more widespread in spleen in Y-infected ducklings than in PS-infected ducklings (Figure 3E). Collectively, our data indicate that the marked differences in virulence in 5-day-old Pekin duckling model between Y and PS is associated with their capacity to replicate in the periphery and the central nervous (CNS) and to produce and sustain the level of viremia.

TMUV Y and PS induce similar levels of neutralizing antibody

Earlier works in our laboratory showed that strains Y and PS elicited comparable levels of neutralizing antibody in a 2-day-old Pekin duckling model (11). To provide further support to the neutralizing antibody responses induced by PS and Y, we repeated the neutralizing antibody analysis using the 5-day-old Pekin duckling model described above (Figure 4). A similar kinetics of neutralizing antibody response was observed for Y and PS, both of which elicited detectable neutralizing antibodies

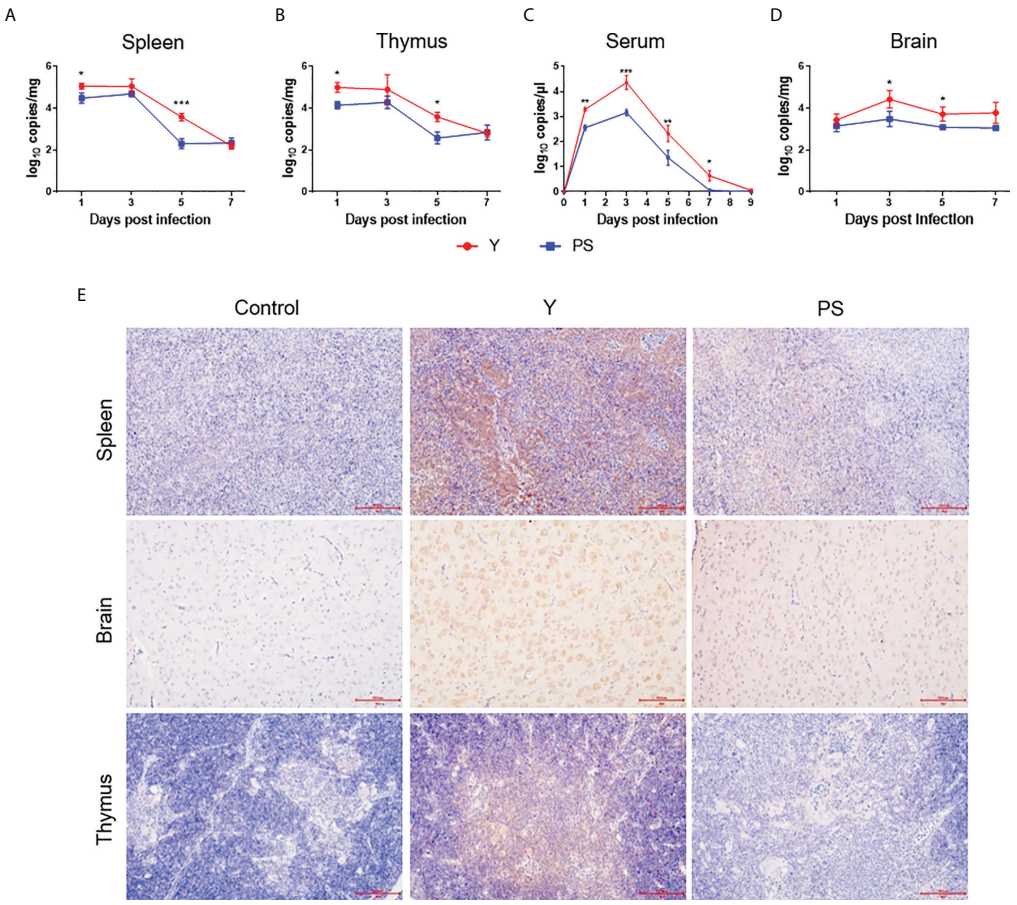

FIGURE 3
TMUV strain Y replicates in Pekin ducklings more efficiently than strain PS. Tissues were sampled from survivors in each group at different time points pi in experiments shown in Figure 2. Viral RNA levels in spleen **(A)**, thymus **(B)**, serum **(C)**, and brain **(D)** of three ducklings in each group were determined at different time points pi by the RT-qPCR assay. Data are presented as mean ± SD. *, $P<0.05$; **, $P<0.01$; ***, $P<0.001$. Tissues (brain, spleen, and thymus) collected at 5 days pi were subjected to immunohistochemical analysis **(E)**. Paraformaldehyde-fixed, paraffin-embedded tissues were immunolabeled with the TMUV E-specific mAb F3B4 and HRP-conjugated goat anti-mouse IgG.

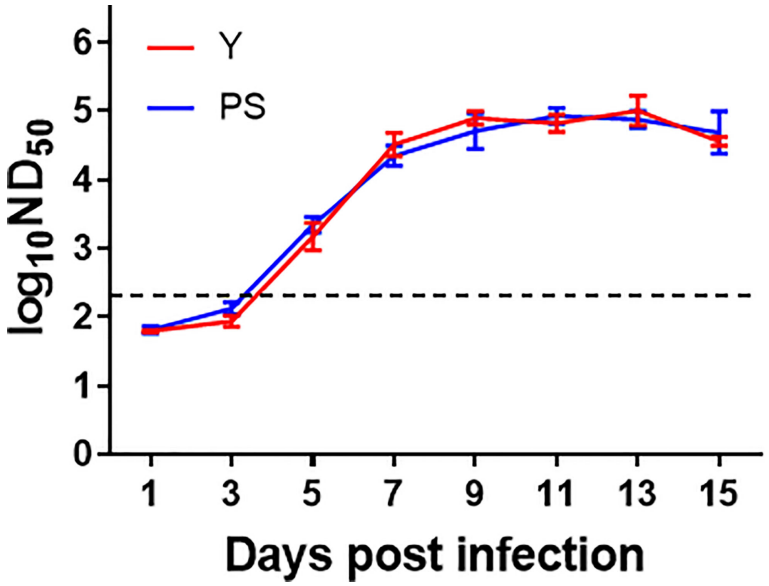

FIGURE 4
TMUV strains Y and PS elicit similar levels of neutralizing antibody in Pekin ducklings. Sera of survivors were collected from each group in experiments shown in FIGURE 2 were tested for neutralizing antibodies at different time points pi using PRNT. Dotted line indicates cut-off value defined recently for negative and positive sera (12). Data are presented as mean ± SD of the $\log_{10}$ ND_{50} from three ducklings.

at 5 day pi that peaked at 9 days pi. No significant differences in neutralizing antibody between Y and PS were detected at any time point pi. Our data further confirm that TMUV strains Y and PS induce similar levels of neutralizing antibody response.

TMUV Y induces higher magnitude of cellular immune responses than PS

The marked differences in virulence and the similarity in neutralizing antibody responses between Y and PS suggest that there may be a link between the magnitude of cellular immune responses and TMUV virulence. To confirm the hypothesis, we measured the expression of cytokines (IL-2, IL-17, IFN-γ, and TNF-β) and T cell markers (CD4 and CD8) in brain, thymus, and spleen (Figure 5A) and the frequencies of $CD4^+$ and $CD8^+$ T cells in PBMCs (Figure 5B) at different time points pi. Infection with Y induced 2- to 13-fold increases in expression of cytokines and T cell markers tested in brain and thymus (except CD4 mRNA in thymus) at 5 and 7 days pi (3 and 5 days pi for IFN-γ response in brain; 7 days pi for CD8 expression in brain) ($P<0.05$), relative to infection with PS. These data indicate that strain Y induces stronger cellular immune response in brain and thymus than strain PS. Infection with Y induced 2- to 4-fold decreases in expression of IL-2 at 7 days pi, IFN-γ at 3 and 5 days pi, TNF-β at 5 and 7 days pi, and CD8 at 3 dpi ($P<0.05$) and 2- to 4-fold increases in CD8 expression at 5 and 7 dpi ($P<0.05$) in spleen, as compared to infection with PS, suggesting that strain Y exerts an inhibitory effect on expression of cytokines in spleen. Significant differences in frequency of $CD8^+$ T cells between Y- and PS-infected ducklings were observed. Infection with Y resulted in more significant decrease in frequency of $CD8^+$ T cells at 3 days pi (0.5-fold; $P<0.05$), and more significant increase in frequency of $CD8^+$ T cells at 9 and 11 days pi (1-fold and 0.5-fold, respectively; $P<0.05$), relative to those observed for PS. These data reveal a negative correlation between TMUV virulence and frequency of $CD8^+$ T cells at the peak of viremia and a positive correlation between TMUV virulence and frequency of $CD8^+$ T cells after virus clearance from the circulation. Altogether, these data suggest that strain Y induces higher magnitude of cellular immune responses than PS, which can be reflected by measurement of expression of cytokines and T cell markers in brain and thymus of infected ducklings.

Transfer of Y-specific T cells provide more significant protection relative to PS

To compare the protection conferred by Y- and PS-specific T cells, we performed adoptive cell transfer using 3-day-old Pekin ducklings as recipients. Contrasting with the high mortalities of ducklings received PBS (100%), naïve $CD4^+$ T cells (90%), and naïve $CD8^+$ T cells (100%), transfer of Y- and PS-specific $CD8^+$ T cells and Y-specific $CD4^+$ T cells provided significant protection (100%, 85%, and 75%, respectively) against lethal infection. Whereas PS-specific $CD4^+$ T cells conferred only 30%

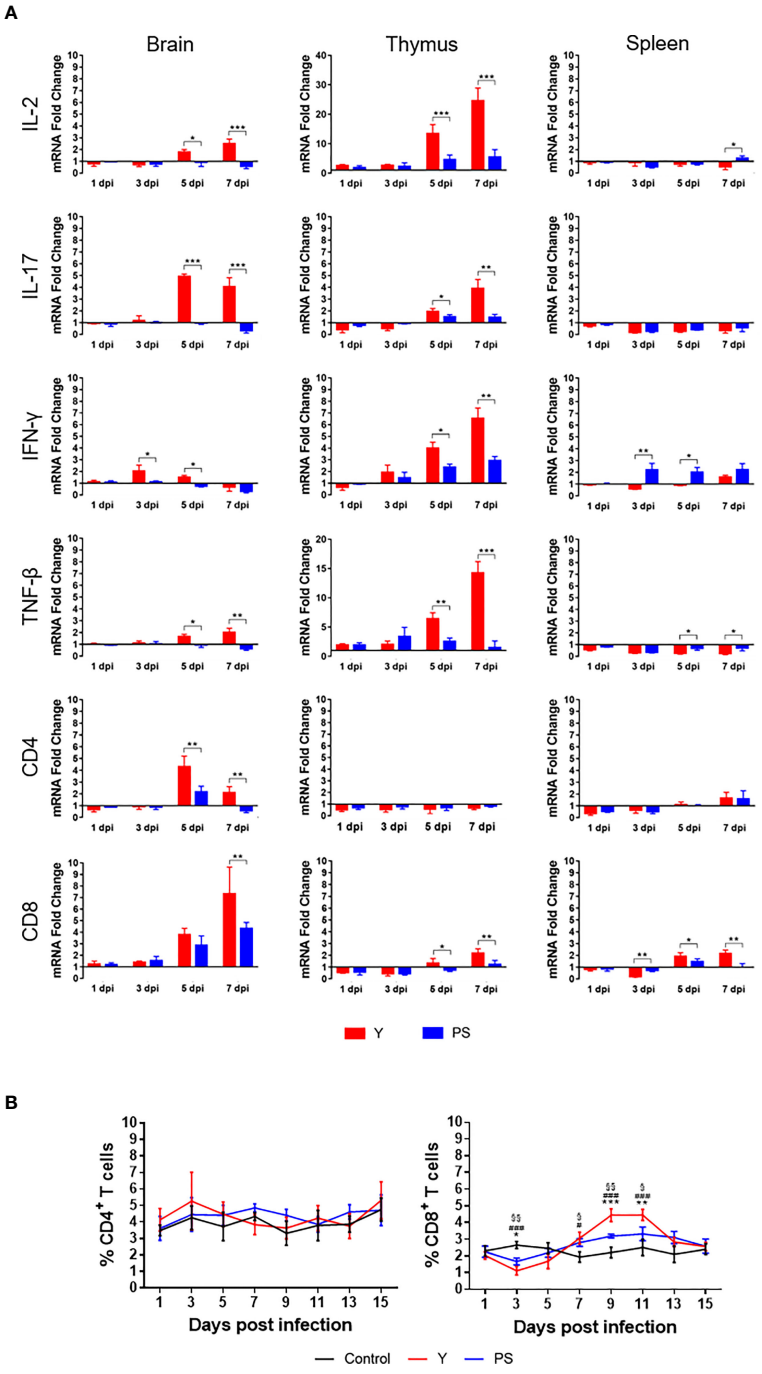

FIGURE 5
TMUV strain Y induces stronger cellular immune response in Pekin ducklings than strain PS. **(A)** Effect of infections with strains Y and PS on expression of cytokines (IL2, IL-17, IFN-γ, and TNF-β) and T cell markers (CD4 and CD8) in brain, thymus, and spleen of Pekin ducklings. Tissues of three survivors from each group were collected at different time points pi in experiments shown in FIGURE 2 and tested for relative expression of the cellular immune-related genes using RT-qPCR. Data are presented as means ± SD. *, $P<0.05$; **, $P<0.01$; ***, $P<0.001$. **(B)** Effect of infections with strains Y and PS on frequencies of $CD4^+$ and $CD8^+$ T cells in PBMCs of Pekin ducklings. Y- and PS-specific and naïve $CD4^+$ and $CD8^+$ T cells were isolated from PBMCs of three survivors from each group at different time points pi and counted. Data are presented as mean ± SD. Asterisks indicate significant differences between Y and PS viruses (*, $P<0.05$; **, $P<0.01$; ***, $P<0.001$). The # signs indicate significant differences between the groups infected with Y and the controls(#, $P<0.05$; ###, $P<0.001$). The § signs indicate significant differences between the groups infected with PS and the controls (§, $P<0.05$; §§, $P<0.01$; §§, $P<0.001$).

protection to recipient ducklings (Figure 6A). Transfer of Y- and PS-specific $CD4^+$ and $CD8^+$ T cells was also effective in preventing signs of encephalitis, weight loss, and tissue injury upon TMUV Y infection, with Y-specific T cells being more effective than PS-specific T cells (Supplementary Figures 2, 3). Together, these data indicate that Y-specific T cells induce stronger protection against TMUV-related disease than PS-specific T cells and that for TMUV, $CD8^+$ T cells induce stronger protection against TMUV-related disease than $CD4^+$ T cells.

To investigate the contribution of Y- and PS-specific T cells in production of neutralizing antibodies, we determined neutralizing antibody titers between 1 and 15 days after challenge with strain Y. Significantly higher levels of neutralizing antibody were detected in ducklings received TMUV-specific $CD4^+$ T cells between 1 and 7 days after challenge, as compared to those derived from ducklings received PBS and naïve $CD4^+$ T cells. The neutralizing antibodies in ducklings received Y- and PS-specific $CD4^+$ T cells peaked at 5 and 7 days after challenge, respectively. By

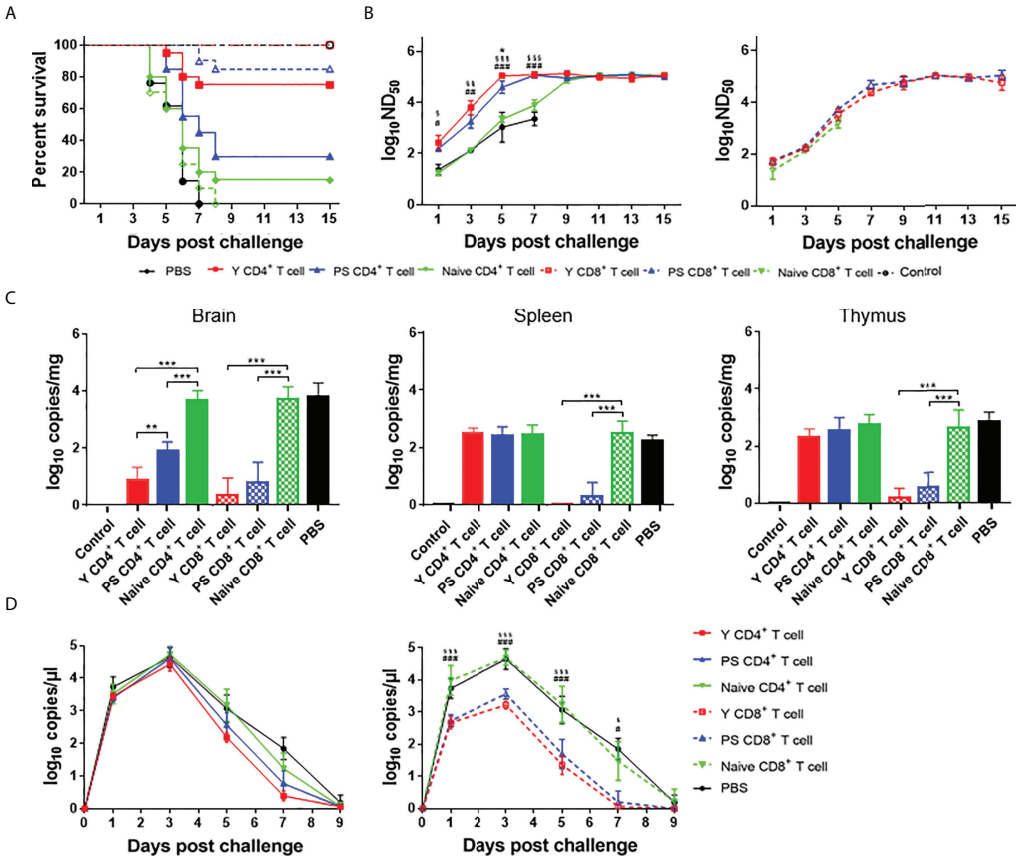

FIGURE 6
$CD4^+$ and $CD8^+$ T cells participate in protective response to TMUV. Groups of 23 3-day-old recipient ducklings were inoculated by iv route with Y-specific $CD4^+$ T cells (Y $CD4^+$ T cell), PS-specific $CD4^+$ T cells (PS $CD4^+$ T cell), Y-specific $CD8^+$ T cells (Y $CD8^+$ T cell), PS-specific $CD8^+$ T cells (PS $CD8^+$ T cell)), naïve $CD4^+$ T cells (Naive $CD4^+$ T cell), naïve CD8+ T cells (Naive $CD8^+$ T cell) (10^7/duck), or PBS. The recipient ducklings were challenged by im route with 2×10^3 PFU of TMUV Y 12 h later, and monitored for 15 days. **(A)** Survival curves of recipient ducklings. Significant difference in survival was detected between groups received Y- and PS-specific $CD4^+$ T cells ($P<0.01$); PS-specific and naïve $CD4^+$ T cells ($P<0.05$); and Y-specific and naïve $CD4^+$ T cells, Y-specific and naïve $CD8^+$ T cells, and PS-specific and naïve $CD8^+$T cells ($P<0.0001$). **(B)** Effect of transferred $CD4^+$ (left) and $CD8^+$ (right) T cells on the production of neutralizing antibodies in recipient ducklings. Neutralizing antibodies in sera were determined using PRNT. Data are presented as mean ± SD of the $\log_{10}$ ND_{50} from three ducklings. Asterisks indicate significant differences between groups received Y- and PS-specific T cells (*, $P<0.05$). The # signs indicate significant differences between Y-specific T cells adoptive groups and the control (#, $P<0.05$; ##, $P<0.01$; ###, $P<0.001$). The § signs indicate significant differences between PS-specific T cell adoptive group and the control (§, $P<0.05$; §§, $P<0.01$; §§§, $P<0.001$). **(C)** Effect of transferred $CD4^+$ and $CD8^+$ T cells on viral RNA levels in tissues (spleen, thymus, and brain) of recipient ducklings at 7 days after challenge. Data are presented as mean ± SD of the $\log_{10}$ RNA copies per mg of tissue from three ducklings. **, $P<0.01$; ***, $P<0.001$. **(D)** Effect of transferred $CD4^+$ and $CD8^+$ T cells on viremia of recipient ducklings between 1 and 9 days after challenge. Data are presented as mean ± SD of the $\log_{10}$ RNA copies per μl for sera from three ducklings. The # signs indicate significant differences between Y-specific T cells adoptive group and the control (#, $P<0.05$; ###, $P<0.001$). The § signs indicate significant differences between PS-specific T cells adoptive group and the control (§, $P<0.05$; §§§, $P<0.001$).

comparison, the neutralizing antibodies in ducklings received naïve $CD4^+$ T cells peaked at 11 days after challenge. In addition, significantly higher levels of neutralizing antibody were detected in ducklings received Y-specific $CD4^+$ T cells between 3 and 5 days after challenge than in ducklings received PS-specific $CD4^+$ T cells (Figure 6B, left panel). These data indicate that TMUV-specific $CD4^+$ T cells provide help for neutralizing antibody response, whereas Y-specific $CD4^+$ T cells contribute to a more beneficial effect on production of neutralizing antibodies than PS-specific $CD4^+$ T cells. All ducklings received naïve $CD8^+$ T cells died before 7 days after challenge. There was no significant difference in neutralizing antibody response between groups received TMUV-specific $CD8^+$ T cells and naïve $CD8^+$ T cells within 1 to 5 days after challenge, and between groups received Y- and PS-specific $CD8^+$ T cells within 1 to 15 days after challenge (Figure 6B, right panel). These data indicate that Y- and PS-specific $CD8^+$ T cells make no contribution to neutralizing antibody response.

To compare the effect of Y- and PS-specific T cells on viral load, we measured viral RNA levels in tissues (brain, spleen, and thymus) at 7 days after challenge and in serum samples between 1 and 9 days after challenge (Figures 6C, D). Adoptive transfer of Y- and PS-specific $CD4^+$ T cells reduced viral RNA levels in brain (353-fold and 59-fold, respectively; $P<0.001$), and had no significant effect on viral RNA levels in spleen, thymus, and serum. By comparison, transferred Y- and PS-specific $CD8^+$ T cells reduced viral RNA levels in brain (1549-fold and 590-fold, respectively; $P<0.001$), spleen (355-fold and 252-fold, respectively; $P<0.001$), and thymus (443-fold and 157-fold, respectively; $P<0.001$) and in serum (32- to 103-fold and 28- to 38-fold, respectively; $P<0.001$) between 1 and 5 days after challenge, and cleared virus from the blood at 7 days after challenge. There was no significant difference in viral RNA levels in brain, spleen, thymus, and serum between groups received Y- and PS-specific $CD8^+$ T cells. Overall, our data suggest that virus-specific $CD8^+$ T cells play an important role in clearing infection from tissues and preventing virus persistence, with Y- and PS-specific $CD8^+$ T cells being similar in this function.

The E protein plays a major role in determining the differences in cellular immune response between Y and PS

To determine which protein is responsible for the differences in cellular immune response between Y and PS, 5-day-old Pekin ducks were infected with chimeric viruses rPS-YE and rPS-YNS1-3'UTR and control viruses rY and rPS. We measured the expression of IL-2, IL-17, IFN-γ, TNF-β, CD4, and CD8 mRNAs in brain and thymus at 7 days pi (Figure 7A). rY and rPS behaved like Y and PS (Figure 5A) respectively. Infection with rPS-YE significantly increased the levels of IL-2, IL-17, TNF-β, and CD8 in brain and thymus, CD4 in brain, and IFN- γ in thymus, and significantly reduced the levels of IFN-γ in brain and CD4 in thymus, as compared to those observed for the parental backbone virus rPS. As a result, rPS-YE infection induced mRNAs of these cytokines and T cell makers to similar levels as measured for rY. In general, infection with rPS-YNS1-3'UTR had little or no contribution to the expression of cytokines (except TNF-β) and T cell markers in brain and thymus ($P<0.05$). These data indicate that the E protein plays a major role in determining the differences in cellular immune response between Y and PS.

The T151A and R304M mutations in the E protein contribute to significant enhanced cellular immune response to TMUV

We then identify E protein residues responsible for the differences in cellular immune response between Y and PS. 5-day-old Pekin ducklings were infected with the R38K, T151A, and R304M mutant viruses and the rY and rPS control viruses, and the levels of IL-2, IL-17, IFN-γ, TNF-β, CD4, and CD8 mRNAs in brain and thymus were measured at 7 days after infection (Figure 7B). In this experiment, rY and rPS also behaved like Y and PS (Figure 5A) respectively. Infections with both T151A and R304M significantly increased the levels of IL-2, IL-17, TNF-β, and CD8 in brain and thymus, IFN-γ in thymus, and CD4 in brain, as compared to infection with the rPS parental backbone virus ($P<0.05$). Thus, both T151A and R304M induced mRNAs of these cytokines and T cell makers to similar levels as measured for rY. Infection with R38K had little or no effect on expression of the tested cytokines (except TNF-β in thymus) and T cell markers in brain and thymus ($P<0.05$). Our data indicate that mutations T151A and R304M in the E protein contribute to the differences in cellular immune response between Y and PS.

Mutations of E protein residues 151 and 304 affect $CD4^+$ T cell-mediated immunity

Our studies indicate that the marked differences in $CD4^+$ T cell-induced protection and neutralizing antibody response and some differences in $CD8^+$ T cell-induced protection exist between Y- and PS-infected ducklings, which might be attributed to E protein residues 151 and 304. To confirm the hypothesis, $CD4^+$ and $CD8^+$ T cells from ducklings infected with mutant viruses T151A and R304M were used in the adoptive transfer experiments.

We evaluated adoptive transfer of $CD8^+$ T cells from ducklings infected with mutant viruses T151A and R304M for its effect on protection of recipient ducklings from lethal

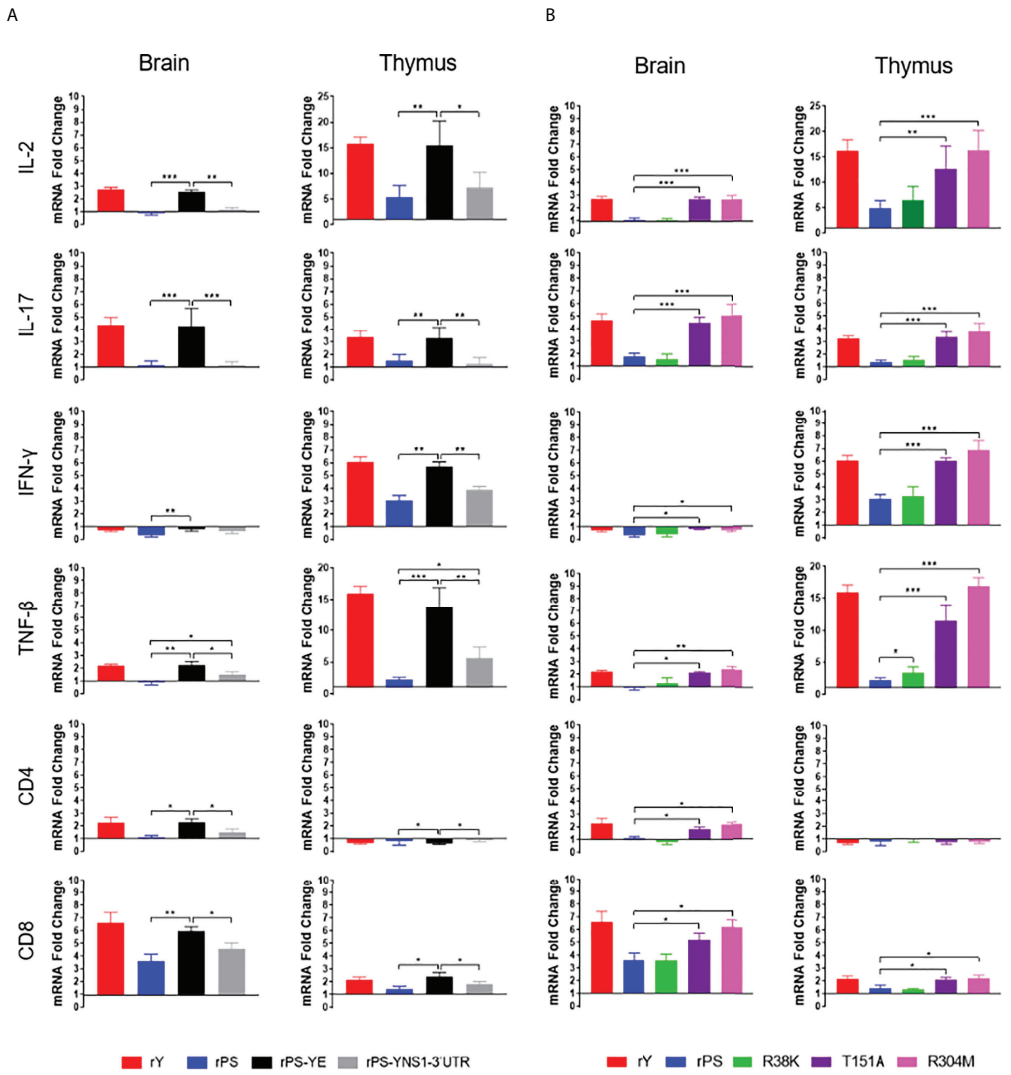

FIGURE 7
E protein residues 151 and 304 are responsible for the differences in cellular immune response between Y- and PS-infected Pekin ducklings. Groups of 23 5-day-old ducklings were inoculated with virus at a dose of 2×10^3 PFU of virus or mock infected. **(A)** Expression of cellular immune-related genes in ducklings infected with chimeric (rPS-YE and rPS-YNS1-3'UTR) and control (rPS and rY) viruses. **(B)** Expression of cellular immune-related genes in ducklings infected with mutant (R38K, T151A, and M304R) and control (rPS and rY) viruses. The expression of the cellular immune-related genes in tissues (brain and thymus) of three individuals in each group was determined at 7 days pi using RT-qPCR. Data are represented as mean ± SD. *, $P<0.05$; **, $P<0.01$; ***, $P<0.001$.

challenge (Figure 8A). Survivals in groups received T151A-and R304M-specific $CD8^+$T cells (80% and 75%, respectively) were comparable to those in group received rPS-specific $CD8^+$ T cells (75%), but lower than those in group received rY-specific $CD8^+$T cells (100%). The result indicates that the R304M and T151A mutations have little or no contribution to $CD8^+$ T cell-mediated protection.

We assessed adoptive transfer of $CD4^+$ T cells from ducklings infected with mutant viruses T151A and R304M for its effects on protective capacity, neutralizing antibody response, and TMUV burden in brain (Figures 8B–D). Varying degrees of increases in survival occurred in group received T151A- and R304M-specific $CD4^+$T cells (50% and 65%, respectively), as compared to that in group received rPS-specific $CD4^+$T cells (20%). The data indicate that both T151A and R304M mutations contribute to markedly enhanced $CD4^+$ T cell-induced protective efficacy, with the R304M mutation contributing more to protection against lethality. Neutralizing antibodies in ducklings received rPS-specific $CD4^+$T cells peaked at 7 days after challenge. By comparison, neutralizing antibodies in ducklings received T151A- and R304M-specific $CD4^+$T cells peaked 2 days earlier, like that observed for rY-specific $CD4^+$T

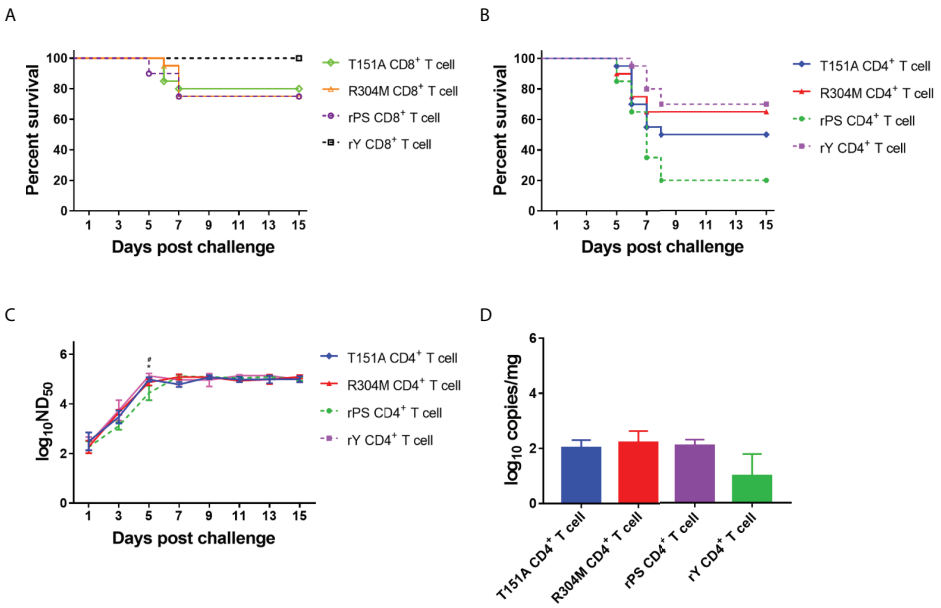

FIGURE 8
E protein residues 151 and 304 contribute to the differences in T cell-mediated immunity between Y- and PS-infected Pekin ducklings. Groups of 23 3-day-old recipient ducklings were inoculated by iv route with rY-specific CD4$^+$ T cells (rY CD4$^+$ T cell), rPS-specific CD4$^+$ T cells (rPS CD4$^+$ T cell), T151A CD4$^+$ T cells (T151A CD4$^+$ T cell), R304M CD4$^+$ T cells (R304M CD4$^+$ T cell), rY-specific CD8$^+$ T cells (rY CD8$^+$ T cell), rPS-specific CD8$^+$ T cells (rPS CD8$^+$ T cell)), T151A CD8$^+$ T cells (Naive CD8$^+$ T cell), R304M CD8$^+$ T cells (R304M CD8$^+$ T cell) (10^7/duck). The recipient ducklings were challenged by im route with 2×10^3 PFU of TMUV Y 12 h later, and monitored for 15 days. **(A)** Effect of transferred T151A- and R304M-specific CD8$^+$ T cells on survival of recipient ducklings. **(B)** Effect of transferred T151A- and R304M-specific CD4$^+$ T cells on survival of recipient ducklings. Significant difference in survival was detected between groups received T151A- and rPS-specific CD4$^+$ T cells (P<0.05) as well as R304M- and rPS-specific CD4$^+$ T cells (P<0.01) groups. **(C)** Effect of transferred T151A- and R304M-specific CD4$^+$ T cells on neutralizing antibody response in recipient ducklings. Neutralizing antibodies in sera were determined using PRNT. Data are presented as mean ± SD of the $\log_{10}$ ND_{50} from three ducklings. Asterisks indicate significant differences between groups received T151A- and rPS-specific T CD4$^+$ cells (*, P<0.05). The # signs indicate significant differences between R304M- and rPS-specific CD4$^+$ducklings (#, P<0.05). **(D)** Measurement of TMUV burden in ducklings received CD4$^+$ T cells. Viral RNA levels in brain of three ducklings in each group were determined at 7 days after challenge by the RT-qPCR assay. Data are presented as mean ± SD.

cells. The levels of neutralizing antibody detected in ducklings received T151A-, R304M-, and rY-specific CD4$^+$T cells between 1 and 5 days after challenge were similar, all of which were higher than those detected in ducklings received rPS-specific CD4$^+$T cells, with significant higher antibody titers occurring at 5 days after challenge. These data indicate that both R304M and T151A mutations contribute to significantly increased CD4$^+$ T cell-mediated neutralizing antibody response. The levels of viral RNA detected in brain of ducklings received T151A- and R304M-specific CD4$^+$T cells at 7 days after challenge were similar to those derived from ducklings received rPS-specific CD4$^+$T cells, indicating that both R304M and T151A mutations have no contribution to CD4$^+$ T cell-mediated viral clearance from the brain.

Discussion

The primary goal of the present study was to investigate the protective role for TMUV-specific CD4$^+$ and CD8$^+$ T cells by using the high-virulence TMUV strain Y and the low-virulence TMUV strain PS. Because strain Y caused very high mortality in recently reported 2-day-old Pekin duckling model (11), we first evaluated the pathogenicity of strain Y in 3, 5, and 7-day-old Pekin ducklings. We showed that strain Y presented distinct pathogenicity in 3-, 5-, and 7-day-old Pekin ducklings, indicating that the pathogenic outcome is age dependent even in the age range of 3 to 7 days. Strain Y presented a lower virulence phenotype in 5-day-old Pekin ducklings and a similarly high virulence phenotype in 3-day-old Pekin ducklings when compared with that observed in 2-day-old Pekin ducklings (11). Thus, the 5-day-old-Pekin duck model is a useful tool for the assessment of immune responses to TMUV strains with different virulence phenotypes, whereas the 3-day-old Pekin duckling model can be used as recipients in the adoptive transfer experiments.

The present observation confirmed recent findings in which TMUV strains Y and PS were shown to elicit comparable levels of neutralizing antibody in 2-day-old Pekin duck model (11). This indicates that the neutralizing antibody response fails to

correlate with the difference in virulence between Y and PS. Considering that PS elicits significantly higher levels of neutralizing antibody than those observed for sufficiently attenuated PS180 strain derived from 180 passages of PS in BHK-21 cells (26), we can conclude that no correlation exists between the levels of neutralizing antibodies and virulence above a baseline level of low virulence represented by PS. In the investigation of Y- and PS-induced cellular immune responses, we observed more marked IL-2, IL-17, IFN-γ, and TNF-β responses and higher up-regulation of CD4 and CD8 genes at 5 and 7 days pi as well as more markedly increased frequencies of $CD8^+$ T cells between 7 and 11 days pi in Y-infected ducklings than in PS-infected ducklings. These findings indicate that strain Y elicits stronger cellular immune response than PS, suggesting a positive correlation between the magnitude of TMUV-specific T cell immune response (especially $CD8^+$ T cell response) and the virulence of TMUV.

We observed that the viral RNA levels in brain, thymus, spleen, and blood in both Y- and PS-infected ducklings tended to decline from 3 to 7 days pi, indicating that virus-induced immune responses have exerted their functions in inhibiting virus replication, limiting virus dissemination, clearing infection from tissues, and preventing viral persistence. The levels of viral RNA in Y-infected duckling were reduced to those in PS-infected ducklings at 7 days pi, suggesting a role of the excess of Y-specific T cell immunity over PS-specific T cell immunity in controlling TMUV burden. It is likely that more rapid clearance of virus from the blood of PS-infected ducklings than from Y-infected ducklings might be attributed to the role of glycosaminoglycan-binding motif at residue 304 in the E protein of PS. TMUV burden in brain of both Y- and PS-infected ducklings were reduced more slowly as compared to those in the extraneural tissues, which might be associated with immune responses in the CNS involve recruitment of peripheral immune cells to the CNS (36–38).

Using adoptive T cell transfer, we demonstrated that Y-specific $CD4^+$ T cells and Y- and PS-specific $CD8^+$ T cells provided significant protection against a lethal infection with TMUV Y, indicating a crucial role of T cells in the protective immune response to TMUV. $CD8^+$ T cells were shown to confer more robust protection to recipient ducklings than $CD4^+$ T cells, suggesting that for TMUV, similarly to dengue virus (DENV) (39, 40), $CD8^+$ T cells are more relevant to the control of TMUV-related disease. It is interesting to observe a more marked difference in protection between Y- and PS-specific $CD4^+$ T cells in comparison to that between Y- and PS-specific $CD8^+$ T cells. This may indicate that the difference in T cell-mediated protective immune response between Y and PS is primarily attributed to $CD4^+$ T cells.

The measurement of neutralizing antibodies in sera and viral RNA levels in tissues revealed that for TMUV, $CD4^+$ T cells primarily made contribution to the production of neutralizing antibodies, and $CD8^+$ T cells primarily mediated viral clearance for brain, thymus, spleen, and blood, similar to other flaviviruses (e.g., DENV, West Nile virus, Japanese encephalitis virus, and yellow fever virus) (39, 41–45). Nevertheless, TMUV-specific $CD4^+$ T cells also mediated viral clearance from the brain, similar to DENV-specific $CD4^+$ T cells (44). Whereas Y- and PS-specific $CD4^+$ T cells were distinct from each other in terms of contribution to neutralizing antibody response and viral clearance from the brain. It is likely that the difference in T cell-mediated protective immune response between Y and PS can be attributed to the different contribution of Y- and PS-specific $CD4^+$ T cell to the production of neutralizing antibodies and the clearance of virus from the brain.

From studies on expression of cytokines and T cell markers in ducklings infected with chimeric and mutant viruses we conclude that E protein residues 151 and 304 are the key determinants of the magnitude of TMUV-specific T cell immune response. Based on adoptive transfer of mutant virus-specific T cells, this work has also shown that E protein residues 151 and 304 are the key determinants of protection against lethal infection and neutralizing antibody production mediated by TMUV-specific $CD4^+$ T cells. We observed that the contribution of both T151A- and R304M-specific $CD4^+$ T cells to protection and antibody production failed to achieve the levels conferred by rY-specific $CD4^+$ T cells, suggesting that a combination of the T151A and R304M mutations might synergistically enhance virus-specific $CD4^+$ T cell immunity.

Previous studies with other flaviviruses (e.g., DENV and JEV) have shown that $CD4^+$ T cells mainly target the E, C, and NS1 proteins, whereas $CD8^+$ T cells preferentially recognize the NS3, NS4B, and NS5 proteins (46–52). We speculate that E protein residues 151 and 304 are likely to be located within one of epitopes recognized by TMUV-specific $CD4^+$ T cells, that the difference in viral clearance from the brain between Y- and PS-specific $CD4^+$ T cells might be associated with one or more of the three residues in the NS1 protein that differ between Y and PS (11), and that the difference in protection between Y- and PS-specific $CD8^+$ T cells could be related to one or more of the 10 residues in NS2A, NS3, NS4B, and NS5 proteins that differ between Y and PS (11). Further studies are needed to confirm the hypothesis.

Taken together, our studies demonstrate a critical role of $CD4^+$ and $CD8^+$ T cells in the protective immune response and the control of TMUV infection. A positive correlation exists between the virulence of TMUV and T cell immunity, including $CD8^+$ T cell-mediated protection and $CD4^+$ T cell-mediated protection, neutralizing antibody response, and viral clearance from the brain. We have also demonstrated that the difference in $CD4^+$ T cell-mediated immunity is mainly related to residues 151 and 304 in the E protein. Our studies contribute to the better understanding of the role of T cell immunity in the protective immune response and the molecular basis of TMUV-induced $CD4^+$ T cell immunity.

Data availability statement

The original contributions presented in the study are included in the article/Supplementary Material. Further inquiries can be directed to the corresponding author.

Ethics statement

The animal study was reviewed and approved by Animal Welfare and Ethics Committee of China Agricultural University.

Author contributions

RM conducted experiments, analysis, and writing of the original manuscript draft. BY, CF, and JH were involved in sample collection, sample processing, analysis, and data collection. XW was involved in the analysis and interpretation of data. DZ performed analysis, writing, and reviewing. All authors contributed to the article and approved the submitted version.

Funding

This project was supported by grants from China Agriculture Research System of MOF and MARA for DZ and the National Key Research and Development Program of China (2016YFD0500107) for DZ.

Acknowledgments

We thank Lixin Yang (China Agricultural University) for advice and suggestions in duck experiments; Duo Peng, Qiong Li, Jiaying Wang, and Zixin Feng (China Agricultural University) for their support in sample collection.

Conflict of interest

The authors declare that the research was conducted in the absence of any commercial or financial relationships that could be construed as a potential conflict of interest.

Publisher's note

All claims expressed in this article are solely those of the authors and do not necessarily represent those of their affiliated organizations, or those of the publisher, the editors and the reviewers. Any product that may be evaluated in this article, or claim that may be made by its manufacturer, is not guaranteed or endorsed by the publisher.

Supplementary material

The Supplementary Material for this article can be found online at: https://www.frontiersin.org/articles/10.3389/fimmu.2022.890263/full#supplementary-material

References

1. Yun T, Zhang D, Ma X, Cao Z, Chen L, Ni Z, et al. Complete genome sequence of a novel flavivirus, duck tembusu virus, isolated from ducks and geese in China. *J Virol* (2012) 86:3406–7. doi: 10.1128/JVI.07132-11

2. Yun T, Ye W, Ni Z, Zhang D, Zhang C. Identification and molecular characterization of a novel flavivirus isolated from pekin ducklings in China. *Vet Microbiol* (2012) 157:311–9. doi: 10.1016/j.vetmic.2012.01.013

3. Cao Z, Zhang C, Liu Y, Liu Y, Ye W, Han J, et al. Tembusu virus in ducks, China. *Emerg Infect Dis* (2011) 17:1873–5. doi: 10.3201/eid1710.101890

4. Homonnay ZG, Kovács EW, Bányai K, Albert M, Fehér E, Mató T, et al. Tembusu-like flavivirus (Perak virus) as the cause of neurological disease outbreaks in young pekin ducks. *Avian Pathol* (2014) 43:552–60. doi: 10.1080/03079457.2014.973832

5. Thontiravong A, Ninvilai P, Tunterak W, Nonthabenjawan N, Chaiyavong S, Angkabkingkaew K, et al. Tembusu-related flavivirus in ducks, Thailand. *Emerg Infect Dis* (2015) 21:2164–7. doi: 10.3201/eid2112.150600

6. Liang T, Liu X, Qu S, Lv J, Yang L, Zhang D. Pathogenicity of egg-type duck-origin isolate of tembusu virus in pekin ducklings. *BMC Vet Res* (2019) 15:362. doi: 10.1186/s12917-019-2136-x

7. Ninvilai P, Tunterak W, Oraveerakul K, Amonsin A, Thontiravong A. Genetic characterization of duck tembusu virus in Thailand, 2015-2017: Identification of a novel cluster. *Transbound Emerg Dis* (2019) 66:1982–92. doi: 10.1111/tbed.13230

8. Sun XY, Diao YX, Wang J, Liu X, Lu AL, Zhang L, et al. Tembusu virus infection in cherry valley ducks: The effect of age at infection. *Vet Microbiol* (2014) 168:16–24. doi: 10.1016/j.vetmic.2013.10.003

9. Li N, Lv C, Yue R, Shi Y, Wei L, Chai T, et al. Effect of age on the pathogenesis of duck tembusu virus in cherry valley ducks. *Front Microbiol* (2015) 6:581. doi: 10.3389/fmicb.2015.00581

10. Ninvilai P, Limcharoen B, Tunterak W, Prakairungnamthip D, Oraveerakul K, Banlunara W, et al. Pathogenesis of Thai duck tembusu virus in cherry valley ducks: The effect of age on susceptibility to infection. *Vet Microbiol* (2020) 243:108636. doi: 10.1016/j.vetmic.2020.108636

11. Yang L, Liang T, Lv J, Qu S, Meng R, Yang B, et al. Substantial attenuation of virulence of tembusu virus strain PS is determined by an arginine at residue 304 of the envelope protein. *J Virol* (2021) 95:e02331–20. doi: 10.1128/JVI.02331-20

12. Lv J, Yang L, Qu S, Meng R, Li Q, Liu H, et al. Detection of neutralizing antibodies to tembusu virus: Implications for infection and immunity. *Front Vet Sci* (2019) 6:442. doi: 10.3389/fvets.2019.00442

13. Zhao D, Huang X, Han K, Liu Y, Yang J, Liu Q, et al. Protective immune response against newly emerging goose tembusu virus infection induced by immunization with a recombinant envelope protein. *Lett Appl Microbiol* (2015) 61:318–24. doi: 10.1111/lam.12459

14. Zhao D, Han K, Zhang L, Wang H, Tian Y, Huang X, et al. Identification and immunogenic evaluation of T cell epitopes based on tembusu virus envelope protein in ducks. *Virus Res* (2018) 257:74–81. doi: 10.1016/j.virusres.2018.09.008

15. Ma T, Liu Y, Cheng J, Liu Y, Fan W, Cheng Z, et al. Liposomes containing recombinant e protein vaccine against duck tembusu virus in ducks. *Vaccine* (2016) 34:2157–63. doi: 10.1016/j.vaccine.2016.03.030

16. Li L, Zhang Y, Dong J, Zhang J, Zhang C, Sun M, et al. The truncated e protein of DTMUV provide protection in young ducks. *Vet Microbiol* (2020) 240:108508. doi: 10.1016/j.vetmic.2019.108508

17. Han K, Zhao D, Liu Y, Huang X, Yang J, Liu Q, et al. Design and evaluation of a polytope construct with multiple b and T epitopes against tembusu virus infection in ducks. *Res Vet Sci* (2016) 104:174–80. doi: 10.1016/j.rvsc.2015.09.011

18. Huang J, Jia R, Shen H, Wang M, Zhu D, Chen S, et al. Oral delivery of a DNA vaccine expressing the PrM and e genes: A promising vaccine strategy against flavivirus in ducks. *Sci Rep* (2018) 8:12360. doi: 10.1038/s41598-018-30258-3

19. Tang J, Bi Z, Ding M, Yin D, Zhu J, Zhang L, et al. Immunization with a suicidal DNA vaccine expressing the e glycoprotein protects ducklings against duck tembusu virus. *Virol J* (2018) 15:140. doi: 10.1186/s12985-018-1053-0

20. Chen P, Liu J, Jiang Y, Zhao Y, Li Q, Wu L, et al. The vaccine efficacy of recombinant duck enteritis virus expressing secreted e with or without PrM proteins of duck tembusu virus. *Vaccine* (2014) 32:5271–7. doi: 10.1016/j.vaccine.2014.07.082

21. Zou Z, Liu Z, Jin M. Efficient strategy to generate a vectored duck enteritis virus delivering envelope of duck tembusu virus. *Viruses* (2014) 6:2428–43. doi: 10.3390/v6062428

22. Zou Z, Huang K, Wei Y, Chen H, Liu Z, Jin M. Construction of a highly efficient CRISPR/Cas9-mediated duck enteritis virus-based vaccine against H5N1 avian influenza virus and duck tembusu virus infection. *Sci Rep* (2017) 7:1478. doi: 10.1038/s41598-017-01554-1

23. Sun M, Dong J, Li L, Lin Q, Sun J, Liu Z, et al. Recombinant Newcastle disease virus (NDV) expressing duck tembusu virus (DTMUV) pre-membrane and envelope proteins protects ducks against DTMUV and NDV challenge. *Vet Microbiol* (2018) 218:60–9. doi: 10.1016/j.vetmic.2018.03.027

24. Chen L, Yu B, Hua J, Ni Z, Ye W, Yun T, et al. Optimized expression of duck tembusu virus e gene delivered by a vectored duck enteritis virus. *In Vitro. Mol Biotechnol* (2019) 61:783–90. doi: 10.1007/s12033-019-00206-1

25. Tang J, Yin D, Wang R, Zhou Q, Zhou X, Xing X, et al. A recombinant adenovirus expressing the e protein of duck tembusu virus induces protective immunity in duck. *J Vet Med Sci* (2019) 81:314–20. doi: 10.1292/jvms.18-0036

26. Lv J, Liu X, Cui S, Yang L, Qu S, Meng R, et al. The neutralizing antibody response elicited by tembusu virus is affected dramatically by a single mutation in the stem region of the envelope protein. *Front Microbiol* (2020) 11:585194. doi: 10.3389/fmicb.2020.585194

27. Huang J, Shen H, Jia R, Wang M, Chen S, Zhu D, et al. Oral vaccination with a DNA vaccine encoding capsid protein of duck tembusu virus induces protection immunity. *Viruses* (2018) 10:180. doi: 10.3390/v10040180

28. Lv C, Li R, Liu X, Li N, Liu S. Pathogenicity comparison of duck tembusu virus in different aged cherry valley breeding ducks. *BMC Vet Res* (2019) 15:282. doi: 10.1186/s12917-019-2020-8

29. Thontiravong A, Nedumpun T, Ninvilai P, Tunterak W, Techakriengkrai N, Banlunara W, et al. Dynamics of cellular and humoral immune responses following duck tembusu virus infection in ducks. *Transbound Emerg Dis* (2022). doi: 10.1111/tbed.14467

30. Yu C. *Isolation identification and fluorescence quantitative RT-PCR assay of tembusu virus. [master's thesis]*. Shandong: Shandong Agricultural University (2013).

31. Wang X, Zhang J, Meng R, Jiang Y, Liang S, Zhang Y, et al. Host differences affecting resistance and susceptibility of the second generation of a pekin duck flock to duck hepatitis a virus genotype 3. *Front Microbiol* (2017) 8:1128. doi: 10.3389/fmicb.2017.01128

32. Beaufrère A, Bessières B, Bonnière M, Driessen M, Alfano C, Couderc T, et al. A clinical and histopathological study of malformations observed in fetuses infected by the zika virus. *Brain Pathol* (2019) 29:114–25. doi: 10.1111/bpa.12644

33. Enlow W, Piret J, Boivin G. Droplet digital PCR and immunohistochemistry techniques to detect zika virus in the central nervous system of mice. *Methods Mol Biol* (2020) 2142:41–57. doi: 10.1007/978-1-0716-0581-3_4

34. Dai W. *Preparation of monoclonal antibody (MAb) against e protein of duck tembusu virus and identification of antigen epitope recognized by the MAb. [master's thesis]*. Beijing: China Agricultural University (2019).

35. Livak KJ, Schmittgen TD. Analysis of relative gene expression data using real-time quantitative PCR and the 2(-delta delta C(T)) method. *Methods* (2001) 25:402–8. doi: 10.1006/meth.2001.1262

36. Maximova OA, Pletnev AG. Flaviviruses and the central nervous system: Revisiting neuropathological concepts. *Annu Rev Virol* (2018) 5:255–72. doi: 10.1146/annurev-virology-092917-043439

37. Feng C, Jin M, Yang L, Lv J, Qu S, Meng R, et al. Pathogenicity of a jinding duck-origin cluster 2.1 isolate of tembusu virus in 3-week-old pekin ducklings. *Vet Microbiol* (2020) 251:108870. doi: 10.1016/j.vetmic.2020.108870

38. Ma Y, Liang Y, Wang N, Cui L, Chen Z, Wu H, et al. Avian flavivirus infection of Monocytes/Macrophages by extensive subversion of host antiviral innate immune responses. *J Virol* (2019) 93:e00978–19. doi: 10.1128/JVI.00978-19

39. Yauch LE, Zellweger RM, Kotturi MF, Qutubuddin A, Sidney J, Peters B, et al. A protective role for dengue virus-specific $CD8^+$ T cells. *J Immunol* (2009) 182:4865–73. doi: 10.4049/jimmunol.0801974

40. Yauch LE, Prestwood TR, May MM, Morar MM, Zellweger RM, Peters B, et al. $CD4^+$ T cells are not required for the induction of dengue virus-specific $CD8^+$ T cell or antibody responses but contribute to protection after vaccination. *J Immunol* (2010) 185:5405–16. doi: 10.4049/jimmunol.1001709

41. Shrestha B, Diamond MS. Role of $CD8^+$ T cells in control of West Nile virus infection. *J Virol* (2004) 78:8312–21. doi: 10.1128/JVI.78.15.8312-8321.2004

42. Sitati EM, Diamond MS. $CD4^+$ T-cell responses are required for clearance of West Nile virus from the central nervous system. *J Virol* (2006) 80:12060–9. doi: 10.1128/JVI.01650-06

43. Larena M, Regner M, Lee E, Lobigs M. Pivotal role of antibody and subsidiary contribution of $CD8^+$ T cells to recovery from infection in a murine model of Japanese encephalitis. *J Virol* (2011) 85:5446–55. doi: 10.1128/JVI.02611-10

44. Zellweger RM, Miller R, Eddy WE, White LJ, Johnston RE, Shresta S. Role of humoral versus cellular responses induced by a protective dengue vaccine candidate. *PloS Pathog* (2013) 9(10):e1003723. doi: 10.1371/journal.ppat.1003723

45. Bassi MR, Kongsgaard M, Steffensen MA, Fenger C, Rasmussen M, Skjødt K, et al. $CD8^+$ T cells complement antibodies in protecting against yellow fever virus. *J Immunol* (2015) 194:1141–53. doi: 10.4049/jimmunol.1402605

46. Duangchinda T, Dejnirattisai W, Vasanawathana S, Limpitikul W, Tangthawornchaikul N, Malasit P, et al. Immunodominant T-cell responses to dengue virus NS3 are associated with DHF. *Proc Natl Acad Sci USA* (2010) 107:16922–7. doi: 10.1073/pnas.1010867107

47. Mathew A, Townsley E, Ennis FA. Elucidating the role of T cells in protection against and pathogenesis of dengue virus infections. *Future Microbiol* (2014) 9:411–25. doi: 10.2217/fmb.13.171

48. Weiskopf D, Yauch LE, Angelo MA, John DV, Greenbaum JA, Sidney J, et al. Insights into HLA-restricted T cell responses in a novel mouse model of dengue virus infection point toward new implications for vaccine design. *J Immunol* (2011) 187:4268–79. doi: 10.4049/jimmunol.1101970

49. Weiskopf D, Angelo MA, de Azeredo EL, Sidney J, Greenbaum JA, Fernando AN, et al. Comprehensive analysis of dengue virus-specific responses supports an HLA-linked protective role for $CD8^+$ T cells. *Proc Natl Acad Sci USA* (2013) 110:E2046–53. doi: 10.1073/pnas.1305227110

50. Weiskopf D, Angelo MA, Bangs DJ, Sidney J, Paul S, Peters B, et al. The human $CD8^+$ T cell responses induced by a live attenuated tetravalent dengue vaccine are directed against highly conserved epitopes. *J Virol* (2015) 89:120–8. doi: 10.1128/JVI.02129-14

51. Vaughan K, Greenbaum J, Blythe M, Peters B, Sette A. Meta-analysis of all immune epitope data in the flavivirus genus: Inventory of current immune epitope data status in the context of virus immunity and immunopathology. *Viral Immunol* (2010) 23:259–84. doi: 10.1089/vim.2010.0006

52. Rivino L, Lim MQ. $CD4^+$ and $CD8^+$ T-cell immunity to dengue-lessons for the study of zika virus. *Immunology* (2017) 150:146–54. doi: 10.1111/imm.12681

frontiers | Frontiers in Immunology

TYPE Review
PUBLISHED 12 August 2022
DOI 10.3389/fimmu.2022.899559

OPEN ACCESS

EDITED BY
Pei-Hui Wang,
Shandong University, China

REVIEWED BY
Jean-Pierre Routy,
McGill University, Canada
Brandon Beddingfield,
Tulane University, United States

*CORRESPONDENCE
Cristian Apetrei
apetreic@pitt.edu

†These authors have contributed equally to this work

‡These authors have contributed equally to this work

SPECIALTY SECTION
This article was submitted to Viral Immunology, a section of the journal Frontiers in Immunology

RECEIVED 18 March 2022
ACCEPTED 25 July 2022
PUBLISHED 12 August 2022

CITATION
Pandrea I, Brooks K, Desai RP, Tare M, Brenchley JM and Apetrei C (2022) I've looked at gut from both sides now: Gastrointestinal tract involvement in the pathogenesis of SARS-CoV-2 and HIV/SIV infections.
Front. Immunol. 13:899559.
doi: 10.3389/fimmu.2022.899559

I've looked at gut from both sides now: Gastrointestinal tract involvement in the pathogenesis of SARS-CoV-2 and HIV/SIV infections

Ivona Pandrea[1,2†], Kelsie Brooks[3†], Rahul P. Desai[1,4], Minali Tare[1,4], Jason M. Brenchley[3‡] and Cristian Apetrei[2,4*‡]

[1]Department of Pathology, School of Medicine, University of Pittsburgh, Pittsburgh, PA, United States, [2]Department of Infectious Diseases and Microbiology, Graduate School of Public Health, University of Pittsburgh, Pittsburgh, PA, United States, [3]Barrier Immunity Section, Laboratory of Viral Diseases, Division of Intramural Research, National Institute of Allergy and Infectious Diseases, National Institutes of Health, Bethesda, MD, United States, [4]Division of Infectious Diseases, Department of Medicine, School of Medicine, University of Pittsburgh, Pittsburgh, PA, United States

The lumen of the gastrointestinal (GI) tract contains an incredibly diverse and extensive collection of microorganisms that can directly stimulate the immune system. There are significant data to demonstrate that the spatial localization of the microbiome can impact viral disease pathogenesis. Here we discuss recent studies that have investigated causes and consequences of GI tract pathologies in HIV, SIV, and SARS-CoV-2 infections with HIV and SIV initiating GI pathology from the basal side and SARS-CoV-2 from the luminal side. Both these infections result in alterations of the intestinal barrier, leading to microbial translocation, persistent inflammation, and T-cell immune activation. GI tract damage is one of the major contributors to multisystem inflammatory syndrome in SARS-CoV-2-infected individuals and to the incomplete immune restoration in HIV-infected subjects, even in those with robust viral control with antiretroviral therapy. While the causes of GI tract pathologies differ between these virus families, therapeutic interventions to reduce microbial translocation-induced inflammation and improve the integrity of the GI tract may improve the prognoses of infected individuals.

KEYWORDS

HIV - human immunodeficiency virus, SIV, SARS-CoV-2, AIDS - acquired immunodeficiency syndrome, COVID - 19, inflammation, microbial translocation, barrier integrity

Introduction

Differently from Joni Mitchell, the Canadian-American singer-songwriter and painter who doesn't know love at all (in spite of looking at it from both sides), we know gastrointestinal (GI) tract tissue as an immune organ very well. It contains about 80% of the total leukocytes in the body (1), and most of the human microbiota (2–4) (Figure 1A). The GI tract is constantly exposed to foreign antigens from food and this exposure is critical for normal development of the mucosal immune system and immune tolerance (5–8).

The GI tract has the largest surface area exposed to the environment and the intestinal epithelia confers protection against toxic substances from food and microbes, both those normally present in the human microbiome, as well as those carried with food and water. The intestinal mucosal barrier is

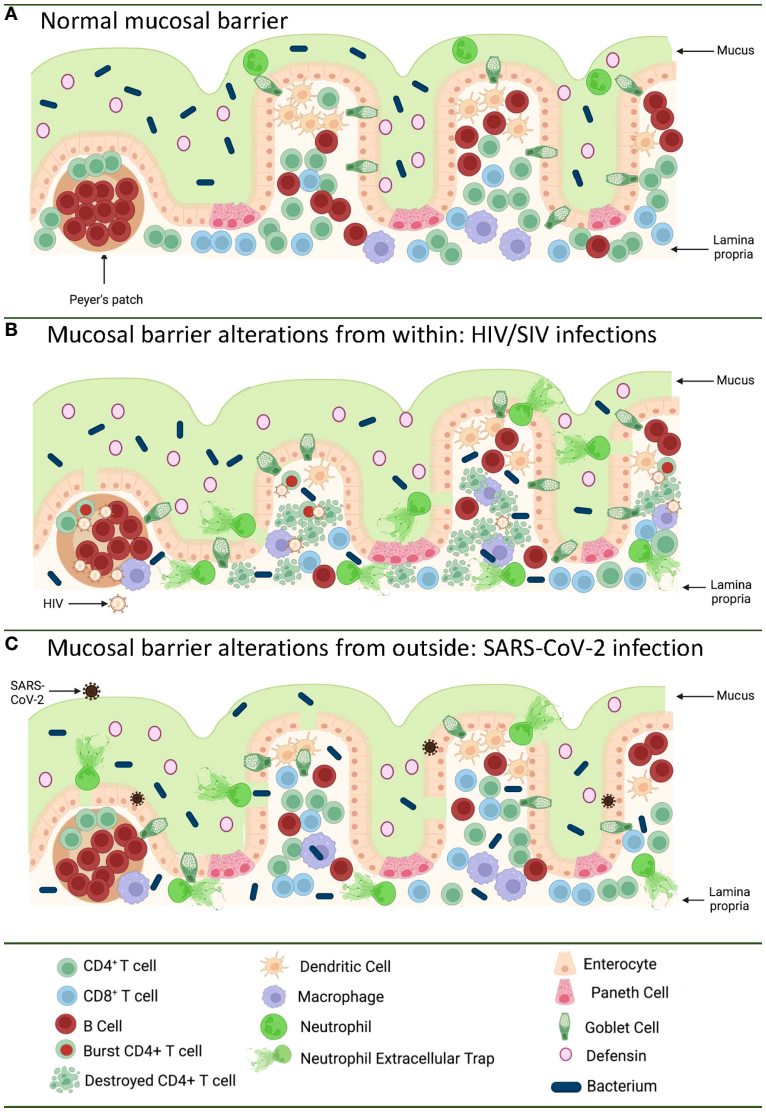

FIGURE 1
Pathways of the gastrointestinal tract damage in HIV/SIV and SARS-CoV-2 infections. **(A)** Normal GI tract is a continuous barrier which protects the internal milieu by the damage of an enormous microbiota existent in the GI lumen. This barrier is multistratified, being represented by mucus, a continuous intestinal epithelium, and immune effectors that capture translocated microbes. **(B)** While HIV/SIV penetrates the body at mucosal sites, GI infection occurs through systemic seeding. $CD4^+$ T cell destruction and the inflammatory responses contribute to the destruction of the mucosal barrier from within, leading to the translocation of the intestinal flora in the lamina propria and then systemically; **(C)** SARS-CoV-2 infection of the enterocytes (that express high levels of the ACE-2 and TMPRSS-2 receptor) produce direct epithelial destructions also leading to translocation of the intestinal microbiota to the lamina propria and then systemically. Mucosal damage is both a major determinant of long COVID, as well as of an incomplete immune recovery even in HIV-infected individuals receiving suppressive antiretroviral therapy. Was created with BioRender.com.

multilayered, with intestinal mucus, commensal bacteria, GI tract epithelium and the lamina propria immune system all contributing to host defense (9, 10) (Figure 1A). Protection is not limited to a physical barrier, but includes numerous active cell populations that exert secretory functions: goblet cells which produce mucus glycoproteins (11, 12); Paneth cells which produce antimicrobials that have the ability to specifically lyse bacteria (13); and B cells from the lamina propria which produce immunoglobulins (IgA) that capture bacteria that arriving to this gut level, preventing their successful translocation (14) (Figure 1A).

Breaches of the mucosal integrity of the GI tract are central to the pathogenesis of multiple chronic metabolic, autoimmune, and aging-related diseases (9, 10). Multiple infections can alter the integrity of the mucosal barrier including (15): human and simian immunodeficiency viruses (16–21); influenza virus infection (22); dengue (23); hepatitis B virus infection (24); hepatitis C virus infection (25); and SARS-CoV-2 (26, 27).

Furthermore, the quality of our intestinal microbiome is driving our overall morbidity (28–32). An inflammatory flora, such as the one associated with a Western diet (i.e. rich in saturated fats and sugars) drives a state of chronic inflammation, which triggers multiple systemic diseases and is roughly responsible for more than 50% of the deaths on the planet (33). Replacement with a healthy diet (i.e., Mediterranean diet rich in fiber, minerals and vitamins, and Omega 3) can alter the microbiome in as little as 3 weeks and change its phenotype to an anti-inflammatory one (34–42).

The interplay of the GI tract immune system and pathogens which disrupt this complex mucosal barrier is critically important in understanding pathogenesis, and providing targets for reducing damage. We will explore the well-studied impacts of HIV and SIV on the GI tract in addition to the parallels and distinctions that can be made in a recently emerged pandemic virus, SARS-CoV-2, and its corresponding disease, COVID-19.

Breaching the barrier from within: Mucosal pathogenesis of HIV and SIV infection

Even since the discovery of HIV, the involvement of the GI tract in the pathogenesis of AIDS was suggested by the high frequency of the gut dysfunction and wasting disease (43). Yet, the paradigm of HIV infection as a mucosal disease emerged only after the detailed characterization of the interactions between HIV and SIVs and their CD4-expressing target cells. It was reported that only the $CD4^+$ T cell subsets that expressed high levels of CCR5 (i.e. central memory cells, transitional memory cells, and effector memory cells) are preferentially targeted by HIV and SIV (44–47) and that the main reservoir is represented by the central memory cells (48). From a functional perspective, Th-17 $CD4^+$ T cells contribute to the maintenance of the gut integrity and are preferentially lost during progressive HIV and SIV infections (49–51). As such, since the vast majority of the effector memory cells are located at mucosal surfaces, numerous studies have shown that the first major immunologic injury inflicted by HIV/SIV to the immune system is the massive depletion of mucosal $CD4^+$ T cells (>95%) that occurs at the mucosal sites within three weeks from infection (52–54). As memory $CD4^+$ T cells are the preferential targets of HIV infection, their depletion is more prominent at the effector sites, such as the lamina propria, compared to inductive sites (i.e. the Peyer patches) which contain naïve $CD4^+$ T cells (55). $CD4^+$ T cell depletion within effector sites persists throughout chronic infection, irrespective of the virological and clinical outcome (56). Furthermore, differently from the circulating $CD4^+$ T cells, which can be rapidly restored to preinfection levels after administration of combination antiretroviral therapy (cART), mucosal $CD4^+$ T cell restoration is slow and incomplete (35-50% from the baseline levels) (56–58).

The severe immunologic insult produced following the interactions between HIV/SIV and their target cells within the GI tract trigger key pathogenic features of chronic SIV/HIV infection that drive disease progression (Figure 1B). Indeed, Th17 cells contribute to the maintenance of GI tract immunity through induction of mucins, claudins, and defensins, which are key components of the mucosal junctions and have antimicrobial activities; therefore, loss of Th17 cells directly compromises mucosal integrity (59). Their loss results in reduced levels of IL-17 and IL-22, which promote the recruitment of neutrophils and myeloid cells at the effector sites of the mucosa and lead to growth of epithelial cells (59–61). Alteration of the Th17/Treg ratio is associated with increased indoleamine-2,3-dioxygenase (IDO) expression by antigen-presenting cells (62–65). IDO is involved in the tryptophan metabolization (64), and IDO metabolites directly inhibit Th17 cell differentiation (66). IDO increases are also associated with decreased frequencies of CD103 antigen-presenting cells, which can induce Th17 cells (67). Altogether these features, which are specifically associated with pathogenic SIV infection and absent during the SIV infection of natural NHP hosts (in which Th17 cells are preserved) (49, 51), point to a vicious circle that leads to a continuous depletion of the Th17 population, the consequence of which is the occurrence and intensification of the mucosal damage during HIV/SIV infections.

The impact of HIV/SIV infection on the innate immune cell populations at the mucosal sites has also been extensively investigated. Progressive HIV and SIV infections lead to a reduction of both plasmacytoid dendritic cells (pDCs) and myeloid dendritic cells (mDCs) in both the peripheral blood and spleen, and alter their homing to the gut (68). Progressive infection leads to their excessive activation, leading to increased

turnover in tissues (68). Similar profiles of increased apoptosis and an altered functional profile upon HIV/SIV infections are observed for the gut-resident innate lymphocyte type III cells (69–71). As a result, instead of facilitating control of the virus through recruitment to the mucosal sites, the innate immune cells produce excess of cytokines; meanwhile their high mortality triggers release of more inflammatory cytokines by the surrounding cells, further enhancing mucosal inflammation and epithelial cell activation (72). Interestingly, mDC and macrophage recruitment to the mucosal sites also occurs during the nonprogressive SIV infections of the natural hosts or controller rhesus macaques (68). This process is, however, only transient, is not associated with excessive production of inflammatory cytokines, and does not result in their excessive death, strongly suggesting that the fate of the immune cell subsets and their functions in the GI tract is driven by the local environment (73). As such, the current view is that, being programmed to fight against the infections, the innate cells migrate to the gut in progressive, as well as in nonprogressive and controlled SIV infections. Yet, the innate cells become hyperactivated only in the pathogenic infections, due to their mucosal environment, which is altered by both the virus and translocated microbial products, and thus further fuel the inflammation, deepen the damage of the mucosal barrier, and contribute to the negative outcome of HIV/SIV infection (74, 75) (Figure 1B).

The HIV/SIV-associated immunological alterations at the mucosal sites result in structural and functional pathologies of the GI tract. Virus replication, inflammation and immune activation together with bystander apoptosis of the epithelial cells throughout the GI tract result in enterocyte loss and alterations of mucosal integrity (16). Progressive HIV and SIV infections trigger enterocyte loss through multiple mechanisms: (i) the virus itself can decrease glucose uptake by enterocytes through a Tat-mediated microtubule disruption or through GP120 binding to GPR15 on epithelial cells (76, 77); (ii) increased enterocyte apoptosis occurs through bystander effects, similar to other colitis (i.e. celiac disease) (78); (iii) excessive production of inflammatory cytokines (i.e., tumor necrosis factor-TNFα by innate and adaptive immune cells from the lamina propria) at the mucosal sites lead to increased apoptosis of the epithelial cells and perturbations of the tight junction epithelial barrier (79); and (iv) loss of IL22-producing innate lymphoid cells and Th17 cells leads to decreased proliferation of enterocytes (59, 61). Loss of epithelial GI tract integrity through any of these mechanisms in progressive HIV/SIV infection is associated with inflammation (80–83).

Enterocyte loss and subsequent intestinal alterations are associated with: (i) low levels of serum citrulline (a protein that is produced by the enterocytes); (ii) decreased ratio of the villous height/crypt depth (i.e., atrophy) (84); (iii) hyperproliferation of the crypt stem cells (resulting in malabsorption) (85); (iv) Increased plasma levels of the biomarkers of enterocyte damage, i.e., intestinal fatty acid binding protein (I-FABP) (86); (v) abnormal enterocyte differentiation through alterations of the sodium glucose transport and of the concentrations of intraepithelial calcium (87–89). GI tract dysfunction occurs as early as 14 days during progressive HIV/SIV infections and is associated with colitis, diarrhea, and malabsorption (43, 90).

These pathologies are specific to pathogenic SIV infections in macaques and absent during nonpathogenic SIV infections of the African nonhuman primates that are natural hosts of SIV (91–93). In these species, the mucosal lesions characteristic to pathogenic SIV infections do not occur during either the acute or chronic stages of infection (84, 94) due to an exquisite ability to maintain gut health throughout the SIV infection (94, 95).

Breaching the barrier from outside: Mucosal pathogenesis of SARS-CoV-2 infection

SARS-CoV-2 is the etiological agent of COVID-19, a respiratory disease characterized by severe pneumonia and a plethora of symptoms suggestive of viral pneumonia: cough and sputum production, sore throat, shortness of breath, fever, myalgia, and fatigue (96–99). However, despite SARS-CoV-2 infection's main clinical presentation as a respiratory tract infection, it may also cause symptoms associated with multiple organs, including the GI tract (diarrhea, anorexia, nausea, vomiting, and abdominal pain), liver (abnormal enzymes levels), pancreas (pancreatitis), kidney (proteinuria and hematuria, abnormal creatinine levels), brain (strokes, seizures, confusion, and brain inflammation), heart and blood vessels (elevations of cardiac injury biomarkers, palmus, chest distress, cardiac inflammation and injury, arrhythmias, and blood clots), eyes (conjunctivitis, membrane inflammation), anosmia (loss of smell), and ageusia (loss of sense of taste) (100–124).

To enter target cells, SARS-CoV-2 engages angiotensin-converting enzyme 2 (ACE2) as the entry receptor and serine protease TMPRSS2 for the Spike (S) protein priming (125, 126). Use of ACE2 is shared with SARS (127), but not with MERS, which uses a different receptor, DPP4 (128). ACE2 is widely distributed in the body, being identified in up to 72 tissues (129), and SARS-CoV-2 infection is likewise highly disseminated (130). The ACE2 protein is expressed in enterocytes, renal tubules, gallbladder, cardiomyocytes, male reproductive cells, placental trophoblasts, ductal cells, eyes, and vasculature (131). Notably, limited ACE2 expression is observed in the respiratory system both on the protein and mRNA level (132). However, a relatively limited number of cells express high levels of both ACE2 and TMPRSS2: Type II pneumocytes, nasal secretory cells, and absorptive enterocytes (131).

ACE2 expression in the human respiratory tract is highly heterogenous, being highest within regions of the sinonasal

cavity (in the nasal ciliated cells) and pulmonary alveoli; these are the sites of viral transmission and severe disease development, respectively (133–137). In the lung parenchyma, ACE2 is expressed on the apical surface of a small subset of alveolar type II cells, where it was colocalized with TMPRSS2 (133–137). Interestingly, ACE2 protein expression is not reported to be lower in children, who have a lower incidence of severe COVID-19, in some studies (133); however, other investigations have described lower levels of the protein transcript in children's airways (138).

ACE2 expression is increased in physiologic and pathologic circumstances: smoking is correlated with increased expression of the *ACE2* gene in the upper airway, but lower expression in certain lung cells (139). As such, smokers are 14 times more likely to develop a severe form of the disease (140). Interferon and influenza increase *ACE2* in human nasal epithelia and lung tissue (131). Some ACE2 inhibitors (i.e. lisinopril) have the ability to raise tissue levels of ACE2 in mice (141), while other studies did not find an increase of ACE2 expression in people treated with ACE2 inhibitors (137). Severe COVID-19, which is associated with high levels of inflammatory cytokines (IL-1β and type I and type III interferons), upregulates ACE2 expression, which has the potential to increase target cell availability and, thus, viral replication (131, 134, 139, 142). Yet, the impact on the variations of ACE2 expression on disease severity it is not known, and recently, it was reported that interferon-stimulated expression of ACE2 yields a truncated isoform that cannot bind SARS-CoV-2 (143).

Different clinical conditions were also reported to modulate ACE2 expression: hypertension, hyperlipidaemia, diabetes, chronic pulmonary diseases, and aging (134) (144). All these conditions are also risk factors for more severe clinical expression of COVID-19 (145–157). Note, however, that these data regarding ACE2 are highly debated and, to date, no comorbidity has been unambiguously associated with ACE2 expression level (144).

Several molecules were reported as alternative receptors for SARS-CoV-2, such as the C-type lectins DC-SIGN and L-SIGN (158–160), and TIM1 and AXL (161, 162). However, lectins and phosphatidylserine are not classical receptors for the virus: they are nonspecific and do not function efficiently in binding SARS-CoV-2 in the absence of ACE2 (163). Therefore, it was proposed that a more correct term for these molecules would be that of 'attachment factors' (144). CD147 is a transmembrane glycoprotein expressed ubiquitously in epithelial and immune cells, that was proposed as a receptor for SARS-CoV-2, yet its role as a viral receptor is downplayed by the observation that CD147 cannot bind to the S protein (164–166). Neuropilin 1 (NRP1) was also reported to be a host factor for SARS-CoV-2 (167, 168). NRP1 is expressed in olfactory and respiratory epithelial cells (167), yet its expression is low in the SARS-CoV-2 target cells (ciliated cells) and high in the goblet cells, which are not susceptible to SARS-CoV-2 (134, 169). B0AT1 is a virus cofactor that is expressed in the GI tract and kidney, but not in the lung; B0AT1 expression in the small intestine depends on interaction with ACE2 (170). Additional human genes are important for SARS-CoV-2 infection of lung epithelial cells: the GTPase encoded by *RAB7A* is critical for endocytosis, and *CTSL* encoding cathepsin L contributes to SARS-CoV-2 spike cleavage; yet more genes support other viral life cycle stages (171). Integrins were also reported to mediate cell entry of SARS-CoV-2 (172, 173), although other studies did not confirm these observations (174). Reduction of human *ACE2* in the epithelia of K18 transgenic mice in concert with increased *CTSL* did not alter the pathogenesis of SARS-CoV-2 (175), further suggesting the importance of the interplay between host factors at mucosal sites for successful viral entry and propagation.

Enterocytes express ACE2 and support viral replication that is enhanced by TMPRSS2 and 4 (176, 177), and SARS-CoV-2 virions have been directly visualized in the GI tracts of COVID-19 patients (178). SARS-CoV-2 infection rapidly induces activated $CD8^+$ T cell infiltration to the intestinal epithelium (179) and increased effector $CD4^+$ and $CD8^+$ T cells in the lamina propria (180). This is in spite of a lack of gross pathological changes in histological findings on endoscopy in the same patients (179, 180), though others have reported abnormalities such as crypt hyperplasia with necrotic cell debris in the absence of inflammation following a positive SARS-CoV-2 test (181). Similar to this dichotomy, several studies have reported presence (182, 183) or absence (184) of viable virus isolation from stool, while viral RNA may be shed in feces for prolonged periods compared to respiratory tract samples (185, 186); persistence of viral antigens have also been reported in GI biopsies for approximately three months following infection while nasopharyngeal swabs were negative for SARS-CoV-2 RNA (187). Such a paucity of consensus regarding the impact of viral replication on GI inflammation and/or pathology is in stark contrast to HIV/SIV infection, in which ongoing viral replication in untreated infection is a clear determinant of mucosal and systemic inflammation, although such inflammation is reduced but not eliminated with the drastic reduction of viral replication during ART (188–190).

SARS-CoV-2 infection of an *in vitro* GI tract model demonstrates direct damage to tight junctions and upregulated proinflammatory cytokine transcripts (191) (Figure 1C). GI symptoms in COVID-19 have also been associated with elevated liver enzymes (192) while increased markers of inflammation such as TNFα and IL-6 have separately been associated with severe and/or fatal disease (193–195). The capability of SARS-CoV-2 to enter and replicate in GI barrier cells, with corresponding immune responses and GI symptoms, suggests GI tract damage may be a critical component of COVID-19 disease.

Microbial translocation and its role in inflammation: Are lessons learned from HIV/SIV relevant to SARS-CoV-2?

GI tract dysfunction in progressive HIV and SIV infection leads to translocation of microbial products from the lumen. However, this phenomenon is not specific to SIV/HIV infection, and occurs in multiple clinical conditions in which mucosal epithelium is altered and gut permeability is increased (17). Microbial translocation is a key determinant of systemic inflammation, which is the most important driver of progressive HIV/SIV disease progression. The intestinal flora is large and diverse (approximately 10^{14} bacteria, fungi, protozoans, helminths, and viruses) and is composed of numerous antigens which can directly stimulate the immune system, including: peptidoglycan and lipoteichoic acid (through TLR2), lipopolysaccharide (LPS, through TLR4), flagellin (through TLR5), CpG-containing DNA (through TLR9 and other cytoplasmic sensors), and double stranded and single stranded RNAs (through TLR 7/8 and other cytoplasmic sensors) (88). Microbial translocation also includes fungal products that have relevance for immune activation and clinical outcome independently of bacterial products (196, 197). GI tract dysfunction, therefore, leads to significant inflammation with increased production of proinflammatory cytokines IL-1β, IL-6, TNFα and interferons (88).

Microbial translocation is specifically associated with progressive SIV/HIV infections and is nearly absent in African nonhuman primates that are natural hosts of SIV (198), and studies in nonhuman primates have established a direct link between microbial translocation and inflammation. Chronically SIV-infected African green monkeys (AGMs) that do not progress to AIDS maintain a healthy mucosal barrier and lack evidence of microbial translocation and systemic inflammation (91, 92, 94). However, intravenous administration of LPS, either in single dose or in prolonged administration over a three-week duration, resulted in increased levels of inflammation and coagulation markers (199). Similarly, alcohol or dextran sulphate administration to rhesus macaques increased GI tract permeability, induced microbial translocation, and resulted in increased levels of inflammation and SIV replication (200). Conversely, direct blockade of microbial translocation in progressively SIV infected Asian macaques with sevelamer, a chelator of LPS, resulted in a significant reduction of systemic inflammation and coagulation markers (201). Altogether, these studies provide direct evidence for microbial translocation as a key determinant of immune activation and associated pathologies, such as non-AIDS comorbidities, in SIV infection (202, 203).

Due to the key role of microbial translocation in the pathogenesis of HIV/SIV infection, studies have also focused on characterization of the impact of infection on the composition of the GI microbiome. Analysis of longitudinal samples from Asian macaques has shown that, while levels of enteric virus genomes increase, the bacterial microbiome is not dramatically altered (204–206). However, analyses of cross-sectional cohorts of HIV-infected and uninfected individuals routinely demonstrate the bacterial microbiomes of infected humans are altered (207–209). Recent studies have shown that one major contributor to the bacterial dysbiosis observed in HIV-infected individuals are risk factors for HIV acquisition (210, 211); when these risk factors are controlled for, significant dysbiosis is observed only in individuals with advanced HIV disease (210, 212). Moreover, while high fat diets lead to accelerated SIV disease in Asian macaques, with significantly increased inflammation (213), antibiotic-induced dysbiosis of the GI tract microbiome is insufficient to accelerate SIV disease (214).

Alteration to the GI tract virome may also play a role in disease. A significant increase in the size of the fecal virome was reported to occur in the progressive SIV infection of macaques, while no such change was detected in the nonprogressive SIV infection of AGMs (204). Furthermore, potentially pathogenic viruses, such as adenoviruses, are specifically colocalized with the areas of structural damage of the GI tract in progressively SIV-infected macaques (204). Finally, analysis of circulating microbial nucleic acids and those in tissues have demonstrated that microbes which translocate are not a representation of those present within the lumen, and the individual types of translocating organisms can be associated with prognosis (20, 205). Taken together it is clear that GI tract dysfunction, microbial translocation, and resulting inflammation play important roles in progressive HIV and SIV infections.

Alterations to the GI tract bacterial microbiome have been reported in hospitalized (215, 216) and even asymptomatic COVID-19 patients (217), though it is challenging to control for the confounding effects of diet, environment, and chronic conditions between infected and uninfected individuals to assess changes in microbial communities. K18 transgenic mice with a controlled diet and environment demonstrate dose-dependent GI tract microbiome alterations with SARS-CoV-2 infection (218), but the integrity of the intestinal barrier was not assessed. However, inflammation of the intestine itself has been implicated in SARS-CoV-2 infection, as COVID-19 patients with diarrhea demonstrated significantly higher levels of fecal calprotectin, largely produced by neutrophils and an indication of neutrophilic inflammation, which correlated with systemic IL-6 levels (219). Additionally, GI tract microbial dysbiosis and an increase in LPS-binding protein (LBP) were observed in severe COVID-19 patients over those with mild COVID-19, with LBP correlating to other inflammatory markers such as C-reactive protein (CRP) and IL-6 (220). Furthermore, bacterial proteins were found in COVID-19 patient blood plasma (220). Finally, in a comprehensive study by Giron

et al., the tight junction protein zonulin was significantly elevated in COVID-19 patients with moderate or severe disease over controls, as were LBP and the product of monocyte inflammation in response to LPS, soluble CD14 (221). The levels of zonulin and LBP were correlated with a number of systemic inflammatory markers, again including IL-6 and CRP (221). Interestingly, both in Giron et al. (221) and another study from Hoel et al. investigating GI tract barrier integrity in COVID-19 patients (222), there was an increase in LBP without an increase in I-FABP indicative of enterocyte damage, suggesting that the epithelial barrier is disrupted by another means. The translocation of microbes and/or microbial products across a damaged intestinal epithelium, however, can induce systemic inflammation and contribute to the pathogenesis of SARS-CoV-2 infection (Figure 1C), as in HIV and SIV infection. Furthermore, intestinal dysbiosis in HIV infection was reported to be associated with low $CD4^+$ T cell reconstitution, which may be relevant for COVID-19-associated lymphopenia (223).

While systemic inflammation, including that which may be induced by microbial translocation, is associated with COVID-19 mortality, there are additional mechanisms in which inflammation influences COVID-19 morbidity. Symptoms may persist or recur after primary infection, leading to the diagnosis of Post-Acute Sequalae of SARS-CoV-2 (PASC) or "long COVID-19" (https://recovercovid.org). Multisystem inflammatory syndrome can also occur in children (MIS-C) or adults (MIS-A) following COVID-19 diagnosis (https://www.cdc.gov/mis/about.html), and is manifested by severe organ system inflammation similar to Kawasaki disease that can occur in the presence or absence of viral antigen (224) and may be attributed to super-antigen-like attributes of SARS-CoV-2 spike protein (225). Notably, children and adults exhibit differential inflammatory responses during primary COVID-19, with adults demonstrating higher levels of LBP and IL-6, while healthy adult and pediatric controls were not significantly different in these markers (226). However, children with MIS had higher rates of GI symptoms than children with primary COVID-19, as well as increased zonulin, LBP, and IL-6 in the early stage of MIS-C (226, 227). Furthermore, mortality in MIS-C cases and primary severe pediatric COVID-19 is similar (228), suggesting that the high levels of inflammation in MISC-C may contribute to mortality as in adult COVID-19 cases. The impact of GI tract barrier disruption has been minimally explored in MIS-A or PASC cases, with one study reporting gut microbiome dysbiosis in adults with PASC at six months post-infection versus convalescent COVID-19 patients without PASC, who had returned to microbial communities similar to previously uninfected individuals (229). An additional study observed higher TNFα and IP-10 in the early recovery phase from primary COVID-19 in adults who would go on to experience PASC (230). Understanding the mechanisms of PASC and MIS, including GI damage, microbial translation, and resulting inflammation that may contribute to mortality, is therefore of critical importance. Insights from HIV/SIV infections that persistent immune activation and inflammation may occur with low levels or absence of viral antigen during virologically suppressive antiretroviral therapy (188–190) are the foundation upon which a more detailed knowledge of inflammation following primary COVID-19 may be built to provide prevention and treatment strategies.

Therapeutic approaches aimed at limiting the impact of gut dysfunction on the outcome of HIV and SARS-CoV-2 infections

Although ART has dramatically improved the lifespan of individuals living with HIV, with life expectancy reaching near that of uninfected individuals (231, 232), treatment neither eliminates the virus nor all inflammation (233, 234). Therapeutics to complement ART and reduce the GI tract dysfunction and inflammation experienced from early infection on have taken many forms, from microbial products to probiotics to small peptides such as an apoA-I mimetic (235). Additionally, immunomodulatory treatments for reducing GI inflammation in inflammatory bowel diseases (IBD) have been assessed, and at least one therapy was evaluated for loss of gut barrier integrity and inflammation in a MIS-C case (227). The shared mechanisms of GI tract permeability and resulting inflammation in these infectious and chronic conditions suggest that strategies to effectively address inflammation in one condition may prove beneficial in another as well.

Gut microbiota are key regulators of GI tract immunity, and promotion of anti-inflammatory functions can be attempted in many ways, including provision of prebiotics, probiotics, and microbial metabolic products. Prebiotic therapies including bacterial energy sources such as short and long chain oligosaccharides have shown modest improvements to gut-related inflammation in HIV infected individuals, with significant reductions in CRP and IL-6 (236) or sCD14 (237). However, these studies were conducted in small numbers of individuals, and only demonstrated these effects in people not receiving cART (237) or individuals who had initiated treatment but poorly reconstituted $CD4^+$ T cell counts of <350, and without significant change to gut microbiota alpha diversity (236). Polyphenol, a key component of the Amazonian fruit *Camu Camu* (CC), has also been suggested as a prebiotic candidate based on its anti-inflammatory and antioxidant properties in animal models and tobacco smokers, and is under investigation for use in HIV infected individuals (238, 239).

Directly modifying the gut microbiota through administration of microbial strains as probiotics has also been

trialed in HIV patients receiving cART to mixed results: men with $CD4^+$ T cell counts <350 did not experience changes in systemic inflammation with probiotics including eight bacterial strains, and may have experienced increased T cell activation (240); two additional studies with distinct single bacterial strain probiotics observed no significant changes with treatment (241, 242); a study with multi-strain bacterial probiotics has demonstrated reductions in systemic inflammatory markers (D-dimer, IL-6, CRP), but no reductions in LPS or sCD14 (243); one study has shown improved gut barrier health with lower enterocyte apoptosis in the intestine and increased Th17 cell in GALT with high-dose, multi-strain bacterial probiotics (244). Probiotic effects (or lack thereof) may be influenced by a number of factors such as the strain(s) used, dose, and duration of treatment; in the studies detailed above, gut bacterial microbiome alterations were not assessed (241) or not observed (242) in the single bacterial strain probiotic treatments, with only multi-strain treatments demonstrating changes to the microbial communities (243, 244). Attempts to alter the complex gut microbiota may therefore require complex therapeutics, and indeed combinations of pre- and probiotics (synbiotics) have been utilized. However, like their probiotic counterparts, these studies have shown mixed results, with unaltered sCD14 and CRP levels in women (245), reduction in IL-6 in ART-naïve individuals (246), and lessened gut dysfunction in ART-treated macaques (247).

Supplementation with microbial metabolic products such as short-chain fatty acids, which are produced by GI tract microbiota through fiber fermentation and promote intestinal homeostasis (248, 249), has long been sought as a means of reducing GI tract inflammation (250). A recent study utilizing sodium propionate in conjunction with cART has shown a transient increase in circulating IL-17, but consistent decline in $CD4^+$ Th17 and Treg cells (251), which may not promote improved gut dysfunction.

Additional microbial therapies to promote intestinal barrier integrity warrant further investigation, however: mucosaly-associated fungi promoted IL-22 and IL-17 production in the intestine of mice, promoting barrier integrity and reducing damage during infection (252). Modulating bacterial communities to specifically reduce those associated with enhanced inflammation, rather than providing beneficial bacteria as probiotics, also may be a promising alternative approach: bacteriophage mediated delivery of CRISPR-Cas9 has successfully reduced specific bacterial strains in the intestines of mice (253).

Although most therapies for reduced inflammation induced by GI tract damage target the gut microbiota, another means of modulating dysregulated gut inflammation includes apoA-I mimetics, which bind LPS and lipids. Not only has an apoA-I mimetic peptide demonstrated reduction of HDL cholesterol *ex vivo* (254), but the molecule and another mimetic have also reduced inflammatory cytokines such as TNFα and IL-6 in the plasma of HIV-infected humanized mice (235). These peptides do not directly interact with the virus, and have already been implicated in treatment of chronic non-infectious inflammatory GI tract conditions such as inflammatory bowel disease (IBD) (255). Investigated as a complement to ART, apoA-I mimetics could be an excellent candidate for reduction of HIV or SARS-CoV-2 induced GI tract dysregulation and inflammation.

Steroids are a clear treatment for consideration to reduce inflammation, but are not components of standard therapies for individuals living with HIV. However, in an acute infection characterized by hyperinflammatory conditions such as COVID-19, the immunosuppressive effects of corticosteroids have been beneficial: in severe COVID-19 patients, moderate doses of dexamethasone administered for a short duration reduced the duration of hospitalization and mortality (256–260).

Finally, cell signaling approaches have been taken to reduce inflammation resulting from GI tract disruption. In a case of severe MIS-C, inhibiting zonulin signaling with a zonulin receptor agonist was undertaken to improve tight junctions, with tight junction loss hypothesized to lead to antigenemia and severe systemic inflammation (227). The child's condition did improve with treatment, as evidenced by decreased CRP, D-dimer, and indeed lower SARS-CoV-2 spike protein in the blood (227). This virus-independent means of reducing GI tract disruption, which is currently approved for a clinical trial for celiac disease treatment (261), may be appropriate for HIV as well, as might anti-inflammatory treatments for other chronic immune conditions such as IBD. Although TNF antagonist and immunosuppressive thiopurine treatment was associated with risk of hospitalization or death from COVID-19, TNF antagonist treatment alone was associated with lower odds ratios of hospitalization or death (262). Treatment with anti-TNFα antibodies has proven successful at reducing inflammation in clinical trials (263) and may be a safe strategy for reducing GI tract inflammation that results from viral infection, either chronically in HIV or acutely in SARS-CoV-2; indeed anti-TNFα antibodies were successful at reducing pulmonary pathology in a case study of a COVID-19 patient (264) and in inflammation and pathology in progressive SIV infection (79). Furthermore, anti-IL-6 therapies have been investigated for HIV and SARS-CoV-2 and proposed for inflammatory gut diseases, though efficacy has been mixed for both viral infections (265–268).

In conclusion, despite the distinctions of SARS-CoV-2 and HIV infections in terms of target cells, viral persistence, and symptomatology, there are considerable parallels in the loss of gut barrier integrity and corresponding inflammation that results. These parallels suggest that therapies to address chronic HIV inflammation, as well as that of non-infectious diseases, may be appropriate for treating SARS-CoV-2. Although the infection is acute rather than chronic, MIS cases strongly suggest persistent or recrudescent damage of organ systems including the GI tract that can lead to serious and fatal

inflammation. Treatment therapies to reduce GI tract damage and/or resulting inflammation may therefore not only improve acute SARS-CoV-2 infection outcomes, but also improve morbidity and mortality associated with subsequent multisystem inflammation.

Author contributions

IP KB, JB, and CA designed, wrote, and edited the manuscript. All authors contributed to literature screening, writing, and editing and approved the submitted version.

Funding

IP and CA are supported by grants from the National Institutes of Health/National Institute of Diabetes and Digestive and Kidney Diseases/National Heart, Lung and Blood Institute/ National Institute of Allergy and Infectious Diseases: R01 DK130481 (IP), R01 DK113919 (IP/CA), R01 DK119936 (CA), R01 DK131476 (CA), RO1 HL117715 (IP), R01 HL123096 (IP), R01 HL154862 (IP), R01 AI119346 (CA). This study was funded, in part, by the Division of Intramural Research, NIAID. The content of this publication does not necessarily reflect the views or policies of the Department of Health and Human Services, nor does mention of trade names, commercial products, or organizations imply endorsement by the U.S. Government. The funders had no role in study design, data collection and analysis, decision to publish, or preparation of the manuscript.

Acknowledgement

Figure 1 was created with BioRender.com.

Conflict of interest

The authors declare that the research was conducted in the absence of any commercial or financial relationships that could be construed as a potential conflict of interest.

Publisher's note

References

1. Wiertsema SP, van Bergenhenegouwen J, Garssen J, Knippels LMJ. The interplay between the gut microbiome and the immune system in the context of infectious diseases throughout life and the role of nutrition in optimizing treatment strategies. *Nutrients 13* (2021). doi: 10.3390/nu13030886

2. Dickson RP. The microbiome and critical illness. *Lancet Respir Med* (2016) 4:59–72. doi: 10.1016/S2213-2600(15)00427-0

3. Miniet AA, Grunwell JR, Coopersmith CM. The microbiome and the immune system in critical illness. *Curr Opin Crit Care* (2021) 27:157–63. doi: 10.1097/MCC.0000000000000800

4. Virgin HW. The virome in mammalian physiology and disease. *Cell* (2014) 157:142–50. doi: 10.1016/j.cell.2014.02.032

5. Rodriguez-Sillke Y, Visekruna A, Glauben R, Siegmund B, Steinhoff U. Recognition of food antigens by the mucosal and systemic immune system: Consequences for intestinal development and homeostasis. *Int J Med Microbiol* (2021) 311:151493. doi: 10.1016/j.ijmm.2021.151493

6. Ku HJ, Kim YT, Lee JH. Microbiome study of initial gut microbiota from newborn infants to children reveals that diet determines its compositional development. *J Microbiol Biotechnol* (2020) 30:1067–71. doi: 10.4014/jmb.2002.02042

7. Mohammadkhah AI, Simpson EB, Patterson SG, Ferguson JF. Development of the gut microbiome in children, and lifetime implications for obesity and cardiometabolic disease. *Children (Basel) 5* (2018). doi: 10.3390/children5120160

8. Mendez CS, Bueno SM, Kalergis AM. Contribution of gut microbiota to immune tolerance in infants. *J Immunol Res* (2021) 2021:7823316. doi: 10.1155/2021/7823316

9. Martel J, Chang SH, Ko YF, Hwang TL, Young JD, Ojcius DM. Gut barrier disruption and chronic disease. *Trends Endocrinol Metab* (2022). doi: 10.1016/j.tem.2022.01.002

10. Turner JR. Intestinal mucosal barrier function in health and disease. *Nat Rev Immunol* (2009) 9:799–809. doi: 10.1038/nri2653

11. Knoop KA, Newberry RD. Goblet cells: multifaceted players in immunity at mucosal surfaces. *Mucosal Immunol* (2018) 11:1551–7. doi: 10.1038/s41385-018-0039-y

12. Paone P, Cani PD. Mucus barrier, mucins and gut microbiota: The expected slimy partners? *Gut* (2020) 69:2232–43. doi: 10.1136/gutjnl-2020-322260

13. Bevins CL, Salzman NH. Paneth cells, antimicrobial peptides and maintenance of intestinal homeostasis. *Nat Rev Microbiol* (2011) 9:356–68. doi: 10.1038/nrmicro2546

14. Allaire JM, Crowley SM, Law HT, Chang SY, Ko HJ, Vallance BA. The intestinal epithelium: Central coordinator of mcosal immunity. *Trends Immunol* (2018) 39:677–96. doi: 10.1016/j.it.2018.04.002

15. Serek P, Oleksy-Wawrzyniak M. The effect of bacterial infections, probiotics and zonulin on intestinal barrier integrity. *Int J Mol Sci 22* (2021). doi: 10.3390/ijms222111359

16. Brenchley JM, Douek DC. The mucosal barrier and immune activation in HIV pathogenesis. *Curr Opin HIV AIDS* (2008) 3:356–61. doi: 10.1097/COH.0b013e3282f9ae9c

17. Brenchley JM, Douek DC. Microbial translocation across the GI tract. *Annu Rev Immunol* (2012) 30:149–73. doi: 10.1146/annurev-immunol-020711-075001

18. Brenchley JM, Price DA, Douek DC. HIV Disease: fallout from a mucosal catastrophe? *Nat Immunol* (2006) 7:235–9. doi: 10.1038/ni1316

19. Brenchley JM, Price DA, Schacker TW, Asher TE, Silvestri G, Rao S, et al. Microbial translocation is a cause of systemic immune activation in chronic HIV infection. *Nat Med* (2006) 12:1365–71. doi: 10.1038/nm1511

20. Nganou-Makamdop K, Talla A, Sharma AA, Darko S, Ransier A, Laboune F, et al. Translocated microbiome composition determines immunological outcome in treated HIV infection. *Cell* (2021) 184:3899–914.e16. doi: 10.1016/j.cell.2021.05.023

21. Kleinman AJ, Pandrea I, Apetrei C. So pathogenic or so what?-A brief overview of SIV pathogenesis with an emphasis on cure research. *Viruses 14* (2022). doi: 10.3390/v14010135

22. Sencio V, Gallerand A, Gomes Machado M, Deruyter L, Heumel S, Soulard D, et al. Influenza virus infection impairs the gut's barrier properties and favors secondary enteric bacterial infection through reduced production of short-chain fatty acids. *Infect Immun* (2021) 89:e0073420.

23. van de Weg CA, Pannuti CS, de Araujo ES, van den Ham HJ, Andeweg AC, Boas LS, et al. Microbial translocation is associated with extensive immune activation in dengue virus infected patients with severe disease. *PLoS Negl Trop Dis* (2013) 7:e2236.

24. Kassa Y, Million Y, Gedefie A, Moges F. Alteration of gut microbiota and its impact on immune response in patients with chronic HBV infection: A review. *Infect Drug Resist* (2021) 14:2571–8. doi: 10.2147/IDR.S305901

25. Preveden T, Scarpellini E, Milic N, Luzza F, Abenavoli L. Gut microbiota changes and chronic hepatitis c virus infection. *Expert Rev Gastroenterol Hepatol* (2017) 11:813–9. doi: 10.1080/17474124.2017.1343663

26. Devaux CA, Lagier JC, Raoult D. New insights into the physiopathology of COVID-19: SARS-CoV-2-associated gastrointestinal illness. *Front Med (Lausanne)* (2021) 8:640073. doi: 10.3389/fmed.2021.640073

27. Johnson SD, Olwenyi OA, Bhyravbhatla N, Thurman M, Pandey K, Klug EA, et al. Therapeutic implications of SARS-CoV-2 dysregulation of the gut-brain-lung axis. *World J Gastroenterol* (2021) 27:4763–83. doi: 10.3748/wjg.v27.i29.4763

28. Fromentin S, Forslund SK, Chechi K, Aron-Wisnewsky J, Chakaroun R, Nielsen T, et al. Microbiome and metabolome features of the cardiometabolic disease spectrum. *Nat Med* (2022) 28:303–14. doi: 10.1038/s41591-022-01688-4

29. Blaser MJ. Antibiotic use and its consequences for the normal microbiome. *Science* (2016) 352:544–5. doi: 10.1126/science.aad9358

30. Cox LM, Blaser MJ. Antibiotics in early life and obesity. *Nat Rev Endocrinol* (2015) 11:182–90. doi: 10.1038/nrendo.2014.210

31. Poore GD, Kopylova E, Zhu Q, Carpenter C, Fraraccio S, Wandro S, et al. Microbiome analyses of blood and tissues suggest cancer diagnostic approach. *Nature* (2020) 579:567–74. doi: 10.1038/s41586-020-2095-1

32. Jasinska AJ, Dong TS, Lagishetty V, Katzka W, Jacobs JP, Schmitt CA, et al. Shifts in microbial diversity, composition, and functionality in the gut and genital microbiome during a natural SIV infection in vervet monkeys. *Microbiome* (2020) 8:154. doi: 10.1186/s40168-020-00928-4

33. Furman D, Campisi J, Verdin E, Carrera-Bastos P, Targ S, Franceschi C, et al. Chronic inflammation in the etiology of disease across the life span. *Nat Med* (2019) 25:1822–32. doi: 10.1038/s41591-019-0675-0

34. Del Chierico F, Vernocchi P, Dallapiccola B, Putignani L. Mediterranean Diet and health: food effects on gut microbiota and disease control. *Int J Mol Sci* (2014) 15:11678–99. doi: 10.3390/ijms150711678

35. De Filippis F, Pellegrini N, Vannini L, Jeffery IB, La Storia A, Laghi L, et al. High-level adherence to a Mediterranean diet beneficially impacts the gut microbiota and associated metabolome. *Gut* (2016) 65:1812–21. doi: 10.1136/gutjnl-2015-309957

36. Mitsou EK, Kakali A, Antonopoulou S, Mountzouris KC, Yannakoulia M, Panagiotakos DB, et al. Adherence to the Mediterranean diet is associated with the gut microbiota pattern and gastrointestinal characteristics in an adult population. *Br J Nutr* (2017) 117:1645–55. doi: 10.1017/S0007114517001593

37. Nagpal R, Shively CA, Appt SA, Register TC, Michalson KT, Vitolins MZ, et al. Gut microbiome composition in non-human primates consuming a Western or Mediterranean diet. *Front Nutr* (2018) 5:28. doi: 10.3389/fnut.2018.00028

38. Podadera-Herreros A, Alcala-Diaz JF, Gutierrez-Mariscal FM, Jimenez-Torres J, Cruz-Ares S, Arenas-de Larriva AP, et al. Long-term consumption of a mediterranean diet or a low-fat diet on kidney function in coronary heart disease patients: The CORDIOPREV randomized controlled trial. *Clin Nutr* (2022) 41:552–9. doi: 10.1016/j.clnu.2021.12.041

39. Estruch R, Ros E, Salas-Salvado J, Covas MI, Corella D, Aros F, et al. Primary prevention of cardiovascular disease with a Mediterranean diet. *N Engl J Med* (2013) 368:1279–90. doi: 10.1056/NEJMoa1200303

40. Pauwels EK. The protective effect of the Mediterranean diet: focus on cancer and cardiovascular risk. *Med Princ Pract* (2011) 20:103–11. doi: 10.1159/000321197

41. Panagiotakos DB, Dimakopoulou K, Katsouyanni K, Bellander T, Grau M, Koenig W, et al. Mediterranean Diet and inflammatory response in myocardial infarction survivors. *Int J Epidemiol* (2009) 38:856–66. doi: 10.1093/ije/dyp142

42. Feart C, Samieri C, Alles B, Barberger-Gateau P. Potential benefits of adherence to the Mediterranean diet on cognitive health. *Proc Nutr Soc* (2013) 72:140–52. doi: 10.1017/S0029665112002959

43. Kotler DP, Gaetz HP, Lange M, Klein EB, Holt PR. Enteropathy associated with the acquired immunodeficiency syndrome. *Ann Intern Med* (1984) 101:421–8. doi: 10.7326/0003-4819-101-4-421

44. Veazey RS, DeMaria M, Chalifoux LV, Shvetz DE, Pauley DR, Knight HL, et al. Gastrointestinal tract as a major site of CD4+ T cell depletion and viral replication in SIV infection. *Science* (1998) 280:427–31. doi: 10.1126/science.280.5362.427

45. Veazey RS, Lackner AA. The gastrointestinal tract and the pathogenesis of AIDS. *AIDS 12 Suppl A* (1998), S35–42.

46. Smit-McBride Z, Mattapallil JJ, McChesney M, Ferrick D, Dandekar S. Gastrointestinal T lymphocytes retain high potential for cytokine responses but have severe CD4+ T-cell depletion at all stages of simian immunodeficiency virus infection compared to peripheral lymphocytes. *J Virol* (1998) 72:6646–56. doi: 10.1128/JVI.72.8.6646-6656.1998

47. Jasinska AJ, Pandrea I, Apetrei C. CCR5 as a coreceptor for human immunodeficiency virus and simian immunodeficiency viruses: A prototypic love-hate affair. *Front Immunol* (2022) 13:835994. doi: 10.3389/fimmu.2022.835994

48. Chomont N, El-Far M, Ancuta P, Trautmann L, Procopio FA, Yassine-Diab B, et al. HIV Reservoir size and persistence are driven by T cell survival and homeostatic proliferation. *Nat Med* (2009) 15:893–900. doi: 10.1038/nm.1972

49. Brenchley JM, Paiardini M, Knox KS, Asher AI, Cervasi B, Asher TE, et al. Differential Th17 CD4 T-cell depletion in pathogenic and nonpathogenic lentiviral infections. *Blood* (2008) 112:2826–35. doi: 10.1182/blood-2008-05-159301

50. Cecchinato V, Trindade CJ, Laurence A, Heraud JM, Brenchley JM, Ferrari MG, et al. Altered balance between Th17 and Th1 cells at mucosal sites predicts AIDS progression in simian immunodeficiency virus-infected macaques. *Mucosal Immunol* (2008) 1:279–88. doi: 10.1038/mi.2008.14

51. Favre D, Lederer S, Kanwar B, Ma ZM, Proll S, Kasakow Z, et al. Critical loss of the balance between Th17 and T regulatory cell populations in pathogenic SIV infection. *PLoS Pathog* (2009) 5:e1000295. doi: 10.1371/journal.ppat.1000295

52. Li Q, Duan L, Estes JD, Ma ZM, Rourke T, Wang Y, et al. Peak SIV replication in resting memory CD4+ T cells depletes gut lamina propria CD4+ T cells. *Nature* (2005) 434:1148–52. doi: 10.1038/nature03513

53. Mattapallil JJ, Douek DC, Hill B, Nishimura Y, Martin M, Roederer M. Massive infection and loss of memory CD4+ T cells in multiple tissues during acute SIV infection. *Nature* (2005) 434:1093–7. doi: 10.1038/nature03501

54. Pandrea IV, Gautam R, Ribeiro RM, Brenchley JM, Butler IF, Pattison M, et al. Acute loss of intestinal CD4+ T cells is not predictive of simian immunodeficiency virus virulence. *J Immunol* (2007) 179:3035–46. doi: 10.4049/jimmunol.179.5.3035

55. Veazey RS, Marx PA, Lackner AA. The mucosal immune system: primary target for HIV infection and AIDS. *Trends Immunol* (2001) 22:626–33. doi: 10.1016/S1471-4906(01)02039-7

56. Le Hingrat Q, Sereti I, Landay AL, Pandrea I, Apetrei C. The hitchhiker guide to CD4+ T-cell depletion in lentiviral infection. A critical review of the dynamics of the CD4+ T cells in SIV and HIV infection. *Front Immunol* (2021) 12:695674. doi: 10.3389/fimmu.2021.695674

57. Mehandru S, Poles MA, Tenner-Racz K, Jean-Pierre P, Manuelli V, Lopez P, et al. Lack of mucosal immune reconstitution during prolonged treatment of acute and early HIV-1 infection. *PLoS Med* (2006) 3:e484.

58. Saluzzo S, Pandey RV, Gail LM, Dingelmaier-Hovorka R, Kleissl L, Shaw L, et al. Delayed antiretroviral therapy in HIV-infected individuals leads to irreversible depletion of skin- and mucosa-resident memory T cells. *Immunity* (2021) 54:2842–58.e5. doi: 10.1016/j.immuni.2021.10.021

59. Stockinger B, Omenetti S. The dichotomous nature of T helper 17 cells. *Nat Rev Immunol* (2017) 17:535–44. doi: 10.1038/nri.2017.50

60. Neil JA, Matsuzawa-Ishimoto Y, Kernbauer-Holzl E, Schuster SL, Sota S, Venzon M, et al. IFN-I and IL-22 mediate protective effects of intestinal viral infection. *Nat Microbiol* (2019) 4:1737–49. doi: 10.1038/s41564-019-0470-1

61. Pickert G, Neufert C, Leppkes M, Zheng Y, Wittkopf N, Warntjen M, et al. STAT3 links IL-22 signaling in intestinal epithelial cells to mucosal wound healing. *J Exp Med* (2009) 206:1465–72. doi: 10.1084/jem.20082683

62. Page EE, Greathead L, Metcalf R, Clark SA, Hart M, Fuchs D, et al. Loss of Th22 cells is associated with increased immune activation and IDO-1 activity in HIV-1 infection. *J Acquir Immune Defic Syndr* (2014) 67:227–35. doi: 10.1097/QAI.0000000000000294

63. Vujkovic-Cvijin I, Swainson LA, Chu SN, Ortiz AM, Santee CA, Petriello A, et al. Gut-resident lactobacillus abundance associates with IDO1 inhibition and Th17 dynamics in SIV-infected macaques. *Cell Rep* (2015) 13:1589–97. doi: 10.1016/j.celrep.2015.10.026

64. Byakwaga H, Boum Y, Huang 2Y, Muzoora C, Kembabazi A, Weiser SD, et al. Hunt, the kynurenine pathway of tryptophan catabolism, CD4+ T-cell recovery, and mortality among HIV-infected ugandans initiating antiretroviral therapy. *J Infect Dis* (2014) 210:383–91. doi: 10.1093/infdis/jiu115

65. Favre D, Mold J, Hunt PW, Kanwar B, Loke P, Seu L, et al. Tryptophan catabolism by indoleamine 2,3-dioxygenase 1 alters the balance of TH17 to regulatory T cells in HIV disease. *Sci Transl Med 2* (2010), 32ra36.

66. Brenchley JM, Douek DC. HIV Infection and the gastrointestinal immune system. *Mucosal Immunol* (2008) 1:23–30. doi: 10.1038/mi.2007.1

67. Klatt NR, Estes JD, Sun X, Ortiz AM, Barber JS, Harris LD, et al. Loss of mucosal CD103+ DCs and IL-17+ and IL-22+ lymphocytes is associated with mucosal damage in SIV infection. *Mucosal Immunol* (2012) 5:646–57. doi: 10.1038/mi.2012.38

68. Wijewardana V, Kristoff J, Xu C, Ma D, Haret-Richter G, Stock JL, et al. Kinetics of myeloid dendritic cell trafficking and activation: impact on progressive, nonprogressive and controlled SIV infections. *PLoS Pathog* (2013) 9:e1003600. doi: 10.1371/journal.ppat.1003600

69. Li H, Richert-Spuhler LE, Evans TI, Gillis J, Connole M, Estes JD, et al. Hypercytotoxicity and rapid loss of NKp44+ innate lymphoid cells during acute SIV infection. *PLoS Pathog* (2014) 10:e1004551. doi: 10.1371/journal.ppat.1004551

70. Mudd JC, Brenchley JM. Innate lymphoid cells: Their contributions to gastrointestinal tissue homeostasis and HIV/SIV disease pathology. *Curr HIV/AIDS Rep* (2019) 16:181–90. doi: 10.1007/s11904-019-00439-4

71. Mudd JC, Busman-Sahay K, DiNapoli SR, Lai S, Sheik V, Lisco A, et al. Hallmarks of primate lentiviral immunodeficiency infection recapitulate loss of innate lymphoid cells. *Nat Commun* (2018) 9:3967. doi: 10.1038/s41467-018-05528-3

72. Sivanandham R, Brocca-Cofano E, Krampe N, Falwell E, Venkatraman SMK, Ribeiro RM, et al. Neutrophil extracellular trap production contributes to pathogenesis in SIV-infected nonhuman primates. *J Clin Invest* (2018) 128:5178–83. doi: 10.1172/JCI99420

73. van Wijk F, Cheroutre H. Mucosal T cells in gut homeostasis and inflammation. *Expert Rev Clin Immunol* (2010) 6:559–66. doi: 10.1586/eci.10.34

74. Schechter ME, Andrade BB, He T, Richter GH, Tosh KW, Policicchio BB, et al. Inflammatory monocytes expressing tissue factor drive SIV and HIV coagulopathy. *Sci Transl Med 9* (2017). doi: 10.1126/scitranslmed.aam5441

75. Reno TA, Tarnus L, Tracy R, Landay AL, Sereti I, Apetrei C, et al. Complement, and NET formation in HIV/SIV pathogenesis. *Front Virol* (2022).

76. de Mareuil J, Carre M, Barbier P, Campbell GR, Lancelot S, Opi S, et al. HIV-1 tat protein enhances microtubule polymerization. *Retrovirology* (2005) 2:5. doi: 10.1186/1742-4690-2-5

77. Lien K, Mayer W, Herrera R, Rosbe K, Tugizov SM. HIV-1 proteins gp120 and tat induce the epithelial-mesenchymal transition in oral and genital mucosal epithelial cells. *PLoS One* (2019) 14:e0226343. doi: 10.1371/journal.pone.0226343

78. Blander JM. Death in the intestinal epithelium-basic biology and implications for inflammatory bowel disease. *FEBS J* (2016) 283:2720–30. doi: 10.1111/febs.13771

79. Tabb B, Morcock DR, Trubey CM, Quinones OA, Hao XP, Smedley J, et al. Reduced inflammation and lymphoid tissue immunopathology in rhesus macaques receiving anti-tumor necrosis factor treatment during primary simian immunodeficiency virus infection. *J Infect Dis* (2013) 207:880–92. doi: 10.1093/infdis/jis643

80. Sim JH, Mukerji SS, Russo SC, Lo J. Gastrointestinal dysfunction and HIV comorbidities. *Curr HIV/AIDS Rep* (2021) 18:57–62. doi: 10.1007/s11904-020-00537-8

81. Alzahrani J, Hussain T, Simar D, Palchaudhuri R, Abdel-Mohsen M, Crowe SM, et al. Inflammatory and immunometabolic consequences of gut dysfunction in HIV: Parallels with IBD and implications for reservoir persistence and non-AIDS comorbidities. *EBioMedicine* (2019) 46:522–31. doi: 10.1016/j.ebiom.2019.07.027

82. Tincati C, Douek DC, Marchetti G. Gut barrier structure, mucosal immunity and intestinal microbiota in the pathogenesis and treatment of HIV infection. *AIDS Res Ther* (2016) 13:19. doi: 10.1186/s12981-016-0103-1

83. Pandrea I, Xu C, Stock JL, Frank DN, Ma D, Policicchio BB, et al. Antibiotic and antiinflammatory therapy transiently reduces inflammation and hypercoagulation in acutely SIV-infected pigtailed macaques. *PLoS Pathog* (2016) 12:e1005384. doi: 10.1371/journal.ppat.1005384

84. Estes JD, Harris LD, Klatt NR, Tabb B, Pittaluga S, Paiardini M, et al. Damaged intestinal epithelial integrity linked to microbial translocation in pathogenic simian immunodeficiency virus infections. *PLoS Pathog* (2010) 6:e1001052. doi: 10.1371/journal.ppat.1001052

85. Batman PA, Kotler DP, Kapembwa MS, Booth D, Potten CS, Orenstein JM, et al. HIV Enteropathy: crypt stem and transit cell hyperproliferation induces villous atrophy in HIV/Microsporidia-infected jejunal mucosa. *AIDS* (2007) 21:433–9. doi: 10.1097/QAD.0b013e3280142ee8

86. He T, Brocca-Cofano E, Gillespie DG, Xu C, Stock JL, Ma D, et al. Critical role for the adenosine pathway in controlling simian immunodeficiency virus-related immune activation and inflammation in gut mucosal tissues. *J Virol* (2015) 89:9616–30. doi: 10.1128/JVI.01196-15

87. Das B, Okamoto K, Rabalais J, Young JA, Barrett KE, Sivagnanam M. Aberrant epithelial differentiation contributes to pathogenesis in a murine model of congenital tufting enteropathy. *Cell Mol Gastroenterol Hepatol* (2021) 12:1353–71. doi: 10.1016/j.jcmgh.2021.06.015

88. Sandler NG, Douek DC. Microbial translocation in HIV infection: causes, consequences and treatment opportunities. *Nat Rev Microbiol* (2012) 10:655–66. doi: 10.1038/nrmicro2848

89. Hartigan-O'Connor DJ, Hirao LA, McCune JM, Dandekar S. Th17 cells and regulatory T cells in elite control over HIV and SIV. *Curr Opin HIV AIDS* (2011) 6:221–7. doi: 10.1097/COH.0b013e32834577b3

90. Li Q, Estes JD, Duan L, Jessurun J, Pambuccian S, Forster C, et al. Simian immunodeficiency virus-induced intestinal cell apoptosis is the underlying mechanism of the regenerative enteropathy of early infection. *J Infect Dis* (2008) 197:420–9. doi: 10.1086/525046

91. Ma D, Jasinska A, Kristoff J, Grobler JP, Turner T, Jung Y, et al. SIVagm infection in wild African green monkeys from south Africa: Epidemiology, natural history, and evolutionary considerations. *PLoS Pathog* (2013) 9:e1003011. doi: 10.1371/journal.ppat.1003011

92. Ma D, Jasinska AJ, Feyertag F, Wijewardana V, Kristoff J, He T, et al. Factors associated with siman immunodeficiency virus transmission in a natural African nonhuman primate host in the wild. *J Virol* (2014) 88:5687–705. doi: 10.1128/JVI.03606-13

93. Pandrea I, Silvestri G, Onanga R, Veazey RS, Marx PA, Hirsch V, et al. Simian immunodeficiency viruses replication dynamics in African non-human primate hosts: Common patterns and species-specific differences. *J Med Primatol* (2006) 35:194–201. doi: 10.1111/j.1600-0684.2006.00168.x

94. Raehtz KD, Barrenas F, Xu C, Busman-Sahay K, Valentine A, Law L, et al. African Green monkeys avoid SIV disease progression by preventing intestinal dysfunction and maintaining mucosal barrier integrity. *PLoS Pathog* (2020) 16:e1008333. doi: 10.1371/journal.ppat.1008333

95. Barrenas F, Raehtz K, Xu C, Law L, Green RR, Silvestri G, et al. Macrophage-associated wound healing contributes to African green monkey SIV pathogenesis control. *Nat Commun* (2019) 10:5101. doi: 10.1038/s41467-019-12987-9

96. Huang C, Wang Y, Li X, Ren L, Zhao J, Hu Y, et al. Clinical features of patients infected with 2019 novel coronavirus in wuhan, China. *Lancet* (2020) 395:497–506. doi: 10.1016/S0140-6736(20)30183-5

97. Huang D, Lian X, Song F, Ma H, Lian Z, Liang Y, et al. Clinical features of severe patients infected with 2019 novel coronavirus: A systematic review and meta-analysis. *Ann Transl Med* (2020) 8:576. doi: 10.21037/atm-20-2124

98. Li J, Gong X, Wang Z, Chen R, Li T, Zeng D, et al. Clinical features of familial clustering in patients infected with 2019 novel coronavirus in wuhan, China. *Virus Res* (2020) 286:198043. doi: 10.1016/j.virusres.2020.198043

99. Chen N, Zhou M, Dong X, Qu J, Gong F, Han Y, et al. Epidemiological and clinical characteristics of 99 cases of 2019 novel coronavirus pneumonia in Wuhan, China: A descriptive study. *Lancet* (2020) 395:507–13. doi: 10.1016/S0140-6736(20)30211-7

100. Mukherjee R, Smith A, Sutton R. Covid-19-related pancreatic injury. *Br J Surg* (2020) 107:e190. doi: 10.1002/bjs.11645

101. Lin L, Jiang X, Zhang Z, Huang S, Zhang Z, Fang Z, et al. Gastrointestinal symptoms of 95 cases with SARS-CoV-2 infection. *Gut* (2020) 69:997–1001. doi: 10.1136/gutjnl-2020-321013

102. de-Madaria E, Siau K, Cardenas-Jaen K. Increased amylase and lipase in patients with COVID-19 pneumonia: Don't blame the pancreas just yet! *Gastroenterology* (2021) 160:1871. doi: 10.1053/j.gastro.2020.04.044

103. Wang D, Yin Y, Hu C, Liu X, Zhang X, Zhou S, et al. Clinical course and outcome of 107 patients infected with the novel coronavirus, SARS-CoV-2, discharged from two hospitals in wuhan, China. *Crit Care* (2020) 24:188. doi: 10.1186/s13054-020-02895-6

104. Wu Y, Xu X, Chen Z, Duan J, Hashimoto K, Yang L, et al. Nervous system involvement after infection with COVID-19 and other coronaviruses. *Brain Behav Immun* (2020) 87:18–22. doi: 10.1016/j.bbi.2020.03.031

105. Adao R, Guzik TJ. Inside the heart of COVID-19. *Cardiovasc Res* (2020) 116:e59–61. doi: 10.1093/cvr/cvaa086

106. Akhmerov A, Marban E. COVID-19 and the heart. *Circ Res* (2020) 126:1443–55. doi: 10.1161/CIRCRESAHA.120.317055

107. Azarkish M, Laleh Far V, Eslami M, Mollazadeh R. Transient complete heart block in a patient with critical COVID-19. *Eur Heart J* (2020) 41:2131. doi: 10.1093/eurheartj/ehaa307

108. Bader F, Manla Y, Atallah B, Starling RC. Heart failure and COVID-19. *Heart Fail Rev* (2021) 26:1–10. doi: 10.1007/s10741-020-10008-2

109. Bohm M, Frey N, Giannitsis E, Sliwa K, Zeiher AM. Coronavirus disease 2019 (COVID-19) and its implications for cardiovascular care: expert document from the German cardiac society and the world heart federation. *Clin Res Cardiol* (2020) 109:1446–59. doi: 10.1007/s00392-020-01656-3

110. Cheng R, Leedy D. COVID-19 and acute myocardial injury: The heart of the matter or an innocent bystander? *Heart* (2020) 106:1122–4. doi: 10.1136/heartjnl-2020-317025

111. Dhakal BP, Sweitzer NK, Indik JH, Acharya D, William P. SARS-CoV-2 infection and cardiovascular disease: COVID-19 heart. *Heart Lung Circ* (2020) 29:973–87. doi: 10.1016/j.hlc.2020.05.101

112. Goha A, Mezue K, Edwards P, Nunura F, Baugh D, Madu E. COVID-19 and the heart: An update for clinicians. *Clin Cardiol* (2020) 43:1216–22. doi: 10.1002/clc.23406

113. Khalid N, Chen Y, Case BC, Shlofmitz E, Wermers JP, Rogers T, et al. COVID-19 (SARS-CoV-2) and the heart - an ominous association. *Cardiovasc Revasc Med* (2020) 21:946–9. doi: 10.1016/j.carrev.2020.05.009

114. Khan IH, Zahra SA, Zaim S, Harky A. At The heart of COVID-19. *J Card Surg* (2020) 35:1287–94. doi: 10.1111/jocs.14596

115. Libby P. The heart in COVID-19: Primary target or secondary bystander? *JACC Basic Transl Sci* (2020) 5:537–42. doi: 10.1016/j.jacbts.2020.04.001

116. Mehra MR, Ruschitzka F. COVID-19 illness and heart failure: A missing link? *JACC Heart Fail* (2020) 8:512–4. doi: 10.1016/j.jchf.2020.03.004

117. Mishra AK, Sahu KK, Lal A, Sargent J. Patterns of heart injury in COVID-19 and relation to outcome. *J Med Virol* (2020) 92:1747. doi: 10.1002/jmv.25847

118. Otto CM. Heartbeat: Heart disease and COVID-19. *Heart* (2020) 106:1115–6. doi: 10.1136/heartjnl-2020-317674

119. Strabelli TMV, Uip DE. COVID-19 and the heart. *Arq Bras Cardiol* (2020) 114:598–600.

120. Terpos E, Ntanasis-Stathopoulos I, Elalamy I, Kastritis E, Sergentanis TN, Politou M, et al. Hematological findings and complications of COVID-19. *Am J Hematol* (2020) 95:834–47. doi: 10.1002/ajh.25829

121. Al-Namaeh M. COVID-19 and conjunctivitis: a meta-analysis. *Ther Adv Ophthalmol* (2021) 13:25158414211003368. doi: 10.1177/25158414211003368

122. Loffredo L, Fallarino A, Paraninfi A, Pacella F, Pacella E, Oliva A, et al. Different rates of conjunctivitis in COVID-19 eastern and western hospitalized patients: a meta-analysis. *Intern Emerg Med* (2021). doi: 10.1007/s11739-021-02880-z

123. Loffredo L, Pacella F, Pacella E, Tiscione G, Oliva A, Violi F. Conjunctivitis and COVID-19: A meta-analysis. *J Med Virol* (2020) 92:1413–4. doi: 10.1002/jmv.25938

124. Vaira LA, Salzano G, Fois AG, Piombino P, De Riu G. Potential pathogenesis of ageusia and anosmia in COVID-19 patients. *Int Forum Allergy Rhinol* (2020) 10:1103–4. doi: 10.1002/alr.22593

125. Hoffmann M, Kleine-Weber H, Schroeder S, Kruger N, Herrler T, Erichsen S, et al. SARS-CoV-2 cell entry depends on ACE2 and TMPRSS2 and is blocked by a clinically proven protease inhibitor. *Cell* (2020) 181:271–80.e8. doi: 10.1016/j.cell.2020.02.052

126. Yan R, Zhang Y, Li Y, Xia L, Guo Y, Zhou Q. Structural basis for the recognition of SARS-CoV-2 by full-length human ACE2. *Science* (2020) 367:1444–8. doi: 10.1126/science.abb2762

127. Li W, Moore MJ, Vasilieva N, Sui J, Wong SK, Berne MA, et al. Angiotensin-converting enzyme 2 is a functional receptor for the SARS coronavirus. *Nature* (2003) 426:450–4. doi: 10.1038/nature02145

128. Wang N, Shi X, Jiang L, Zhang S, Wang D, Tong P, et al. Structure of MERS-CoV spike receptor-binding domain complexed with human receptor DPP4. *Cell Res* (2013) 23:986–93. doi: 10.1038/cr.2013.92

129. Hamming I, Timens W, Bulthuis ML, Lely AT, Navis G, van Goor H. Tissue distribution of ACE2 protein, the functional receptor for SARS coronavirus. *A first step understanding SARS pathogenesis. J Pathol* (2004) 203:631–7. doi: 10.1002/path.1570

130. Chertow D, Stein S, Ramelli S, Grazioli A, Chung J-Y, Singh M, et al. *SARS-CoV-2 infection and persistence throughout the human body and brain* (2022). Available at: https://www.researchsquare.com/article/rs-1139035/v1.

131. Ziegler CGK, Allon SJ, Nyquist SK, Mbano IM, Miao VN, Tzouanas CN, et al. Lung-network@humancellatlas.org and H.C.A.L.B. network, SARS-CoV-2 receptor ACE2 is an interferon-stimulated gene in human airway epithelial cells and is detected in specific cell subsets across tissues. *Cell* (2020) 181:1016–35 e19.

132. Hikmet F, Mear L, Edvinsson A, Micke P, Uhlen M, Lindskog C. The protein expression profile of ACE2 in human tissues. *Mol Syst Biol* (2020) 16:e9610. doi: 10.15252/msb.20209610

133. Ortiz ME, Thurman A, Pezzulo AA, Leidinger MR, Klesney-Tait JA, Karp PH, et al. Heterogeneous expression of the SARS-Coronavirus-2 receptor ACE2 in the human respiratory tract. *EBioMedicine* (2020) 60:102976. doi: 10.1016/j.ebiom.2020.102976

134. Hou YJ, Okuda K, Edwards CE, Martinez DR, Asakura T, Dinnon KH, et al. SARS-CoV-2 reverse genetics reveals a variable infection gradient in the respiratory tract. *Cell* (2020) 182:429–46.e14. doi: 10.1016/j.cell.2020.05.042

135. Sungnak W, Huang N, Becavin C, Berg M, Queen R, Litvinukova M, et al. SARS-CoV-2 entry factors are highly expressed in nasal epithelial cells together with innate immune genes. *Nat Med* (2020) 26:681–7. doi: 10.1038/s41591-020-0868-6

136. Zou X, Chen K, Zou J, Han P, Hao J, Han Z. Single-cell RNA-seq data analysis on the receptor ACE2 expression reveals the potential risk of different human organs vulnerable to 2019-nCoV infection. *Front Med* (2020) 14:185–92. doi: 10.1007/s11684-020-0754-0

137. Lee IT, Nakayama T, Wu CT, Goltsev Y, Jiang S, Gall PA, et al. ACE2 localizes to the respiratory cilia and is not increased by ACE inhibitors or ARBs. *Nat Commun* (2020) 11:5453. doi: 10.1038/s41467-020-19145-6

138. Bunyavanich S, Do A, Vicencio A. Nasal gene expression of angiotensin-converting enzyme 2 in children and adults. *JAMA* (2020) 323:2427–9. doi: 10.1001/jama.2020.8707

139. Smith JC, Sausville EL, Girish V, Yuan ML, Vasudevan A, John KM, et al. Cigarette smoke exposure and inflammatory signaling increase the expression of the SARS-CoV-2 receptor ACE2 in the respiratory tract. *Dev Cell* (2020) 53:514–29.e3. doi: 10.1016/j.devcel.2020.05.012

140. Liu W, Tao ZW, Wang L, Yuan ML, Liu K, Zhou L, et al. Analysis of factors associated with disease outcomes in hospitalized patients with 2019 novel coronavirus disease. *Chin Med J (Engl)* (2020) 133:1032–8. doi: 10.1097/CM9.0000000000000775

141. Brooks SD, Smith RL, Moreira A, Ackerman HC. Oral lisinopril raises tissue levels of ACE2, the SARS-CoV-2 receptor, in healthy male and female mice. *bioRxiv* (2022) 2021:10. doi: 10.3389/fphar.2022.798349

142. Zhuang MW, Cheng Y, Zhang J, Jiang XM, Wang L, Deng J, et al. Increasing host cellular receptor-angiotensin-converting enzyme 2 expression by coronavirus may facilitate 2019-nCoV (or SARS-CoV-2) infection. *J Med Virol* (2020) 92:2693–701. doi: 10.1002/jmv.26139

143. Baker SA, Kwok S, Berry GJ, Montine TJ. Angiotensin-converting enzyme 2 (ACE2) expression increases with age in patients requiring mechanical ventilation. *PLoS One* (2021) 16:e0247060. doi: 10.1371/journal.pone.0247060

144. Jackson CB, Farzan M, Chen B, Choe H. Mechanisms of SARS-CoV-2 entry into cells. *Nat Rev Mol Cell Biol* (2022) 23:3–20. doi: 10.1038/s41580-021-00418-x

145. Blair RV, Vaccari M, Doyle-Meyers LA, Roy CJ, Russell-Lodrigue K, Fahlberg M, et al. Acute respiratory distress in aged, SARS-CoV-2-Infected African green monkeys but not rhesus macaques. *Am J Pathol* (2021) 191:274–82. doi: 10.1016/j.ajpath.2020.10.016

146. Loske J, Rohmel J, Lukassen S, Stricker S, Magalhaes VG, Liebig J, et al. Pre-activated antiviral innate immunity in the upper airways controls early SARS-CoV-2 infection in children. *Nat Biotechnol* (2022) 40:319–24. doi: 10.1038/s41587-021-01037-9

147. Rossi AD, de Araujo JLF, de Almeida TB, Ribeiro-Alves M, de Almeida Velozo C, Almeida JM, et al. Association between ACE2 and TMPRSS2 nasopharyngeal expression and COVID-19 respiratory distress. *Sci Rep* (2021) 11:9658. doi: 10.1038/s41598-021-88944-8

148. Saheb Sharif-Askari N, Saheb Sharif-Askari F, Alabed M, Temsah MH, Al Heialy S, Hamid Q, et al. Airways expression of SARS-CoV-2 receptor, ACE2, and TMPRSS2 is lower in children than adults and increases with smoking and COPD. *Mol Ther Methods Clin Dev* (2020) 18:1–6. doi: 10.1016/j.omtm.2020.05.013

149. Su Y, Yuan D, Chen DG, Ng RH, Wang K, Choi J, et al. Multiple early factors anticipate post-acute COVID-19 sequelae. *Cell* (2022) 185:881–95.e20. doi: 10.1016/j.cell.2022.01.014

150. Toh ZQ, Anderson J, Mazarakis N, Neeland M, Higgins RA, Rautenbacher K, et al. Comparison of seroconversion in children and adults with mild COVID-19. *JAMA Netw Open* (2022) 5:e221313. doi: 10.1001/jamanetworkopen.2022.1313

151. Weisberg SP, Connors TJ, Zhu Y, Baldwin MR, Lin WH, Wontakal S, et al. Distinct antibody responses to SARS-CoV-2 in children and adults across the COVID-19 clinical spectrum. *Nat Immunol* (2021) 22:25–31. doi: 10.1038/s41590-020-00826-9

152. Yoshida M, Worlock KB, Huang N, Lindeboom RGH, Butler CR, Kumasaka N, et al. Local and systemic responses to SARS-CoV-2 infection in children and adults. *Nature* (2022) 602:321–7. doi: 10.1038/s41586-021-04345-x

153. Prendergast H, Tyo C, Colbert C, Kelley M, Pobee R. Medical complications of obesity: heightened importance in a COVID era. *Int J Emerg Med* (2022) 15:29. doi: 10.1186/s12245-022-00431-7

154. Sharma P, Behl T, Sharma N, Singh S, Grewal AS, Albarrati A, et al. COVID-19 and diabetes: Association intensify risk factors for morbidity and mortality. *BioMed Pharmacother* (2022) 151:113089. doi: 10.1016/j.biopha.2022.113089

155. Kastora S, Patel M, Carter B, Delibegovic M, Myint PK. Impact of diabetes on COVID-19 mortality and hospital outcomes from a global perspective: An umbrella systematic review and meta-analysis. *Endocrinol Diabetes Metab* (2022) 5:e00338. doi: 10.1002/edm2.338

156. Boden I, Bernabeu MO, Dhillon B, Dorward DA, MacCormick I, Megaw R, et al. Pre-existing diabetic retinopathy as a prognostic factor for COVID-19 outcomes amongst people with diabetes: A systematic review. *Diabetes Res Clin Pract* (2022) 187:109869. doi: 10.1016/j.diabres.2022.109869

157. Karampela I, Vallianou N, Magkos F, Apovian CM, Dalamaga M. Obesity And COVID-19: The Bermuda triangle in public health. *Curr Obes Rep* (2022). doi: 10.1007/s13679-022-00471-3

158. Jeffers SA, Tusell SM, Gillim-Ross L, Hemmila EM, Achenbach JE, Babcock GJ, et al. CD209L (L-SIGN) is a receptor for severe acute respiratory syndrome coronavirus. *Proc Natl Acad Sci USA* (2004) 101:15748–53.

159. Yang ZY, Huang Y, Ganesh L, Leung K, Kong WP, Schwartz O, et al. pH-dependent entry of severe acute respiratory syndrome coronavirus is mediated by the spike glycoprotein and enhanced by dendritic cell transfer through DC-SIGN. *J Virol* (2004) 78:5642–50. doi: 10.1128/JVI.78.11.5642-5650.2004

160. Amraei R, Yin W, Napoleon MA, Suder EL, Berrigan J, Zhao Q, et al. CD209L/L-SIGN and CD209/DC-SIGN act as receptors for SARS-CoV-2. *ACS Cent Sci* (2021) 7:1156–65. doi: 10.1021/acscentsci.0c01537

161. Mori Y, Fink C, Ichimura T, Sako K, Mori M, Lee NN, et al. KIM-1/TIM-1 is a receptor for SARS-CoV-2 in lung and kidney. *medRxiv* (2022).

162. Wang S, Qiu Z, Hou Y, Deng X, Xu W, Zheng T, et al. AXL is a candidate receptor for SARS-CoV-2 that promotes infection of pulmonary and bronchial epithelial cells. *Cell Res* (2021) 31:126–40. doi: 10.1038/s41422-020-00460-y

163. Jemielity S, Wang JJ, Chan YK, Ahmed AA, Li W, Monahan S, et al. TIM-family proteins promote infection of multiple enveloped viruses through virion-associated phosphatidylserine. *PLoS Pathog* (2013) 9:e1003232. doi: 10.1371/journal.ppat.1003232

164. Chen Z, Mi L, Xu J, Yu J, Wang X, Jiang J, et al. Function of HAb18G/CD147 in invasion of host cells by severe acute respiratory syndrome coronavirus. *J Infect Dis* (2005) 191:755–60. doi: 10.1086/427811

165. Wang K, Chen W, Zhang Z, Deng Y, Lian JQ, Du P, et al. CD147-spike protein is a novel route for SARS-CoV-2 infection to host cells. *Signal Transduct Target Ther* (2020) 5:283. doi: 10.1038/s41392-020-00426-x

166. Shilts J, Crozier TWM, Greenwood EJD, Lehner PJ, Wright GJ. No evidence for basigin/CD147 as a direct SARS-CoV-2 spike binding receptor. *Sci Rep* (2021) 11:413. doi: 10.1038/s41598-020-80464-1

167. Cantuti-Castelvetri L, Ojha R, Pedro LD, Djannatian M, Franz J, Kuivanen S, et al. Neuropilin-1 facilitates SARS-CoV-2 cell entry and infectivity. *Science* (2020) 370:856–60. doi: 10.1126/science.abd2985

168. Daly JL, Simonetti B, Klein K, Chen KE, Williamson MK, Anton-Plagaro C, et al. Neuropilin-1 is a host factor for SARS-CoV-2 infection. *Science* (2020) 370:861–5. doi: 10.1126/science.abd3072

169. Ahn JH, Kim J, Hong SP, Choi SY, Yang MJ, Ju YS, et al. Nasal ciliated cells are primary targets for SARS-CoV-2 replication in the early stage of COVID-19. *J Clin Invest 131* (2021). doi: 10.1172/JCI148517

170. Camargo SM, Singer D, Makrides V, Huggel K, Pos KM, Wagner CA, et al. Tissue-specific amino acid transporter partners ACE2 and collectrin differentially interact with hartnup mutations. *Gastroenterology* (2009) 136:872–82. doi: 10.1053/j.gastro.2008.10.055

171. Daniloski Z, Jordan TX, Wessels HH, Hoagland DA, Kasela S, Legut M, et al. Identification of required host factors for SARS-CoV-2 infection in human cells. *Cell* (2021) 184:92–105.e16. doi: 10.1016/j.cell.2020.10.030

172. Liu J, Lu F, Chen Y, Plow E, Qin J. Integrin mediates cell entry of the SARS-CoV-2 virus independent of cellular receptor ACE2. *J Biol Chem* (2022) 298:101710. doi: 10.1016/j.jbc.2022.101710

173. Huntington KE, Carlsen L, So EY, Piesche M, Liang O, El-Deiry WS. Integrin/TGF-beta1 inhibitor GLPG-0187 blocks SARS-CoV-2 delta and omicron pseudovirus infection of airway epithelial cells *In vitro*, which could attenuate disease severity. *Pharm (Basel) 15* (2022). doi: 10.1101/2022.01.02.22268641

174. Othman H, Messaoud HB, Khamessi O, Ben-Mabrouk H, Ghedira K, Bharuthram A, et al. SARS-CoV-2 spike protein unlikely to bind to integrins *via* the arg-Gly-Asp (RGD) motif of the receptor binding domain: Evidence from structural analysis and microscale accelerated molecular dynamics. *Front Mol Biosci* (2022) 9:834857. doi: 10.3389/fmolb.2022.834857

175. Alvarado DM, Son J, Thackray LB, Gomez Castro MF, Prasad S, Cui X, et al. Mesalamine reduces intestinal ACE2 expression without modifying SARS-CoV-2 infection or disease severity in mice. *Inflammation Bowel Dis* (2022) 28:318–21. doi: 10.1093/ibd/izab274

176. Lamers MM, Beumer J, van der Vaart J, Knoops K, Puschhof J, Breugem TI, et al. SARS-CoV-2 productively infects human gut enterocytes. *Science* (2020) 369:50–4. doi: 10.1126/science.abc1669

177. Zang R, Gomez Castro MF, McCune BT, Zeng Q, Rothlauf PW, Sonnek NM, et al. TMPRSS2 and TMPRSS4 promote SARS-CoV-2 infection of human small intestinal enterocytes. *Sci Immunol 5* (2020). doi: 10.1126/sciimmunol.abc3582

178. Qian Q, Fan L, Liu W, Li J, Yue J, Wang M, et al. Direct evidence of active SARS-CoV-2 replication in the intestine. *Clin Infect Dis* (2021) 73:361–6. doi: 10.1093/cid/ciaa925

179. Lehmann M, Allers K, Heldt C, Meinhardt J, Schmidt F, Rodriguez-Sillke Y, et al. Human small intestinal infection by SARS-CoV-2 is characterized by a mucosal infiltration with activated CD8+ T cells. *Mucosal Immunol* (2021) 14:1381–92. doi: 10.1038/s41385-021-00437-z

180. Livanos AE, Jha D, Cossarini F, Gonzalez-Reiche AS, Tokuyama M, Aydillo T, et al. Intestinal host response to SARS-CoV-2 infection and COVID-19 outcomes in patients with gastrointestinal symptoms. *Gastroenterology* (2021) 160:2435–50.e34. doi: 10.1053/j.gastro.2021.02.056

181. Yantiss RK, Qin L, He B, Crawford CV, Seshan S, Patel S, et al. Intestinal abnormalities in patients with SARS-CoV-2 infection: Histopathologic changes reflect mechanisms of disease. *Am J Surg Pathol* (2022) 46:89–96. doi: 10.1038/s41385-021-00437-z

182. Wang W, Xu Y, Gao R, Lu R, Han K, Wu G, et al. Detection of SARS-CoV-2 in different types of clinical specimens. *JAMA* (2020) 323:1843–4. doi: 10.1097/PAS.0000000000001755

183. Xiao F, Sun J, Xu Y, Li F, Huang X, Li H, et al. Infectious SARS-CoV-2 in feces of patient with severe COVID-19. *Emerg Infect Dis* (2020) 26:1920–2. doi: 10.1001/jama.2020.3786

184. Wolfel R, Corman VM, Guggemos W, Seilmaier M, Zange S, Muller MA, et al. Virological assessment of hospitalized patients with COVID-2019. *Nature* (2020) 581:465–9. doi: 10.3201/eid2608.200681

185. Wu Y, Guo C, Tang L, Hong Z, Zhou J, Dong X, et al. Prolonged presence of SARS-CoV-2 viral RNA in faecal samples. *Lancet Gastroenterol Hepatol* (2020) 5:434–5. doi: 10.1038/s41586-020-2196-x

186. Xu Y, Li X, Zhu B, Liang H, Fang C, Gong Y, et al. Characteristics of pediatric SARS-CoV-2 infection and potential evidence for persistent fecal viral shedding. *Nat Med* (2020) 26:502–5. doi: 10.1016/S2468-1253(20)30083-2

187. Ramakrishnan RK, Kashour T, Hamid Q, Halwani R, Tleyjeh IM. Unraveling the mystery surrounding post-acute sequelae of COVID-19. *Front Immunol* (2021) 12:686029. doi: 10.1038/s41591-020-0817-4

188. Guadalupe M, Sankaran S, George MD, Reay E, Verhoeven D, Shacklett BL, et al. Viral suppression and immune restoration in the gastrointestinal mucosa of human immunodeficiency virus type 1-infected patients initiating therapy during primary or chronic infection. *J Virol* (2006) 80:8236–47. doi: 10.3389/fimmu.2021.686029

189. Mendez-Lagares G, Romero-Sanchez MC, Ruiz-Mateos E, Genebat M, Ferrando-Martinez S, Munoz-Fernandez MA, et al. Long-term suppressive combined antiretroviral treatment does not normalize the serum level of soluble CD14. *J Infect Dis* (2013) 207:1221–5. doi: 10.1128/JVI.00120-06

190. Zevin AS, McKinnon L, Burgener A, Klatt NR. Microbial translocation and microbiome dysbiosis in HIV-associated immune activation. *Curr Opin HIV AIDS* (2016) 11:182–90. doi: 10.1093/infdis/jit025

191. Guo Y, Luo R, Wang Y, Deng P, Song T, Zhang M, et al. SARS-CoV-2 induced intestinal responses with a biomimetic human gut-on-chip. *Sci Bull (Beijing)* (2021) 66:783–93. doi: 10.1097/COH.0000000000000234

192. Pan L, Mu M, Yang P, Sun Y, Wang R, Yan J, et al. Clinical characteristics of COVID-19 patients with digestive symptoms in Hubei, China: A descriptive, cross-sectional, multicenter study. *Am J Gastroenterol* (2020) 115:766–73. doi: 10.1016/j.scib.2020.11.015

193. Liu F, Li L, Xu M, Wu J, Luo D, Zhu Y, et al. Prognostic value of interleukin-6, c-reactive protein, and procalcitonin in patients with COVID-19. *J Clin Virol* (2020) 127:104370. doi: 10.14309/ajg.0000000000000620

194. Hadjadj J, Yatim N, Barnabei L, Corneau A, Boussier J, Smith N, et al. Impaired type I interferon activity and inflammatory responses in severe COVID-19 patients. *Science* (2020) 369:718–24. doi: 10.1016/j.jcv.2020.104370

195. Mandel M, Harari G, Gurevich M, Achiron A. Cytokine prediction of mortality in COVID19 patients. *Cytokine* (2020) 134:155190. doi: 10.1126/science.abc6027

196. Isnard S, Lin J, Bu S, Fombuena B, Royston L, Routy JP. Gut leakage of fungal-related products: Turning up the heat for HIV infection. *Front Immunol* (2021) 12:656414. doi: 10.1016/j.cyto.2020.155190

197. Mehraj V, Ramendra R, Isnard S, Dupuy FP, Ponte R, Chen J, et al. Circulating (1–>3)-beta-D-glucan is associated with immune activation during human immunodeficiency virus infection. *Clin Infect Dis* (2020) 70:232–41. doi: 10.3389/fimmu.2021.656414

198. Pandrea I, Apetrei C. Where the wild things are: pathogenesis of SIV infection in African nonhuman primate hosts. *Curr HIV/AIDS Rep* (2010) 7:28–36. doi: 10.1093/cid/ciz212

199. Pandrea I, Gaufin T, Brenchley JM, Gautam R, Monjure C, Gautam A, et al. Cutting edge: Experimentally induced immune activation in natural hosts of simian

immunodeficiency virus induces significant increases in viral replication and CD4+ T cell depletion. *J Immunol* (2008) 181:6687–91. doi: 10.1007/s11904-009-0034-8

200. Hao XP, Lucero CM, Turkbey B, Bernardo ML, Morcock DR, Deleage C, et al. Experimental colitis in SIV-uninfected rhesus macaques recapitulates important features of pathogenic SIV infection. *Nat Commun* (2015) 6:8020. doi: 10.4049/jimmunol.181.10.6687

201. Kristoff J, Haret-Richter G, Ma D, Ribeiro RM, Xu C, Cornell E, et al. Early microbial translocation blockade reduces SIV-mediated inflammation and viral replication. *J Clin Invest* (2014) 124:2802–6. doi: 10.1038/ncomms9020

202. Deeks SG, Tracy R, Douek DC. Systemic effects of inflammation on health during chronic HIV infection. *Immunity* (2013) 39:633–45. doi: 10.1172/JCI75090

203. Pandrea I, Landay A, Wilson C, Stock J, Tracy R, Apetrei C. Using the pathogenic and nonpathogenic nonhuman primate model for studying non-AIDS comorbidities. *Curr HIV/AIDS Rep* (2015) 12:54–67. doi: 10.1016/j.immuni.2013.10.001

204. Handley SA, Thackray LB, Zhao G, Presti R, Miller AD, Droit L, et al. Pathogenic simian immunodeficiency virus infection is associated with expansion of the enteric virome. *Cell* (2012) 151:253–66. doi: 10.1007/s11904-014-0245-5

205. Klase Z, Ortiz A, Deleage C, Mudd JC, Quinones M, Schwartzman E, et al. Dysbiotic bacteria translocate in progressive SIV infection. *Mucosal Immunol* (2015) 8:1009–20. doi: 10.1016/j.cell.2012.09.024

206. Brenchley JM, Ortiz AM. Microbiome studies in non-human primates. *Curr HIV/AIDS Rep* (2021) 18:527–37. doi: 10.1038/mi.2014.128

207. Rosel-Pech C, Chavez-Torres M, Bekker-Mendez VC, Pinto-Cardoso S. Therapeutic avenues for restoring the gut microbiome in HIV infection. *Curr Opin Pharmacol* (2020) 54:188–201. doi: 10.1007/s11904-021-00584-9

208. Ashuro AA, Lobie TA, Ye DQ, Leng RX, Li BZ, Pan HF, et al. Review on the alteration of gut microbiota: The role of HIV infection and old age. *AIDS Res Hum Retroviruses* (2020) 36:556–65. doi: 10.1016/j.coph.2020.09.010

209. Dillon SM, Frank DN, Wilson CC. The gut microbiome and HIV-1 pathogenesis: a two-way street. *AIDS* (2016) 30:2737–51. doi: 10.1089/aid.2019.0282

210. Vujkovic-Cvijin I, Sortino O, Verheij E, Sklar J, Wit FW, Kootstra NA, et al. HIV-Associated gut dysbiosis is independent of sexual practice and correlates with noncommunicable diseases. *Nat Commun* (2020) 11:2448. doi: 10.1097/QAD.0000000000001289

211. Noguera-Julian M, Rocafort M, Guillen Y, Rivera J, Casadella M, Nowak P, et al. Gut microbiota linked to sexual preference and HIV infection. *EBioMedicine* (2016) 5:135–46. doi: 10.1038/s41467-020-16222-8

212. Guillen Y, Noguera-Julian M, Rivera J, Casadella M, Zevin AS, Rocafort M, et al. Low nadir CD4+ T-cell counts predict gut dysbiosis in HIV-1 infection. *Mucosal Immunol* (2019) 12:232–46. doi: 10.1016/j.ebiom.2016.01.032

213. He T, Xu C, Krampe N, Dillon SM, Sette P, Falwell E, et al. High-fat diet exacerbates SIV pathogenesis and accelerates disease progression. *J Clin Invest* (2019) 129:5474–88. doi: 10.1038/s41385-018-0083-7

214. Ortiz AM, Flynn JK, DiNapoli SR, Vujkovic-Cvijin I, Starke CE, Lai SH, et al. Experimental microbial dysbiosis does not promote disease progression in SIV-infected macaques. *Nat Med* (2018) 24:1313–6. doi: 10.1172/JCI121208

215. Yeoh YK, Zuo T, Lui GC, Zhang F, Liu Q, Li AY, et al. Gut microbiota composition reflects disease severity and dysfunctional immune responses in patients with COVID-19. *Gut* (2021) 70:698–706. doi: 10.1038/s41591-018-0132-5

216. Reinold J, Farahpour F, Fehring C, Dolff S, Konik M, Korth J, et al. A pro-inflammatory gut microbiome characterizes SARS-CoV-2 infected patients and a reduction in the connectivity of an anti-inflammatory bacterial network associates with severe COVID-19. *Front Cell Infect Microbiol* (2021) 11:747816. doi: 10.1136/gutjnl-2020-323020

217. Liu Y, Zhang H, Tang X, Jiang X, Yan X, Liu X, et al. Distinct metagenomic signatures in the SARS-CoV-2 infection. *Front Cell Infect Microbiol* (2021) 11:706970. doi: 10.3389/fcimb.2021.747816

218. Seibert B, Caceres CJ, Cardenas-Garcia S, Carnaccini S, Geiger G, Rajao DS, et al. Mild and severe SARS-CoV-2 infection induces respiratory and intestinal microbiome changes in the K18-hACE2 transgenic mouse model. *Microbiol Spectr* (2021) 9:e0053621. doi: 10.3389/fcimb.2021.706970

219. Effenberger M, Grabherr F, Mayr L, Schwaerzler J, Nairz M, Seifert M, et al. Faecal calprotectin indicates intestinal inflammation in COVID-19. *Gut* (2020) 69:1543–4. doi: 10.1128/Spectrum.00536-21

220. Sun Z, Song ZG, Liu C, Tan S, Lin S, Zhu J, et al. Gut microbiome alterations and gut barrier dysfunction are associated with host immune homeostasis in COVID-19 patients. *BMC Med* (2022) 20:24. doi: 10.1136/gutjnl-2020-321388

221. Giron LB, Dweep H, Yin X, Wang H, Damra M, Goldman AR, et al. Plasma markers of disrupted gut permeability in severe COVID-19 patients. *Front Immunol* (2021) 12:686240. doi: 10.1186/s12916-021-02212-0

222. Hoel H, Heggelund L, Reikvam DH, Stiksrud B, Ueland T, Michelsen AE, et al. Elevated markers of gut leakage and inflammasome activation in COVID-19 patients with cardiac involvement. *J Intern Med* (2021) 289:523–31. doi: 10.3389/fimmu.2021.686240

223. Ferrari B, Da Silva AC, Liu KH, Saidakova EV, Korolevskaya LB, Shmagel KV, et al. Gut-derived bacterial toxins impair memory CD4+ T cell mitochondrial function in HIV-1 infection. *J Clin Invest 132* (2022). doi: 10.1111/joim.13178

224. Patel P, DeCuir J, Abrams J, Campbell AP, Godfred-Cato S, Belay ED. Clinical characteristics of multisystem inflammatory syndrome in adults: A systematic review. *JAMA Netw Open* (2021) 4:e2126456. doi: 10.1172/JCI149571

225. Porritt RA, Paschold L, Rivas MN, Cheng MH, Yonker LM, Chandnani H, et al. HLA class I-associated expansion of TRBV11-2 T cells in multisystem inflammatory syndrome in children. *J Clin Invest 131* (2021). doi: 10.1001/jamanetworkopen.2021.26456

226. Sacco K, Castagnoli R, Vakkilainen S, Liu C, Delmonte OM, Oguz C, et al. Immunopathological signatures in multisystem inflammatory syndrome in children and pediatric COVID-19. *Nat Med* (2022). doi: 10.1172/JCI146614

227. Yonker LM, Gilboa T, Ogata AF, Senussi Y, Lazarovits R, Boribong BP, et al. Multisystem inflammatory syndrome in children is driven by zonulin-dependent loss of gut mucosal barrier. *J Clin Invest 131* (2021).

228. Feldstein LR, Tenforde MW, Friedman KG, Newhams M, Rose EB, Dapul H, et al. Characteristics and outcomes of US children and adolescents with multisystem inflammatory syndrome in children (MIS-c) compared with severe acute COVID-19. *JAMA* (2021) 325:1074–87. doi: 10.1172/JCI149633

229. Liu Q, Mak JWY, Su Q, Yeoh YK, Lui GC, Ng SSS, et al. Gut microbiota dynamics in a prospective cohort of patients with post-acute COVID-19 syndrome. *Gut* (2022) 71:544–52. doi: 10.1001/jama.2021.2091

230. Peluso MJ, Lu S, Tang AF, Durstenfeld MS, Ho HE, Goldberg SA, et al. Markers of immune activation and inflammation in individuals with postacute sequelae of severe acute respiratory syndrome coronavirus 2 infection. *J Infect Dis* (2021) 224:1839–48. doi: 10.1136/gutjnl-2021-325989

231. Antiretroviral Therapy Cohort C. Survival of HIV-positive patients starting antiretroviral therapy between 1996 and 2013: A collaborative analysis of cohort studies. *Lancet HIV* (2017) 4:e349–56. doi: 10.1093/infdis/jiab490

232. Marcus JL, Leyden WA, Alexeeff SE, Anderson AN, Hechter RC, Hu H, et al. Comparison of overall and comorbidity-free life expectancy between insured adults with and without HIV infection, 2000-2016. *JAMA Netw Open* (2020) 3:e207954.

233. Siliciano JD, Siliciano RF. Nonsuppressible HIV-1 viremia: A reflection of how the reservoir persists. *J Clin Invest* (2020) 130:5665–7. doi: 10.1001/jamanetworkopen.2020.7954

234. Babu H, Ambikan AT, Gabriel EE, Svensson Akusjarvi S, Palaniappan AN, Sundaraj V, et al. Systemic inflammation and the increased risk of inflamm-aging and age-associated diseases in people living with HIV on long term suppressive antiretroviral therapy. *Front Immunol* (2019) 10:1965. doi: 10.1172/JCI141497

235. Daskou M, Mu W, Sharma M, Vasilopoulos H, Heymans R, Ritou E, et al. ApoA-I mimetics reduce systemic and gut inflammation in chronic treated HIV. *PLoS Pathog* (2022) 18:e1010160. doi: 10.3389/fimmu.2019.01965

236. Serrano-Villar S, Vazquez-Castellanos JF, Vallejo A, Latorre A, Sainz T, Ferrando-Martinez S, et al. The effects of prebiotics on microbial dysbiosis, butyrate production and immunity in HIV-infected subjects. *Mucosal Immunol* (2017) 10:1279–93. doi: 10.1371/journal.ppat.1010160

237. Gori A, Rizzardini G, Van't Land B, Amor KB, van Schaik J, Torti C, et al. Specific prebiotics modulate gut microbiota and immune activation in HAART-naive HIV-infected adults: Results of the "COPA" pilot randomized trial. *Mucosal Immunol* (2011) 4:554–63. doi: 10.1038/mi.2016.122

238. Isnard S, Fombuena B, Ouyang J, Royston L, Lin J, Bu S, et al. Camu camu effects on microbial translocation and systemic immune activation in ART-treated people living with HIV: Protocol of the single-arm non-randomised camu camu prebiotic pilot study (CIHR/CTN PT032). *BMJ Open* (2022) 12:e053081. doi: 10.1038/mi.2011.15

239. Messaoudene M, Pidgeon R, Richard C, Ponce M, Diop K, Benlaifaoui M, et al. And circumvents anti-PD-1 resistance through effects on the gut microbiota. *Cancer Discov* (2022) 12:1070–87. doi: 10.1136/bmjopen-2021-053081

240. Rousseau RK, Walmsley SL, Lee T, Rosenes R, Reinhard RJ, Malazogu F, et al. Randomized, blinded, placebo-controlled trial of de Simone formulation probiotic during HIV-associated suboptimal CD4+ T cell recovery. *J Acquir Immune Defic Syndr* (2022) 89:199–207. doi: 10.1158/2159-8290.CD-21-0808

241. Yang OO, Kelesidis T, Cordova R, Khanlou H. Immunomodulation of antiretroviral drug-suppressed chronic HIV-1 infection in an oral probiotic double-blind placebo-controlled trial. *AIDS Res Hum Retroviruses* (2014) 30:988–95. doi: 10.1097/QAI.0000000000002840

242. Tenore SB, Avelino-Silva VI, Costa PR, Franco LM, Sabino EC, Kalil J, et al. Immune effects of lactobacillus casei shirota in treated HIV-infected patients with poor CD4+ T-cell recovery. *AIDS* (2020) 34:381–9. doi: 10.1089/aid.2014.0181

243. Stiksrud B, Nowak P, Nwosu FC, Kvale D, Thalme A, Sonnerborg A, et al. Reduced levels of d-dimer and changes in gut microbiota composition after probiotic intervention in HIV-infected individuals on stable ART. *J Acquir Immune Defic Syndr* (2015) 70:329–37. doi: 10.1097/QAD.0000000000002420

244. Christensen AD, Skov S, Haase C. The role of neutrophils and G-CSF in DNFB-induced contact hypersensitivity in mice. *Immun Inflammation Dis* (2014) 2:21–34. doi: 10.1097/QAI.0000000000000784

245. Schunter M, Chu H, Hayes TL, McConnell D, Crawford SS, Luciw PA, et al. Randomized pilot trial of a synbiotic dietary supplement in chronic HIV-1 infection. *BMC Complement Altern Med* (2012) 12:84. doi: 10.1002/iid3.16

246. Gonzalez-Hernandez LA, Jave-Suarez LF, Fafutis-Morris M, Montes-Salcedo KE, Valle-Gutierrez LG, Campos-Loza AE, et al. Synbiotic therapy decreases microbial translocation and inflammation and improves immunological status in HIV-infected patients: a double-blind randomized controlled pilot trial. *Nutr J* (2012) 11:90. doi: 10.1186/1472-6882-12-84

247. Klatt NR, Canary LA, Sun X, Vinton CL, Funderburg NT, Morcock DR, et al. Probiotic/prebiotic supplementation of antiretrovirals improves gastrointestinal immunity in SIV-infected macaques. *J Clin Invest* (2013) 123:903–7. doi: 10.1186/1475-2891-11-90

248. Topping DL, Clifton PM. Short-chain fatty acids and human colonic function: roles of resistant starch and nonstarch polysaccharides. *Physiol Rev* (2001) 81:1031–64. doi: 10.1172/JCI66227

249. Koh A, De Vadder F, Kovatcheva-Datchary P, Backhed F. From dietary fiber to host physiology: Short-chain fatty acids as key bacterial metabolites. *Cell* (2016) 165:1332–45. doi: 10.1152/physrev.2001.81.3.1031

250. Parada Venegas D, de la Fuente MK, Landskron G, Gonzalez MJ, Quera R, Dijkstra G, et al. Short chain fatty acids (SCFAs)-mediated gut epithelial and immune regulation and its relevance for inflammatory bowel diseases. *Front Immunol* (2019) 10:277. doi: 10.1016/j.cell.2016.05.041

251. Brauckmann V, Nambiar S, Potthoff A, Hoxtermann S, Wach J, Kayser A, et al. Influence of dietary supplementation of short-chain fatty acid sodium propionate in people (PLHIV). *J Eur Acad Dermatol Venereol* (2022). doi: 10.3389/fimmu.2019.00277

252. Leonardi I, Gao IH, Lin WY, Allen M, Li XV, Fiers WD, et al. Mucosal fungi promote gut barrier function and social behavior *via* type 17 immunity. *Cell* (2022) 185:831–46.e14. doi: 10.1111/jdv.18006

253. Lam KN, Spanogiannopoulos P, Soto-Perez P, Alexander M, Nalley MJ, Bisanz JE, et al. Phage-delivered CRISPR-Cas9 for strain-specific depletion and genomic deletions in the gut microbiome. *Cell Rep* (2021) 37:109930. doi: 10.1016/j.cell.2022.01.017

254. Kelesidis T, Yang OO, Currier JS, Navab K, Fogelman AM, Navab M. HIV-1 infected patients with suppressed plasma viremia on treatment have pro-inflammatory HDL. *Lipids Health Dis* (2011) 10:35. doi: 10.1016/j.celrep.2021.109930

255. Meriwether D, Sulaiman D, Volpe C, Dorfman A, Grijalva V, Dorreh N, et al. Apolipoprotein a-I mimetics mitigate intestinal inflammation in COX2-dependent inflammatory bowel disease model. *J Clin Invest* (2019) 129:3670–85. doi: 10.1186/1476-511X-10-35

256. Benfield T, Bodilsen J, Brieghel C, Harboe ZB, Helleberg M, Holm C, et al. Improved survival among hospitalized patients with coronavirus disease 2019 (COVID-19) treated with remdesivir and dexamethasone. A nationwide population-based cohort study. *Clin Infect Dis* (2021) 73:2031–6. doi: 10.1172/JCI123700

257. Calabrese LH, Calabrese C. Baricitinib and dexamethasone for hospitalized patients with COVID-19. *Cleve Clin J Med* (2021). doi: 10.1093/cid/ciab536

258. Calzetta L, Aiello M, Frizzelli A, Rogliani P, Chetta A. Dexamethasone in patients hospitalized with COVID-19: Whether, when and to whom. *J Clin Med 10* (2021). doi: 10.3949/ccjm.88a.ccc073

259. Group RC, Horby P, Lim WS, Emberson JR, Mafham M, Bell JL, et al. Dexamethasone in hospitalized patients with covid-19. *N Engl J Med* (2021) 384:693–704. doi: 10.3390/jcm10081607

260. Ranjbar K, Moghadami M, Mirahmadizadeh A, Fallahi MJ, Khaloo V, Shahriarirad R, et al. Methylprednisolone or dexamethasone, which one is superior corticosteroid in the treatment of hospitalized COVID-19 patients: A triple-blinded randomized controlled trial. *BMC Infect Dis* (2021) 21:337. doi: 10.1056/NEJMoa2021436

261. Leffler DA, Kelly CP, Green PH, Fedorak RN, DiMarino A, Perrow W, et al. Larazotide acetate for persistent symptoms of celiac disease despite a gluten-free diet: a randomized controlled trial. *Gastroenterology* (2015) 148:1311–9.e6. doi: 10.1186/s12879-021-06045-3

262. Ungaro RC, Brenner EJ, Agrawal M, Zhang X, Kappelman MD, Colombel JF. Surveillance epidemiology of coronavirus under research exclusion for inflammatory bowel disease research, impact of medications on COVID-19 outcomes in inflammatory bowel disease: Analysis of more than 6000 patients from an international registry. *Gastroenterology* (2022) 162:316–19.e5. doi: 10.1053/j.gastro.2015.02.008

263. Zhou HY, Guo B, Lufumpa E, Li XM, Chen LH, Meng X, et al. Comparative of the effectiveness and safety of biological agents, tofacitinib, and fecal microbiota transplantation in ulcerative colitis: Systematic review and network meta-analysis. *Immunol Invest* (2021) 50:323–37. doi: 10.1053/j.gastro.2021.09.011

264. Bezzio C, Manes G, Bini F, Pellegrini L, Saibeni S. Infliximab for severe ulcerative colitis and subsequent SARS-CoV-2 pneumonia: A stone for two birds. *Gut* (2021) 70:623–4. doi: 10.1080/08820139.2020.1714650

265. Gupta S, Leaf DE. Tocilizumab in COVID-19: some clarity amid controversy. *Lancet* (2021) 397:1599–601. doi: 10.1136/gutjnl-2020-321760

266. Gupta S, Padappayil RP, Bansal A, Daouk S, Brown B. Tocilizumab in patients hospitalized with COVID-19 pneumonia: Systematic review and meta-analysis of randomized controlled trials. *J Investig Med* (2022) 70:55–60. doi: 10.1016/S0140-6736(21)00712-1

267. Nagao A, Nakazawa S, Hanabusa H. Short-term efficacy of the IL6 receptor antibody tocilizumab in patients with HIV-associated multicentric castleman disease: report of two cases. *J Hematol Oncol* (2014) 7:10. doi: 10.1136/jim-2021-002001

268. Minkove SJ, Geiger G, Llibre JM, Montgomery MW, West NE, Chida NM, et al. Clinical outcomes after IL-6 blockade in patients with COVID-19 and HIV: A case series. *AIDS Res Ther* (2022) 19:6. doi: 10.1186/1756-8722-7-10

frontiers | Frontiers in Immunology

TYPE Perspective
PUBLISHED 30 August 2022
DOI 10.3389/fimmu.2022.904342

OPEN ACCESS

EDITED BY
Eric Hunter,
Emory University, United States

REVIEWED BY
Juan C. De La Torre,
The Scripps Research Institute,
United States

*CORRESPONDENCE
Gennady Bocharov
gbocharov@gmail.com
Andreas Meyerhans
andreas.meyerhans@upf.edu

SPECIALTY SECTION
This article was submitted to Viral Immunology, a section of the journal Frontiers in Immunology

RECEIVED 25 March 2022
ACCEPTED 12 August 2022
PUBLISHED 30 August 2022

CITATION
Bocharov G, Grebennikov D, Cebollada Rica P, Domenjo-Vila E, Casella V and Meyerhans A (2022) Functional cure of a chronic virus infection by shifting the virus - host equilibrium state.
Front. Immunol. 13:904342.
doi: 10.3389/fimmu.2022.904342

Functional cure of a chronic virus infection by shifting the virus - host equilibrium state

Gennady Bocharov[1,2,3]*, Dmitry Grebennikov[1,2,3], Paula Cebollada Rica[4], Eva Domenjo-Vila[4], Valentina Casella[4] and Andreas Meyerhans[4,5]*

[1]Marchuk Institute of Numerical Mathematics, Russian Academy of Sciences, Moscow, Russia, [2]Moscow Center for Fundamental and Applied Mathematics at INM RAS, Moscow, Russia, [3]Institute for Computer Science and Mathematical Modelling, Sechenov First Moscow State Medical University, Moscow, Russia, [4]Infection Biology Laboratory, Department of Medicine and Life Sciences, Universitat Pompeu Fabra, Barcelona, Spain, [5]Catalan Institution for Research and Advanced Studies (ICREA), Barcelona, Spain

The clinical handling of chronic virus infections remains a challenge. Here we describe recent progress in the understanding of virus - host interaction dynamics. Based on the systems biology concept of multi-stability and the prediction of multiplicative cooperativity between virus-specific cytotoxic T cells and neutralising antibodies, we argue for the requirements to engage multiple immune system components for functional cure strategies. Our arguments are derived from LCMV model system studies and are translated to HIV-1 infection.

KEYWORDS

Chronic virus infections, multi-stability, shifting equilibrium states, cure strategies, LCMV (lymphocytic choriomeningitis virus), HIV (human immunodeficiency virus)

Introduction

Chronic virus infections like those with Human Immunodeficiency Viruses (HIV) and Hepatitis B (HBV) and C (HCV) viruses continue to threaten global health. A common feature of these infections is the persistence of virus antigen and the associated exhaustion of virus-specific T lymphocytes (1–5). Although the latter reduces immune-cell-mediated pathology, it is associated with a reduction of virus control that enables antigen persistence and has per se pathological consequences. For example, untreated HIV infection mediates CD4 T cell depletion, chronic immune activation, lymphoid tissue destruction and dysregulation of immune homeostasis (6, 7). Chronic hepatitis virus infections deteriorate liver functions and can lead to liver cirrhosis and hepatocellular carcinoma (8–10). Globally these 3

infections are carried by close to 400 million individuals and thus are a significant burden for public health care systems (11).

The existing approaches to treat chronic infections may be subdivided into 2 fundamentally different categories, (i) targeting of virus replication by antiviral drugs including interferons or therapeutic target cell modifications, and (ii) targeting virus-specific immune responses to improve host control by restoration of immune functions i.e. through therapeutic vaccination or immune checkpoint inhibitors that reinvigorate exhausted lymphocytes. While most of these options are still experimental, antiviral drugs are by far the most common therapeutic modality in use and very successful. For example, the current virus-specific anti-HCV drugs are highly potent and enable virus clearance in around 95% of infected individuals (12). Current antivirals against HIV can reduce virus loads to below detectable levels however fail to eliminate the latently infected cells (13, 14). As a consequence, treatment interruptions lead to rapid viral rebounds from viral reservoirs and the continuation of a high viral load infection state (15). To overcome the need for life-long antiviral HIV therapy with its side effects and the inherent financial burden for health care systems, numerous concepts for curing chronic infections have been developed and experimentally tested. These include "shock-and-kill" strategies that aim to purge the latent virus reservoir by latency reversal agents with subsequent killing of infected cells (16, 17), "block-and-lock" strategies that aim to permanently silence all HIV proviruses (18) and the potential "rinse-and-replace" strategy that predicts a "washing-out" of infected cells by uninfected naive and memory T cells *via* sequential waves of polyclonal T cell stimulation under combination antiretroviral therapy (19). While still being far from clinical practice, the combined delivery of broadly neutralising antibodies or CD8 T cell-inducing therapeutic vaccines with latency-reversal-agents (LRAs) including TLR7 agonists showed encouraging first results in experimental SIV/SHIV infections of rhesus monkeys (20, 21) and in humans (22).

Cure strategies for chronic virus infections can be divided into sterilising and functional cure strategies. While the former attempts to completely eliminate the virus from the host e.g. by HIV-resistant hematopoietic stem cell transplantation (23, 24) or provirus deletion approaches (25–27), the latter solely aims to shift the dynamic virus - host immune system balance into a state in which the virus is sufficiently controlled without causing pathology (Figure 1A). Given that HIV elimination was only successful in possibly 4 cases worldwide with a procedure that has a high mortality rate (30), functional cure approaches appear more feasible. However, is there any evidence that a shift from a high-virus-load to a low-virus-load equilibrium is possible? And what would the requirements be for such a shift? Here, we discuss the evidence that indeed such a shift should be possible and define the conditions under which it may occur.

LCMV model system-based analyses

Many features of virus - immune system interactions within the lymphocytic choriomeningitis virus (LCMV) mice model system resemble those of human chronic HIV and hepatitis virus infections (31, 32). In the early stages, LCMV infections are mainly controlled by CTLs. Infection with a low dose of e.g. LCMV-Docile or a high dose of LCMV-Arm leads to the clearance of virus below the detection level and formation of immune memory (33). In contrast, infection with high doses of LCMV-Docile or LCMV-Cl13 results in chronic viral persistence at high levels and exhaustion of antigen-specific cytotoxic CD8 T cells (CTLs) (1, 34). Nonetheless, they differ in their long-term kinetics of infections i.e. clearance of LCMV Clone 13 by late neutralizing antibodies versus persistence of LCMV Docile (1).

To explore the necessary conditions for the co-existence of virus-host equilibria that differ in viral loads as well as the possibilities for transferring a high-viral load state to a more favourable equilibrium, one can utilise the analytical power of existing mathematical models that have been calibrated using experimental data. Our previously developed mathematical model of LCMV infection considers the population dynamics of viruses, precursor and effector CTLs (35), and utilises LCMV data assimilation procedures and bifurcation analysis (36). The results suggested that the reduction in the net viral growth rate β is a necessary condition for a stable low level LCMV infection state within an immunocompetent host (Figure 1B). Specifically, the existence of replication competent LCMV below the detection limit of about 100 FFU per spleen in immune mice requires a more than 2-times reduction of the exponential virus growth rate of the acute infection phase. Given that LCMV-specific neutralising antibodies (nAbs) can block free virus particles and thus reduce the net virus growth rate, it was hypothesised that such antibodies could be decisive for virus control. And indeed, subsequent experimental work by Greczmiel *et al.* demonstrated that it is the late appearance of nAbs that finally controls a chronic LCMV infection to below detectable levels (37) (Figure 1C).

A conceptual dynamic view of the above observations is summarized in Figure 2A which considers the outcome of virus-host interactions as a 'numbers game' between the rate of infection growth and the activation of the immune system (38). If the virus outcompetes the CTL response, a high virus load state is established that is characterised by T cell exhaustion and maintained through the interaction of inhibitory receptors on T cells with their ligands on antigen-presenting cells (APCs) (5). However, this harmful equilibrium can be shifted in favour of the host by inducing a virus-specific neutralising antibody response or by providing antibodies as a therapeutic intervention (37, 39). Since the cooperativity of remaining CTLs and the newly induced antibody response can be considered as multiplicative rather than just additive, the demand for both specific immune response components is less stringent in absolute numbers (40).

10.3389/fimmu.2022.904342

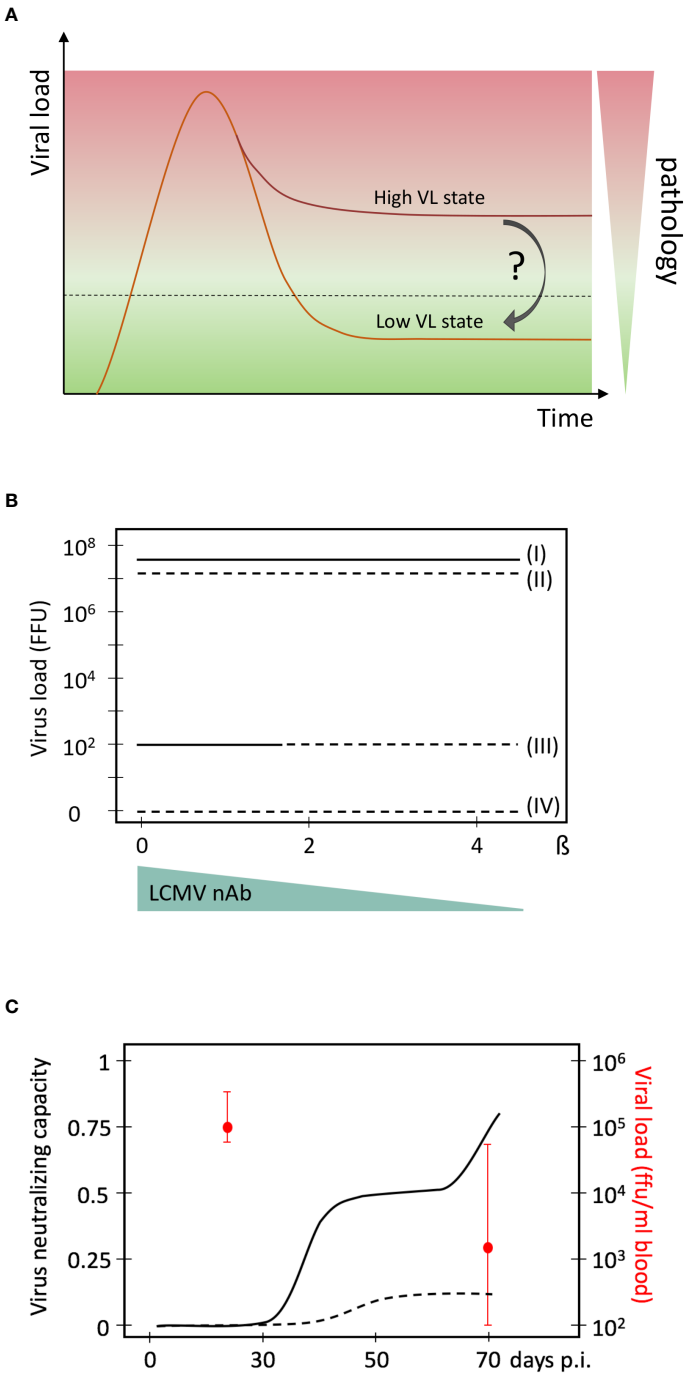

FIGURE 1
High and low virus load (VL) equilibrium states in persistent chronic virus infections. **(A)** Schematic presentation of a high and low virus load state, and the associated pathology. **(B)** Mathematical model predictions of multiple virus equilibrium states (I to IV) in LCMV infections of mice as a function of the net virus growth rate β. Data are from (28). The four virus equilibrium states differ in their values of the virus load from the highest (state I) to the lowest (state IV). Stability of an equilibrium state or steady state means that the system returns back after some perturbation. Only stable equilibrium states are biologically observable. State I is always stable while state III is stable for a certain range of β (solid lines). States II and IV are unstable (broken lines) and cannot be observed biologically. A possible reduction of β by neutralising antibodies is indicated below. It represents the natural occurrence of a late, specific neutralizing antibody response during chronic LCMV infection that reduces the net virus growth rate represented by β. **(C)** Evolution of virus neutralising capacity of mouse sera during an experimental LCMV infection of mice. Experimental data are from (29) and converted into this presentation. Medians of viral loads at days 30 and 70 and their interquartile ranges are indicated in red. Solid line, sera from chronic infection; broken line, sera from acute infection.

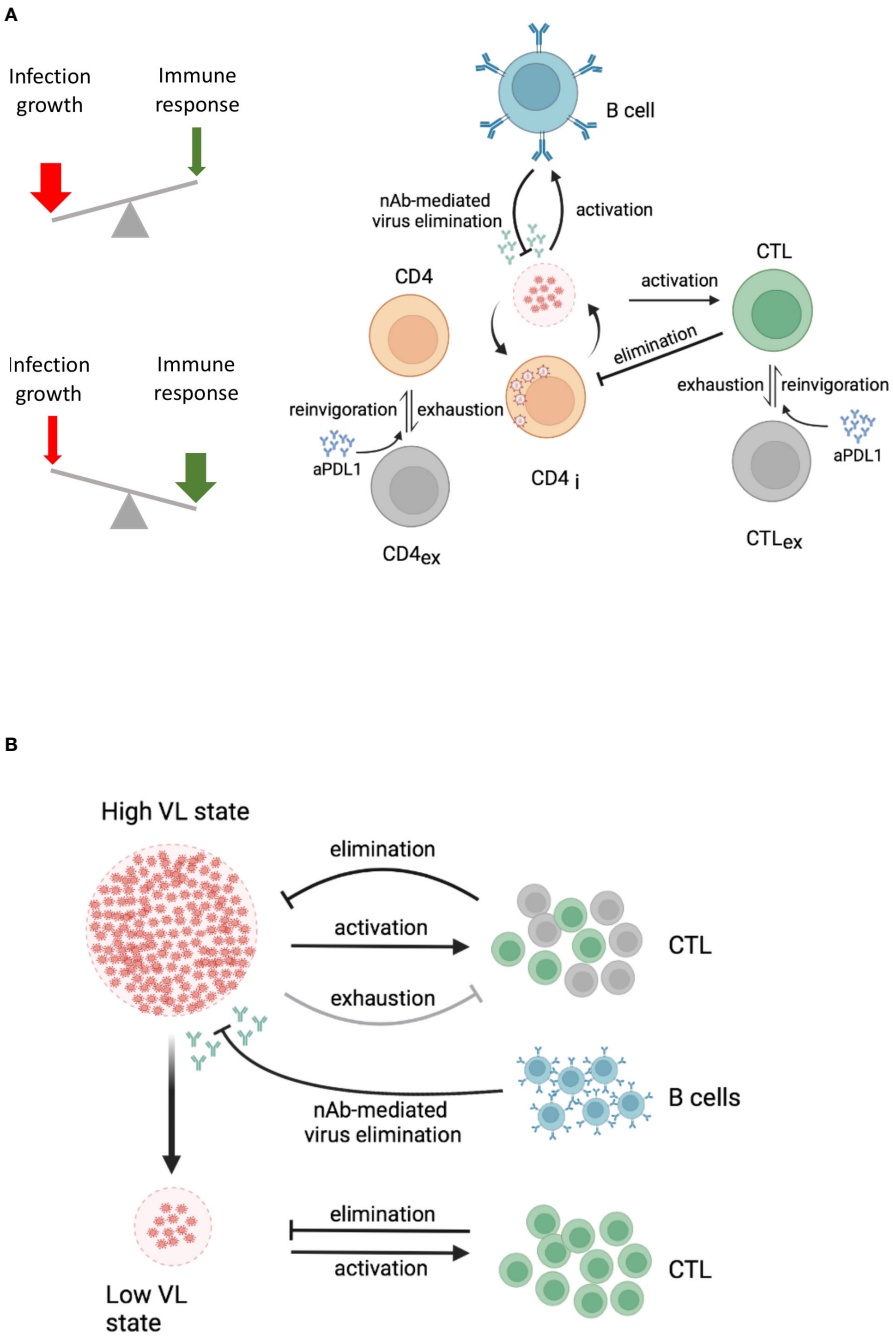

FIGURE 2
Dynamic views of virus-host interactions. Lines with an arrow or T end represent expansion or reduction/suppression of the corresponding virus or cell populations, respectively. The specific processes by which this occurs are specified above the lines. **(A)** Conceptual dynamic view of a high and a low virus load state within an infected host. The underlying processes are indicated. A high VL state drives CTL exhaustion (grey cells) and reduces the population of effector CTL (green cells). B cells (blue cells) produce antibodies that eliminate infectious viruses. Both, effector CTL and antibodies from B cells, depending on their strength, contribute to the control of the virus load. **(B)** Cooperative engagement of individual immune components for functional cure strategies in HIV-1 infection. The combination of immune checkpoint inhibitors with CTL-based immunotherapy and neutralising antibody responses is indicated. aPDL1, anti-PDL1 antibodies; CTL, cytotoxic T cells; CTLex, exhausted CTL; CD4i, infected CD4 T cells; VL, virus load. The figure was created with BioRender.com.

Extrapolation to HIV infections

To translate these results and considerations from the LCMV mouse model system to human infections like HIV infections and functional cure strategies, two fundamental questions arise: Is there evidence for different dynamic steady states in HIV infection? How can one reduce viral growth rate β and restore functional immune control in a therapeutic setting? Answer to the first question is yes. There are several different dynamic states that can be defined by viral loads and disease progression rates (41). These are related to the virus set point, the dynamic equilibrium state at which the virus settles after the primary infection phase (42–44). For example, from the infected individuals in which the virus load settles to above 36,000 virions/ml blood, more than 62% will develop AIDS within 5 years. In contrast, only 8% of individuals with a virus set point below 4,500 virions/ml blood will develop AIDS in this time frame. Thus, at least in HIV-1 infection, virus loads are directly linked to pathology and the low virus load stage, as observed in so-called "elite controllers" (EC) (45, 46), may be regarded as a non-pathogenic virus infection state that should be the target for functional cure strategies (Figure 1A). Indeed, elite controllers are exceptional HIV-infected individuals that control virus replication without the requirement of antiretroviral therapy. Based on studies during their chronic steady state, many potential immunological and virological factors have been linked to this. It includes virus-specific CTLs and CD4 T cells, innate immune responses like NK cells and plasmacytoid dendritic cells as well as virus attenuation and provirus integration into repressed chromatin sites (47–49). Since the EC state is associated with certain HLA types, and the antiviral functionality of CTLs from EC against HIV-infected autologous CD4 T cells is superior to those of HIV non-controllers (50), HIV-specific CTL seem to be a prime component in achieving virus control. The role of virus-specific neutralizing antibody responses in EC is less clear as high titres of these are often lacking in respective individuals (47).

The answer to the second question is much more demanding because one needs to consider the state of the whole immune system and virus population at the time the functional cure strategy is to be initiated. In the chronic infection state in which T cells are exhausted (5) and the virus is a complex quasispecies population (51, 52) and partially hiding within latently infected cells (53, 54), the simple reduction of the virus growth rate by antiviral drugs is not sufficient to self-maintain a stable low virus load state. Likewise, it is not sufficient to invigorate exhausted T and B cells by checkpoint inhibitors in the presence of antiviral drugs because only a fraction of HIV disease phenotypes would benefit. This was demonstrated in our modelling study of anti-PD-L1 blockage in HIV-1 infection (55). In this we showed that a favourable effect in terms of viral load reduction and restoration of functional T cells strongly depends on the antibody-mediated elimination rate of infectious virus in a threshold dependent manner. Furthermore, taking into account spatial aspects of HIV-1 infection spreading within lymphatic tissue and CTL motility, we estimated that the minimum frequency of HIV-specific effector CTLs should be above 5% to ensure localisation and elimination of an infected cell within a virus life cycle time (56). Recent vaccine studies against simian–human immunodeficiency virus (SHIV) infection in macaques demonstrated that the threshold requirements for virus infection control were much lower when neutralizing antibodies and CTLs were induced (57) suggesting multiplicative cooperation between both arms of the adaptive immune system (40). Taken together and considering the multiplicative cooperativity between cellular and humoral responses, it would appear that only a multi-modal empowerment of antiviral immunity could enable a permanent shift from a high virus load to a low virus load state in HIV-1 infection. This would require invigoration of exhausted T cells by checkpoint inhibitors in the presence of antiviral drugs (58) and induction of novel CTLs together with neutralising antibodies that cover a broad spectrum of viral epitopes (Figure 2B).

Discussion

Here we summarise the evidence for multiple stable virus load states in persistent chronic virus infections and provide a perspective for a functional cure.

Multi-stability is a relevant property of complex biological systems with normal feedback regulation (59) to which virus infections belong to. It provides the possibility of switching between different virus load states. Computational models are helpful in this context as they can identify the required parameter values for the multiple steady states (28). For example, a 2-times reduction of the net virus growth rate β is the necessary condition for the existence of the low virus load state in persistent LCMV infection (Figure 1B). Once this condition is identified, the challenge becomes to define the required manipulations for shifting the whole system to that favourable state. Again, computational approaches can provide useful insight. Amongst them is the recently developed optimal disturbance approach which can predict multi-modal impacts (combination therapies) with maximal effects on the immune system (60). When applied to LCMV infection, the results demonstrated that a systems shift is possible and requires a combination of different initial state perturbations like virus load and functional T cell state. While this will translate to a combination therapy e.g. of checkpoint inhibitors and neutralising antibodies, the respective quantities and time lines are not yet determined and await experimental elaboration. Nonetheless, these mathematically-driven experimental LCMV system-based studies provide a proof-of-concept for a possible system shift to a favourable virus-host interaction dynamics. Respective analyses of multi-stability and optimal disturbances for HIV-1 or other persistent chronic infections in humans are still lacking and clearly represent a challenge and direction for

further interdisciplinary research. The recent progress of immunotherapies to induce and boost antiviral immunity are encouraging but also highlight the need to cooperatively engage individual immune system components that may eventually allow moving from a drug-based virus containment to a long-term immune system-based functional cure.

In summary, the currently explored strategies for functionally curing an HIV infection are "shock-and-kill", "block-and-lock" and "rinse-and-replace". None of them considers and explores the concept of multiplicative cooperativity between individual immune system components that is proposed here. A proof of concept in a clinical setting is eagerly waited for.

Data availability statement

The original contributions presented in the study are included in the article/supplementary material. Further inquiries can be directed to the corresponding authors.

Author contributions

All authors listed have made a substantial, direct and intellectual contribution to the work, and approved it for publication. All authors contributed to the article and approved the submitted version.

Funding

The authors are supported by the Russian Science Foundation (RSF grant no. 18-11-00171), the Russian Foundation of Basic Research (RFBR grant no. 20-01-00352), "la Caixa" Foundation under the project code HR17-00199, the Spanish Ministry of Science and Innovation grant no. PID2019-106323RB-I00 AEI//10.13039/501100011033, and "Unidad de Excelencia María de Maeztu", funded by the MCIN and the AEI (DOI: 10.13039/501100011033) Ref: CEX2018-000792-M.

Conflict of interest

The authors declare that the research was conducted in the absence of any commercial or financial relationships that could be construed as a potential conflict of interest.

Publisher's note

All claims expressed in this article are solely those of the authors and do not necessarily represent those of their affiliated organizations, or those of the publisher, the editors and the reviewers. Any product that may be evaluated in this article, or claim that may be made by its manufacturer, is not guaranteed or endorsed by the publisher.

References

1. Moskophidis D, Lechner F, Pircher H, Zinkernagel RM. Virus persistence in acutely infected immunocompetent mice by exhaustion of antiviral cytotoxic effector T cells. *Nature* (1993) 362:758–61. doi: 10.1038/362758a0

2. Day CL, Kaufmann DE, Kiepiela P, Brown JA, Moodley ES, Reddy S, et al. PD-1 expression on HIV-specific T cells is associated with T-cell exhaustion and disease progression. *Nature* (2006) 443:350–4. doi: 10.1038/nature05115

3. Boni C, Fisicaro P, Valdatta C, Amadei B, Vincenzo PD, Giuberti T, et al. Characterization of hepatitis B virus (HBV)-specific T-cell dysfunction in chronic HBV infection. *J Virol* (2007) 81:4215–25. doi: 10.1128/jvi.02844-06

4. Bengsch B, Seigel B, Ruhl M, Timm J, Kuntz M, Blum HE, et al. Coexpression of PD-1, 2B4, CD160 and KLRG1 on exhausted HCV-specific CD8+ T cells is linked to antigen recognition and T cell differentiation. *PLoS Pathog* (2010) 6: e1000947. doi: 10.1371/journal.ppat.1000947

5. Wherry EJ, Kurachi M. Molecular and cellular insights into T cell exhaustion. *Nat Rev Immunol* (2015) 15:486–99. doi: 10.1038/nri3862

6. Stevenson M. HIV-1 pathogenesis. *Nat Med* (2003) 9:853–60. doi: 10.1038/nm0703-853

7. Lackner AA, Lederman MM, Rodriguez B. HIV Pathogenesis: The host. *Csh Perspect Med* (2012) 2:a007005. doi: 10.1101/cshperspect.a007005

8. Liang TJ, Rehermann B, Seeff LB, Hoofnagle JH. Pathogenesis, natural history, treatment, and prevention of hepatitis C. *Ann Intern Med* (2000) 132:296. doi: 10.7326/0003-4819-132-4-200002150-00008

9. Chisari FV, Isogawa M, Wieland. SF. Pathogenesis of hepatitis b virus infection. *Pathol Biol* (2010) 58:258–66. doi: 10.1016/j.patbio.2009.11.001

10. Iannacone M, Guidotti LG. Immunobiology and pathogenesis of hepatitis B virus infection. *Nat Rev Immunol* (2022) 22:19–32. doi: 10.1038/s41577-021-00549-4

11. Global progress report on HIV, viral hepatitis and sexually transmitted infections. In: *Accountability for the global health sector strategies 2016–2021: actions for impact*. Geneva: World Health Organization. Available at: https://www.who.int/publications/i/item/9789240027077.

12. Villani R, Monami M, Cosimo FD, Fioravanti G, Mannucci E, Vendemiale G, et al. Direct-acting antivirals for HCV treatment in older patients: A systematic review and meta-analysis. *J Viral Hepat* (2019) 26:1249–56. doi: 10.1111/jvh.13169

13. Cohn LB, Chomont N, Deeks SG. The biology of the HIV-1 latent reservoir and implications for cure strategies. *Cell Host Microbe* (2020) 27:519–30. doi: 10.1016/j.chom.2020.03.014

14. Saag MS, Gandhi RT, Hoy JF, Landovitz RJ, Thompson MA, Sax PE, et al. Antiretroviral drugs for treatment and prevention of HIV infection in adults. *JAMA* (2020) 324:1651–69. doi: 10.1001/jama.2020.17025

15. Wen Y, Bar KJ, Li JZ. Lessons learned from HIV antiretroviral treatment interruption trials. *Curr Opin HIV AIDS* (2018) 13:416–21. doi: 10.1097/coh.0000000000000484

16. Deeks SG. Shock and kill. *Nature* (2012) 487:439–40. doi: 10.1038/487439a

17. Siliciano JD, Siliciano RF. *In vivo* dynamics of the latent reservoir for HIV-1: New insights and implications for cure. *Annu Rev Pathol Mech Dis* (2021) 17:1–24. doi: 10.1146/annurev-pathol-050520-112001

18. Vansant G, Bruggemans A, Janssens J, Debyser Z. Block-And-Lock strategies to cure HIV infection. *Viruses* (2020) 12:84. doi: 10.3390/v12010084

19. Grossman Z, Singh NJ, Simonetti FR, Lederman MM, Douek DC, Deeks SG, et al. 'Rinse and replace': Boosting T cell turnover to reduce HIV-1 reservoirs. *Trends Immunol* (2020) 41:466–80. doi: 10.1016/j.it.2020.04.003

20. Borducchi EN, Cabral C, Stephenson KE, Liu J, Abbink P, Ng'ang'a D, et al. Ad26/MVA therapeutic vaccination with TLR7 stimulation in SIV-infected rhesus monkeys. *Nature* (2016) 540:284–7. doi: 10.1038/nature20583

21. Borducchi EN, Liu J, Nkolola JP, Cadena AM, Yu W-H, Fischinger S, et al. Antibody and TLR7 agonist delay viral rebound in SHIV-infected monkeys. *Nature* (2018) 563:360–4. doi: 10.1038/s41586-018-0600-6

22. Mothe B, Rosás-Umbert M, Coll P, Manzardo C, Puertas MC, Morón-López S, et al. HIVconsv vaccines and romidepsin in early-treated HIV-1-Infected individuals: Safety, immunogenicity and effect on the viral reservoir (Study BCN02). *Front Immunol* (2020) 11:823. doi: 10.3389/fimmu.2020.00823

23. Hütter G, Nowak D, Mossner M, Ganepola S, Müßig A, Allers K, et al. Long-term control of HIV by CCR5 Delta32/Delta32 stem-cell transplantation. *New Engl J Med* (2009) 360:692–8. doi: 10.1056/nejmoa0802905

24. Gupta RK, Abdul-Jawad S, McCoy LE, Mok HP, Peppa D, Salgado M, et al. HIV-1 remission following CCR5Δ32/Δ32 haematopoietic stem-cell transplantation. *Nature* (2019) 568:244–8. doi: 10.1038/s41586-019-1027-4

25. Mancuso P, Chen C, Kaminski R, Gordon J, Liao S, Robinson JA, et al. CRISPR based editing of SIV proviral DNA in ART treated non-human primates. *Nat Commun* (2020) 11:6065. doi: 10.1038/s41467-020-19821-7

26. *Excision BioTherapeutics (U.S.). (2022, January -). study of EBT-101 in aviremic HIV-1 infected adults on stable ART*. Available at: https://clinicaltrials.gov/ct2/show/NCT05144386.

27. Sarkar I, Hauber I, Hauber J, Buchholz F. HIV-1 proviral DNA excision using an evolved recombinase. *Science* (2007) 316:1912–5. doi: 10.1126/science.1141453

28. Nechepurenko Y, Khristichenko M, Grebennikov D, Bocharov G. Bistability analysis of virus infection models with time delays. *Discret Contin Dyn Syst - S* (2020) 13:2385–401. doi: 10.3934/dcdss.2020166

29. Kräutler NJ, Yermanos A, Pedrioli A, Welten SPM, Lorgé D, Greczmiel U, et al. Quantitative and qualitative analysis of humoral immunity reveals continued and personalized evolution in chronic viral infection. *Cell Rep* (2020) 30:997–1012.e6. doi: 10.1016/j.celrep.2019.12.088

30. Styczyński J, Tridello G, Koster L, Iacobelli S, van BiezenA, van der Werf S, et al. Death after hematopoietic stem cell transplantation: changes over calendar year time, infections and associated factors. *Bone Marrow Transpl* (2020) 55:126–36. doi: 10.1038/s41409-019-0624-z

31. Klenerman P, Zinkernagel RM. What can we learn about human immunodeficiency virus infection from a study of lymphocytic choriomeningitis virus? *Immunol Rev* (1997) 159:5–16. doi: 10.1111/j.1600-065x.1997.tb01003.x

32. Abdel-Hakeem MS. Viruses teaching immunology: Role of LCMV model and human viral infections in immunological discoveries. *Viruses* (2019) 11:106. doi: 10.3390/v11020106

33. Ciurea A, Klenerman P, Hunziker L, Horvath E, Odermatt B, Ochsenbein AF, et al. Persistence of lymphocytic choriomeningitis virus at very low levels in immune mice. *Proc Natl Acad Sci* (1999) 96:11964–9. doi: 10.1073/pnas.96.21.11964

34. Zajac AJ, Blattman JN, Murali-Krishna K, Sourdive DJD, Suresh M, Altman JD, et al. Viral immune evasion due to persistence of activated T cells without effector function. *J Exp Med* (1998) 188:2205–13. doi: 10.1084/jem.188.12.2205

35. Bocharov GA. Modelling the dynamics of LCMV infection in mice: Conventional and exhaustive CTL responses. *J Theor Biol* (1998) 192:283–308. doi: 10.1006/jtbi.1997.0612

36. Luzyanina T, Engelborghs K, Ehl S, Klenerman P, Bocharov G. Low level viral persistence after infection with LCMV: A quantitative insight through numerical bifurcation analysis. *Math Biosci* (2001) 173:1–23. doi: 10.1016/s0025-5564(01)00072-4

37. Greczmiel U, Kräutler NJ, Pedrioli A, Bartsch I, Agnellini P, Bedenikovic G, et al. Sustained T follicular helper cell response is essential for control of chronic viral infection. *Sci Immunol* (2017) 2(18):eaam8686. doi: 10.1126/sciimmunol.aam8686

38. Zinkernagel RM, Hengartner H, Stitz L. ON THE ROLE OF VIRUSES IN THE EVOLUTION OF IMMUNE RESPONSES. *Brit Med Bull* (1985) 41:92–7. doi: 10.1093/oxfordjournals.bmb.a072033

39. Ertuna YI, Fallet B, Marx A-F, Dimitrova M, Kastner AL, Wagner I, et al. Vectored antibody gene delivery restores host B and T cell control of persistent viral infection. *Cell Rep* (2021) 37:110061. doi: 10.1016/j.celrep.2021.110061

40. Bocharov G, Grebennikov D, Argilaguet J, Meyerhans A. Examining the cooperativity mode of antibody and CD8+ T cell immune responses for vaccinology. *Trends Immunol* (2021) 42(10):852–5. doi: 10.1016/j.it.2021.08.003

41. Gurdasani D, Iles L, Dillon DG, Young EH, Olson AD, Naranbhai V, et al. A systematic review of definitions of extreme phenotypes of HIV control and progression. *Aids* (2014) 28:149–62. doi: 10.1097/qad.0000000000000049

42. Mellors JW, Rinaldo CR Jr, Gupta P, White RM, Todd JA, Kingsley LA. Prognosis in HIV-1 infection predicted by the quantity of virus in plasma. *Science* (1996) 272:1167–70. doi: 10.1126/science.272.5265.1167

43. Ho DD. Viral counts count in HIV infection. *Science* (1996) 272:1124–5. doi: 10.1126/science.272.5265.1124

44. Robb ML, Eller LA, Kibuuka H, Rono K, Maganga L, Nitayaphan S, et al. Prospective study of acute HIV-1 infection in adults in East Africa and Thailand. *New Engl J Med* (2016) 374:2120–30. doi: 10.1056/nejmoa1508952

45. Baker B, Block B, Rothchild A, Walker B. Elite control of HIV infection: implications for vaccine design. *Expert Opin Biol Th* (2008) 9:55–69. doi: 10.1517/14712590802571928

46. Moyano A, Ndungu T, Mann JK. Determinants of natural HIV-1 control. *AIDS Rev* (2022) 24(2):51–8. doi: 10.24875/aidsrev.21000048

47. Deeks SG, Walker BD. Human immunodeficiency virus controllers: mechanisms of durable virus control in the absence of antiretroviral therapy. *Immunity* (2007) 27(3):406–16. doi: 10.1016/j.immuni.2007.08.010

48. Navarrete-Muñoz MA, Restrepo C, Benito JM, Rallón N. Elite controllers: A heterogeneous group of HIV-infected patients. *Virulence* (2020) 11(1):889–97. doi: 10.1080/21505594.2020.1788887

49. Jiang C, Lian X, Gao C, Sun X, Einkauf KB, Chevalier JM, et al. Distinct viral reservoirs in individuals with spontaneous control of HIV-1. *Nature* (2020) 585 (7824):261–7. doi: 10.1038/s41586-020-2651-8

50. Domingo E, García-Crespo C, Perales C. Historical perspective on the discovery of the quasispecies concept. *Ann Rev Virol* (2021) 8:51–72. doi: 10.1146/annurev-virology-091919-105900

51. Chun T-W, Fauci AS. Latent reservoirs of HIV: Obstacles to the eradication of virus. *Proc Natl Acad Sci* (1999) 96:10958–61. doi: 10.1073/pnas.96.20.10958

52. Siliciano RF, Greene WC. HIV Latency. *Csh Perspect Med* (2011) 1:a007096. doi: 10.1101/cshperspect.a007096

53. Zheltkova V, Argilaguet J, Peligero C, Bocharov G, Meyerhans A. Prediction of PD-L1 inhibition effects for HIV-infected individuals. *PLoS Comput Biol* (2019) 15:e1007401. doi: 10.1371/journal.pcbi.1007401

54. Grebennikov D, Bouchnita A, Volpert V, Bessonov N, Meyerhans A, Bocharov G. Spatial lymphocyte dynamics in lymph nodes predicts the cytotoxic T cell frequency needed for HIV infection control. *Front Immunol* (2019) 10:1213. doi: 10.3389/fimmu.2019.01213

55. Sáez-Cirión A, Lacabaratz C, Lambotte O, Versmisse P, Urrutia A, Boufassa F, et al. HIV Controllers exhibit potent CD8 T cell capacity to suppress HIV infection ex vivo and peculiar cytotoxic T lymphocyte activation phenotype. *Proc Natl Acad Sci USA* (2007) 104(16):6776–81. doi: 10.1073/pnas.0611244104

56. Meyerhans A, Cheynier R, Albert J, Seth M, Kwok S, Sninsky J, et al. Temporal fluctuations in HIV quasispecies *in vivo* are not reflected by sequential HIV isolations. *Cell* (1989) 58:901–10. doi: 10.1016/0092-8674(89)90942-2

57. Arunachalam PS, Charles TP, Joag V, Bollimpelli VS, Scott MKD, Wimmers F, et al. Pulendran b. T cell-inducing vaccine durably prevents mucosal SHIV infection even with lower neutralizing antibody titers. *Nat Med* (2020) 26(6):932–40. doi: 10.1038/s41591-020-0858-8

58. Peligero C, Argilaguet J, Güerri-Fernandez R, Torres B, Ligero C, Colomer P, et al. PD-L1 blockade differentially impacts regulatory T cells from HIV-infected individuals depending on plasma viremia. *PLoS Pathog* (2015) 11:e1005270. doi: 10.1371/journal.ppat.1005270

59. Angeli D, Ferrell JE, Sontag ED. Detection of multistability, bifurcations, and hysteresis in a large class of biological positive-feedback systems. *Proc Natl Acad Sci* (2004) 101:1822–7. doi: 10.1073/pnas.0308265100

60. Bocharov GA, Nechepurenko Y, Khristichenko M, Grebennikov DS. Optimal disturbances of bistable time-delay systems modeling virus infections. *Dokl Math* (2018) 98:313–6. doi: 10.1134/s1064562418050058

Frontiers in Immunology

Explores novel approaches and diagnoses to treat immune disorders.

The official journal of the International Union of Immunological Societies (IUIS) and the most cited in its field, leading the way for research across basic, translational and clinical immunology.

Discover the latest Research Topics

See more →

Frontiers

Avenue du Tribunal-Fédéral 34
1005 Lausanne, Switzerland
frontiersin.org

Contact us

+41 (0)21 510 17 00
frontiersin.org/about/contact